

JOINT INSTITUTE FOR AERONAUTICS AND ACOUSTICS



National Aeronautics and
Space Administration

Ames Research Center



Stanford University

(NASA-CR-168662) THE AERODYNAMICS OF
CIRCULATION CONTROL (Stanford Univ.) 366 p
HC A16/HF A01 CSCL 01A

N82-20148

Unclas
G3/02 16984

SU- JIAA TR - 41

THE AERODYNAMICS OF CIRCULATION CONTROL AEROFOILS



N.J. Wood

STANFORD UNIVERSITY
Department of Aeronautics and Astronautics
Stanford, California 94305

JULY 1981

JIAA TR - 41

THE AERODYNAMICS
OF
CIRCULATION CONTROL AEROFOILS

N. J. WOOD

JULY 1981

The results from the calculation procedure CIRCON were obtained by the author at the NASA Ames Research Center and may not necessarily reflect the latest version of the program. The work here presented has been partially supported by the National Aeronautics and Space Administration under NASA Grant NCC 2-89 to the Joint Institute for Aeronautics and Acoustics.

SUMMARY

Two dimensional subsonic wind tunnel tests have been conducted on a 20% thickness, chord ratio circulation controlled elliptic aerofoil section equipped with forward and reverse blowing slots. Overall performance measurements were made over a range of trailing edge blowing momentum coefficients from 0 to 0.04; some included the effect of leading edge blowing. The effective incidence was determined experimentally and lift augmentations, $\partial C_L / \partial C_{\mu}$, of 70 were obtained at low blowing rates.

A detailed investigation of the trailing edge wall jet, using split film probes, hot wire probes and total head tubes, provided measurements of mean velocity components, Reynolds normal and shear stresses, and radial static pressure. Corrections for the effects of ambient temperature variation, flow angle and shear flow gradient upon the various probes were examined and some corrections for the low bandwidth of the split film probes proposed.

In some cases, the effects of slot height and slot lip thickness were investigated. The results were mostly taken at a geometric incidence of 0° .

The closure of the two dimensional angular momentum and continuity equations was examined using the measured data, with and without correction, and the difficulty of obtaining a satisfactory solution illustrated.

The experimental results have led to some suggestions regarding the nature of the flow field which should aid the understanding of Coanda effect and the theoretical solution of highly curved wall jet flows.

ACKNOWLEDGEMENT

The author would like to thank all of his friends and colleagues at both the University of Bath, England and Stanford University, California for their help and encouragement to produce this work.

Special mention should be given to:

- the many academic and technical staff of the University of Bath who assisted my efforts. In particular Dr. J.F. Henderson, Mr. J. G. Burt, Mr. T. Keston and Mr. H. Cox.
- Professor I. C. Cheeseman of the University of Southampton and Mr. R. M. Williams of the NSRDC for their help, enthusiasm and encouragement.
- Miss T. Sherrin and Mrs. J. Fossen for completing the dubious task of typing this thesis.

This work was supported by a Research Grant from the Science Research Council and also the National Aeronautics and Space Administration under NASA Grant NCC 2-89 to the Joint Institute for Aeronautics and Acoustics

CONTENTS

page
no

SUMMARY

NOTATION

1. INTRODUCTION	1
1.1 The Coanda Effect	1
1.2 The Applications of Circulation Control	2
1.3 Previous Experimental Work	4
1.3.1 Plane jet experiments	5
1.3.2 Curved jet experiments	6
1.3.3 Circulation control aerofoil experiments	7
1.4 Previous Theoretical Work	9
1.4.1 The Integral method	10
1.4.2 The finite difference method of Dvorak and Kind	10
1.4.3 The discrete vortex method of Smith	12
1.5 The Present Investigation	12
1.6 A Brief Guide to the Contents	14
2. APPARATUS	16
2.1 Aerofoil Design	16
2.1.1 Design considerations	16
2.1.1.1 Aerodynamic	16
2.1.1.2 Mechanical	18
2.1.1.3 Constructional	19
2.1.1.4 Operational	19
2.1.2 Final scheme	21
2.1.3 Slot design	22
2.1.3.1 Two-dimensionality of slot flow	23
2.1.4 Traversing gear	24
2.1.4.1 Mechanical system	25
2.1.5 Position control system	26
2.1.5.1 Typical operation of traversing gear/position control system for a boundary layer traverse	28

	page no
2.2 The 7 ft x 5 ft Wind Tunnel	29
2.2.1 Calibration of the 7 ft x 5 ft working section	30
2.2.2 Investigation of free stream turbulence	30
2.2.3 Proposed testing conditions	31
2.2.3.1 Effect of tip jets	31
2.2.4 Blockage corrections	33
2.3 The Blowing Air Supply	34
2.3.1 Description of system	34
2.3.2 Calibration of orifice plates	35
2.3.3 Blowing supply control and instrumentation	36
2.3.4 Evaluation of the blowing momentum coefficient C_μ	37
3. INSTRUMENTATION	41
3.1 Pressure Data Acquisition System	41
3.1.1 Evaluation of the aerofoil effective incidence	42
3.1.2 Low pressure transducer calibration	44
3.1.3 High pressure transducer calibration	45
3.2 Hot Wire Anemometry	45
3.2.1 Calibration rig	45
3.2.2 General comments on hot wire anemometry	46
3.2.3 Operation of single sensor wire probes	51
3.2.4 Operation of dual sensor wire probes	52
3.2.5 Sources of error in the hot wire anemometry measurements	55
3.2.5.1 The temperature gradient across the wall jet	55
3.2.5.2 Non radial traversing path	56
3.2.5.3 Wall and probe interference effects	56
3.3 Split Film Anemometry	57
3.3.1 Calibration	60
3.3.2 Data reduction	63
3.3.3 Operation	67
3.3.4 Sources of error in the split film anemometry measurements	68
3.3.4.1 Wall effects	68
3.3.4.2 Probe geometry	69
3.3.4.3 Flow curvature	69

	page no
3.3.4.4 Frequency response	69
3.3.4.5 Probe interference	70
3.3.4.6 Shear flow effects	70
3.4 Radial Static Pressure Measurement	70
3.4.1 Sources of error in the radial static pressure measurement	73
3.4.1.1 Effect of turbulence	73
3.4.1.2 Effect of shear flow	74
3.4.1.3 Errors in hot wire anemometry	75
3.4.1.4 Probe geometry	75
3.4.1.5 Air density	75
4. PRESENTATION OF RESULTS	76
4.1 Overall Performance	76
4.1.1 No blowing performance	76
4.1.2 Trailing edge blowing only	76
4.1.3 Leading edge blowing only	77
4.1.4 Leading and trailing edge blowing	78
4.2 Trailing Edge Investigation	78
4.2.1 Upstream boundary layer	78
4.2.2 Wall jet velocity profiles	79
4.2.3 Turbulence results	81
4.2.4 Radial static pressure distributions	83
5. DISCUSSION OF RESULTS	85
5.1 Overall Performance	85
5.1.1 Unblown aerofoil	85
5.1.2 Trailing edge blowing only	87
5.1.3 Leading and trailing edge blowing	89
5.2 Velocity and Turbulence Profiles in the Upstream Boundary Layer	91
5.3 Trailing Edge Wall Jet	92
5.3.1 Radial static pressure measurements	92
5.3.1.1 Physical significance of results	93
5.3.1.2 Comparison of experimental results with the radial momentum equation	95
5.3.1.3 An observation of the anemometer signals	97

	page no
5.3.2 Proposed flow field	97
5.3.2.1 Supporting evidence for the proposed flow field	98
5.4 Discussion of the Experimental Results in the Light of the Proposed Flow Field	100
5.4.1 Overall performance	100
5.4.1.1 Effect of increasing slot height	100
5.4.1.2 Effect of probe interference	100
5.4.2 Velocity profiles	101
5.4.2.1 Effect of slot height variations	101
5.4.2.2 Effect of slot lip thickness	102
5.4.2.3 Variations of the parameters which describe the velocity profiles	102
5.4.2.4 Streamline patterns and their radii of curvature	103
5.4.3 Turbulence results	104
5.4.3.1 The longitudinal turbulence intensity	105
5.4.3.2 The normal turbulence intensity	108
5.4.3.3 The Reynolds shear stress $\overline{u'v'}$	109
5.4.3.4 The radial static pressure distribution	110
5.5 General Conclusions Regarding the Experimental Results	111
6. THE THEORETICAL IMPLICATIONS OF THE PRESENT RESULTS AND THE PROPOSED FLOW FIELD	112
6.1 The Deficiencies of the Existing Method of Dvorak and Kind	112
6.2 Some Comments Upon the Incorporation of a Discrete Vortex Model into an Aerofoil Calculation Scheme	114
6.2.1 Determination of the initial vortex strength	114
6.2.2 Determination of the vortex shedding frequency	117
6.2.3 On the growth and dissipation of the vortex stream	119
6.2.4 Some further consideration	122
6.2.4.1 Effect of longitudinal pressure gradient	122
6.2.4.2 Effect of the presence of shock waves	122
7. CONCLUSIONS	124

	page no
8. SUGGESTIONS FOR FURTHER RESEARCH	127
REFERENCES	128
APPENDIX I. The Scanivalve Control Program	136
APPENDIX II. Hot Wire Anemometry	143
TABLES OF RESULTS	
FIGURES	

LIST OF TABLES

- TABLES 1 - 17 : Detailed trailing edge wall jet measurements for $C_u = 0.0065, 0.0139, 0.0197, 0.0284$.
- TABLE 18 : Comparison of experimental and predicted pressure gradients in the trailing edge wall jet, $C_u = 0.0284$.
- TABLE 19 : Overall conditions for the four blowing cases at which detailed trailing edge wall jet measurements were made.

LIST OF FIGURES

- 1 : Examples of the application of Coanda effect.
- 2 : Performance trends of a circulation controlled aerofoil.
- 3 : A sketch of the X-wing stopped rotor aircraft.
- 4 : Growth of reversed flow regions with increasing advance ratios.
- 5 : Velocity profiles in typical circulation control flow fields.
- 6 : Downstream development of typical wall jet velocity profiles.
- 7 : Block diagram of the calculation method of Kind³².
- 8 : Schematic layout of the calculation method of Dvorak and Kind (CIRCON)³⁸.
- 9 : Calculation procedure of Dvorak and Kind³⁸.
- 10 : The discrete vortex potential flow model of Smith et al³⁹.

- 11 : An example of the jet sheet development from the method of Smith et al³⁹.
- 12 : Comparison of experimental and theoretical results from Smith et al³⁹.
- 13 : The Bath University Wind tunnel.
- 14 : Possible secondary blowing schemes.
- 15 : General arrangement of circulation controlled 20% elliptic aerofoil mounted in 7 ft x 5 ft wind tunnel.
- 16 : Model during final assembly.
- 17 : Static tapping positions on model centreline.
- 18 : Slot geometry model.
- 19 : Slot geometry and sealing.
- 20 : A check on the two-dimensionality of the slot flow including the effect of the tip jets.
- 21 : A check on the two-dimensionality of the slot flow close to the model centreline.
- 22 : Traversing gear assembly.
- 23 : Block diagram of stepper control and position detection system.
- 24 : Position control system: variation of probe output with distance from the surface.

- 25 : A check on the vibration of a hot wire probe during a radial traverse from the surface.
- 26 : The circulation controlled aerofoil located in the 7 ft x 5 ft working section.
- 27 : Tunnel reference pressure difference calibration.
- 28 : Contours of q/q_{CL} in working section before cleaning gauze.
- 29 : Contours of q/q_{CL} in working section after cleaning gauze.
- 30 : Turbulence intensities in high speed working section before cleaning gauze.
- 31 : Reynolds shear stresses in the high speed working section before cleaning gauze.
- 32 : Effect of tip jets upon overall lift coefficient.
- 33 : Schematic diagram of blowing supply.
- 34 : Orifice plate calibration nozzle geometry.
- 35 : Orifice plate calibration.
- 36 : Calibration nozzle rig.
- 37 : Estimation of jet velocity by three methods.
- 38 : Block diagram of aerofoil pressure measuring system.
- 39 : Block diagram of Scanivalve control program.
- 40 : Examples of the effective incidence estimation technique for the unblown aerofoil.

- 41 : Scanivalve transducer calibration.
- 42 : Velocity profiles downstream of calibration nozzle exit as measured by a dual sensor hot wire probe.
- 43 : Longitudinal turbulence intensity downstream of calibration nozzle exit from a dual sensor hot wire probe.
- 44 : Frequency response of hot wire signals.
- 45 : Effect of temperature upon the calibration of a single hot wire probe.
- 46 : Two hot wire calibration techniques.
- 47 : Block diagram of single sensor system.
- 48 : Yaw effects on the response of a single hot wire probe.
- 49 : Co-ordinate system for dual sensor hot wire probes.
- 50 : Measured direction sensitivity coefficient of a hot wire probe.
- 51 : Block diagram of dual sensor system.
- 52 : Block diagram of the dual sensor hot wire probe sampling and analysis programs.
- 53 : Error in probe angular position due to non radial traversing.
- 54 : Detail of a split film probe : TSI type 1287.
- 55 : Split film angular calibration: determination of the angular offset of the plane of the splits to the probe axis.

- 56 : Validity of the chosen function for angular calibration.
- 57 : Angular calibration of a split film probe.
- 58 : Normal calibration of a split film probe.
- 59 : Experimental and derived angular functions of a split film probe.
- 60 : Illustration of the excellent repeatability of the split film probe measurements.
- 61 : Normal static pressure variation across wall jet from Englar²⁸.
- 62 : Radial static pressure measurement technique.
- 63 : Effects on the radial static pressure distribution of offsets for "sheared flow" correction (Young & Maas⁵⁰) and for possible errors in velocity measurement.
- 64 : Effects of total head tube size upon the radial static pressure distribution.
- 65 : Lift curve slope of the unblown ellipse compared with the two-dimensional case⁵¹ and the theory of Dvorak and Kind³⁸.
- 66 : Measured pressure distributions for the unblown aerofoil compared with a simple potential flow prediction method.
- 67 : Measured pressure distributions of the unblown aerofoil compared with the viscous/potential flow method of Dvorak and Kind³⁸.
- 68 : Variations of centreline lift coefficient with geometric incidence. Trailing edge blowing only.

- 69 : Effect of slot height and probe interference upon measured lift coefficient for trailing edge blowing only.
- 70 : Examples of the effective incidence estimation technique for trailing edge blowing only.
- 71 : Experimental pressure distribution with trailing edge blowing only.
- 72 : Deduced effective incidence correction.
- 73 : Lifting performance of the aerofoil as a function of effective incidence for trailing edge blowing only.
- 74 : Examples of the lifting performance of other aerofoils compared with the present study.
- 75 : Aerofoil pressure drag coefficient with and without the jet thrust component.
- 76 : Effect of leading edge blowing alone upon the centreline lift coefficient.
- 77 : Experimental centreline pressure distributions for leading edge blowing only.
- 78 : Effect of simultaneous leading and trailing edge blowing upon lift coefficient.
- 79 : Experimental centreline pressure distributions for simultaneous leading and trailing edge blowing.
- 80 : Variation of lift coefficient with trailing edge blowing for a fixed leading edge blowing rate, $Cu_{LE} = 0.0125$.

- 81 : Boundary layer velocity profiles upstream of slot.
- 82 : Longitudinal turbulence intensity through boundary layer upstream of slot.
- 83 : Velocity profiles in the boundary layer upstream of the slot compared with $y/\delta = (\frac{\bar{U}}{U_m})^{1/7}$
- 84 : Velocity profiles in the trailing edge wall jet for $Cu = 0.0065, \alpha_G = 0^\circ$.
- 85 : Velocity profiles in the trailing edge wall jet as a function of the half velocity point, $y_{m/2}, Cu = 0.0065, \alpha_G = 0^\circ$.
- 86 : Velocity profiles in the trailing edge wall jet for $Cu = 0.0139, \alpha_G = 0$.
- 87 : Velocity profiles in the trailing edge wall jet as a function of the half velocity point, $y_{m/2}, Cu = 0.0139, \alpha_G = 0$.
- 88 : Velocity profiles in the trailing edge wall jet for $Cu = 0.0197, \alpha_G = 0$.
- 89 : Velocity profiles in the trailing edge wall jet as a function of the half velocity point, $y_{m/2}, Cu = 0.0197, \alpha_G = 0$.
- 90 : Velocity profiles in the trailing edge wall jet for $Cu = 0.0284, \alpha_G = 0$.
- 91 : Velocity profiles in the trailing edge wall jet as a function of the half velocity point $y_{m/2}, Cu = 0.0284, \alpha_G = 0$.
- 92 : Local flow angle in the trailing edge wall jet, $Cu = 0.0065$.
- 93 : Local flow angle in the trailing edge wall jet, $Cu = 0.0139$.

- 94 : Local flow angle in the trailing edge wall jet, $C_\mu = 0.0197$.
- 95 : Local flow angle in the trailing edge wall jet, $C_\mu = 0.0284$.
- 96 : Mean normal velocity in trailing edge wall jet for two blowing rates.
- 97 : Comparison of experiment with continuity in prediction of mean normal velocity, \bar{V} , $C_\mu = 0.0284$.
- 98 : Non-dimensional velocity profile comparison with Kind³².
- 99 : Comparison of velocity profiles in the trailing edge wall jet from three different measurement techniques, $C_\mu = 0.0284$.
- 100 : Mean streamline pattern in trailing edge wall jet $C_\mu = 0.0065$.
- 101 : Deduced mean streamline radii of curvature, $C_\mu = 0.0065$.
- 102 : Mean streamline pattern in trailing edge wall jet $C_\mu = 0.0139$.
- 103 : Deduced mean streamline radii of curvature, $C_\mu = 0.0139$.
- 104 : Mean streamline pattern in trailing edge wall jet $C_\mu = 0.0284$.
- 105 : Deduced mean streamline radii of curvature, $C_\mu = 0.0284$.
- 106 : Effect of slot height and lip thickness on the velocity profile 5° from slot.
- 107 : Effect of slot height and lip thickness on the velocity profile 15° from slot.
- 108 : Changes in angle from slot to separation with trailing edge blowing for a variety of aerofoils and evaluation techniques.

- 109 : Locus of half velocity point for varying C_u .
- 110 : Decay of wall jet edge velocity with distance from slot.
- 111 : Decay of wall jet maximum velocity with distance from slot.
- 112 : Variation of wall jet minimum velocity with distance from slot.
- 113 : Longitudinal turbulence intensity in the trailing edge wall jet, $C_u = 0.0065$.
- 114 : Longitudinal turbulence intensity in the trailing edge wall jet, $C_u = 0.0139$.
- 115 : Longitudinal turbulence intensity in the trailing edge wall jet, $C_u = 0.0197$.
- 116 : Longitudinal turbulence intensity in the trailing edge wall jet, $C_u = 0.0284$.
- 117 : Comparison of longitudinal turbulence in the trailing edge wall jet with Kind's³² results.
- 118 : Effect of slot height and lip thickness upon the longitudinal turbulence intensity in the trailing edge wall jet.
- 119 : Loci of the maxima and minima of the mean velocity and the longitudinal turbulence intensity in the trailing edge wall jet, $C_u = 0.0065$.
- 120 : Loci of the maxima and minima of the mean velocity and the longitudinal turbulence intensity in the trailing edge wall jet, $C_u = 0.0284$.
- 121 : Normal turbulence distribution in the trailing edge wall jet, $C_u = 0.0065$.

- 122 : Normal turbulence distributions in the trailing edge wall jet, $C_\mu = 0.0139$.
- 123 : Normal turbulence distribution in the trailing edge wall jet, $C_\mu = 0.0197$.
- 124 : Normal turbulence distribution in the trailing edge wall jet, $C_\mu = 0.0284$.
- 125 : Comparison of longitudinal and normal turbulence quantities in the trailing edge wall jet, $C_\mu = 0.0139$.
- 126 : Comparison of development of longitudinal and normal turbulence maxima in the trailing edge wall jet.
- 127 : Reynolds shear stress distribution in the trailing edge wall jet, $C_\mu = 0.0065$.
- 128 : Reynolds shear stress distribution in the trailing edge wall jet, $C_\mu = 0.0139$.
- 129 : Reynolds shear stress distribution in the trailing edge wall jet, $C_\mu = 0.0197$.
- 130 : Reynolds shear stress distribution in the trailing edge wall jet, $C_\mu = 0.0284$.
- 131 : Correlation coefficient of split film results in the trailing edge wall jet, $C_\mu = 0.0065$.
- 132 : An example of the proposed correction for low anemometer bandwidth of the normal turbulence intensity, $C_\mu = 0.0284$.
- 133 : An example of the proposed correction for low anemometer bandwidth on the Reynolds shear stress, $C_\mu = 0.0284$.

- 134 : Comparison between the shear stress results of the present study and typical values from the calculation method of Dvorak and Kind³⁸.
- 135 : Comparison between the shear stress results of the present study and those from Jones³³ and Wilson and Goldstein²¹.
- 136 : Upstream boundary layer radial static pressure distribution, $\alpha_G = 0$.
- 137 : Actual measurements used to derive figure 136.
- 138 : Trailing edge static pressure distribution indicating separation point.
- 139 : Radial static pressure distribution in the trailing edge wall jet, $C = 0.0065$.
- 140 : Radial static pressure distribution in the trailing edge wall jet, $C = 0.0139$.
- 141 : Radial static pressure distribution in the trailing edge wall jet, $C = 0.0197$.
- 142 : Radial static pressure distribution in the trailing edge wall jet, $C = 0.0284$.
- 143 : Static pressure variation normal to a slotted flap surface from reference 49.
- 144 : Effect of split film probe position on the measured centreline lift coefficient.
- 145 : A comparison between the present results and the theoretical normal stress calculation of Kind⁵³.

- 146 : Comparison between measured static pressure gradients and those obtained from the radial momentum equation, $C_\mu = 0.0284$.
- 147 : Sketch of observed hot wire output signals.
- 148 : Proposed Coanda flow field.
- 149 : Spatial correlation of the experimental results with the proposed vortex stream $C_\mu = 0.0284$, $\alpha_G = 0^\circ, 55^\circ$ from slot.
- 150 : Decay of the velocity difference across the free shear layer with angle from the slot.
- 151 : Interpretation of the measured turbulence quantities with respect to the proposed vortex stream.
- 152 : Wall shear stress under a highly curved wall jet measured by a surface mounted hot film sensor, from Englar²⁸.
- 153 : A sample of the variation of longitudinal pressure gradient in the trailing edge wall jet from the calculation program CIRCON³⁸.
- 154 : The roll-up of a uniform vortex sheet to produce the 'cats-eye' shape.
- 155 : Simplified vortex array to determine the true vortex strength from a time averaged velocity profile.
- 156 : An example of the variation of instantaneous to time averaged velocity at the edge of the proposed vortex stream as a function of vortex strength, speed and geometry.
- 157 : Variation of the proposed vortex streaming speed with angle from the slot.
- 158 : The proposed vortex shedding frequency as a function of the velocity difference at the slot for a variety of typical length scales.
- 159 : A comparison of half velocity point growth rates for various wall jet configurations.

NOTATION

a	speed of sound hot wire direction sensitivity coefficient in plane of prongs
A	area hot sensor calibration constant
b	hot wire direction sensitivity coefficient normal to wire
B	hot sensor calibration constant ratio of normal:longitudinal turbulence for film measurements
c	aerofoil chord
C	split film angular calibration constant
C_1	constant, equation (1.4)
C_D	drag coefficient
C_{Dp}	drag coefficient due to surface static pressure
C_L	lift coefficient
C_N	normal force coefficient
C_p	pressure coefficient
C_T	thrust coefficient
$C_u, C_{u_{TE}}$	trailing edge blowing momentum coefficient
$C_{u_{LE}}$	leading edge blowing momentum coefficient

C_p	normal stress coefficient, $\frac{p + \overline{\rho v'^2}}{\frac{1}{2}\rho U_\infty^2}$
d	internal bore of tube distance between vortex centres typical length in Strouhal number
D	outside diameter of tube
e	fluctuating component of bridge voltage, angular error of hot wire probe position
E_B	anemometer bridge voltage
E_o	hot sensor zero flow voltage
f	vortex frequency
G	constant, equation (5.6)
h	slot height
Δh	pressure difference across orifice plates
J_{ex}	excess momentum flux in the wall jet
K	correction for non perfect matching of split film sensors vortex strength
m	split film angular calibration index
\dot{m}	mass flowrate
M_j	jet Mach number
n	hot sensor normal calibration, index, vortex number

P	static pressure
P	total pressure
q	dynamic pressure
	effective cooling velocity of a hot wire
r	hot sensor resistance
	vortex radius
R	radius of curvature
	gas constant
R_e	Reynolds number
R_o	surface radius of curvature
S	surface distance from slot exit
S_T	Strouhal number
t	maximum aerofoil thickness
T	temperature
u', v', w'	fluctuating components of velocities
\tilde{u}	periodic velocity function
U, V, W	instantaneous velocities
$\bar{U}, \bar{V}, \bar{W}$	time averaged velocities
U_T	empty working section centreline velocity, translational velocity of vortex centres

U_∞, V_∞ free stream velocity in x direction
 V_j jet exit velocity
 ω vorticity
 x, y, z cartesian co-ordinates
 Z offset from pitot tube centreline due to shear flow

Greek symbols

α incidence
 hot sensor ambient temperature correction
 wire resistance temperature coefficient
 α_{eff} effective incidence
 α_G geometric incidence
 γ gas constant
 angular position of the rear stagnation line on an ellipse
 in potential flow
 Γ vortex strength
 δ boundary layer thickness
 θ angular position from slot
 ellipse co-ordinate angle
 λ vortex stream wavelength
 μ advance ratio
 angle of exit of blowing jet to horizontal

ν_t	eddy viscosity
ρ	air density
σ	helicopter rotor solidity ratio hot sensor overheat ratio
τ	shear stress
ϕ	angular offset of hot wire probe from the radial traversing axis

Subscripts

D	duct or plenum condition
e	boundary layer edge condition
J	jet parameter
m	measured (voltages) maximum (velocities)
min	minimum
$\frac{m}{2}$	half velocity point
o	stagnation conditions
∞	free stream condition

1. INTRODUCTION

1.1 The Coanda Effect

The effect by which a fluid jet attaches itself to an adjacent surface and remains attached was initially observed by M. Henri Coanda, after whom the effect was named. 'Coanda effect' is capable not only of attaching a free jet to a surface but can also enable a tangential jet to negotiate and remain attached to a highly curved wall. The effect produces very strong entrainment of the surrounding fluid, independently of whether the external fluid is moving or stationary, and significantly reduces the surface static pressure under the jet. The point at which the flow separates from a curved surface in a two dimensional case can be controlled by the jet blowing momentum. The detailed physics of the effect are still not wholly understood.

M. Coanda investigated many applications of the effect including leading edge blown aerofoils and thrust augmentors. Reference 1 is an example of this work, reproduced after the war. Further applications have been investigated by other researchers, for example, the blown cylinder, upper surface wing/flap blowing (as on the Buccaneer and VC-14 aircraft), fluidic amplifiers and wall blowing to improve wind tunnel diffuser operation (see Figure 1). More recently interest has been focused upon circulation control aerofoils and their potential benefits for helicopter rotors.

If aerofoils are considered, then a conventional sharp trailing edged aerofoil exhibits the well known 'Kutta' condition. This states that the rear stagnation streamline must emerge from the trailing edge in order to avoid discontinuities in velocity and pressure. Hence the circulation around the aerofoil is uniquely defined by the aerofoil geometry, incidence and free stream velocity. If however, the trailing edge of the aerofoil is rounded, then the rear stagnation point is free to move, depending upon the other parameters. If the aerofoil is an ellipse aligned at zero incidence to the free stream direction, then the upper and lower surface separation points should be located at the same chordwise station and the nett circulation will be zero. If now a jet of fluid is injected tangentially into the upper surface boundary

layer, near the trailing edge, the Coanda effect will entrain the boundary layer and delay the separation of the upper surface flow. This causes a nett increase in the circulation around the aerofoil. The momentum of the blowing jet now controls the position of the rear stagnation point; the aerofoil is subject to 'Circulation Control' by blowing. If the blowing jet is strong enough to discharge excess momentum into the wake, then the aerofoil performs in a similar manner to one fitted with a jet flap. The lift is no longer produced solely by delaying the upper surface separation but has a jet reaction thrust component which reduces the nett lift augmentations $\partial C_L / \partial C_M$, (see Figure 2).

1.2 The Applications of Circulation Control

The application of circulation control-by-blowing to helicopter rotors and more recently to stopped rotor aircraft (X-wing, see Figure 3) is shown in References 2 and 3.

Conventional helicopter rotor systems suffer from a variety of problems, including vibration, mechanical complexity, high drag and retreating blade stall at high forward speed. It has been shown (References 4, 5 and 6) that a circulation control rotor is capable of reducing many of these problems.

Circulation control aerofoils are able to develop lift independently of incidence, and to a first approximation, at low blowing rates, velocity. Hence the rotor may develop lift purely as a function of blowing rate. At low advance ratios - μ = helicopter forward speed/rotor tip speed less than 0.5 - the lift may be increased at the fore and aft azimuth positions of the rotor disc to produce a more efficient value of the thrust coefficient/solidity ratio (C_T/σ). In particular, the hover performance may be greatly improved since a circulation control rotor is capable of producing high lift coefficients compared with conventional rotors. At advance ratios in excess of 0.7 the area of reversed flow on the retreating blade side tends to increase (see Figure 4). It has been shown by Ottensmeyer⁷

that incorporation of a second blowing slot on the leading edge of the blade, ejecting air tangential to the surface and in an opposite sense to the normal free stream direction, enables the blade to produce lift in a reversed flow region. The dual slots may be blown independently as required or continuously with little significant loss of lift. Typical flows around a dual slotted aerofoil are shown in Figure 5. Useful lift has been shown on test rigs at advance ratios greater than 2 (approximately 400 knots forward speed).

Three distinct flight regimes of improved VTOL performance arise as a consequence of circulation control:

- i) High forward speed (advance ratios of the order of 2) by incorporating blowing slots at the leading and trailing edges.
- ii) High forward speed at higher advance ratios permitted by slowing the rotor and incorporating leading edge blowing only.
- iii) Low speed performance as a conventional helicopter and transition to a 'stopped rotor' for high speed flight (X-wing mode). Transition would be between 100 - 180 Kts. In this case dual blowing would be available for the helicopter mode and 'trailing edge' only blowing would be used to augment the lift whilst operating as a stopped rotor aircraft.

All of these techniques would use the blowing system as an attitude control system offering improved control response at low forward speed.

Each of these systems offers many advantages over the current technology improvements in helicopter performance being made available by tip geometry, blade construction and airframe improvements.

Inherent in circulation control aerofoils is the increased blade stiffness which will enable the rotor to be smaller and lighter. A circulation control blade may be as much as 10 times stiffer in bending compared with a conventional 'D' spar blade.

Since collective and cyclic blowing can be substituted for collective and cyclic pitch, the complexity, size and weight of a circulation control hub can be significantly less than its conventional counterpart. This offers three main advantages:

- i) reduced hub aerodynamic drag
- ii) reduced hub weight
- iii) reduced rotor system maintenance

The third advantage being most significant in terms of operating costs and time on the ground. A circulation control rotor also has the advantage of having fewer dynamic force components and hence a higher harmonic control system is possible giving less vibration and improved gust response.

Reference 8 describes the first practical application of circulation control to a helicopter rotor (Kaman XH-2/CCR) and indicates the simplicity and effectiveness of installing a circulation control rotor on an existing airframe. The Kaman flight demonstrator is essentially a low speed test bed; a more realistic stopped rotor has been tested in the NASA-Ames 40 ft x 80 ft wind tunnel.

1.3 Previous Experimental Work

With the advent of these advanced technology applications, the existing knowledge of the Coanda effect and circulation control aerofoils has had to be reviewed. The basic aim of the research was, and still is, to produce a reliable prediction method for estimating the performance of practical applications of the Coanda effect, in particular, circulation control aerofoils.

Accepting that the heart of the problem is to solve the highly curved wall jet flow, experimental research over the last two decades can be

grouped in three categories:

- i) plane jets
- ii) curved jets
- iii) circulation control aerofoils

An excellent recent summary of wall jet experiments is given in Reference 9.

1.3.1 Plane jet experiments

References 10 - 18 are given as examples of experimental work available on plane wall jets. These reports cover a variety of effects including longitudinal pressure gradient, external flow, jet turbulence level and slot geometry.

The self preserving, simple plane wall jet flow has been shown to exhibit a linear half velocity growth rate given by

$$\frac{d y_{m/2}}{dx} = 0.073 \pm 0.002 \quad (1.1)$$

however, this region may not begin until some 50 slot widths downstream. The growth rate is some 30% less than the corresponding free jet value. Few useful measurements exist within the important starting region of the flow, although the study of Irwin¹⁰ is particularly thorough in the self preserving region. Also, good agreement with general momentum balances is somewhat lacking and it has been suggested in Reference 9 that this is due mainly to unsatisfactory turbulence measurements. The problem of matching results from different test apparatus will be further illustrated in the later sections of this report.

Several examples for the case of a plane turbulent wall jet in the presence of an external stream have been given. These have a more direct relationship to the blown boundary layer application, but the addition of a further variable, the external flow, merely appears to complicate the test situation. The work of Kruka and Eskinazi¹¹ is considered to be one of the most reliable in this field. Indicated in this work are the variation of maximum velocity decay, jet and free shear layer growth. Additionally the difficulty of providing a single similarity profile which applies across the whole flow is demonstrated. Gartshore and Newman¹⁸ provide some interesting comparisons between various test results and a proposed theory. The theory was used to investigate some assumptions generally made regarding the shear stress profile across a plane wall jet. This work emphasises how any prediction method has to be based on well documented, reliable test results.

1.3.2 Curved jet experiments

References 19 - 25 are a selection of works concerned with wall jets around curved surfaces. The radial pressure gradient and extra strain on the fluid due to curvature make a convex curved flow more susceptible to spanwise irregularities and hence many of the experimental results must be viewed with suspicion. True two-dimensional flow around a cylinder is considerably more difficult to obtain than with a plane jet. The interaction effects at the extremities of the blowing jet may cause large longitudinal vortices to be shed into the jet flow. The slot geometry and, in particular, small spanwise irregularities in the slot lip, may also cause severe three-dimensional effects. The growth rate of the curved jet is considerably higher than that of a plane jet due to the extra strain imposed by the curvature upon the flow. A further problem involved with the testing of curved, rather than plane, wall jets is the provision of satisfactory instrumentation for measurements in the highly curved flow. In general, to avoid excessive blowing requirements, a small cylinder and slot height is chosen and this reduces the width of the flow and hence demands smaller spatial resolution of any probes

positioned within the flow. With the higher growth rate, the flow also ceases to be effectively parallel to the local surface. This, coupled with the high turbulence levels experienced at the edge of the jet and the increased entrainment, make determination of any turbulence parameters exceedingly difficult. Reference 21, by Wilson and Goldstein, may be considered to give a good indication of the turbulence properties within a highly curved wall jet in still air.

In an attempt to produce a self preserving curved wall jet some researchers have investigated the log spiral surface, in which the curvature is a function of the distance from the slot.

$$R_o = K S \quad (1.2)$$

where R_o = surface radius

S = distance from slot.

Giles et al²³ is an example of this work. An approximately self preserving wall jet is created, although the growth rate is larger than for circular cylinders of comparable surface radius. Little reliable turbulence data is available for this type of flow.

1.3.3 Circulation control aerofoil experiments

There are two main areas of interest in the aerofoil experiments:

- i) overall force and pitching moment coefficients
- ii) mean values and turbulence parameters in the curved wall jet.

Early work at N.G.T.E. and N.P.L. provided much information upon the high lift capabilities of cylinders and ellipses with circulation control by blowing. The majority of the work however was performed at high blowing momentum coefficients, C_μ , in excess of 0.5,

$$C_\mu = \frac{\dot{m} V_j}{\frac{1}{2} \rho V_\infty^2 S} \quad (1.3)$$

and hence was not of significant use in the current applications. More recently a series of studies have been performed; References 7, 26 - 34 are good examples of this work. Typically, lift coefficients in excess of 6.5 for $C_{\mu} < 0.25$, lift augmentations $\partial C_L / \partial C_{\mu}$ of greater than 70, and section effective lift/drag ratios of more than 30 have been demonstrated.

Only references 28, 32, 33 indicate any detailed trailing edge measurements. Englar²⁸ used a hot film surface mounted shear stress meter to measure wall shear stress beneath the wall jet. Some indications of radial static pressure distributions were also obtained from static tappings located on a machined flange mounted normal to the trailing edge surface. The aerofoil was a modified 20% ellipse of 11 inch chord, tested up to high subsonic speeds. Kind³² produced velocity profiles and longitudinal turbulence profiles at various angular positions around the trailing edge using a single hot wire probe. This aerofoil was again a 20% uncambered ellipse of 14 1/2 inch chord and was tested at low subsonic speeds. Jones³³ produced a large chord (~ 4 ft) modified elliptic model in an attempt to increase the size of the measuring zone. Velocity and shear stress profiles were produced, again at low subsonic speeds, using a single slant hot wire probe. Examples of these results, where of interest, will be used in Chapter 5.

The main reason for the lack of detailed investigations around the trailing edge of a circulation control aerofoil arises from the complexity of the testing environment. The small scale of the flow (slot heights of 0.5 mm are typical), the high curvature of the trailing edge and the problem of establishing two-dimensional flow around the aerofoil have restricted many researchers to simple overall pressure measurements.

1.4 Previous Theoretical Work

The theoretical work can be divided into two areas:

- i) The wall jet without a co-flowing stream
- ii) The wall jet with a co-flowing stream/aerofoil trailing edge wall jet flow.

The theoretical prediction of the first type of flow is greatly simplified since the boundary conditions are invariant from case to case. This suggests that both integral and differential methods should succeed since the velocity profile can be described simply, by a single equation. The bases of the two methods are summarised by Newman and Irwin³⁵ and their relative qualities discussed. In general the technique used is to split the flow into a series of strips and to solve the assumed equations by establishing the boundary conditions at the edges of the strips. Unfortunately the extension of these types of technique to a trailing edge wall jet flow appears impractical.

A great variety of wall jet velocity profiles may exist around the highly curved trailing edge of a circulation control aerofoil (see Figure 6) and this precludes the use of a simple universal set of equations to describe the velocity profiles. For this reason, the integral technique will be only briefly discussed (see Section 1.4.1) and the reader is referred to the work of Kind³² for further details.

In general, the solution of the flow around a circulation control aerofoil follows a similar pattern regardless of closure technique.

- i) determine the pressure distribution around the aerofoil using a potential flow solution.
- ii) calculate the lower surface boundary layer development to separation using a suitable method, usually of the integral type.

- iii) calculate the upper surface flow development as far as the blowing slot, again usually by an integral method.
- iv) close the flow by calculating the curved wall jet development, from the starting conditions of the upper surface boundary layer at the slot and C_u , to separation. It is usually assumed that the wall jet separates at the same pressure as the lower surface boundary layer as suggested by Thwaites³⁶.

1.4.1 The integral method

Dunham³⁷ modified Spalding's plane wall jet method by incorporating corrections for curvature and entrainment to represent a wall jet on a circular cylinder. Kind³² then extended the method to an elliptic aerofoil; a block diagram of his method is given as Figure 7. However as previously mentioned, these integral type calculations have limited applicability.

1.4.2 The finite-difference method of Dvorak and Kind³⁸

Dvorak and Kind³⁸ used a similar overall calculation scheme which includes allowance for viscous effects, and uses a finite difference calculation to determine the wall jet development (see Figures 8, 9). The finite difference scheme is initiated by merging the final boundary layer profile at the slot with a nearly uniform slot flow profile. The calculation mesh distribution is arranged with points concentrated in the regions of high shear.

The static pressure distribution both normal and tangential to the surface is obtained from the potential flow calculation. A correction to take account of the excess momentum flux in the jet (J_{ex}) is applied to the deduced radial static pressure distribution. A variation of $(-J_{ex}/R)$ at the surface to zero at the velocity minimum is superimposed upon the distribution.

The equations of motion are then closed using an eddy viscosity model

for the Reynold's shear stress term. The model in its final form is

$$\begin{aligned} -\overline{u'v'} &= \nu_t \frac{\partial u}{\partial y} - C_1 \frac{uk}{1+ky} \\ \nu_t &= \text{eddy viscosity} \\ k &= f(x) = \frac{1}{R} \end{aligned} \quad (1.4)$$

This is largely based on simple mixing length arguments. Values for the additional empirical curvature correction, C_1 , have been quoted from 1 to 25 by various researchers. In this model, the value of C_1 has largely been tailored to fit the small amount of existing experimental data (Kind³²) and varies thus:

$$\begin{aligned} \text{For } y < y_m \\ C_1 &= 182\eta - 32\eta^2 + 190\eta^3 \\ \eta &= \frac{y}{y_m} \\ \text{For } y > y_m \\ C_1 &= 33 - 32\eta \\ \eta &= \frac{(y - y_m)}{(y_{\max} - y_m)} \end{aligned} \quad (1.5)$$

This type of variation is assumed since, at some small distance from the wall ($y < y_m$), where $\partial U/\partial y$ is still large and positive, C_1 must also be large to allow $\overline{u'v'}$ to become positive, as has been shown by Jones³³ and Wilson and Goldstein²¹. This is a possible indication that the present eddy viscosity model is inappropriate for this type of flow.

The finite difference scheme which develops the wall jet flow to separation is checked against the previously stated Thwaites equal pressure criterion, and the aerofoil calculations are then iterated to a satisfactory closure.

1.4.3 The discrete vortex method of Smith³⁴

Recently, however, a new technique has been developed by Smith³⁴, et al³⁸ to determine the development of the curved wall jet on an aerofoil. At present, the method uses a simple potential flow solution around a cylinder with the wall jet represented by a series of discrete point vortices (and their images) shed from the slot lip at discrete time intervals. The vortices rotate in the sense which describes the outer free shear layer of the wall jet. The development of the wall jet is then calculated using the mutual influence of the vortices to predict steady state separation. The summation of the induced effects of the vortices upon each other is calculated and the locus of the vortex stream is predicted (see Figures 10, 11). The initial strength of the vortices is based upon the velocity difference at the slot, representing C , and the vortex strength then decays exponentially representing the dissipation of the vortex energy. An artificial viscosity has also been found necessary to stabilise the vortex motion.

This method, simple in technique, has shown reasonable agreement with experiment, as shown in Figure 12, but is very dependent upon the prescribed decay rate of the vortex strength and the vortex shedding frequency (i.e. the time interval between each successive vortex). At present, the technique is undergoing development in order to remove the empirical decay rate and improve prediction. Further discussion of this technique and its relevance to the current study will be given in Chapters 5 and 6.

1.5 The Present Investigation

As has been stated, there exists a requirement to be able to predict the performance of Coanda flows, in particular for circulation control aerofoils of various geometries. The existing theories lack universal applicability and so it was decided to undertake a detailed experimental study in order to provide more data and a better understanding of the mechanics of a Coanda flow.

The test aerofoil was to be mounted in the 7 ft x 5 ft high speed working section of the Bath University wind tunnel (see Figure 13 and Section 2.2). The blowing supply was to be delivered from a compressor capable of supplying 1300 c.f.m. (F.A.D.) at a nominal 80 p.s.i.g.

The following design guidelines were adopted in the light of previous work and the available facilities.

- i) The chosen aerofoil section should be an ellipse as this is a section which is easily transformed mathematically, simplifying the evaluation of the theoretical pressure distribution around the aerofoil.
- ii) The thickness: chord ratio of the ellipse was chosen as 20% to enable direct comparison with previous research, particularly the work of Kind³².
- iii) The chord should be as large as possible within the restraints of the working section in order to enlarge the scale of the boundary layer at the trailing edge.
- iv) It should be possible to adjust the incidence over the range $\pm 10^\circ$ from the tunnel centreline.
- v) The aerofoil should incorporate a plenum chamber and the skin of the aerofoil should not deflect significantly when blowing pressure was applied.
- vi) Slots should be incorporated at the leading and trailing edges in order to examine the dual/reverse blowing cases. The slots should exhaust as near tangentially to the local surface as possible and should cause a minimum of discontinuity of the surface profile.

- vii) The slot height should be adjustable within the optimum range of slot height : chord ratio as suggested by previous work ($0.001 < h/c < 0.002$ Englar and Williams⁴⁰).
- viii) The flow should be as near to the two-dimensional case as possible, either by using a large aspect ratio or by incorporating a secondary blowing system.
- ix) A traversing system was to be mounted on, or in, the model, to enable hot wire and pressure probes to be accurately positioned around the trailing edge of the aerofoil.

It was proposed to examine the performance of this circulation control aerofoil within the range of blowing momentum coefficients of 0 to 0.1, this being the most efficient regime in terms of maximum lift augmentation.

1.6 A Brief Guide to the Contents of the Remainder of this Thesis

The design considerations raised in Section 1.5 will be discussed in more detail in Chapter 2. Also in Chapter 2, a full explanation of the precautions taken to control the two-dimensionality of the flow, a description of the probe positioning devices, the wind tunnel and the blowing air supply will be given.

Chapter 3 contains all the information on the instrumentation used in this experiment. The calibration, operation and sources of errors of both wire and split film anemometer probes are considered.

Chapter 4 is a presentation of the results obtained both for the overall performance and the detailed trailing edge investigation.

In Chapter 5 some suggestions are made regarding the mechanics of a Coanda flow field in the light of the experimental results. The implications of the suggestions and their effect upon the interpretation of the results is discussed. Justification for the

suggested flow field is given and the limitations of the instrumentation are illustrated.

Chapter 6 reviews the incorporation of the suggested flow field into a full aerofoil performance scheme and also discusses the deficiencies of current methods.

Where possible, the parameters used have been made non-dimensional. Some references to both the Imperial and Metric systems has been unavoidable; however the units are clearly stated in all cases and the author apologises for any inconvenience this may cause.

2. APPARATUS

2.1 Aerofoil Design

2.1.1 Design considerations

Many of the points made in the following sections have been gleaned from the problems encountered by previous workers, notably, Kind³², Jones³³, Englar²⁸ and in particular Englar and Williams⁴⁰.

2.1.1.1 Aerodynamic

Three-dimensional effects dominate the aerodynamic considerations when designing a circulation control aerofoil model. They arise from three sources:

- i) high lift testing of large models in closed tunnels.
- ii) effects of low, undefined aspect ratio (of the order of 1) and endplate boundary layer interactions due to the large adverse pressure gradients at the aerofoil trailing edge.
- iii) spanwise irregularities in the slot flow.

The recommendations of Englar and Williams⁴⁰ cover many of these points and suggest that the chord to tunnel height ratio should be less than 0.3 and that some form of secondary blowing should be incorporated to re-energise the spanwise extremities of the flow.

The secondary blowing could take the forms (shown in Figure 14) of either

- i) blowing on the end plates aft of the half chord point
- ii) blowing between the leading edge and the half chord tangentially over the aerofoil surface.

- iii) blowing with excess momentum compared to the main jet at the spanwise extremities of the main trailing edge slot. These are called 'tip jets', (see Figure 14).

For reasons of blowing air economy and manufacturing simplicity, the tip jet option was chosen.

To reduce the boundary layer growth on the end plates, they were positioned with less than a half chord projecting in front of the leading edge of the aerofoil. The position and dimensions of the end plates is discussed further in Section 2.1.1.2.

The reason for the low aspect ratio is primarily an attempt to increase the chord and hence the size of the trailing edge wall jet. The bigger the wall jet, the fewer the problems encountered when velocity profiles and turbulence surveys are required. A compromise must be drawn between this and the overall tunnel constraints. Jones³³ outlines qualitatively the problems involved in obtaining a reasonable solution.

The thickness of the boundary layer just upstream of the blowing slot and hence the chord, also indicates the range of slot widths which may be used. For example, if the boundary layer is too thin, then manufacture of narrow, accurate slots ($h < 0.25$ mm (0.010 inch)) becomes extremely difficult, while if the boundary layer is too thick, there is a chance of causing shear layer separation in the wall jet, as found by McGahan⁴¹. It was proposed in this work to vary the slot height : chord ratio (h/c) around the optimum value of 0.002 proposed by Englar et al⁴⁰. The slot itself should be free from obstruction for at least 2.5 cm (1 inch) from the slot exit (this limit allowed the majority of the contraction to be 'clean') and the slot flow should exhaust as near tangentially to the outer surface as physically possible, with the minimum cross section occurring at the exit itself.

The slot chordwise position was chosen to be between 96 and 96.5% x/c in order that the slot exit was close to the point at which the unblown boundary layer would normally separate; this was expected to be the most efficient location. The final position was calculated as a function of the geometry of the trailing edge and the optimum slot height, and was located at 96.45% x/c , as shown in Figure 15.

As a further aerodynamic consideration the model geometric incidence, α_G , was made adjustable by $\pm 10^\circ$ relative to the tunnel centreline.

2.1.1.2 Mechanical

The two main problem areas concerned the blowing air and the model mounting in the tunnel.

Following the experiences of Kind³², it was noted that the aerofoil should not be allowed to deform under blowing pressure. This placed limitations on the model construction and in particular, on the choice of materials. Other researchers have found that if the plenum air pressure is allowed to act on retaining screws in the outer skin, the screws tend to loosen and leakage and loss of structural integrity may occur.

The vertical mounting of the model in the wind tunnel working section (to reduce chord : height ratio) and the size and position of the access panels (see Section 2.2) imposed restrictions on the end plate design. In particular, in allowing the end plates to extend less than a half chord in front of the leading edge, the axis of the model and the end plate size were fixed by their positions relative to the roof and floor access panels. It was also a requirement that the model should be easily removable from the working section to allow the tunnel to be available for other testing and to permit easy model maintenance. For this reason the model was mounted on its own 'floor' and could be lifted into place as a complete unit including control instrumentation, on a simple hoist system.

2.1.1.3 Constructional

The model overall dimensions were restricted by the capacity of the available workshop machinery. This was a major factor in arriving at the final design scheme.

Care was also taken over the choice of materials, with particular reference to corrosion. Wherever possible aluminium or brass were used, but where steel could not be avoided, the components were cadmium plated.

To further simplify production it was decided that the leading and trailing edges should be constructed from drawn steel tube of a suitable diameter.

2.1.1.4 Operational

Consideration was given to shortening the actual tunnel running time, by optimising the model operation at the design stage. It was assumed that, since the investigation was concerned with detailed trailing edge surveys, variations of geometric incidence were of secondary importance compared with the accurate positioning of a probe (wire, film or pressure) around the trailing edge, without stopping the tunnel or the blowing air supply. For this reason, any probe traversing system had to be operable externally from the working section and should not change its effect upon the flow field. Further discussion of these points is included in Sections 2.1.4, 3.2, 3.3.

Following consideration of the above requirements, certain aspects of the aerofoil were finalised irrespective of span.

- 1) An elliptic 20% section with 24 inch chord was chosen to match previous work, provide a relatively thick section for ease of manufacture and to reduce the curvature at the leading and trailing edges.

- ii) The leading and trailing edges should be made from 2 inch (50.8 mm) O.D., 10 G wall, drawn steel tube.
- iii) The positioning of the tubes should be such that all external surfaces should join tangentially.
- iv) The leading and trailing edge slots should be symmetrically placed at 3.55% and 96.45% chord. These figures were defined from the assumed geometry, an optimum slot height and slot lip thickness and the condition of surface tangency.
- v) The slot width h , should be variable by ± 0.015 inch (0.375 mm) about $h = 0.035$ inch (0.875 mm) giving $h/c = 0.0015$ and $R_o/h = 28.5$, where R_o is the radius of the trailing edge.
- vi) The radial traversing gear should be housed within the trailing edge tube, rotatable from outside the tunnel and have a resolution of better than ± 0.001 inch (± 0.025 mm).
- vii) Blowing air supply to the model plenum should be from both ends of the model.
- viii) No pressurised surface should deflect more than 0.005 inch (0.125 mm).
- ix) The slot contraction should be free from obstruction for at least 1 inch (25.4 mm) ahead of the slot exit.

The first model design was of 54 inch (1.37 m) span, aspect ratio ≈ 2.2 , mounted vertically in the working section. Three inches (7.5 cm) were allowed on both sides for removal of the working section wall boundary layer and the model was to be of rib and skin aluminium construction. This design was abandoned mainly due to production difficulties (for long lengths) and a smaller span model (27 inch, 0.685 m) of simpler construction was adopted. This consisted of an inner steel box

plenum with wooden contour blocks to add the outer profile. Among its many advantages, the plenum could be built and sealed, specifically to eliminate leakage, without the constraint of having a desired aerodynamic profile. Also the load upon the blocks was minimised since there were only aerodynamic forces upon them. This model had to be modified because of warping difficulties in manufacturing the wooden contour blocks. The final production model was a compromise between these two designs and is the latter plenum design with a rib and skin outer profile (Section 2.1.2).

2.1.2 Final scheme

The final production model (see Figures 15, 16) consisted of a simple box plenum constructed from $\frac{1}{4}$ inch (6.34 mm) aluminium alloy plate with a rib and skin outer profile. The plenum geometry was maintained by 16 small internal ribs, which also located the leading and trailing edge cylinders. Aluminium spacers, $\frac{1}{4}$ inch (12.7 mm) O.D. were also used to add rigidity to the plenum surfaces. The plenum was divided in two by a spanwise main spar, separating the leading and trailing edge blowing plenums. Six $\frac{1}{4}$ inch (9.53 mm) aluminium ribs on the top and bottom plates provided the contour for the $\frac{1}{4}$ inch (3.18 mm) aluminium alloy outer skin which was held in place by 6BA countersunk head bolts, at $\frac{1}{4}$ inch (19 mm) pitch, in the ribs. The inner surfaces of the plenum were coated with non setting adhesive (Lion liquid jointing) before assembly to provide sealing against air leaks. The plenum stagnation pressure and temperature were measured via a pitot tube and a thermocouple mounted in the middle of each plenum.

The slots were made by two numerically machined slot lips (see Section 2.1.3) which located directly onto the plenum chamber plates. The slot gap was adjustable and could be locked by 24 locating bolts in each lip. The lower surface was sealed using two strips similar to the slot lips, machined to fit flush against the cylinders. Sealing between the lips, sealing strips and the plenum walls was achieved by 1/16 inch (1.6 mm) thick, soft rubber strips secured between them. "Sealastik" was also used between the sealing strips

and the edge cylinders to provide additional sealing. The slot lips, sealing strips and leading and trailing edge cylinders were cadmium plated to protect the slot contraction against corrosion.

The aerofoil was supported by two spigots attached to the end ribs and rotating in thrust bearings housed in the support assemblies. The support assemblies and leading and trailing edge cylinders which extended to the tunnel walls, were left unfaired. This ensured that the unfaired cylinders would not produce any lift and therefore could not produce the asymmetric interference encountered by Kind³².

End plates were fitted and they located into the end outer ribs and rotated with the model. The end plates measured 34 in x 54 in (0.86 m x 1.37 m), the longest side parallel to the aerofoil chord, and projected approximately half a chord in front of the model leading edge. The end plates were wire braced to each other and the tunnel walls to provide additional stiffness.

The final overall model chord was 23.425 in (0.595 m).

There were 44 static pressure tapings located around the model centreline (see Figure 17). One of the tapings proved unserviceable due to being drilled incorrectly. Tubes from the static tapings were routed through the outer ribs to avoid contact with the high pressure plenum air.

Details of the blowing air supplies are given in Section 2.3 and of the pressure data reduction system in Chapter 3.

The aerofoil incidence was set by rigidly mounted incidence locking arms located near the tunnel walls.

2.1.3 Slot design

The importance of good slot design was highlighted by the variable performance obtained by other researchers. While the main model was

being designed a small slot geometry model was built, and this is shown in Figure 18. It consisted of a 2 in (50.8 mm) square section tube, with optical glass sides and contained adjustable liners. The tube was constricted by an offset 2 in (50.8 mm) diameter cylinder, creating a variable height slot. The liners could be interchanged to represent various slot geometries. A vertical splitter plate was inserted to check that slot flow interference was minimal and that no significant wake was present over the cylinder. Liquid film, smoke flow visualisation and schlieren were used to check on the flow within the slot. This simple model was used to establish the production slot geometry.

The production slot geometry is shown in Figure 19; details of the location and sealing are also shown. The geometry was initially drawn by eye and dimensioned later.

Both the slot lips and the lower surface sealing strips were produced on a numerically controlled milling machine, this being the only complex machining involved in the final model design scheme. The slot lips were designed to have an optimum geometric position at $h = 0.035$ in (0.875 mm) and contraction ratios in excess of 50 were typical. The actual slot lip thickness was 0.010 in (0.25 mm), this being a precaution against lip deflection under aerodynamic or blowing load.

2.1.3.1 Two-dimensionality of slot flow

Many researchers, notably Gartshore and Newman¹⁸ have indicated severe problems arising from slot flow which is not two-dimensional. Figures 20, 21 show the slot flow for this model with a slot gap of 0.021 in (0.52 mm) measured with a flattened pitot tube and a multi-tube rake. Apart from the various surface and plenum irregularities, the uniformity of the flow is excellent. The slot gap was constant to within ± 0.001 in (0.025 mm) across the span and the slot lip had been machined to a sharp 90° edge to ensure a strong fixed separation from the slot lip. The excess tip jet blowing is clearly seen (in Figure 20) at the edge of the main jet flow. The

inflections in the total pressure distribution at the boundary of the main and tip jets may also indicate the presence of a secondary longitudinal vortex caused by excessive tip jet blowing as discussed in Section 2.2.3.1. Apart from the inflections, the tip jet blowing is shown to have little harmful effect upon the main jet blowing distribution.

2.1.4 Traversing gear

It was required to be able to position a probe at any position within 1 inch (25.4 mm) of the surface of the trailing edge cylinder, mainly on the centreline, although some spanwise movement was desirable. The accuracy was required to be within 0.001 in (0.025 mm) radially and $\pm 1^\circ$ on θ (angular position from slot). The θ position was to be adjustable from outside the working section and the probe supports should offer a minimum of flow disturbance:

There were three possible arrangements for the traversing gear:

- i) housed externally from the model with the probe brought to the trailing edge, (Kind³²).
- ii) housed internally within the plenum or trailing edge cylinder and projecting the probe radially through the surface, (Jones³³).
- iii) housed within the trailing edge cylinder with the probe returning to the surface some distance away from the traversing gear.

The third option was chosen, in view of the problems encountered on the first two systems by previous researchers, and also because of its improved rigidity and interference properties. The one problem with this option was that the gear system was to be housed within a tube of 1½ in (94 mm) internal diameter.

2.1.4.1 Mechanical system

A detail of the final layout of the traversing gear system is shown in Figure 22. The drive unit chosen was an Impex 48 pole stepper motor type 9904 112 0400 with a step angle of $7^{\circ}30'$ and a maximum working torque of 12 mNm. The drive shaft from the motor was positioned inside the trailing edge cylinder and its rotation was then translated into radial movement within the traversing gear. Many systems were investigated including, rack and pinion, bevel gears, worm gears and cams. Eventually a worm gear system was chosen as this offered several advantages; including:- small size for large built in gear reduction; the teeth are in constant mesh; cheap; less susceptible to wear.

To eliminate backlash in the system two features were incorporated. Firstly, the mesh of the gears was adjustable to keep the worm in firm contact with the wheel. Secondly, a sprung collar was fitted to the drive shaft inside the worm wheel to keep the threads in permanent one way contact irrespective of the direction of motion.

The two probe supports were required to give adequate rigidity to the probe and so the worm system was duplicated at a 4 inch (10 cm) pitch, spanwise.

The rotation of the traversing gear as a unit was achieved via a fixed shaft on the axis of the trailing edge cylinder, extending between the traversing gear body and the stepper motor mounting block. Since the stepper motor was at a fixed relative angular position, rotation of the unit did not affect the zero setting of the traversing gear. The stepper motor mounting plate was held in position by grub screws, which clamped onto the trailing edge cylinder.

The resolution of the system was as follows:-

1 pulse of motor = $7^{\circ}30'$

50:1 worm gear reduction = 9'

32.6 t.p.i. on shaft = 0.0307 inches per revolution

\therefore 1 pulse = 1.279×10^{-5} inches

\therefore approximately 75 steps = 0.001 in (0.025 mm)

The motor could be driven either remotely by the PDP-11 computer or via a manual control. The position of the probe was recorded on a counter as a number of steps from a zero datum and was also available as a BCD output from the stepper drive.

To obtain maximum advantage of the accuracy of the traversing gear a reliable zero setting procedure was required. This is described in the next section.

2.1.5 Position control system

Previous researchers have used either a mechanical or optical, wind off, zero setting device for the positioning of hot wire probes. These systems have many disadvantages, the main one being the deflection of the probe under airflow, and hence can only be considered accurate to within ± 0.001 in (0.025 mm) at best.

To obtain improved accuracy, the capacitance position control system, shown in Figure 23, was developed.

Simply, the probe was used to detect the capacitance between itself and the surface of the model. The model as a whole was energised with a 5 volt r.m.s., 5 KHz a.c. signal; the charge detected was amplified and passed through a phase sensitive detector set at the same frequency. The final output voltage was compared with a preset reference voltage which enabled inhibition of the stepper drive system. A typical output for measured voltage against distance from the surface is shown in Figure 24. The voltage produced was a function of probe orientation relative to the local surface, but for any run the orientation was constant. Using this system, the probe could be positioned optically wind off and the zero returned to, reliably, wind on, even if the drive system miscounted the number of step pulses or the probe was moved to a new angular location around the trailing edge. There were four main advantages with this system:-

- 1) the electric field is unaffected by airflow and thus the probe could be positioned whilst the tunnel was running.

- ii) when close to the surface, the repeatable resolution was better than 0.0001 in (0.0025 mm).
- iii) any wire or film probe can use this system. Any insulated metallic pressure probe could also use the system, although this was not investigated in the current work.
- iv) a probe can be positioned over any metallic part of the model.

Using this system and a travelling microscope, a single sensor probe can easily and repeatably be positioned at its minimum distance from the surface dictated by the prong tip diameter.

The potential of this system for probe positioning over the entire surface area of the model was not realised at the initial design stage. Hence a thin brass strip was inserted around the trailing edge, on the centreline, to enable probe positioning on the model centreline. During the experimental work however, the anemometry probes were positioned over the steel cylinder away from the pressure tappings to avoid the majority of interference effects from the surface discontinuities.

It should also be made clear that the anemometer probes were electrically isolated from the model. This was achieved by supporting the probe holders in non-conducting nylon bushes and isolating the model from a common earth. The probe connecting cable was also isolated from the fluctuating field by the addition of a further braided wire sheath around the cable. The field was automatically inhibited when the probes were activated.

The system has been shown to be accurate enough to be used to test for vibration of the probe mounting and probe supports. The probe was driven into and out from the surface and the output monitored on a storage oscilloscope, (see Figure 25). The results show little detectable vibration, wind on or off.

2.1.5.1 Typical operation of traversing gear/position control system for a boundary layer traverse

The following section illustrates the use of the position control/traversing gear/anemometer systems to perform a simple boundary layer traverse.

- i) switch stepper control to 'Manual' and 'Ref. pt'.
- ii) mount probe and align with surface.
- iii) move probe towards the surface, monitoring the gap with a travelling microscope.
- iv) when the probe is at the desired zero position, adjust the reference voltage to match the probe output voltage. Note, all metallic equipment other than the model and probe should be removed from the working section as they affect the field around the probe and hence the reference voltage would be incorrect.
- v) set step counter to zero.
- vi) move probe away from the surface and switch to 'DISA'. This enables the probe to be heated and the zero flow voltage measured. It should be noted that the proximity of the model may significantly affect the measured zero flow voltage. It was found necessary to determine the variation of zero flow voltage against distance from the surface so that a true zero flow voltage could be determined at any known position from the surface.
- vii) switch back to 'Ref. pt.' having switched off the probe; start up the tunnel.
- viii) whilst monitoring the probe output voltage, drive the probe towards the surface. If the probe stops due to reference point

voltage, then the probe has deflected towards the surface; zero the counter. If the probe stops due to zero on the counter, the probe has deflected away from the surface; allow the counter to go through zero until the reference point voltage is encountered and then zero the counter. Typical deflections due to airflow were of the order of 0.001 in (0.025 mm).

- ix) the probe is now positioned at the original set point. Switch to 'DISA' and activate the probe. The probe can now be driven away from the surface and the anemometer output voltages recorded.
- x) having completed a traverse, switch off the anemometer (note: tunnel still running) and switch the stepper control to 'Ref. pt.'. The traversing gear can now be moved to its new angular position and locked in place.
- xi) repeat viii), ix), x)

Using this procedure the probe could be accurately reset close to the surface, taking account of small surface irregularities and deflection of the probe due to airflow.

2.2 The 7 ft x 5 ft Wind Tunnel

The wind tunnel used was the Bath University large dual purpose tunnel, shown in Figure 13. The model was mounted vertically in the 7 ft x 5 ft high speed working section as shown in Figure 26. The tunnel is powered by a 170 h.p. motor which drives a 4 bladed fan, 10 ft (3.05 m) in diameter. The high speed working section has a 4:1 contraction upstream, fitted with a gauze, and downstream there is a multicell diffuser. The maximum continuous centreline velocity in the high speed section is 160 f.p.s. (49 ms^{-1}). The return duct of the tunnel is a 12 ft x 10 ft industrial working section with a maximum centreline velocity of 40 f.p.s. (12.3 ms^{-1}). A three component balance is mounted above the high speed working section but this was not used as the model was mounted vertically to obtain the maximum tunnel height: chord ratio.

2.2.1 Calibration of the 7 ft x 5 ft working section

Prior to testing the aerofoil, the working section was recalibrated to take into account the effect of the aerofoil upon the reference static pressure difference tapping located on the side wall at the entrance to the working section. A series of new tapings was positioned in the ceiling at the end of the contraction and the static pressure difference across the contraction was recorded with and without the model in place. The static pressure difference was measured on a Betz micromanometer and referenced to the dynamic pressure at the gauze measured by a pitot static tube and an alcohol micromanometer. The static pressure tapping which suffered least model interference for maximum contraction static pressure difference was chosen and a calibration of Betz manometer readings against working section dynamic pressure obtained (Figure 27). The third tapping from the start of the working section was found to best satisfy these conditions.

The tunnel was operated with the low speed working section vented to atmosphere to avoid air inflow through the alternative vents in the high speed test section.

During initial commissioning runs of the aerofoil it was apparent that the flow in the working section was severely disturbed and an initial rake survey showed the flow field to be asymmetric as shown in Figure 28. On examination of the tunnel, the contraction gauze was found to be partially blocked with dirt causing a recirculating separation bubble in the contraction. The gauze was cleaned and the calibration and rake survey repeated. The flow was shown to be greatly improved (Figure 29).

2.2.2 Investigation of free stream turbulence

During the calibration of the high speed working section, the free stream turbulence levels were investigated using a dual sensor DISA hot wire probe. The results (Figures 30, 31) clearly show the disturbed nature of the lower flow prior to the cleaning of the gauze. The free stream turbulence in the undisturbed region is less than 1%

and can be considered isotropic. The anemometer was operated as described in section 3.2.4.

2.2.3 Proposed testing conditions

All experiments were carried out at a constant free stream velocity of 31.9 ms^{-1} given by a reference pressure difference of 60 mm of water on the Betz micromanometer. The velocity was kept at this modest value to enable a better comparison with the work of Kind³², and also to ease the noise problem for the operator during the anticipated long run times. These conditions gave a test Reynolds number of approximately 1.3×10^6 based on the aerofoil chord.

The slot blowing rate was seen to have a slight effect upon the reference pressure difference but it was small compared with its effect upon the downwash corrections. At each test point, the tunnel r.p.m. was adjusted to give a constant reference pressure difference.

The low speed return section of the wind tunnel was vented to atmosphere, providing a free stream stagnation pressure slightly less than atmospheric.

$$(P_{\text{atmos}} - P_{O_w}) < 1 \text{ cm of water}$$

This proved to be of advantage in the determination of the radial static pressure distributions (see section 3.4).

2.2.3.1 Effect of tip jets

Following the recommendations of Englar and Williams⁴⁰ discussed in Section 2.1.1.1, small tip jets were installed at the extreme spanwise positions of the trailing edge blowing slot. The basic idea was to blow the tip jets two or three times harder than the main jet and effectively disrupt any vorticity which might be shed at the junction of the aerofoil and the end plates. The vorticity present can be reduced by careful filletting between the end plate and the model skin.

In addition, the large adverse pressure gradients which exist at the trailing edge of the aerofoil have a very pronounced effect upon the end plate inner surface boundary layer.

An attempt was made to ascertain the effectiveness of the tip jets by measuring the flatness of the spanwise, upper surface, half chord pressure distribution. Eight static pressure tappings were incorporated at the 50% chord station, equispaced to within $1\frac{1}{4}$ in (76 mm) of either end plate. It was found however that little non-linearity could be detected with or without tip jet blowing.

The overall effect of the tip jets, as shown in Figure 32, was to increase the value of C_L by an amount which increased in proportion to the amount of tip jet blowing. Since no plateau or peak was indicated in the production of extra C_L , it was decided to attempt an optimisation using flow visualisation. It was found that a single wool tuft positioned over the splitter between the tip and main jets, extending over the trailing edge, proved most successful.

When no tip jet blow was used, the main jet caused the tuft to deflect towards the centreline of the model. The amount of tip jet blow could then be adjusted until the tuft was parallel to the endplates, indicating no crossflow in the stream. This is suggested as one of the best methods of ensuring two-dimensionality in circulation control testing, particularly at low free stream velocities. It should be noted that the tip jet blowing system became less effective at increased slot heights due primarily to the nature of the non-adjustable sealing strips between the main and tip plenum chambers in the slot contraction. Also, if the tip jets were blown too hard, a secondary vortex was created between the tip and main jet flows, re-introducing three-dimensional effects.

The optimum amount of tip jet blowing was not obvious but is thought to be a function of the main jet momentum, the overall circulation and the geometry of the end plates.

2.2.4 Blockage corrections

A simple solid blockage correction was applied to the free stream dynamic pressure since the effects of the high lift coefficients, model mounting, air supply pipes and the impingement of the strong wake on the multicell diffuser were difficult to determine individually. The correction applied was from Pankhurst and Holder⁴² and it was assumed that the model spanned the tunnel, to take account of the end plates and mounting tubes.

The correction is given by

$$U_{\infty} = U_T(1 + \epsilon_s) \quad (2.1)$$

where $\epsilon_s = \tau \lambda \left(\frac{t}{h}\right)^2$

$$\tau = 0.822 \text{ for a closed tunnel}$$

$$\frac{t}{h} = \frac{\text{maximum aerofoil thickness}}{\text{tunnel height}}$$

$$\lambda = \frac{1}{2} \left(1 + \frac{c}{t}\right) \text{ for an ellipse}$$

$$\frac{c}{t} = \frac{\text{aerofoil chord}}{\text{aerofoil thickness}}$$

This gave a blockage factor of 1.0275 for the free stream dynamic pressure. The test conditions were then

$$\frac{1}{2} \rho U_{\infty}^2 = 613 \text{ Nm}^{-2}$$

throughout the experiments.

2.3 The Blowing Air Supply

2.3.1 Description of system

A schematic diagram of the blowing system is shown in Figure 33. The blowing supply system was based on a Bellis and Morcom, oil-less, 3 cylinder compressor delivering 1300 c.f.m. F.A.D. up to 80 p.s.i.g. $\pm 10\%$. The compressor delivered the air direct to a settling tank. A self regulating Arca valve installed at the outlet from the settling tank, provided initial regulation of the air supply. A galvanised pipe was installed, external to the buildings, between the settling tank and the wind tunnel, and a Hattersly stop valve was provided at the entry to the wind tunnel building. To improve hot wire/film life and reliability a Domnick Hunter 0.1 μ m filter was fitted immediately downstream of the stop valve.

The flow then passed through a manifold into three separate channels, each controlled by its own Hale Hamilton RL6D dome valve. Each RL6D was operated by an L15 controller, powered from a tapping just downstream of the filter. This provided a system with independent control for the leading and trailing edge slots and for the tip jets. Each flow, regulated by an RL6D, was then split into two to supply each side of the model. Shortly after splitting, the flow for the main slots was transferred to 2 in (50.8 mm) I.D. braid reinforced nylon tube of 40 p.s.i.g. maximum working pressure connected to the model manifolds. Orifice plates (see Section 2.3.2) were positioned in the flexible hose for the main leading and trailing edge flows only. The tip jet flow passed to the model through $\frac{1}{4}$ in (9.5 mm) bore nylon tube.

The maximum pipe flow Mach number was kept below 0.45 to reduce losses; the worst possible conditions were evaluated thus:

		Worst flow case (c.f.m)	Maximum Mach number
6" pipe	settling tank to stop valve	1300	0.1
4" pipe	stop valve to 3-way manifold	1300	0.22
3" pipe	3-way manifold to 2-way manifold	1300	0.395
2" pipe	final supply to model	650	0.44

The final case was equivalent to nearly three times the flow required to choke the main trailing edge slot.

It was not considered necessary to accurately monitor the tip jet flow and the dome regulation pressure was found to be sufficient for control.

2.3.2 Calibration of orifice plates

The orifice plates fitted in the upper and lower, leading and trailing edge main jet supply lines were designed to BS1042⁴³. Since the required operating flow range was large and the connecting tubing was unable to comply with the recommendations of BS1042⁴³, in terms of minimum straight lengths either side of the orifice plates, a calibration was made.

A series of nozzles was manufactured to the general design shown in Figure 34. These could be fitted in turn to the upper leading edge air supply pipeline, the lower leading edge hose being blanked off. By ensuring that the flow through the nozzle was choked, the following relationship could be assumed:

$$\dot{m}_{\text{nozzle}} = 0.585 \frac{AP_0}{\sqrt{T_0}} \left(\frac{\gamma}{R} \right)^{\frac{1}{2}} \text{ kg s}^{-1} \quad (2.2)$$

where A = area of exit (m²)

T_0 = stagnation temperature (°K) measured
by a thermocouple upstream of the nozzle

P_0 = stagnation pressure in Bars, measured
by a Statham pressure transducer upstream
of the orifice plate

γ, R are the usual gas constants, for air

Three nozzles were made with different exit areas, enabling wide coverage of the flow range.

With the mass flow, P_o and T_o obtained as above and the pressure difference across the plates measured on a specially constructed water manometer, the calibration was obtained as:-

$$\dot{m} \sqrt{\frac{T_o}{P_o}} = 0.146 \sqrt{\Delta h} \quad (\text{figure 35}) \quad (2.3)$$

where Δh is the pressure difference across the orifice plate measured in cm of water.

It was later found that there was a difference between the flows of the upper and lower supplies, but, since the calibration applies to all flow rates, it applied equally well to all four individual supplies.

2.3.3 Blowing supply control and instrumentation

With the blowing system coupled to the model, it was found possible, in the mass flow calibration, to replace the stagnation pressure upstream of the orifice plate by the model plenum stagnation pressure, with negligible error. The system was thus controlled primarily by monitoring the plenum pressure on a Statham O - 25 p.s.i.d. pressure transducer. Although small variations in Δh and T_o occurred from day to day, in using constant P_o settings, the overall repeatability of the values of C_u was found to be better than 2%, the transducer sensitivity being adjusted accordingly. Full details of the calculation of C_u are given in Section 2.3.4.

Alternatively, the upper leading edge blowing supply could also be used as the supply for the anemometer calibration rig (see Section 3.2 and Figure 36). Dependent upon the nozzle size, a similar accuracy for nozzle exit velocity as for C_u could be attained.

As mentioned in Section 2.3.2 a difference existed between the upper and lower model plenum supplies, due to the difference in length of

pipe runs. This was also the case on the tip jet supply. Where the main supplies exhausted into a near stagnant plenum, the tip jets maintained the asymmetry through the blowing slot. For this reason, a small restrictor valve was placed in the shorter tip jet supply line enabling equalisation of the blowing rates. This valve had to be adjusted according to the slot height and unfortunately slightly reduced the capability of the tip jets to control three-dimensional effects.

Serious instabilities were encountered on the RL6D dome valves in the form of a resonance between the valve lip and seat just as the valve opened. As the valve 'cracked', a region of high suction was formed between the lip and seat causing the valve to close and then open, once more, under the dome pressure. The resultant 'trumpeting' was so severe as to prevent testing of the aerofoil. After extended tests the only satisfactory solution was to increase the valve spindle damping by filling the spindle support cavity with Tate and Lyle 'Golden Syrup'. All oils tested lacked sufficient viscosity and all greases failed to flow back to the closed position. The application of syrup not only stopped the resonance but also reduced the low frequency variations in blowing supply from sundry causes such as interactions with the Arca valve.

2.3.4 Evaluation of the blowing momentum coefficient, C_μ

The blowing momentum coefficient is given by

$$C_\mu = \frac{\dot{m} V_J}{\frac{1}{2} \rho V_\infty^2 S} \quad (2.4)$$

now for two-dimensional tests

$$C_\mu = \frac{\dot{m}_{2D} V_J}{\frac{1}{2} \rho V_\infty^2 C} \quad (2.5)$$

where \dot{m}_{2D} = mass flow per unit span

V_J = jet velocity

The value of the jet velocity was obtained from a small iterative procedure based on an isentropic expansion in the nozzle.

Since the stagnation temperature and pressure in the plenum are known, a value for ρ_o can be found.

$$\rho_o = \frac{P_o}{RT_o} \quad (2.6)$$

Assuming that the flow is incompressible, an initial value of the slot Mach number can be found.

$$M_J = \frac{\dot{m}}{\rho_o \times \sqrt{\gamma RT_o} \times \text{area of slot}} \quad (2.7)$$

Due allowance was made for the reduction in slot span due to the presence of the tip jets, when relating the orifice plate calibrated flowrate to the aerofoil slot flow.

This now allows a first estimate for ρ , since

$$\frac{\rho_o}{\rho} = \left(1 + \frac{M_J^2}{5} \right)^{2.5} \quad (2.8)$$

The procedure can be repeated and the value found for M_J which solves the loop. This takes no account of any losses or boundary layer growth within the slot.

The value of the plenum stagnation pressure is found relative to the unblown slot exit static pressure. The error caused by not referring to the actual slot exit static pressure in the presence of the jet was small since low blowing rates were used and the free stream dynamic pressure was small compared with the plenum stagnation pressure.

As a check on the calculation procedure, the trailing edge jet velocity was determined by three independent methods.

- i) Assuming isentropic conditions at the nozzle gives,

$$V_J = \left[2RT_D \left(\frac{\gamma}{\gamma - 1} \right) \left(1 - \left(\frac{P_\infty}{P_D} \right) \right)^{\frac{\gamma-1}{\gamma}} \right]^{\frac{1}{2}} \quad (2.9)$$

$$\dot{m}_{isen} = A_J P_D \left[\frac{2\gamma}{(\gamma - 1)RT_D} \left(\left(\frac{P_\infty}{P_D} \right)^{2/\gamma} - \left(\frac{P_\infty}{P_D} \right)^{\frac{\gamma+1}{\gamma}} \right) \right]^{\frac{1}{2}} \quad (2.10)$$

where T_D = duct temperature ($^{\circ}\text{K}$)

P_D = duct pressure (Nm^{-2})

P_∞ = free stream static pressure (Nm^{-2})

The duct variables were assumed to be the plenum stagnation quantities. The slot contraction ratio for this test was 70 : 1.

- ii) A single sensor hot wire probe was placed in the middle of the jet and the velocities calculated from its calibration. The probe was moved 0.001 in (0.025 mm) either side of the centre-line of the slot and no velocity change was apparent. The heat loss to the model had a large effect on the performance of the probe.

- iii) The C_p calculation program could be used to determine the slot velocity.

The results of the three methods are shown in Figure 37. The agreement is surprisingly good. The deviation of the C_p calculation could be due to losses in the slot, while the apparent increase measured by the hot wire could be due to boundary layer build-up in the slot and probe blockage at high speeds, and to model interference effects at low speeds.

The slot height for this test was 0.021 in (0.52 mm) and the agreement for jet velocity over the test range (up to $V_j/V_\infty = 4$) was considered satisfactory and not to warrant further investigations.

3. INSTRUMENTATION

3.1 Pressure Data Acquisition System

A block diagram of the system is shown in Figure 28. Two 48 port 'J' series Scanivalves were used, allowing alternate tapings on alternate Scanivalves to provide the sequence for the static tapings. This enabled each transducer to return to ambient pressure before the experimental pressure was applied, thus avoiding pressure lag problems.

The Scanivalves were controlled by an online PDP-8 computer which stepped them in sequence and analysed the data. At each measuring point the transducer was allowed a settling time of 250 ms and then the pressure at the transducer face was found as the average of 50 samples over a 50 ms period.

The transducers were a Statham ± 2.5 p.s.i.d. and a Setra ± 5 p.s.i.d.; they were identically calibrated over the same range using the low pressure transducer calibration system (see Section 3.1.1). The range of the calibration was determined to give the maximum signal permissible for the tests envisaged within the 10 volt A/D converter range of the PDP-8 computer. The derived transducer sensitivity was then input as a program constant. The maximum pressure coefficients allowed were ± 5.5 based on a free stream dynamic pressure of 613 Nm^{-2} . This range was only possible because of the low blowing rates being used; previous researchers had encountered pressure coefficients in excess of -20 in the trailing edge suction peak.

The analysis of the data was performed, as shown in Figure 39, by a Scanivalve control program on the PDP-8, discussed further in Appendix I. Briefly, points were interpolated midway between adjacent data points using a Lagrangian interpolation technique. At the leading and trailing edges, where high curvature of the distributions was present, certain restrictions were placed on the interpolation routine to reduce instabilities. These had a small effect upon the overall performance results. The lift coefficients and pressure drag coefficients were evaluated using a simple numerical integration technique.

It is usual to evaluate the normal force coefficients including allowances for the reaction thrust of the jet.

$$\begin{aligned} C_N &= C_{N_m} + C_\mu \sin \mu \\ C_D &= C_{D_m} - C_\mu \cos \mu \end{aligned} \quad (3.1)$$

where μ is the angle of the jet exit to the horizontal and the subscript m indicates the initial measured quantity. Since this work was mainly concerned with the detailed trailing edge investigation, these corrections were not included in the computer program. The effect on the lift coefficient would be small since C_μ was generally less than 0.03 and μ was small. The effect on the drag force is much larger; however the initial accuracy of the drag integration was questionable due to the lack of static pressure tappings around the trailing edge.

The results, including the interpolated values, were displayed on a CRT display at the tunnel console, enabling an immediate visual check on the flow.

The aerofoil pressure distributions were used to evaluate the effective incidence of the aerofoil and this will be described in detail in the next section.

3.1.1 Evaluation of the aerofoil effective incidence

Since an aerofoil with a rounded trailing edge does not exhibit the well known 'Kutta' condition of conventional sharp trailing edged aerofoil sections, the determination of the effective incidence is complex and subject to error. Kind³² used a method of comparing pre-drawn potential flow pressure distributions with the experimental results. This enabled the downwash correction to be calculated and the effective incidence deduced. This method has been adopted and improved in this study, by matching the experimental and theoretical pressure distributions over the leading half chord. The leading half chord was chosen

in order to avoid the major direct effects of the blowing jet which occur round the trailing edge.

The theoretical pressure distribution around an ellipse, given by Jones³³ for example, is

$$C_p = 1 - \left(\frac{A}{U_\infty}\right)^2 \left[\left(\frac{t}{c}\right)^2 + \left(1 - \left(\frac{t}{c}\right)^2\right) \sin^2(\alpha + \theta) \right] \quad (3.2)$$

$$\text{where } \frac{A}{U_\infty} = \frac{2\left(1 + \frac{t}{c}\right) (\sin \theta + \sin(\alpha + \gamma))}{1 + \left(\frac{t}{c}\right)^2 - \left(1 - \left(\frac{t}{c}\right)^2\right) \cos(2\alpha + 2\theta)}$$

$$\text{and } \gamma = \arcsin \left(\frac{C_L}{2\pi \left(1 + \frac{t}{c}\right)} \right) - \alpha$$

α = effective incidence, α_{eff}

$$0 < \theta < 2\pi \text{ such that } \frac{x}{c} = \frac{1}{2}(1 + \cos \theta)$$

$$\frac{y}{c} = \frac{1}{2}\left(\frac{t}{c}\right) \sin \theta$$

Thus, if θ is defined at the static tapping positions the theoretical pressure coefficients at these points could be determined for a given C_L and α_{eff} . The experimental leading edge half chord C_L was calculated as a first step. The value of the estimated α_{eff} was input to the Scanivalve control program by the operator. The program then evaluated a set of theoretical points and adjusted the value of the theoretical C_L until the integrated areas of the theoretical and experimental leading half chord distributions were equal.

A comparison of the measured pressure distribution with the potential flow solution was shown on a CRT display in the wind tunnel. The operator then 'visually' iterated to obtain the best fit to the pressure distribution over the leading half chord by successive estimates of the effective incidence.

The three major problems with this technique were:

- i) the model geometry differed slightly from that of the true ellipse, due to the circular arc leading edge and the forward facing blowing slot.
- ii) the effective incidence could only be determined to $\pm 1^\circ$ at any single data point.
- iii) the technique could not be used when the leading edge was blown since the forward jet flow caused too great a disparity between the theoretical and experimental distributions.

Examples of the displays produced by this technique are shown in Figure 40. Further discussion of the accuracy of this simple theoretical calculation is given in Section 5.1.1.

3.1.2 Low pressure transducer calibration

This system was for use where the required pressures were less than ± 30 in (0.76 m) of water. It consisted of a small pneumatic actuator which was coupled to the transducer and a water manometer. This simple system proved to be very reliable and accurate over its small range. Also it was simply adopted to enable both Scanivalve transducers to be calibrated at the same time, thus avoiding any sensitivity errors between them.

3.1.3 High pressure transducer calibration

This system was originally produced for use on the supersonic wind tunnel facility at Bath University. It consisted of a needle valve controller which allowed simultaneous pressure supply to two 'calibration standard' Wallace and Tiernan gauges, giving differential and absolute pressures, and to the required pressure transducer. The supply was vented to atmosphere via a short section of fine glass capillary tubing which allowed the system pressure to stabilise quickly.

The whole system was fed from the main blowing supply via the tip jet valve controller. This enabled the maximum calibration pressure to be set, avoiding any possible over pressures being applied to the transducer face.

The maximum range of this system was 80 p.s.i.g.

All transducers were calibrated using either of these two systems and showed negligible hysteresis. An example of the calibration of the two Scanivalve transducers using the low pressure system is shown in Figure 41.

It is important to note that the Scanivalve transducers were calibrated in situ as it was apparent that the operating temperature within the Scanivalve housing had a definite effect upon the calibration. The zero of these transducers was also found to be affected by the securing tension of the transducer retaining caps in the Scanivalves.

3.2 Hot Wire Anemometry

3.2.1 Calibration rig

All investigations and calibrations of the anemometer equipment were performed on the nozzle rig shown in Figure 36. This is a similar arrangement to that described in Section 2.3.2. for calibrating the orifice plates. By use of different size nozzles, velocities from

25 ms⁻¹ to 300 ms⁻¹ could be produced. The nozzles were all produced to the same geometric form shown in Figure 34.

The calibration rig used filtered air, as mentioned in Section 2.3.1, to improve probe life and reliability and was fitted with a rotating table which supported the various probe configurations.

An experimental investigation of the calibration jet was performed using a DISA dual sensor wire probe, the operation of which is discussed in Section 3.2.4. The results obtained showed the extent and development of the constant velocity core and the turbulence levels within the jet. These tests indicated that a probe could be centrally positioned up to 1 inch (25.4 mm) from the nozzle face without loss of jet velocity. The results are shown in Figures 42, 43. The orifice plate calibration discussed in Section 2.3.2 was used to determine the jet velocity at the nozzle.

The ability to position a probe away from the face of the nozzle increased the rotational limit of the rotary table by some 40°. This was of particular importance in the calibration of the split film probe since it enabled the flow angle to become negative for the chosen probe geometry (see Section 3.3).

3.2.2 General comments on hot wire anemometry

In general the hot wires and the associated instrumentation were operated in accordance with the relevant operation manual.

The wire anemometer bridges were adjusted to operate at their maximum bandwidth at a typical expected flow velocity and an upper limit frequency response of 40 KHz was attainable (see Figure 44).

It was assumed that the wire probes followed a Kings Law type relationship given by:-

$$E_B^2 = E_O^2 + BU^n \quad (3.3)$$

where B and n are the calibration constants.

The constant n was to be measured as it was felt that the value of 0.5, usually assumed, was unreliable over such a wide velocity range.

It can be shown that the effects of ambient temperature drift are confined to a variation of B , the intercept of the log plot, rather than the slope n . Kristensen⁴⁴ proposed a solution to this problem, which has been extended by Starsmore⁴⁵ and as a final exact solution (see Appendix II for details) can be shown to be

$$E_B^2 = E_O^2 + B \left(\frac{1}{1 + \frac{\alpha}{\sigma}} \right) U^n \quad (3.4)$$

where

σ = overheat ratio

$$\alpha = \frac{(T_{\text{fluid}} - T_{\text{cal}})}{T_{\text{fluid}}}$$

T measured in $^{\circ}\text{K}$

This relationship not only allowed correction to calibrations for ambient temperature drift but also allowed the calibration temperature to be corrected to a single value if the run temperature varied. The effect of varying the required calibration temperature at a fixed overheat ratio is shown in Figure 45.

The standard equation can be reduced to:-

$$\left(\frac{E_B^2}{E_O^2} - 1 \right) \left(1 + \frac{\alpha}{\sigma} \right) = \frac{B}{E_O^2} U^n \quad (3.5)$$

and by plotting the log of both sides, the values of B/E_O^2 and n can be found.

The following correction to the measured zero flow voltage was assumed, to take account of the influence of convective cooling. With the wire

aligned in the vertical plane:

$$E_o = 0.92 \times E_o \text{ measured} \quad (3.6)$$

An extensive investigation was performed into the effects of flow temperature upon the overheat ratio and calibration of wire probes. The usually adopted probe setting procedure is outlined below:

- i) zero probe cable resistance on anemometer bridge.
- ii) measure probe resistance r_p
- iii) set operating resistance on anemometer decades.

$$r_o = (1 + \sigma) r_p \quad (3.7)$$

- iv) operate probe in flow field.

Throughout this work, the DISA anemometers were unable to zero the cable resistances and consequently the resistance used to calculate the operating resistance was assumed to be

$$r_p = r_{\text{probe} + \text{cable}} - r_{\text{cable}} \quad (3.8)$$

The value of r_{cable} could be found from the resistance decades as that value necessary to give zero cable resistance.

It was also apparent that if allowance was made for variations in ambient fluid temperature while operating, then allowance should also be made for the value of the probe cold resistance varying with the moving fluid temperature. An extensive series of tests indicated that the value of n significantly decreased with increasing overheat ratio. Since the overheat ratio is a function of the difference between the probe operating temperature and the ambient fluid temperature, it seemed advisable to evaluate the operating resistance from a probe resistance measured in the presence of the moving fluid. This was

thought to be the only way of maintaining constant overheat ratio and hence constant calibration, over a period of time.

Equation (3.8) now becomes

$$r_p = r_{\text{probe} + \text{cable}} (\text{at moving fluid temp}) - r_{\text{cable}} \quad (3.9)$$

In the experimental arrangement already described, variations of fluid temperature from $+20^{\circ}\text{C}$ to -5°C were common, dependent upon the outside weather conditions and the air mass flow rate, whilst the ambient tunnel air varied from $+10^{\circ}\text{C}$ to $+35^{\circ}\text{C}$ depending on how long the wind tunnel had been running. The importance of the revised technique is apparent and tests indicated an improvement in the repeatability of the calibration constants for a given wire from $\pm 5\%$ to $\pm 1\%$.

A typical wire resistance temperature coefficient, α , given by

$$r_1 = r_0 (1 + \alpha(T_1 - T_0)) \quad (3.10)$$

was found to be

$$\alpha = 3.695 \times 10^{-3} \Omega \text{ per } ^{\circ}\text{C}$$

Hence a 10°C variation in ambient temperature would change the operating resistance by nearly 0.07Ω at an overheat ratio of 0.8. This would have a significant effect upon the zero flow voltage and the probe calibration in general.

The reason for the variation of calibration with overheat ratio is not clearly understood but may be a function of the change in thermal stress of the wire between the prongs caused by the change of operating temperature. The easiest solution was to adopt the above procedure and run at a constant overheat ratio of 0.8. This overheat ratio was chosen as a compromise between frequency response and probe life.

A further series of experiments indicated little variation in the calibration constants over extended periods of time. The reason for

this is thought to be the 'clean' air supplied by the 0.1 μm filter.

The calibration equation (3.5) was initially used in these tests; however, the small variations in n that have previously been discussed caused large variations in B because of the remoteness of the data points from the vertical scale. It was found more reliable to use the following equation:

$$\left(\frac{E_B^2}{E_O^2} - 1 \right) \left(1 + \frac{\alpha}{\sigma} \right) = \frac{B}{E_O^2} (10\rho M)^n \quad (3.11)$$

Examples of the two techniques are given in Figure 46. The values of n obtained from both techniques were consistently close to 0.4 and the improved confidence in the intercept from the second method is obvious.

The calibrations were all obtained by a linear regression method programmed on a PDP11/34. Typically, greater than 99.9% correlation was achieved and it was found sufficient to take only 5 or 6 experimental points to determine the calibration constants.

Boundary layer wire probes (5 μm diameter) and DISA D series bridges were used throughout the single sensor experiments.

Two data reduction techniques are available for hot wire anemometry. The unlinearised signals can be analysed by either an analogue or digital technique. The analogue technique is particularly suited to single wire operation and will be discussed in Section 3.2.3, while the digital technique offers many advantages where more than one sensor is used (see Section 3.2.4). It was decided not to use linearisers in this work since the controlling parameters were susceptible to ambient temperature variations evident as changes in the wire calibration constants.

3.2.3 Operation of single sensor wire probes

All single sensor probes were operated on the simple analogue system shown in Figure 47. The reduction of the turbulence data and determination of the mean velocity, including the effects of ambient temperature drift, were performed on a pocket programmable calculator using the inverse calibration equation and the recommendations of Mojola⁴⁶.

$$\bar{U} = \frac{a}{10\rho} \left[\frac{\left(\frac{\bar{E}_B^2}{\bar{E}_O^2} - 1 \right) \left(1 + \frac{\alpha}{\sigma} \right)}{\frac{B}{\bar{E}_O^2}} \right]^{1/n} \text{ ms}^{-1} \quad (3.12)$$

where a = speed of sound = $\sqrt{\gamma R T_F}$ ms^{-1}

$$\frac{\sqrt{u'^2}}{\bar{U}} = \sqrt{e^2} \frac{2}{n} \frac{\bar{E}_B}{(\bar{E}_B^2 - \bar{E}_O^2)} \quad (3.13)$$

where $\sqrt{e^2}$ is the r.m.s. of the fluctuating portion of the bridge signal and the bar signifies a time averaged quantity.

Extension of the simple analogue technique to dual and triple sensor probes is possible but requires the use of summing and multiplying circuits. Full details of the necessary relationships are given by Mojola⁴⁶.

An example of the effect of yaw angles in the plane of the prongs and normal to the wire is given in Figure 48. It is clear from this figure that the contraction effect of the prongs when the flow is normal to the prongs and wire produces approximately a 10% increase in the effective cooling velocity of the flow. Whereas when the flow is angled in the plane of the prongs, the effective cooling velocity

is a function of the sine of the yaw angle, representing the effective length of the wire in yaw.

3.2.4 Operation of dual sensor wire probes

Whilst it was not expected to use these probes for investigations around the trailing edge of the aerofoil due to their lack of spatial resolution, their operation was investigated to gain experience in the use of dual sensor probes. Each sensor of an X-array wire probe was calibrated normal to the airflow in exactly the same manner as a single sensor probe.

The digital analysis technique used by Starsmore⁴⁵ was adopted for this work since it was simpler and more adaptable than the equivalent analogue dual sensor technique. It consists of sampling the output of both wires at discrete time intervals and calculating the instantaneous velocity vectors for each time step. It has been shown that the instantaneous velocity vectors for an X-array dual sensor probe in the XY plane (see Figure 49 for co-ordinate system) are:

$$U = \frac{1}{\sqrt{2}} \sqrt{\frac{(q_1^2 + q_2^2)}{(1 + a^2)}} + \sqrt{\frac{(q_1^2 + q_2^2)^2}{(1 + a^2)^2} - \frac{(q_1^2 - q_2^2)^2}{(a^2 - 1)^2}}$$

$$V = \frac{(q_1^2 - q_2^2)}{2(a^2 - 1)U}$$
(3.14)

where q_1 = effective cooling velocity wire #1

q_2 = effective cooling velocity wire #2

a = direction sensitivity coefficient

A full derivation of these equations is given in Appendix II.

If a total of n samples is taken at a frequency f , then the time averaged mean quantities are given by

$$\begin{aligned}\bar{U} &= \frac{1}{n} \sum_{n=1}^n U_n \\ \bar{V} &= \frac{1}{n} \sum_{n=1}^n V_n\end{aligned}\tag{3.15}$$

At each sample point, the fluctuating velocities are then given by:

$$\begin{aligned}u'_n &= U_n - \bar{U} \\ v'_n &= V_n - \bar{V}\end{aligned}\tag{3.16}$$

$$\begin{aligned}\text{and } \overline{u'^2} &= \frac{1}{n} \sum_{n=1}^n (U_n - \bar{U})^2 \\ \overline{v'^2} &= \frac{1}{n} \sum_{n=1}^n (V_n - \bar{V})^2 \\ \overline{u'v'} &= \frac{1}{n} \sum_{n=1}^n (U_n - \bar{U})(V_n - \bar{V})\end{aligned}\tag{3.17}$$

Thus the time averaged mean and fluctuating quantities are simply deduced. Full details of the program developed for this method are given in Appendix II. The procedure can be repeated by reorientating the probe in the XZ plane to produce \bar{W} , w'^2 and $\overline{u'w'}$.

The value of a , where

$$a = \frac{\text{measured velocity}}{\text{actual velocity}}, \text{ for flow parallel to the wire}$$

is generally accepted to be 0.2. This was shown to be a reasonable assumption compared with the results measured in this work (see Figure 50).

The sampling frequency f , is desired to be as high as possible, or the sample size should be increased in order to 'capture' the maximum turbulence contribution. The sampling rate of the PDP11/34 A/D converter has a nominal maximum value of 3.4 KHz using the supplied system library routines. In practice this figure can only be approached dependent on the type of storage file management employed. A maximum rate of 2.6 KHz was attained for this study.

A total sample size of 2560 samples per wire was finally used as a compromise between accuracy and analysis time. This sample size showed negligible error in turbulence measurement compared to one of 32000, and gave an order of magnitude decrease in analysis time.

Block diagrams of the dual sensor analysis system and the related computer programs are given in Figures 51, 52 (and see also Appendix II). The filtered fluctuating components of each bridge signal are amplified to the maximum ± 2.5 volts permissible by the PDP11/34 A/D converter. The amplified fluctuating inputs were monitored on an oscilloscope to avoid saturating the A/D converter. The base signal r.m.s. and time averaged mean voltages, input to the computer, were then used to recreate the actual voltage, and hence the velocity, time history. In this manner the maximum fluctuating signal definition was obtained.

This data reduction technique was used to investigate the tunnel free stream turbulence levels and the calibration jet development (see Sections 2.2.2, 3.2.1).

3.2.5 Sources of error in the hot wire anemometry measurements

3.2.5.1 The temperature gradient across the wall jet

As has already been stated in Section 2.3.1, the blowing air supply temperature was very dependent upon the outside weather conditions. It was usual for the jet air temperature to be of the order of 10°C cooler than the surrounding tunnel air. Having indicated the dependence of a hot wire probe calibration on ambient temperature, the importance of the techniques previously described (see Section 3.2.2) to account for these variations becomes apparent. However since the wall jet produces a strong entrainment effect between the jet and the external flow, the existence of a temperature difference between the flows produces a temperature gradient across the flow which varies with downstream position, the cold blowing jet air gradually being heated to the ambient conditions.

Since the temperature gradients were indeterminate for this study, the effects were allowed for by using the jet temperature at slot exit to adjust the wire calibration. In this way the error was reduced for the high velocity measurements, but some discrepancies were apparent in the wall jet edge velocities compared with the split film measurements (see Figure 98, 99). Had the tunnel air temperature been used, the edge velocities would be more realistic but an equal percentage error to the previous low velocity measurements would have produced increased velocity errors in the jet velocity measurements. Short of attaching a small temperature sensor to the wire probe and measuring the actual temperature at each measurement point, the adopted method seems to be an acceptable compromise.

An attempt was made to measure the temperature gradient across the flow by detecting variations of the resistance of an unheated wire probe. However, lack of time for the necessary adjustment of the anemometer bridges prohibited precise measurements. It was also

considered unnecessary since the bulk of the trailing edge survey was to be performed using a split film probe which apparently was less susceptible to ambient temperature variations (see Section 3.3.1).

3.2.5.2 Non-radial traversing path

Due to the finite size and positioning of the traversing gear probe supports and the desire to place the hot wire probe as near to the slot as possible, it was necessary to offset the wire from the radial traversing plane (see Figure 53). When the probe was traversed in the configuration shown, an angular offset at the extent of travel of approximately 2° was typical. In the presence of longitudinal velocity gradients, errors in the measurement of the wall jet outer layer velocities were apparent.

The angular error was given by

$$\epsilon = \frac{\phi}{\left(1 + \frac{R}{y}\right)} \quad (\text{see figure 53 for notation}) \quad (3.18)$$

ϕ was typically less than 10° which gives an error of less than 2° for $R/y < 5$.

It was possible to position the probes such that the offset angle was zero, however it was felt that the advantages in being able to approach the slot exit with the probes outweighed the errors produced.

3.2.5.3 Wall and probe interference effects

The most usual consideration when using wire probes in close proximity to a solid wall is heat loss to the surface. It is usually assumed that the heat loss to the surface does not become significant until the probe is less than 0.004 in (0.1 mm) from the surface. However, in this study, velocity measurements as close as physically allowed by the probe prong radius (0.003 in, 0.075 mm) were apparently unaffected. This was thought to be due to the unusually high shear gradient close to the wall reducing the relative increase in measured velocity.

The probe support geometry (see Figure 53) was designed to minimise interference at the measuring point. The introduction of a normal obstruction in the curved wall jet tends to 'split' the flow and generate three-dimensional instabilities. It was assumed that the small projected area of the prong tips would cause minimal disturbance of the flow. The effect of probe interference upon the measured lift coefficient is discussed in Section 4.1.2, 5.4.1.2.

The results obtained in Section 3.2.3 for the effects of yaw in the plane normal to the wire indicate that negligible error would arise from small changes in orientation relative to the curved surface. This conclusion also implies that the normal velocity measured on a single hot wire will also include the V contribution.

$$U_n^2 = U^2 + b^2 V^2 \quad (3.19)$$

where b is the direction sensitivity coefficient in the plane normal to the prongs, usually equal to 1.1. Hence in regions of high flow angle relative to the surface (due to entrainment and jet growth), the hot wire will tend to overestimate the velocity. The wire probes were, in general, orientated slightly angled to the surface (~ 2 or 3°) to improve the definition of the reference point for the position control system.

To summarise, the maximum error in the wall jet velocity profiles occurred at the outer edge of the wall jet boundary layer and could be as high as $\pm 5 \text{ ms}^{-1}$ dependent upon flow conditions and probe position.

3.3 Split Film Anemometry

Split film probes are a relatively new type of probe marketed by Thermo Systems Inc.⁴⁷, and consist of two semicylindrical separate platinum films, sputtered onto a 0.006 in (0.15 mm) quartz rod. They offer a much improved spatial resolution (of the order of 8 times) compared with a conventional cross wire sensor and are approximately half the focussed volume of a laser anemometer system. A boundary

layer type probe is sketched in Figure 54.

The probe operates on the principle that:-

- i) The total heat transfer on both films gives a measure of the velocity vector perpendicular to the sensor.
- ii) The difference of heat transfer for the two films gives a measure of the velocity vector perpendicular to the plane of the splits on the sensor.

Hence, from i) assuming a Kings Law type relationship,

$$E_1^2 + k^2 E_2^2 = A + B U_n^n \quad (3.20)$$

This assumption is valid, since if the splits are considered small compared with the total film surface area, then the total heat transfer would follow a law similar to that of a single wire.

From ii)

$$E_1^2 - k^2 E_2^2 = f(U_n) \sin \theta \quad (3.21)$$

where θ is the angle between the plane of the splits and the normal velocity vector.

Therefore

$$U = U_n \cos \theta$$

$$V = U_n \sin \theta \quad (3.22)$$

$$\text{and } U = \sqrt{U_n^2 - V^2}$$

The constant K is described by the manufacturers as a correction for non perfect matching of sensors. In the limit, K must be equal to the ratio of the zero flow voltages and T.S.I. suggests that adjustment of the overheat ratios should be used to set K to unity. In the light of the experiments with hot wires, it was felt to be more reasonable to adjust the probe cold resistances on the bridge resistance decades to obtain $K = 1$: this enables a finer control of the value of K . It should also be noted that in order to minimise the offset from the actual resistances, as one film is increased in resistance so the other should be reduced, or vice versa. This means that the total resistance is unchanged and the total heat loss due to normal velocity U_n is also unchanged. In this manner, K is assumed equal to unity from here on.

Originally, it was hoped to operate these probes from two 55D01 DISA anemometers: however, one of these anemometers was found to be insufficiently stable to run the films concurrently. The films were therefore driven by a Prosser 6100 twin channel anemometer system. This system has a high/low bandwidth switch which simplifies the running of these probes. The low setting limits the bandwidth to 10 kHz while the high setting allows adjustment similar to that on a DISA anemometer. It was found that instability of these probes, due to thermal couplings across the quartz rod, was their major drawback. Three different modes of behaviour were experienced:-

- i) When using the DISA anemometers, since one channel was less stable, only 1 film could be run at a time. The large thermal couplings caused one film to drive the other and the situation was reversible but always of a 'hard over' nature. The phenomenon occurred even when the anemometers were run at the lowest gains and bandwidth with an overheat ratio of less than 0.1, independently of which film was started first and the duration of the probe cut-in time.
- ii) Using the Prosser system with the low bandwidth selected, a stable situation occurred and the probe operated normally.

- iii) With the Prosser system set to high bandwidth, a situation occurred where both films were running and film⁺2 was found to be slaved to film⁺1 i.e. for an increase in E_1 due to a change in flow angle, E_2 increased by the same amount.

The results of the above observations was that the probe had to be run at a reduced bandwidth. This showed however, only a 2% drop in detected r.m.s. readings compared with the high setting at the chosen overheat ratio of 0.5 and this was considered satisfactory.

3.3.1 Calibration

The calibration of these probes requires that the probes be set at a series of angles (in this case -5° to $+30^\circ$) relative to the plane of the splits and the bridge voltages recorded for a series of speeds. This provides the data necessary for all the constants to be derived. From equation (3.20)

$$E_1^2 + E_2^2 = E_{O1}^2 + E_{O2}^2 + BU_n^n$$

where

$$E_{O1,2} = E_{O1,2} \text{ measured} \times 0.92$$

to account for the effects of convective cooling upon the zero flow voltage.

The constants B, n can be derived in a similar manner to those for a single sensor hot wire, using only the zero angle data.

$$\log \left[\frac{E_1^2 + E_2^2}{E_{O1}^2 + E_{O2}^2} - 1 \right] = \log \frac{B}{(E_{O1}^2 + E_{O2}^2)} + n \log U_n \quad (3.23)$$

No allowance for the variation of the ambient temperature was included in the calibration. If a similar correction to the wire probe was used, the induced effects were found to be far more significant on results. This is thought to be due to running at a lower overheat ratio, $\sigma = 0.5$, compared with that used for the wire probes and to the large thermal capacity of the probes. Time did not allow a full investigation of this effect and good repeatability was achieved without the inclusion of a temperature correction. This will be shown in Section 3.3.3.

It should be noted that, without further investigation, it is not recommended to run these probes up to the same wind speeds as wire probes for two reasons:-

- i) structural integrity
- ii) the frequency of vortex shedding from the probe becomes significant relative to the effects of turbulence.

The author is aware of experiments at up to sonic speeds (Boeing Corpⁿ, private communication) but is unable to comment on the results achieved.

The angular calibration constants are somewhat more difficult to obtain. From equation (3.21)

$$E_1^2 - E_2^2 = f(U_n) \sin\theta$$

At $\theta = 0^\circ$, E_1 should equal E_2 ; this is arranged by setting K to unity and is also dependent upon the actual split geometry relative to the datum probe axis. The manufacturers suggest that,

$$f(U_n) = C U_n^m$$

$$\therefore E_1^2 - E_2^2 = C U_n^m \sin\theta$$

(3.24)

The system for derivation of these constants C, m is suggested as follows.

- i) Plot E_1 and E_2 versus θ for each speed. These are straight lines for a fixed U_n and the crossover point, θ_{error} , is the deviation of the probe setting from the plane of the splits. θ_{error} should be a constant for a given probe unless the probe deflects under wind load.
- ii) Amend the yaw angles, using the deduced θ_{error} , and plot $(E_1^2 - E_2^2)$ versus $\sin(\theta - \theta_{\text{error}})$. This results in a series of straight lines for each given speed. The lines should all pass through the origin if K has been correctly measured. They also show the equation (3.24) to be of the right form, since the gradient of each line, $C U_n^m$, is a constant for any given speed.
- iii) Plot the log of the gradients in ii) against the log of the fixed speeds. The slope of this line represents m.
- iv) The value of C can be found to give the best fit to the experimental data. It should be noted that extrapolation to the axis to give C is not possible as the response of the probe changes considerably at lower speeds, as will be indicated.

Figure 55 - 59 show a typical set of calibration data for these probes. The normal and angular calibration for the probe used in the experimental work were found to be,

$$E_1^2 + E_2^2 = E_{O_1}^2 + E_{O_2}^2 + 41.77 U_n^{0.386} \quad (3.25)$$

and

$$E_1^2 - E_2^2 = 9.856 U_n^{0.566} \sin \theta \quad (3.26)$$

It is interesting to note that the value of the normal index, n , was very similar to that typical of a single wire probe. This would seem reasonable since, if the splits are assumed small in area compared with the total sensor surface area, then the split film probe would lose heat to the air in a similar manner to that of a fine wire.

It should also be stated that the validity of this type of angular calibration has not been demonstrated at high angles to the plane of the splits. Obviously, as θ approaches 90° to the plane of the splits, the calibration loses its sensitivity to angular variation. Since this area was not of interest in the current work it was not pursued further.

Also, at very low speeds, the split film sensor ceases to respond to angular variations altogether. This is due to the flow at low Reynolds numbers approaching the simple inviscid flow case. It is suggested that the use of this type of probe in either, flows of high angular variation or, flows giving low probe Reynolds numbers should be regarded with caution.

The calibration of the split film probe was not found to vary with time by any significant amount indicating a resistance to contamination and oxidation, problems associated with wire probes. It is however advised that the probes are 'burnt-in' for a short period (15 - 30 minutes) prior to establishing a calibration. This technique appears to stabilise the films and their quartz coatings to provide a more repeatable operation.

3.3.2 Data reduction

In terms of data reduction, split film probes can be treated exactly like a dual sensor wire probe. The discussion given in Sections 3.2.2, 3.2.3, 3.2.4. regarding the use of analogue or digital analysis techniques applies equally well.

The digital technique is very similar to that described in Section 3.2.4 except that the instantaneous velocities of each sample are derived directly from the calibration equations. Equation (3.25) can be used to give the value of U_n and θ can be obtained from (3.26). This gives the magnitude and direction of the instantaneous velocity vector, allowing the normal components to be derived from (3.22). The time averaged means of the normal components are found and used to deduce the normal fluctuations of each sample point. The normal and shear stresses are then simply obtained, similarly to the dual wire sensor system. Appendix II gives full details and a listing of the analysis program. The digital method was used throughout this work. The major advantage of the simplicity of the data reduction equations was that the computer analysis time was an order of magnitude less than the comparable cross wire system. This enabled a real time analysis to be performed.

The analogue method is inherently more complicated electronically since it involves the use of a number of summing and multiplication circuits. Since little has been published regarding the use of split film probes, a full derivation of the analogue turbulence equations, and the assumptions made, is given here for the benefit of other researchers. These equations have previously been published in T.S.I. TB20⁴⁷ but unfortunately the equation for $\overline{u'v'}$ was incorrect. The equation was given as

$$\overline{u'v'} = \frac{\overline{U}^2}{(m-1)CU^m} \overline{(E_1 e_1 - E_2 e_2)} \quad (3.27)$$

where e_1 and e_2 are the fluctuating portions of E_1 and E_2 . This is obviously wrong, since

$$\overline{E_1 e_1 - E_2 e_2} = 0$$

The correct derivation for $\overline{u'^2}$, $\overline{v'^2}$ and $\overline{u'v'}$ is as follows:-

From equations (3.20), assuming $K = 1$ and

$$E_{1,2} = \bar{E}_{1,2} + e_{1,2}$$

$$U = \bar{U} + u'$$

$$V = \bar{V} + v'$$

then

$$\begin{aligned} (\bar{E}_1 + e_1)^2 + (\bar{E}_2 + e_2)^2 &= A + BU^n \\ &= A + \bar{B}\bar{U}^n \left(1 + \frac{u'}{\bar{U}} + \frac{av'^2}{2\bar{U}^2} \right)^n \end{aligned}$$

Multiplying out the L.H.S. and expanding the R.H.S. gives, ignoring third order terms

$$\begin{aligned} (\bar{E}_1^2 + \bar{E}_2^2) + 2(\bar{E}_1 e_1 + \bar{E}_2 e_2) + (e_1^2 + e_2^2) \\ = A + \bar{B}\bar{U}^n + \bar{B}\bar{U}^n n \left(\frac{u'}{\bar{U}} + \frac{a^2 v'^2}{2\bar{U}^2} + \frac{(n-1)u'^2}{2\bar{U}^2} \right) \end{aligned}$$

now, if the mean flow is aligned with the plane of the splits

$$\bar{E}_1^2 + \bar{E}_2^2 = A + \bar{B}\bar{U}^n$$

then

$$2(\bar{E}_1 e_1 + \bar{E}_2 e_2) + (e_1^2 + e_2^2) = n\bar{B}\bar{U}^n \left(\frac{u'}{\bar{U}} + \frac{a^2 v'^2}{2\bar{U}^2} + \frac{(n-1)u'^2}{2\bar{U}^2} \right)$$

squaring both sides and ignoring triple products

$$\left[2(\bar{E}_1 e_1 + \bar{E}_2 e_2) \right]^2 = \left[n \bar{B} \bar{U} n \right]^2 \frac{u'^2}{\bar{U}^2}$$

therefore, time averaging and taking the square root

$$\frac{\sqrt{\overline{u'^2}}}{\bar{U}} = \frac{2}{n \bar{B} \bar{U} n} \left[\overline{(\bar{E}_1 e_1 + \bar{E}_2 e_2)^2} \right]^{1/2} \quad (3.28)$$

To obtain the shear stress equation, consider (3.24). If the mean flow is aligned in the plane of the splits, such that

$$\bar{E}_1^2 - \bar{E}_2^2 = 0$$

$$\text{and} \quad \sin \theta = \frac{v'}{U_n}$$

then

$$2(\bar{E}_1 e_1 - \bar{E}_2 e_2) + (e_1^2 - e_2^2) = C U_n^{m-1} v'$$

Therefore, by expanding U_n as before

$$\text{R.H.S.} = C v' \bar{U}^{m-1} \left(1 + (m-1) \left(\frac{u'}{\bar{U}} + \frac{a^2 v'^2}{2 \bar{U}^2} \right) \right)$$

$$2(\bar{E}_1 e_1 - \bar{E}_2 e_2) + (e_1^2 - e_2^2) = C \bar{U}^m \frac{v'}{\bar{U}} + (m-1) u' v' \frac{C \bar{U}^m}{\bar{U}^2} \quad (3.29)$$

time averaging

$$\overline{e_1^2} - \overline{e_2^2} = (m-1) C \bar{U}^m \frac{\overline{u' v'}}{\bar{U}^2}$$

$$\therefore \quad \overline{u' v'} = \frac{\bar{U}^2}{(m-1) C \bar{U}^m} (\overline{e_1^2} - \overline{e_2^2}) \quad (3.30)$$

This is an interesting comparison with the usual analogue cross wire equation which is also a function of the difference of the two wire r.m.s. values.

If equation (3.29) is squared, then, ignoring triple products

$$4(\bar{E}_1 e_1 - \bar{E}_2 e_2)^2 = (\bar{C}\bar{U}^m)^2 \frac{v'^2}{\bar{U}^2}$$

Time averaging and taking the square root yields

$$\frac{\sqrt{v'^2}}{\bar{U}} = \frac{2}{\bar{C}\bar{U}^m} \left[(\bar{E}_1 e_1 - \bar{E}_2 e_2)^2 \right]^{\frac{1}{2}} \quad (3.31)$$

These equations are not particularly difficult to solve but they do require that the mean flow vector is aligned in the plane of the splits. Any deviation from this is significant since $(\bar{E}_1^2 - \bar{E}_2^2)$ has been ignored and this could be orders of magnitude greater than the other terms left in the equation. The digital method is far simpler in assumptions and does not require the mean flow to be aligned in the plane of the splits, providing obvious advantages in a highly curved flow.

3.3.3 Operation

The split film probes were powered from a Prosser 6100 twin channel anemometer as discussed in Section 3.3. The probes were mounted with the plane of the splits tangential to the local surface and traversed radially using the traversing gear previously described in Section 2.1.4. The position control system (see Section 2.1.5) was used to set the datum zero position of the probes relative to the local surface and the sensor axis could be brought to within 0.009 inches (0.23 mm) of the surface. This was the minimum distance possible dictated by the ceramic support tubes at the ends of the sensor. It was assumed that the measurement position coincided with the sensor

axis. Traverses of the wall jet could then be performed as for a wire probe described in Section 2.1.5.1.

Excellent repeatability was obtained for velocity profiles around the trailing edge of the aerofoil (see Figure 60) justifying the assumptions regarding ambient temperature variations. The data from the probes was analysed at each measurement point and took approximately 10 seconds to give values of \bar{U} , \bar{V} , $\overline{u'^2}$, $\overline{v'^2}$, $\overline{u'v'}$.

3.3.4 Sources of errors in the split film anemometry measurements

Unlike the single wire probes, the split film probes did not suffer from being offset from the traversing gear radial axis nor did the flow temperature gradient across the flow appear to affect the results. However a number of other possible sources of error must be mentioned.

3.3.4.1 Wall effects

Because of the large thermal capacity of the split film probe compared with a wire probe (the diameter of a split film probe is approximately 30 times that of a wire probe) and the orientation of the plane of the splits, the split film probe is more subject to errors caused by heat loss to the surface. Since it was necessary to bring the probe as close to the wall as physically possible, a technique of equalising the bridge voltages, in the presence of the airflow, at some small distance from the wall was adopted. The technique was similar to that for reducing K to unity, (see Section 3.3) and involved small changes in the film cold resistances on the anemometer resistance decades. These adjustments seemed valid since at some small distance from the surface, the local flow angle should still be nearly tangential to the local surface. Also, it was attempted to make these adjustments at or near the velocity maximum to avoid problems of shear flow on the finite probe diameter (see Section 3.3.4.6). This technique obviously is open to criticism but appeared to provide good representative results for the time average mean velocities down to the minimum distance from the wall.

However a distinct effect upon the turbulence measurements close to the wall was also apparent. The heat loss to the surface appeared to increase the measured turbulence within a given distance from the wall (see Section 5.4.3.1). This would seem reasonable since the presence of the wall would cause an asymmetry in the response of the films and hence an increase in the measured turbulence. From the data recorded it was decided that all split film turbulence data within 0.036 in (0.9 mm) should be regarded as unreliable.

3.3.4.2 Probe geometry

From Figure 52 it is clear that the plane of the splits is offset from the probe support axis by approximately 1° . The offset whilst appearing positive from Figure 52 would be of the sense to produce a negative offset in measured flow angle.

3.3.4.3 Flow curvature

Due to the finite size of the sensor cylinder, the high curvature of the flow produces a movement of the front stagnation point towards the surface. The effect can be shown to be small compared with the geometrical considerations of the previous sections, being of the order of only 10 seconds of arc.

3.3.4.4 Frequency response

As has already been stated, (see Section 3.3), the split film probes had to be operated at a reduced bandwidth in order to maintain probe stability. This caused a severe reduction in the detected turbulence levels, in some cases by a factor of 4 compared with hot wire results. Also it is reasonable to suggest that the large relative size of the split film probe will cause it to be unaffected by eddies of smaller size than the probe diameter. This would also appear as a reduction of the detected turbulence levels. Examples of these effects will be shown and discussed in more detail in Section 5.4.3.

3.3.4.5. Probe interference

The flow effects produced by introducing a split film probe into a highly curved wall jet with severe positive and negative pressure gradients were difficult to determine. In general any interference with the flow causes the jet to shear and roll-up behind the obstruction. The extent to which the film probe affected the flow was not investigated but all possible precautions were taken in the probe support geometry to minimise the effects. A similar but slightly smaller reduction in lift coefficient to that noted in Section 3.2.5.3 for wire probes was observed suggesting that the film probes disturbed the flow to a lesser extent than the wire probes and their supports.

3.3.4.6 Shear flow effects

This was effectively an error of spatial resolution. If the probe is in the presence of positive shear an effect opposite to heat loss to the surface would result: vice versa for negative shear. No corrections were applied to the results to account for the effects of shear gradient; however it is suggested that the correction would be of similar form to that for a pitot tube in shear flow (see Section 3.4.1.2). Little noticeable error was produced between the mean velocity profiles from the split film probes compared with the wire probes as discussed in Section 5.4.2.

3.4 Radial Static Pressure Measurement

In the majority of boundary layer research the determination of normal static pressure distributions is not necessary and the assumption of $\partial p / \partial y = 0$ is sufficient. However, in the case of a highly curved flow a static pressure gradient must exist due to the streamline curvature. In particular, where jet flow exists and the velocities and shear gradients are high, the $\partial p / \partial y$ terms in the radial angular momentum equations become dominant. In general, past researchers have made two basic assumptions regarding the flow:-

- i) that the streamlines are all locally parallel and concentric about the centre of curvature of the local surface, thus:-

$$R = R_0 \left(1 + \frac{y}{R_0} \right) \quad (3.32)$$

This assumption will be shown to be invalid in Section 5.4.2.

- ii) that the radial static pressure distribution can be given by a simple force balance

$$\frac{\partial p}{\partial y} = \frac{\rho U^2}{R} \quad (3.33)$$

Provided that U could be defined as a function of y and that the streamlines were concentric about some known centre such that R could be found also as a function of y , this simple balance could be of use. However neither U nor R is a simple function of y . Many researchers have recorded the overall static pressure difference across curved wall jets and have shown some agreement between experiment and the simple force balance if a mean value for U is assumed to apply across the flow. However, a detailed knowledge of the radial static pressure distribution is of great importance if a satisfactory closure of the governing equations of highly curved wall jets is to be achieved.

Englar²⁸ attempted to measure the distribution within the jet by using a vertical sharp edged plate mounted on the trailing edge, with a series of static tapings normal to the trailing edge cylinder. These results indicated a departure from the expected pressure distribution, (see Figure 61) and will be further discussed in Section 5.3.1. Englar's technique was thought unsatisfactory due to the interference effects at the junction of the plate and the trailing edge cylinder. The effect of having a vertical plate within the wall jet flow was also suspected to be causing large three dimensional disturbances.

Conventional static pressure probes cannot be used because of the highly curved nature of the wall jet flow, the large induced flow angles and the small scale of the flow to be examined.

Pache⁴⁸ described a method using a hot wire probe positioned alongside a total head tube, the static pressure being deduced from Bernoulli's incompressible equation. The method was shown to work for flat plate boundary layers and was adopted in this work for a survey of the trailing edge wall jet. This method was also used by Dvorak and Woodward⁴⁹ to determine the radial static pressure distribution over a slotted flap arrangement. The major problem with this method was the relative magnitudes of the terms in Bernoulli's equation.

$$(p - p_{\text{atmos}}) = (P_o - p_{\text{atmos}}) - \frac{1}{2} \rho (\bar{u}^2 + \bar{v}^2 + \bar{w}^2) \quad (3.34)$$

Usually, the working section static pressure is set to atmospheric pressure by venting the high speed working section. This implies that, P_o (relative to atmosphere) and the dynamic head are of equal magnitude. Hence the differencing of two equal large quantities to obtain a small quantity is subject to large errors. As mentioned in Section 2.2.1. the tunnel used for this research was run with the high speed working section vents closed to avoid air inflow problems. Consequently, the total head of the airflow was approximately atmospheric. This implies a much greater confidence in the values of the static pressure deduced from (3.34) since $(p - p_{\text{atmos}})$ was of the same magnitude as the dynamic head and the total pressure relative to atmosphere was comparatively small.

A sketch of the system used is shown in Figure 62. The total head tube was a flattened stainless steel tube (0.019 in, 0.48 mm thick) and the pressure was measured on an alcohol manometer. This type of probe is far less sensitive to flow angle compared with a conventional static pressure probe. A correction, suggested by Young and Maas⁵⁰

as:-

C-2

$$\frac{Z}{D} = 0.13 + 0.08 \frac{d}{D} \quad (3.35)$$

Z = offset

d = internal bore of tube

D = outside diameter of tube

was applied to take account of the effect of the sheared flow field on the pitot tube.

The pitot tube and the hot wire were mounted approximately 0.25 in (6.35 mm) apart to avoid lateral interference effects and were positioned on a common axis using a travelling microscope. The position control system described in Section 2.1.5. was used to control the datum zero position of the probe combination. The hot wire was used as the position detector and the rigidity of the system could be estimated since the reference point cut off could be set to allow the pitot tube to just contact the surface. As the pitot probe contacted the surface, so it became energised with the 5 kHz signal. This gave a step in the field intensity around the wire sensor and increased its positional sensitivity. Relative movement of the two probes could then simply be judged by the difference in the datum positions as shown on the step counter. The deflection using this probe arrangement was shown to be negligible.

3.4.1 Sources of error in the radial static pressure measurement

A summary of the effects of possible errors in the measurements on a typical wall jet static pressure distribution is shown in Figures 63, 64.

3.4.1.1 Effect of turbulence

Equation (3.34) contains an allowance for the turbulent energy in the flow. If it is assumed that:-

$$p = p_o - \frac{1}{2} \rho U^2$$

and that

$$U = \bar{U} + u' + v' + w'$$

then

$$u^2 = \bar{U}^2 \left(1 + \frac{2(u' + v' + w')}{\bar{U}} + \frac{(u' + v' + w')^2}{\bar{U}^2} \right)$$

Time averaging gives

$$\overline{u^2} = \bar{U}^2 \left(1 + \frac{\overline{u'^2} + \overline{v'^2} + \overline{w'^2}}{\bar{U}^2} \right)$$

assuming the shear terms to be small.

Then since the measured pressures are automatically time averaged quantities, equation (3.34) can be deduced.

If the longitudinal turbulence intensity $\sqrt{\overline{u'^2}}/\bar{U}$ was of the order of 10% at a velocity of 50 ms^{-1} , then the correction $\overline{u'^2}$ was approximately 1% of the dynamic pressure. Variations of this order can be ignored. Similarly even if $\overline{v'^2}$ and $\overline{w'^2}$ were assumed of the same magnitude, the overall effect could still be ignored.

Turbulence levels of 10% were assumed not to affect the total head tube readings.

3.4.1.2 Effect of shear flow

The effects of the highly sheared flow are significant only for the pitot tube assuming the hot wire to be negligibly small. The existing data on the effects of sheared flow on pitot tube measurements are very scant and most researchers use the standard corrections proposed by Young and Maas⁵⁰ (see Section 3.4). The effect of this correction was to provide a constant effective tube centreline offset in the direction opposite to the shear gradient and takes no account of the actual magnitude of the shear. This is not considered satisfactory but must suffice in the absence of an alternative. For the pitot tube used the offset was only approximately 0.002 in. (0.05 mm). Results for two different sized pitot tubes showed little difference in the measured total pressure. It was therefore assumed that while a correction should be applied, it had no pronounced effect upon the trends of the results.

A third even smaller probe was also tested, this being round, square faced and 0.011 in (0.27 mm) outside diameter, but two problems prevented its use:

- i) the excessive lag time required to achieve a steady pressure reading.
- ii) the probe was insufficiently rigid and the highly curved flow accentuated this problem.

3.4.1.3 Errors in hot wire anemometry

All the relevant precautions discussed in Section 3.2.5 were used and the anemometry results were considered satisfactory.

3.4.1.4 Probe geometry

The two probes were mounted approximately 0.25 in (6.35 mm) apart laterally and the cross interference was assumed to be negligible.

The probes were assumed not to have deflected under aerodynamic load. This seemed reasonable considering the accuracy of the position control system for the hot wire and the rigidity of the pitot probe support. No deflection was apparent when checked after each run.

The flow angle data provided by the split film probes showed angles not greater than $\pm 10^\circ$. Hence, if it could be assumed that both the hot wire and total head tubes would provide acceptable data for flow angles up to $\pm 10^\circ$ from the probe axes, then the angular effects on the radial static pressure distribution should be negligible.

3.4.1.5 Air density

The problem was not simply of compressibility, although density gradients must exist within a high velocity wall jet, but of defining the datum density value in the flow which had a temperature gradient. As a compromise, the density of the air at the jet exit was used, as calculated by the Cu calculation program (see Section 2.3.4). This value was based on the flow rate and ambient conditions.

4. PRESENTATION OF RESULTS

This section summarises the results obtained; detailed discussion of the results is reserved for Chapter 5.

4.1 Overall Performance

4.1.1 No blowing performance

Figure 65 shows the lifting performance of the unblown aerofoil measured using the pressure data acquisition system (see Section 3.1) at a test Reynolds number of 1.3×10^6 based on the aerofoil chord. The free stream velocity was 31.9 ms^{-1} including a solid blockage correction (see Section 2.2.4). An estimation of the performance obtained from the method of Dvorak³⁸ is also shown and is in good agreement.

The measured three-dimensional lift curve slope was found to be 3.25 per radian. The value for a two-dimensional ellipse at a similar Reynolds number from Hoerner⁵¹ was found to be 4.0 per radian. The experimental results contain no allowance for the low aspect ratio of the model or wall/end plate interference effects. The tip jet blowing system was not used for these tests.

Examples of the measured pressure distributions for the unblown ellipse are given in Figures 66, 67. Theoretical pressure distributions obtained from equation (3.2) assuming the measured lift coefficients and incidences are shown together with distributions obtained from the viscous/potential flow calculation of Dvorak and Kind³⁸.

4.1.2 Trailing edge blowing only

Figures 68, 69 show the overall performance of the aerofoil as a function of trailing edge blowing momentum coefficient for a range of geometric incidences. The effects of slot height, hot wire probe interference and tip jet blowing are indicated for a range of blowing rates at $\alpha_0 = 0^\circ$. The increased slot height shows an improved performance, whilst it is obvious that the probe interference may account for a reduction of as much as 20% in the lift coefficient by

disrupting the trailing edge suction peak. The hot wire probe was positioned approximately 1 in (25 mm) to one side of the static tapings.

Figures 70, 71 show examples of the CRT display from the effective incidence calculation (see Section 3.1.1) and also some examples of the measured pressure distributions in the presence of trailing edge blowing. The effective incidence calculation was used to produce the downwash corrections for a range of α_G and C_{μ} shown in Figure 72. The corrections deduced by Kind³² are indicated and show good agreement with the positive α_G results. Using those corrections, curves of C_L against C_{μ} for constant effective incidence are obtained (see Figure 73). Results from Kind³² and the program CIRCON³⁵ are also indicated in Figure 73, the agreement with the experimental work being satisfactory. Some further typical results for different ellipses and aerofoil section are shown in Figure 74 and indicate the high lift augmentation capability of circulation controlled aerofoils compared with jet flap arrangements.

The measured pressure drag coefficients are shown in Figure 75 for a range of α_G and blowing momentum coefficients. The increase in the pressure drag due to the high suction around the trailing edge is clearly evident. The effect of including the jet reaction component, equation (3.1) is indicated.

4.1.3 Leading edge blowing only

Figure 76 shows the effect of leading edge blowing alone upon the aerofoil performance at $\alpha_G = 5^\circ$. Initially the C_L reduces quickly, then a more linear reduction at C_{μ} 's greater than 0.003 - 0.004 occurs. The reason for this change in slope is not fully understood since the changeover in flow pattern (see Section 1.2) occurs at a much higher C_{μ} . Figure 77 shows examples of the measured pressure distributions for a range of leading edge blowing momentum coefficients.

4.1.4 Leading and trailing edge blowing

The effect of leading edge blowing at zero geometric incidence for a range of trailing edge blowing momentum coefficients is shown in Figure 78. The expected reduction in performance is apparent. Figure 79 shows examples of the measured pressure distributions around the aerofoil for various amounts of blowing and the two possible flow cases are clearly indicated. The first flow case, at low $C_{p_{LE}}$ and high incidence indicates that the flow 'folds-back' and flows along the upper surface causing a more positive value of C_p at the leading edge. The second case, at high $C_{p_{LE}}$ and low incidence indicates the continuation of the leading edge jet flow onto the lower surface of the aerofoil as shown by an increased leading edge suction.

The inability of the effective incidence calculation to match the measured pressure distributions in the presence of leading edge blowing is shown on the CRT displays. Figure 80 shows the effect of dual blowing for a variety of geometric incidences and trailing edge blowing rates at a fixed $C_{p_{LE}}$ of 0.0125.

4.2 Trailing Edge Investigation

The numerical results of the trailing edge investigation are given in Tables 1 - 17. Tip jet blowing was used at its estimated optimum throughout these experiments (see Section 2.2.3.7).

4.2.1 Upstream boundary layer

The boundary layer approximately 4 slot widths (0.084 in, 2.1 mm) upstream of the blowing jet was measured using a boundary layer single sensor hot wire, in the presence of the leading and trailing edge jet flows. The no-blowing case was also investigated. Values for the shape factor of the profiles were determined but are subject to some error due to the lack of definition of the boundary layer edge. The longitudinal turbulence intensity distribution across the layer was also measured. A comparison between the results of Kind³², the

present study and the usual power law assumption

$$\left(\frac{U}{U_m}\right) = \left(\frac{y}{\delta}\right)^{\frac{1}{7}} \quad (4.1)$$

is also shown in Figure 83. The results indicate a deviation from the power law in the presence of the blowing jet. The leading edge flow is also shown to increase the turbulence intensity within the boundary layer, as might be expected.

4.2.2 Wall jet velocity profiles

Figures 84 - 91 show, for 0° geometric incidence, the mean velocity (\bar{U}) profiles through the trailing edge wall jet for the four tabulated blowing cases (see Table 19) and measured by a split film sensor. The results are given for values of θ at 10° intervals up to separation, starting at 15° from the slot. In some cases intermediate traverses have also been performed.

The mean normal velocity is shown as the local flow angle \bar{V}/\bar{U} in Figures 92 - 95. Inflow angles as high as 10° towards the surface are indicated near the slot. The entrainment process and jet growth rate are also clearly visible. Figure 96 shows the actual variation of \bar{V} across the wall jet for two blowing rates. Figure 97 is an indication of the compatibility of the results with the continuity equation

$$\frac{1}{R} \frac{\partial U}{\partial \theta} + \frac{\partial V}{\partial y} = 0 \quad (4.2)$$

Figures 98, 99 show comparison of \bar{U}/\bar{U}_m against $y/y_{m/2}$ with the work of Kind³² and also direct comparisons of the various methods used in the current study: hot wire, split film and the velocity data used to derive the radial static pressure. The hot wire results are subject to the errors discussed in Section 3.2.5., most obvious of which is the temperature gradient across the wall jet.

Figures 100 - 105 show the streamline patterns, lines of constant $(y \cdot \bar{U} / \bar{U}_m)$, deduced from the split film results for the four blowing rates. The inflow and jet growth quantities show reasonable agreement with those indicated by the local flow angle measurements. The curvature of the streamlines, deduced by a numerical curve fitting technique and the use of the standard equation

$$\text{Radius of curvature} = \frac{\left(1 + \left(\frac{dy}{dx}\right)^2\right)^{\frac{3}{2}}}{\frac{d^2y}{dx^2}} \quad (4.3)$$

are shown for three blowing rates and compared with

$$R = R_0 \left(1 + \frac{y}{R_0}\right) \quad (4.4)$$

usually assumed in theories and computations. The results clearly show that the streamlines are not concentric with the local surface centre of curvature. It is interesting to note that at higher blowing rates, the distributions tend to be parallel to the results from (4.4). At positions closer to the slot, the outer layer curvature is less than expected indicating entrainment effects.

The effects of different slot heights and slot lip thicknesses are shown in Figures 106, 107. The results were obtained using a single sensor hot wire probe.

The increased slot height allowed a constant velocity core to exist in the jet and enabled estimation of the boundary layer thickness within the slot contraction.

The increased slot lip thicknesses were obtained by successive addition of adhesive tape (0.007 in, 0.18 mm thick) to the upper surface of the slot lip. Interestingly the wake of the lip appears to alter little in downstream extent.

A comparison of angular position of separation measured from the slot for the present study compared with the results of Kind¹² and Englar²⁸ is shown in Figure 108. It would appear that the current results show good agreement with Englar²⁸ while Kind³² was not operating at the optimum blowing rate for the test conditions. Two sets of results are shown from Englar²⁸, the first being the published results deduced from a surface mounted shear stress probe, the second being taken from the pressure distributions published in the same reference. The separation point was assumed to be the point where the static pressure reached a constant value, as in the separation bubble. A marked difference exists between the two sets of data; this will be further discussed in Section 5.1.2.

Figures 109 - 112 show the variation of the jet parameters $y_{m/2}$, U_e , U_m , U_{min} against angular position from the slot for a variety of trailing edge blowing rates. These results are taken mainly from the split film velocity profiles.

4.2.3 Turbulence results

All the wall jet turbulence measurements were taken at zero geometric incidence. Figures 113 - 116 show the longitudinal turbulence intensity, $\sqrt{u'^2}/\bar{U}$, distribution across the wall jet for four blowing cases. The measurements were taken at 10° intervals of θ starting at 15° from the slot exit. Radial positioning closer than 15° from the slot was not possible with the split film probes and although the hot wires could be positioned almost anywhere, the error due to radial misalignment (discussed in 3.2.5.2) became increasingly noticeable. The results shown are from both the split film probe and a single sensor hot wire; they clearly indicate the effect of probe size and operational bandwidth. The results of Kind³² are compared in Figure 117 with the split film results at the one data point at which the majority of the flow parameters (e.g. angle from slot, C_u) are similar. Figure 118 shows the effects of varying the slot height and slot lip thickness upon the longitudinal turbulence intensity as recorded by a hot wire probe.

Figures 119, 120 show the relative positions of U_m , U_{min} , $(\sqrt{u'^2}/U)_{max}$ and $(\sqrt{u'^2}/U)_{min}$ for two blowing cases. The maximum turbulence intensity is shown to remain just outboard of the centre of the free shear layer while the minimum intensity closely follows the velocity maximum in the jet flow. The origin of the turbulence intensity maximum is shown to be the slot lip.

Figures 121 - 124 show the normal stress $\sqrt{v'^2}/\bar{U}$ for the four blowing cases as recorded by the split film investigation. The results again are shown for 10° intervals of θ through the wall jet, starting at 15° from the slot exit.

Figure 125 shows a direct comparison between the longitudinal and normal r.m.s. fluctuation. The normal r.m.s. is shown to be roughly 60% of the longitudinal intensity. The relative radial positions of the longitudinal and normal turbulence intensities maxima for a variety of C_μ 's is shown in Figure 126.

The results obtained for the Reynolds's shear stress, $\overline{u'v'}$, from the split film probe are shown in Figures 127 - 130. An example of the correlation coefficient, given by

$$\text{correlation coefficient} = \frac{\overline{u'v'}}{\sqrt{\overline{u'^2}} \sqrt{\overline{v'^2}}} \quad (4.5)$$

is shown in Figure 131. The usually accepted value is 0.4 although this is subject to error at points near areas of high $\partial^2 U / \partial y^2$ (i.e. the velocity maxima and minima).

It is suggested that the correlation coefficient as measured by a split film probe can be used to produce results representative of a higher bandwidth device. If it is assumed that the relative magnitudes of the turbulence intensities are constant compared with each sensor bandwidth, then let

$$B = \frac{\overline{v'^2}_{\text{film}}}{\overline{u'^2}_{\text{film}}} \quad (4.6)$$

Then

$$\overline{v'^2}_{\text{wire}} = B \times \overline{u'^2}_{\text{wire}}$$

Also assuming a consistent correlation coefficient, then:-

$$\overline{u'v'}_{\text{wire}} = \sqrt{B} \times \overline{u'^2}_{\text{wire}} \times \text{film correlation coefficient} \quad (4.7)$$

In this manner it is possible to produce more realistic values for $\overline{u'v'}$ and $\overline{v'^2}$ and to indicate the bandwidth limitations. The results of these adjustments are shown in Figures 132, 133 for one blowing case. This technique is only approximate since the relative sizes of the sensors will affect the ability of a given eddy size to cause a fluctuation of the bridge voltage.

The shear stress results are compared with the assumed distribution in the program of Dvorak et al.³⁸ and with the measurements of Wilson and Goldstein²¹ and Jones³³ in Figures 134, 135.

4.2.4 Radial static pressure distributions

As a check on the validity of the technique of Pache⁴⁸ (see Section 3.4), the static pressure distribution across the boundary layer, just upstream of the trailing edge blowing slot was determined. The results, with and without trailing edge blowing, are given in Figures 136, 137. The results show excellent agreement with the usual assumption within the boundary layer that, for low curvature

$$\frac{\partial p}{\partial y} = 0 \quad (4.8)$$

The indicated pressure coefficient for the unblown case is also in good agreement with a value obtained from the surface pressure measuring equipment.

Figure 138 shows the measured wall static pressures around the trailing edge for three blowing cases. These results were used

to provide the wall datum pressure for the radial static pressure distributions given in Figures 139 -- 142. The convergence of the flow quantities with the wall datum points is excellent. Figures 63, 64 show examples of the raw measurements used to deduce p , the static pressure. The effects of total head tube size and shape, shear flow correction and errors in velocity measurements are indicated, and discussed in Section 3.4.1. The free stream total pressure for these experiments was approximately 0.5 cm of Alcohol below atmospheric.

The results of Dvorak and Woodward⁴⁹ using a similar twin probe technique to evaluate the radial static pressure distribution over a slotted flap are shown in Figure 143. The similarity in shape of the distributions is remarkable, and perhaps the flow fields could be taken to be similar in nature.

5. DISCUSSION OF RESULTS

5.1 Overall Performance

5.1.1 Unblown aerofoil

The three dimensional lifting performance of the unblown aerofoil, Figure 65, was shown to be less than the two dimensional value predicted by Hoerner⁵¹ for a similar Reynolds number, as might be expected due to the low effective aspect ratio,

$$\left(\frac{\partial C_L}{\partial \alpha} \right)_{\text{exp}} = 3.25 \text{ per radian}$$

$$\left(\frac{\partial C_L}{\partial \alpha} \right)_{\text{Hoerner}} = 4.0 \text{ per radian}$$

The low, indeterminate, aspect ratio of the model clearly affected the unblown performance. Due to the endplates the downwash at the trailing edge was increased compared to the two-dimensional case, affecting the estimation of the lift curve slope. It is interesting to note that the effects of the end plates are usually confined to reducing the effective incidence of a sharp trailing edged aerofoil where the rear stagnation point is fixed. This has the result of reducing the measured lift curve slope. The rounded trailing edge of the current model however allows the rear stagnation point to move to produce an opposite, but apparently, smaller effect upon the lift curve slope. In general, the measured unblown performance and pressure distributions were satisfactory.

Examination of Figure 66 indicates one further contribution to the lift curve slope discrepancy. The theoretical pressure distribution shown was calculated for a true ellipse of identical thickness:chord ratio to the model. However the model is not a true ellipse:-

- i) the leading and trailing edges are circular cylinders

- ii) blowing slots cause surface irregularities at the leading and trailing edges.

It should be noted that the calculation does not take account of viscous effects, i.e. boundary layer growth over the surface, and therefore cannot be totally representative of the flow over the latter half of the model. However it does indicate that the increase in the leading edge suction peak observed experimentally was produced by the circular leading edge compared with a true ellipse. The effect of the leading edge slot was not obvious from the measured pressure distribution although oil film flow visualisation indicated a small (< 0.1 in, 2.5 mm) separation bubble followed by a turbulent reattachment. The lack of asymmetry in the lift generation at positive or negative incidences suggests the effect of the slot lip on C_L to be small.

Figure 67 shows comparisons of the experimental three-dimensional no blowing pressure distributions and those obtained from the two-dimensional viscous/potential flow analysis of Dvorak et al.³⁸. These results clearly show the presence of the non-elliptic leading edge. On the suction surface a high suction peak is indicated in a region short of pressure tappings, and on the high pressure surface a similar effect is produced. The discrepancies in the pressure distributions over the trailing half chord are not fully understood although this may be a surface roughness effect.

No boundary layer trips were included on the model due to the presence of the leading edge slot lip and the relatively large test Reynolds number of 1.3×10^6 . If the model surface had been smooth, natural transition would be expected at approximately 35% chord.

No signs of approaching stall were indicated over the limited incidence range ($\pm 7.5^\circ$) examined.

The measured pressure coefficient at the leading edge stagnation point, (see Figure 67) was shown to be within 1% of unity, indicating a reasonable evaluation of the blockage correction.

5.1.2 Trailing edge blowing only

The performance of the aerofoil shown in Figures 68 - 69 was very much as expected. The effect of the tip jets was significant and is indicated in Figure 68.

The advantages of operating at lower values of C_u are obvious and lift augmentations ($\partial C_L / \partial C_u$) of the order of 60 were attained. Figure 69 indicates the effects of increasing the slot height:chord ratio and the effect of the presence of a hot wire probe in the wall jet. The improved performance obtained at the higher slot height was expected from the information given in reference 40, which suggests that an optimum value for the slot height:chord ratio exists (typically 0.002) and would appear to be a function of the slot design, exit angle relative to the local surface and of the relative mass flows between the jet and upstream boundary layer flow.

The presence of the hot wire probe causes a premature local separation of the flow and since the probe was located approximately 1 in (25 mm) to the side of the static pressure tappings, the full effect was not measured. In some cases the measured lift was reduced by 20% with the probe in place at the trailing edge. It could also be shown that the proximity of the probe to the surface affected the measured performance, the maximum reduction of C_L being when the probe was closest to the surface (see Figure 144). All the overall performance measurements (static pressures) were taken with the probe and probe support arrangement well removed from the static pressure tappings. The question of probe interference with regard to the anemometer results is not so serious since the hot wire is a relatively long distance in front of the probe holder, and the split film probe, whilst bulkier compared with a hot wire, does not require the same physical support (see Figure 53 and Sections 3.2.5.3, 3.3.4.5.).

The pressure distributions recorded (see Figures 70, 71) exhibit the typical 'saddle-back' form associated with circulation control aerofoils.

Figure 72 shows the estimated downwash corrections from the effective incidence calculation (Section 3.1.1). At positive geometric incidence the agreement with the results of Kind³² was excellent. The change in slope for negative geometric incidence is suggested to be due to the reduced effect of the wall jet wake upon the upstream flow. The more negative the incidence the closer the wake trajectory approaches the tunnel centreline, reducing the under surface wake blockage effect.

Figures 72 and 68 were used to produce Figure 73, the lifting performance of the aerofoil for constant effective incidence. The results are shown compared with Kind³² and those predicted by CIRCON³⁸ for the current aerofoil. Whilst the agreement with Kind³² is excellent, some doubts do exist since the current results were obtained at a higher Reynolds number. It is also apparent from Figure 108 that there is a large discrepancy in the angle to separation for the various comparable flows. In general, the current model exhibited much lower angles to separation for similar C_u 's than those of Kind³² or CIRCON³⁸ while still producing similar lift coefficients. However, the current results appeared to fit well with those of Englar²⁸, certainly for angle to separation. There are several factors which may account for these inconsistencies:-

- i) the theoretical calculation procedure was incorrect.
- ii) variations of slot design, slot height:chord ratio between experimental aerofoils.
- iii) test Reynolds number variations.
- iv) definition of separation point from experimental results e.g. onset of constant surface static pressure, zero shear stress or $\partial U/\partial y = 0$ at wall from velocity profiles.
- v) surface roughness.

It appears that of these, the two main reasons for these inconsistencies are:-

- i) Firstly the experimental results were obtained for a relatively low slot height:chord ratio (0.000897) compared with Kind³² (0.0012) and as shown in Figure 69, increased slot height produced a significant improvement in the lifting performance of the aerofoil.
- ii) Secondly, the trailing edge cylinder was not quite smooth and this reduced the angle to separation of the Coanda jet and hence the circulation for a given C_μ . These two effects have opposite results on the generation of C_L and hence the dominant factor is difficult to determine. Further work to investigate the effects of the surface finish of the trailing edge cylinder on the current aerofoil may be performed at Bath University.

Figure 74 shows a family of typical performance curves for various aerofoil shapes and indicates the advantages of circulation control over the simple jet flap.

Figure 75 shows the expected increase in C_{Dp} with C_μ caused by the reduction of surface pressure around the trailing edge and the expected influence of the jet thrust. Since the drag of the aerofoil was not the main area of interest in the current study, it was not fully investigated.

5.1.3 Leading and trailing edge blowing

The effects of leading edge blowing indicated in Figures 76 - 80 show a smaller lift decrement than might be expected. The two distinct leading edge flow fields are indicated by the pressure distributions with and without trailing edge blowing. The boundary between the two flow cases was not easily defined since many parameters are involved. No hysteresis effect was apparent. It is suggested that the parameters involved are those which determine the position of the leading edge stagnation point relative to the leading edge blowing

slot, namely:-

- i) $C_{\mu_{LE}}$. This obviously is the major parameter involved since it dictates the ability of the jet to remain attached to the curved surface.
- ii) $C_{\mu_{TE}}$. Since the trailing edge blowing momentum coefficient controls the trailing edge separation point and hence the circulation, it must also have great influence upon the position of the leading edge stagnation point. Thus, as was found experimentally, the higher the value of $C_{\mu_{TE}}$, the longer the flow 'folded-back' for increasing $C_{\mu_{LE}}$ at constant effective incidence.
- iii) Effective incidence. The evaluation of the boundary condition for the two flow fields was not simple when attempted in a closed tunnel since the effective incidence was a function of $C_{\mu_{TE}}$. Hence, controlled experiments at constant effective incidence were impractical. However, the variation of incidence must have a direct effect since it requires a movement of the leading edge stagnation point. This implies that at more positive incidence the leading edge flow would 'fold-back' until a higher $C_{\mu_{LE}}$ was reached.

The technique used to determine the effective incidence of the aerofoil (see Section 3.1.1) was unsuitable when leading edge blowing was used. The theoretical pressure distribution used in the technique was not able to account for the jet flow around the leading edge and hence no practical comparison with the experimental results was possible. There is as yet no theoretical method capable of solving the leading edge jet flow cases.

The lack of a large number of static tapings in the leading edge cylinder and in the very thin slot lip precluded any detailed estimations of either the extent or nature of the separation bubble under the fold back flow or whether the stagnation point was detached from the surface when the jet continued on to the lower surface.

5.2 Velocity and Turbulence Profiles in the Upstream Boundary

Figures 81, 82, 83 show the velocity and longitudinal turbulence profiles measured upstream of the blowing slot. The trailing edge blowing jet was expected to influence the velocity profiles in two ways.

- i) The increased circulation and associated static pressure distribution was expected to change the boundary layer growth along the upper surface. This is clearly shown by the profiles, the boundary layer thickness being reduced in the presence of the blowing jet.
- ii) Close to the slot, the strong entrainment of the boundary layer by the blowing jet was expected to change the form of the boundary layer velocity profile from the usually assumed power law

$$\left(\frac{U}{U_m}\right) = \left(\frac{y}{\delta}\right)^{\frac{1}{7}} \quad (5.1)$$

This is shown in Figure 83 and the effect of blowing is to increase the velocity gradient close to the wall. The difficulty in accurately defining the edge of the boundary layer makes qualitative comparison of the velocity profiles unreliable.

The effect of the leading edge blowing (Figures 81, 82) upon the velocity profiles was to produce a nett deficit in the circulation of the aerofoil and hence a nett decrease in the velocity at the edge of the boundary layer. When the leading edge jet flow folded back on the upper surface, no wake of the jet was observed in the velocity profile just upstream of the blowing slot.

The shape factors shown in Figure 81 are in good agreement considering the indeterminate nature of the boundary layer edge and compare well with those of Kind³².

The longitudinal turbulence intensities, $\sqrt{u'^2}/\bar{U}$ (Figure 82) across the boundary layer were very much as expected, showing an increase as the wall was approached due to the suppression of the normal turbulence and the velocity tending to zero. At the edge of the boundary layer the values approached those measured for the wind tunnel free stream turbulence levels (see Section 2.2.2).

The introduction of the trailing edge blowing jet greatly reduced the measured turbulence intensities, primarily due to the removal of the onset of separation, the change in the boundary layer growth and pressure distribution over the upper surface and the strong entrainment of the blowing jet. The introduction of leading edge blowing increased the turbulence intensities compared with the trailing edge blowing only case. At the flow conditions indicated in Figure 82, the leading edge jet flow was found to be folded back along the upper surface and the increase in the turbulence is taken to be a residue of the disturbed upstream flow.

5.3 Trailing Edge Wall Jet

Of all the detailed trailing edge wall jet measurements, the radial static pressure results indicated the most unexpected trends. Prior to this work, the radial static pressure distribution had always been represented by a simple radial force balance based on a streamline curvature, assumed concentric with the local surface. This was shown to be invalid and was then the area in which the interpretation of the results was concentrated.

5.3.1 Radial static pressure measurements

The results, shown in Figures 139 - 142, were at first viewed with some scepticism, and a thorough examination of the possible sources of error (Section 3.4.1) was undertaken. However it was shown that the measured distributions indicated valid trends and in some cases the removal of possible errors merely accentuated those trends.

Figure 136 shows the radial static pressure distribution just upstream of the blowing slot with and without the blowing jet. The agreement with the usually assumed zero pressure gradient for the no blowing case provides an excellent check on the validity of the experimental technique. The measured static pressure values are in good agreement with the measured surface pressure coefficient values from Figure 67.

5.3.1.1 Physical significance of results

Whilst the measured radial static pressure distributions were not as expected, they were not without some physical justification.

- i) Close to the wall, the pressure gradients became negative as is predicted if the radial momentum equation is allowed to tend to $y = 0$, giving

$$\frac{1}{\rho} \frac{\partial p}{\partial y} \rightarrow - \frac{\partial (\overline{v'^2})}{\partial y} \quad (5.2)$$

since $\overline{v'^2}$ must tend to zero at the wall due to the suppression of v' fluctuations by the wall, then $\partial \overline{v'^2} / \partial y$ is positive. Hence, $\partial p / \partial y$ is negative.

- ii) the large positive gradient, in excess of that required for a radial force balance, suggests a reason for strong flow attachment on a highly curved surface - the Coanda effect.
- iii) the two inner pressure gradients tend to equalise as separation is approached. This could be suggested as a separation criterion, since a large inner negative gradient would tend to reverse the flow curvature.
- iv) the outer negative pressure gradient, which extends approximately from $y_m/2$ to y_{min} was in general less steep than the positive inner gradient. This pressure gradient was thought to influence the growth of the shear layer and the mixing rate of the two streams.

- v) at the edge of the flow, the pressure gradient again becomes positive with a slope consistent with an overall radial force balance.

For comparison, pressure distributions calculated using a simple force balance applied over two layers, the jet and the boundary layer, are shown on Figures 139 - 142. The slopes were calculated assuming a constant average velocity across each layer from the measured velocity profiles (Figures 84 - 91) and a mean radius of curvature for each layer from the deduced radii of curvature (Figures 101, 103, 105). Good agreement between the gradients in the outer layer is indicated.

Static pressure distributions of this form have previously been shown by other researchers, but little discussed in their reports. As mentioned in Section 4.2.4, Figure 143, Dvorak and Woodward⁴⁹ used a similar experimental technique to investigate the static pressure distribution over a trailing edge slotted flap. The results are very similar to the present study but are not discussed in their report in any detail. The flow through a flap slot could be simply represented as a low speed wall jet and consequently the similarity in the results should not be unexpected. The large physical scale of the flap results would also indicate fewer measurement errors due to flow angle, wall interference and shear flow, providing further justification for the present results.

Kruka and Eskinazi¹¹ also indicated radial static pressure measurements of similar form for a plane wall jet, but failed to comment on their results.

Miller and Comings⁵² showed similar pressure distributions in a round free jet flow. Their work used a flat plate probe which was optically aligned in the mean flow direction. The results indicated a positive/negative pressure variation in the vicinity of the shear layer very similar to that of the present study.

Englar²⁸ used a radially mounted trailing edge flange plate with radial static tapings and gave the first results for a highly curved trailing edge wall jet. Interestingly, the results showed a more severe positive pressure gradient much closer to the wall than would normally be expected. At some radial positions and blowing conditions there was a tendency for a negative gradient to appear (see Figure 61). However these results must be questioned and perhaps considered unreliable due to plate interference and corner flow interaction in the region of high positive and negative longitudinal pressure gradients. Unfortunately Englar²⁸ published no velocity profiles for this study.

The present experimental results for the normal stress ($p + \rho \overline{v'^2}$) were compared with those predicted by Kind⁵³. Kind used a simple numerical method to predict the normal stress based on satisfying a radial force balance with two equations to represent the velocity profiles. The normal stress was given as

$$\frac{C_{\sigma} - C_{\sigma_s}}{C_{\sigma_\delta} - C_{\sigma_s}}, \text{ suffix } s \text{ denotes surface} \quad (5.3)$$

$$\text{suffix } \delta \text{ denotes edge}$$

where

$$C_{\sigma} = \frac{p + \rho \overline{v'^2}}{\frac{1}{2} \rho U_{ref}^2}$$

The results are shown as Figure 145 and indicate reasonable agreement until the experimental results change slope in the outer part of the shear layer. This is associated with the negative static pressure gradients obtained in this region.

5.3.1.2 Comparison of experimental results with the radial momentum equation

While the measured pressure changes were small, the small distances over which they occurred gave rise to very large pressure gradients. It was hoped to determine values of $\partial p / \partial y$ by direct substitution of the measured velocities, radii of curvature and fluctuating

components into the radial momentum equation.

$$\frac{\bar{U}}{R} \frac{\partial v}{\partial \theta} + \frac{v \partial v}{\partial y} - \frac{(\bar{U}^2 + \overline{u'^2} - \overline{v'^2})}{R} = - \frac{\partial}{\partial y} \left(\frac{p}{\rho} + \overline{v'^2} \right) - \frac{1}{R} \frac{\partial}{\partial \theta} (\overline{u'v'}) \quad (5.4)$$

All of the terms of this equation could be directly obtained from the experimental results and used to provide values for $\partial p / \partial y$ at various radial positions. It was assumed that

$$(\overline{u'^2} - \overline{v'^2}) \ll \bar{U}^2$$

and that values for $\overline{v'^2}$ and $\overline{u'v'}$ should be corrected as discussed in Section 4.2.3, Figures 132, 133 to take account of the low operational bandwidth of the split film probes. The results obtained are given in Table 18 and Figure 146 and indicate that the equation underestimates the measured gradients in some cases by more than an order of magnitude. The errors appear to be largest at the limits of the y values examined, i.e. the edges of the free shear layer. It is of interest also to note the magnitude of the normal stress gradient $\partial \overline{v'^2} / \partial y$ in relation to the other terms in the radial equation. Clearly if a solution to the wall jet problem uses this equation then extreme care must be taken in eliminating or modelling these fluctuating terms.

Since great care had been taken in the evaluation of the experimental results, the inability of the radial momentum equation to produce the measured pressure distributions posed a serious problem. It was suspected that the actual flow field was not adequately described by the time averaged results.

5.3.1.3 An observation of the anemometer signals

During the hot wire anemometer survey of the trailing edge flow field, it was observed that the high pass filtered signal consistently exhibited a 'bias' dependent upon the position of the probe in the flow. Figure 147 is an illustration of the observed signals. Near \bar{U}_m , the signal showed a distinct positive bias which reversed near \bar{U}_{min} . This effect was mainly confined to measurements within the first 30° of the flow from the jet. Away from these points the signal was seen to fluctuate around the zero voltage point as would normally be expected. This observation coupled with the unsatisfactory solution of the radial momentum equation led to a suggestion that the flow field was not of the simple nature usually assumed.

5.3.2 Proposed flow field

It is now proposed that the actual Coanda jet flow is of the general nature shown in Figure 148. The flow consists of a stream of coherent vortices emanating from the slot lip region. The vortices are formed from the excess vorticity produced by the difference in velocities of the two flows and the instability of the ensuing vortex sheet. An instantaneous flow pattern between the vortices is suggested and indicates the mechanism for the strong entrainment associated with Coanda flow. The attachment of the wall jet to the surface, Coanda effect, may be explained in two ways.

- i) Smith et al³⁹ have shown that in inviscid potential flow, the flow remains attached and spreads due to the mutually induced velocities of the vortices. This phenomenon also produces separation of the flow at some distance from the slot, dependent upon the initial vortex strength assumed. It is interesting to also note the similarity between the proposed flow field and the calculation method of Smith et al³⁹.
- ii) the concentration of the streamlines between each vortex and the surface must produce a local reduction of static pressure hence, each vortex attaches itself. The entrainment produced by such a vortex stream is sufficiently strong, dependent upon the jet strength, to delay separation of the external flow.

It is suggested that it is the growth of the discrete vortices due to entrainment, the loss of angular momentum due to surface viscous effects and the loss of total angular momentum to negotiate the curved surface which dictate the extent of the attachment of the wall jet.

The frequency of the vortex stream, the decay of the vortex strength, the estimation of the initial vortex strength and the effects of geometry, external flow and blowing rate will be further discussed in relation to the production of an improved theoretical wall jet model in Chapter 6.

It will be shown in the following sections how the time averaged results can be deduced from the suggested instantaneous flow field, and its relation to the measured turbulence and pressure distributions will also be shown. The passing frequency of the proposed flow field vortices was indeterminate but must have been above the upper limit of the hot wire anemometer to explain the observations of Section 5.3.1.3. If it is assumed that the vortices are convected at approximately the half velocity, $\bar{U}_m/2$ and are initially a slot width in diameter, then a typical frequency of 100 KHz is easily attainable. It is suggested that the vortex centres follow the locus of the half velocity point.

5.3.2.1 Supporting evidence for the proposed flow field

Evidence of the suggested flow structure has been noted by a variety of researchers although the influence of these vortices upon a Coanda flow field has been neglected.

Horne and Karamcheti⁵⁴ obtained some detailed schlieren photographs of this type of flow in a plane laminar jet in the presence of a variable length wall. The photographs were coupled with hot wire probe outputs which clearly indicated the periodic nature of the flow. The vortices were shown to exist even in the presence of a curved wall, although the growth rate of the vortices was far greater than that for a plane wall.

Davies and Baxter⁵⁵ discuss the development of ring vortices in a free air jet from the Kelvin-Helmholtz instability of the vortex sheet and the importance of the vortices upon the transition of the free shear flow. Their results indicated a strong Reynolds number dependence and the flow appeared to be well ordered below a Reynolds number of 15000 based on the jet diameter. At Reynolds numbers above 20000, the onset of chaotic motion is increased. A hydrogen bubble technique was used to visualise the flow field.

Damms and Kuchemann⁵⁶ proposed a similar flow field to predict the mixing region between two parallel streams of different velocities in the wake of a splitter plate. Their vortices were allowed to have cores and the effects of either equidistant or exponential spacings of the cores were investigated. The growth rates of the cores were investigated, and time averaged velocities across a shear layer produced. The work was based upon the experimental results of Brown and Roshko⁵⁷. They used a shadowgraph technique to trace the vortex cores formed behind a splitter plate between two streams of different density (nitrogen and air) in a pressurised working section (~ 6 atmos). A vortex streaming frequency of approximately 10 KHz was found at a streaming speed of approximately 11 ms^{-1} . The vortex cores were apparently formed as the vortex sheet between the fluids rolled up at regular intervals. The experiments were run at relatively high Reynolds numbers. Other experimental evidence is given in reference 56, in particular, Clark and Markland⁵⁸ found evidence of a core type structure in the free shear layer of a plane wall jet.

Further evidence and discussion of the cause, structure and persistence of large vortical structures is given in references 59 - 62. In particular, Wygnanski et al⁵⁹ show photographic evidence of the structure and Chandrsuda et al⁶² show the process of helical pairing which will be further discussed in Section 6.2.3.

The proposed flow field is therefore well supported by previous research.

5.4 Discussion of the Experimental Results in the Light of the Proposed Flow Field

The spatial correlation of the proposed vortex stream and the experimental velocity profiles, turbulence quantities and radial static pressure distributions for a single angular position and blowing rate is given in Figure 149. A full interpretation of each of the experimental parameters with respect to the vortex stream is given in Sections 5.4.2, 5.4.3, 5.4.4. It is immediately obvious from Figure 149 how the vortex stream relates to the time averaged velocity profiles and also in particular how the stream allows the radial static pressure to depart from the normally smooth distributions within the bounds of the free shear layer.

5.4.1 Overall performance

The proposed flow field now provides a simple physical explanation of the Coanda attachment, its dependence upon the jet blowing rate and a number of the variations of overall performance previously indicated (Section 5.1).

5.4.1.1 Effect of increasing slot height

For identical C_u values an increased slot height produces a lower jet velocity; this would tend to suggest a weaker vortex strength at the initiation of the vortex stream. Also, the streaming speed will be reduced. In general, it would be expected that an increase in slot height would reduce the lifting performance of a given aerofoil. This is shown to be true in reference 40 for slot height:chord ratios of greater than 0.0166. The current tests were conducted at ratios lower than this figure (generally 0.000897) and hence it would appear that an optimum ratio would exist dependent upon the relative width of the jet, the boundary layer within the jet and the upstream boundary layer, below which the trend was reversed. Section 5.4.2.1 contains a further discussion on this point.

5.4.1.2 Effect of probe interference

Whilst it is not suggested that the individual vortices are of full spanwise extent, the shedding frequency should be high enough to avoid

discontinuities in attachment. The effect however of introducing an obstruction into the Coanda flow (an anemometer probe for example) would be to rupture the vortex sheet and cause a 'roll-up' of the vortices either side of the obstruction. The resulting longitudinal vortices are a well known phenomenon, as is the tendency of the jet sheet to split in the wake of an obstruction.

5.4.2 Velocity profiles

The time averaged velocity profiles \bar{U} , as measured by a split film probe, (Figures 84 - 91) were much as expected. It is obvious from Figure 148, how the proposed flow field could be used to produce these time averaged results. Further discussion of this point will be given in Section 6.2.1 in relation to determining the true vortex strength from a given time averaged velocity profile.

The \bar{U} results show excellent agreement with the one comparable profile of Kind³², (Figure 98) and the other two hot wire techniques used in this study, (Figure 99). A discussion of the profile errors of the anemometer equipment is given in Section 3.2.5.

5.4.2.1 Effect of slot height variations

The effect of increasing the slot height upon the measured velocity profiles (Figure 106) is seen to be primarily a change in jet velocity profile. The existence of an approximately constant velocity core is apparent although outside the velocity minimum, little difference exists in the profile. Unfortunately time did not permit further downstream investigation of the wall jet at the increased slot height. With reference to the effects of increasing slot height upon overall performance discussed in Section 5.4.1.1, it is suggested that the optimum performance is influenced by the boundary layers in the jet. The presence of the boundary layers in the jet produces a concentration of vorticity within these boundary layers proportional to the velocity gradient. The presence of a constant velocity core provides the optimum conditions for this vorticity concentration, i.e. maximum $\partial U / \partial y$. Therefore since the magnitude of the vorticity defines the distance to separation of the wall jet, it is proposed that it is the

size and gradient of the jet boundary layer (dependent upon the existence of a core, or not), coupled with the effects of the proximity of the vortex stream to the wall which produces the variation of performance of circulation control aerofoils.

5.4.2.2 Effects of slot lip thickness

The effect of increasing the thickness of the slot lip, (Figure 107) is very interesting. It was expected that the effect would be to lengthen the starting region of the flow in the wake of the lip and reduce the lift coefficient. However, this was not apparent from the results, which implied that the entrainment process was strong enough to produce inflow angles of up to 25° . This also suggests that the formation of the proposed vortex stream does not require a starting length dependent upon geometry, but rather on velocity ratio.

5.4.2.3 Variations of the parameters which describe the velocity profiles

Figure 109 shows the variation of the position of the half velocity point, $y_{m/2}$ with θ for a variety of blowing rates. The half velocity point may be defined two ways:

$$\begin{aligned} \text{where} \quad \bar{U}_{\frac{m}{2}} &= \frac{\bar{U}_m + \bar{U}_{\min}}{2} \\ \text{or} \quad \bar{U}_{\frac{m}{2}} &= \frac{\bar{U}_m + \bar{U}_\delta}{2} \end{aligned} \quad (5.5)$$

Figure 109 gives both variations. However it is shown (Figure 109) that at higher blowing rates where a fully developed wall jet profile is attained, the two half velocity points coincide ($\bar{U}_{\min} \rightarrow \bar{U}_\delta$).

Figure 110 shows the variation of the wall jet profile edge velocity with θ and C_p . In some cases, determination of \bar{U} was difficult due to the variety of wall jet velocity profiles obtained.

Figure 111 shows the variation of \bar{U}_{\min} with θ and C_u . \bar{U}_{\min} is assumed to tend to zero at the slot. Figure 112 shows the variation of \bar{U}_m with θ and C_u . These two figures give some indication of the variation of vortex strength in the wall jet. It could be assumed, allowing for the fact that the velocity profiles are time averaged, that the vortex strength is given by

$$K = f \left[(\bar{U}_m - \bar{U}_{\min}), G, (y_m - y_{\min}) \right] \quad (5.6)$$

where G is a factor to allow for the effects of time averaging upon the individual vortex strengths. $(y_m - y_{\min})$ represents a typical length scale for the vortices, assumed to be their diameter, and is equal to the width of the free shear layer. The velocity difference across the shear layer $(\bar{U}_m - \bar{U}_{\min})$, coupled with G , indicates the velocity increment across the vortices. Figure 150 shows the variation of $(\bar{U}_m - \bar{U}_{\min})$ with θ and C_u which can be seen to be an exponential type decay. The method of Smith et al.³⁹ uses a similar type decay to model the vortex strength distribution along the wall jet. Some comments upon the relative size of G will be made in Chapter 6.

5.4.2.4 Streamline patterns and their radii of curvature

The time averaged results, \bar{U} , shown in Figures 84 - 91 were used to produce the streamline patterns and their radii of curvature (Figures 100 - 105). The effects of the strong entrainment close to the slot and the growth rate of the jet are obvious from the streamline patterns. The radii of curvature were produced, as described in Section 4.2.2 and show a distinct departure from the usually assumed concentricity with the local centre of surface curvature:

$$R = R_o + y \quad (5.7)$$

Equation (5.7) is shown on the figures for comparison and it can be seen that at higher blowing rates and angles from the slot, the variation of the deduced radius of curvature becomes parallel to

equation (5.7). This would appear to indicate the occurrence of a fully developed wall jet profile once clear of the slot and the associated strong entrainment. The deduced radius of curvature can be as much as twice that usually assumed by equation (5.7). This would produce significant errors in many theories particularly where the radial static pressure gradient is given by a simple force balance (equation 3.33).

The measured local flow angles \bar{V}/\bar{U} , (Figures 92 - 95) seemed to indicate the expected trends of entrainment and jet growth. However the results when compared with the requirements of continuity, (Figure 97)

$$\frac{\partial \bar{U}}{\partial x} + \frac{\partial \bar{V}}{\partial y} = 0 \quad (5.8)$$

were shown to be too negative. It was suspected that the errors discussed in Section 3.3.4. produced this apparent negative offset and allowing for this, the results provide a reasonable representation of the streamline patterns shown in Figures 100, 102, 104.

The derivation of the normal velocity profiles from equation (5.8) is suggested as realistic since the vortices in the proposed flow field, although markedly different from the time averaged streamline patterns, would produce no nett effect upon \bar{V} ; as each vortex passes, then equal and opposite V influences are experienced producing a nett zero effect for a constant radial position above the surface.

5.4.3 Turbulence results

The first consideration regarding the measured turbulence parameters in the light of the proposed flow field is, exactly what has the equipment measured? The instantaneous velocity vector instead of being simply represented thus

$$U = \bar{U} + u'$$

could now be

$$U = \bar{U} + \tilde{u} + u'$$

(5.9)

where \tilde{u} now represents a periodic function the value of which is dependent upon the measuring position relative to the vortex stream. Since the passing frequency of the stream has been shown to be above the anemometer frequency response, it can only be assumed that the measured turbulence represents \tilde{u} . Apart from the regions close to the wall and in the outer boundary layer the turbulence levels should be explained by their relative positions to the vortex stream.

5.4.3.1 The longitudinal turbulence intensity

There is a great lack of reliable turbulence data in highly curved wall jet flows. As is common with all turbulence results, normalisation and comparison is difficult and subject to many errors. Differences in equipment, technique and datum flow quantities can provide order of magnitude errors in the measurements even if the flow situations are well reproduced. Comparable data for this flow field is limited to the work of Kind³² as the only reliable and well documented set of results.

Two techniques (single wire and split film probe) were used in the present study to determine the longitudinal turbulence intensity $\sqrt{u'^2}/\bar{U}$ and these are described in Sections 3.2, 3.3. The comparison between the split film and single wire results, shown in Figures 113 - 116, indicates the effects of probe size and operational bandwidth. The edge of the wall jet ($y > 0.3$ in, 7.5 mm) indicates that the free stream turbulence levels tended to be less than 4%, in good agreement with those originally measured in Section 2.2.2. using a crossed wire probe. In the outer part of the wall jet the intensity gradually decreases to the free stream levels as would be expected.

Close to the wall, a minimum intensity exists in the region of the velocity maximum and increases as the wall is approached. This is

consistent with the suppression of the normal turbulence at the wall,

$$\overline{v'^2} \rightarrow 0 \text{ as } y \rightarrow 0$$

The effects of heat loss to the surface from the hot wire probe did not seem to be a problem, although the closest points were within the region ($y < 0.004$ in, 0.1 mm) generally regarded with suspicion for wire probes of 5 μ m diameter. The effects of the wall upon the split film probe results are however more noticeable. Whilst heat loss to the surface may have affected the mean velocity measurements, the effects of probe interference are more evident in the turbulence measurements. This is because the turbulence parameters are calculated as the fluctuations upon the mean, which is calculated at each step; hence the turbulence levels are relatively insensitive to changes in mean flow angle or heat loss to the surface. All split film probe turbulence measurements within 6 probe diameters (~ 0.035 in, 0.88 mm) of the surface have been ignored. It should be remembered that the film probes were run at a much lower overheat ratio (0.5) compared with the wire probes (0.8). The effect of the wall interference on the split film probe is clearly shown in Figure 117 as an increase in $\sqrt{u'^2}/\bar{u}$ beyond that expected as the wall is approached. Figure 117 also shows a comparison between the present split film results and the hot wire results of Kind³². The agreement is remarkable and not only provides justification for the assumptions regarding the extent of probe interference but also indicates that the results of Kind³² were taken at a similarly low operational bandwidth.

In the region of the shear layer, Figures 113 - 116, the turbulence results must now be reinterpreted for the presence of the vortex stream. The time averaged longitudinal intensity ($\sqrt{u'^2}/\bar{u}$) indicates a peak value in the outer half of the shear layer. This is explained simply as the region in which the longitudinal velocity vector experiences the greatest variations. Dependent upon the relative position of a vortex, the velocity vector can be rotated through a full 180° as indicated in Figure 151.

Figures 119, 120 more clearly illustrate the relative positions of the maximum and minimum longitudinal turbulence intensities to the velocity maximum and minimum.

The effects of the excessive surface roughness mentioned in Section 5.1.2, upon the turbulence results is not obvious since no suitable data exists to provide a comparison.

The longitudinal turbulence intensities, (Figures 113 - 116) exhibit a minimum time averaged profile a short distance downstream of the slot, in common with the other turbulence parameters. This is thought to be an indication of the change in sign of the longitudinal pressure gradient. The negative pressure gradient suppresses the turbulence while the positive gradient has the opposite effect. The θ position of this minimum in the turbulence profiles appears to be nearly constant for varying C_u and was consistent with the position of the measured suction peak. A similar effect was noticed by Englar²⁸ on measurements of surface shear stress, an example of which is given as Figure 151.

As separation is approached, Figures 113 - 116 indicate that the intensity of the turbulence increases rapidly with distance from the slot, as would be expected.

Figure 118 shows the longitudinal turbulence intensity as measured by a hot wire probe at similar C_u values but for variations of slot height and lip thickness. Increasing the slot height reduces the minimum intensity due to the presence of a near constant velocity core. However, the maximum intensity near the slot lip has been nearly doubled. The doubled slot height effectively reduces the jet velocity for a given C_u by nearly 30%, thus reducing the initial mixing process and the formation of the vortex stream. This results in a higher net turbulence intensity in the wake of the lip.

Thickening the lip shows an increase in the value of the peak intensity in the shear layer and a corresponding expansion of the wake of the lip. The effects upon the velocity profiles, (Section 5.4.2.2, Figure 107) were shown to be small and this indicates that the

starting length was little changed by the lip thickness. The effects of thickening the lip upon the overall lift coefficients were within the experimental accuracy of the measurement system and hence could not be used to indicate any trends.

In both doubling the slot heights and thickening the slot lip, the typical eddy size of the flow in the wake of the lip has been increased by reducing the velocity gradients and increasing the typical lengths. This could also be a factor in the apparent increase in the measured turbulence in the wake of the lip.

5.4.3.2. The normal turbulence intensity

The normal turbulence distributions are shown in Figures 121 - 124. The measurements for this parameter were only obtained using the split film probe and as such are subject to the operational limitations discussed in Sections 3.3.3, 3.3.4. The values close to the wall have had to be ignored due to probe interference effects as discussed in Section 5.4.3.1. It is interesting to note that as the wall was approached, the lower film would cause a small contraction between the probe and the surface and therefore reduce the fluctuations measured by the lower film. Now, since the normal fluctuations were a function of the difference of the two film signals, this asymmetry would cause an apparent increase in the measured fluctuations. This can be seen to be the case as shown at one blowing rate in Figure 124. In general the values for the normal turbulence were approximately 60% of the longitudinal values as shown in Figure 125.

The normal turbulence intensity maximum appeared to be located at the centre of the shear layer, this being the proposed centreline of the vortex stream. This result seems reasonable since, at the vortex centreline, as each vortex passes, the velocity vector rotates through 180° to give the maximum variation of V , (see Figure 151).

Figure 126 shows that, at lower blowing rates, the positions of the maxima of the normal and longitudinal turbulence intensities do not coincide, the normal turbulence being closer to the surface. This

relates well to the proposed vortex stream. However, at higher blowing rates, the longitudinal turbulence maximum moves closer to the surface to coincide with the normal maximum. This phenomenon is not fully understood but may be due to the vortices not being circular. As the jet velocity is increased, so the vortices are deformed allowing the turbulence intensity maxima to converge.

5.4.3.3 The Reynolds shear stress $u'v'$

Figures 127 - 130 show the shear stress distributions measured by a split film probe for various angular positions and blowing rates. The results, although subject to the errors discussed in Section 3.3.4, 5.4.3.2 indicated the expected trends. A negative value near the wall was not measured but was indicated by the results, in agreement with a positive wall shear

$$\tau = - \rho \overline{u'v'}$$

An example of the wall shear stress as measured by Englar²⁸ is given in Figure 152.

Just inboard of the velocity maximum a zero shear stress point was indicated although it was apparently at a greater y/y_m value than was suggested for a curved wall jet by Wilson and Goldstein²¹. This may be an effect of the surface roughness of the trailing edge cylinder.

A maximum value of the shear stress occurred close to $y_m/2$ and the distributions then quickly reduced to a second zero value at approximately y_{min} . Outboard of this zero point the shear stress became negative, consistent with the return of a positive velocity gradient.

Figures 134, 135 give a comparison between the measured distributions, those produced by CIRCON³⁸ and those measured by Wilson and Goldstein²¹. They indicate the large difference in the distribution caused by the presence of the external flow and also the inability of the eddy viscosity model used in CIRCON³⁸ to predict the shear stress in the

outer region of the flow. Figures 134, 135 use the results shown in Figure 133 for the measured $\overline{u'v'}$ factored to take account of the limited bandwidth of the split film probes, as discussed in Section 4.2.3.

The interpretation of these shear stress results with regard to the proposed vortex stream is more complex than for the normal stresses $\overline{u'^2}$, $\overline{v'^2}$. It would seem reasonable however to expect the maximum shear to occur in the vicinity of the counter flowing stream between each vortex (see Figure 151). Also, since the fluctuating velocity at the inner edge of the vortex stream imparts a shear force on the surrounding fluid of constant sign, then it is reasonable for the time averaged shear stress at that point to be finite and non-zero. Hence the zero shear stress may well occur away from the velocity maximum.

At the outer edge of the vortex stream however, the shear stress is of fluctuating sign. This suggests that the time averaged shear stress should be zero; as was shown to be the case (Figure 127 - 130).

It is necessary to remember that the measured shear stresses ($\overline{u'v'}$) are perhaps not a realistic representation of the actual shears experienced by the fluid since the measurements were time averaged with respect to a fixed co-ordinate system.

5.4.3.4 The radial static pressure distribution

These results have already been discussed in Section 5.3.1. The unusual shape of the static pressure distributions is however now simply explained by the proposed discrete vortex flow field. The high pressure gradients that were measured represented the time averaged values of the pressure gradients appropriate to the high curvature of the streamlines of the flow around their local centres of curvature for each passing vortex, combined with the spacing of the vortices.

The radii of the proposed streamlines around the vortices is roughly an order of magnitude smaller than the surface radius (see Figure 148). This explains the disagreement between the measured pressure gradients

and those produced by the radial momentum equation.

5.5 General Conclusions Regarding the Experimental Results

Great care was taken in obtaining and evaluating the experimental results. The unexpected trends of the radial static pressure distributions led to a new understanding of a Coanda flow field which not only allowed a full interpretation of the turbulence measurements, but also explained many of the unusual phenomena associated with the performance of circulation control aerofoils.

It is hoped that the proposed flow field will lead to an improved theoretical prediction and the incorporation of such a discrete vortex calculation into an aerofoil prediction scheme will now be discussed in some detail in Chapter 6.

6. THE THEORETICAL IMPLICATIONS OF THE PRESENT RESULTS AND THE PROPOSED FLOW FIELD

6.1 The Deficiencies of the Method of Dvorak³⁸

The discussion of the current results in Chapter 5 indicated a number of deficiencies, other than the assumed flow field, in the time averaged parameters used in the trailing edge wall jet calculation of Dvorak and Kind³⁸.

i) Radial shear stress distribution

Figure 134 gives a comparison between a typical shear stress distribution predicted by Dvorak and Kind³⁸ and the current results. The eddy viscosity model used by Dvorak and Kind³⁸ equation (1.4) is used to calculate the shear stress distribution and it can clearly be seen how the model fails to predict the negative values in the outer region. This negative shear stress region was also shown to exist by Jones³³ but only close to the slot exit.

ii) Radial static pressure gradient

The measured static pressure gradients (Figures 139 - 142) indicate a significant departure from the usually assumed distribution given by an overall radial force balance. The values used in CIRCON³⁸ are taken from the potential flow calculation with a correction for excess jet momentum. Only the longitudinal pressure gradient is calculated by CIRCON³⁸ and an example of the distribution is shown in Figure 153.

iii) Local streamline radius of curvature

The experimental results (Figures 101, 103, 105) indicated that the local streamline radius of curvature was considerably larger than the usually assumed value of $(R_0 + y)$. This would have an effect throughout the wall jet calculation, most obviously in the continuity equation,

$$\frac{1}{R} \frac{\partial U}{\partial \theta} + \frac{\partial V}{\partial y} = 0 \quad (6.1)$$

and in the calculation of the following terms in the radial momentum equation.

$$\frac{U}{R} \frac{\partial V}{\partial \theta} + \frac{U^2}{R} + \frac{1}{R} \frac{\partial (\bar{u}' \bar{v}')}{\partial \theta}$$

It should of course be noted that the use of such time averaged relationships has produced a calculation method that is not based on a true representation of the flow field. The above deficiencies exist within the present calculation scheme; however there are some other aspects of the assumed flow field that CIRCON³⁸ is unable to account for, such as:

- i) jet exit angle relative to the local surface
- ii) surface roughness
- iii) variation of jet contraction geometry
- iv) variation of slot lip geometry

It is suggested that all of these may produce large changes in the performance of a given aerofoil.

If a wall jet calculation scheme is to be based upon the solution of the momentum equation, closed by a suitable turbulence model, then the finite difference technique is considered to be the most suitable. However, if the proposed flow field is to be accurately modelled then an inordinately fine mesh grid would be necessary, creating problems in terms of computer time and storage. It is proposed that a more physically representative approach would be to incorporate a discrete vortex wall jet model into the overall viscous/potential flow interaction technique.

6.2 Some Comments Upon the Incorporation of a Discrete Vortex Model Into an Aerofoil Calculation Scheme

Viscous/potential flow interaction techniques exist which enable the calculation of the boundary conditions around the trailing edge wall jet of a circulation control aerofoil. These boundary conditions are very important in this type of calculation since the conditions at the slot determine the initial vorticity and the lower surface boundary conditions usually define the wall jet separation pressure. The present results may be used to make some suggestions regarding the improvement of the existing discrete vortex wall jet calculation scheme (Smith et al^{34, 39}).

6.2.1 Determination of the initial vortex strength

Since it is known that apart from viscous effects the vorticity cannot be destroyed in a flow, merely dissipated, the determination of the initial vortex strength becomes of prime importance. It is this parameter that will control the extent of the Coanda attachment for a given surface geometry.

It would seem reasonable that the jet:free stream velocity difference should be the major factor in determining the vorticity; the external and slot flow are assumed steady. A realistic value should be obtained by considering the velocity profiles and in particular the instantaneous value of $(U_m - U_{min})$ close to the slot. It can be seen from Figure 149, that the time averaged values of this velocity difference exhibit an exponential type decay, suggesting some similarity between this parameter and the proposed vortex decay of Smith et al³⁹ in terms of energy dissipation. Before considering the actual vortex strength within a Coanda jet, two other factors must be considered; the frequency of the vortex shedding and the starting length of the flow. The frequency is considered in Section 6.2.2.

The question of starting length has long been a problem in all wall jet calculation methods, although problems are usually centred around the possible existence of a potential core and the extent of the slot lip wake. In the case of the log spiral trailing edge it is usual to assume

a false origin to the Coanda surface in order to produce the required similarity. As shown in Figure 148 the proposed flow field is more complex when considering starting length.

From the experimental results (Figure 107) the extent of the slot lip wake appeared to be small, of the order of 5 slot widths, and did not vary significantly with changes in slot lip thickness. This would suggest that a value for the wake length as a function of the blowing rate would be reasonable and not significantly in error. It is proposed that the wake length would reduce with increasing blowing due to the increased entrainment of the stronger jet.

The more difficult problem is that of the transition from the assumed vortex sheet at the end of the lip wake to the fully developed vortex flow. More recently Jimenez⁶³ has considered this problem without the presence of the wall. Considering an infinite uniform vortex sheet with strength ΔU , then if the sheet is perturbed locally it will tend to roll up into a tight spiral whose evolution and growth rate can be determined.

A double armed spiral is formed with a tight almost circular, central core. The streamlines form the familiar 'cats-eye' type pattern (Figure 154) and indicate that the large vortical structures are elliptical in shape with a semi axis ratio of 1.76. The growth rate of a free shear layer constructed of a number of such structures has been shown by Jimenez⁶³ to be:

$$\frac{\delta}{x} = \frac{4}{\pi^2} \frac{\Delta U}{(U_1 + U_2)} \quad (6.2)$$

This is in good agreement with the experimental observations of Brown and Roshko⁵⁷.

The distance over which the vortex sheet rolls up to form such discrete structures is not clear. However it would be logical to suggest that, providing the perturbation was not a randomly occurring event but

continuous, then the starting length could be approximated to one wavelength of the vortex stream, similar to the photographic evidence of Chandrsuda et al⁶².

The required perturbation could be due to either three dimensional effects within the turbulence structure or, as is more likely in the case of the wall jet, to the strong entrainment of the outer flow at the jet exit.

It is clear that these suggestions are reasonable for free shear layers. The effects of the presence of the wall and viscosity upon the formation of the structures is as yet undetermined. The wall will presumably have a more significant effect upon the growth rate than on the formation of the structures and this will be discussed in Section 6.2.3.

Having determined some criteria for the starting length, the problem of relating the time averaged velocity profiles to the instantaneous vortex strengths is now considered. Assuming the simplified vortex array and with the notation as shown in Figure 155 it can be shown that, assuming the vortices to exactly span the shear layer and that locally, the vortex strengths and size are constant, then

$$U_{x,r} = \sum_{-n}^n \frac{2K_n r}{(nd - x)^2 + r^2} + U_T \quad (6.3)$$

If this is integrated to produce the time averaged velocity then:

$$\bar{U}_{x,r} = \frac{2K_n r}{d} \sum_{-n}^n \left(-\frac{1}{r} \tan^{-1} \frac{nd}{r} + \frac{1}{r} \tan^{-1} \frac{d(n-1)}{r} \right) + \bar{U}_T \quad (6.4)$$

Hence the ratio of instantaneous to time averaged velocity at the edge of the simplified vortex stream is given by,

$$\frac{U}{\bar{U}} = \frac{\sum_{-n}^n \frac{2K_n r}{n^2 d^2 + r^2} + U_T}{\frac{2K_n r}{d} \sum_{-n}^n \left(\tan^{-1} \frac{nd}{r} - \tan^{-1} \frac{d(n-1)}{r} \right) + U_T} \quad (6.5)$$

This is taken at a point on the edge of the shear layer coincident with a vortex centreline. The parameter d is the wavelength of the stream. Figure 154 shows some results from this calculation for ratios of vortex strength for typical length scales and indicates the magnitude of the corrections in order to allow for time averaged flow.

Using the simple model of Figure 155 it is obvious that the instantaneous value of V , the normal velocity at any vortex centre, providing it is not at the extremities of the stream, will always be zero, since the normal components of the vortices tend to cancel. Thus it becomes clear that the dissipation of the vortex strength and changes in vortex spacing dictate the locus of the vortex stream. This will be further discussed in Section 6.2.3.

6.2.2 Determination of the vortex shedding frequency

The determination of the vortex shedding frequency is of vital importance to any discrete vortex theoretical method since it dictates the time step interval of the calculation. The current experimental work suggested that the frequencies of the stream were above the normal operating bandwidth (20 - 40 KHz) of the hot wire anemometers. This would tend to be supported by other experimental evidence, such as Brown and Roshko⁵⁷, Horne et al⁵⁴. It is also reasonable to suggest that, not including vortex pairing or dissipation, which will be discussed in the next section, the time interval between vortices remains constant for the wall jet. Now, since

$$\text{frequency} = \frac{1}{\text{time interval}} = \frac{\text{streaming speed}}{\text{separation distance}} \quad (6.6)$$

the distance between adjacent vortices must vary with changes in streaming speed as well as with their mutual interaction. Figure 157 shows the variation of $\bar{U}_{m/2}$, the proposed streaming speed, with angle from the jet exit. Since $\bar{U}_{m/2}$ is measured at the vortex centres, its variation will be almost independent of the size, strength and frequency of the vortex stream.

The shedding frequency is usually determined, such as in the cases of cylinders, blunt aerofoils and spoilers, from the Strouhal number.

$$S_T = \frac{f d}{U} \quad (6.7)$$

where d and U are assumed typical lengths and velocities (such as the free stream velocity and the diameter in the case of the cylinder). For a given situation, the Strouhal number remains constant and the frequency then becomes a linear variable with velocity.

For the case of the highly curved wall jet with an external stream, it is proposed that,

$$d = f_n \text{ (slot lip thickness, jet boundary layer displacement thickness)}$$

$$U = \text{velocity difference at the slot}$$

The effect of slot height upon the value of d , given as δ_{JET}^* , the displacement thickness of the jet boundary layer, is suggested in order to account for the presence of the jet boundary layers, as these are the source of the majority of the vorticity flux $(-\partial U / \partial y)$, and the possible existence of a constant velocity core. It is possible that a similar effect for the upstream boundary layers should be included. However the strong entrainment at the slot exit has been shown to alter the shape of the upstream boundary layer velocity profile and insufficient data is available on which to base any qualitative suggestions. Certainly, since the vorticity of a fluid element is defined as

$$\omega = \frac{\partial v}{\partial x} - \frac{\partial u}{\partial y} \quad (6.8)$$

the largest contribution will come from the jet boundary layer/slot lip wake interaction and the suggested scaling length is representative. From the current geometry where $d = 0.25 \times 10^{-3} \text{ m}$ (0.010 inches) and

assuming a constant Strouhal number of 0.2 (typical of vortex shedding flows), the frequency variation shown in Figure 158 can be obtained. The frequencies indicated are in the correct range compared with the bandwidth of the anemometer equipment and suggest a wavelength (distance between adjacent vortices) given by

$$\lambda = \frac{U}{f} = \frac{\text{streaming speed}}{\text{frequency}}$$

of the order of 1 + 2 mm (0.04 + 0.08 inches).

Since the formation of the vortices is suggested to be largely dependent upon the interaction of the jet boundary layer and the slot lip wake, the effects of the proximity of the wall are expected to be small.

6.2.3 On the growth and dissipation of the vortex stream

The vortex stream which makes up the shear layer of the wall jet grows due to the individual growth of each vortex by entrainment. As the vortices roll up, they continue to entrain the outer fluid at a rate dependent upon the individual vortex strengths and the spacing between adjacent vortices. In his analysis, Jimenez⁶³ considered the entrainment process of each vortex. He showed that the vortices will continue to grow in the familiar 'cat's-eye' shape but that the expansion of the individual vortex in the lateral direction saturates before the longitudinal axis. The limiting condition then becomes the point at which adjacent vortices touch. At that point it is suggested that the process of pairing occurs. Up to the present time this process has not been allowed for in discrete vortex wall jet calculations.

The pairing process is a very complex one. There are two possibilities to be considered. The first possibility is that, at the very point that the vortices touch, the effect of having opposite velocity vectors at the same point causes a severe disruption of the local streamline pattern and instant amalgamation of the two vortices occurs. Upon amalgamation, the nett vorticity will be conserved while the wavelength

of the local vortex stream is doubled. If the cross sectional area of the 'new' vortex is roughly double that of a previous vortex, then separation between vortices again exists and entrainment continues. The second possibility usually considered is that, upon touching, the two vortices roll round each other for a fraction of a turn before amalgamation; the so called 'helical pairing'. This process is indicated by the results shown by Chandrsuda et al⁶². It is interesting to note that Jimenez⁶³ also shows that the pairing and entrainment process can approach a limit cycle at which point the vortices are no longer generated downstream. This is interesting and could have significance in determining the extent of the wall jet attachment for a given blowing momentum.

The effect of the presence of the wall is obviously important in determining the growth rate of the vortex stream. Compared with a free shear layer, the growth of the vortices is restricted due to the proximity of the solid surface and of course a certain amount of energy will be lost from the stream due to viscosity within the inner layer. The growth of a free shear layer derived by Jimenez⁶³ is given as equation (6.3) and indicated in Figure 159. The reduction due to the presence of the wall and the effect of the conservation of angular momentum in the curved wall case are clear.

The single vortex stream can be simply modelled in potential flow and a wall can be included by adding the usual mirror images. Introduction of the additional boundary condition that $U \rightarrow 0$ as $y \rightarrow 0$ is more complex and is yet to be satisfactorily attempted.

It is generally assumed that the vorticity will be dissipated by the smaller scale eddies within a flow and that large vortical structures will degrade to a smaller scale - the so called 'energy-cascade', although this is usually a strong three dimensional flow. In the proposed flow field it is obvious that no significant degradation of the flow occurs. It is therefore suggested that the energy is dissipated in three ways:-

- i) by the small scale turbulence surrounding each individual vortex
- ii) by the catastrophic pairing phenomenon
- iii) via the wall shear stress, which exerts a moment on the vortices.

It immediately becomes obvious that the modelling of such a flow field is inherently extremely complicated, and the estimation of the dissipation of the vortical energy is a key part of the technique. The work of Jimenez⁶³ would seem to indicate that the pairing process is the dominant factor in the growth of the shear layer and that inclusion of a limit on the size of adjacent vortices is necessary. Once the limit is reached then pairing should be accounted for with a coincident loss in vorticity for the new single structure.

The assumption that the structures can be represented by simple point vortices is valid since, although the deduced theoretical streamline patterns tend to cylindrical cores, when viewed from a distance, a vortex with a cylindrical core will appear to be a simple point vortex. With this in mind it would suggest that the proposed pairing limit should be checked by estimating when two adjacent 'cats-eye' streamlines touch.

The inviscid potential flow method of Smith et al³⁹, has already shown that a discrete vortex stream will remain attached to a highly curved surface. It was however necessary to include an exponential vortex strength decay to obtain reasonable agreement with experimental lift coefficients. It is hoped that incorporation of some of the above suggestions may allow removal of the somewhat arbitrary vortex decay rate without reducing the accuracy.

6.2.4 Some further considerations

The above comments have been concerned primarily with producing more realistic techniques for incorporating a discrete vortex calculation in a curved wall jet method. When considering the true aerofoil, some further considerations may need to be made.

6.2.4.1 Effect of longitudinal pressure gradient

As has been shown, the wall jet exists in the presence of extremely strong positive and negative longitudinal pressure gradients. It appeared from the turbulence results, (Section 5.4.3) that the initial negative pressure gradient stabilised, or in some cases, gradually reduced the measured turbulence levels. As soon as the suction peak was passed and the pressure gradient became positive, the turbulence levels increased. This may well indicate that little vortical energy is dissipated within the flow until after the jet has negotiated the suction peak, with the exception of that due to skin friction.

6.2.4.2 Effect of the presence of shock waves

In some flight cases it becomes necessary to choke the slot exit to obtain sufficient jet mass flow. In these cases the jet is under-expanded and can become locally supersonic at the jet exit. Little is known of the detailed structure of this flow, or of compressibility effects in general, except that an 'expansion fan' appears to emanate from the slot lip and that eventually, at pressure ratios approaching 2.5, the jet will detach.

Since the velocity difference as defined in Section 6.2.2 remains of similar order, the shedding frequency also remains of similar magnitude. However, since the streaming speed of the vortices is greatly increased, the wavelength of the vortices becomes long. This would tend to suggest that at some point, the vortices become insufficiently close to each other to maintain the attachment, and hence the flow separates. This may explain why the change in flow situation occurs so suddenly and also, since the longer wavelengths

reduce entrainment, why the transonic performance declines.

Many of these points will remain unresolved until further experimental data becomes available.

7. CONCLUSIONS

A program of research has been conducted on the aerodynamics of a nominal 20% thickness:chord ratio circulation controlled elliptic aerofoil section equipped with leading and trailing edge blowing slots.

The overall lifting performance results agreed well with the limited amount of previous work available. The detailed investigation of the thin, highly curved trailing edge wall jet demanded the development of new test techniques and equipment as well as the capability to obtain repeatable, steady, two-dimensional flow conditions around the model section. The results obtained have led to a new insight into the nature of Coanda flow which offers the possibility of a simpler theoretical solution to the complex wall jet flow.

7.1 The Nature of the Coanda Flow

The results from the detailed trailing edge wall jet investigation led to the proposed discrete vortex flow field, fully discussed in Chapter 5.

Each passing vortex produces a reduced static pressure between itself and the adjacent surface, drawing the vortex towards the surface. The balance between the 'centrifugal' force of the stream and the attachment of the vortices causes the typical wall jet properties of attachment and growth. The effect of the high frequency vortex stream is also to strongly entrain the outer fluid, be it moving or stationary, due to the influence of the velocity field of the vortices.

The assumption that the initial vortex strength and shedding frequency (and hence the degree of attachment of the wall jet) are dependent upon both C_{μ} and the slot geometry has allowed a variety of observed effects on overall lifting performance of circulation control aerofoils (e.g. slot height, probe interference) to be simply explained.

7.2 Theoretical Implications

The proposed flow field is believed to explain the inability of the existing "time averaged" theoretical methods (either integral or finite difference approximations) to satisfactorily predict circulation control aerofoil or even highly curved wall jet flows.

The existing potential flow discrete vortex method of Smith et al³⁹ provides an indication of the simplicity of replacing a wall jet by a stream of discrete vortices. The present results would tend to suggest that a more successful method would include the effects of viscosity, vorticity dissipation and pairing of adjacent vortices at some critical point in their development. The potential for an extremely quick calculation scheme still exists however.

7.3 Conclusions Regarding the Experimental Techniques and Instrumentation

7.3.1 Two-dimensionality of flow

The attaining of two-dimensional flow, both over the aerofoil and on exit from the slot, was of vital importance to the validity of the experimental results. The use of some form of secondary blowing was shown to be necessary; however experience suggests that the fixed nature of the tip jet sealing strips became a problem when the slot height was varied. It was also apparent that at higher blowing rates the small tip jets were insufficient to fully compensate for the end plate effects. It is suggested that some form of wall blowing on the end plates would be a more universal solution providing sufficient air supplies were available.

7.3.2 Anemometry

The techniques developed for the hot wire and film probes were shown to provide repeatable, accurate results. By using both types of probe, allowance could be made for the frequency response and size limitations of the split film probes.

The digital analysis techniques were shown to be very suitable to this type of data acquisition and extended the applicability of the split film probes by allowing the flow vector to be at some unknown angle to the sensors.

Mention should also be made of the capacitance position control system developed during this research. It had applications for positioning any metal probe in close proximity to any metallic portion of the aerofoil and was unaffected by airflow. Its accuracy and repeatability were excellent and similar systems may be of significant value in a variety of other aerodynamic testing environments.

7.3.3 Determination of aerofoil effective incidence

The use of on-line mini-computers and simple approximate theories to assess the effective incidence of the aerofoil proved to be the quickest, most reliable technique developed thus far. The equipment also provided instant verification of the validity of the experimental pressure distributions and monitored the stability of a given flow condition over an extended period of time.

8. SUGGESTIONS FOR FURTHER RESEARCH

This experimental research has indicated a need for further investigation of the vortex stream that has been shown to exist in the trailing edge wall jet. It would be desirable to investigate a number of different aspects.

- the vortex shedding frequency.
- the pairing processes of the vortices.
- the effects of the geometry of the slot on the vortex formation.
- the effect of the severe longitudinal pressure gradients upon the vortex stream.
- the influence of free stream and jet flow Mach number.

Due to the inherently high shedding frequency of the vortices it is suggested that an optical technique, either a stroboscopic schlieren or holography for example, would yield the most useful results.

It would also be of interest to investigate the effects of non-circular trailing edges to enable the influence of surface curvature on jet attachment to be determined.

From a full scale application viewpoint, further information regarding the drag of circulation control aerofoils is required. This is an area still grossly deficient in experimental and reliable theoretical results.

Taking into account the suggestions of Chapter 6 regarding the inclusion of a discrete vortex method into an aerofoil calculation scheme, it should be possible to replace the somewhat arbitrary vortex strength decay rate from the method of Smith et al³⁹ by a viscous approximation of the dissipation of vorticity and the pairing of adjacent vortices. This should provide an improved prediction method with more relevance to the real flow.

REFERENCES

1. Young D. W. Wind tunnel tests of the Coanda wing and
Zonars D. nozzle.
U.S.A.F. TR 6199, September 1950.
2. Cheeseman I. C. The application of circulation control by
Seed A. R. blowing to helicopter rotors.
Journal of the Royal Aeronautical Society,
Volume 71, July 1967.
3. Williams R. M. Applications of circulation control rotor
 technology to a stopped rotor aircraft design.
Presented at First European Rotorcraft and
Powered Lift Aircraft Forum, Southampton,
September 1975.
4. Reader K. R. Circulation control applied to a high speed
Wilkerson J. B. helicopter rotor.
Presented at the 32nd National V/STOL
Forum of the American Helicopter Society,
Washington D.C., May 1976.
5. Wilkerson J. B. The application of circulation control
Reader K. R. aerodynamics to a helicopter rotor model.
Linck D. W. Presented at the 29th National Forum of the
American Helicopter Society, May 1973.
6. Williams R. M. Design considerations of circulation control
Rogers E. O. rotors.
Presented at the 28th National Forum of the
American Helicopter Society, May 1971.
7. Ottensmeyer J. Two dimensional subsonic evaluation of a 15
 percent thick circulation control airfoil
 with slots at both leading and trailing edges.
NERDC Report 4456, July 1974.

8. Barnes D. R.
Kirkpatrick D. G.
McCoubrey G. A.

Circulation control rotor flight demonstrator presented at American Helicopter Society symposium on rotor technology, August 1976.
9. Launder B. E.
Rodi W.

Summary presentation of the turbulent wall jet - a review of the experimental data presented at the AFOSR-HTTM-Stanford conference on complex turbulent flows. Stanford University, September 1980.
10. Irwin H. P. A. H

Measurements in a self preserving plane wall jet in a positive pressure gradient.
Journal of Fluid Mechanics (1973), Volume 61, Part 1.
11. Kruka V.
Eskinazi S.

The wall jet in a moving stream.
Journal of Fluid Mechanics (1964), Volume 20, Part 4.
12. Goradia S. H.
Colwell G. T.

Parametric study of a two-dimensional turbulent wall jet in a moving stream with arbitrary pressure gradient.
AIAA Journal Volume 9, Number 11, November 1971.
13. North P.

The suppression of flow separation by sequential wall jets.
Journal of Fluids Engineering, September 1976.
14. Kacker S. C.
Whitelaw J. H.

Some properties of the two-dimensional turbulent wall jet in a moving stream.
Journal of Applied Mechanics, December 1968.
15. Kacker S. C.
Whitelaw J. H.

The effect of slot height and slot turbulence intensity on the effectiveness of the uniform density, two-dimensional wall jet.
Journal of Heat Transfer, November 1968.

16. Kacker S. C. The turbulence characteristics of two-dimensional wall jet and wall wake flows.
Whitelaw J. H. Journal of Applied Mechanics, March 1971.

17. Myers G. E. Plane turbulent wall jet flow development and friction factor.
Schauer J. J. Journal of Basic Engineering, March 1963.
Eustis R. H.

18. Gartshore I. S. The turbulent wall jet in an arbitrary pressure gradient.
Newman B. G. The Aeronautical Quarterly, February 1969.

19. Bradshaw P. Turbulent wall jets with and without an external stream.
Gee M. T. Reports and Memoranda 3252, June 1960.

20. Newman B. G. The deflexion of plane jets by adjacent boundaries - Coanda effect.
Boundary Layer and Flow Control (ed Lachmann)
Pergamon Press, 1961, Volume 1.

21. Wilson D. J. Turbulent wall jets with cylindrical stream-wise surface curvature.
Goldstein R. J. Journal of Fluids Engineering, September 1976.

22. Guitton D. E. Self-preserving turbulent wall jets over convex surfaces.
Newman B. G. Journal of Fluid Mechanics (1977) Volume 81, Part 1.

23. Giles J. A. Turbulent wall jets on logarithmic spiral surfaces.
Hays A. P. The Aeronautical Quarterly, August 1966.
Sawyer R. A.

24. Fekete G. I. Coanda flow in a two-dimensional wall jet on the outside of a circular cylinder. McGill University, Mech. Eng. Report 63-11, 1963.
25. Guitton D. E. Some contributions to the study of equilibrium and non-equilibrium wall jets over curved surfaces. PhD Thesis, McGill University, 1970.
26. Englar R. J. Two-dimensional transonic wind tunnel tests of three 15 percent thick circulation control airfoils. NSRDC AL-182, December 1970.
27. Englar R. J. Two-dimensional subsonic wind tunnel tests of two 15 percent thick circulation control airfoils. NSRDC AL-211, August 1971.
28. Englar R. J. Experimental investigation of the high velocity Coanda wall jet applied to bluff trailing edge circulation control airfoils. NSRDC 4708, September 1975.
29. Englar R. J.
Trobaugh L. A.
Hemmerly R. A. STOL potential of the circulation control wing for high performance aircraft. Journal of Aircraft Volume 15, March 1978.
30. Williams R. M.
Howe H. J. Two-dimensional subsonic wind tunnel tests on a 20 percent thick, 5 percent cambered circulation control airfoil. NSRDC AL-176, August 1970.

31. Englar R. J. Two-dimensional subsonic wind tunnel tests of a cambered 30 percent thick circulation control airfoil.
NSRDC AL-201, May 1972.
32. Kind R. J. A proposed method of circulation control.
PhD Thesis, Cambridge 1967.
33. Jones D. G. The performance of circulation controlled airfoils.
PhD Thesis, Cambridge 1970.
34. Smith R. V. A theoretical and experimental study of circulation control with reference to fixed wing applications.
PhD Thesis, Southampton, 1978.
35. Newman B. G. The prevention of separation by blowing in two-dimensional flow.
Irwin H. P. A. H. From 'Flow separation', AG-CP 168, May 1975.
36. Thwaites B. Incompressible Aerodynamics.
Clarendon Press, 1960.
37. Dunham J. A theory of circulation control by slot blowing applied to a circular cylinder.
Journal of Fluid Mechanics (1968), Volume 33, Part 3.
38. Dvorak F. A. Analysis method for viscous flow over circulation controlled airfoils.
Kind R. J. Journal of Aircraft, Volume 16, No. 1.
January 1979.

39. Smith R. V. Discrete vortex modelling applied to the
Soliman M. E. prediction of circulation control.
Cheeseman I. C. Paper submitted to Journal of Fluid
Mechanics, 1980.
40. Englar R. J. Test techniques for high-lift, two-
Williams R. M. dimensional airfoils with boundary layer
and circulation control for application to
rotary wing aircraft.
NSRDC 4645, July 1975.
41. McGahan W. A. The incompressible turbulent wall jet in an
adverse pressure gradient.
PhD Thesis, M.I.T. 1965.
42. Pankhurst R. Wind tunnel technique.
Holder D.
43. British Standard Methods for the measurement of fluid flow
1042 in pipes.
1964.
44. Kristensen H. S. Hot wire measurements in turbulent flows.
DISA information dept.
45. Starsmore N. PhD Thesis, Bath University 1977.
46. Mojola O. O. A hot wire method for three-dimensional
shear flows.
DISA Information No. 16, July 1974.
47. Thermo Systems Inc. Split film sensor.
Report TB20.

48. Pache W. Measuring the mean static pressure in
turbulent or high frequency fluctuating flow.
DISA Information No. 22, December 1977.

49. Dvorak F. A. A viscous/potential flow interaction analysis
Woodward F. A. method for multi-element infinite swept wings.
NASA CR24-76, November 1974.

50. Young A. D. The behaviour of a pitot tube in a transverse
Maas J. N. total pressure gradient.
Reports and Memoranda 1770, September 1936.

51. Hoerner F. Fluid Dynamic Lift.
Borst H. Hoerner, 1975.

52. Miller D. R. Static pressure in the free turbulent jet.
Comings E. W. Journal of Fluid Mechanics (1957).
Volume 3, Part 1.

53. Kind R. J. Calculation of the normal stress distribution
in a curved wall jet.
The Aeronautical Journal, Volume 75,
May 1971.

54. Horne C. Experimental observations of a 2-D planar
Karamcheti K. wall jet.
AIAA paper 79-0208, 1979.

55. Davies P. O. A. L. Transition in free shear layers.
Baxter D. R. J. Institute of Sound and Vibration Research
Southampton University.

56. Dams S. M. On a vortex sheet model for the mixing
Kuchemann D. between two parallel streams.
RAE Tech. Report 72139, August 1972.

57. Brown G. L.
Roshko A.
On density effects and large structure in
turbulent mixing layers.
Journal of Fluid Mechanics (1974).
Volume 64, pp. 775 - 816.

58. Clark J. A.
Markland E.
Vortex structures in the free shear layer
of a plane wall jet.
Queen's University Belfast, Dept. Mech. Eng.
Report 471, 1970.

59. Wagnanski I.
Oster D.
Fiedler H.
Dziomba B.
On the perseverance of a quasi-two-
dimensional eddy-structure in a turbulent
mixing layer.
Journal of Fluid Mechanics (1979).
Volume 93, Part 2.

60. Davis M. R.
Davies P. O. A. L.
Shear fluctuations in a turbulent jet shear
layer.
Journal of Fluid Mechanics (1979)
Volume 93, Part 2.

61. Browand F. K.
Troutt T. R.
A note on spanwise structure in the two-
dimensional mixing layer.
Journal of Fluid Mechanics (1980).
Volume 97, Part 4.

62. Chandrasekara C.
Mehta R. D.
Weir A. D.
Bradshaw P.
Effect of free stream turbulence on large
structure in turbulent mixing layers.
Journal of Fluid Mechanics (1978)
Volume 85, Part 4.

63. Jimenez J.
On the visual growth of a turbulent mixing
layer.
Journal of Fluid Mechanics (1980).
Volume 96, Part 3.

APPENDIX I : THE SCANIVALVE CONTROL PROGRAMAI.1 Main Program

The arrays and control parameters are established and a blockage correction applied to the input dynamic pressure.

```

COMMON TCON1, TCON2, DYNP, SP50(4), SP(44), SPAV
COMMON X(44), XNEW(44), SPNEW(44)
COMMON ZERO1, ALPHA, CD
DIMENSION IDATE(3)
WRITE(4, 1500)
1500  FORMAT(' INPUT RUN NUMBER AND DATE I FORMAT ')
      READ(4, 1000) IRUN, (IDATE(I), I=1, 3)
      WRITE(4, 1510)
1510  FORMAT(' INPUT DYNP, TCON1, TCON2 ')
      READ(4, 1001) DYNP, TCON1, TCON2
1000  FORMAT(I4, 3I3)
C      BLOCKAGE CORRECTION
      DYNP=DYNP*1.0275
1001  FORMAT(3F10.4)
      RUN=FLOAT(IRUN)
99    CONTINUE

```

The scanivalves are checked to their home positions and the program awaits an external event (+5 volts d.c. on A/D channel 4) to begin sampling. The subroutine STEP, steps the Scanivalve 1 port; the passed argument defines which scanivalve is to be stepped. The required D/A channel is held at +9.5 volts for 40 ms and then at 0 volts for 100 ms. The subroutine TDWELL allows a 250 ms delay, enabling the pressure at the transducer face to reach a steady state.

```

C      ZERO D/A CHANNELS
      CALL DAC(0,0,0)
      CALL DAC(1,0,0)
C      HOME SCANIVALVES
5      HMSIG1=ADC(0)
      IF<HMSIG1.GE.0.5> GOTO 10
      CALL STEP(0)
      CALL TDWELL
      GOTO 5
10     CONTINUE
C      S/V1 HOMED AT FIRST PORT
6      HMSIG2=ADC(2)
      IF<HMSIG2.GE.0.5> GOTO 11
      CALL STEP(1)
      CALL TDWELL
      GOTO 6
11     CONTINUE
C      S/V2 HOMED AT FIRST PORT
C      WAIT FOR EXTERNAL EVENT TO TRIGGER SAMPLING
50     STSIG=ADC(4)
      IF <STSIG.GE.2.0> GOTO 12
      GOTO 50
12     CONTINUE

```

Upon the external event trigger, the program samples the four half chord pressures. These were not used in this work. The 44 static tappings around the centreline are then sampled; allowance is made for the fact that tapping ~~4~~ 4 was unusable. The subroutine SCANCL samples and stores the static pressures; an average of 50 samples of each pressure is used. The Scanivalves are then checked to have returned to the home position.

```

C      START BY SCANNING THE FOUR HALF CHORD PRESSURES
      I1=0
      CALL STEP(0)
      CALL STEP(1)
      CALL STEP(0)
      CALL STEP(1)
      CALL TDWELL
      CALL SCAN50(1, I1)
      CALL TDWELL
      CALL SCAN50(3, I1)
      CALL STEP(0)
      CALL STEP(0)
      CALL TDWELL
      CALL SCAN50(1, I1)
      CALL STEP(1)
      CALL STEP(1)
      CALL TDWELL
      CALL SCAN50(3, I1)
C      NOW SCAN THE 44 TAPPINGS ON CENTRELINE CHORD
C
      L=0
      DO 20 J=1, 43
      L=L+1
      L1=L/2
      L2=2*L1
      IF(L2. EQ. L) GOTO 13
      M=0
      N=1
      GOTO 14
13      M=1
      N=3
14      CALL TDWELL
      CALL ZERO(N)
      CALL STEP(M)
      CALL TDWELL
      IF(L. NE. 4) GOTO 80
      L=L+1
      CALL STEP(M)
      M=0
      N=1
      GOTO 14
80      CONTINUE
      CALL SCANCL(N, J)
81      CONTINUE
      CALL STEP(M)
20      CONTINUE
C      BOTH SCANIVALVES SHOULD BE HOMED CHECK
      HMSIG1=ADC(0)
      HMSIG2=ADC(2)
      IF(HMSIG1. GE. 0. 5. AND. HMSIG2. GE. 0. 5) GOTO 30
      WRITE(4, 2000)
      FORMAT(' ', 5X, 'SCANIVALVES OUT OF SYNC', '/')
      GOTO 31
2000
30      WRITE(4, 2001)
2001      FORMAT(' ', 5X, 'SCANIVALVES HOMED IN SYNC', '/')
31      CONTINUE

```

The subroutine CALCS1 interpolates for extra points between the measured pressures using a Lagrangian interpolation technique and then integrates the pressure coefficients to give C_L and C_{Dp} .

Subroutine EFFECT allows for estimation of the effective incidence of the aerofoil from the measured pressure distributions and is shown separately in Section A1.2. The main program then outputs the results.

```

C      RUN COMPLETED - PRESSURE COEFFICIENTS NOW EVALUATED
      CALL CALCS1
      CALL EFFECT
C      OUTPUT RESULTS
      WRITE(4,4000)
4000   FORMAT(' DO YOU WANT OUTPUT? 1=YES')
      READ(4,4010)IDEC
4010   FORMAT(I2)
      WRITE(4,2002)(IDATE(I),I=1,3),RUN
2002   FORMAT(' ',20X,I3,'/',I3,'/',I3,10X,'RUN NUMBER',F5.1,/)
      WRITE(4,2003)
2003   FORMAT(' ',5X,'***** INPUT PARAMETERS *****',/)
      WRITE(4,2004)DYNP,ALPHA
2004   FORMAT(' ',5X,'DYNAMIC PRESSURE =',F6.3,/,
*      5X,'MODEL EFFECTIVE INCIDENCE = ',F8.2,/,
*      5X,'C MU TRAILING EDGE = ',/,)
      IF(IDEC.NE.1)GOTO 75
      WRITE(4,3010)
3010   FORMAT(' MODEL STATIC PRESSURES')
      WRITE(4,2006)(SP(I),I=1,43)
2006   FORMAT(6F9.3)
      WRITE(4,3050)
3050   FORMAT(' INTERPOLATED PRESSURES')
      WRITE(4,3060)(SPNEW(I),I=1,43)
3060   FORMAT(6F9.3)
75     CONTINUE
      WRITE(4,2010)SPAV
2010   FORMAT(' ',5X,'***** LIFT COEFFICIENT *****',/,
*      5X,'CL = ',F10.4,/)
      WRITE(4,2020)CD
2020   FORMAT(6X,'***** DRAG COEFFICIENT *****',/,5X,'CD=',F10.4,/)
      RUN=RUN+0.1
      GOTO 99
      STOP
      END

```

AI.2 Subroutine EFFECT

This subroutine initially calculates the leading edge lift coefficient (as far as $x/c = 0.5$) from the experimental results.

```

C      SUBROUTINE EFFECT
      TO FIND EFFECTIVE INCIDENCE OF MODEL
      COMMON TCON1, TCON2, DYNP, SP50(4), SP(44), SPAV
      COMMON X(44), XNEW(44), SPNEW(44)
      COMMON ZERO1, ALPHA, CD
      DIMENSION THETA(44), CP(44)
      SUM=0.0
      DO 100 I=33, 43
      XFACT2=(XNEW(I)-X(I))
      SUM=SUM+XFACT2*(SPNEW(I)+SP(I))/2.0
100    CONTINUE
      CONTINUE
      DO 150 I=1, 11
      XFACT=(XNEW(I)-X(I))
      SUM=SUM+XFACT*(SPNEW(I)+SP(I))/2.0
150    CONTINUE
      DO 200 I=33, 43
      I1=I+1
      IF(I.EQ.43)GOTO 210
      GOTO 220
210    I1=1
220    CONTINUE
      XFACT1=(X(I1)-XNEW(I))
      SUM=SUM+XFACT1*(SP(I1)+SPNEW(I))/2.0
200    CONTINUE
      DO 250 I=1, 10
      I1=I+1
      XFACT1=(X(I1)-XNEW(I))
      SUM=SUM+XFACT1*(SP(I1)+SPNEW(I))/2.0
250    CONTINUE
      SPAV1=SUM/11.712
      CL=-SPAV1
      CL1=CL
      WRITE(4,1500)CL
1500  FORMAT(' CALCULATED LEADING EDGE CL =',F6.3)

```

The experimental data is then plotted on a CRT display at the tunnel console.

```

312  CONTINUE
      CALL CLRPLT
      CALL SCALE(0,1,24,-2.00)
      CALL PLINE(0,0,24,0)
      CALL PLINE(0,1,0,-2)
C    PLOT EXPERIMENTAL DATA
      DO 500 I=23,42
        CALL PLINE(X(I),SP(I),XNEW(I),SPNEW(I))
        CALL PLINE(XNEW(I),SPNEW(I),X(I+1),SP(I+1))
500  CONTINUE
      DO 550 I=1,22
        CALL PLINE(X(I),SP(I),XNEW(I),SPNEW(I))
        CALL PLINE(XNEW(I),SPNEW(I),X(I+1),SP(I+1))
550  CONTINUE

```

The operator inputs an estimated effective incidence and the program iterates around the overall theoretical lift coefficient (using the equations given in Section 3.1.1) until the theoretical and experimental leading edge lift coefficients ($0 < x/c < 0.5$) are tolerably close.

```

360  WRITE(4,1000)
1000  FORMAT(' INPUT ALPHA EST')
      READ(4,2000)ALPHA
2000  FORMAT(F6.3)
300  CONTINUE
      DO 310 I=1,43
        THETA(I)=ACOS((2.*X(I)/23.425)-1.)
        IF(I.LT.22)GOTO 310
        THETA(I)=2.*3.14159-THETA(I)
310  CONTINUE
      ALPHA=ALPHA/57.296
311  CONTINUE
      DO 320 I=1,43
        DUMMY=CL/(2.*3.14159*1.2)
        GAMMA=ASIN(DUMMY)-ALPHA
        TOP=2.4*(SIN(THETA(I))+SIN(ALPHA+GAMMA))
        BOT=1.04-0.96*COS(2.0*ALPHA+2.0*THETA(I))
        AUINF=TOP/BOT
        BRAKET=0.04+(0.96*(SIN(ALPHA+THETA(I))**2))
        CP(I)=1.-AUINF*AUINF*BRAKET
320  CONTINUE
      TSUM=0.0
      DO 600 I=33,42
        XFACT=X(I+1)-X(I)
        TSUM=TSUM+XFACT*(CP(I)+CP(I+1))/2.0
600  CONTINUE
      DO 650 I=1,17
        XFACT=X(I+1)-X(I)
        TSUM=TSUM+XFACT*(CP(I)+CP(I+1))/2.0
650  CONTINUE
      TCL=-TSUM/11.712
      IF(ABS(TCL-CL1).LT.0.0001)GOTO 610
      CL=CL-(TCL-CL1)/2.
      GOTO 311
610  CONTINUE

```

The theoretical pressure distribution is then superimposed upon the experimental results and the operator evaluates the match visually. A satisfactory incidence is transferred to the main program upon conclusion.

```

C      PLOT THEORY
C
C
      DO 340 I=1, 43
350    CONTINUE
        C1=CP(I)-.05
        C2=CP(I)+.05
        C3=X(I)+.25
        C4=X(I)-.25
        CALL PLINE(C3, CP(I), C4, CP(I))
        CALL PLINE(X(I), C1, X(I), C2)
340    CONTINUE
      WRITE(4, 1100)
1100   FORMAT(' O. K. =1')
      READ(4, 1200) IDEC
1200   FORMAT(I2)
      IF( IDEC. NE. 1) GOTO 312
      ALPHA=ALPHA*57.296
      RETURN
      END

```

APPENDIX II : HOT WIRE ANEMOMETRY

AII.1 Derivation of a Hot Wire Ambient Temperature Correction

The temperature correction given in reference 44, equation 72 is,

$$E^2 = E_{om}^2 + B(\rho U)^n \left(1 - \frac{\alpha}{\sigma} \Delta T_m\right)$$

where

$$\sigma = \frac{T_w - T_m}{T_m} = \text{overheat ratio}$$

$$\Delta T_m = T_m - T_{mc}$$

$$\alpha = \frac{\sigma}{T_m - T_{mc}}$$

and the subscripts are

w = wire

m = ambient fluid

mc = ambient fluid at calibration

then, α can be given by

$$\alpha = \frac{(T_w - T_m)}{(T_w - T_{mc})} \times \frac{1}{T_m}$$

continued

$$1 - \frac{\alpha}{\sigma} \Delta T_m = 1 - \frac{(T_w - T_m)}{(T_w - T_{mc})} \frac{1}{T_m} \frac{(T_m - T_{mc})}{(T_w - T_m)} T_m$$

$$\begin{aligned} \text{L.H.S.} &= 1 - \frac{(T_m - T_{mc})}{(T_w - T_{mc})} \\ &= \frac{(T_w - T_{mc}) - (T_m - T_{mc})}{(T_w - T_{mc})} \\ &= \frac{(T_w - T_m)}{T_m} \frac{T_m}{(T_w - T_{mc})} \\ &= \sigma \frac{T_m}{(T_w - T_{mc})} \\ &= \frac{\sigma T_m}{(T_w - T_m) + (T_m - T_{mc})} \\ &= \frac{1}{\frac{(T_w - T_m)}{\sigma T_m} + \frac{(T_m - T_{mc})}{\sigma T_m}} \\ &= \frac{1}{1 + \frac{(T_m - T_{mc})}{\sigma T_m}} \\ &= \frac{1}{1 + \frac{\alpha}{\sigma}} \end{aligned}$$

$$E^2 = E_{om}^2 + B \left(1 + \frac{\alpha}{\sigma} \right)^{-1} (\rho U)^n$$

AII.2 Derivation of the Equations to Give U and V from an X-array Hot Wire Probe

Assuming the coordinate system and conventions shown in figure 49, and that q_{eff} represents the effective cooling velocity on a wire, then:

$$q_{\text{perp}}^2 = (U \sin \theta - V \cos \theta)^2 + W^2$$

$$q_{\text{along}}^2 = (U \cos \theta + V \sin \theta)^2$$

assuming

$$q_{\text{eff}}^2 = q_{\text{perp}}^2 + a^2 q_{\text{along}}^2$$

where a = wire direction sensitivity coefficient
= 0.2

Then,

$$q_{\text{eff}}^2 = (U \sin \theta - V \cos \theta)^2 + W^2 + a^2 (U \cos \theta + V \sin \theta)^2$$

to calibrate, i.e. $\theta = 90^\circ$

$$q_{\text{eff}}^2 = U^2 + W^2 + a^2 V^2$$

to determine a , i.e. $\theta = 0^\circ$

$$q_{\text{eff}}^2 = (-V)^2 + W^2 + a^2 U^2$$

continued

For a conventional cross wire probe, wire 1, $\theta = 45^\circ$

$$q_{\text{eff}1}^2 = \left(\frac{U}{\sqrt{2}} - \frac{V}{\sqrt{2}} \right)^2 + W^2 + a^2 \left(\frac{U}{\sqrt{2}} + \frac{V}{\sqrt{2}} \right)^2 \quad (i)$$

and for wire 2, $\theta = 135^\circ$

$$q_{\text{eff}2}^2 = \left(\frac{U}{\sqrt{2}} + \frac{V}{\sqrt{2}} \right)^2 + W^2 + a^2 \left(\frac{V}{\sqrt{2}} - \frac{U}{\sqrt{2}} \right)^2 \quad (ii)$$

subtracting (ii) from (i)

$$q_{\text{eff}1}^2 - q_{\text{eff}2}^2 = 2UV(a^2 - 1)$$

$$UV = \frac{(q_{\text{eff}1}^2 - q_{\text{eff}2}^2)}{2(a^2 - 1)} \quad (\text{AII2.1})$$

adding (ii) and (i)

$$\begin{aligned} q_{\text{eff}1}^2 + q_{\text{eff}2}^2 &= U^2 + V^2 + 2W^2 + a^2V^2 + a^2U^2 \\ &= (1 + a^2)(U^2 + V^2) + 2W^2 \end{aligned}$$

substituting for V^2 from (AII2.1)

$$q_{\text{eff}1}^2 + q_{\text{eff}2}^2 = (1 + a^2) \left(U^2 + \frac{(q_{\text{eff}1}^2 - q_{\text{eff}2}^2)^2}{4U^2(a^2 - 1)^2} \right) + 2W^2$$

Multiplying through by $4U^2(a^2 - 1)^2$ and collecting terms leaves,

$$0 = U^4 + U^2 \left(\frac{2W^2}{(1+a^2)} - \frac{(q_{\text{eff}1}^2 + q_{\text{eff}2}^2)}{(1+a^2)} \right) + \frac{(q_{\text{eff}1}^2 - q_{\text{eff}2}^2)^2}{4(a^2 - 1)^2}$$

Therefore

$$U^2 = \frac{q_{\text{eff}1}^2 + q_{\text{eff}2}^2 - 2W^2}{2(1+a^2)} \pm \frac{1}{2} \sqrt{\left(\frac{2W^2 - q_{\text{eff}1}^2 + q_{\text{eff}2}^2}{(1+a^2)} \right)^2 - \frac{(q_{\text{eff}1}^2 - q_{\text{eff}2}^2)^2}{(a^2 - 1)^2}}$$

Now, assuming there is only 1 real root and that

$$W \ll q_{\text{eff}}$$

then the instantaneous value of U given by $q_{\text{eff}1}$ and $q_{\text{eff}2}$, is

$$U = \frac{1}{\sqrt{2}} \sqrt{\frac{q_{\text{eff}1}^2 + q_{\text{eff}2}^2}{(1+a^2)} + \sqrt{\left(\frac{q_{\text{eff}1}^2 + q_{\text{eff}2}^2}{(1+a^2)} \right)^2 - \frac{(q_{\text{eff}1}^2 - q_{\text{eff}2}^2)^2}{(a^2 - 1)^2}}}$$

Substitution of this result into (AII2.1) will yield a corresponding value for V.

AII.3 The Cross Wire Analysis Computer Program

Due to the complexity of the equations derived in the previous section, the analysis of the dual sensor hot wire signals was performed in two parts. Program XRUN sampled the signals, converted them to floating point numbers and then wrote the results, including run parameters, to files on a hard disc. A second program, XSUMS, was then used at a later time, to recall the data and perform the analysis and time averaging.

AII.3.1 Program XRUN

Initially the program defines the various file names to hold the run data and samples, and gathers the required mean and r.m.s. voltages and flow temperatures.

continued over ...

C

```

THIS IS A DUAL CHANNEL SAMPLING PROGRAM
EXTERNAL XRUNBR
COMMON /BLK1/IBUF(5120),IBUF1(512),IBUF2(512)
COMMON /BLK2/IDEF,ICMF
COMMON /BLK3/ICHAN1,ICHAN2
COMMON /BLK4/E1(256),E2(256)
COMMON /CAIN/IRUN,I1,X1CLAA,X2CLAA,X1DTAA,X2DTAA,
*NTOTAL,E01,A1,N1,SIGMA1,TCAL1,E02,A2,N2,SIGMA2,TCAL2,
*IREC2,IREC4,IREC1,IREC3
REAL*4 HT1(2),HT2(2),PROGNUM(2)
REAL N1,N2
DATA HT1/6RDK1X1A,6R DAT/
DATA HT2/6RDK1X2A,6R DAT/
DATA PROGNUM/6RDKOXRU,6RN SAV/
CALL RCHAIN(IFLAG,IRUN,60)
CALL PRINT(' CROSS WIRE SAMPLING PROGRAM','0)
ICHAN1=IGETC()
IF(ICHAN1.LT.0)STOP
IF(IFETCH(HT1).NE.0)STOP
IF(IENTER(ICHAN1,HT1,20).LT.0)STOP
ICHAN2=IGETC()
IF(ICHAN2.LT.0)STOP
IF(IFETCH(HT2).NE.0)STOP
IF(IENTER(ICHAN2,HT2,20).LT.0)STOP
LOGICAL*1 X1DTAA(15),X1CLAA(15),X2DTAA(15),X2CLAA(15)
IF(IFLAG.LT.0)GOTO 10
IRUN=0
I1=0
DATA X1DTAA/'D','K','1',':','X','1','D','A','A','A',
*','D','A','T','0/
DATA X1CLAA/'D','K','1',':','X','1','C','A','A','A',
*','D','A','T','0/
DATA X2DTAA/'D','K','1',':','X','2','D','A','A','A',
*','D','A','T','0/
DATA X2CLAA/'D','K','1',':','X','2','C','A','A','A',
*','D','A','T','0/
CALL PRINT(' HOT WIRE ANALYSIS PROGRAM','0)
CALL PRINT(' INPUT TOTAL NUMBER OF RUNS','0)
READ(7,1000)NTOTAL
1000 FORMAT(I3)
CALL PRINT(' INPUT E01,A1,N1,SIGMA1,TCAL1','0)
READ(7,1010)E01,A1,N1,SIGMA1,TCAL1
1010 FORMAT(5F8.3)
CALL PRINT(' INPUT E02,A2,N2,SIGMA2,TCAL2','0)
READ(7,1010)E02,A2,N2,SIGMA2,TCAL2

C
C
C
CHAIN LOOP COMMENCES
10 LUN1=14
LUN2=15
I1=I1+1
IRUN=IRUN+1
CALL PRINT(' INPUT RUN NUMBER','0)
READ(7,1000)IRUN1

```

```

CALL PRINT(' INPUT EMEAN1,RMS1,T1','0)
READ(7,1030)EMEAN1,RMS1,T1
1030  FORMAT(3F8.4)
CALL PRINT(' INPUT EMEAN2,RMS2,T2','0)
READ(7,1030)EMEAN2,RMS2,T2
LUN3=12
LUN4=13
CALL ASSIGN(LUN1,X1CLAA)
CALL ASSIGN(LUN2,X1DTAA)
CALL ASSIGN(LUN3,X2CLAA)
CALL ASSIGN(LUN4,X2DTAA)
IREC1=1
IREC3=1
DEFINE FILE LUN1(3,256,U,IREC1)
DEFINE FILE LUN2(20,512,U,IREC2)
DEFINE FILE LUN3(3,256,U,IREC3)
DEFINE FILE LUN4(20,512,U,IREC4)
WRITE(7,6000)X1CLAA,X2CLAA
6000  FORMAT(' ',15A1,5X,15A1)
WRITE(7,6190)E01,A1,N1,SIGMA1,TCAL1,IRUN1,EMEAN1,
      *RMS1,T1,NTOTAL
6190  FORMAT(5F5.2,I3,3F5.2,I4)
C
C      WRITE CALIBRATION CONSTANTS TO FILES X1CL**,X2CL**
C
      WRITE(LUN1'1')E01,A1,N1,SIGMA1,TCAL1,IRUN1,EMEAN1,
      *RMS1,T1,NTOTAL
      WRITE(LUN3'1')E02,A2,N2,SIGMA2,TCAL2,IRUN1,EMEAN2,
      *RMS2,T2,NTOTAL

```

The program samples the input signals upon a carriage return by the operator. The completion routine XRUNSB writes the samples to the previously defined data files.

```

C
C      PAUSE 'TYPE <CR> TO SAMPLE DATA'
C
C      SAMPLE DATA
C
      ICMF=0
      CALL RTS(IBUF,5120,10,2560,0,2,1,2,ICMF,IBEF,256,XRUNSB)
      ICMF1=0
      CALL SETR(3,8+1,5.0,ICMF1)
      CALL PRINT(' WAITING RTS','0)
      CALL LWAIT(ICMF,0)
      CALL SETR(-1,,)
      CALL PRINT(' FINISHED SAMPLING','0)

```

ORIGINAL PAGE IS
OF POOR QUALITY

The samples are recalled from the files and converted to floating point numbers.

```
DO 100 J=1,10
  K=J*2-1
  INCODE=IREADW(512,IBUF1,K,ICHAN1)
  INCODE=IREADW(512,IBUF2,K,ICHAN2)
  DO 110 M=1,256
    E1(M)=(FLT16(IBUF1(M))-512.)*2.5/512.
    E2(M)=(FLT16(IBUF2(M))-512.)*2.5/512.
110  CONTINUE
    WRITE(LUN2,J)E1
    WRITE(LUN4,J)E2
100  CONTINUE
    CALL PRINT(' DATA WRITTEN TO FILES',*0)
```

Upon completion, the files are closed. The names of the data files are updated (this provides each run with a dedicated series of file names) and the program chains back to itself to begin a new sample point.

ORIGINAL PAGE IS
OF POOR QUALITY

```

CALL CLOSE(LUN1)
CALL CLOSE(LUN2)
CALL CLOSE(LUN3)
CALL CLOSE(LUN4)
IF(I1.EQ.26)GOTO 20
GOTO 30
20  DO 120 J=1,25
    X1DTAA(10)=X1DTAA(10)-*1
    X1CLAA(10)=X1CLAA(10)-*1
    X2DTAA(10)=X2DTAA(10)-*1
    X2CLAA(10)=X2CLAA(10)-*1
120  CONTINUE
    X1DTAA(9)=X1DTAA(9)+*1
    X1CLAA(9)=X1CLAA(9)+*1
    X2DTAA(9)=X2DTAA(9)+*1
    X2CLAA(9)=X2CLAA(9)+*1
    I1=0
    GOTO 40
30  X1DTAA(10)=X1DTAA(10)+*1
    X1CLAA(10)=X1CLAA(10)+*1
    X2DTAA(10)=X2DTAA(10)+*1
    X2CLAA(10)=X2CLAA(10)+*1
40  CALL IDELET(ICHAN1,HT1)
    CALL IDELET(ICHAN2,HT2)
    CALL CLOSEC(ICHAN1)
    CALL CLOSEC(ICHAN2)
    CALL IFREEC(ICHAN1)
    CALL IFREEC(ICHAN2)
    IREC1=1
    IREC2=1
    IREC3=1
    IREC4=1
    IF(IRUN.EQ.NTOTAL)STOP 'THATS ALL FOLKS!!'
    CALL CHAIN(PROGMM,IRUN,60)
    STOP
    END

```

The completion routine XRUNSB is called every time 1 buffer of data
(256 samples per wire) is collected by the CALL RTS instruction.

ORIGINAL PAGE IS
OF POOR QUALITY

```

C      XRUNSD.FOR WITH XRUN.SAV
      SUBROUTINE XRUNSD
      COMMON /BLK1/IBUF(5120),IBUF1(512),IBUF2(512)
      COMMON /BLK2/IDEF,ICMF
      COMMON /BLK3/ICHAN1,ICHAN2
      DATA ICALL/0/
      ICALL=ICALL+1
      DO 100 I=1,256
      M=256*(ICALL-1)+(I*2-1)
      IBUF1(I)=IBUF(M)
      IBUF2(I)=IBUF(M+1)
100    CONTINUE
      IDUM=ICALL*2-1
      INCODE=IWRITW(512,IBUF1,IDUM,ICHAN1)
      INCODE=IWRITW(512,IBUF2,IDUM,ICHAN2)
      IDEF=IDEF+1
      RETURN
      END

```

AII.3.2 Program XSUMS

This program performs the analysis of the results stored by program XRUN.

Initially the data files created by XRUN are redefined and made accessible. The run constants are read in and the various required parameters calculated. The accumulators are all set to zero.

ORIGINAL PAGE IS
OF POOR QUALITY.

```

C      XSUMS.FOR   NJW   '79
C      CROSS WIRE ANALYSIS
COMMON/DLK1/NTOTAL,I1,I2,X1DAAA,X1CAAA,X2DAAA,X2CAAA
COMMON/DLK2/E1(256),E2(256),U1(256),U2(256)
COMMON/PLT/UIMEAN,U2MEAN,IFLAG,K
REAL*4 N1RUN,N2RUN
REAL*8 ESML18,ESML28
REAL N1,N2
REAL*4 PROGNM(2)
DATA PROGNM/6RDKOXBU,6RMS SAV/
CALL RCHAIN(IFLAG,NTOTAL,60)
IF(IFLAG.LT.0)GOTO 10
LOGICAL*1 X1DAAA(15),X1CAAA(15),X2DAAA(15),X2CAAA(15)
DATA X1DAAA/'D','K','1',':','X','1','D','A','B','A',
*','D','A','T','O'/
DATA X1CAAA/'D','K','1',':','X','1','C','A','B','A',
*','D','A','T','O'/
DATA X2DAAA/'D','K','1',':','X','2','D','A','B','A',
*','D','A','T','O'/
DATA X2CAAA/'D','K','1',':','X','2','C','A','B','A',
*','D','A','T','O'/
CALL PRINT(' DATA RECALL PROGRAM','0)
I1=0
I2=0
10    I1=I1+1
      I2=I2+1
      LUN1=14
      LUN2=15
      LUN3=12
      LUN4=13
      CALL ASSIGN(LUN1,X1CAAA)
      CALL ASSIGN(LUN2,X1DAAA)
      CALL ASSIGN(LUN3,X2CAAA)
      CALL ASSIGN(LUN4,X2DAAA)
      DEFINE FILE LUN1(1,256,U,IREF1)
      DEFINE FILE LUN2(20,512,U,IREF2)
      DEFINE FILE LUN3(1,256,U,IREF3)
      DEFINE FILE LUN4(20,512,U,IREF4)
      READ(LUN1'1')E01,A1,N1,SIGMA1,TCAL1,IRUN1,EMEAN1,RMS1,T1,NTOTAL
      READ(LUN3'1')E02,A2,N2,SIGMA2,TCAL2,IRUN1,EMEAN2,RMS2,T2,NTOTAL
C      SET UP CONSTANTS
      TCAL1=TCAL1+273.
      TCAL2=TCAL2+273.
      N1RUN=1./N1
      N2RUN=1./N2
      E01RUN=E01**2
      E02RUN=E02**2
      T1=T1+273.
      T2=T2+273.
      EPSLN1=(T1-TCAL1)/TCAL1
      EPSLN2=(T2-TCAL2)/TCAL2
      CORR1=1./(1.+EPSLN1/SIGMA1)
      CORR2=1./(1.+EPSLN2/SIGMA2)
      A1RUN=A1*CORR1
      A2RUN=A2*CORR2

```

ORIGINAL PAGE IS
OF POOR QUALITY

```

E1AV=0.
E2AV=0.
E1FRS=0.
E2FRS=0.
E12PR=0.
U1MEAN=0.
U2MEAN=0.
URMS1=0.
URMS2=0.
U12=0.

```

The mean and r.m.s. values of the input signals are calculated and then used to obtain the attenuation due to the unknown input amplifier gain.

```

C      START CALCS
      DO 100 J=1,10
      READ(LUN2,J)(E1(I),I=1,256)
      READ(LUN4,J)(E2(I),I=1,256)
      DO 110 M=1,256
      E1AV=E1AV+E1(M)
      E2AV=E2AV+E2(M)
      E1FRS=E1FRS+E1(M)*E1(M)
      E2FRS=E2FRS+E2(M)*E2(M)
110    CONTINUE
      WRITE(LUN2,J)(E1(I),I=1,256)
      WRITE(LUN4,J)(E2(I),I=1,256)
100    CONTINUE
      E1FRS=E1FRS/2560.
      E2FRS=E2FRS/2560.
      E1AV=E1AV/2560.
      E2AV=E2AV/2560.
      E1FRS=SQRT(E1FRS-(E1AV*E1AV))
      E2FRS=SQRT(E2FRS-(E2AV*E2AV))
      ATTEN1=RMS1/E1FRS
      ATTEN2=RMS2/E2FRS

```

The attenuations are used to scale the samples and the equations derived in AII.2 can be used to obtain U, V.

ORIGINAL PAGE IS
OF POOR QUALITY

```

DO 120 J=1,10
READ(LUN2'J)(E1(I),I=1,256)
READ(LUN4'J)(E2(I),I=1,256)
DO 130 M=1,256
E1(M)=(E1(M)-E1AV)*ATTEN1
E2(M)=(E2(M)-E2AV)*ATTEN2
ESML1S=EXP(N1RUN*ALOG((EMEAN1+E1(M))*2-E01RUN)/A1RUN))
ESML2S=EXP(N2RUN*ALOG((EMEAN2+E2(M))*2-E02RUN)/A2RUN))
E12PR=E12PR+(E1(M)*E2(M))
ESML1S=ESML1S*ESML1S
ESML2S=ESML2S*ESML2S
EP=(ESML1S+ESML2S)/1.04
EM=(ESML1S-ESML2S)/0.96
U1(M)=(SQRT(EP+SQRT(ABS(EP**2-EM*EM))))/1.4142
U2(M)=-EM/(2.*U1(M))
U1MEAN=U1MEAN+U1(M)
U2MEAN=U2MEAN+U2(M)
130 CONTINUE
WRITE(LUN2'J)(U1(I),I=1,256)
WRITE(LUN4'J)(U2(I),I=1,256)
120 CONTINUE
U1MEAN=U1MEAN/2560.
U2MEAN=U2MEAN/2560.
E12PR=E12PR/2560.

```

From the data, now stored as instantaneous U and V components, the required turbulence parameters $\overline{u'^2}$, $\overline{v'^2}$, $\overline{u'v'}$ can be calculated.

```

DO 140 J=1,10
READ(LUN2'J)(U1(I),I=1,256)
READ(LUN4'J)(U2(I),I=1,256)
DO 150 M=1,256
U1PR=U1(M)-U1MEAN
U2PR=U2(M)-U2MEAN
URMS1=URMS1+U1PR*U1PR
URMS2=URMS2+U2PR*U2PR
U12=U12+U1PR*U2PR
150 CONTINUE
140 CONTINUE
URMS1=SQRT(URMS1/2560.)
URMS2=SQRT(URMS2/2560.)
U12=U12/2560.

```

ORIGINAL PAGE IS
OF POOR QUALITY

The results are output; the data files closed and the file names are updated ready to find the next set of stored data.

```

      IF(IFLAG.LT.0)GOTO 20
      WRITE(7,1000)E01,A1,N1,SIGMA1,TCAL1,E02,A2,N2,SIGMA2,TCAL2
      WRITE(7,1100)
20    CONTINUE
      WRITE(7,1200)IRUN1,U1MEAN,U2MEAN,URMS1,URMS2,U12,E12PR
      CALL CLOSE(LUN1)
      CALL CLOSE(LUN2)
      CALL CLOSE(LUN3)
      CALL CLOSE(LUN4)
      IF(I2.EQ.26)GOTO 30
      GOTO 40
30    DO 50 J=1,25
      X1DAAA(10)=X1DAAA(10)-*1
      X1CAAA(10)=X1CAAA(10)-*1
      X2DAAA(10)=X2DAAA(10)-*1
      X2CAAA(10)=X2CAAA(10)-*1
50    CONTINUE
      X1DAAA(9)=X1DAAA(9)+*1
      X1CAAA(9)=X1CAAA(9)+*1
      X2DAAA(9)=X2DAAA(9)+*1
      X2CAAA(9)=X2CAAA(9)+*1
      I2=0
      GOTO 60
40    X1DAAA(10)=X1DAAA(10)+*1
      X1CAAA(10)=X1CAAA(10)+*1
      X2DAAA(10)=X2DAAA(10)+*1
      X2CAAA(10)=X2CAAA(10)+*1
60    IF(I1.EQ.NTOTAL)STOP
      CALL CHAIN(PROGNN,NTOTAL,60)
1000  FORMAT(/,10X,'*****',BX,'DIGITAL HOT WIRE ANALYSIS',BX,
      *'*****',/,5X,'INPUT CALIBRATION CONDITIONS FOR WIRE 1',/,
      *5X,'ZERO VOLTS',15X,F5.3,/,
      *5X,'INTERCEPT',16X,F5.3,/,
      *5X,'SLOPE',20X,F5.3,/,
      *5X,'OVERHEAT RATIO',11X,F5.3,/,
      *5X,'CALIBRATION TEMPERATURE',2X,F6.1,/,
      *5X,'INPUT CALIBRATION CONDITIONS FOR WIRE 2',/,
      *5X,'ZERO VOLTS',15X,F5.3,/,
      *5X,'INTERCEPT',16X,F5.3,/,
      *5X,'SLOPE',20X,F5.3,/,
      *5X,'OVERHEAT RATIO',11X,F5.3,/,
      *5X,'CALIBRATION TEMPERATURE',2X,F6.1,/,)
1100  FORMAT(/,16X,'*****',BX,'CROSS WIRE ANALYSIS'
      *,13X,'*****',/5X,'RUN',5X,'U1MEAN',5X,'U2MEAN'
      *,5X,'URMS1',5X,'URMS2',4X,'U12',5X,'E12PR',/)
1200  FORMAT(5X,I3,3X,F8.2,3X,F8.2,5X,F8.5,5X,F8.5,2X,F8.5,2X,F8.5)
      STOP
      END

```

ORIGINAL PAGE IS
OF POOR QUALITY

AII.4 The Split Film Analysis Program

The split film analysis program (TSIRUN) is essentially very similar to XRUN, XSUMS except that the two functions are combined. The program does not create stored data files but processes each batch as it is taken.

The program initialises the split film constants and defines a temporary data storage file. The run constants are input (\bar{E}_1 , \bar{E}_2 , $\sqrt{e_1^2}$, $\sqrt{e_2^2}$) and the program then waits to start sampling.

```

COMMON /BLK1/IBUF(5120)
DIMENSION IDIG(5),IDIG1(5),NUM(5)
DIMENSION E1(2560),E2(2560)
REAL N1,N2,N1RUN,N2RUN,N,NUM
WRITE(7,1000)
READ(7,2000)E01,E02
A1=41.77
N1=0.386
SIGMA1=.5
A2=9.856
N2=.556
SIGMA2=.5
J=1
NTOTAL=1
LUN=3
CALL ASSIGN(LUN,'DK1:SPLIT1.DAT')
DEFINE FILE LUN(500,20,U,IREC)
10  CONTINUE
    WRITE(7,1100)
    READ(7,2100)EMEAN1,RMS1,EMEAN2,RMS2
    WRITE(7,3000)
3000  FORMAT(' IS INPUT O.K. 1=YES')
    READ(7,3100)ISWCH
3100  FORMAT(I2)
    IF(ISWCH.NE.1)GOTO 10
    PAUSE 'TYPE <CR> TO SAMPLE'

```

The signals are sampled and converted to floating point numbers.

```

      ICMF=0
      CALL RTS(IBUF,5120,1,2560,0,2,1,2,ICMF,IBEF,2560,)
      ICMF1=0
      CALL SETR(3,8+1,5.0,ICMF1)
      CALL LWAIT(ICMF,0)
      CALL SETR(-1,,)
      DO 100 I=1,2560
      M=I*2-1
      E1(I)=(FLT16(IBUF(M))-512.)*2.5/512.
      E2(I)=(FLT16(IBUF(M+1))-512.)*2.5/512.
100  CONTINUE

```

The attenuation of the input signals is calculated.

```

      N1RUN=1./N1
      E012=(E01*.92)**2+(E02*.92)**2
      E1AV=0.
      E2AV=0.
      E1PRS=0.
      E2PRS=0.
      DO 200 M=1,2560
      E1AV=E1AV+E1(M)
      E2AV=E2AV+E2(M)
      E1PRS=E1PRS+E1(M)*E1(M)
      E2PRS=E2PRS+E2(M)*E2(M)
200  CONTINUE
      S=2560.
      E1PRS=E1PRS/S
      E2PRS=E2PRS/S
      E1AV=E1AV/S
      E2AV=E2AV/S
      E1PRS=SQRT(E1PRS-(E1AV*E1AV))
      E2PRS=SQRT(E2PRS-(E2AV*E2AV))
      ATTEN1=RMS1/E1PRS
      ATTEN2=RMS2/E2PRS

```

ORIGINAL PAGE IS
OF POOR QUALITY

The input data is scaled by the attenuation and the values for \bar{U} , \bar{V} are calculated.

```

DO 300 M=1,2560
E1(M)=(E1(M)-E1AV)*ATTEN1
E2(M)=(E2(M)-E2AV)*ATTEN2
300  CONTINUE
DO 400 M=1,2560
E1SQ=(E1(M)-E1AV)**2
E2SQ=(E2(M)-E2AV)**2
UN=((E1SQ+E2SQ-E012)/A1)**N1RUN
E2(M)=(E1SQ-E2SQ)/(A2*(UN**(N2-1)))
E1(M)=SQRT(UN**2-E2(M)**2)
400  CONTINUE
UAV=0.0
VAV=0.0
DO 500 M=1,2560
UAV=UAV+E1(M)
VAV=VAV+E2(M)
500  CONTINUE
UAV=UAV/S
VAV=VAV/S

```

The velocity fluctuations are determined and u'^2 , v'^2 and $u'v'$ simply obtained.

```

UP=0.0
VP=0.0
UV=0.0
DO 600 I=1,2560
U1=E1(M)-UAV
V1=E2(M)-VAV
UP=UP+U1**2
VP=VP+V1**2
UV=UV+U1*V1
600  CONTINUE
UPR=SQRT(UP/S)
VPR=SQRT(VP/S)
UVPR=UV/S

```

ORIGINAL PAGE IS
OF POOR QUALITY

The value of the traversing gear counter is obtained to give the radial location of the measurement point.

```

IDIG(1)="20
IDIG(2)="40
IDIG(3)="60
IDIG(4)="100
IDIG(5)="120
I=1
1 IN=IDIR(1,"160014","177,1,IVAR)
  I70=IDOR(1,"70","177777,IN,IVAR)
  IDIG1(I)=IDIR(1,"70","160,1,IVAR)
  IF(IDIG1(I).NE.IDIG(I))GOTO 1
  IN=IDIR(1,"160014","177,1,IVAR)
  I72=IDOR(1,"72","177777,IN,IVAR)
  IDIG1(I)=IDIR(1,"72","160,1,IVAR)
  IF(IDIG1(I).NE.IDIG(I))GOTO 1
  IN=IDIR(1,"160014","177,1,IVAR)
  I74=IDOR(1,"74","177777,IN,IVAR)
  IDIG1(I)=IDIR(1,"74","160,1,IVAR)
  IF(IDIG1(I).NE.IDIG(I))GOTO 1
  INUM=IDIR(1,"72","17,1,IVAR)
  NUM(I)=FLOAT(INUM)
  NUM(I)=15.-NUM(I)
  I=I+1
  IF(I.EQ.6)GOTO 2
  GOTO 1
2 CONTINUE
  N=NUM(1)+10.*NUM(2)+100.*NUM(3)+1000.*NUM(4)
  N=N+10000*NUM(5)

```

The results are output and written to the temporary storage file and the program loops to enable the next probe position to be sampled.

```

WRITE(7,1300)UAV,UPR,VAU,VPR,UUPR,NTOTAL,N
NTOTAL=NTOTAL+1
WRITE(7,1200)
READ(7,2200)IDEC
IF(IDEC.EQ.2)GOTO 30
IF(IDEC.EQ.0)GOTO 20
WRITE(LUN'J')UAV,UPR,VAU,VPR,UUPR,J,N
J=J+1
20  CONTINUE
    GOTO 10
1000  FORMAT(' SPLIT FILM SAMPLING AND PROCESSING PROGRAM',/
*, ' INPUT E01,E02')
2000  FORMAT(2F8.4)
1100  FORMAT(' INPUT EMEAN1,RMS1,EMEAN1,RMS2')
2100  FORMAT(4F8.4)
1200  FORMAT(' DO YOU WANT THESE RESULTS 1=YES,0=NO 2=EXIT AND WRITE')
2200  FORMAT(I2)
1300  FORMAT(5X,'UBAR=',F8.2,2X,'UPRIME=',F8.3,2X,'VBAR=',
*F8.3,2X,'VPRIME=',F8.3,/,5X,'UV=',F8.3,2X,'RUN ',I3,2X,'POS=',
*F6.0,/)
30    WRITE(LUN'J')UAV,UPR,VAU,VPR,UUPR,J,N
      U=0.123
      J=J+1
      WRITE(LUN'J')U
      CALL CLOSE(3)
      STOP
      END

```

Subroutine TSISB1 is a completion routine called by the CALL RTS routine upon completion of the sampling.

```

C  TSISB1 WITH TSIRUN.SAV NOV 79
SUBROUTINE TSISB1
COMMON /BLK1/IBUF(5120)
COMMON /BLK2/IBEF,ICMF,ICHAN1
INCODE=IWRITW(10240,IBUF,1,ICHAN1)
IBEF=IBEF+1
RETURN
END

```

TABLE 1

BASIC DATA				SLOT HEIGHT = .021"			
$C_\mu = 0.0065$		$\theta = 15^\circ$		$y_{m/2} = .0250"$		$U_\infty = 31.9 \text{ ms}^{-1}$	
$y(\text{in})$	\bar{U}/U_∞	$y/y_{m/2}$	$\sqrt{\bar{u}'^2}/U_\infty$	\bar{V}/U_∞	$\sqrt{\bar{v}'^2}/U_\infty$	$u'v'(\text{m}^2\text{s}^{-2})$	$(P_{Nm} - P_\infty)$
							-587
							-647
0.009	1.703	0.36		-0.035			
0.012	1.712	0.48		-0.011			
0.014	1.674	0.56		0.012			$y=0.016$
0.017	1.600	0.68		0.027			-424
0.020	1.532	0.80		0.038			
0.022	1.450	0.88		0.033			35
0.029	1.259	1.16		0.023			213
0.036	1.030	1.44	0.049	-0.014	0.023	0.267	173
0.049	0.737	1.96	0.036	-0.100	0.016	0.072	-124
0.062	0.709	2.48	0.037	-0.122	0.011	-0.154	-265
0.076	0.731	3.04	0.039	-0.131	0.010	-0.182	-286
0.089	0.751	3.56	0.038	-0.133	0.011	-0.199	-290
0.102	0.776	4.08	0.038	-0.136	0.011	-0.166	-273
0.116	0.803	4.64	0.037	-0.134	0.012	-0.205	-270
0.129	0.823	5.16	0.037	-0.133	0.012	-0.159	-268
0.142	0.845	5.68	0.038	-0.135	0.011	-0.180	-264
0.209	0.942	8.36	0.033	-0.125	0.012	-0.165	-234
0.276	1.005	11.04	0.027	-0.118	0.011	-0.154	-220
0.342	1.028	13.68	0.018	-0.105	0.010	-0.099	

WALL

TABLE 2

BASIC DATA				SLOT HEIGHT = .021"			
$C_V = 0.0065$		$\theta = 25^\circ$		$y_{m/2} = 0.0317"$		$U_\infty = 31.9 \text{ ms}^{-1}$	
$y(\text{in})$	\bar{U}/U_∞	$y/y_{m/2}$	$\sqrt{u'^2}/U_\infty$	\bar{V}/U_∞	$\sqrt{v'^2}/U_\infty$	$\overline{u'v'}(\text{m}^2\text{s}^{-2})$	$(p - p_\infty)/\rho U_\infty^2$
							-507
							WALL
0.009	1.303	0.284		-0.006			-536
0.012	1.318	0.379		0.007			
0.014	1.306	0.442		0.017			$y=0.016$
0.017	1.290	0.536		0.024			-371
0.020	1.275	0.631		0.030			
0.022	1.237	0.694		0.030			-275
0.029	1.171	0.915		0.035			-159
0.036	1.665	1.136	0.039	0.030	0.021	0.356	-90
0.049	0.818	1.546	0.044	0.013	0.018	0.261	-8
0.062	0.692	1.956	0.041	-0.011	0.016	0.145	-62
0.076	0.619	2.366	0.044	-0.032	0.013	-0.092	-127
0.089	0.623	2.808	0.045	-0.041	0.010	-0.147	-163
0.102	0.639	3.218	0.047	-0.035	0.010	-0.089	-178
0.116	0.671	3.659	0.047	-0.031	0.011	-0.079	-192
0.129	0.682	4.069	0.046	-0.025	0.011	-0.073	-185
0.142	0.704	4.479	0.044	-0.019	0.011	-0.137	-177
0.209	0.815	6.593	0.040	0.010	0.012	-0.119	-165
0.276	0.901	8.706	0.037	0.035	0.013	-0.209	-131
0.342	0.938	10.789	0.027	0.055	0.012	-0.195	

TABLE 3

BASIC DATA		SLOT HEIGHT = .021"					
$C_u = 0.0065$		$\theta = 30^\circ$		$y_{m/2} = 0.0349"$		$U_\infty = 31.9 \text{ ms}^{-1}$	
$y(\text{in})$	\bar{U}/U_∞	$y/y_{m/2}$	$\sqrt{u'^2}/U_\infty$	\bar{V}/U_∞	$\sqrt{v'^2}/U_\infty$	$\overline{u'v'}(\text{m}^2\text{s}^{-2})$	$(p - p_\infty)/\rho U_\infty^2$
0.009	1.076	0.258		-0.044			
0.012	1.103	0.344		-0.027			
0.014	1.117	0.401		-0.009			
0.017	1.117	0.487		-0.003			
0.020	1.110	0.573		0.009			
0.022	1.103	0.630		0.009			
0.029	1.056	0.831		0.015			
0.036	0.998	1.032	0.041	0.020	0.021	0.338	
0.049	0.856	1.404	0.041	0.024	0.022	0.322	
0.062	0.716	1.777	0.043	0.007	0.020	0.301	
0.076	0.590	2.178	0.040	-0.006	0.018	0.033	
0.089	0.549	2.550	0.044	-0.018	0.011	-0.034	
0.102	0.551	2.923	0.045	-0.020	0.012	-0.096	
0.116	0.574	3.324	0.045	-0.014	0.010	-0.056	
0.129	0.586	3.696	0.046	-0.006	0.010	-0.072	
0.142	0.618	4.069	0.047	0	0.011	-0.062	
0.209	0.718	5.989	0.045	0.037	0.013	-0.186	
0.276	0.815	7.908	0.041	0.068	0.014	-0.150	
0.342	0.871	9.799	0.034	0.100	0.015	-0.250	

TABLE 4

BASIC DATA				SLOT HEIGHT = .021"			
$C_u = 0.0065$		$\theta = 35^\circ$		$y_{m/2} = 0.0413"$		$U_m = 31.9 \text{ ms}^{-1}$	
$y(\text{in})$	\bar{U}/U_m	$y/y_{m/2}$	$\sqrt{\bar{U}^2}/U_m$	\bar{V}/U_m	$\sqrt{\bar{V}^2}/U_m$	$\overline{u'v'}(\text{m}^2\text{s}^{-2})$	$(p - p_m)/\rho_m$
							-337
							WALL
0.009	0.792	0.218		-0.071			-544
0.012	0.847	0.291		-0.049			
0.014	0.889	0.339		-0.020			$y=0.016$
0.017	1.012	0.412		-0.002			-634
0.020	1.028	0.484		0.007			
0.022	0.996	0.533		0.012			-531
0.029	0.973	0.702		0.031			-375
0.036	0.945	0.872	0.037	0.045	0.023	0.565	-157
0.049	0.852	1.186	0.038	0.052	0.028	0.429	7
0.062	0.759	1.501	0.037	0.051	0.028	0.589	218
0.076	0.624	1.840	0.041	0.044	0.031	0.774	338
0.089	0.527	2.155	0.039	0.032	0.027	0.593	359
0.102	0.469	2.470	0.037	0.022	0.021	0.220	290
0.116	0.451	2.809	0.044	0.012	0.015	0.096	250
0.129	0.444	3.123	0.046	0.016	0.015	0.193	157
0.142	0.465	3.438	0.052	0.023	0.013	0.131	101
0.209	0.574	5.061	0.053	0.076	0.014	0.151	-144
0.276	0.705	6.683	0.038	0.116	0.014	-0.256	-162
0.342	0.771	8.281	0.029	0.153	0.013	-0.308	

TABLE 5

BASIC DATA				SLOT HEIGHT = .021"			
$C_u = 0.0139$		$\theta = 15^\circ$		$y_{m/2} = 0.0274"$		$U_\infty = 31.9 \text{ ms}^{-1}$	
$y(\text{in})$	\bar{U}/U_∞	$y/y_{m/2}$	$\sqrt{\bar{U}^2}/U_\infty$	\bar{V}/U_∞	$\sqrt{\bar{V}^2}/U_\infty$	$\overline{u'v'}(\text{m}^2\text{s}^{-2})$	$(p - p_\infty) \text{ Nm}^{-2}$
							-1127
							-1560
0.009	2.351	0.328		-0.066			
0.012	2.310	0.438		-0.031			
0.014	2.232	0.511		0			
0.017	2.166	0.620		0.031			
0.020	2.103	0.730		0.053			
0.022	1.994	0.803		0.053			
0.029	1.724	1.058		0.044			199
0.036	1.392	1.314	0.054	0	0.027	0.587	125
0.049	0.969	1.788	0.035	-0.116	0.014	0.168	-268
0.062	0.934	2.263	0.031	-0.147	0.011	-0.103	-595
0.076	0.959	2.774	0.030	-0.154	0.012	-0.102	-610
0.089	0.987	3.248	0.031	-0.154	0.011	-0.089	-599
0.102	1.009	3.723	0.028	-0.160	0.016	-0.055	-591
0.116	1.031	4.234	0.030	-0.157	0.011	-0.101	-595
0.129	1.050	4.708	0.030	-0.160	0.011	-0.089	-573
0.142	1.066	5.182	0.028	-0.157	0.012	-0.071	-556
0.209	1.129	7.628	0.025	-0.154	0.009	-0.089	-515
0.276	1.185	10.073	0.017	-0.154	0.008	-0.055	-461

WALL

TABLE 6

BASIC DATA				SLOT HEIGHT = .021"			
$C_\mu = 0.0139$		$\theta = 25^\circ$		$y_{m/2} = 0.0376"$		$U_\infty = 31.9 \text{ ms}^{-1}$	
$y(\text{in})$	\bar{U}/U_∞	$y/y_{m/2}$	$\sqrt{\bar{U}^2}/U_\infty$	\bar{V}/U_∞	$\sqrt{\bar{V}^2}/U_\infty$	$\overline{u'v'}(\text{m}^2\text{s}^{-2})$	$(p - p_\infty) \text{ Nm}^{-2}$
							-1067
							WALL
0.009	1.878	0.239		0.009			-1123
0.016	1.862	0.426		0.047			-873
0.022	1.771	0.585		0.053			-612
0.029	1.661	0.771		0.053			-361
0.036	1.549	0.957	0.046	0.050	0.029	0.657	-231
0.042	1.354	1.117	0.049	0.031	0.027	0.619	-177
0.049	1.179	1.303	0.049	0.013	0.026	0.586	-134
0.062	0.987	1.649	0.040	-0.031	0.020	0.317	-264
0.076	0.934	2.021	0.037	-0.060	0.012	-0.057	-471
0.089	0.972	2.367	0.037	-0.075	0.011	-0.094	-496
0.102	0.975	2.713	0.036	-0.072	0.011	-0.021	-500
0.116	1.000	3.085	0.038	-0.066	0.011	-0.040	-505
0.129	1.006	3.431	0.037	-0.066	0.011	-0.053	-482
0.142	1.022	3.777	0.036	-0.056	0.011	-0.062	-456
0.209	1.075	5.559	0.031	-0.034	0.011	-0.105	-400
0.276	1.097	7.340	0.023	-0.016	0.010	-0.097	-335

TABLE 7

BASIC DATA			SLOT HEIGHT = .021"				
$Cu = 0.0139$		$\theta = 35^\circ$		$y_{m/2} = 0.0483"$		$U_m = 31.9 \text{ ms}^{-1}$	
$y(\text{in})$	\bar{U}/U_m	$y/y_{m/2}$	$\sqrt{\bar{U}^2}/U_m$	\bar{V}/U_m	$\sqrt{\bar{V}^2}/U_m$	$\overline{u'v'}(\text{m}^2\text{s}^{-2})$	$(p - p_m)$ Nm^{-2}
							-847
							WALL
0.009	1.555	0.186		-0.044			-743
0.016	1.621	0.331		-0.013			-709
0.022	1.611	0.455		0.003			-572
0.029	1.561	0.600		0.009			-385
0.036	1.483	0.745	0.054	0.016	0.031	0.971	-223
0.042	1.389	0.870	0.052	0.019	0.031	0.871	-108
0.049	1.270	1.014	0.052	0.016	0.030	0.842	-35
0.062	1.088	1.284	0.053	0.013	0.029	0.790	56
0.076	0.897	1.573	0.046	-0.006	0.023	0.403	57
0.089	0.796	1.843	0.044	-0.019	0.019	0.191	9
0.102	0.746	2.112	0.046	-0.025	0.015	-0.037	-154
0.116	0.746	2.402	0.048	-0.025	0.013	-0.094	-223
0.129	0.799	2.671	0.050	-0.022	0.013	-0.092	-283
0.142	0.809	2.940	0.050	-0.013	0.012	-0.113	-284
0.209	0.881	4.327	0.045	0.034	0.014	-0.161	-221
0.276	0.931	5.714	0.037	0.069	0.013	-0.208	-182
0.342	0.944	7.081	0.028	0.100	0.012	-0.220	

TABLE 8

BASIC DATA

SLOT HEIGHT = .021"

$C_\mu = 0.0139$		$\theta = 40^\circ$		$y_{m/2} = 0.0584"$		$U_\infty = 31.9 \text{ ms}^{-1}$	
$y(\text{in})$	\bar{U}/U_∞	$y/y_{m/2}$	$\sqrt{u'^2}/U_\infty$	\bar{V}/U_∞	$\sqrt{v'^2}/U_\infty$	$\overline{u'v'}(\text{m}^2\text{s}^{-2})$	$(p - p_\infty)/\rho U_\infty^2$
							WALL
0.009	1.276	0.154		-0.053			
0.016	1.386	0.274		-0.013			
0.022	1.392	0.377		0			
0.029	1.376	0.497		0.016			
0.036	1.335	0.616	0.049	0.034	0.026	0.791	
0.049	1.226	0.839	0.040	0.050	0.026	0.808	
0.062	1.097	1.062	0.041	0.047	0.029	1.016	
0.076	0.931	1.301	0.056	0.044	0.031	1.135	
0.089	0.784	1.524	0.053	0.031	0.027	0.895	
0.102	0.687	1.747	0.046	0.019	0.023	0.441	
0.116	0.633	1.986	0.040	0.009	0.018	-0.157	
0.129	0.621	2.209	0.044	0.006	0.016	-0.244	
0.142	0.705	2.432	0.043	0.009	0.013	-0.359	
0.209	0.787	3.579	0.048	0.063	0.015	-0.108	
0.276	0.846	4.726	0.045	0.107	0.014	-0.244	
0.342	0.878	5.856	0.035	0.141	0.013	-0.261	

TABLE 9

BASIC DATA			SLOT HEIGHT = .021"				
$C_\mu = 0.0197$		$\theta = 15^\circ$		$y_{m/2} = 0.0287"$		$U_\infty = 31.9 \text{ ms}^{-1}$	
$y(\text{in})$	\bar{U}/U_∞	$y/y_{m/2}$	$\sqrt{\bar{U}^2}/U_\infty$	\bar{V}/U_∞	$\sqrt{\bar{V}^2}/U_\infty$	$\overline{u'v'}(\text{m}^2\text{s}^{-2})$	$(p - p_\infty)/\rho U_\infty^2$
							WALL
0.009	2.715	0.314		0			-2287
0.012	2.680	0.418		0.028			
0.014	2.608	0.488		0.041			$y=0.016$
0.017	2.489	0.592		0.050			-837
0.020	2.370	0.697		0.053			
0.022	2.248	0.767		0.050			-320
0.029	1.962	1.010		0.025			-13
0.036	1.592	1.254		-0.019			32
0.042	1.248	1.463		-0.091			-197
0.049	1.075	1.707		-0.147			-463
0.062	1.066	2.160		-0.191			-806
0.076	1.088	2.648		-0.210			-835
0.089	1.110	3.101		-0.223			-838
0.102	1.135	3.554		-0.229			-837
0.116	1.150	4.042		-0.229			-848
0.129	1.160	4.495		-0.235			-854
0.142	1.176	4.948		-0.238			-811
0.209	1.219	7.282		-0.245			-766
0.276	1.229	9.617		-0.238			-704

TABLE 10

BASIC DATA				SLOT HEIGHT = .021"			
$C_\mu = 0.0197$		$\theta = 25^\circ$		$y_{m/2} = 0.0367"$		$U_\infty = 31.9 \text{ ms}^{-1}$	
$y(\text{in})$	\bar{U}/U_∞	$y/y_{m/2}$	$\sqrt{\bar{U}^2}/U_\infty$	\bar{V}/U_∞	$\sqrt{\bar{V}^2}/U_\infty$	$\overline{U'V'}(\text{m}^2\text{s}^{-2})$	$(p - p_\infty)/\rho U_\infty^2$
							WALL
0.009	2.273	0.245		-0.003			-2003
0.012	2.248	0.327		0.025			
0.014	2.219	0.381		0.019			$y=0.016$
0.017	2.185	0.463		0.028			-1396
0.020	2.110	0.545		0.022			
0.022	2.066	0.599		0.013			-1053
0.029	1.950	0.790		0.009			-672
0.036	1.762	0.981	0.049	0.003	0.031	0.740	-493
0.042	1.549	1.144	0.054	-0.028	0.028	0.684	-367
0.049	1.339	1.335	0.057	-0.038	0.026	0.713	-346
0.062	1.132	1.689	0.041	-0.085	0.018	0.373	-540
0.076	1.110	2.071	0.029	-0.129	0.011	-0.030	-759
0.089	1.097	2.425	0.031	-0.132	0.011	-0.048	-801
0.102	1.107	2.779	0.032	-0.132	0.010	-0.054	-775
0.116	1.119	3.161	0.031	-0.125	0.010	-0.036	-762
0.129	1.129	3.515	0.030	-0.129	0.010	-0.054	-749
0.142	1.141	3.869	0.029	-0.129	0.011	-0.057	-729
0.209	1.179	5.695	0.025	-0.110	0.008	-0.048	-661
0.276	1.182	7.520	0.018	-0.084	0.008	-0.085	-560
0.342	1.150	9.319	0.015	-0.078	0.008	-0.077	

TABLE 11

BASIC DATA				SLOT HEIGHT = .021"			
$C\mu = 0.0197$		$\theta = 35^\circ$		$y_{m/2} = 0.0480"$		$U_m = 31.9 \text{ ms}^{-1}$	
$y(\text{in})$	\bar{U}/U_m	$y/y_{m/2}$	$\sqrt{\bar{U}^2}/U_m$	\bar{V}/U_m	$\sqrt{\bar{V}^2}/U_m$	$\overline{u'v'}(\text{m}^2\text{s}^{-2})$	$(p - p_m)$ Nm^{-2}
							WALL
0.009	1.799	0.188		0.009			-1304
0.012	1.824	0.250		0.022			
0.014	1.850	0.292		0.034			$y=0.016$
0.017	1.853	0.354		0.047			-1149
0.020	1.843	0.417		0.047			
0.022	1.821	0.458		0.053			-918
0.029	1.771	0.604		0.053			-675
0.036	1.687	0.750	0.056	0.050	0.033	1.250	-517
0.042	1.571	0.875	0.053	0.053	0.031	1.051	-431
0.049	1.445	1.021	0.053	0.053	0.033	1.005	-385
0.062	1.320	1.292	0.055	0.041	0.032	1.021	-265
0.076	1.113	1.583	0.047	0.009	0.025	0.595	-293
0.089	1.009	1.854	0.040	-0.016	0.018	0.180	-410
0.102	0.984	2.125	0.040	-0.022	0.014	-0.043	-530
0.116	0.987	2.417	0.044	-0.019	0.011	-0.024	-548
0.129	1.000	2.688	0.043	-0.016	0.011	-0.041	-541
0.142	1.006	2.958	0.042	-0.009	0.012	-0.087	-532
0.209	1.053	4.354	0.038	0.028	0.012	-0.145	-479
0.276	1.072	5.750	0.029	0.066	0.010	-0.157	-379
0.342	1.053	7.125	0.023	0.091	0.010	-0.160	

TABLE 12

BASIC DATA				SLOT HEIGHT = .021"			
$C\mu = 0.0284$		$\theta = 15^\circ$		$y_m/2 = 0.0297"$		$U_m = 31.19 \text{ ms}^{-1}$	
$y(\text{in})$	\bar{U}/U_m	$y/y_m/2$	$\sqrt{\bar{U}^2}/U_m$	\bar{V}/U_m	$\sqrt{\bar{V}^2}/U_m$	$\overline{u'v'}(\text{m}^2\text{s}^{-2})$	$(p - p_m)/\rho U_m^2$
							-2187
							WALL
0.009	3.556	0.303		-0.050			-2542
0.016	3.348	0.529		-0.006			-452
0.022	2.934	0.751		-0.006			-9
0.029	2.545	0.976		-0.025			479
0.036	2.053	1.202	0.092	-0.085	0.036	1.012	139
0.042	1.577	1.424	0.083	-0.163	0.026	1.159	-341
0.049	1.326	1.650	0.055	-0.232	0.020	0.755	-684
0.062	1.241	2.098	0.029	-0.288	0.011	-0.042	-1091
0.076	1.260	2.549	0.026	-0.307	0.011	-0.080	-1100
0.089	1.273	3.007	0.026	-0.317	0.009	-0.086	-1111
0.102	1.288	3.434	0.025	-0.326	0.010	-0.077	-1110
0.116	1.307	3.906	0.025	-0.332	0.010	-0.075	-1066
0.129	1.313	4.343	0.024	-0.339	0.011	-0.072	-1087
0.142	1.329	4.781	0.024	-0.342	0.011	-0.068	-1078
0.209	1.354	7.037	0.021	-0.357	0.008	-0.058	-982
0.276	1.332	9.293	0.017	-0.357	0.007	-0.062	-869

TABLE 13

BASIC DATA				SLOT HEIGHT = .021"			
$C_u = 0.0284$		$\theta = 25^\circ$		$y_{m/2} = 0.0402'$		$U_\infty = 31.9 \text{ ms}^{-1}$	
$y(\text{in})$	\bar{U}/U_∞	$y/y_{m/2}$	$\sqrt{u'^2}/U_\infty$	\bar{v}/U_∞	$\sqrt{v'^2}/U_\infty$	$\overline{u'v'}(\text{m}^2\text{s}^{-2})$	$(p - p_\infty)/\rho U_\infty^2$
							-2227
							WALL
0.009	2.900	0.224		-0.088			-2440
0.012	2.922	0.299		-0.082			
0.014	2.893	0.348		-0.072			$y=0.016$
0.017	2.843	0.423		-0.053			-1405
0.020	2.787	0.498		-0.053			
0.022	2.765	0.547		-0.038			-960
0.029	2.608	0.721		-0.050			-730
0.036	2.370	0.896	0.025	-0.053	0.014	0.169	-648
0.042	2.066	1.045	0.042	-0.075	0.020	0.449	-566
0.049	1.765	1.219	0.055	-0.103	0.023	0.936	-513
0.062	1.476	1.542	0.033	-0.160	0.016	0.482	-863
0.076	1.376	1.891		-0.207		-0.011	-1212
0.089	1.373	2.214		-0.219			-1223
0.102	1.370	2.537		-0.223			-1191
0.116	1.382	2.886		-0.229			-1189
0.129	1.389	3.209		-0.229			-1163
0.142	1.389	3.2		-0.229			-1126
0.209	1.401	5.199		-0.219			-1000
0.276	1.367	6.866		-0.207			-869

TABLE 14

BASIC DATA

SLOT HEIGHT = .021"

C _D = 0.0284		$\theta = 35^\circ$		$y_{m/2} = 0.0518"$		$U_\infty = 31.9 \text{ ms}^{-1}$	
y(in)	\bar{U}/U_∞	$y/y_{m/2}$	$\sqrt{U'^2}/U_\infty$	\bar{V}/U_∞	$\sqrt{V'^2}/U_\infty$	$\overline{U'V'}(\text{m}^2\text{s}^{-2})$	(p - p _∞) N _m ⁻²
							-1987
							WALL
0.009	2.451	0.174		0.009			-2141
0.012	2.464	0.232		0.019			
0.014	2.470	0.270		0.016			y=0.016
0.017	2.549	0.328		0.025			-1637
0.020	2.542	0.386		0.031			
0.022	2.508	0.425		0.034			-1412
0.029	2.445	0.560		0.034			-1321
0.036	2.332	0.695	0.029	0.034	0.019	0.486	-909
0.042	2.185	0.811	0.029	0.028	0.019	0.469	-852
0.049	2.009	0.946	0.036	0.031	0.023	0.660	-752
0.062	1.774	1.197	0.048	0.003	0.027	1.040	-703
0.076	1.486	1.467	0.036	-0.041	0.021	0.681	-819
0.089	1.386	1.718		-0.066		0.028	-938
0.102	1.354	1.969		-0.078		-0.024	-1083
0.116	1.348	2.239		-0.075			-1052
0.129	1.348	2.490		-0.075			-1039
0.142	1.357	2.741		-0.069			-1037
0.209	1.370	4.035		-0.044			-873
0.276	1.348	5.328		-0.025			-763

TABLE 15

BASIC DATA				SLOT HEIGHT = .021"			
$CU = 0.0284$		$\theta = 45^\circ$		$y_{m/2} = 0.0671"$		$U_m = 31.9 \text{ ms}^{-1}$	
$y(\text{in})$	\bar{u}/U_m	$y/y_{m/2}$	$\sqrt{\bar{u}^2}/U_m$	\bar{v}/U_m	$\sqrt{\bar{v}^2}/U_m$	$\overline{u'v'}(\text{m}^2\text{s}^{-2})$	$(p - p_m) \text{ mm}^{-2}$
							-1707
							WALL
0.009	2.082	0.134		0			-1656
0.016	2.194	0.238		0.019			-1470
0.022	2.223	0.328		0.034			-1144
0.029	2.207	0.432		0.028			-1048
0.036	2.154	0.537	0.066	0.031	0.038	1.660	-842
0.042	2.085	0.626	0.063	0.031	0.039	1.748	-699
0.049	1.994	0.730	0.064	0.034	0.038	1.740	-621
0.062	1.824	0.924	0.065	0.034	0.040	1.676	-562
0.076	1.596	1.133	0.065	0.016	0.034	1.338	-446
0.089	1.426	1.326	0.059	-0.003	0.028	0.986	-462
0.102	1.323	1.520	0.048	-0.016	0.022	0.623	-594
0.116	1.273	1.729	0.037	-0.025	0.016	0.177	-662
0.129	1.257	1.923	0.034	-0.025	0.013	0.046	-730
0.142	1.254	2.116	0.033	-0.022	0.012	-0.013	-746
0.209	1.263	3.115	0.030	0.013	0.012	-0.096	-638
0.276	1.235	4.113	0.023	0.053	0.011	-0.13	-524

TABLE 16

BASIC DATA				SLOT HEIGHT = .021"			
$C_u = 0.0284$		$\theta = 55^\circ$		$y_{m/2} = 0.0881"$		$U_m = 31.9 \text{ ms}^{-1}$	
$y(\text{in})$	\bar{U}/U_m	$y/y_{m/2}$	$\sqrt{U'^2}/U_m$	\bar{V}/U_m	$\sqrt{V'^2}/U_m$	$\overline{u'v'}(\text{m}^2\text{s}^{-2})$	$(p - p_m) \text{ mm}^{-2}$
							-1217
							WALL
0.009	1.436	0.102		-0.031			-1582
0.012	1.621	0.136		0			
0.014	1.708	0.159		0.013			$y=0.016$
0.017	1.784	0.193		0.028			-1957
0.020	1.809	0.227		0.034			
0.022	1.828	0.250		0.041			-1779
0.029	1.862	0.329		0.038			-1622
0.036	1.859	0.409	0.060	0.050	0.029	1.007	-1210
0.049	1.784	0.556	0.056	0.063	0.035	1.443	-745
0.062	1.737	0.704	0.054	0.066	0.037	1.831	-294
0.076	1.589	0.863	0.055	0.063	0.041	2.103	10
0.089	1.442	1.010	0.061	0.060	0.043	2.382	212
0.102	1.310	1.158	0.061	0.047	0.041	2.095	407
0.116	1.169	1.317	0.056	0.044	0.034	1.471	602
0.129	1.103	1.464	0.045	0.044	0.024	0.544	507
0.142	1.053	1.612	0.038	0.034	0.019	0.027	457
0.209	1.041	2.372	0.039	0.069	0.020	-0.726	-81
0.276	1.038	3.133	0.022	0.125	0.015	-0.340	-210
0.342	1.022	3.882	0.016	0.166	0.011	-0.184	
0.409	0.981	4.642	0.014	0.194	0.10	-0.146	

TABLE 17

BASIC DATA				SLOT HEIGHT = .021"			
$C_\mu = 0.0284$		$\theta = 65^\circ$		$y_m/2 = 0.1726"$		$U_\infty = 31.9 \text{ ms}^{-1}$	
$y(\text{in})$	\bar{U}/U_∞	$y/y_m/2$	$\sqrt{u'^2}/U_\infty$	\bar{V}/U_∞	$\sqrt{v'^2}/U_\infty$	$\overline{u'v'}(\text{m}^2\text{s}^{-2})$	$(p - p_m) \text{ mm}^{-2}$
							WALL
0.009	0.354	0.052		-0.075			
0.012	0.618	0.070		-0.053			
0.014	0.687	0.081		-0.053			
0.017	0.793	0.098		-0.022			
0.020	0.843	0.116		-0.025			
0.022	0.950	0.127		-0.031			
0.029	1.078	0.168		0.006			
0.036	1.056	0.209	0.492	0.028	0.088	34.722	
0.049	1.169	0.284	0.476	0.082	0.124	47.790	
0.062	1.150	0.359	0.384	0.107	0.121	29.487	
0.076	1.191	0.440	0.278	0.163	0.137	14.851	
0.089	1.194	0.516	0.256	0.197	0.123	14.870	
0.102	1.232	0.591	0.202	0.179	0.107	0.468	
0.116	1.132	0.672	0.130	0.238	0.193	5.981	
0.129	1.066	0.747	0.117	0.260	0.166	5.874	
0.142	1.019	0.823	0.109	0.282	0.154	6.624	
0.209	0.824	1.211	0.079	0.194	0.127	5.203	
0.276	0.740	1.599	0.092	0.219	0.089	1.543	

$y(\text{in})$	$u \frac{\partial u}{\partial x}$	$+ v \frac{\partial u}{\partial y}$	$+ \frac{uv}{R}$	$-\frac{\partial(u'v')}{\partial y}$	$= -\frac{1}{\rho} \frac{\partial p}{\partial x}$	EXPT. $-\frac{1}{\rho} \frac{\partial p}{\partial x}$	$\frac{\partial v}{u} \frac{\partial v}{\partial x}$	$+ v \frac{\partial v}{\partial y}$	$-\frac{u^2}{R}$	$-\frac{\partial(v'^2)}{\partial y}$	$-\frac{1}{\rho} \frac{\partial p}{\partial y}$	EXPT. $-\frac{1}{\rho} \frac{\partial p}{\partial y}$
0.036	-14700	-2082	3700	67000	-78400	0	3000	780	92900	11970	-50150	-808800
0.049	-128400	-15800	4500	41000	-98700	0	27500	430	78800	1440	-49430	-220000
0.062	-62600	-25200	4580	24000	-59200	-57200	24800	860	65400	4800	-36660	-200000
0.076	-34300	-29700	4000	0	-60000	-130000	21400	-1400	49500	8300	-21200	-200000
0.089	0	-26000	3440	-22000	-44560	-80400	18900	200	39200	-16080	-36180	362000

$$C_F = 0.0284$$

$$\alpha_c = 0^\circ$$

$$\theta = 45^\circ$$

$$Y_m = 0.022 \text{ in}$$

$$Y_{\min} = 0.123 \text{ in}$$

CORRECTED TURBULENCE QUANTITIES USED
ALL UNITS (ms⁻²)

TABLE 18: COMPARISON OF EXPERIMENTAL AND PREDICTED PRESSURE GRADIENTS

	CASE 1	CASE 2	CASE 3	CASE 4
C_p	0.0065	0.0139	0.0197	0.0284
C_L	0.35	0.55	0.68	0.86
α_G	0°	0°	0°	0°
α_{eff}	-1.8°	-2.7°	-3.4°	-4.0°
θ_{sep} (approx)	35°	42°	49°	59°

TABLE 19: OVERALL CONDITIONS FOR THE FOUR BLOWING CASES AT WHICH DETAILED TRAILING EDGE WALL JET MEASUREMENTS WERE MADE

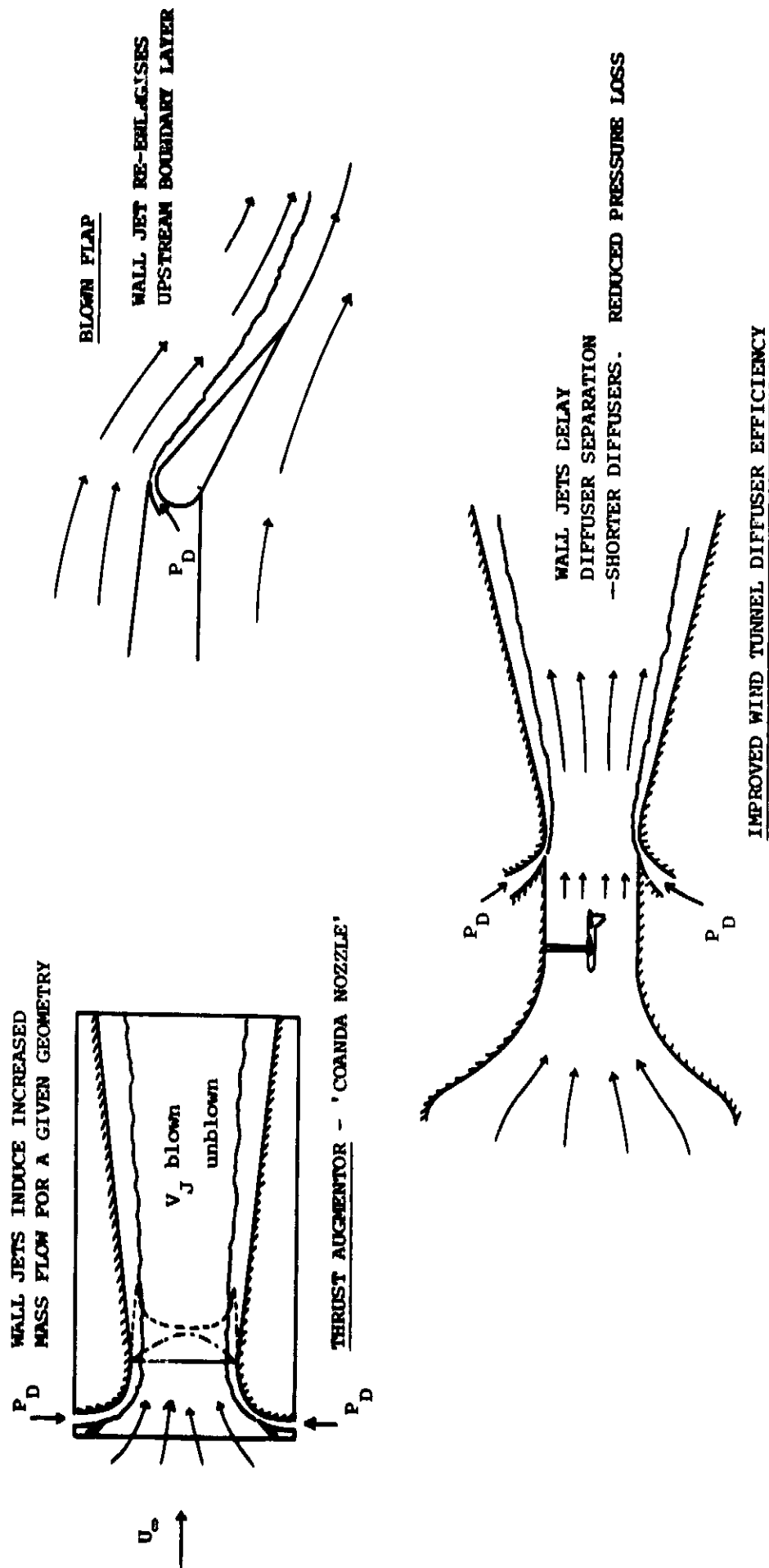


FIGURE 1: EXAMPLES OF THE APPLICATION OF COANDA EFFECT

FIG 2

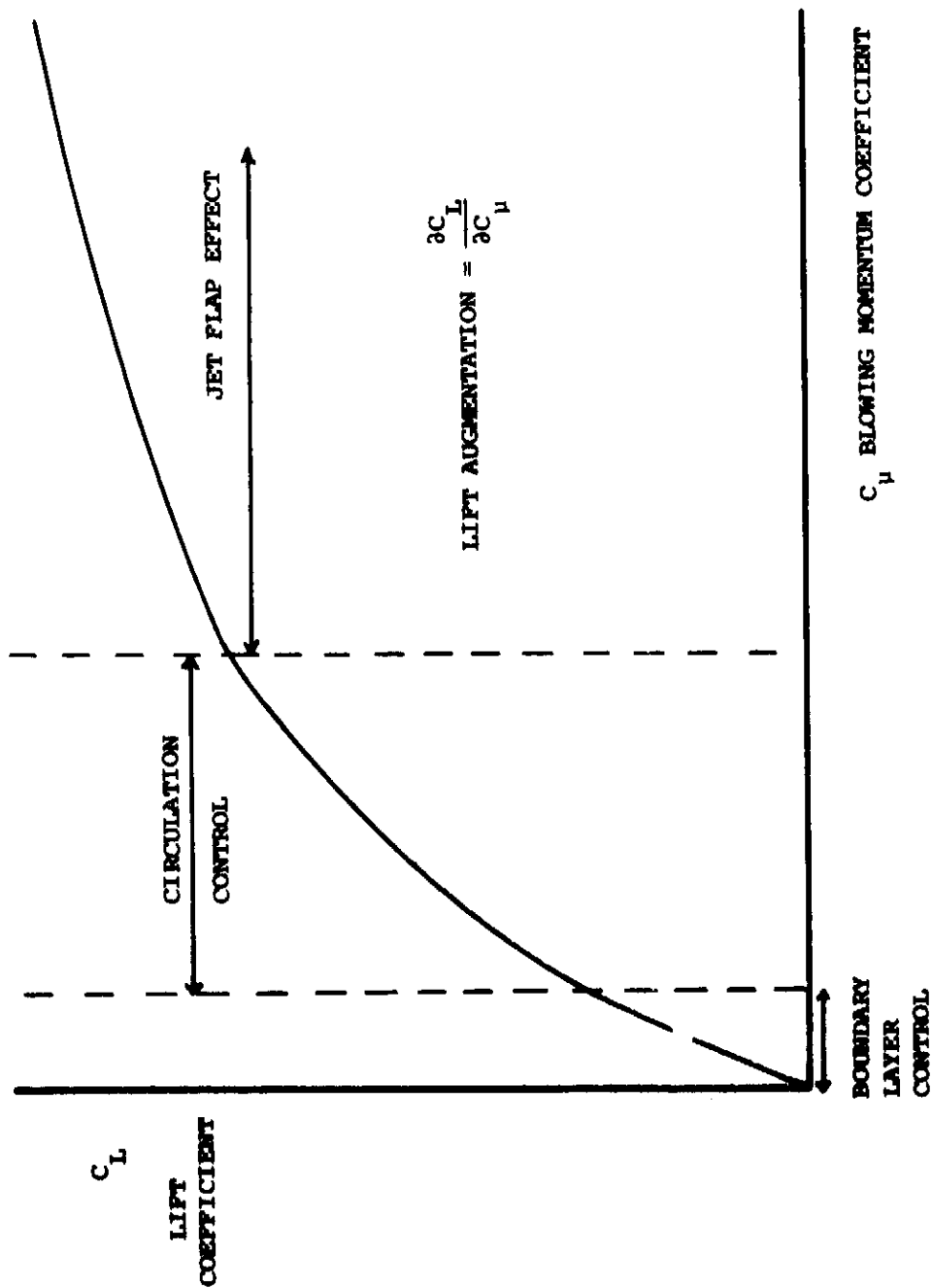


FIGURE 2: PERFORMANCE TRENDS OF A CIRCULATION CONTROLLED AEROFOIL

FIG 3

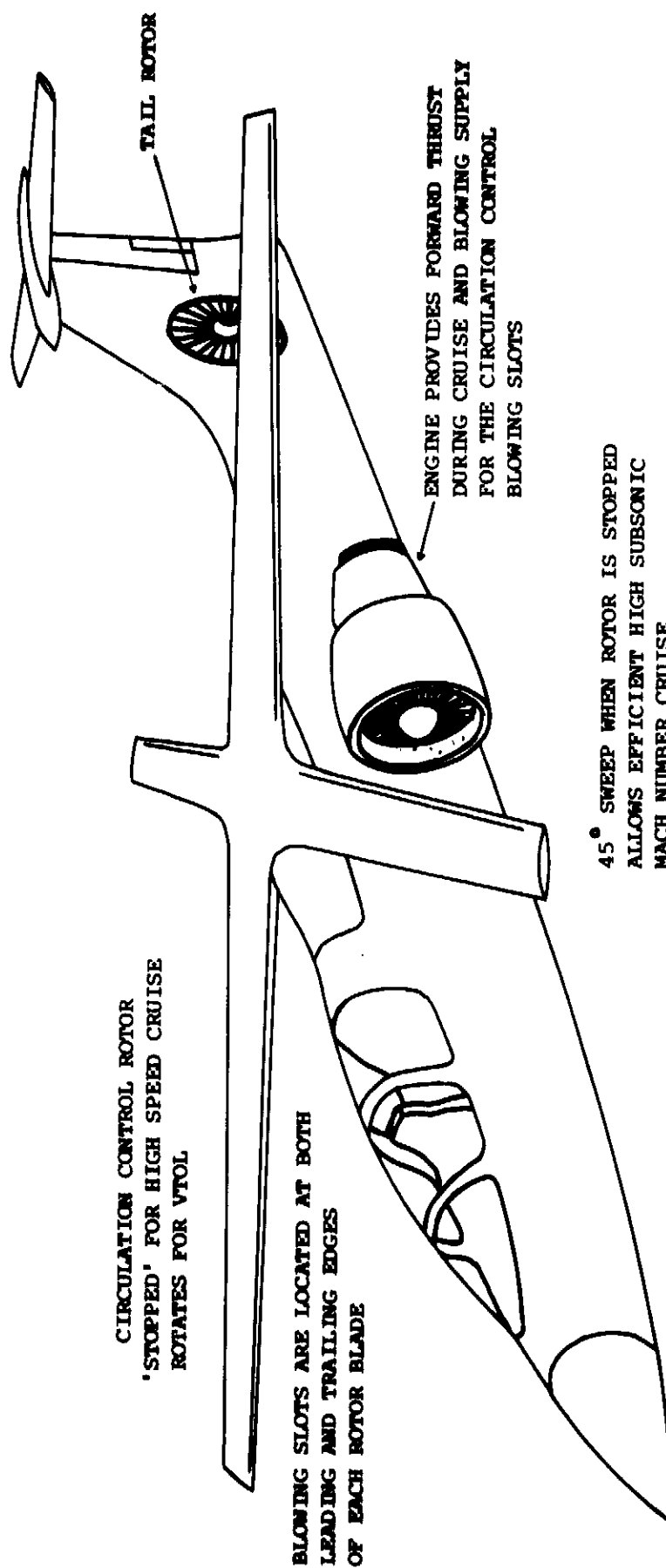
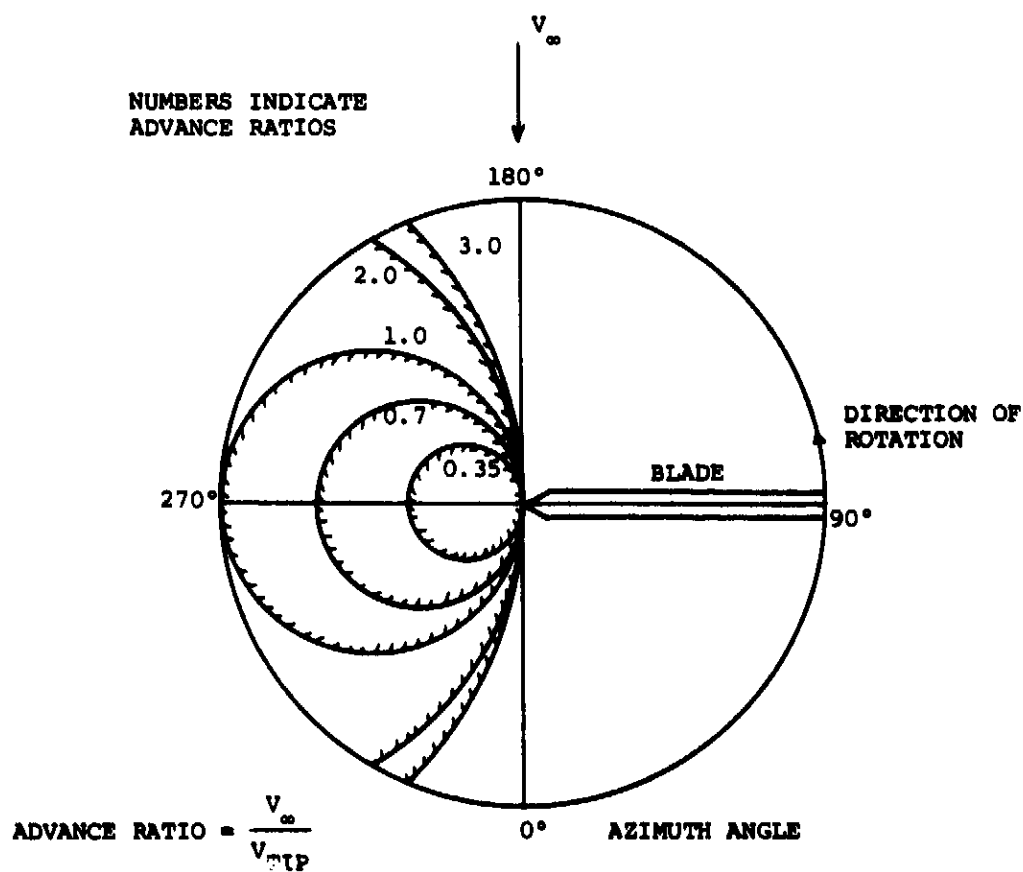


FIGURE 3: A SKETCH OF THE X-WING STOPPED ROTOR AIRCRAFT

FIG 4



NOTE: REVERSED FLOW OCCURS OVER THE PORTION OF THE BLADE WITHIN THE
OPERATING ADVANCE RATIO CIRCLE

**FIGURE 4: GROWTH OF REVERSED FLOW REGIONS WITH INCREASING
ADVANCE RATIOS**

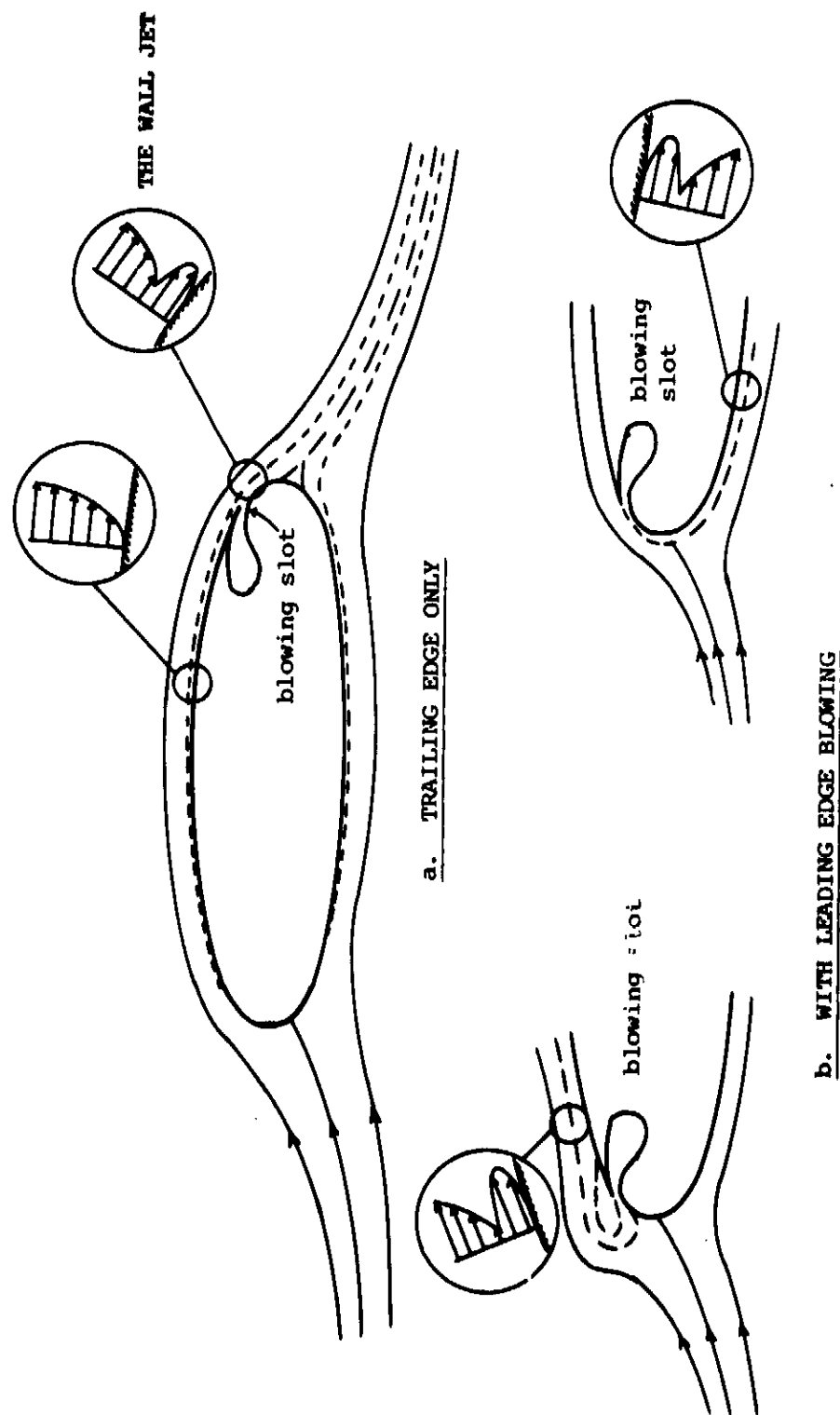


FIGURE 5: VELOCITY PROFILES IN TYPICAL CIRCULATION CONTROL FLOW FIELDS

FIG 6

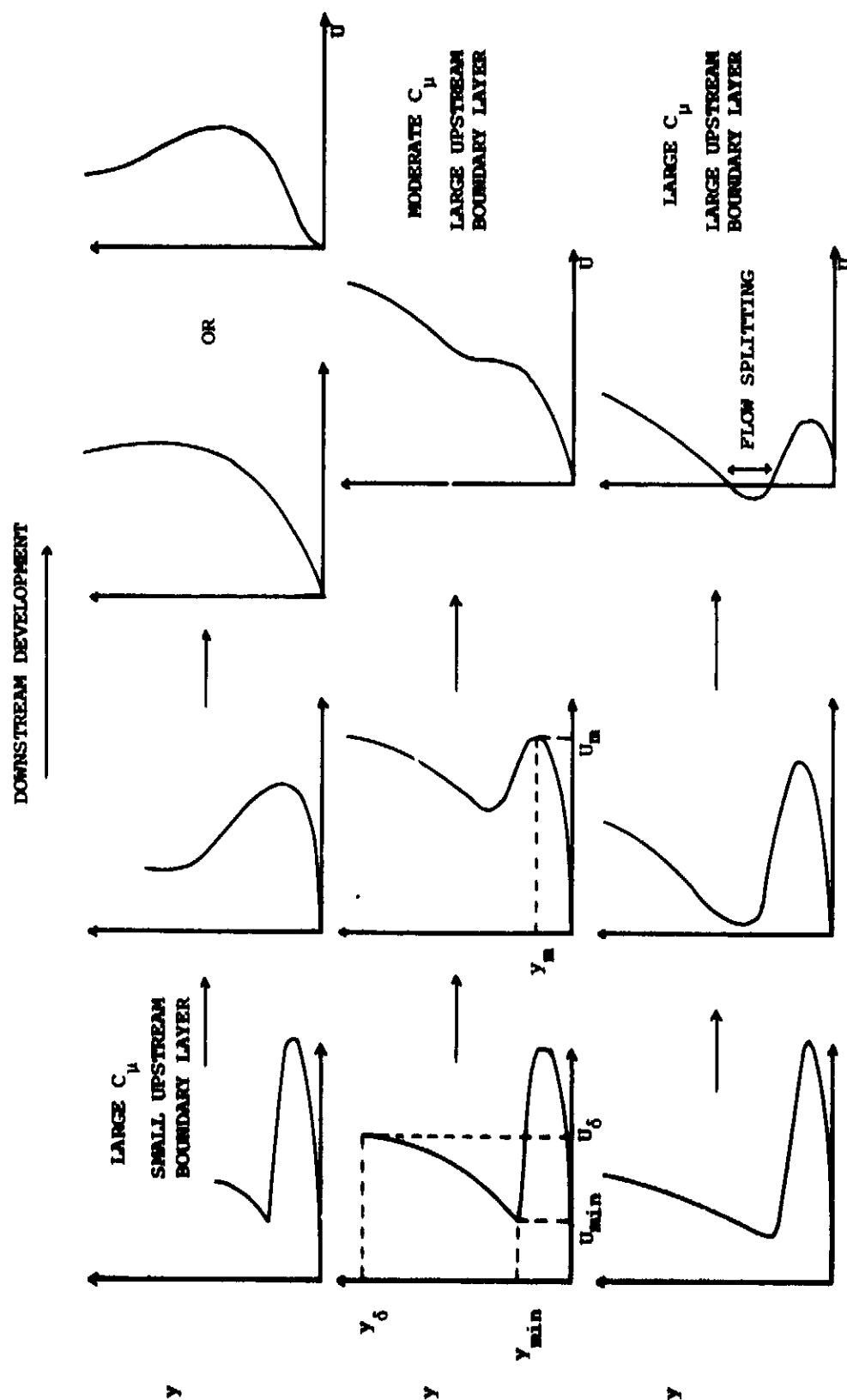


FIGURE 6: DOWNSTREAM DEVELOPMENT OF TYPICAL WALL JET VELOCITY PROFILES

FIG 7

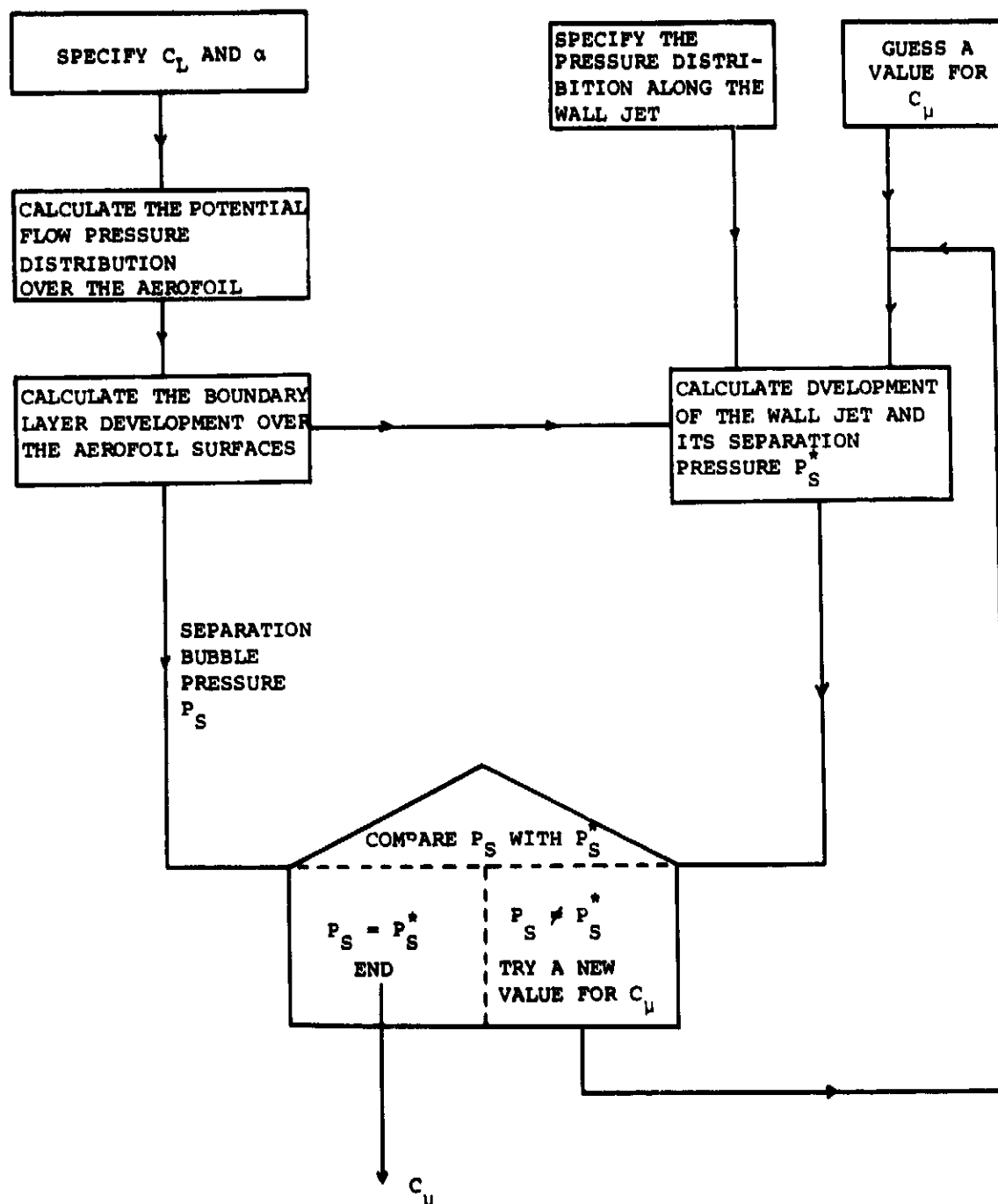


FIGURE 7: BLOCK DIAGRAM OF THE CALCULATION METHOD OF KIND³²

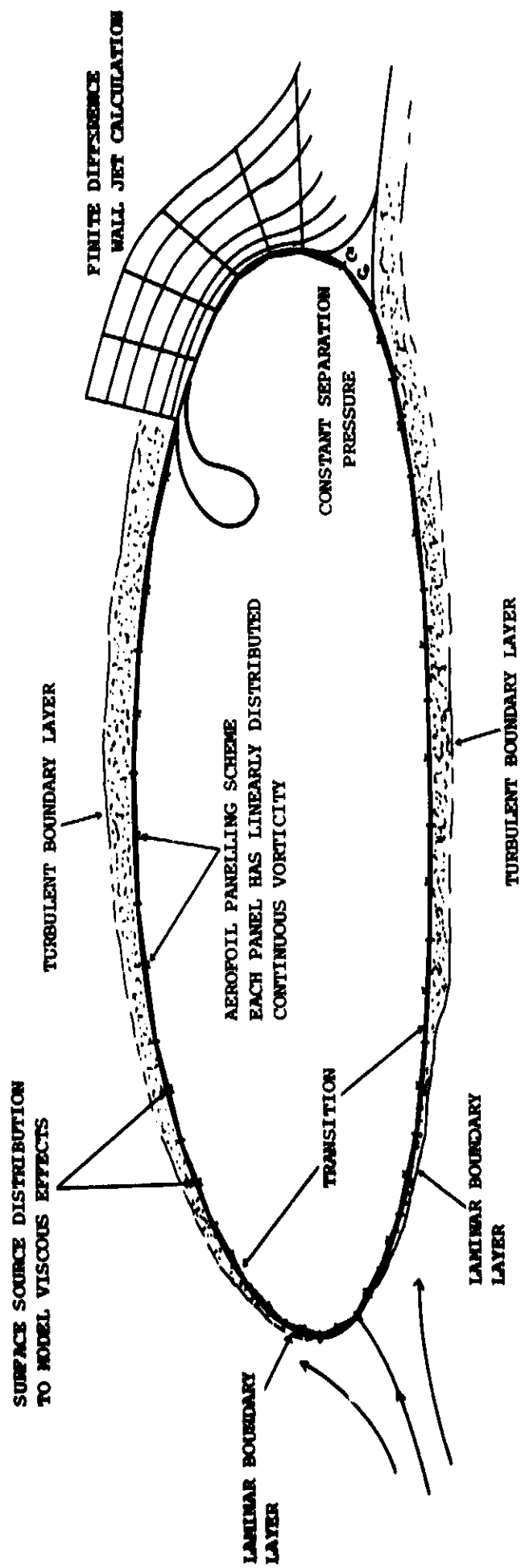


FIGURE 3: SCHEMATIC LAYOUT OF THE CALCULATION METHOD OF DVORAK AND KIND (CIRCON)³⁸

FIG 9

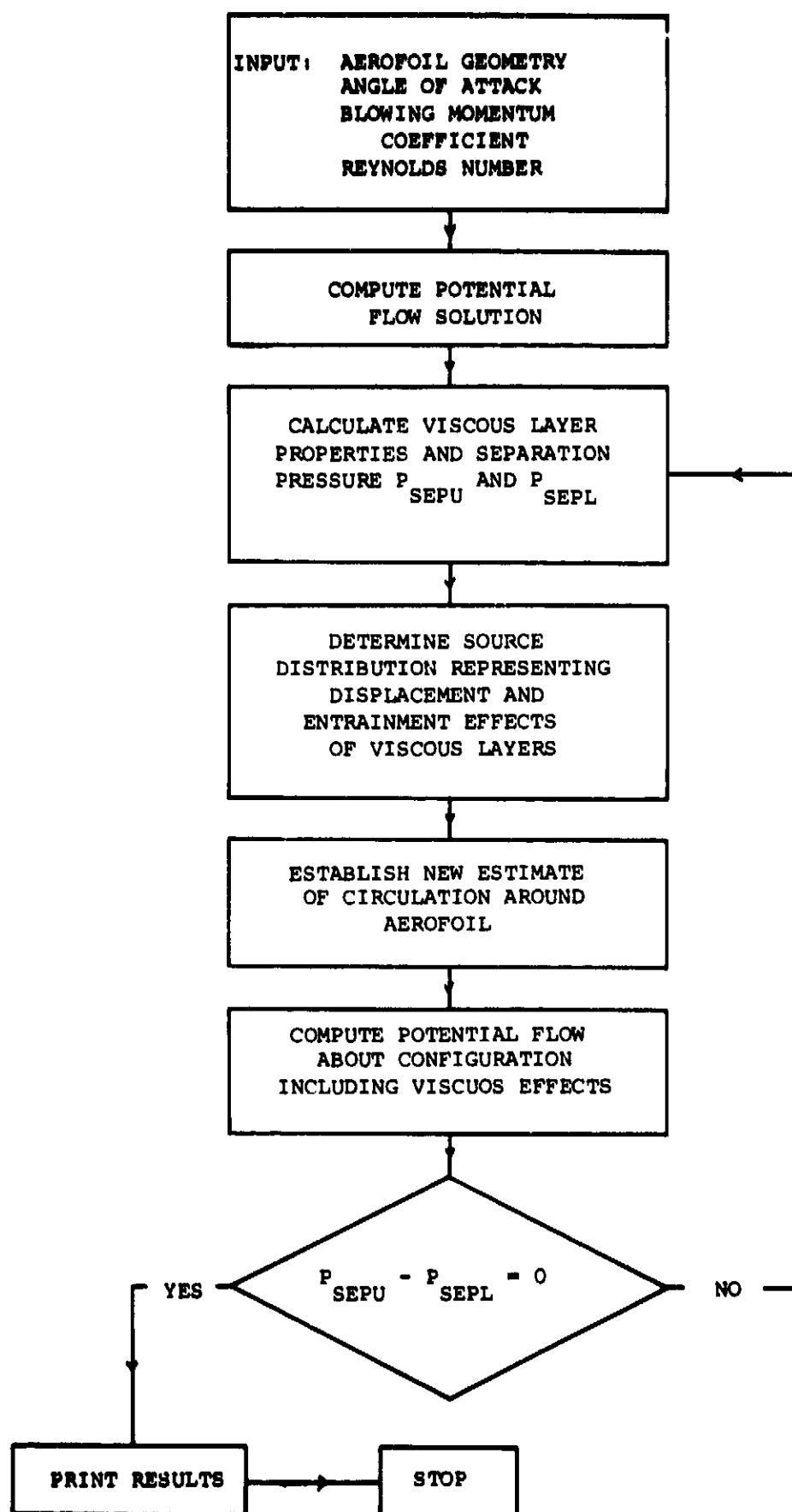


FIGURE 9: CALCULATION PROCEDURE OF DVORAK AND KIND³⁸

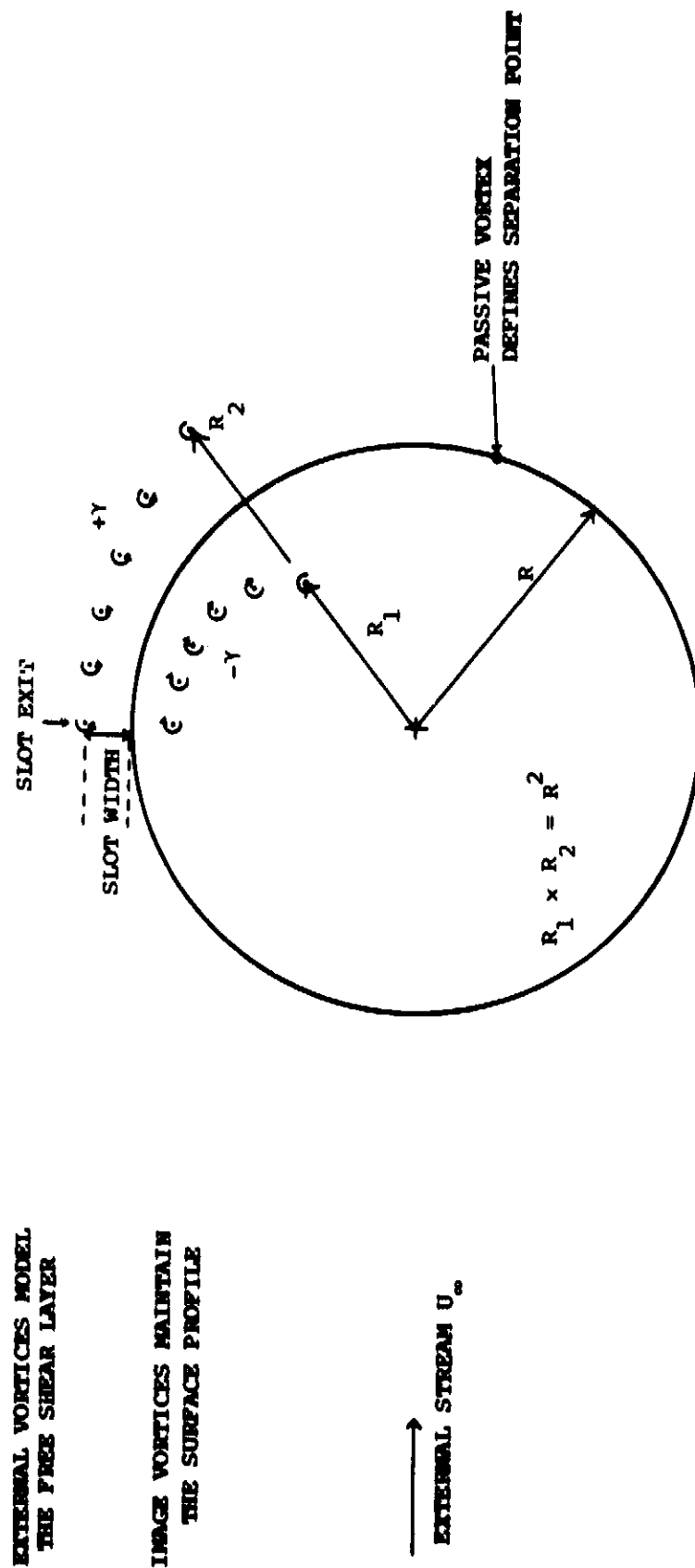


FIGURE 10: THE DISCRETE VORTEX POTENTIAL FLOW MODEL OF SMITH ET AL.³⁹

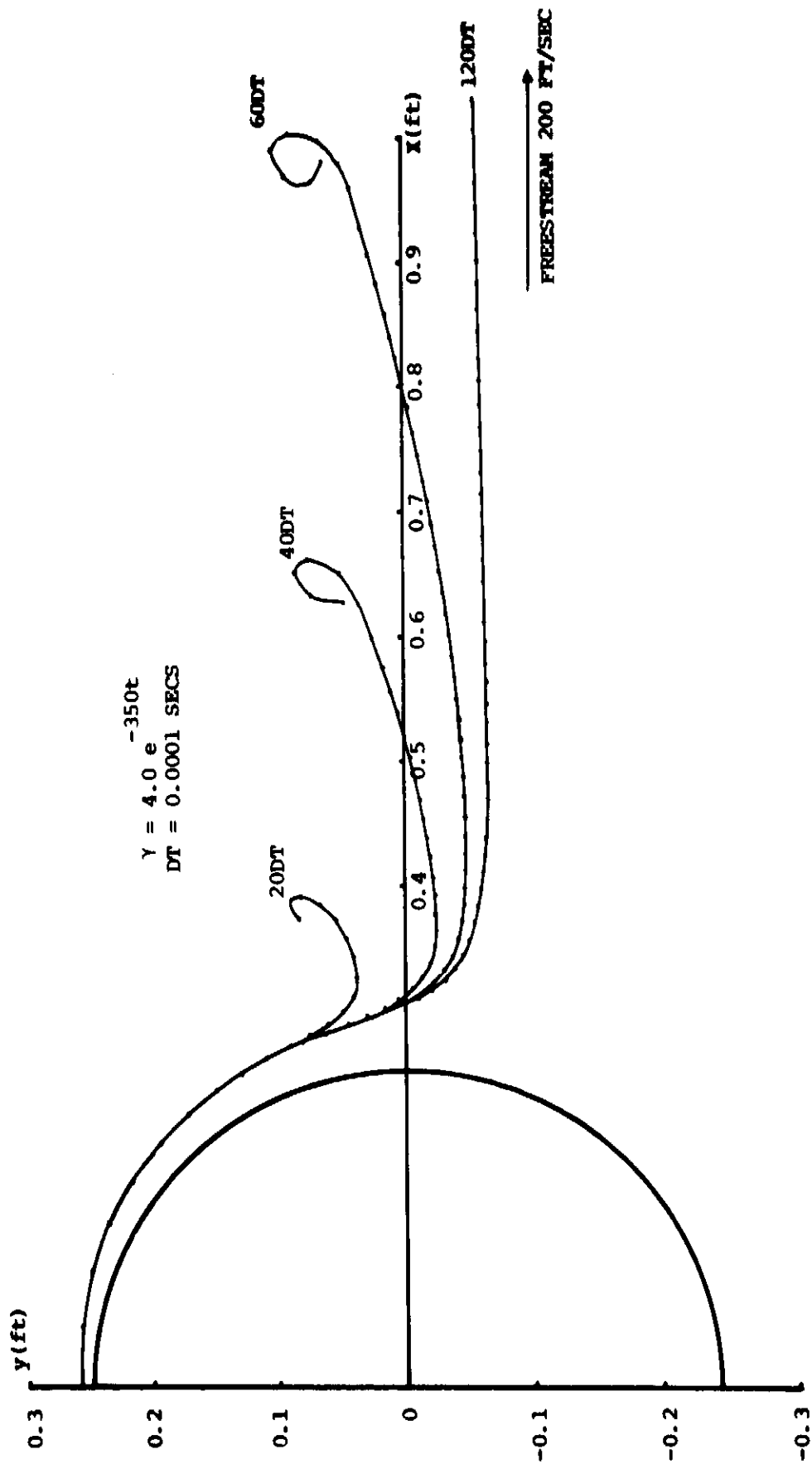


FIGURE 11: AN EXAMPLE OF THE JET SHEET DEVELOPMENT FROM THE METHOD OF SMITH ET. AL.³⁹

——— THEORETICAL PREDICTION
 - - - - -
 - . - . - } SEE REFERENCE 39
 - - - - - } EXPERIMENTAL RESULTS

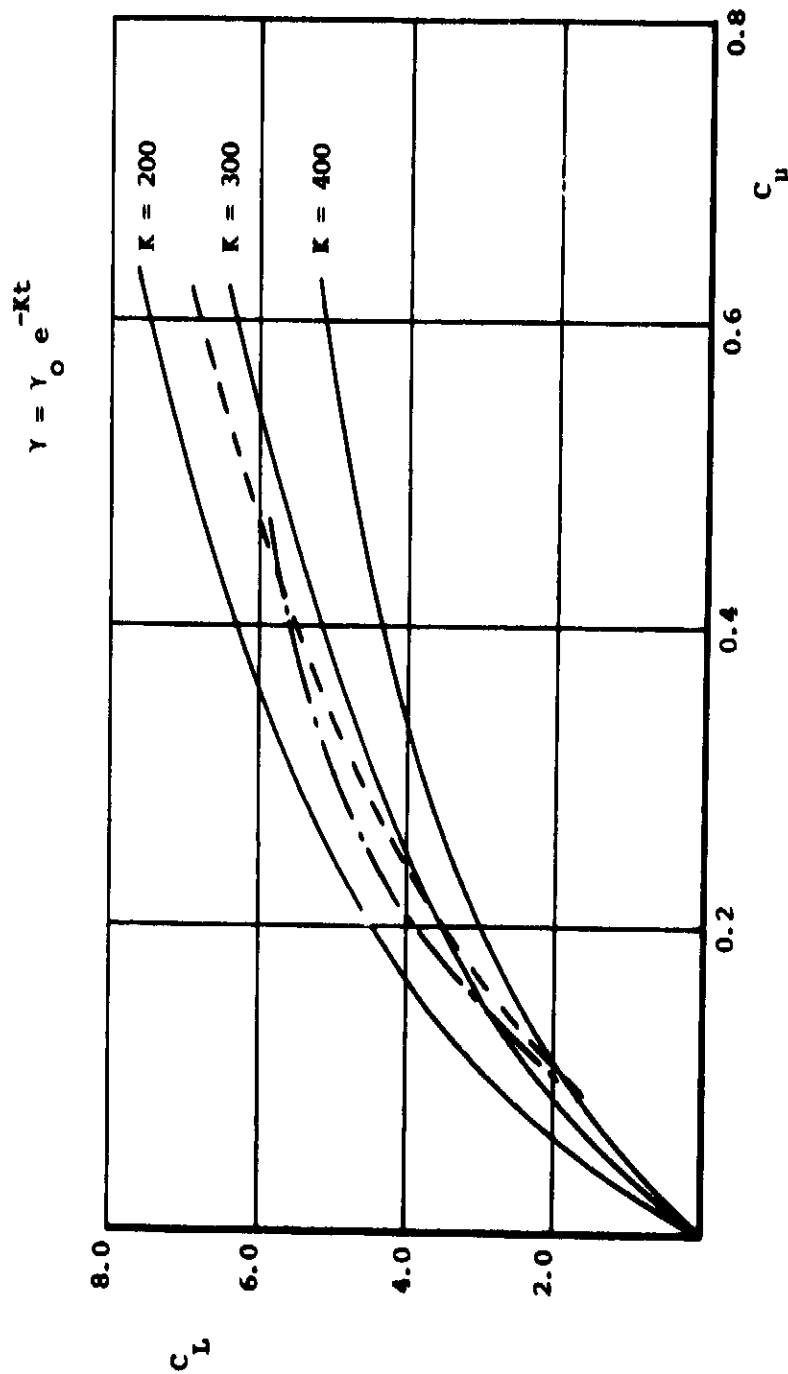


FIGURE 12: COMPARISON OF EXPERIMENTAL AND THEORETICAL RESULTS FROM SMITH ET. AL. 39

FIG 13

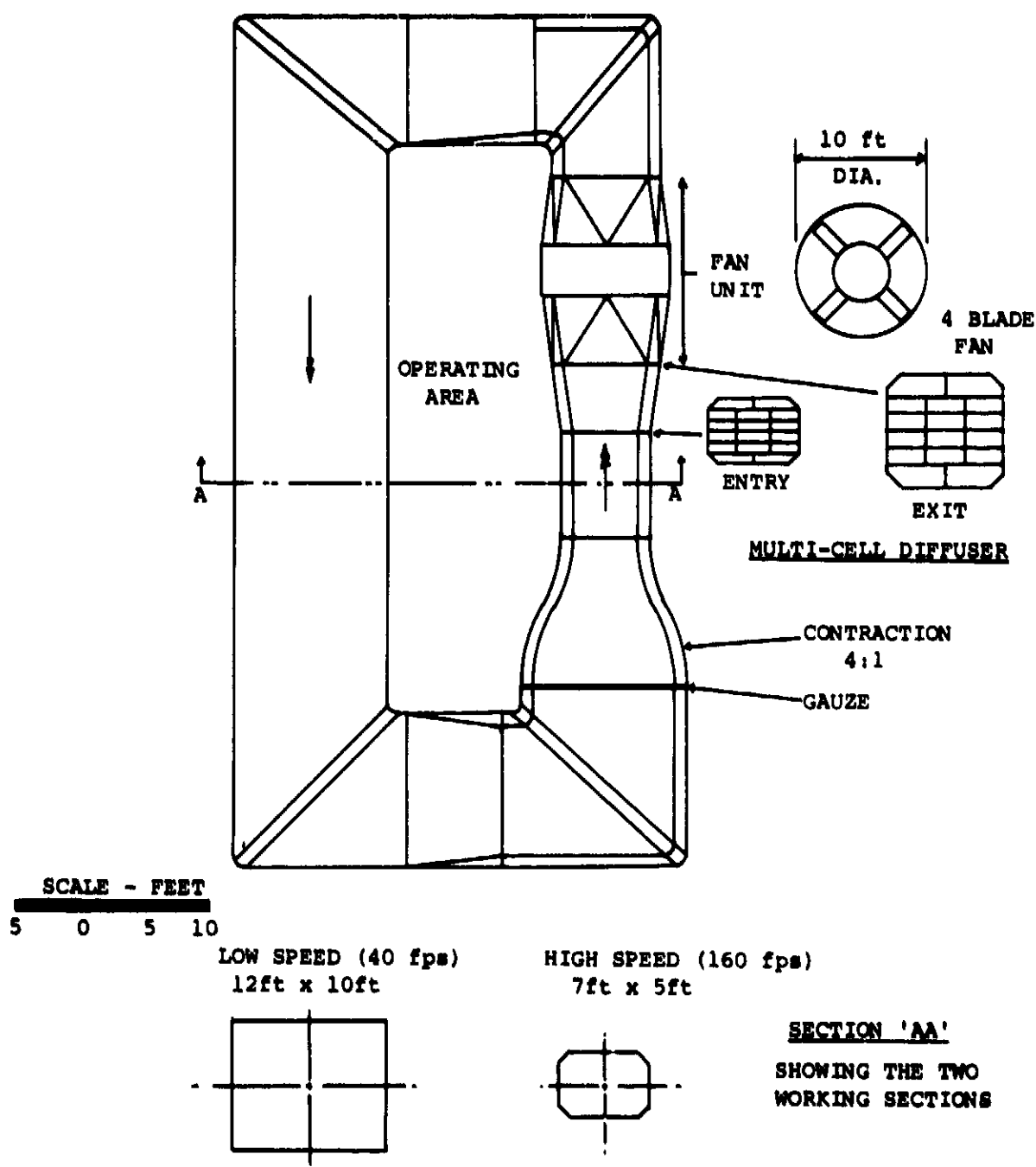


FIGURE 13: LAYOUT OF THE DUAL PURPOSE WIND TUNNEL

FIG 14

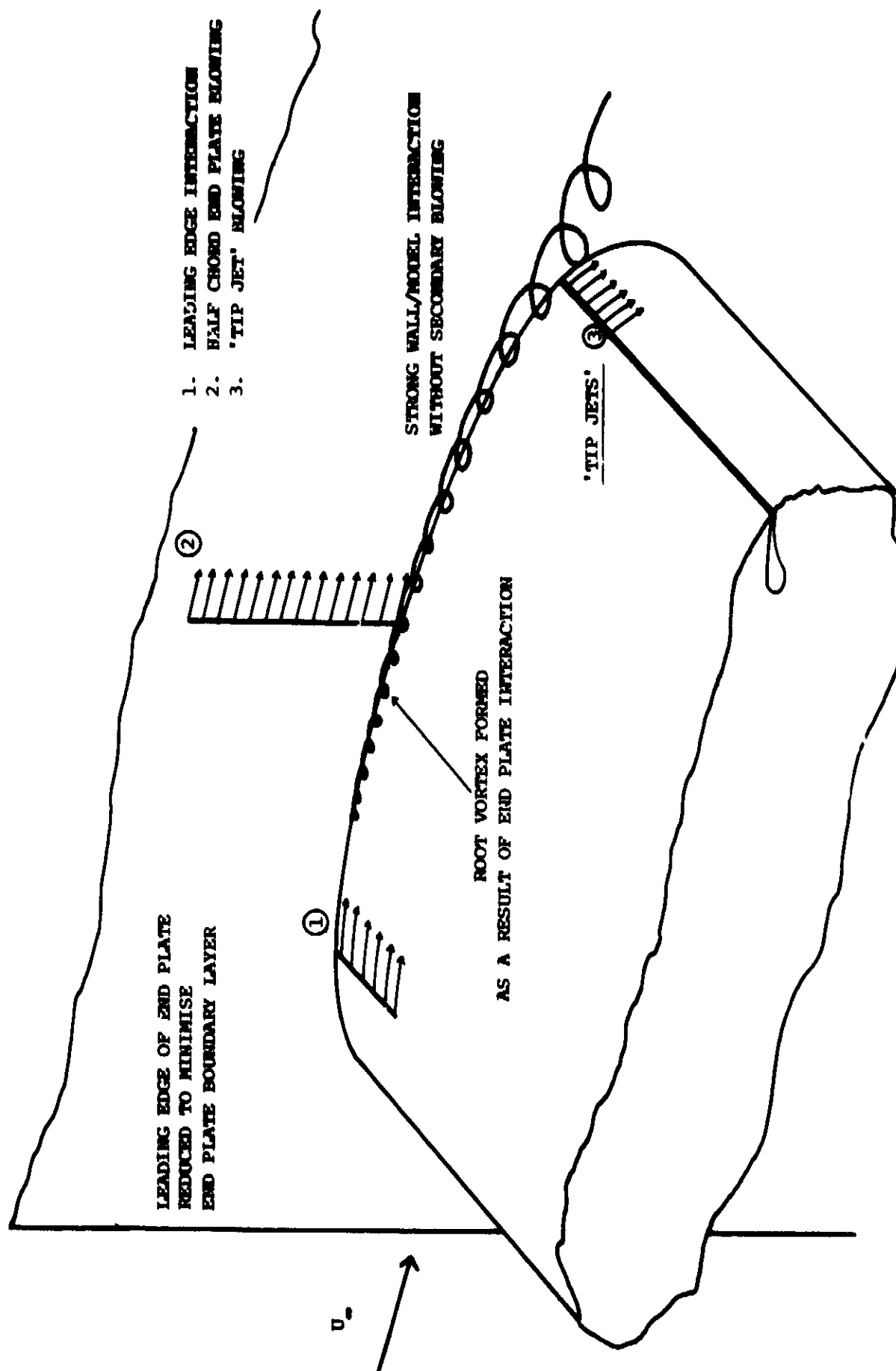


FIGURE 14: POSSIBLE SECONDARY BLOWING SCHEMES

FIG 15

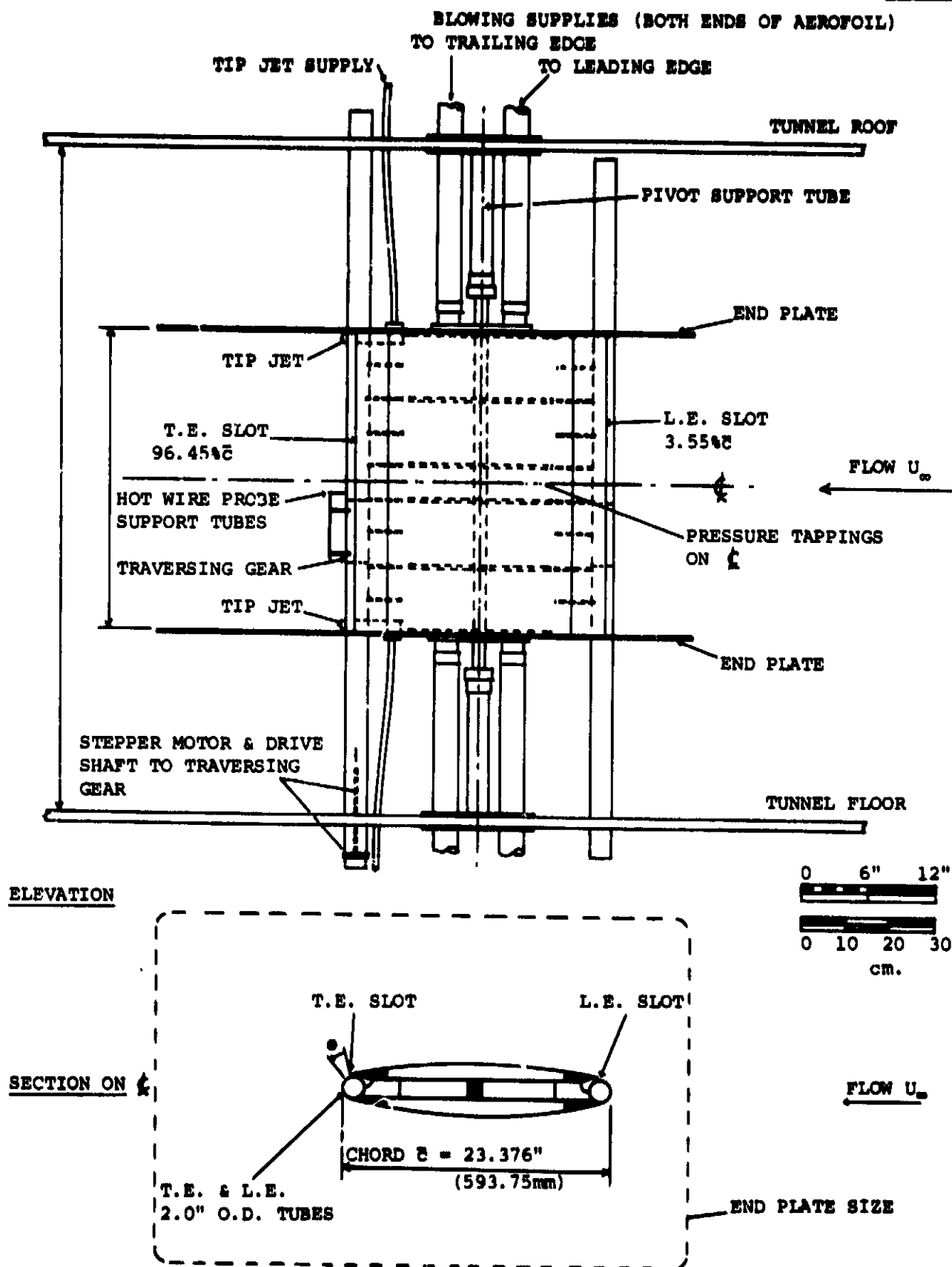
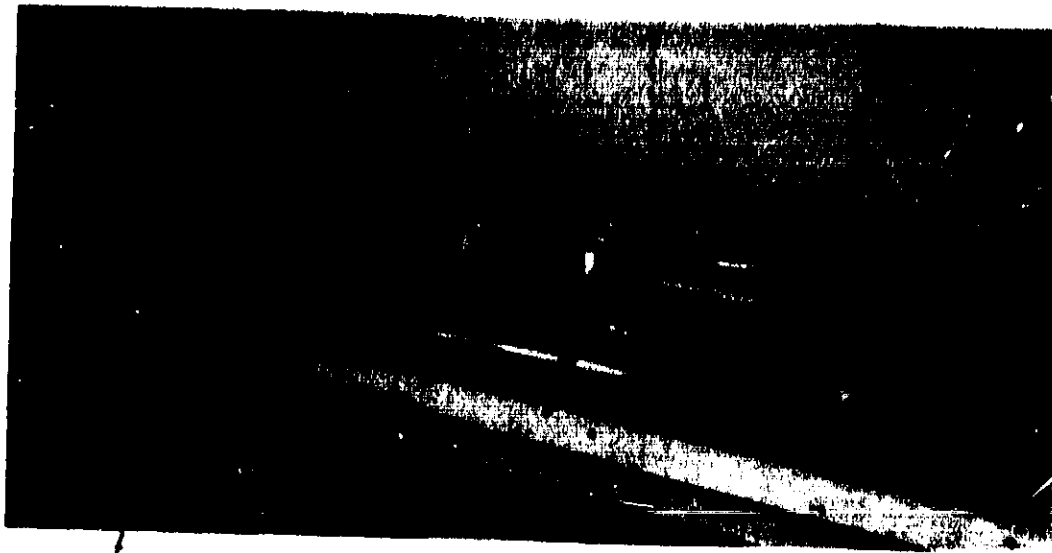


FIGURE 15: GENERAL ARRANGEMENT OF CIRCULATION CONTROLLED 20% ELLIPTIC AEROFOIL MOUNTED IN 7ft x 5ft WIND TUNNEL

OUTER SKIN
SUPPORT RIBS

AEROFOIL SUPPORT
SPIGOTS

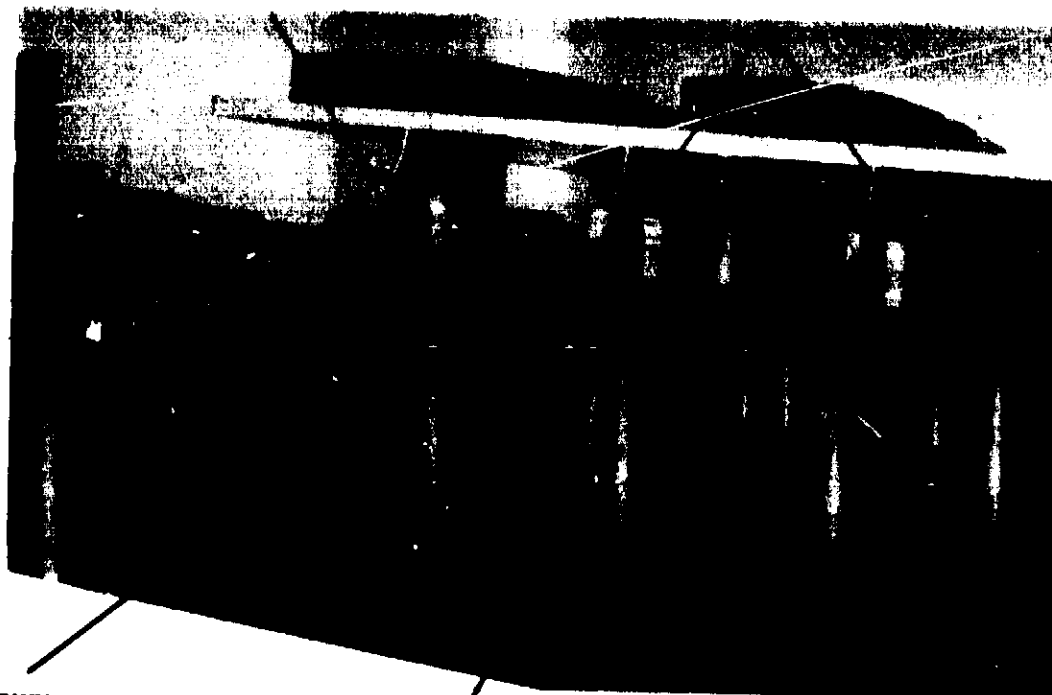


TRAILING EDGE
CYLINDER

ORIGINAL PAGE
BLACK AND WHITE PHOTOGRAPH

AIR INLET

INTERNAL
SPLITTERS



PLENUM
WALLS

INTERNAL PLENUM
SPACERS

CENTRE
SPAR

FIGURE 16: MODEL DURING FINAL ASSEMBLY

ORIGINAL PAGE
BLACK AND WHITE PHOTOGRAPH

FIG 18

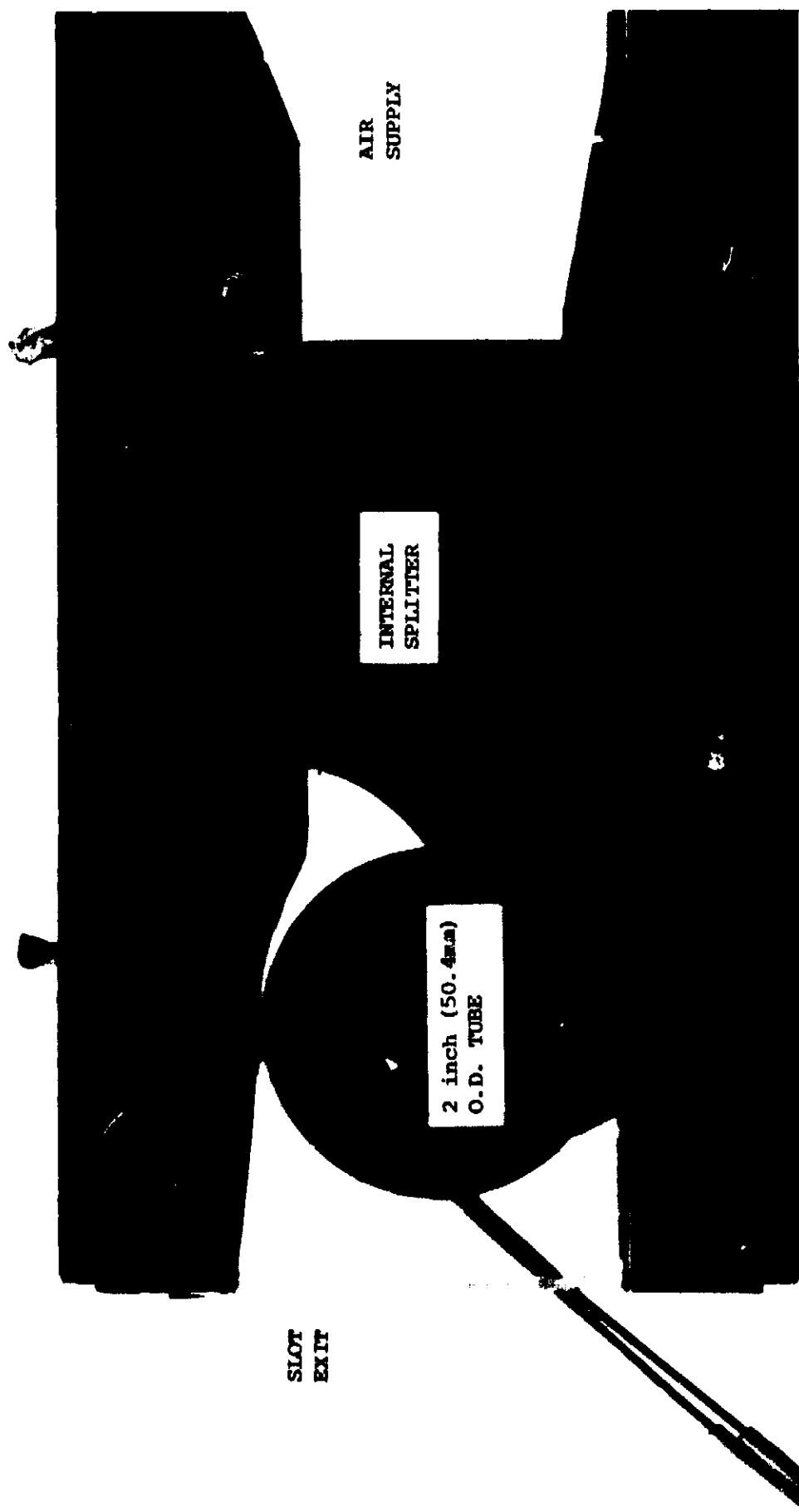


FIGURE 18: SLOT CONTRACTION GEOMETRY MODEL

FIG 19

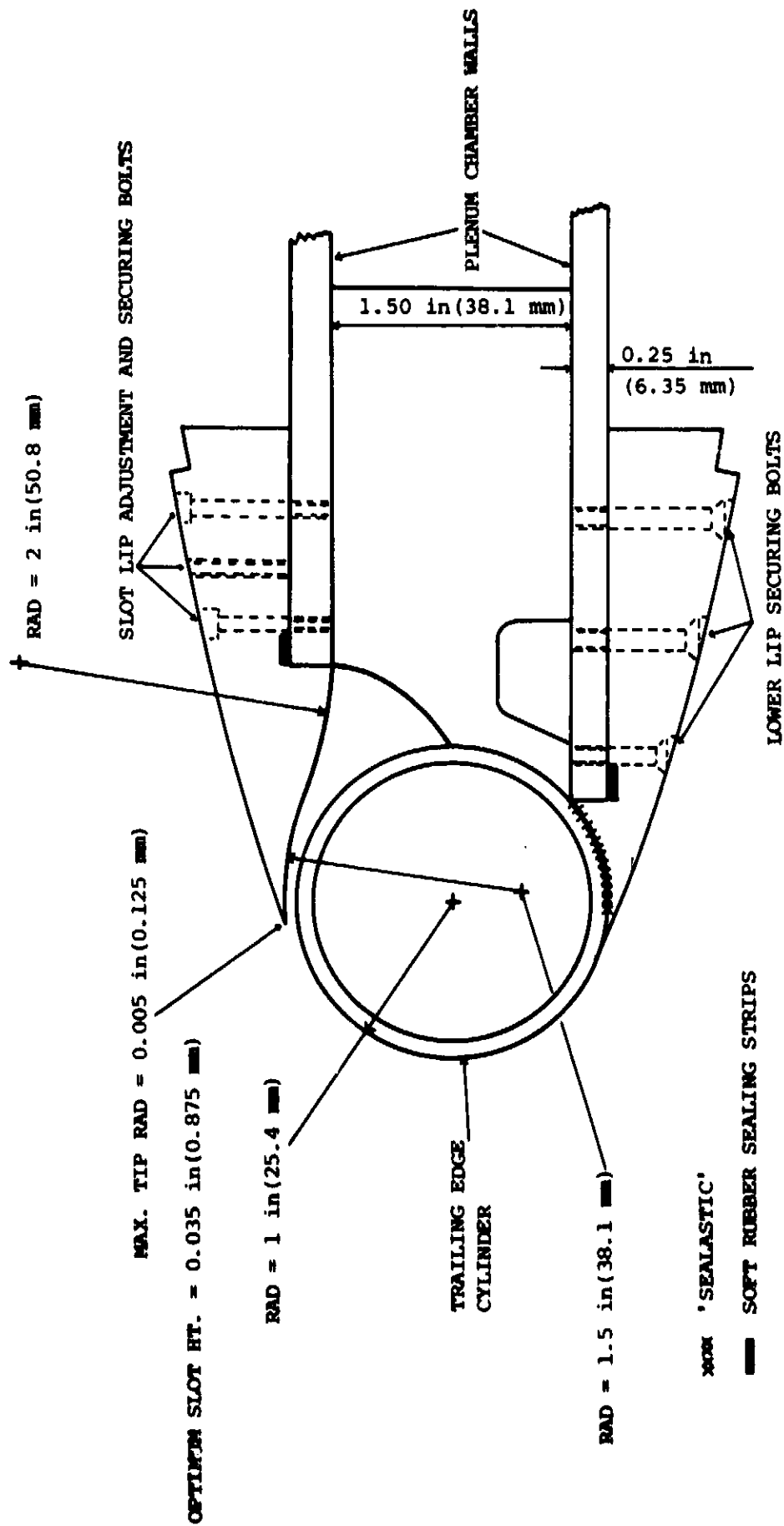


FIGURE 19: SLOT GEOMETRY AND SEALING

FIG 20

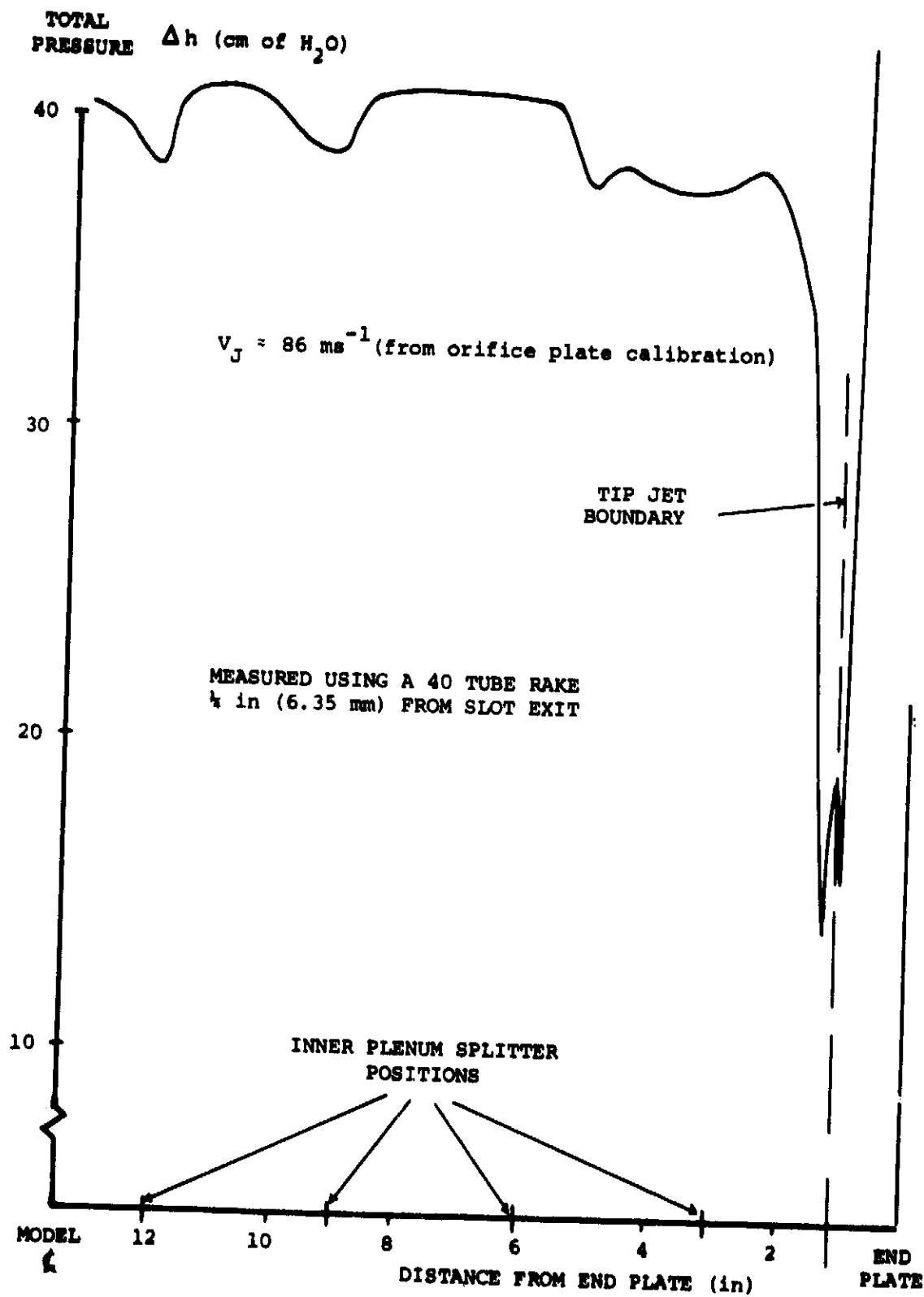


FIGURE 20: A CHECK ON THE TWO-DIMENSIONALITY OF THE SLOT FLOW INCLUDING THE EFFECT OF THE TIP JETS

FIG 21

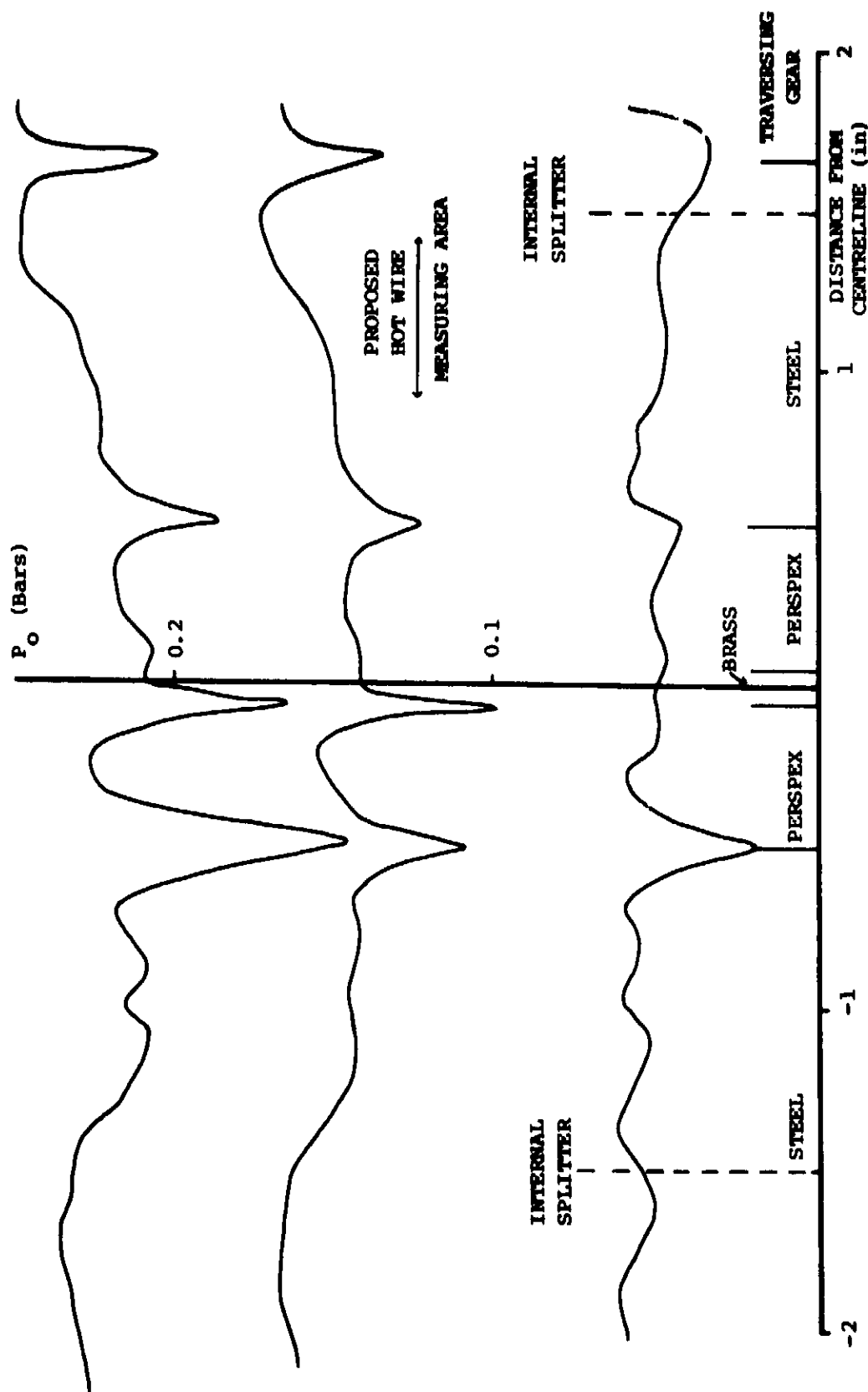


FIGURE 21: A CHECK ON THE TWO-DIMENSIONALITY OF THE SLOT FLOW
CLOSE TO THE MODEL CENTRELINE

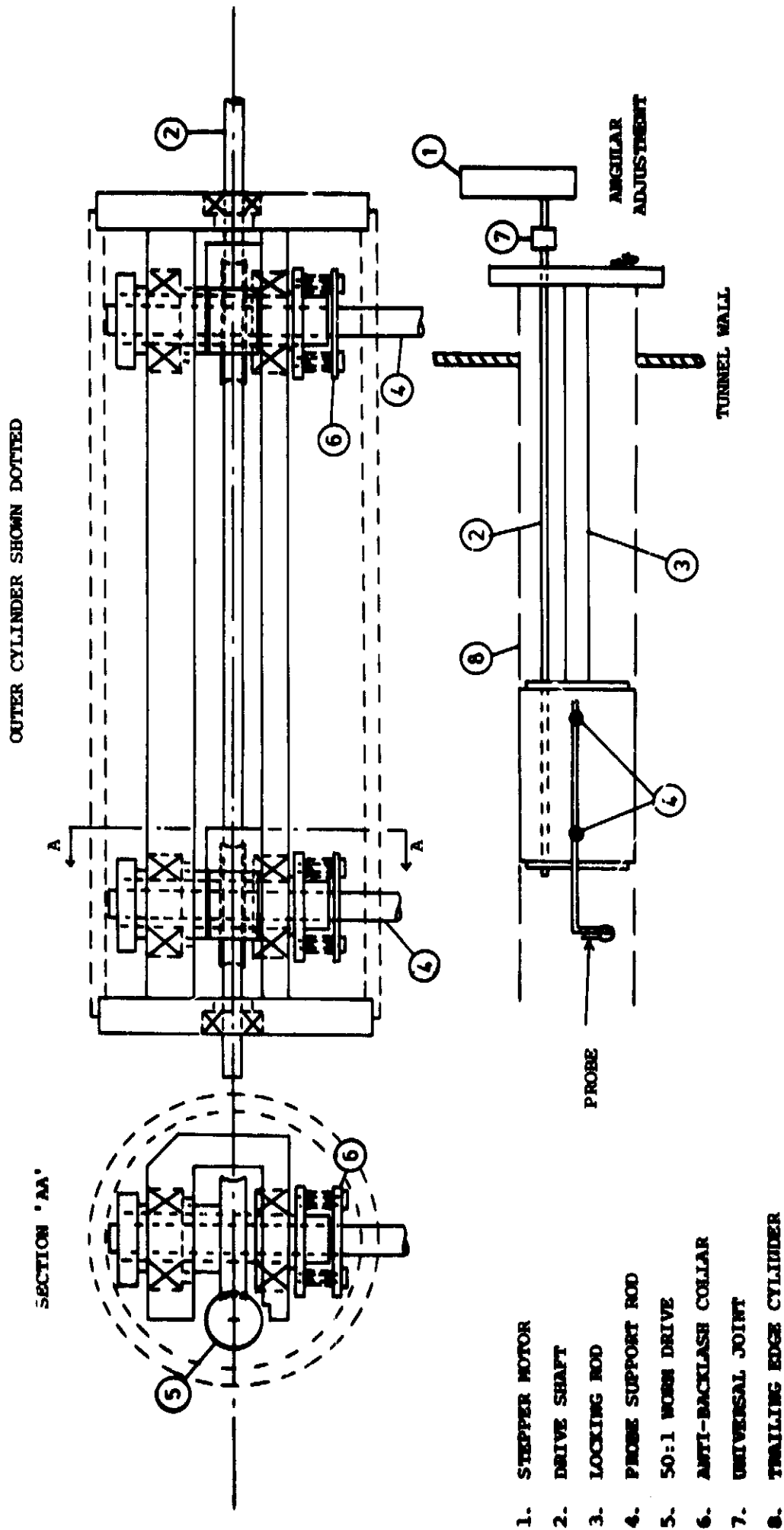


FIGURE 22: TRAVERSING GEAR ASSEMBLY

FIG 23

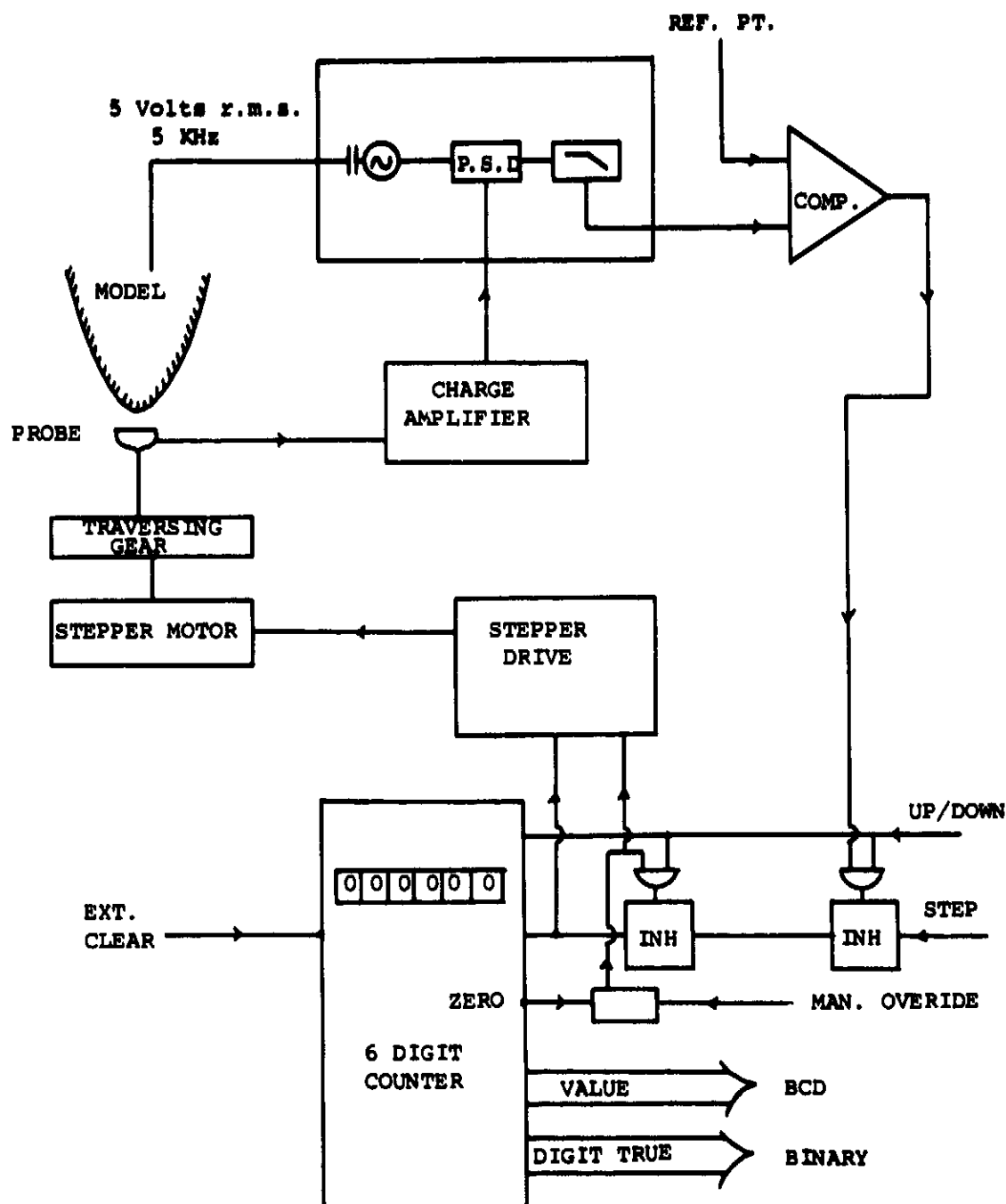


FIGURE 23: BLOCK DIAGRAM OF STEPPER CONTROL AND POSITION DETECTION SYSTEM

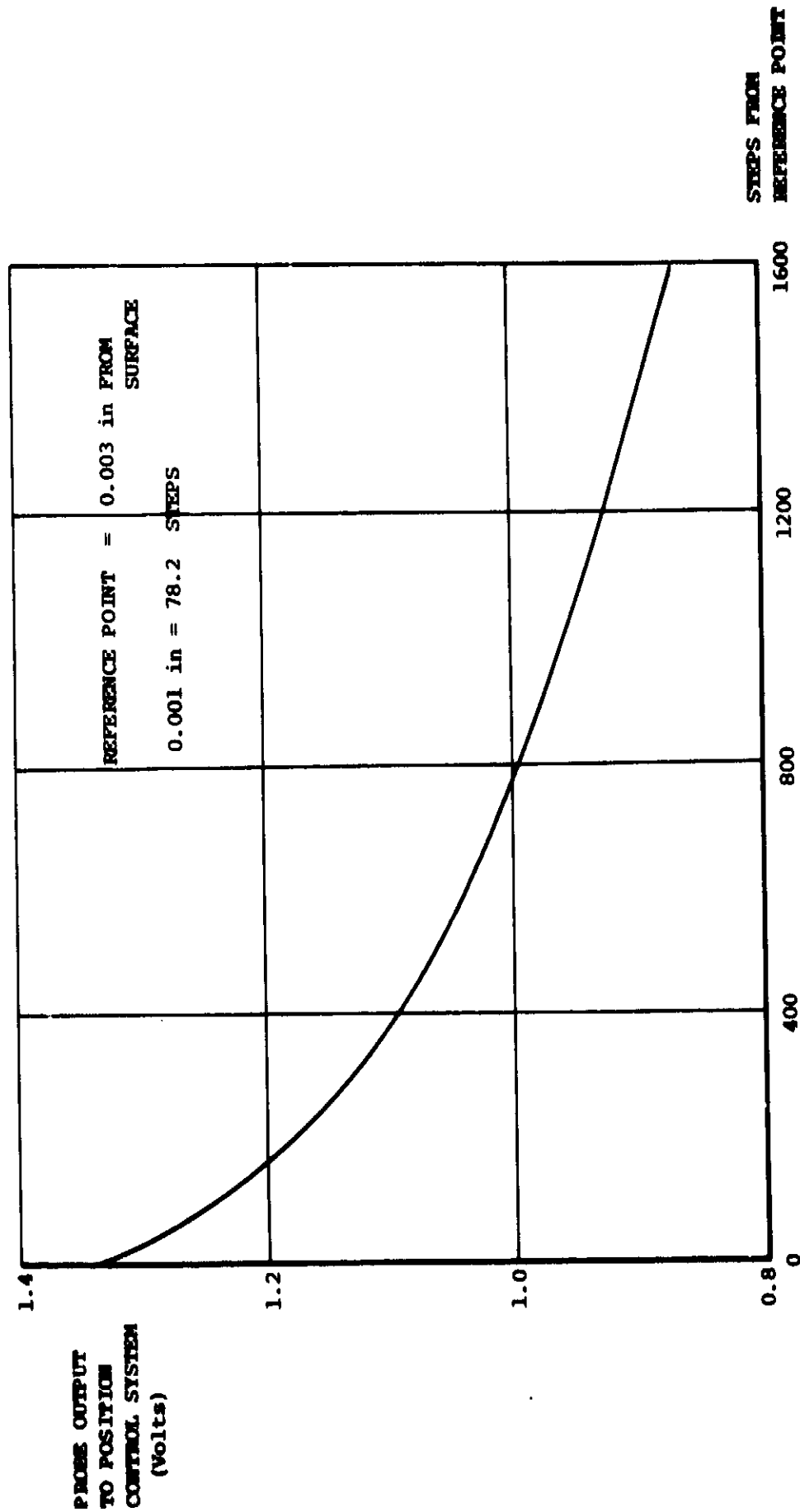
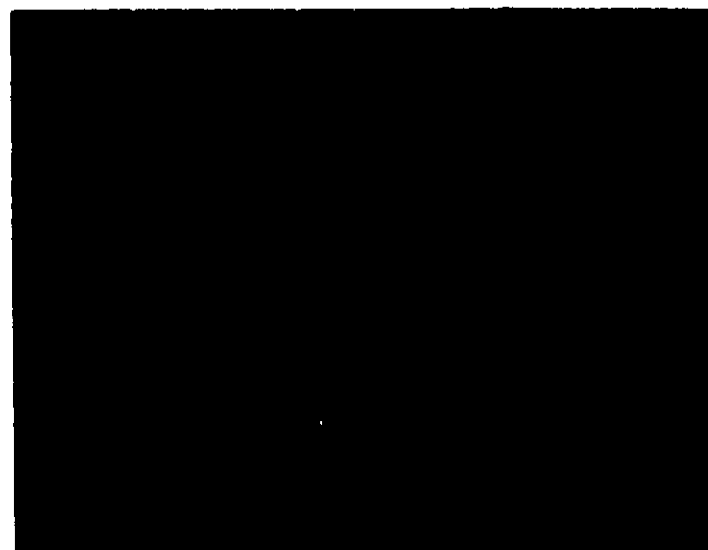


FIGURE 24: POSITION CONTROL SYSTEM: VARIATION OF PROBE OUTPUT WITH DISTANCE FROM THE SURFACE

VERTICAL SCALE = 0.1 V/DIV
 TIMEBASE = 750 STEPS/SWEEP

A. MOVING AWAY FROM SURFACE - NO FLOW



← SURFACE
 PROBE OUTPUT
 DROPS AS
 DISTANCE FROM
 SURFACE
 INCREASES
 ↓

ORIGINAL PAGE
 BLACK AND WHITE PHOTOGRAPH

B. MOVING AWAY FROM SURFACE - $U_{\infty} = 31 \text{ ms}^{-1}$

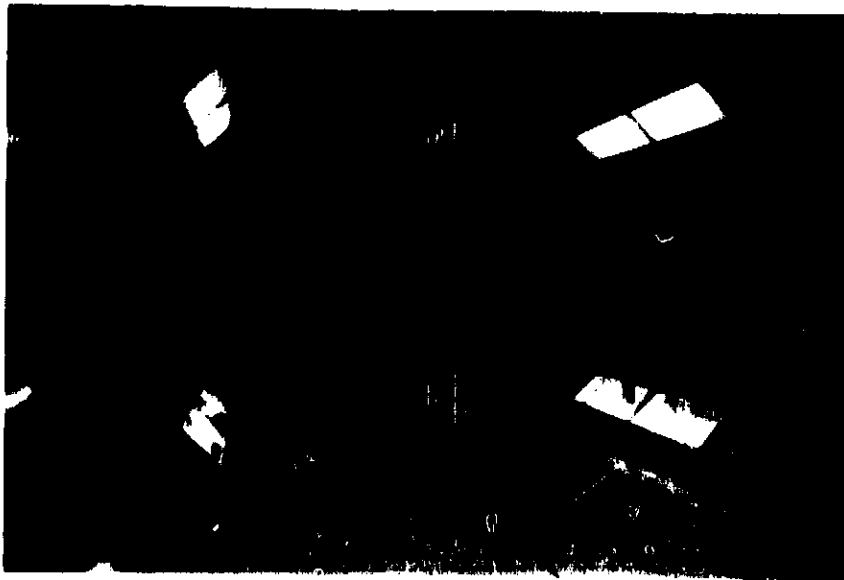


← SURFACE

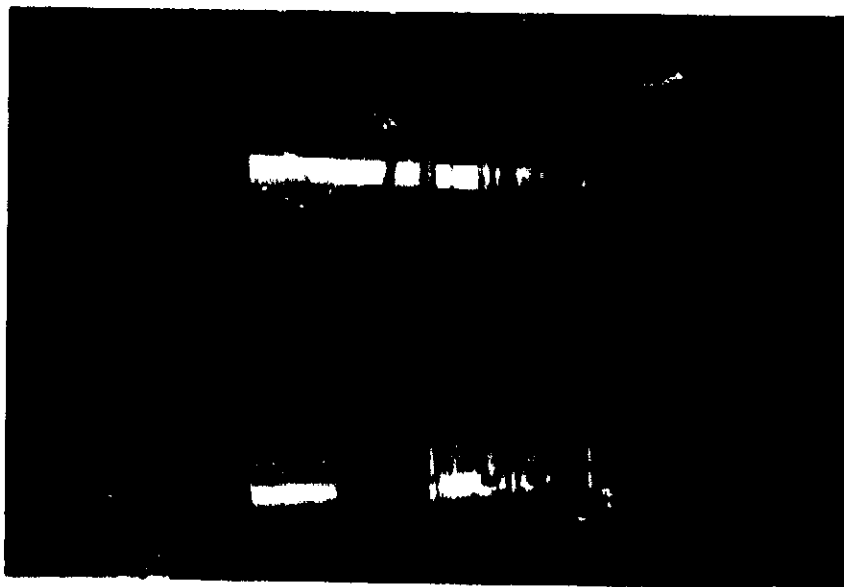
FIGURE 25: A CHECK ON THE VIBRATION OF A HOT WIRE PROBE
 DURING A RADIAL TRAVERSE FROM THE SURFACE

ORIGINAL PAGE
BLACK AND WHITE PHOTOGRAPH

FIG 26
(A) & (B)



(a) VIEW LOOKING DOWNSTREAM



(b) VIEW THROUGH WORKING SECTION WINDOW

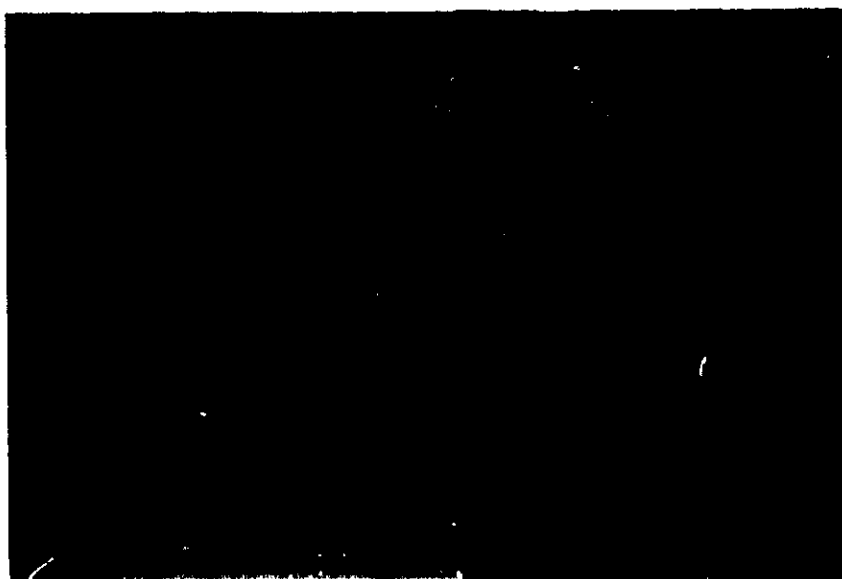
FIGURE 26 THE CIRCULATION CONTROLLED AEROFOIL LOCATED IN THE
7FT X 5FT WORKING SECTION

ORIGINAL PAGE
BLACK AND WHITE PHOTOGRAPH

FIG 26
(c) & (d)



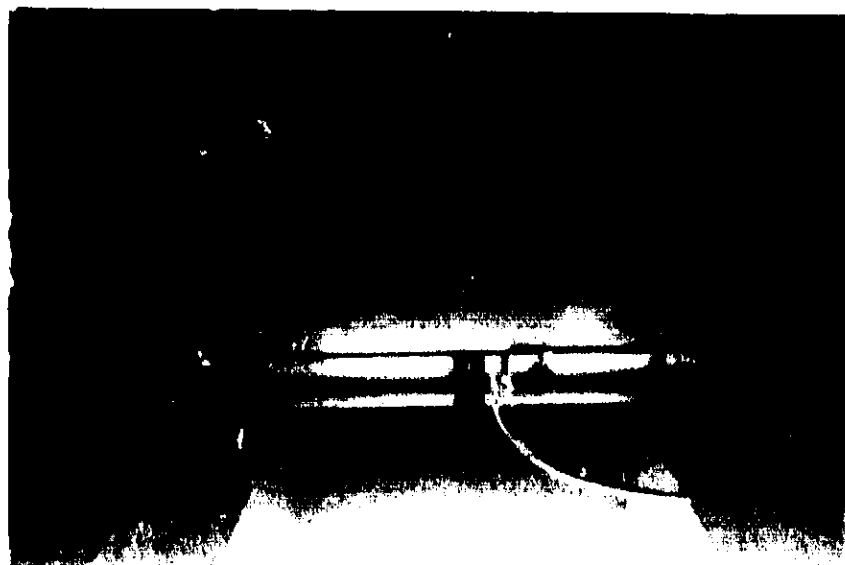
(c) GENERAL LAYOUT OF CONTROL CONSOLES



(d) DETAIL OF PROBES MOUNTED ON AEROFOIL TRAILING EDGE (see also Fig.26(e))

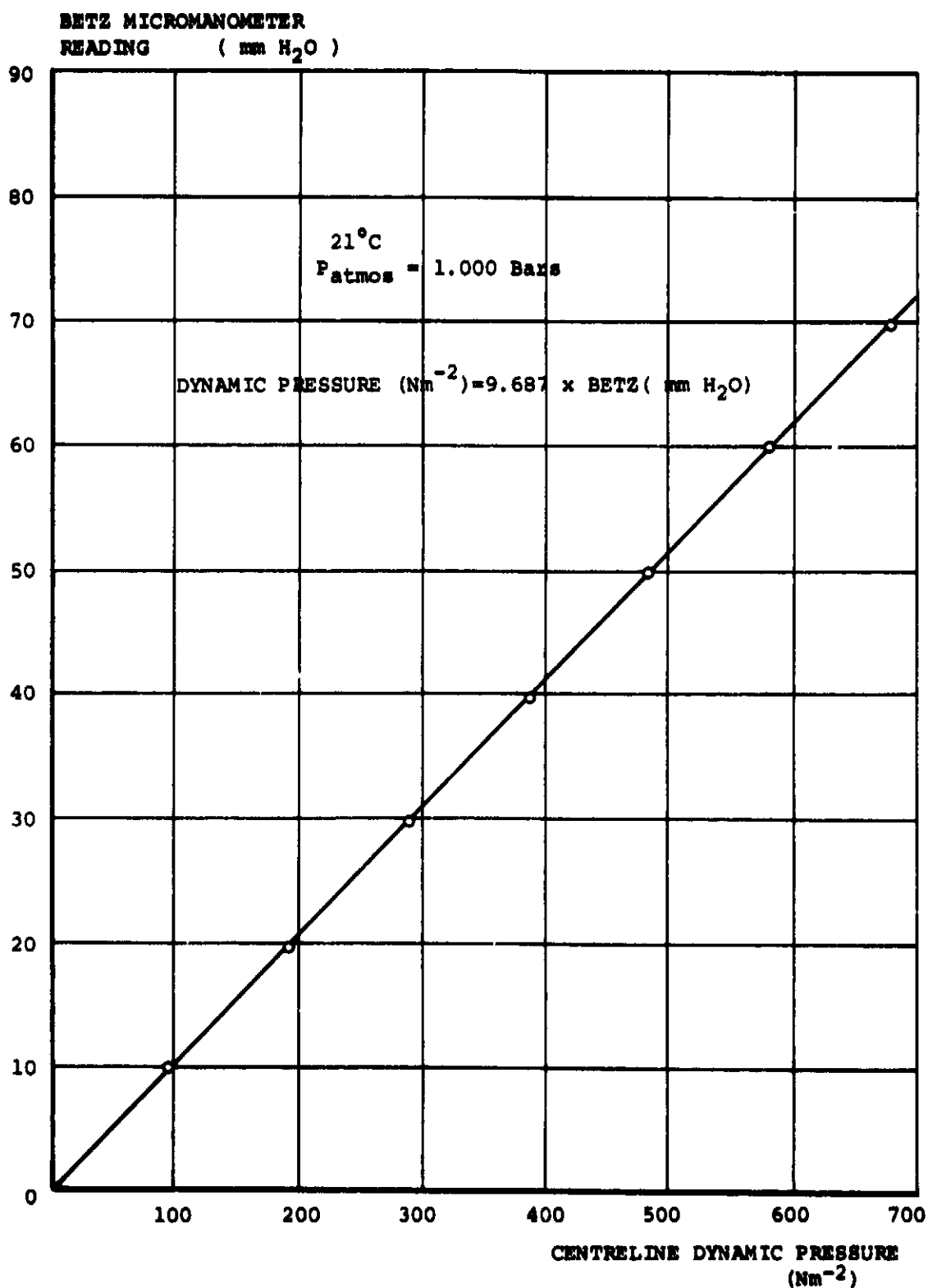
FIGURE 26 CONTINUED

ORIGINAL PAGE
BLACK AND WHITE PHOTOGRAPH

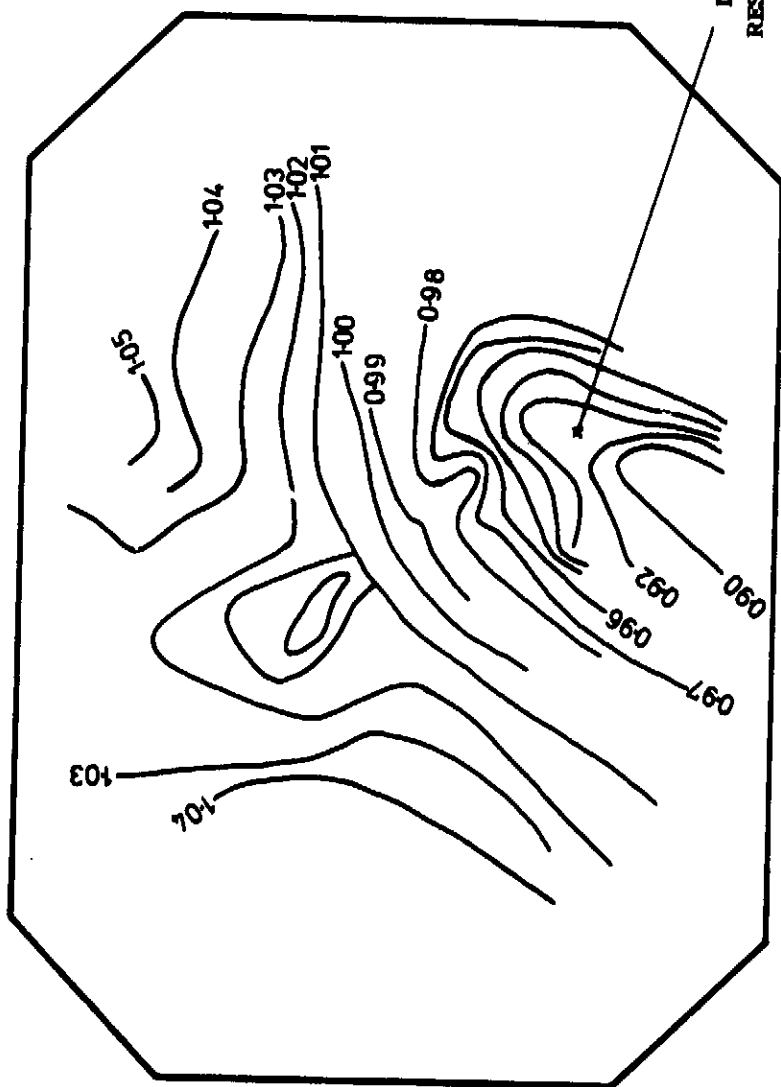


(e) VIEW LOOKING UPSTREAM AT AEROFOIL TRAILING EDGE, SHOWING BLOWING
SLOT AND TRAVERSING GEAR SUPPORTING THE PROBES

FIGURE 26 CONTINUED

FIGURE 27: TUNNEL REFERENCE PRESSURE DIFFERENCE CALIBRATION

HIGH SPEED WORKING SECTION : LOOKING UPSTREAM



$$q / q_{CL}$$

$$q_{CL} = 591 \text{ mm}^{-2}$$

DISTURBANCE AS A
RESULT OF A DIRTY GAUZE

FIGURE 28: CONTOURS OF q/q_{CL} IN WORKING SECTION BEFORE CLEANING GAUZE

FIG 28

HIGH SPEED WORKING SECTION : LOOKING UPSTREAM:



$$\begin{aligned} q/q_{CL} &= 587 \text{ mm}^{-2} \\ v_{CL} &= 30.96 \text{ ms}^{-1} \end{aligned}$$

FIGURE 29: CONTOURS OF Q/Q_{CL} IN WORKING SECTION AFTER CLEANING GAUZE

FIG 30

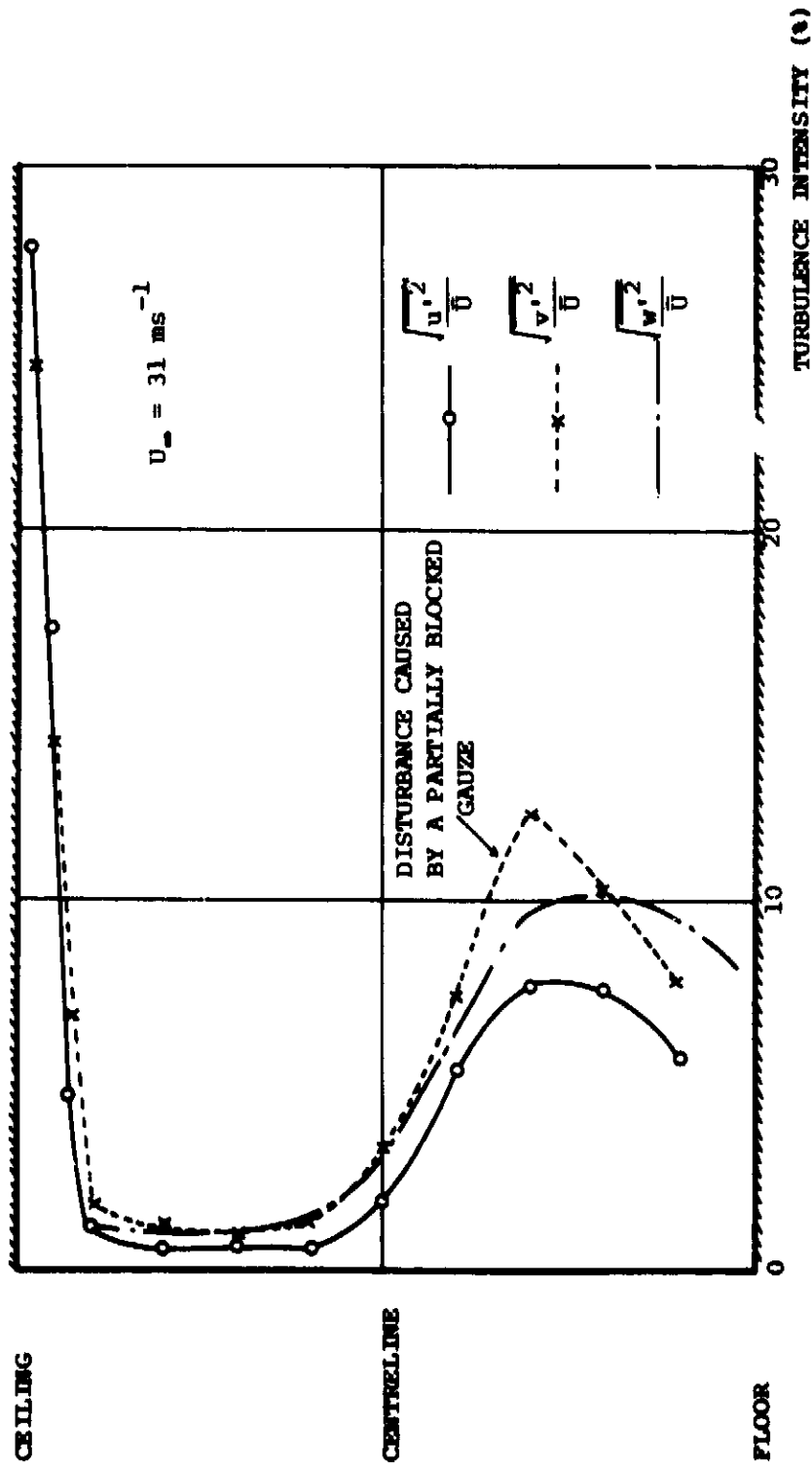


FIGURE 30: TURBULENCE INTENSITIES IN HIGH SPEED WORKING SECTION BEFORE CLEANING GAUZE

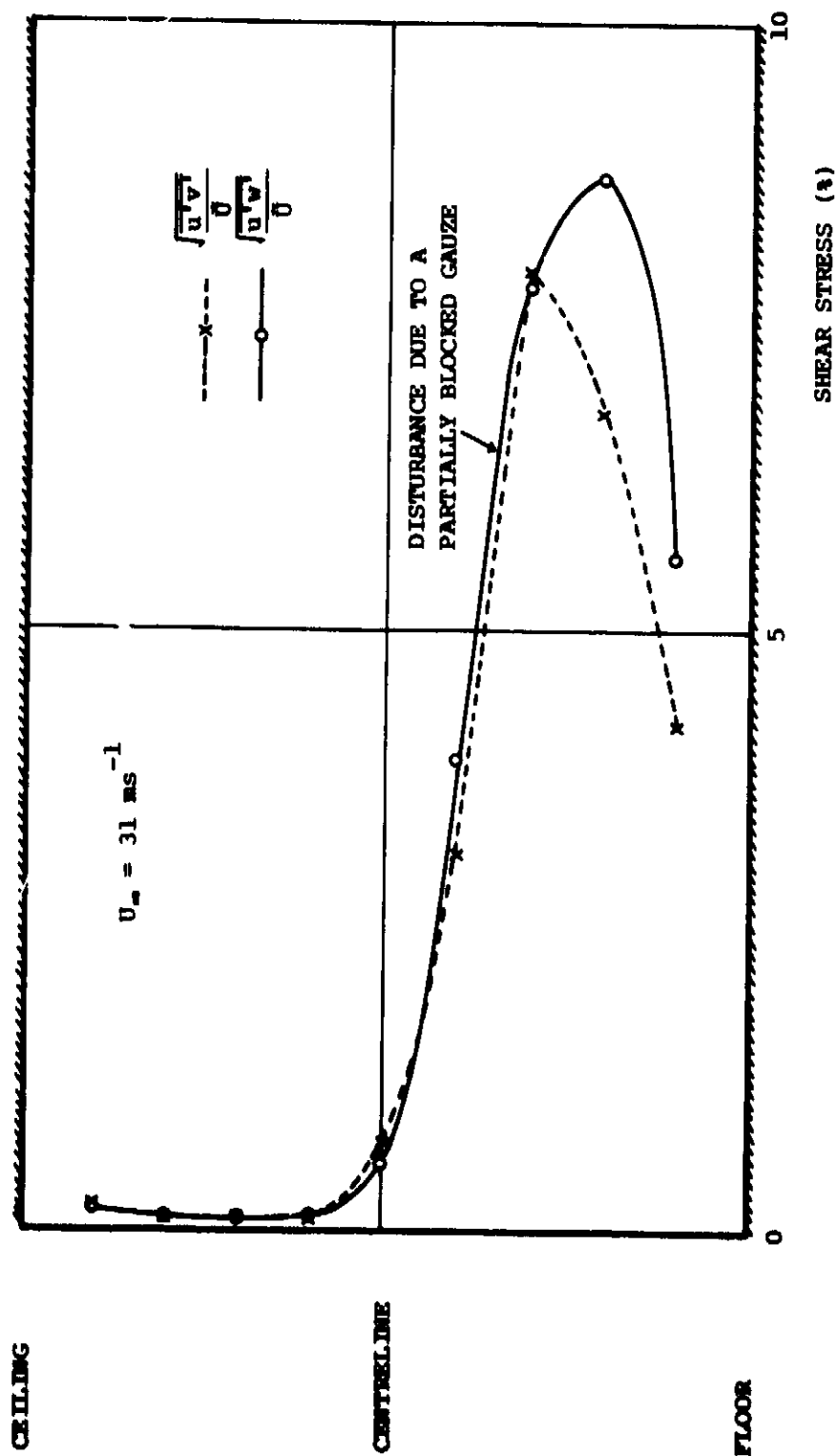


FIGURE 31: REYNOLDS SHEAR STRESSES IN THE HIGH SPEED WORKING SECTION BEFORE CLEANING GAUZE

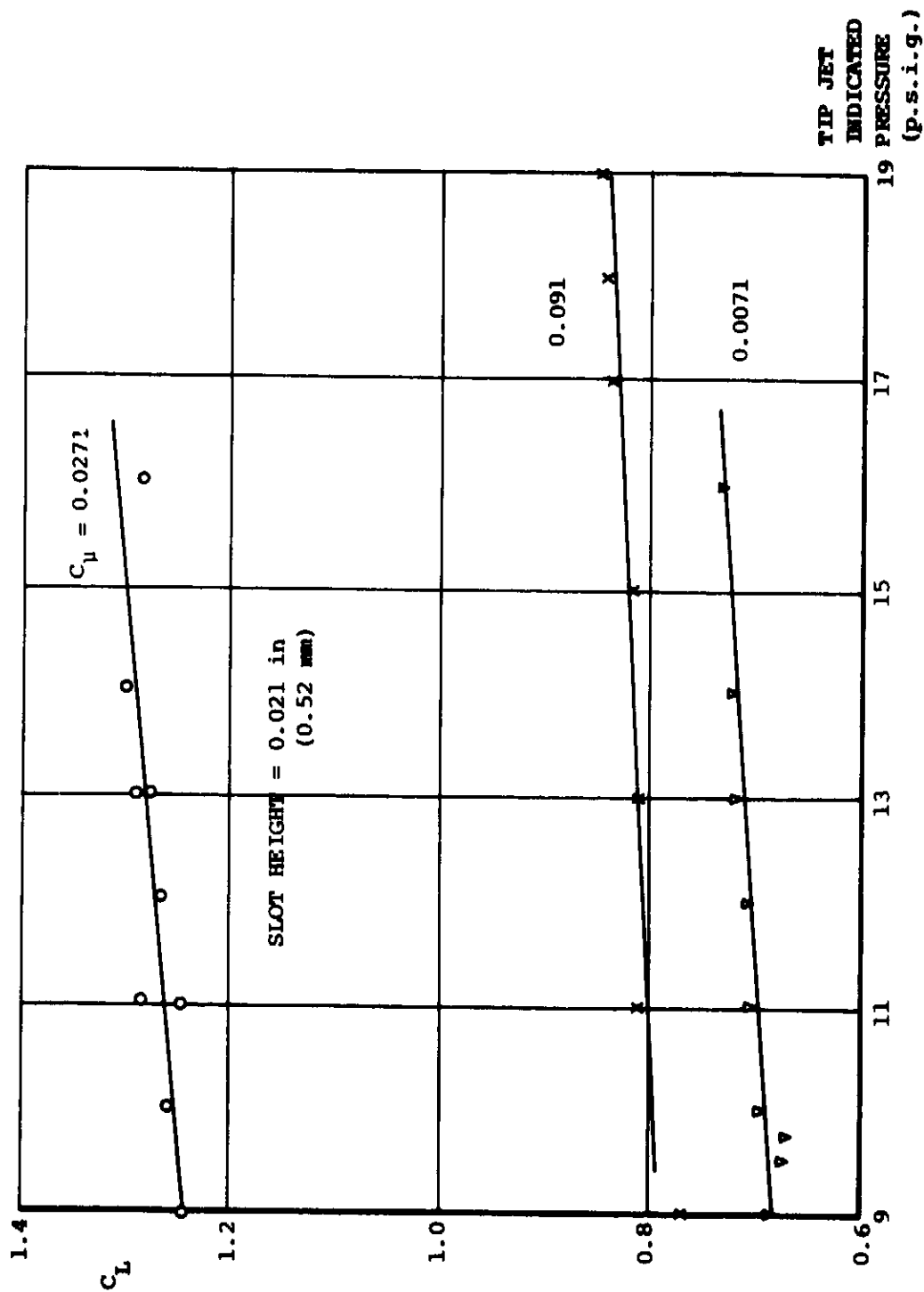


FIGURE 32: EFFECT OF TIP JETS UPON OVERALL LIFT COEFFICIENT

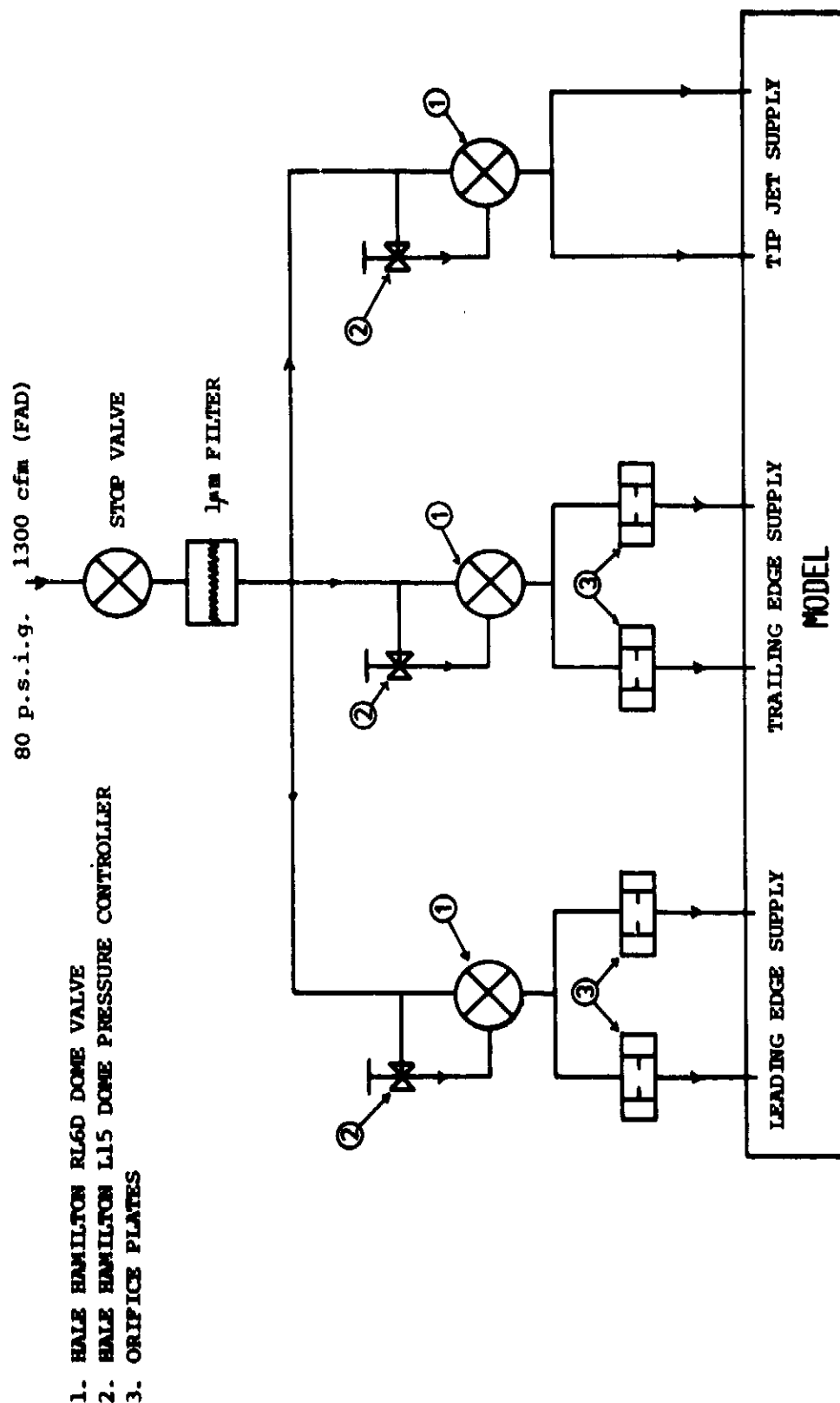


FIGURE 33A: SCHEMATIC DIAGRAM OF BLOWING SUPPLY

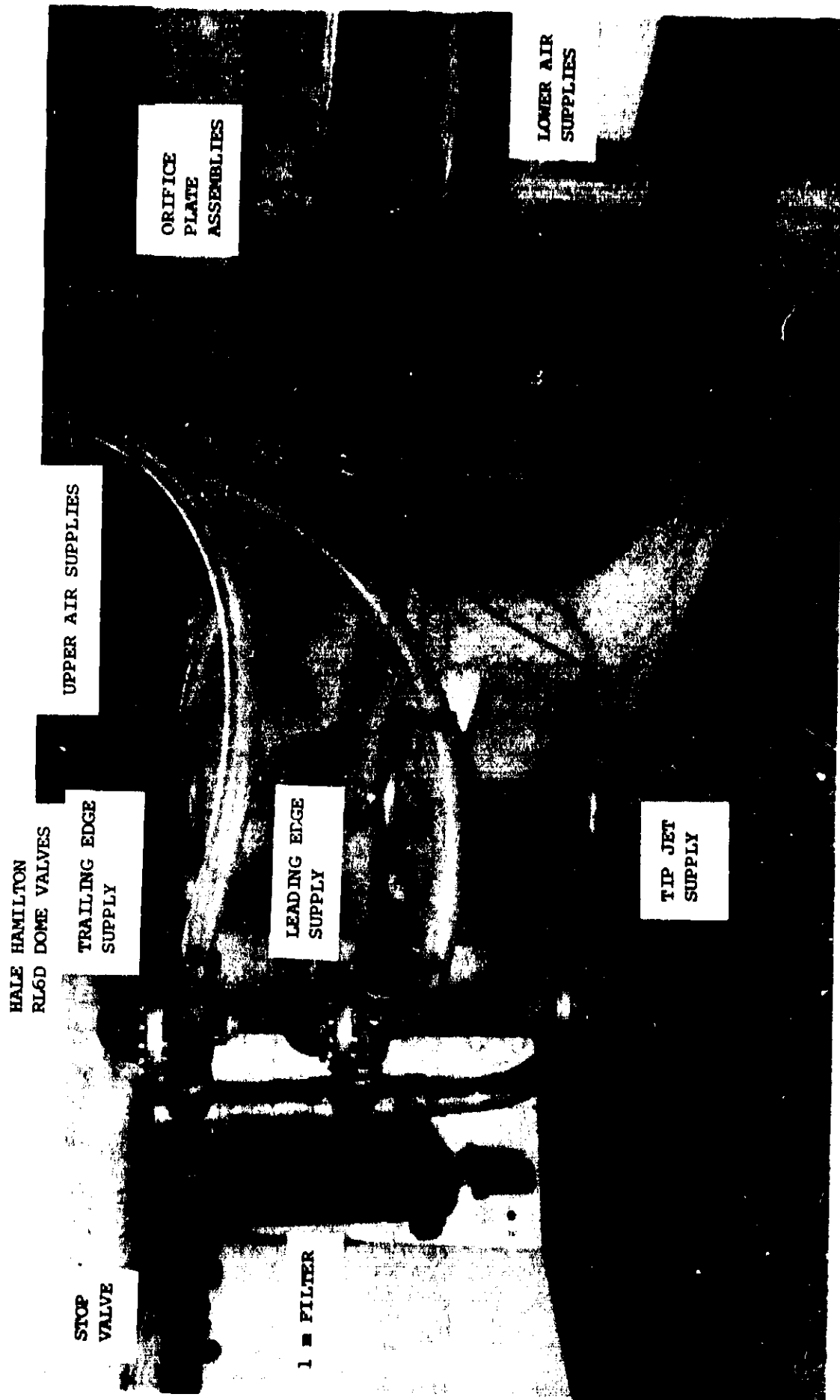


FIGURE 33B: BLOWING SUPPLY SYSTEM INSTALLED UNDER 7FT X 5FT WORKING SECTION

FIG 34

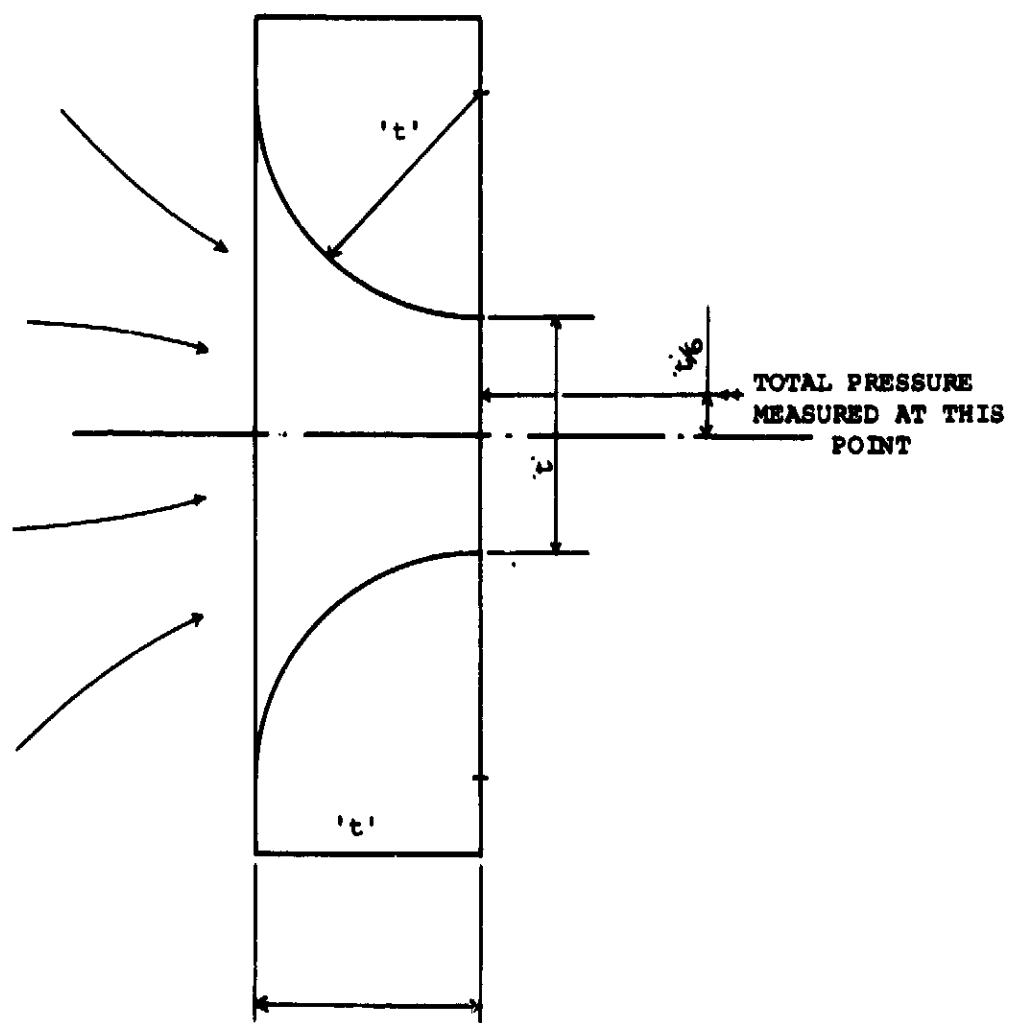
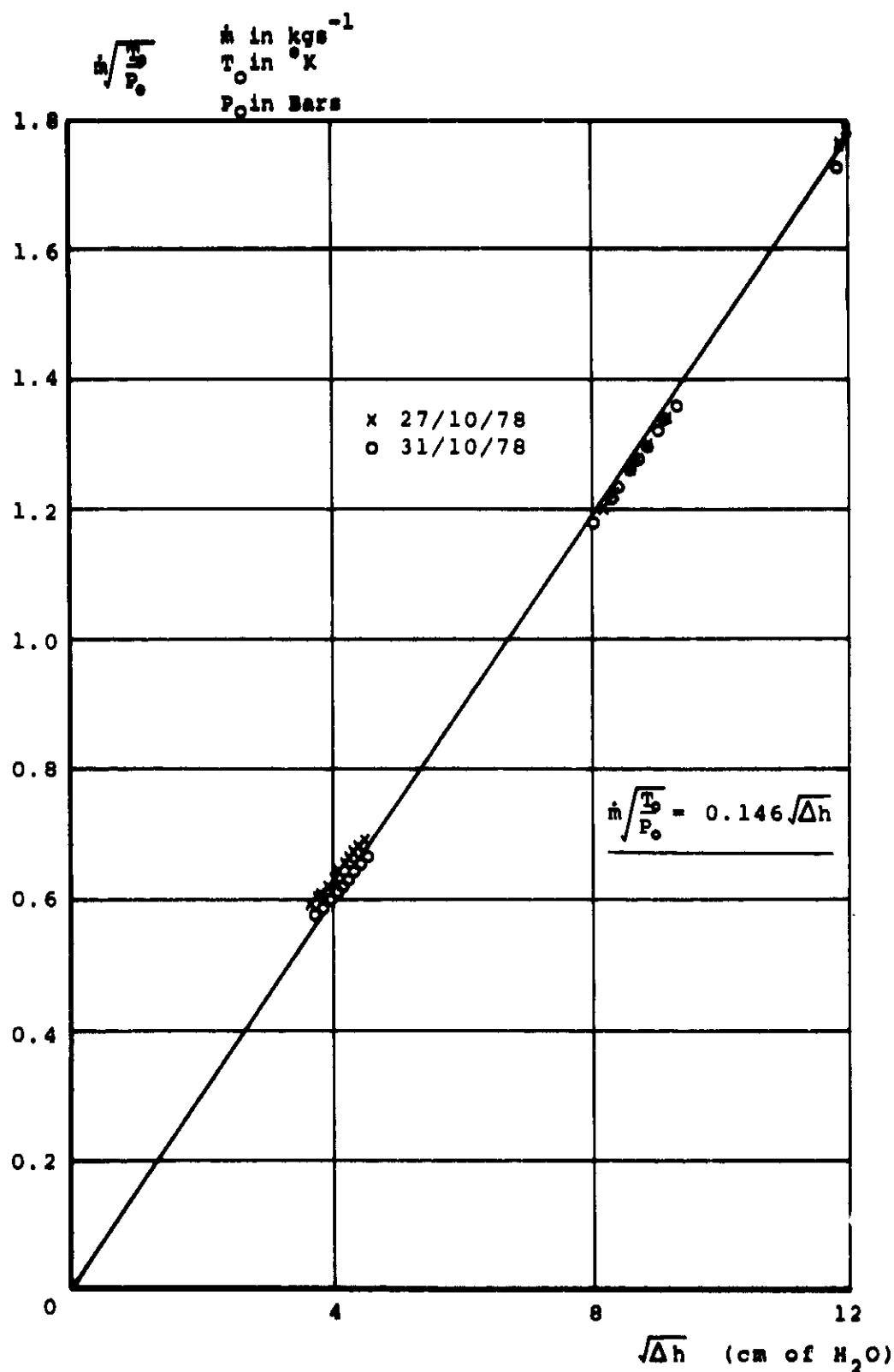


FIGURE 34: ORIFICE PLATE CALIBRATION NOZZLE GEOMETRY

FIG 35

FIGURE 35: ORIFICE PLATE CALIBRATION

ORIGINAL PAGE
BLACK AND WHITE PHOTOGRAPH

FIG 36

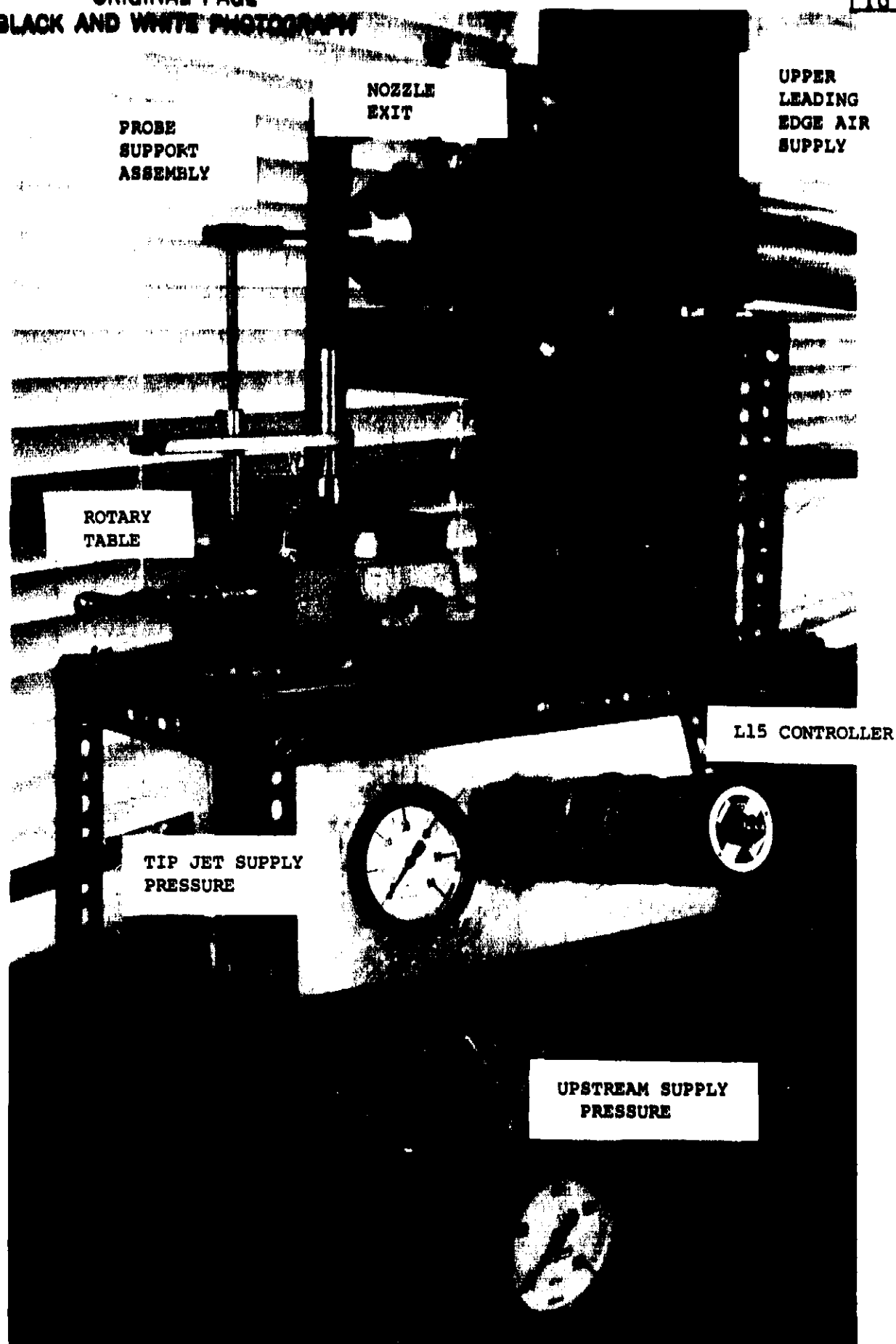


FIGURE 36: CALIBRATION NOZZLE RIG

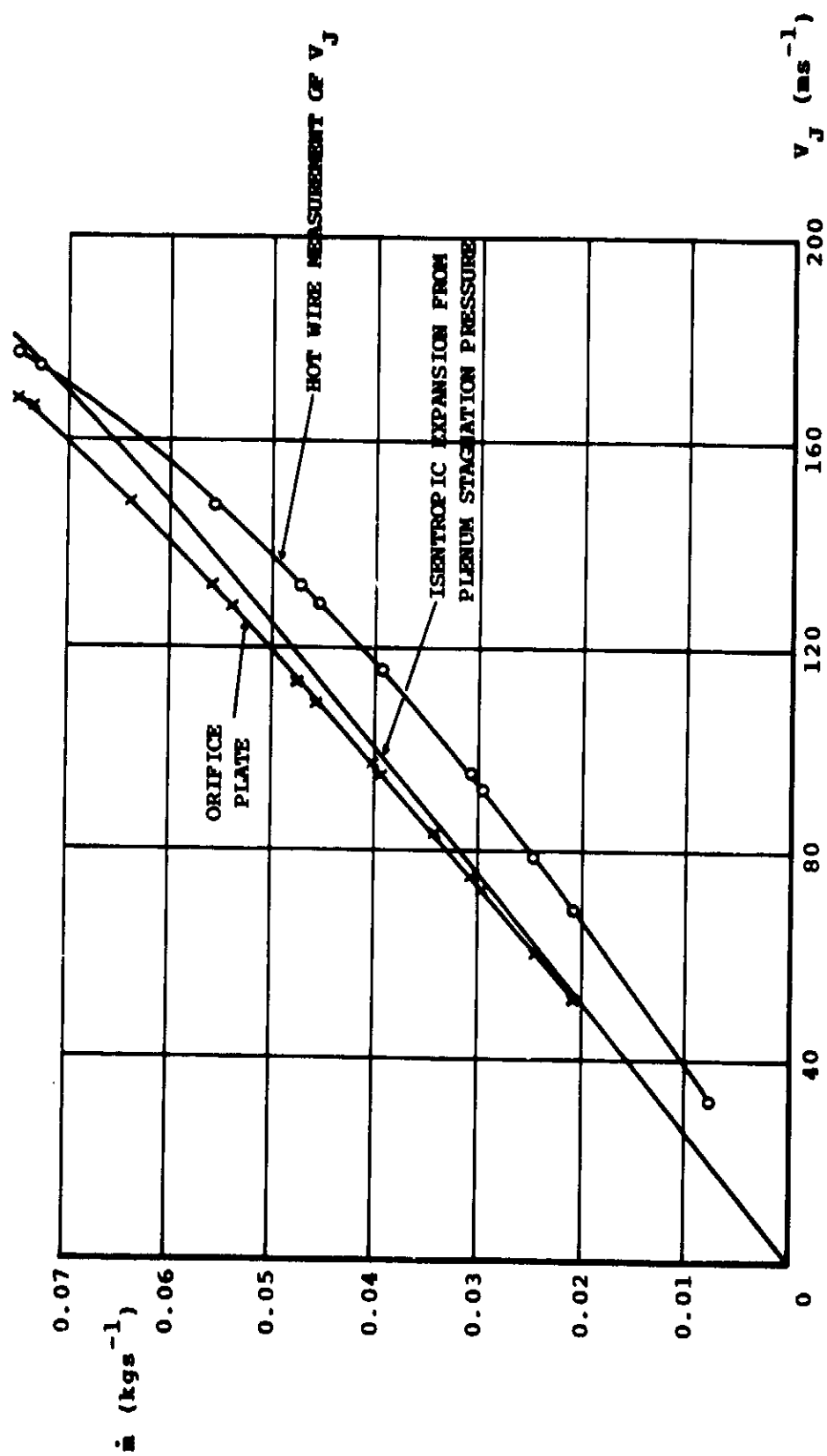


FIGURE 37: ESTIMATION OF JET VELOCITY BY THREE METHODS

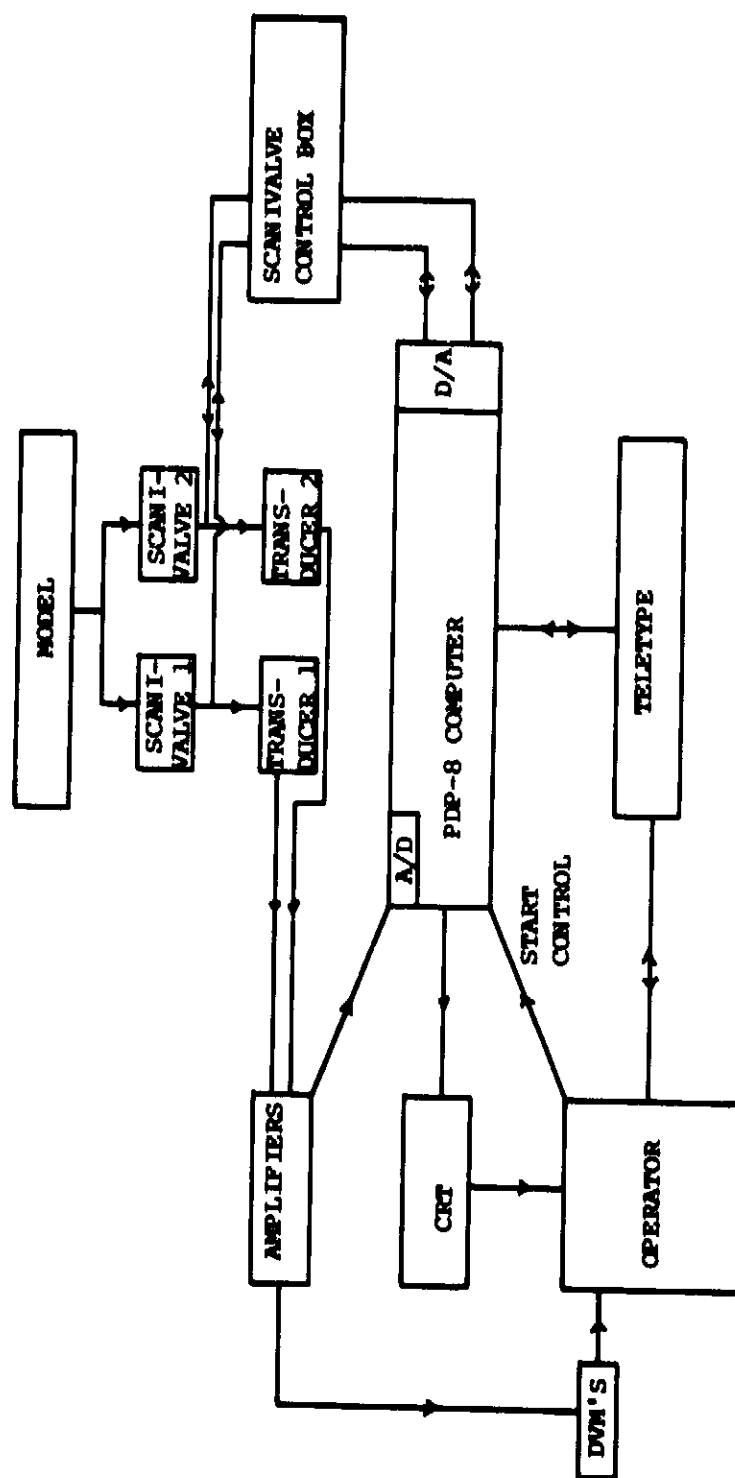


FIGURE 38: BLOCK DIAGRAM OF AEROFOIL PRESSURE MEASURING SYSTEM

FIG 39

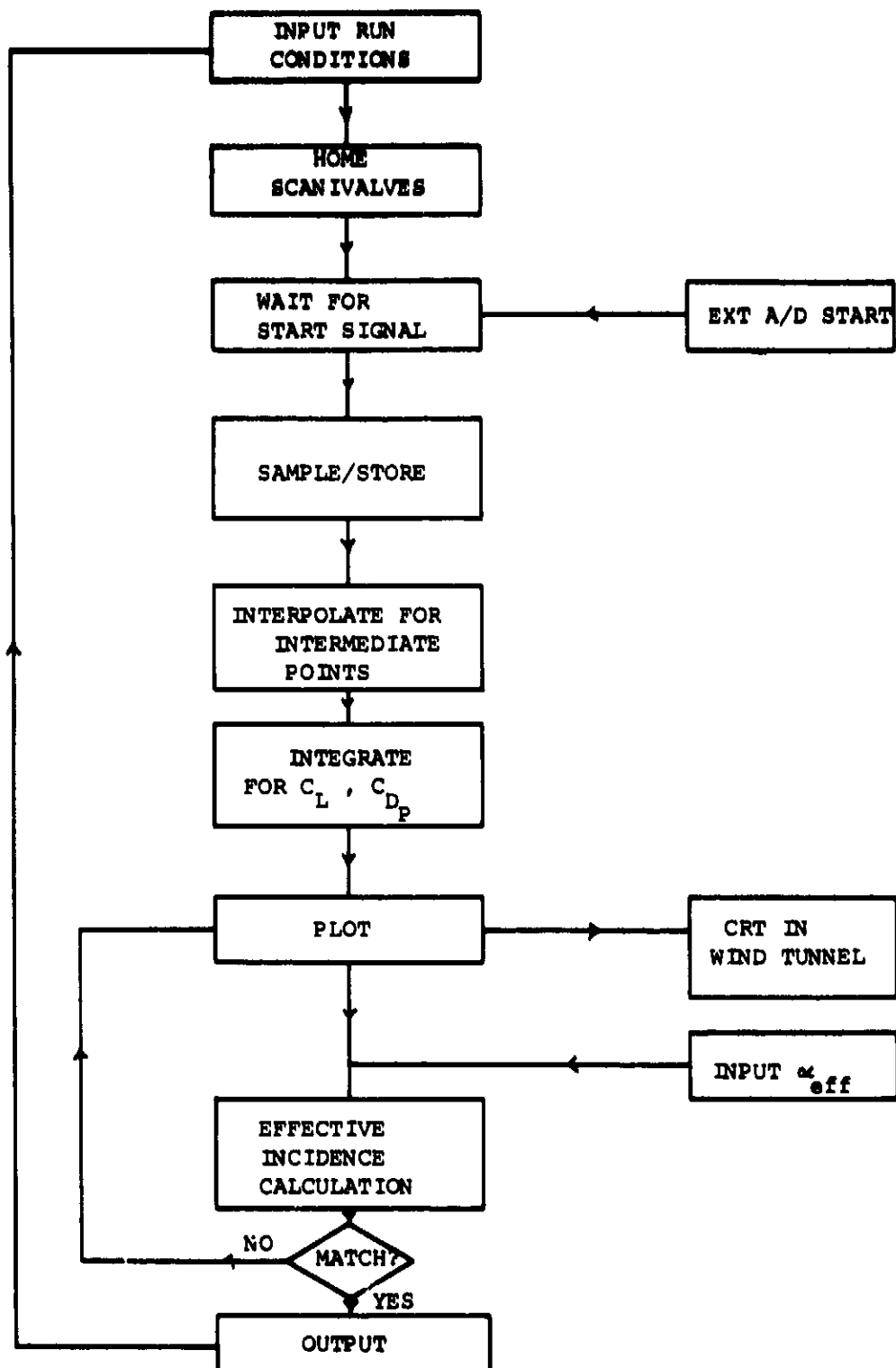
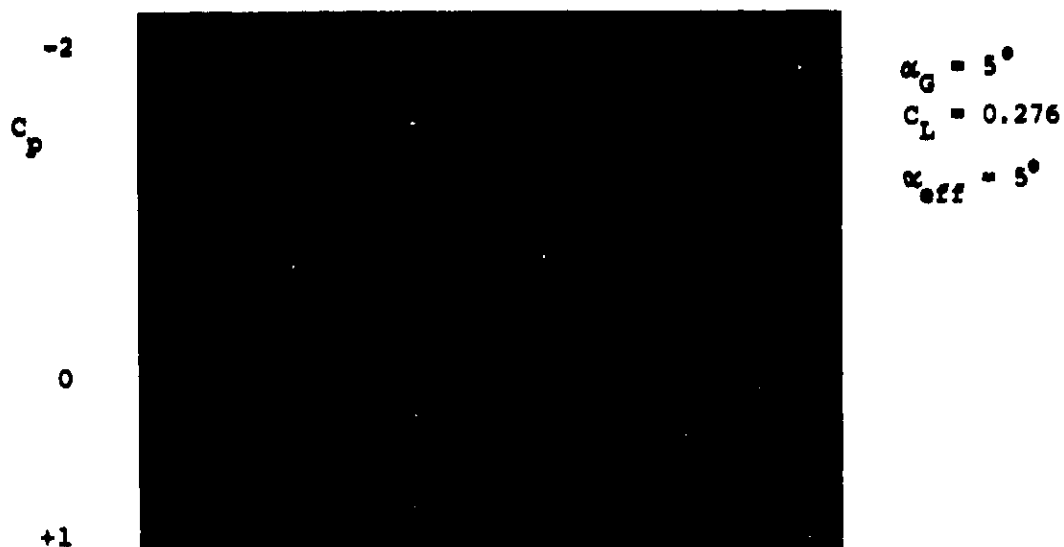


FIGURE 39: BLOCK DIAGRAM OF SCANIVALVE CONTROL PROGRAM

FIG 40

ORIGINAL PAGE
BLACK AND WHITE PHOTOGRAPH



SOLID LINES INDICATE EXPERIMENTAL RESULTS
CROSSES ARE DERIVED FROM SIMPLE THEORY



FIGURE 40: EXAMPLES OF THE EFFECTIVE INCIDENCE ESTIMATION
TECHNIQUE FOR THE UNBLOWN AEROFOIL

FIG 41

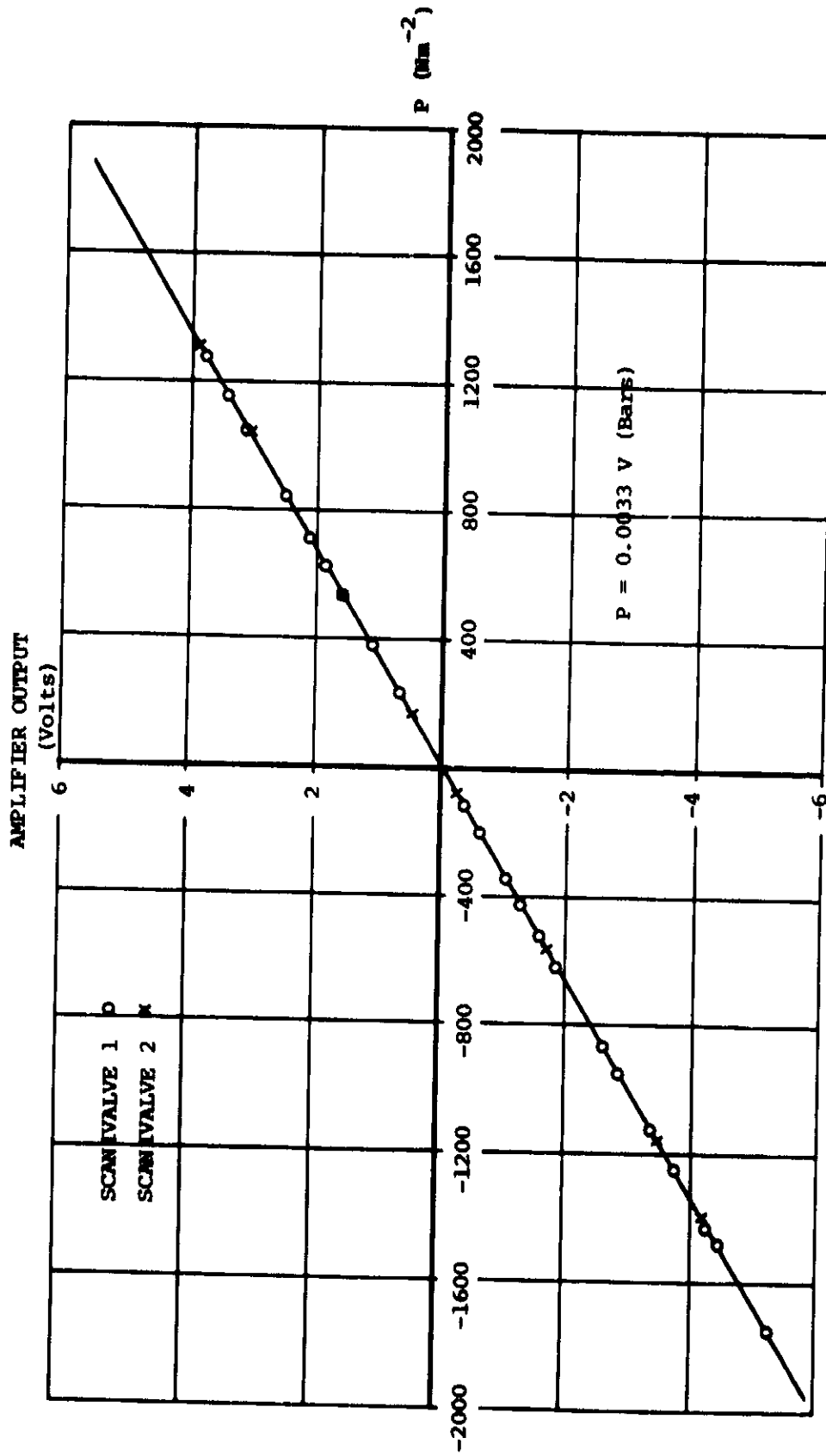


FIGURE 41: SCANIVALVE TRANSDUCER CALIBRATION

FIG 42

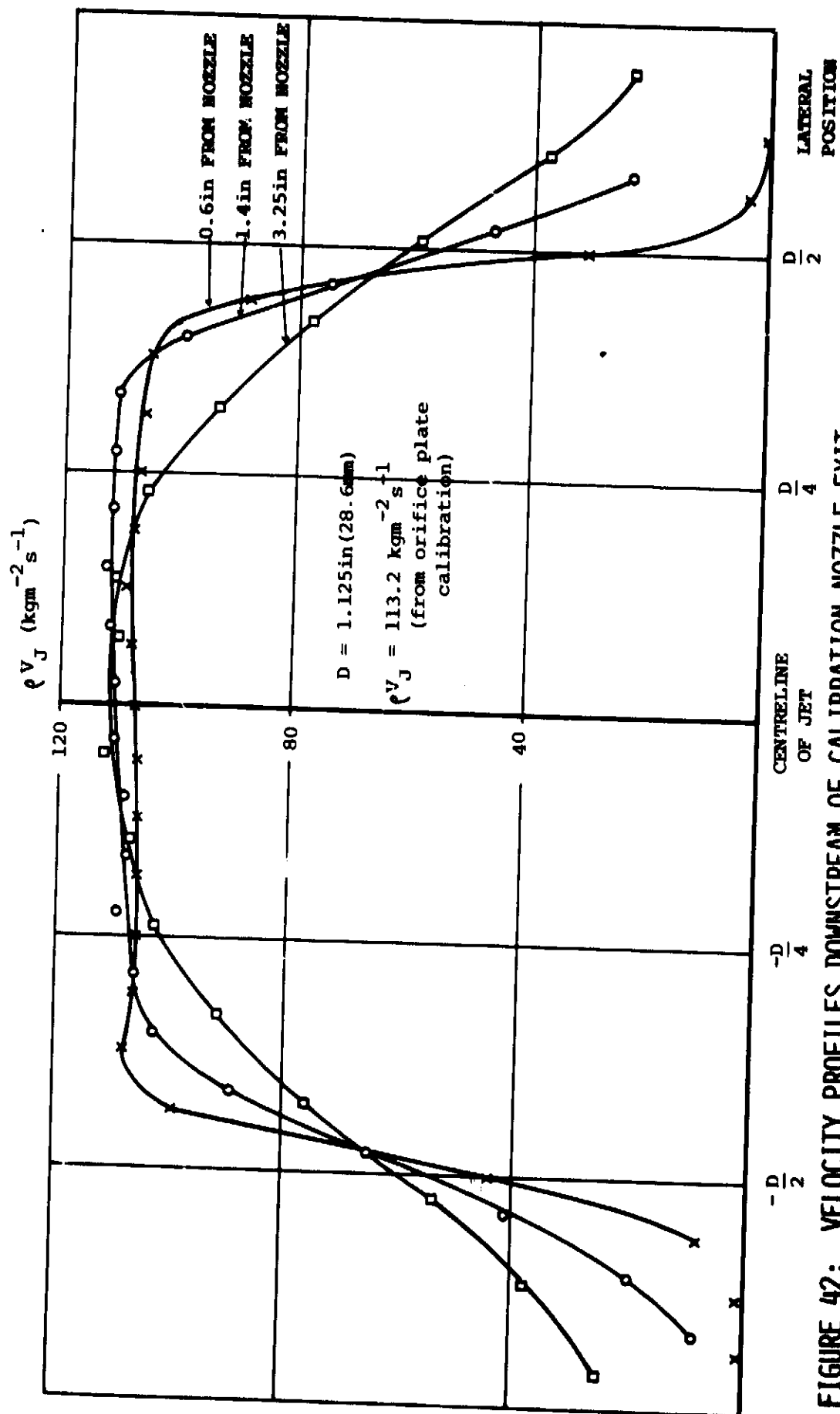


FIGURE 42: VELOCITY PROFILES DOWNSTREAM OF CALIBRATION NOZZLE EXIT
AS MEASURED BY A DUAL SENSOR HOT WIRE PROBE

FIG 43

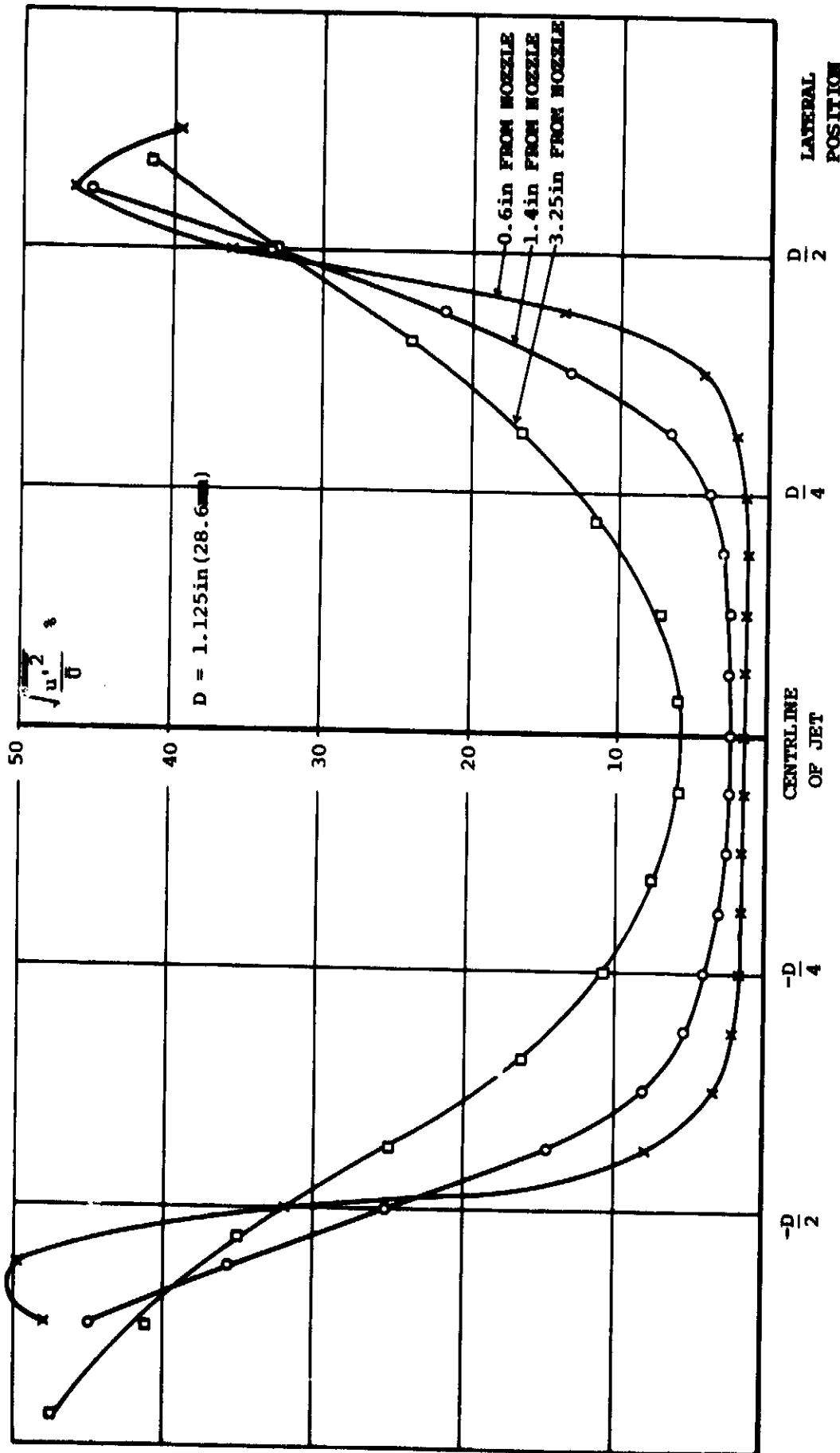


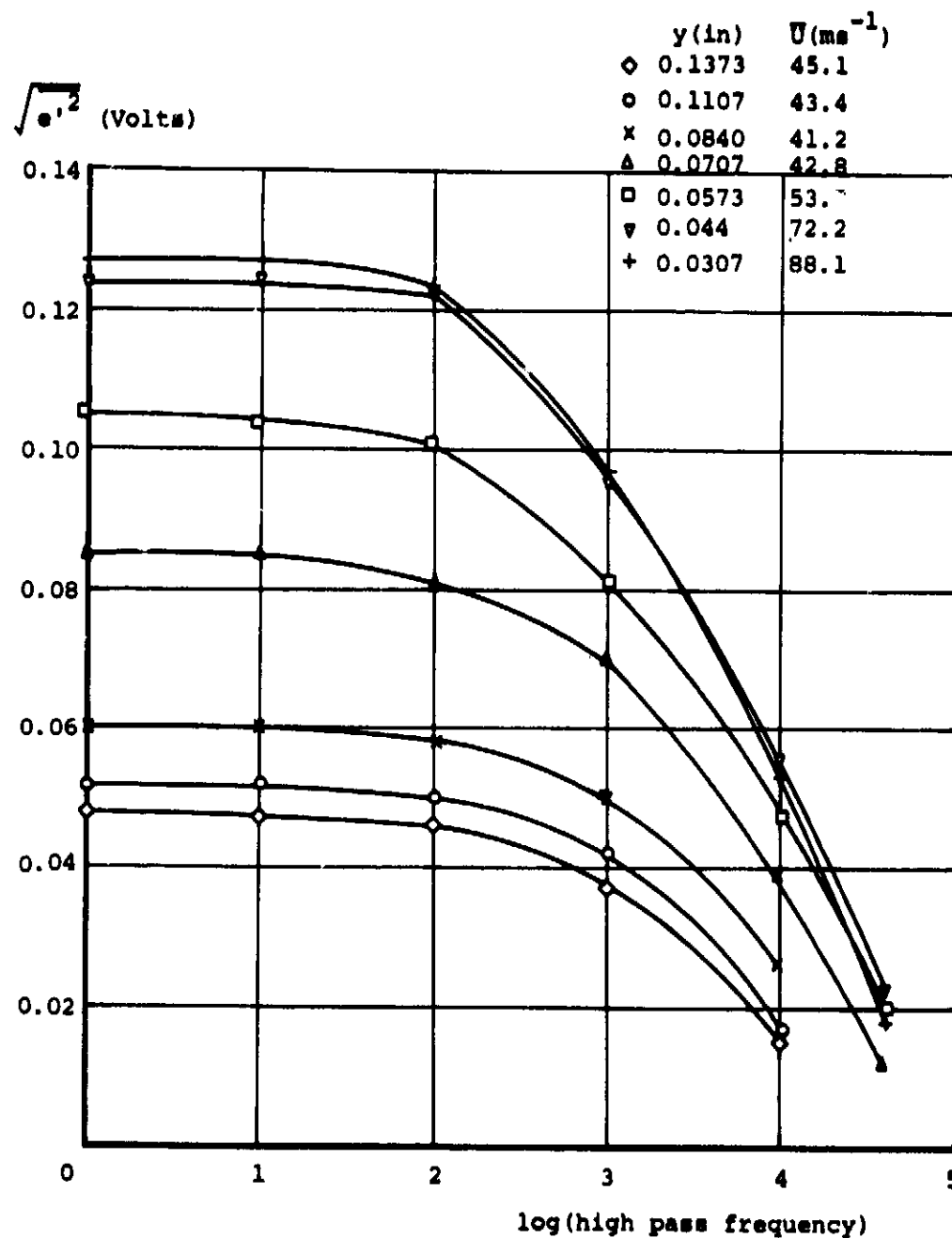
FIGURE 43: LONGITUDINAL TURBULENCE INTENSITY DOWNSTREAM OF CALIBRATION NOZZLE EXIT FROM A DUAL SENSOR HOT WIRE PROBE

FIG 44

15° FROM SLOT
 $C_p = 0.0158$

SLOT HT. = 0.040in
 $\alpha_G = 0^\circ$

LIP = 0.010in

FIGURE 44: FREQUENCY RESPONSE OF HOT WIRE SIGNALS

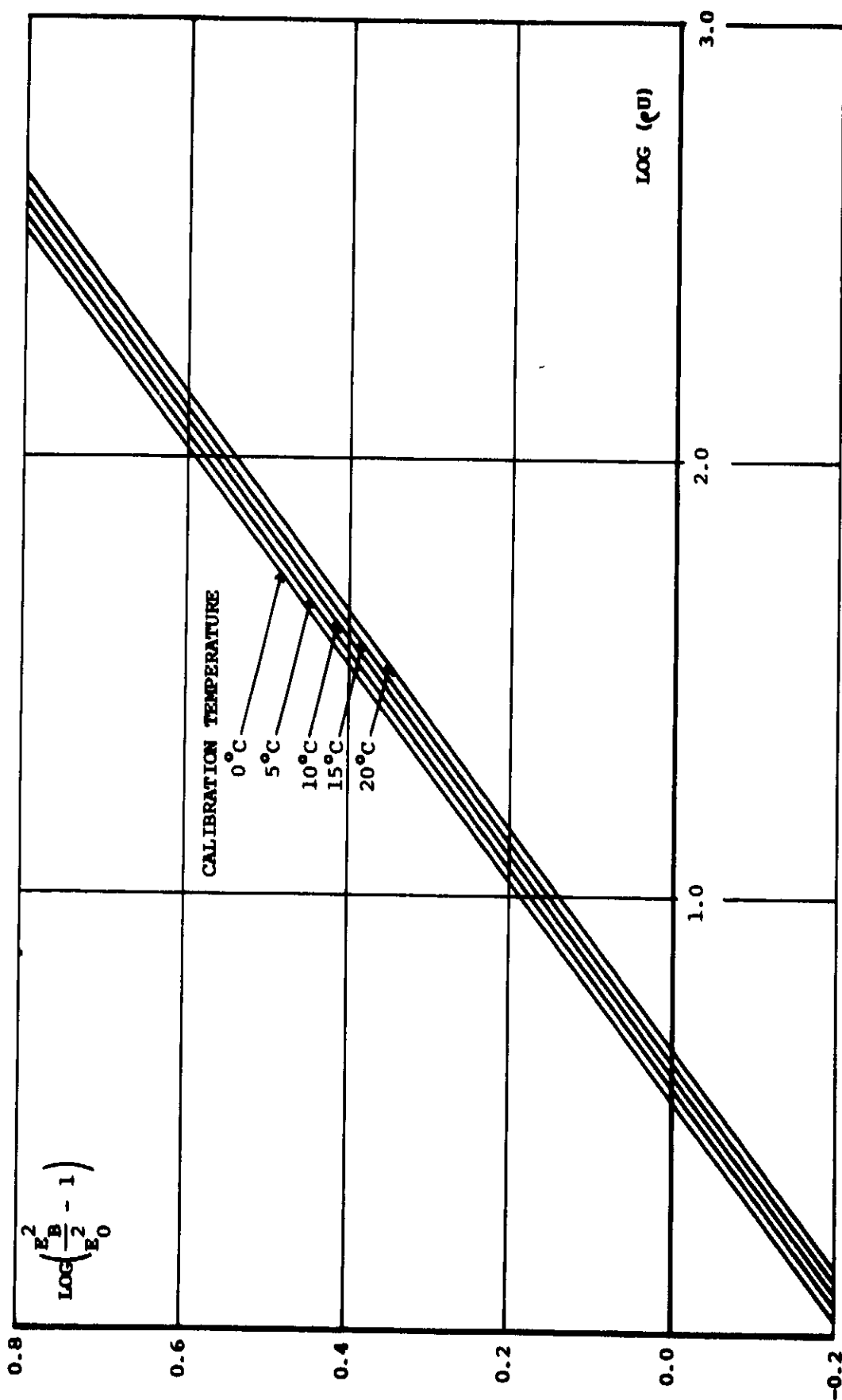


FIGURE 45: EFFECT OF TEMPERATURE UPON THE CALIBRATION OF A SINGLE HOT WIRE PROBE

FIG 46

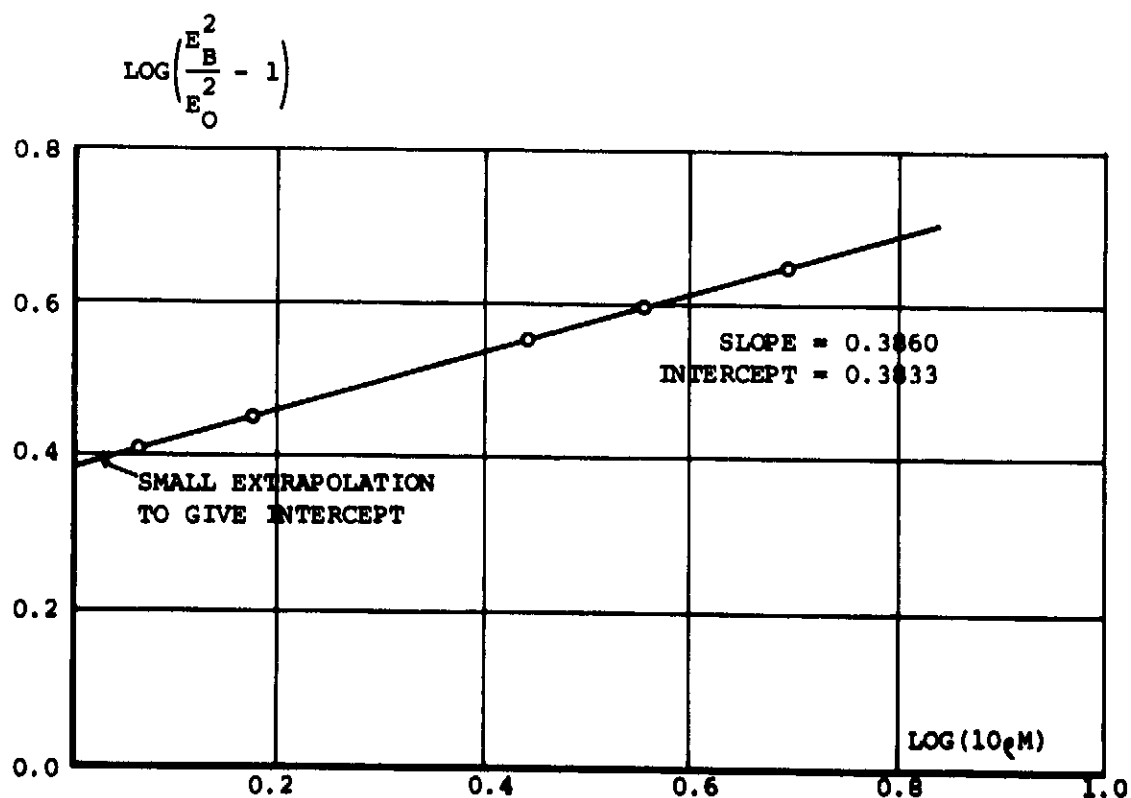
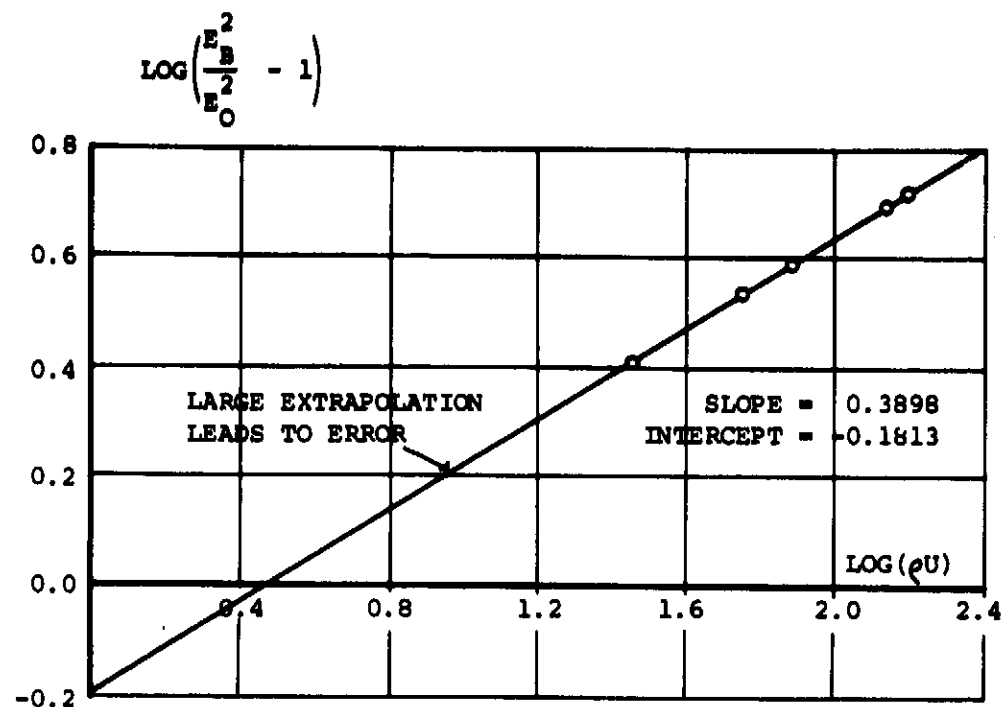


FIGURE 46: TWO HOT WIRE CALIBRATION TECHNIQUES

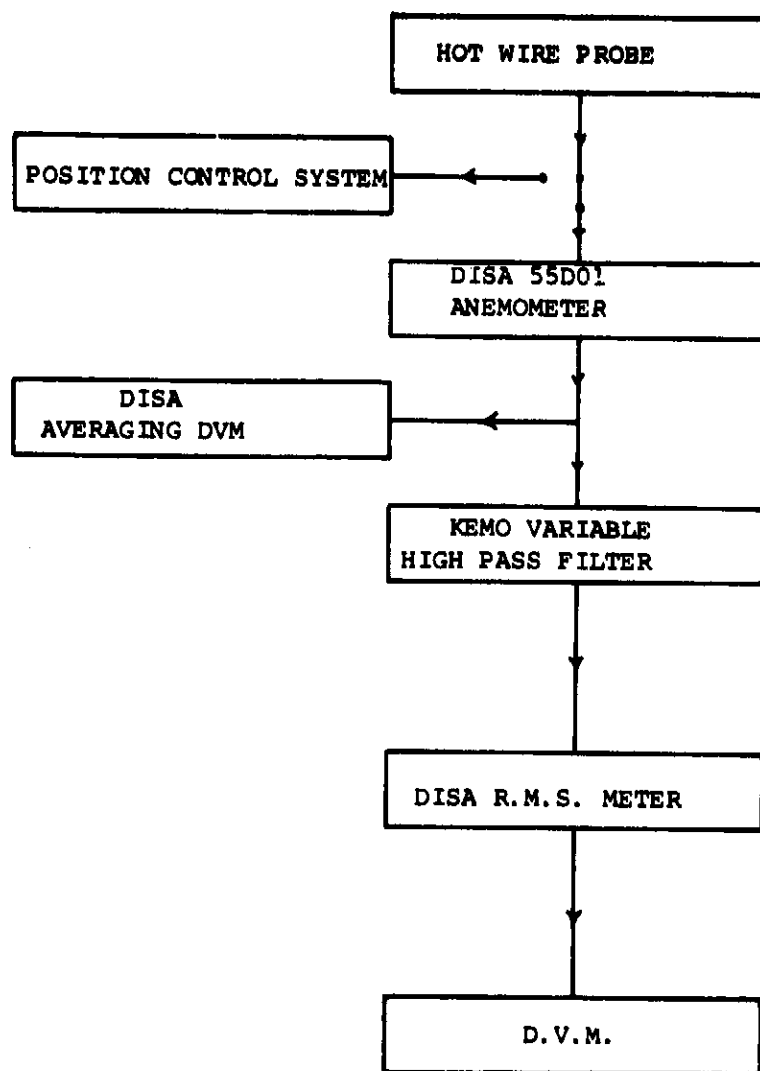
FIGURE 47: BLOCK DIAGRAM OF SINGLE SENSOR SYSTEM

FIG 48

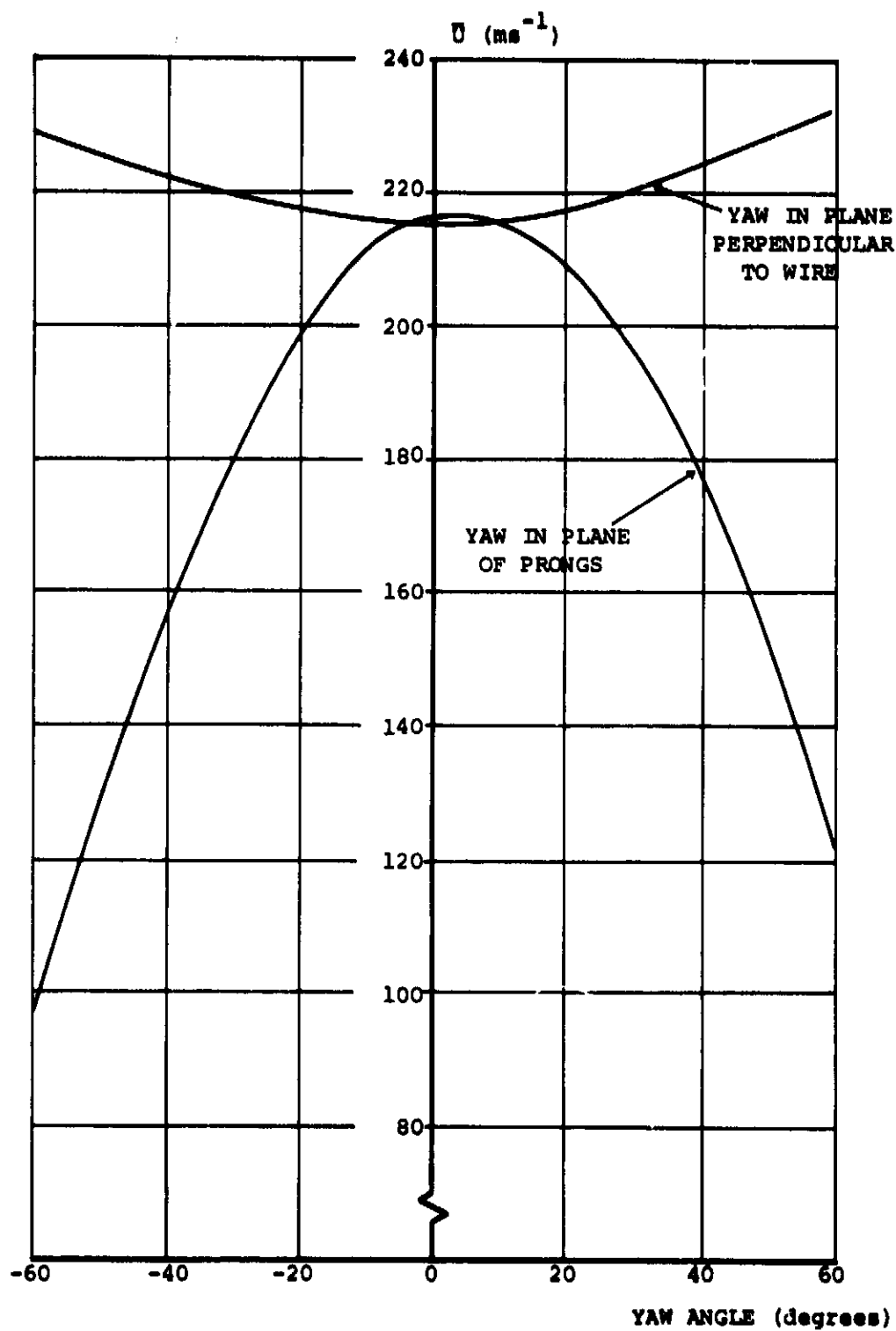


FIGURE 48: YAW EFFECTS ON THE RESPONSE OF A SINGLE HOT WIRE PROBE

FIG 49

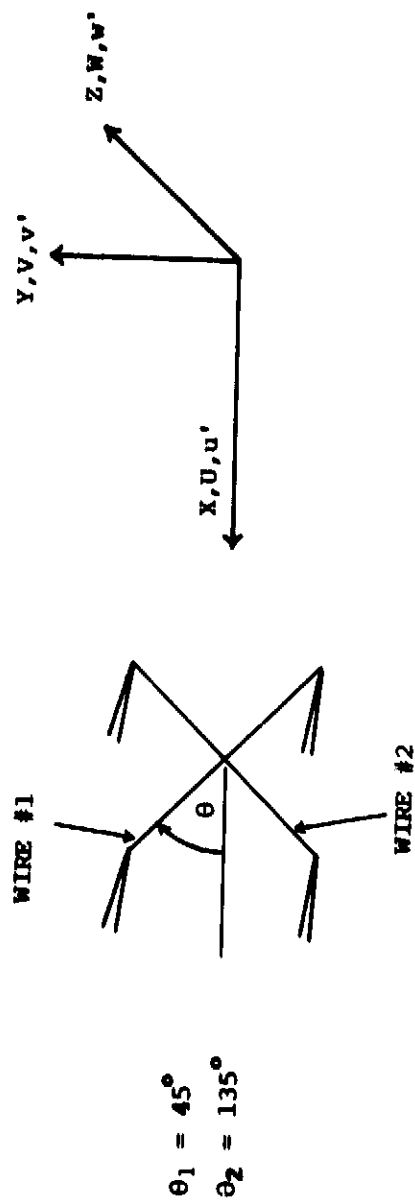


FIGURE 49: COORDINATE SYSTEM FOR DUAL SENSOR HOT WIRE PROBES

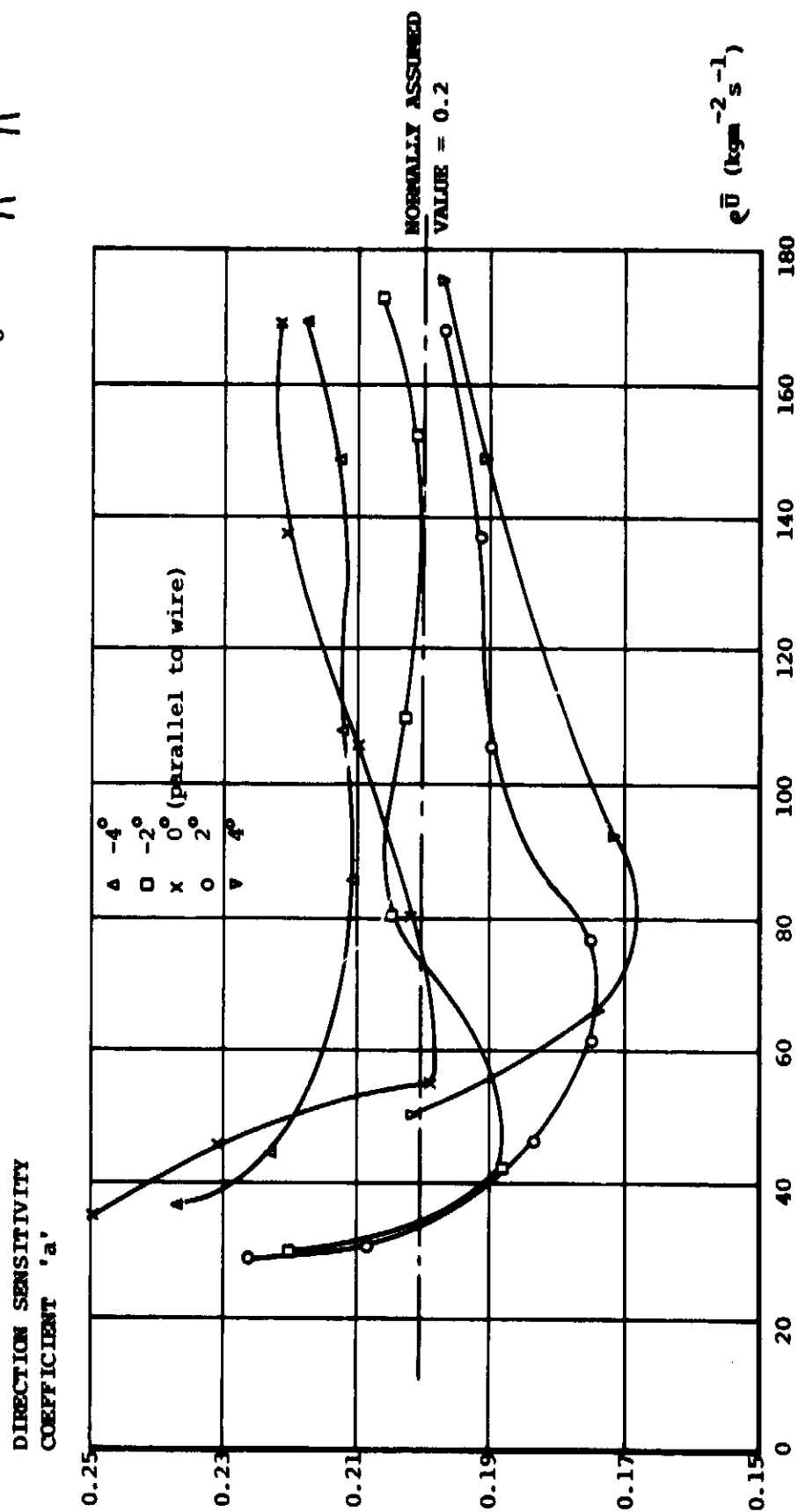


FIGURE 50: MEASURED DIRECTION SENSITIVITY COEFFICIENT OF A HOT WIRE PROBE

FIG 51

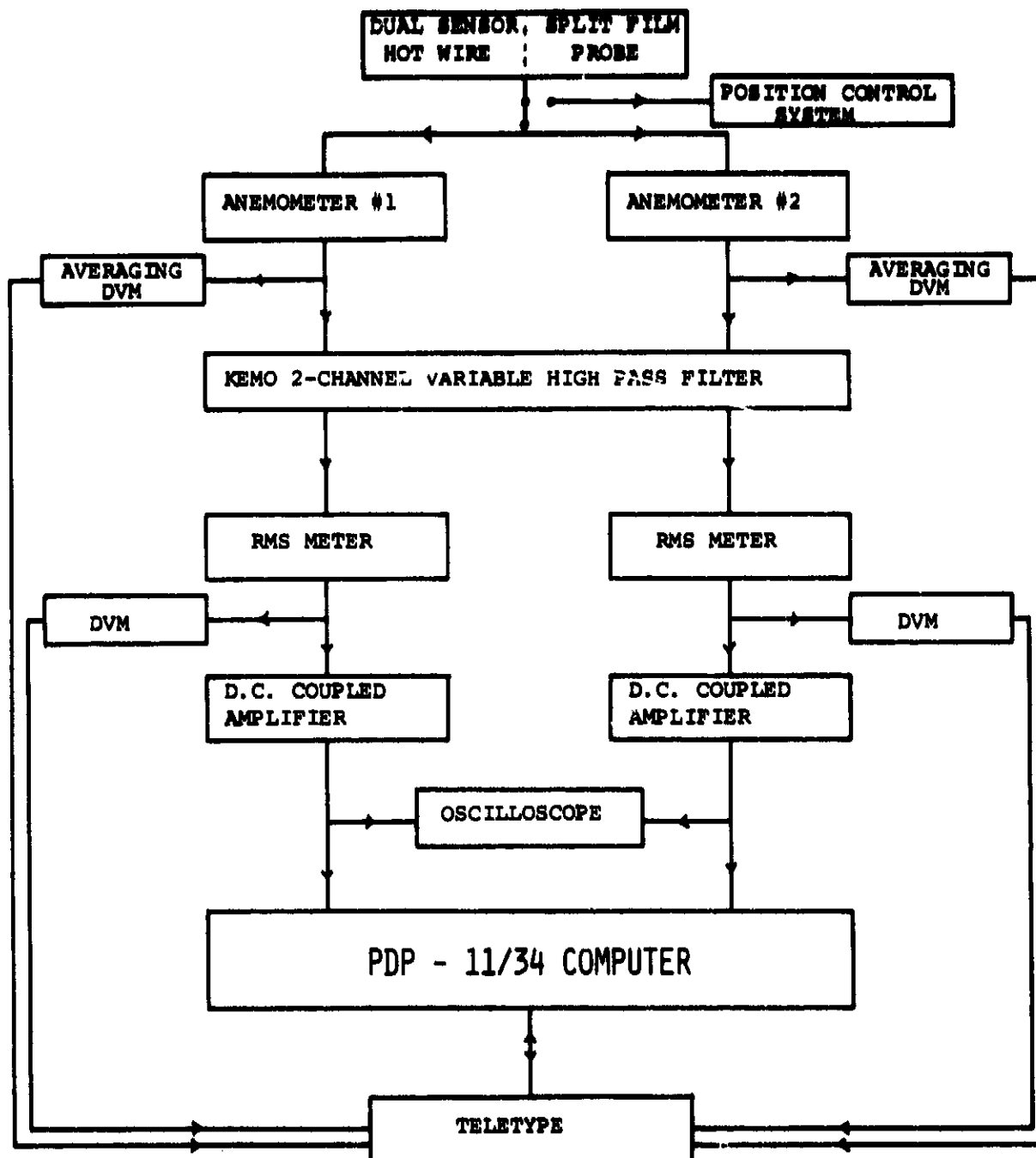


FIGURE 51: BLOCK DIAGRAM OF DUAL SENSOR SYSTEM

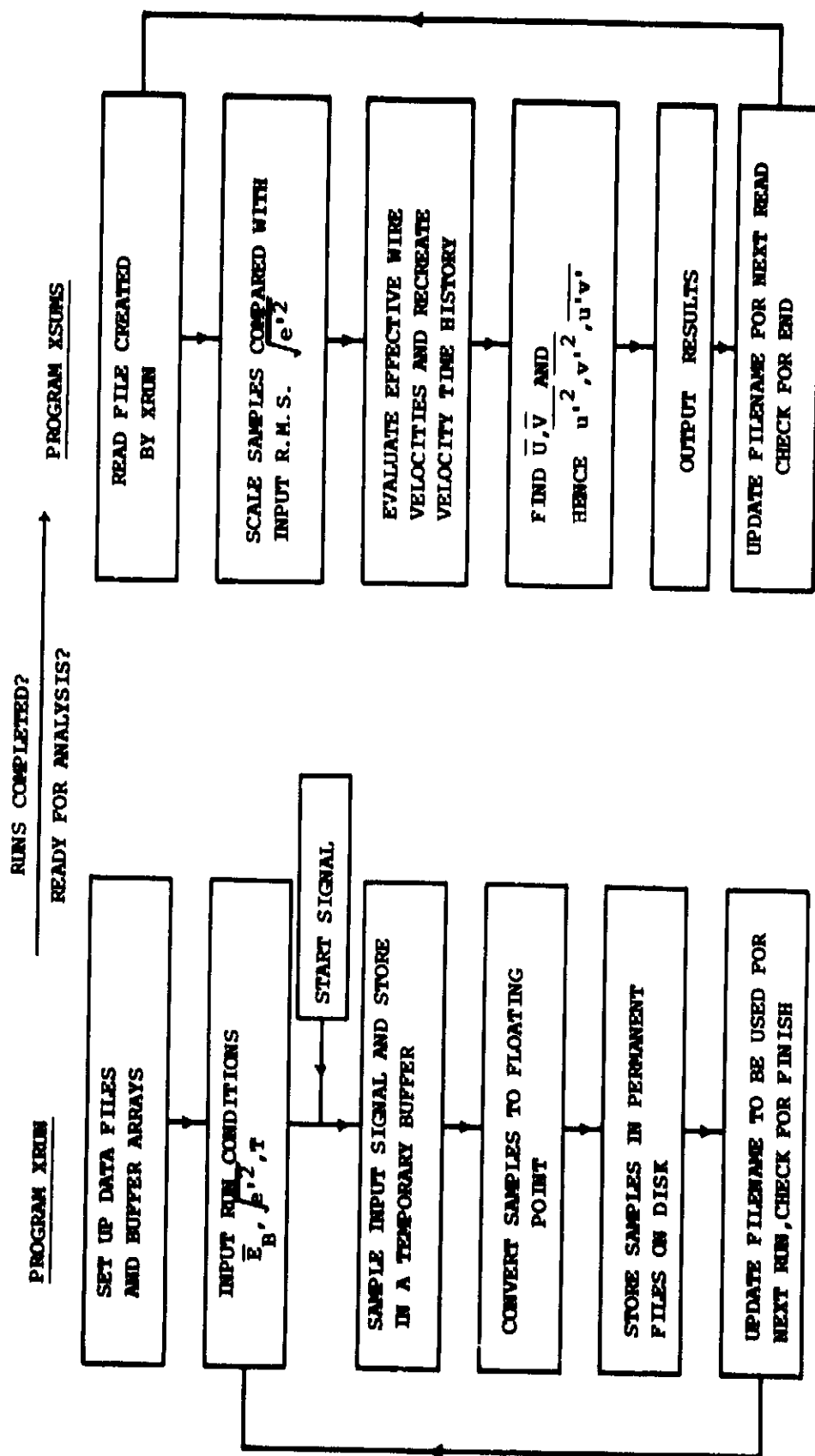
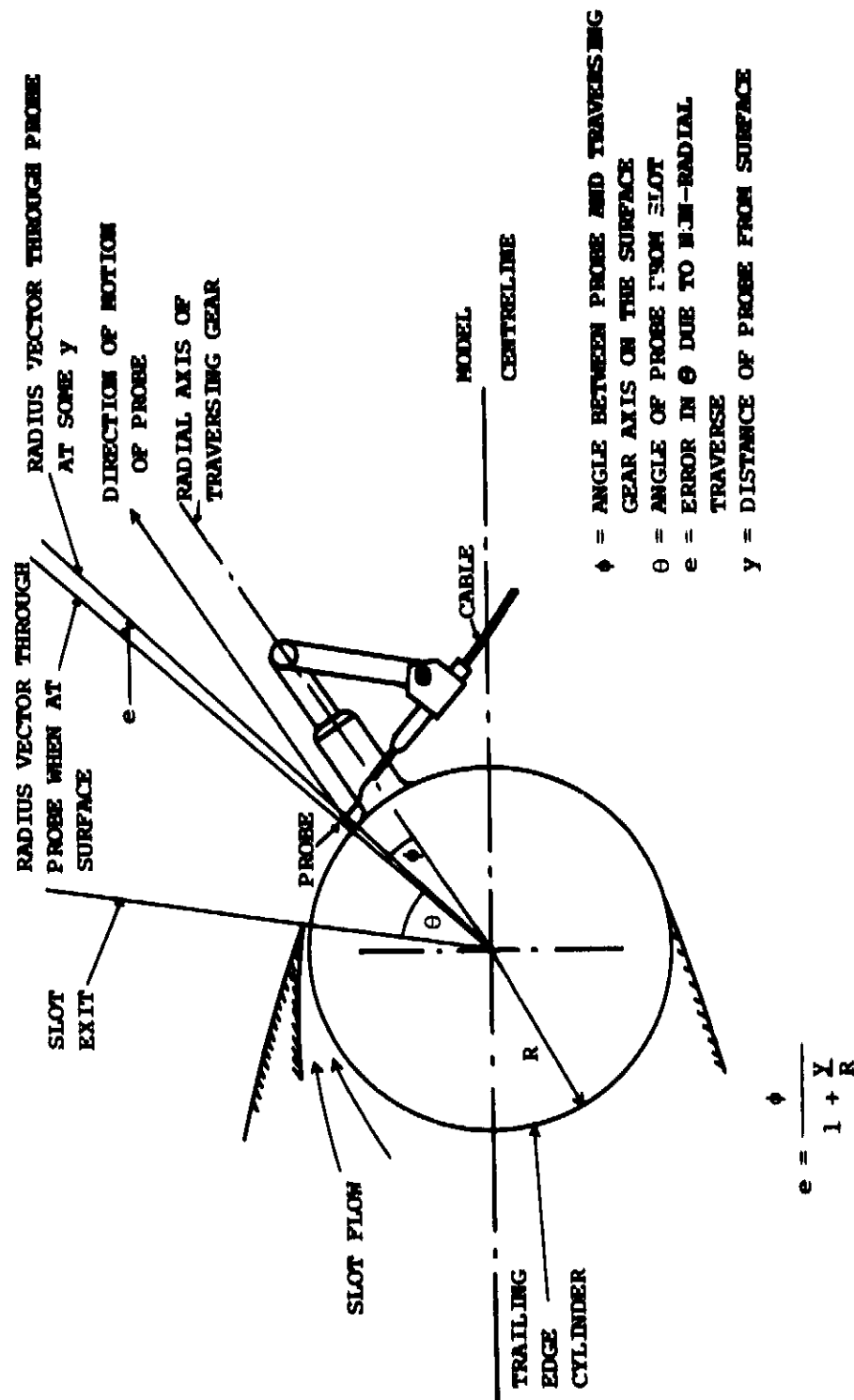


FIGURE 52: BLOCK DIAGRAM OF THE DUAL SENSOR HOT WIRE PROBE SAMPLING AND ANALYSIS PROGRAMS



- ϕ = ANGLE BETWEEN PROBE AND TRAVERSING GEAR AXIS ON THE SURFACE
- θ = ANGLE OF PROBE FROM SLOT
- e = ERROR IN θ DUE TO NON-RADIAL TRAVERSE
- y = DISTANCE OF PROBE FROM SURFACE

FIGURE 53: ERROR IN PROBE ANGULAR POSITION DUE TO NON-RADIAL TRAVERSING
(APPLICABLE TO HOT WIRE PROBES ONLY)

FIG 54

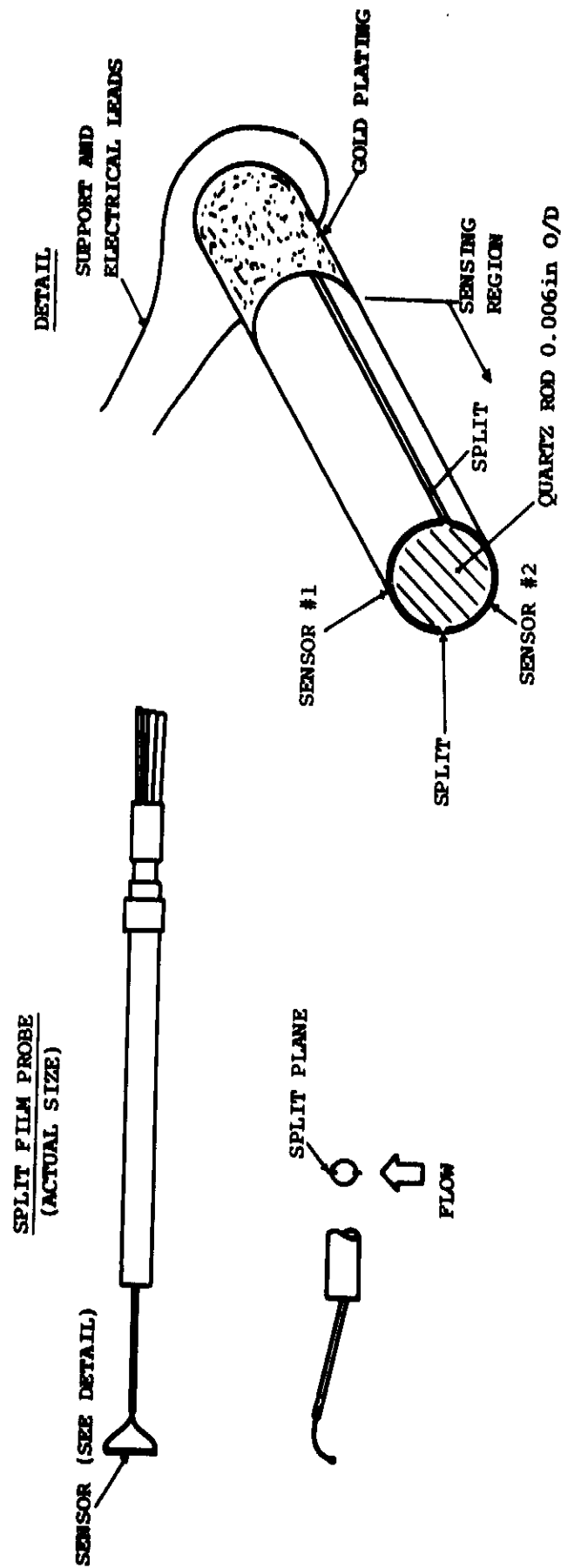


FIGURE 54: DETAIL OF A SPLIT FILM PROBE: TSI TYPE 1287

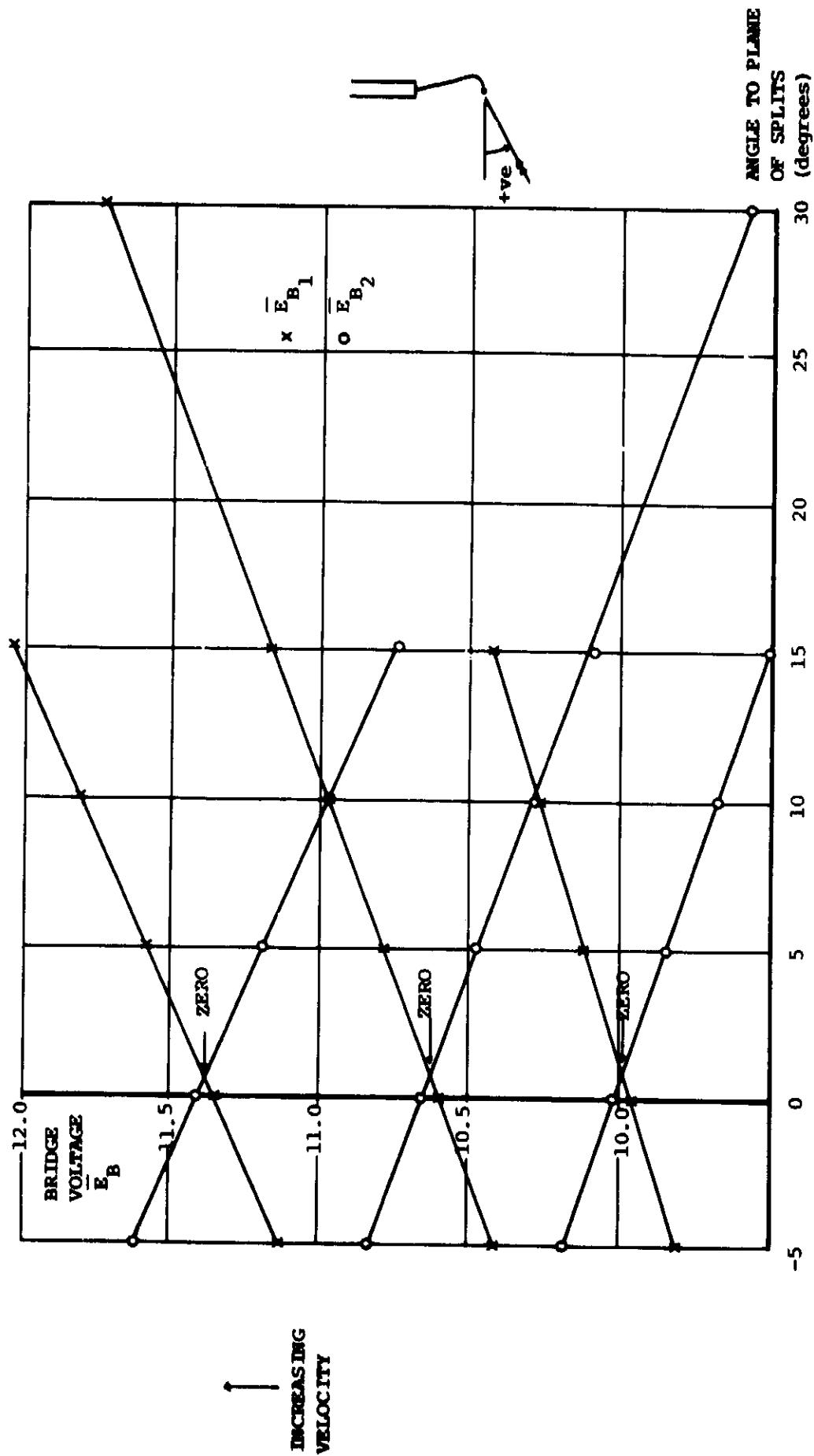


FIGURE 55: SPLIT FILM ANGULAR CALIBRATION: DETERMINATION OF THE ANGULAR OFFSET OF THE PLANE OF THE SPLITS TO THE PROBE AXIS

FIG 56

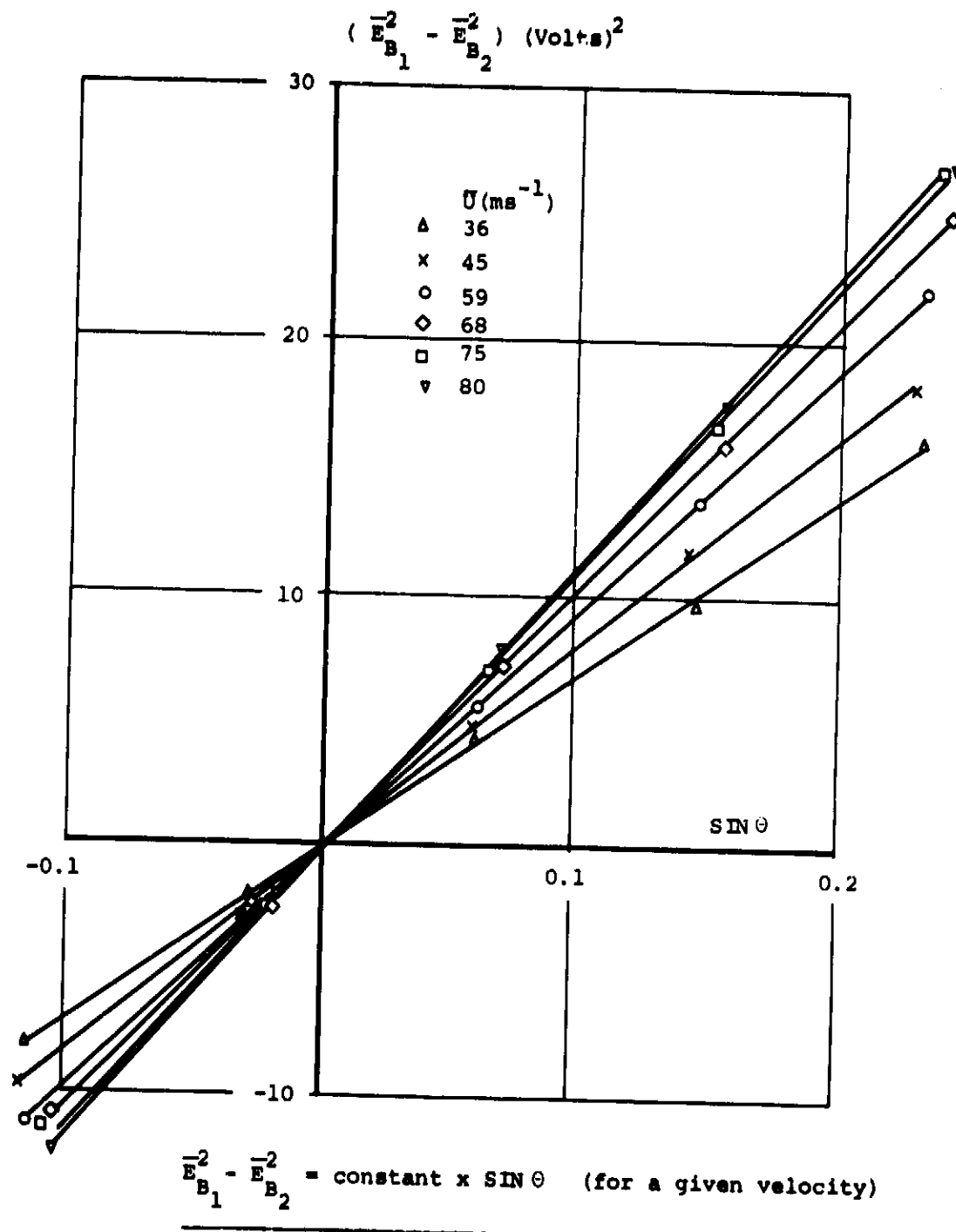
FIGURE 56: VALIDITY OF THE CHOSEN FUNCTION FOR ANGULAR CALIBRATION

FIG 57

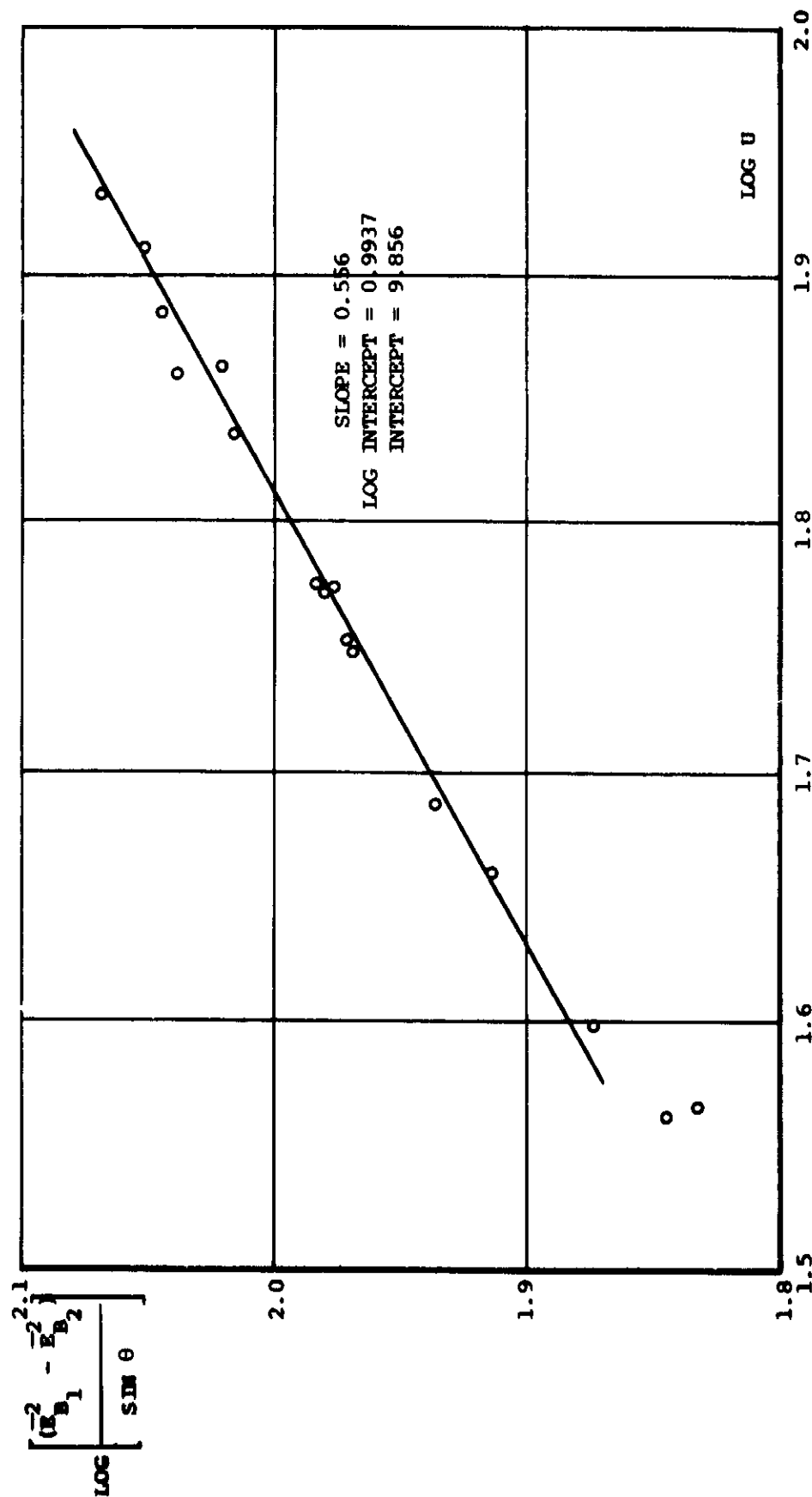
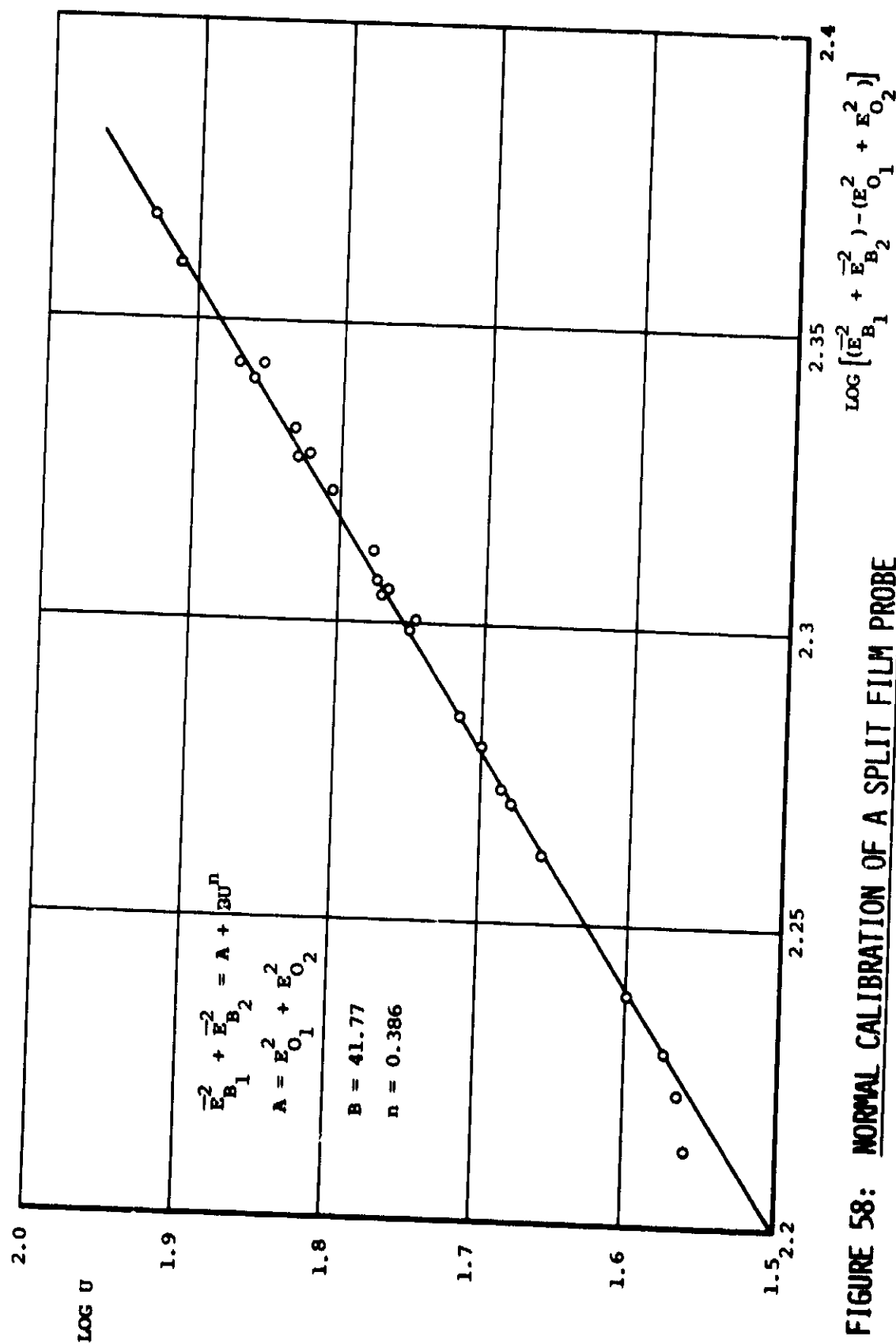


FIGURE 57: ANGULAR CALIBRATION OF A SPLIT FILM PROBE

FIGURE 58: NORMAL CALIBRATION OF A SPLIT FILM PROBE

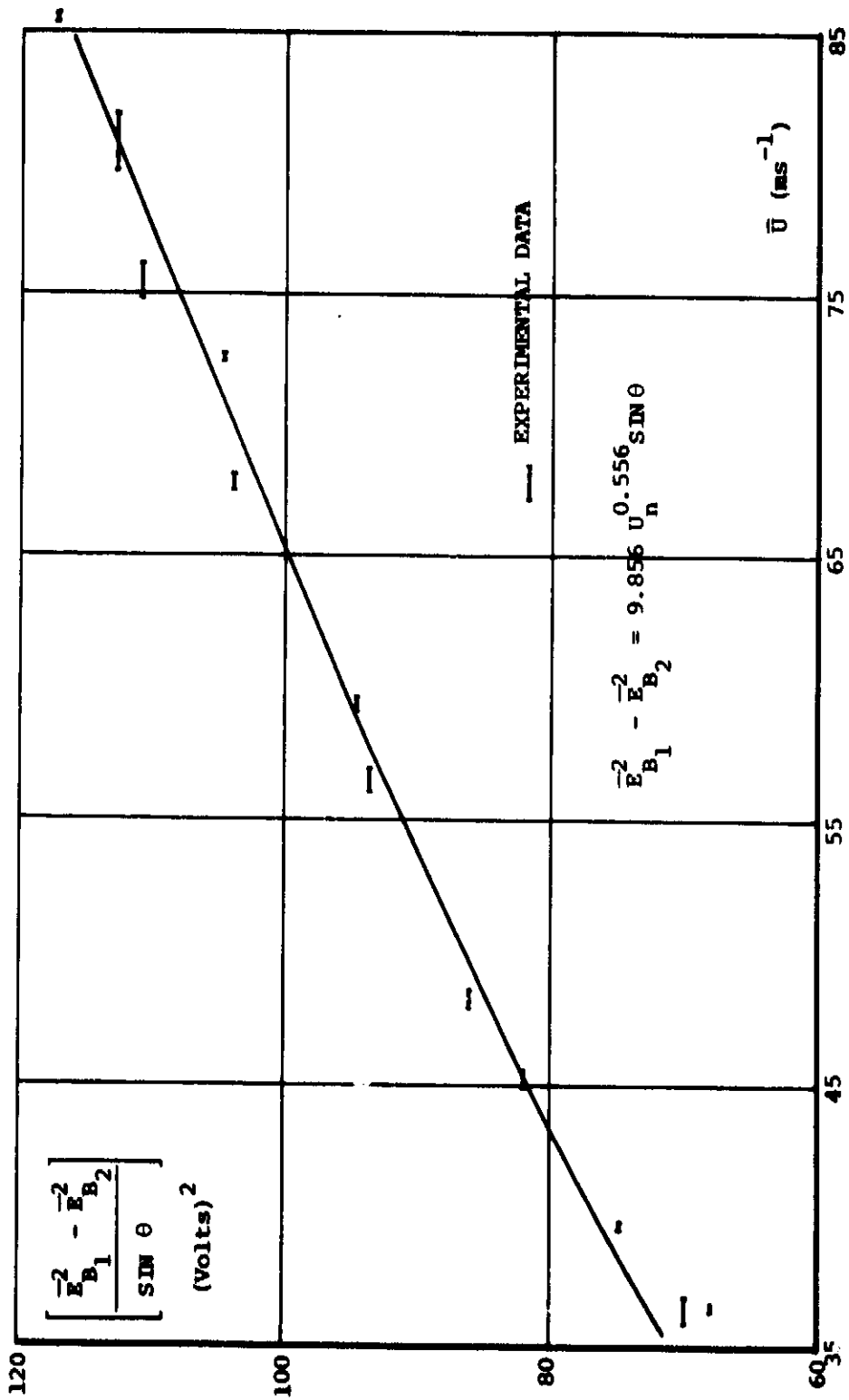


FIGURE 59: EXPERIMENTAL AND DERIVED ANGULAR FUNCTIONS OF A SPLIT FILM PROBE

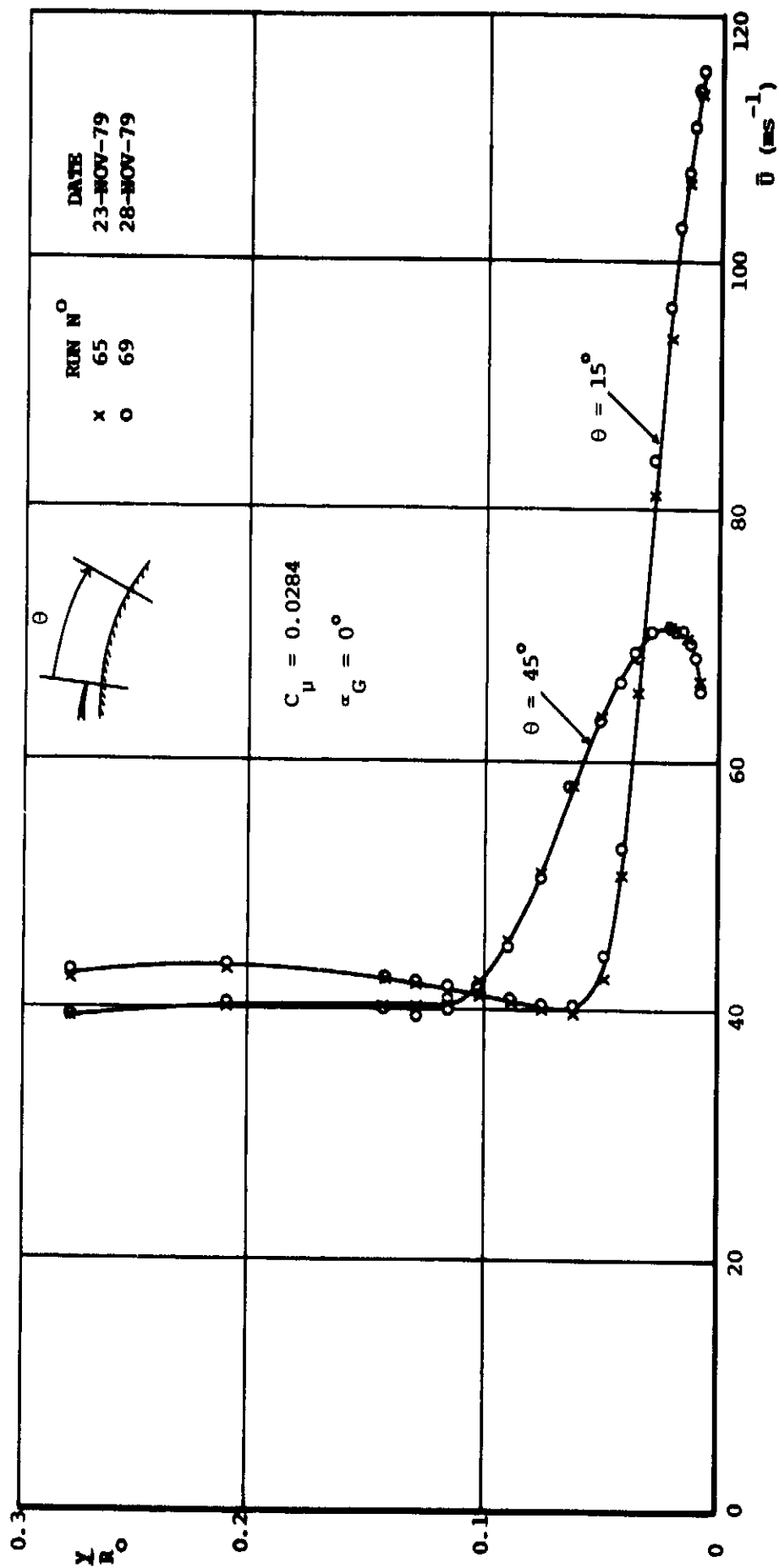


FIGURE 60: ILLUSTRATION OF THE EXCELLENT REPEATABILITY OF THE SPLIT FILM PROBE MEASUREMENTS

FIG 61

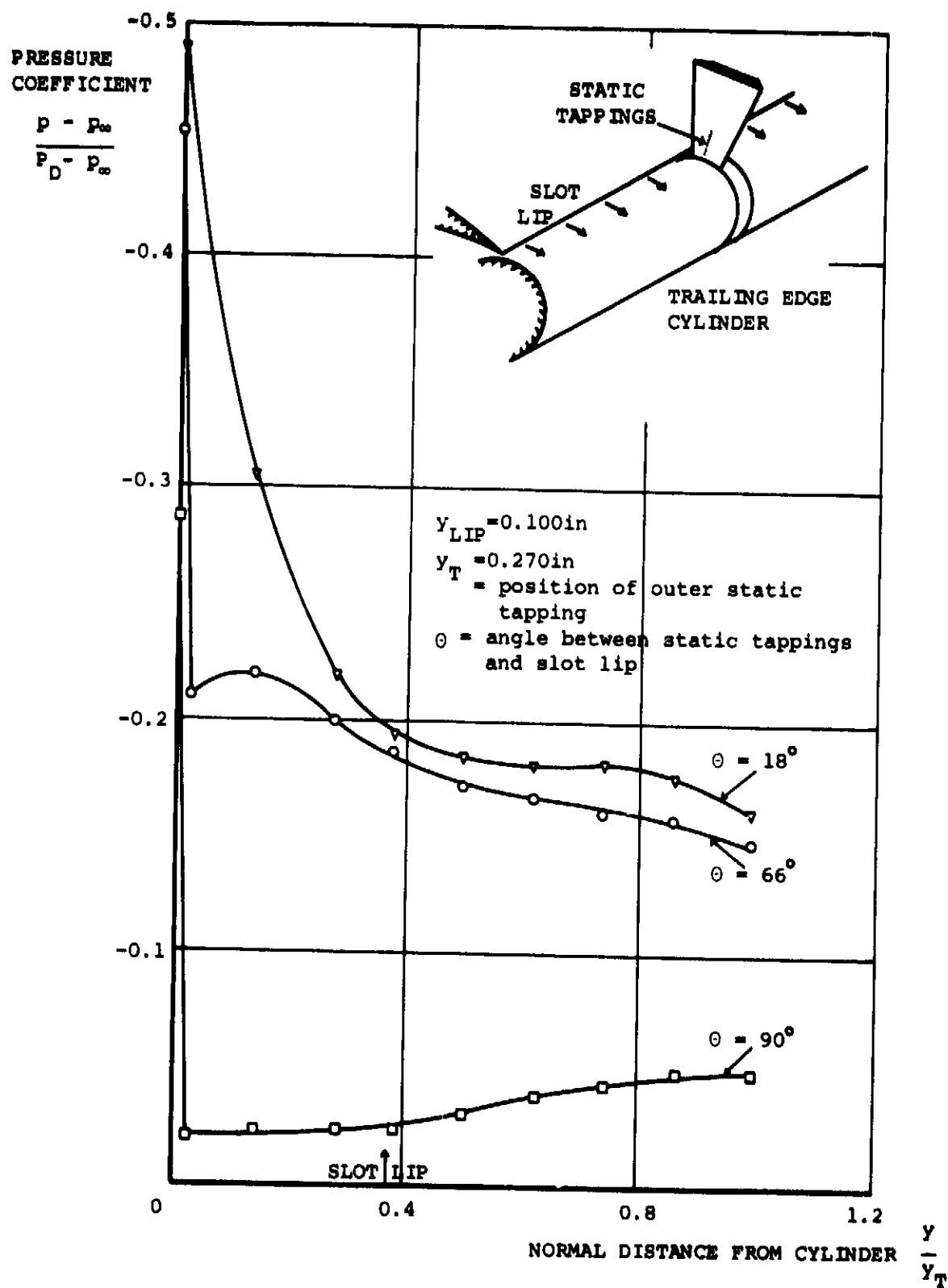


FIGURE 61: NORMAL STATIC PRESSURE VARIATION ACROSS WALL JET
FROM ENGLAR28

FIG 62

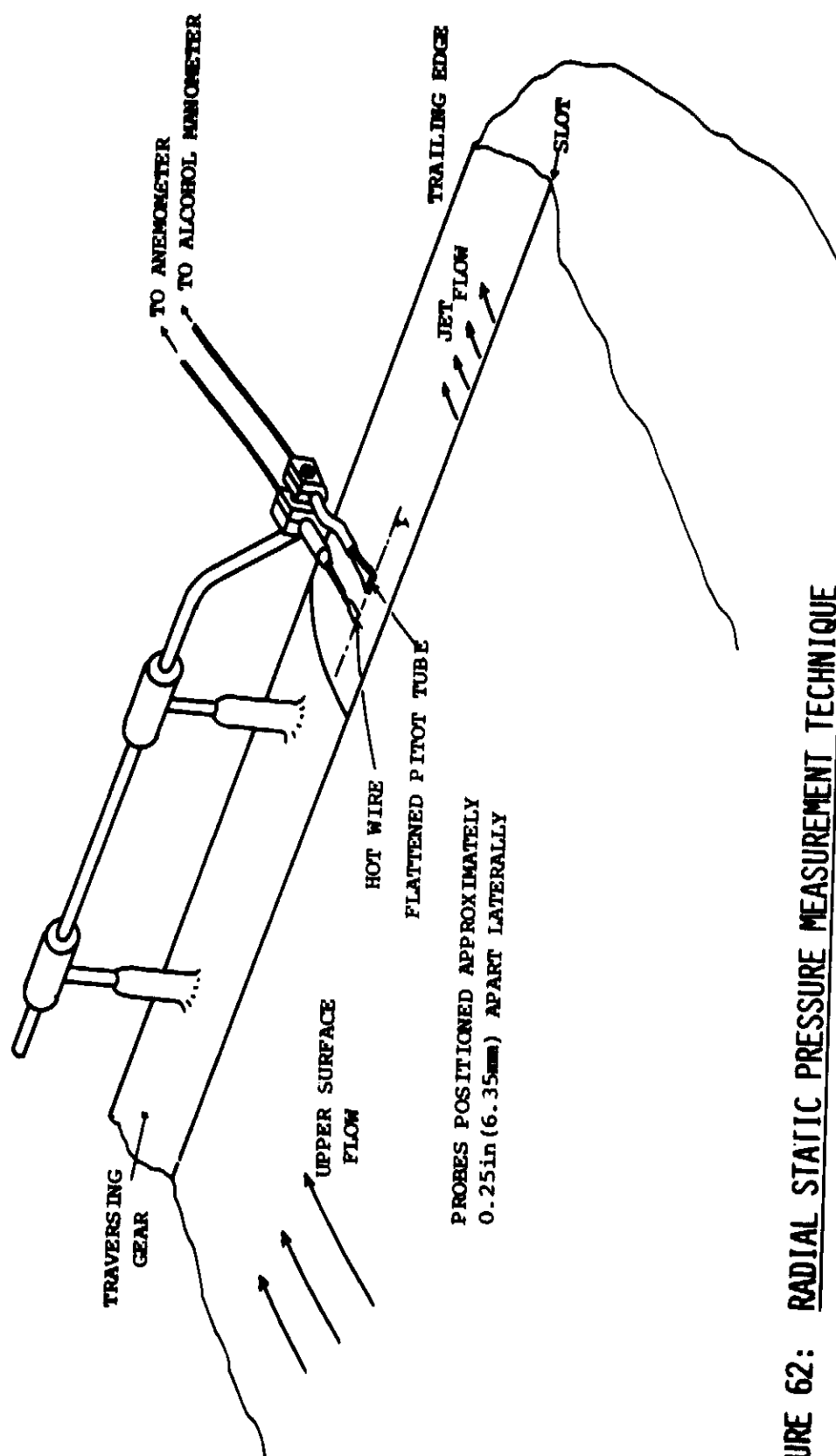


FIGURE 62: RADIAL STATIC PRESSURE MEASUREMENT TECHNIQUE

The graph plots Y/R_0 on the y-axis (ranging from 0.1 to 0.3) against $PRESSURE (P - P_0) (mm^{-2})$ on the x-axis (ranging from -2000 to 400). A series of open circles connected by a line shows a peak around -400 mm^{-2} . Scattered data points marked with 'x' and 'Δ' are also present, particularly at higher pressures.

O	RESULTS DIRECT FROM STATIC PRESSURE TESTS
X	RESULTS USING VELOCITIES DERIVED FROM SPLAT
A	RESULTS WITH FILM VELOCITIES OFFSET -0.007
P	" " " "
	+0.002

**FIGURE 63: EFFECTS ON THE RADIAL STATIC PRESSURE DISTRIBUTION OF OFFSETS FOR 'SHEARED FLOW'
CORRECTION AND FOR POSSIBLE ERRORS IN VELOCITY MEASUREMENT**

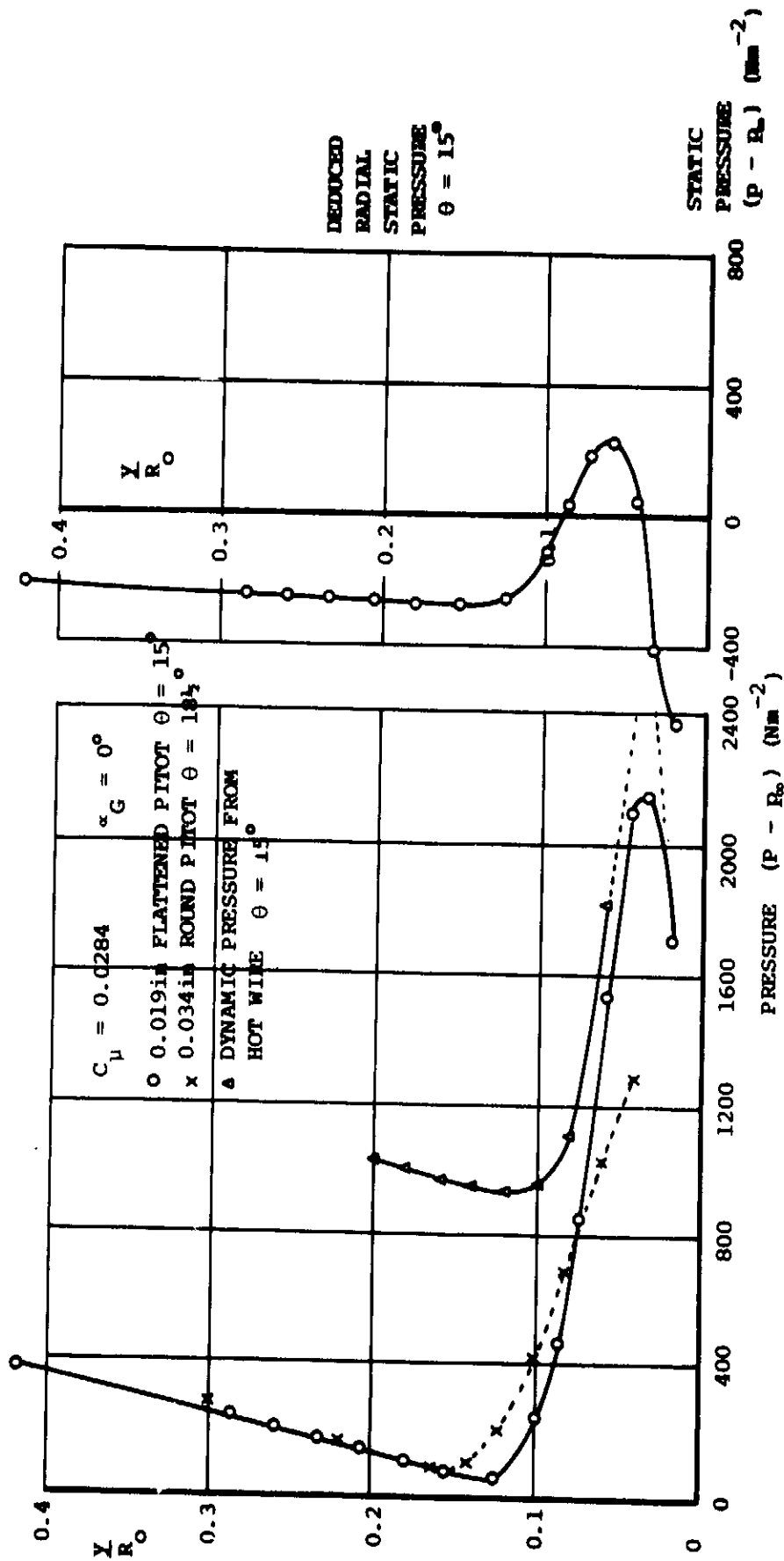


FIGURE 64: EFFECTS OF TOTAL HEAD TUBE SIZE UPON RADIAL STATIC PRESSURE MEASUREMENT

FIG 65

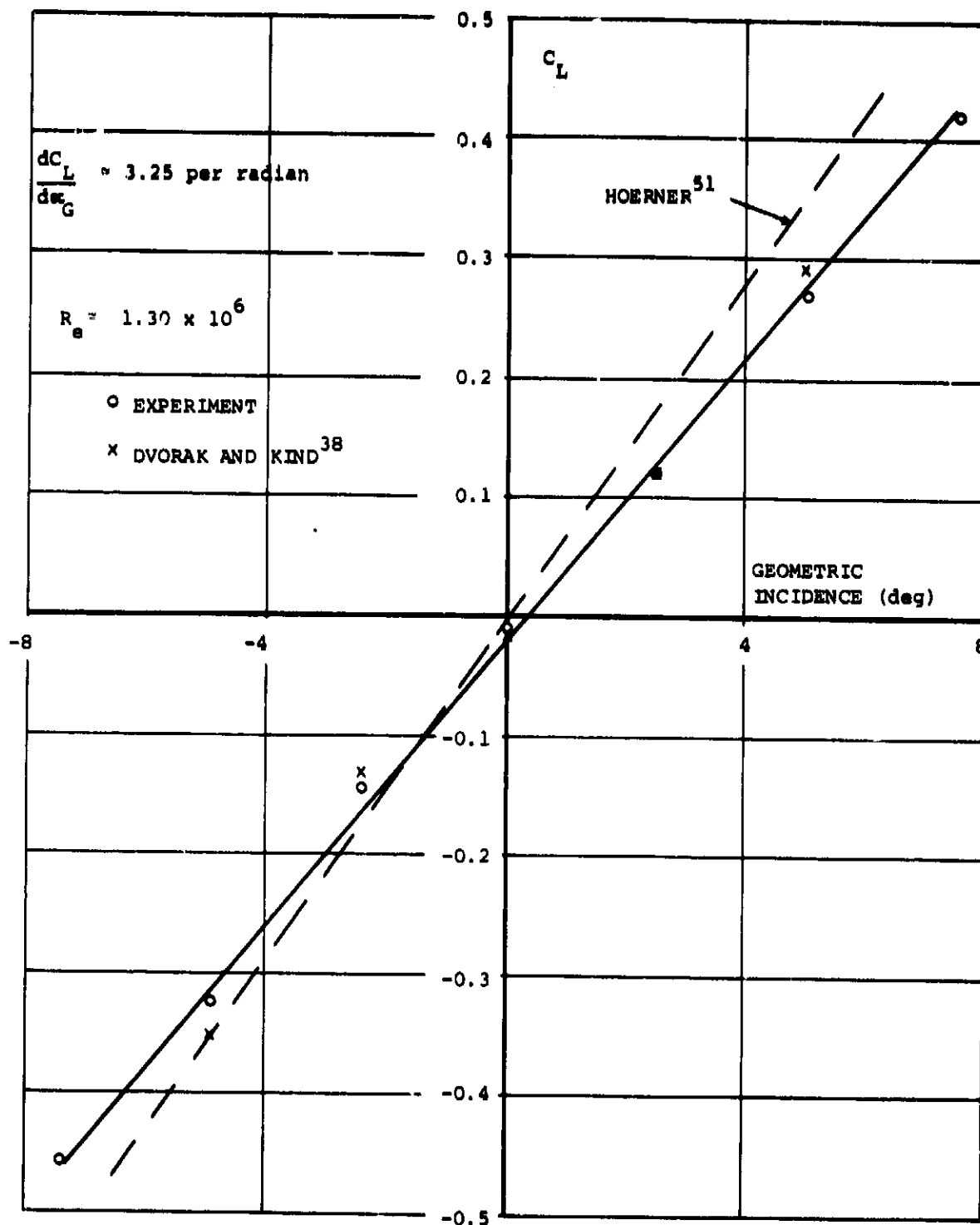


FIGURE 65: LIFT CURVE SLOPE OF THE UNBLOWN ELLIPSE COMPARED WITH THE TWO-DIMENSIONAL CASE⁵¹ AND THE THEORY OF DVORAK AND KIND³⁸

FIG 66

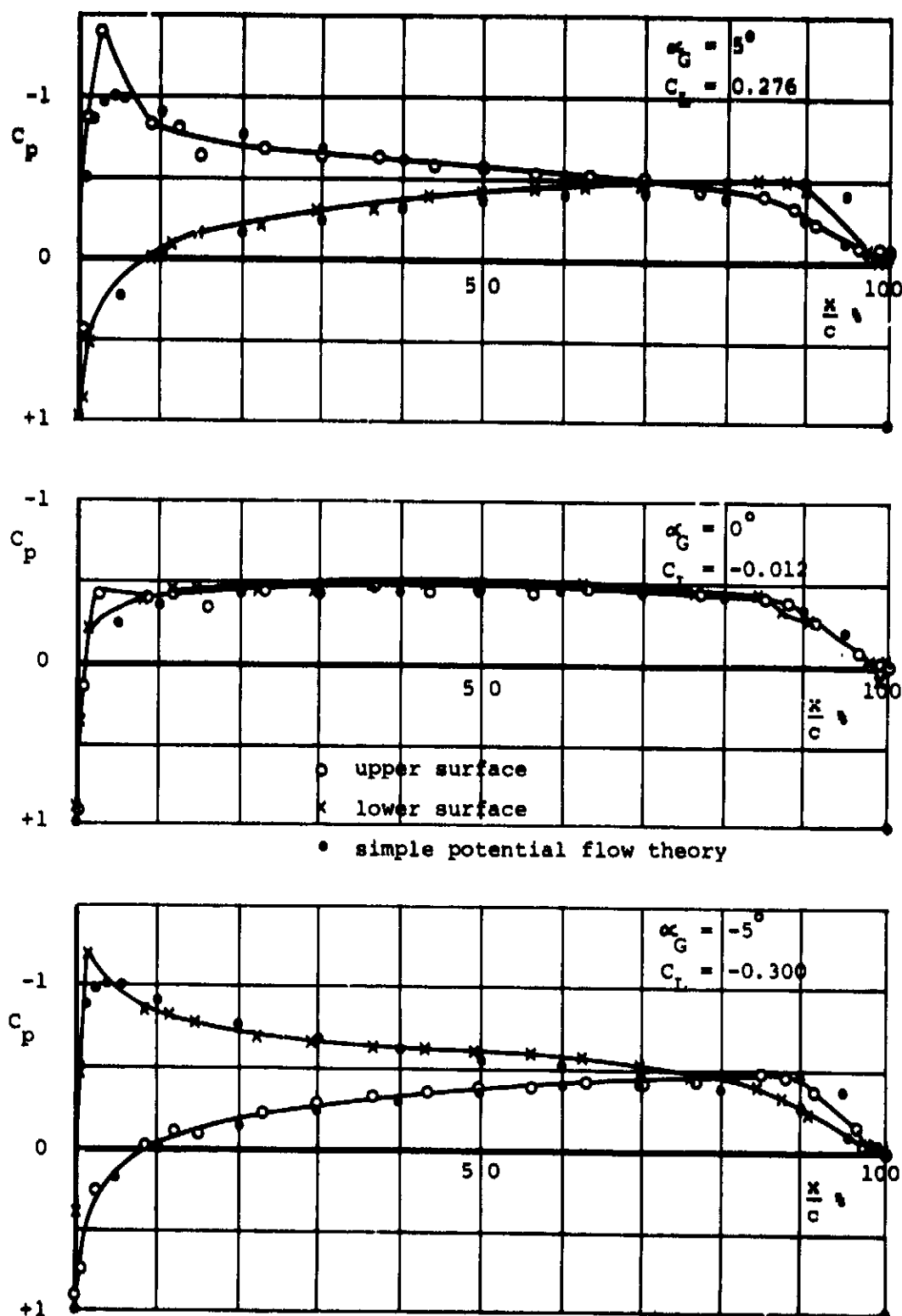


FIGURE 66: MEASURED PRESSURE DISTRIBUTIONS FOR THE UNBLOWN AEROFOIL COMPARED WITH A SIMPLE POTENTIAL FLOW PREDICTION METHOD

FIG 67

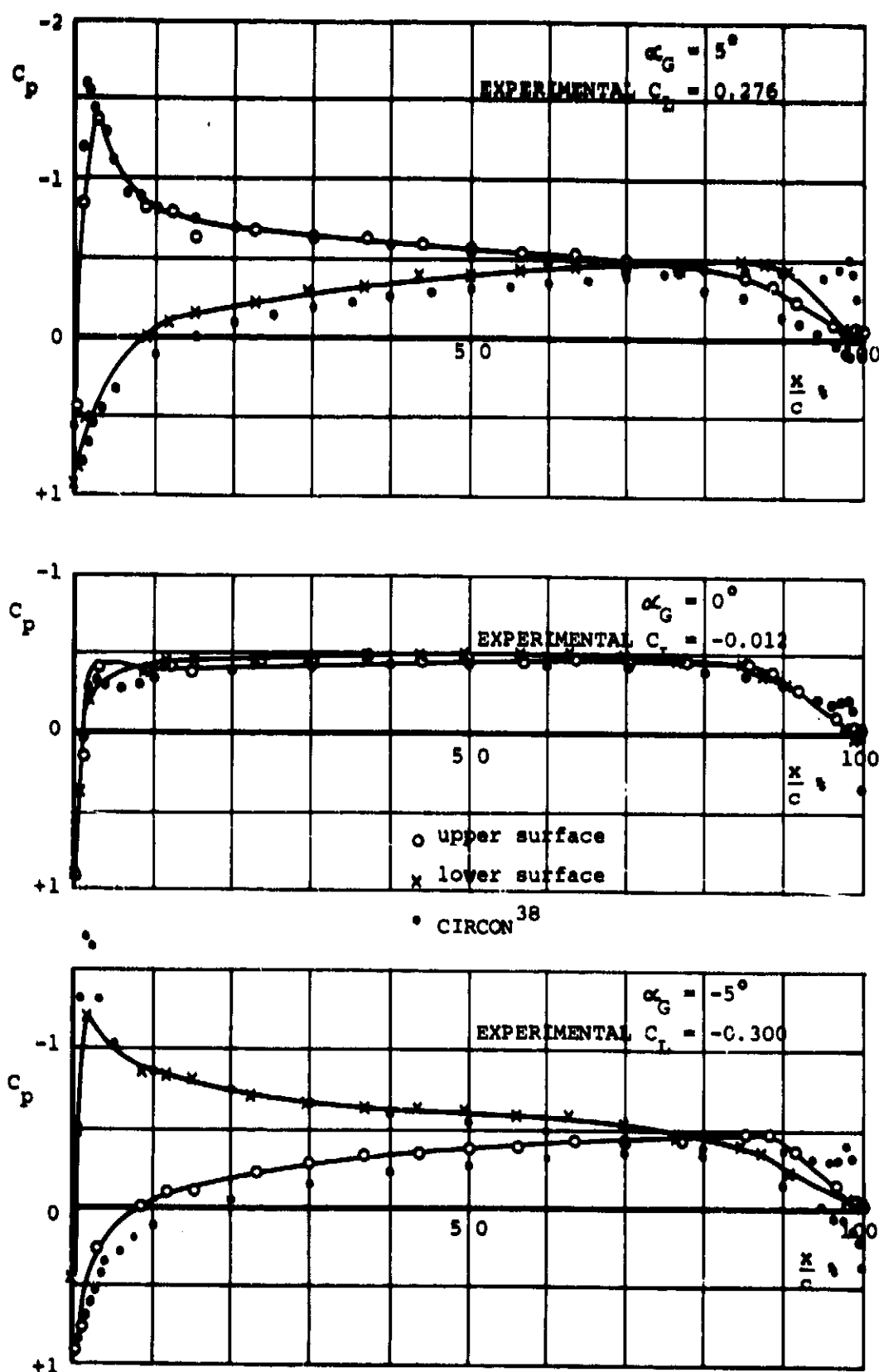


FIGURE 67: MEASURED PRESSURE DISTRIBUTIONS OF THE UNBLOWN AEROFOIL COMPARED WITH THE VISCOUS POTENTIAL FLOW METHOD OF DVORAK AND KIND³⁸

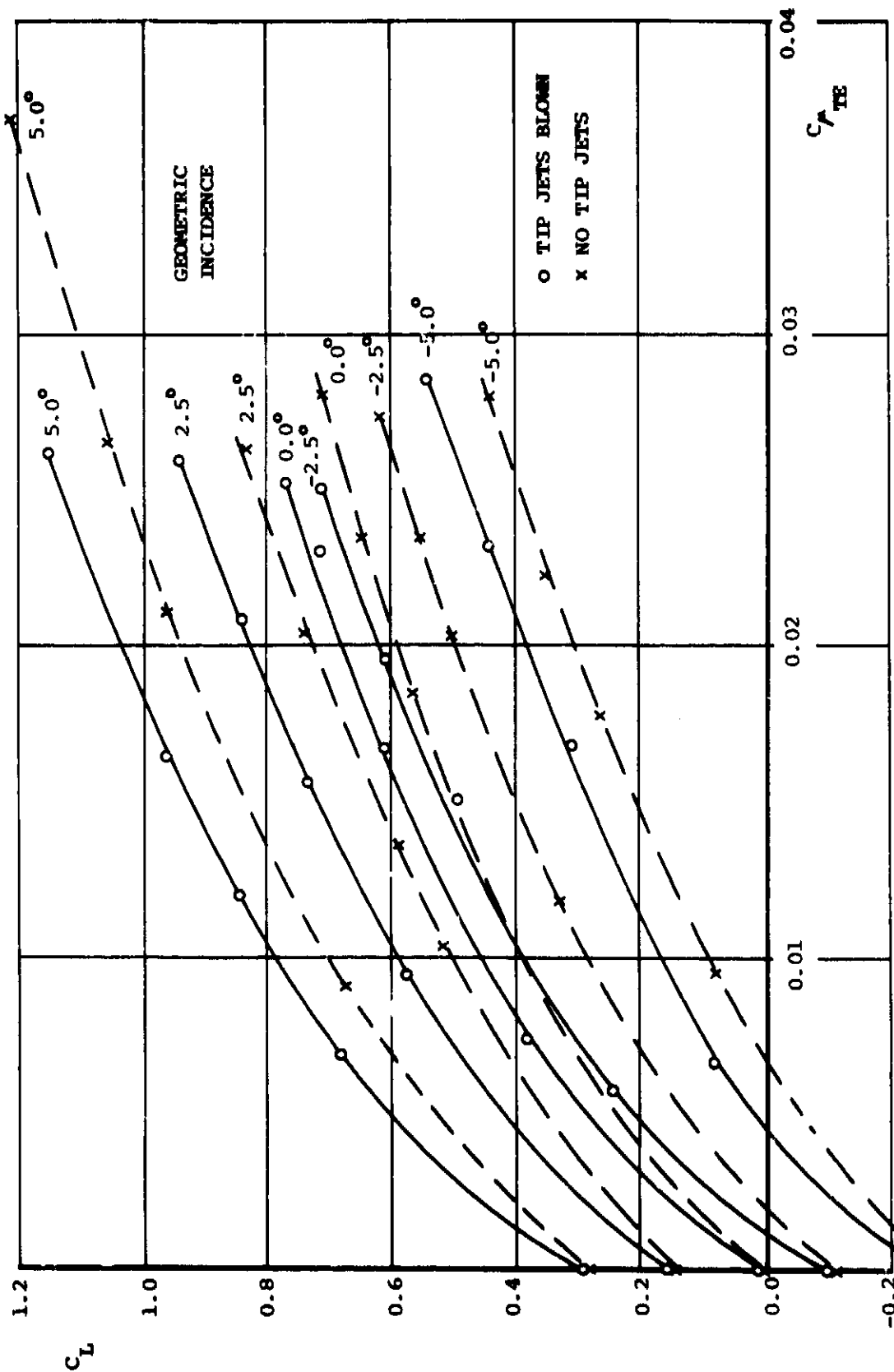


FIGURE 68: VARIATIONS OF CENTRELINE LIFT COEFFICIENT WITH GEOMETRIC INCIDENCE
TRAILING EDGE BLOWING ONLY

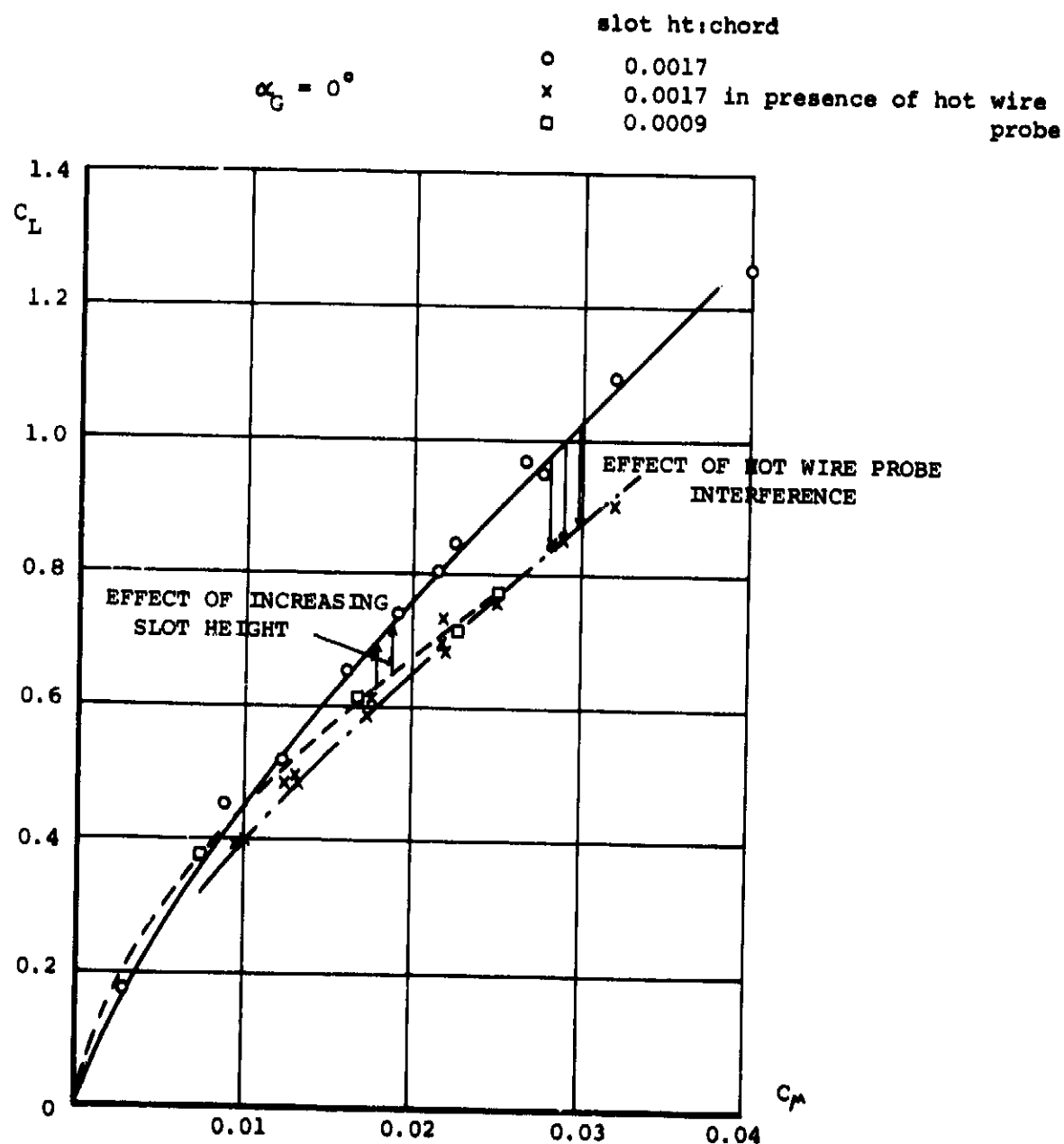
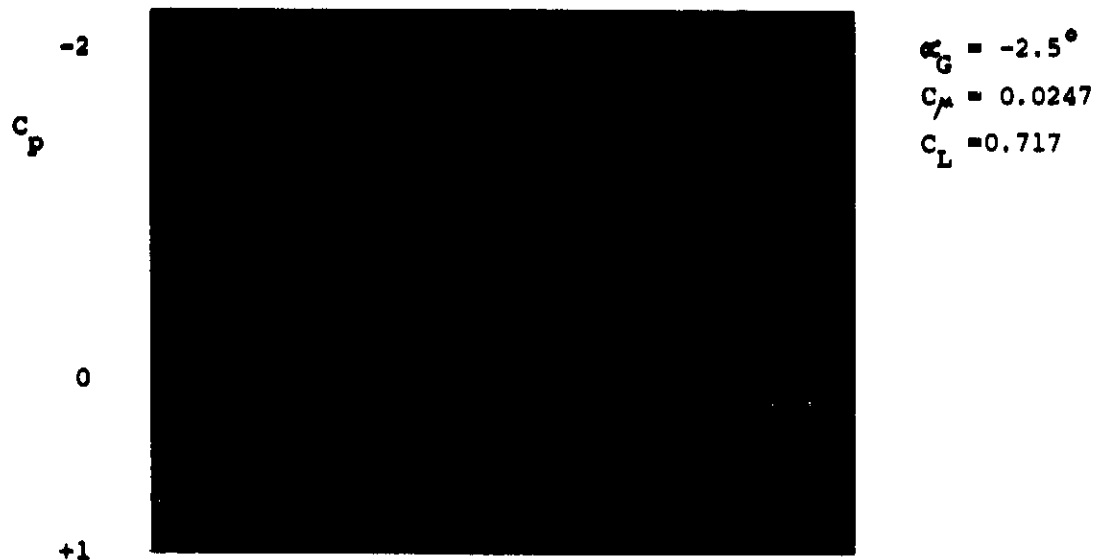


FIGURE 69: EFFECT OF SLOT HEIGHT AND PROBE INTERFERENCE UPON MEASURED LIFT COEFFICIENT FOR TRAILING EDGE BLOWING ONLY

FIG 70

ORIGINAL PAGE
BLACK AND WHITE PHOTOGRAPH

NOTE: SUCTION PEAK
CUT-OFF DUE TO SMALL
VERTICAL SCALE



SOLID LINES INDICATE EXPERIMENTAL RESULTS
CROSSES INDICATE EFFECTIVE INCIDENCE CALCULATION

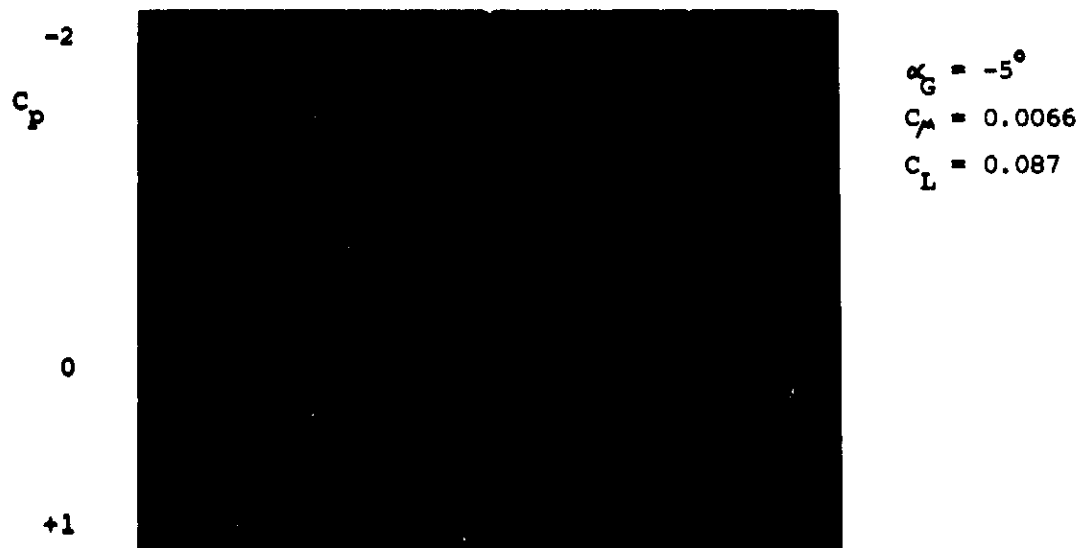


FIGURE 70: EXAMPLES OF THE EFFECTIVE INCIDENCE ESTIMATION
TECHNIQUE FOR TRAILING EDGE BLOWING ONLY

FIG 71A

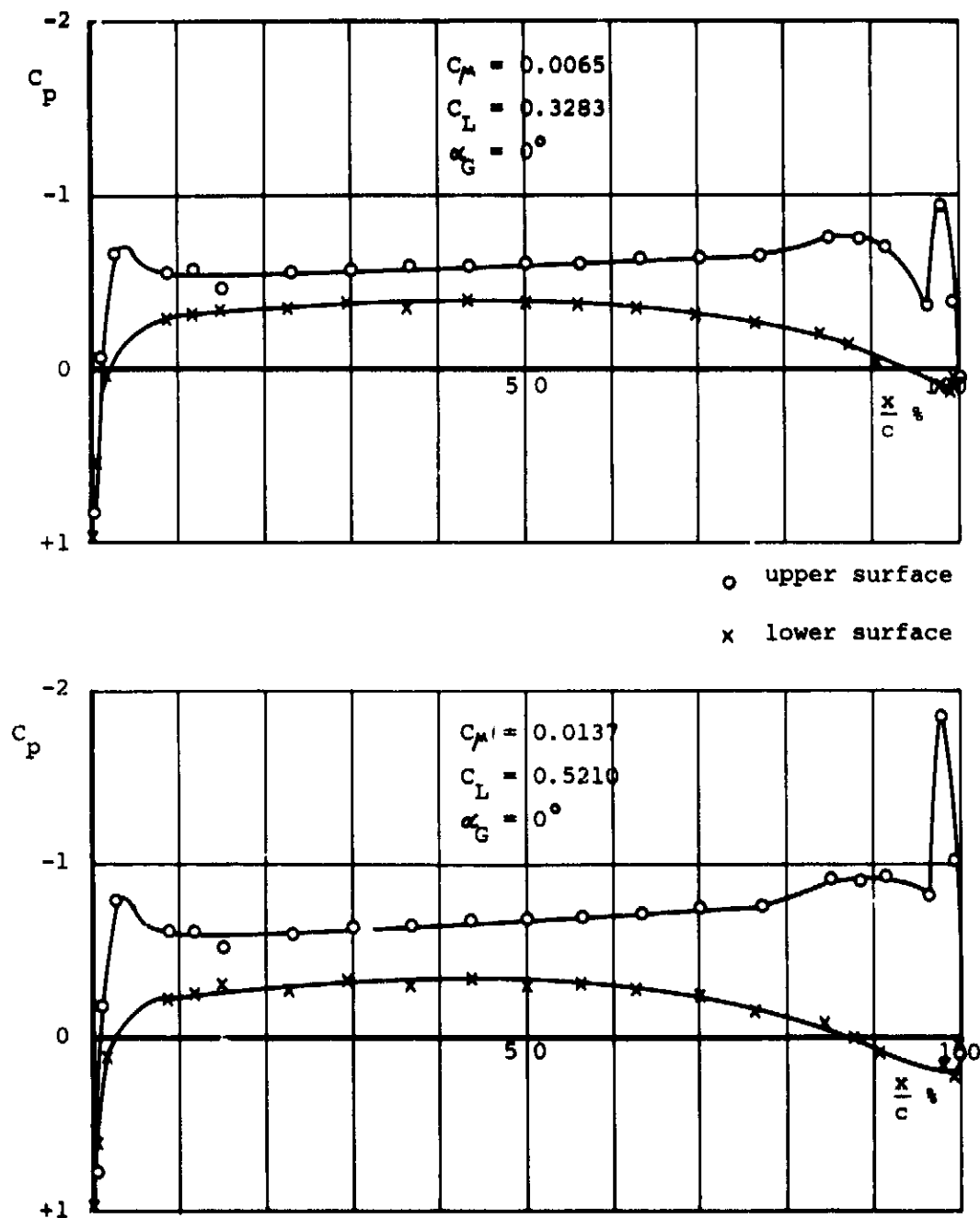


FIGURE 71A: EXPERIMENTAL PRESSURE DISTRIBUTIONS WITH TRAILING EDGE BLOWING ONLY

FIG 71B

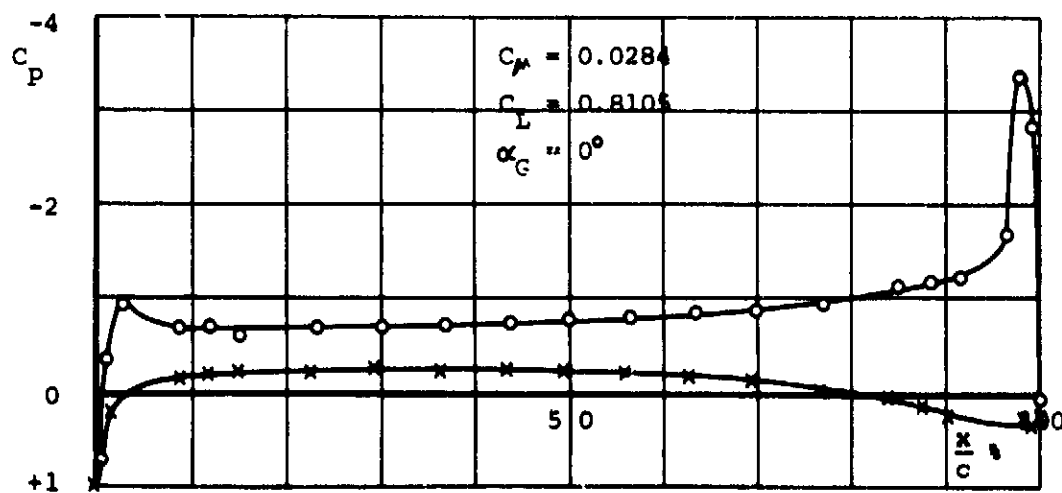
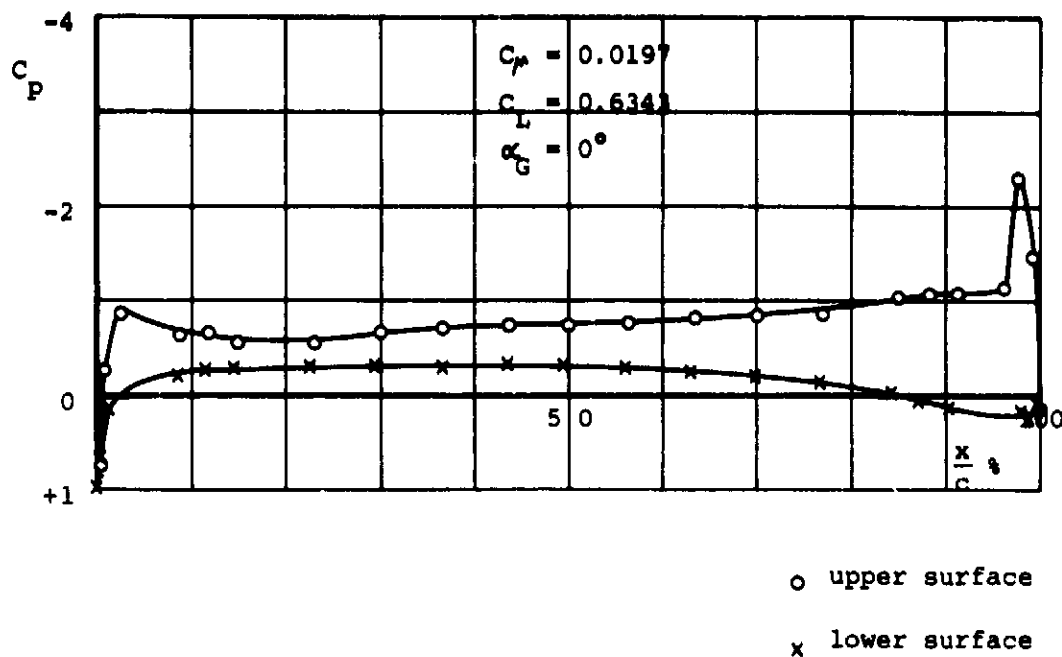


FIGURE 71B: EXPERIMENTAL PRESSURE DISTRIBUTIONS WITH TRAILING EDGE BLOWING ONLY

FIG 72

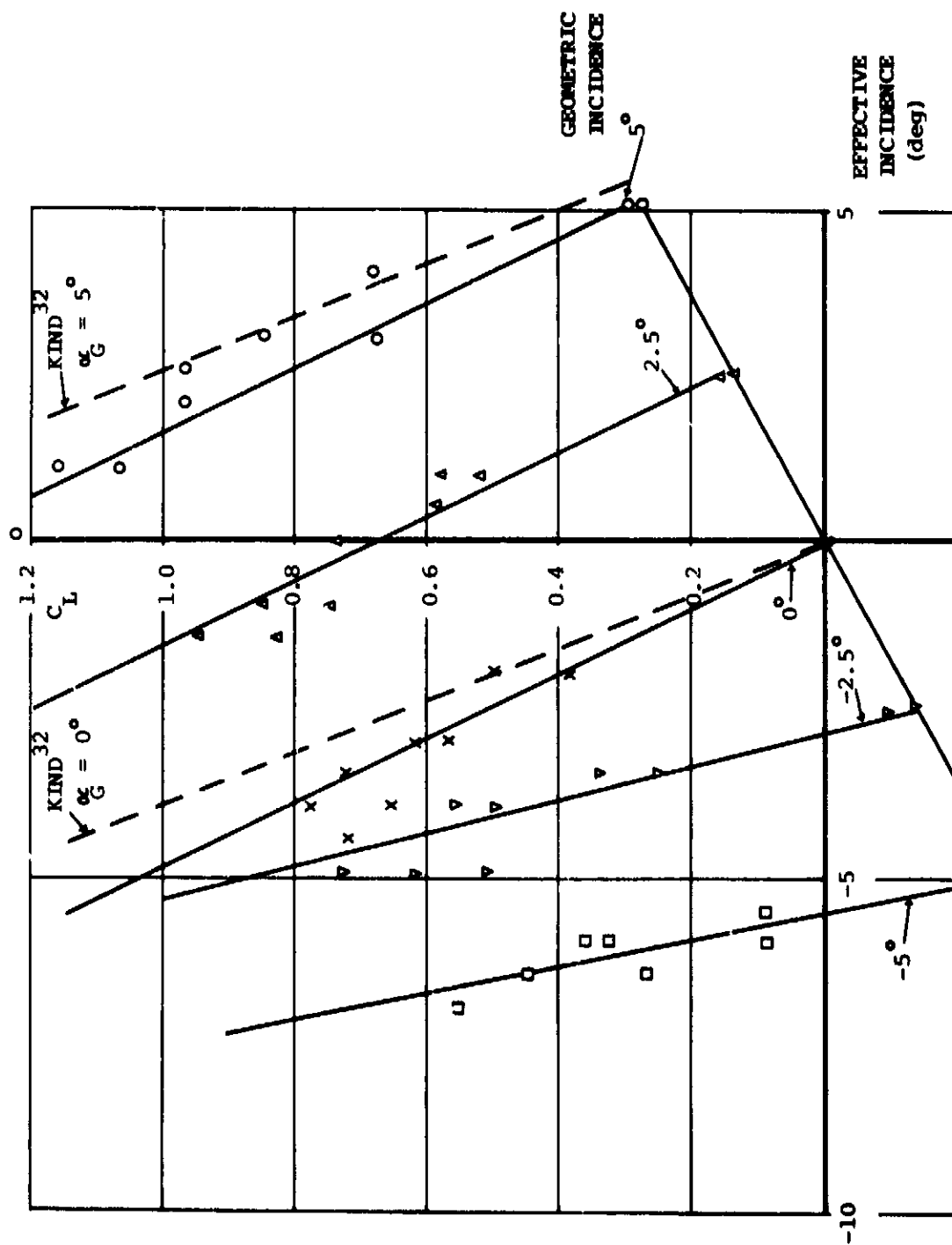


FIGURE 72: DEDUCED EFFECTIVE INCIDENCE CORRECTION

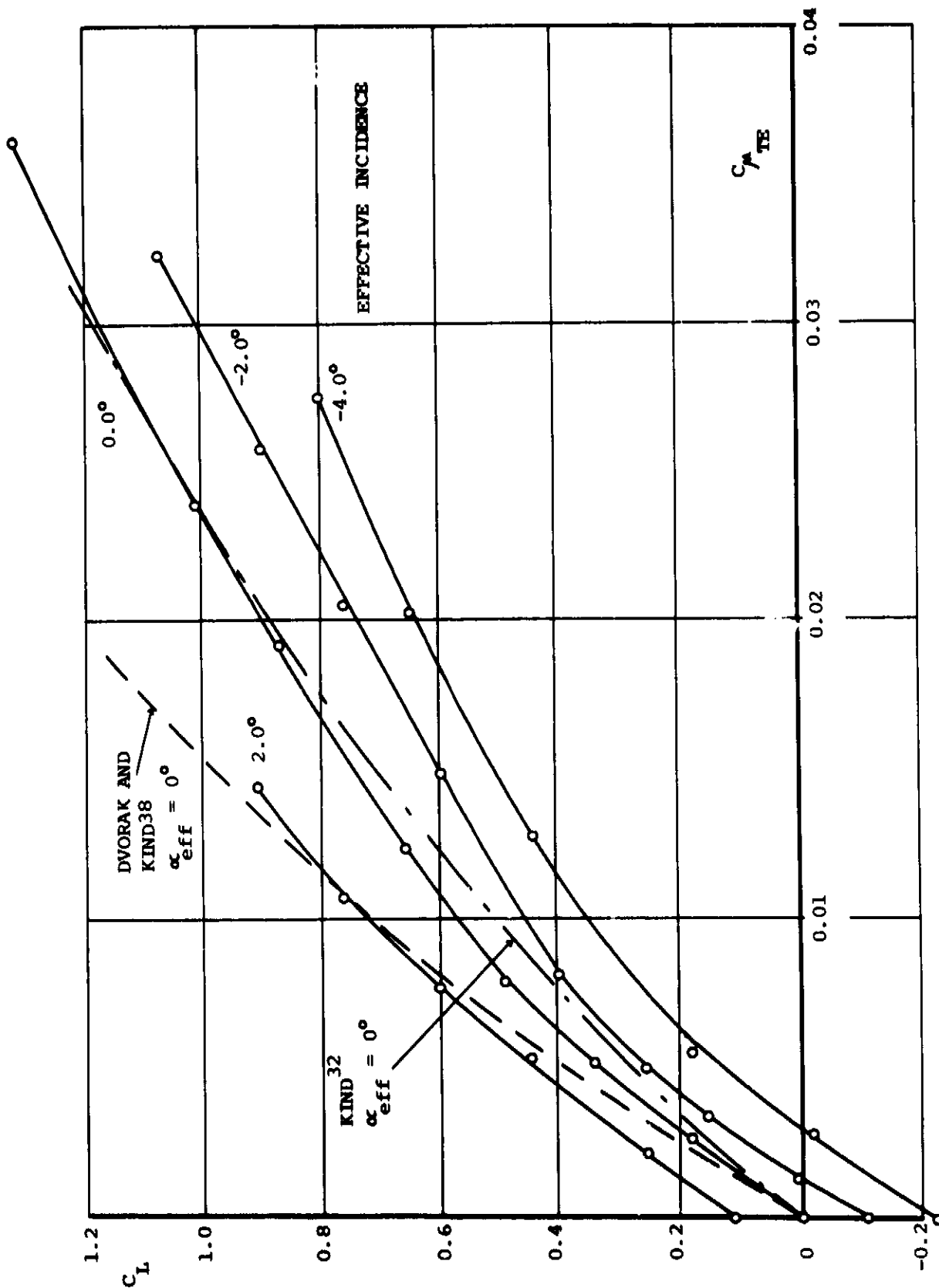


FIGURE 73: LIFTING PERFORMANCE OF THE AEROFOIL AS A FUNCTION OF EFFECTIVE INCIDENCE
FOR TRAILING EDGE BLOWING ONLY

FIG 74

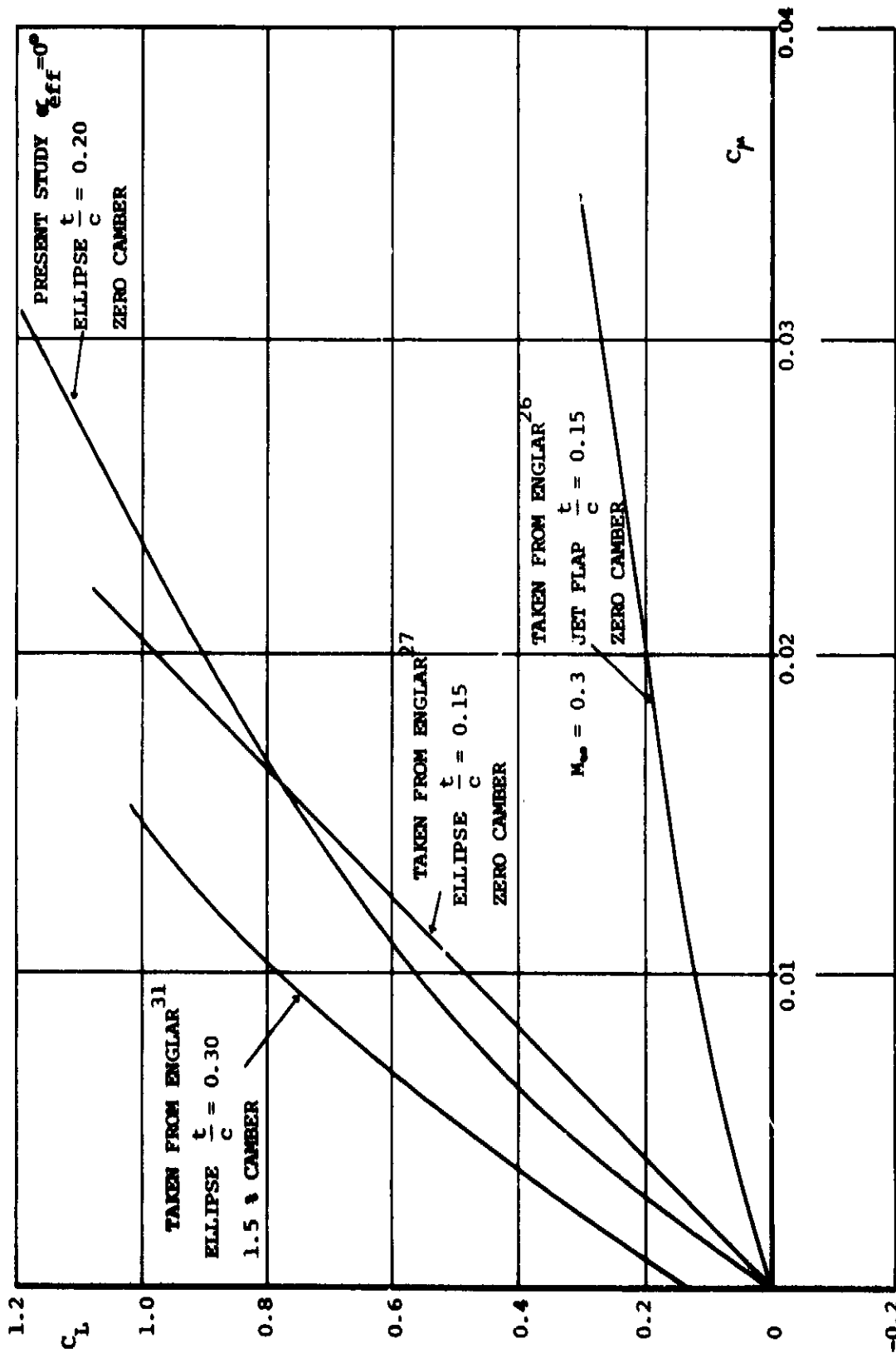


FIGURE 74: EXAMPLES OF THE LIFTING PERFORMANCE OF OTHER AEROFOILS COMPARED WITH THE PRESENT STUDY

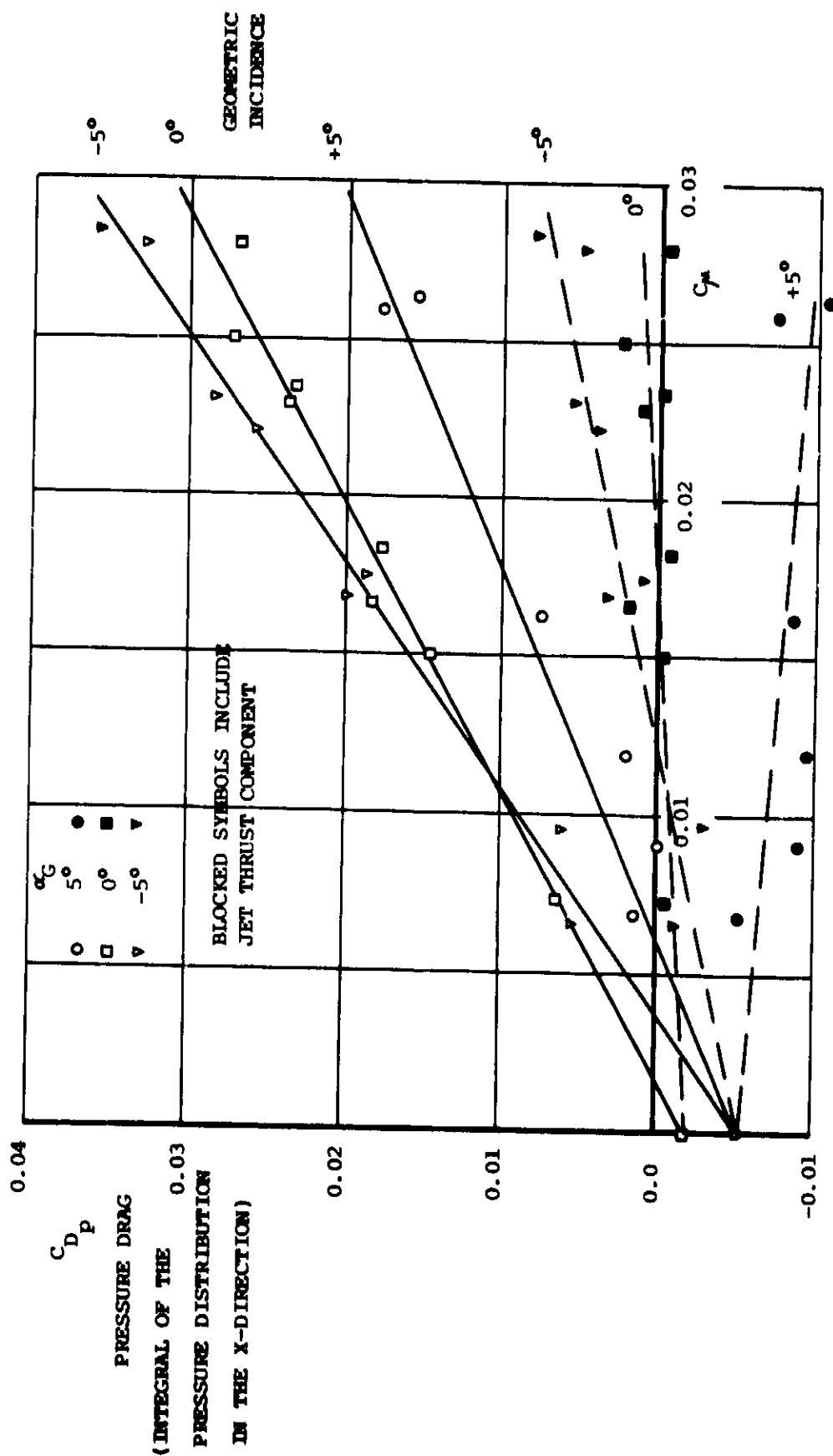


FIGURE 75: AEROFOIL PRESSURE DRAG COEFFICIENT WITH AND WITHOUT THE JET THRUST COMPONENT

FIG 76

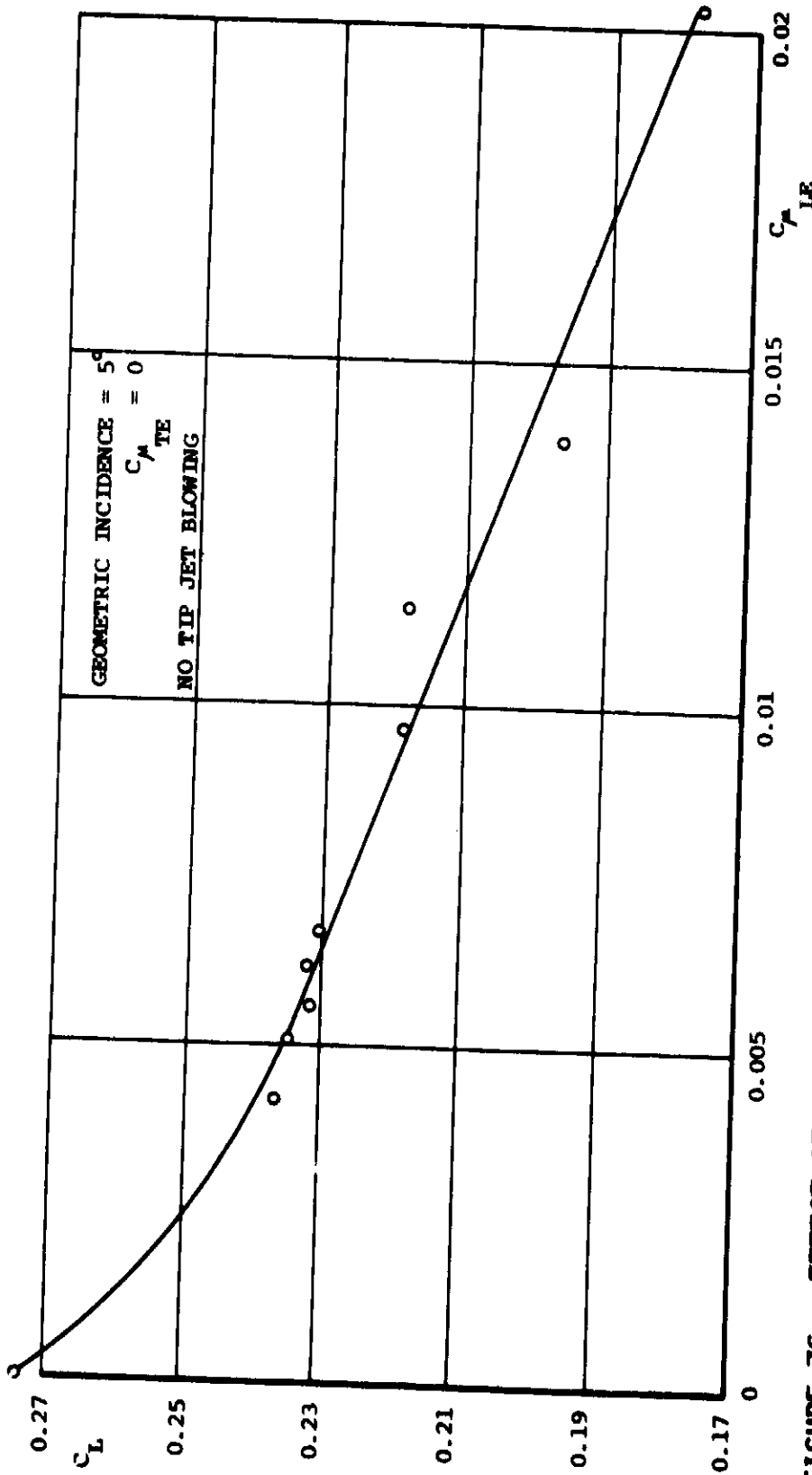


FIGURE 76: EFFECT OF LEADING EDGE BLOWING UPON THE CENTRELINE LIFT COEFFICIENT

FIG 77

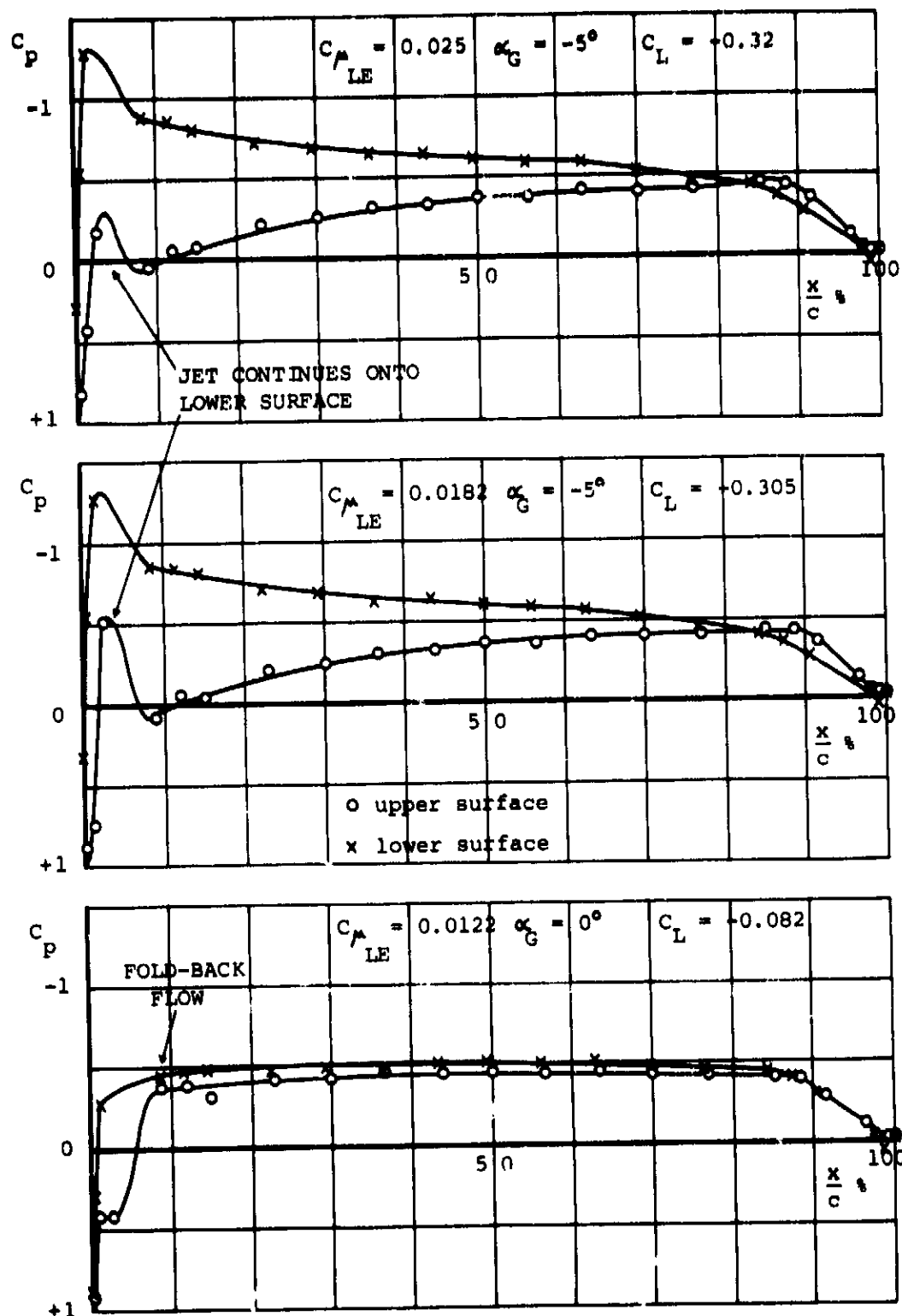
FIGURE 77: EXPERIMENTAL CENTRELINE PRESSURE DISTRIBUTIONS FOR LEADING EDGE BLOWING ONLY

FIG 78

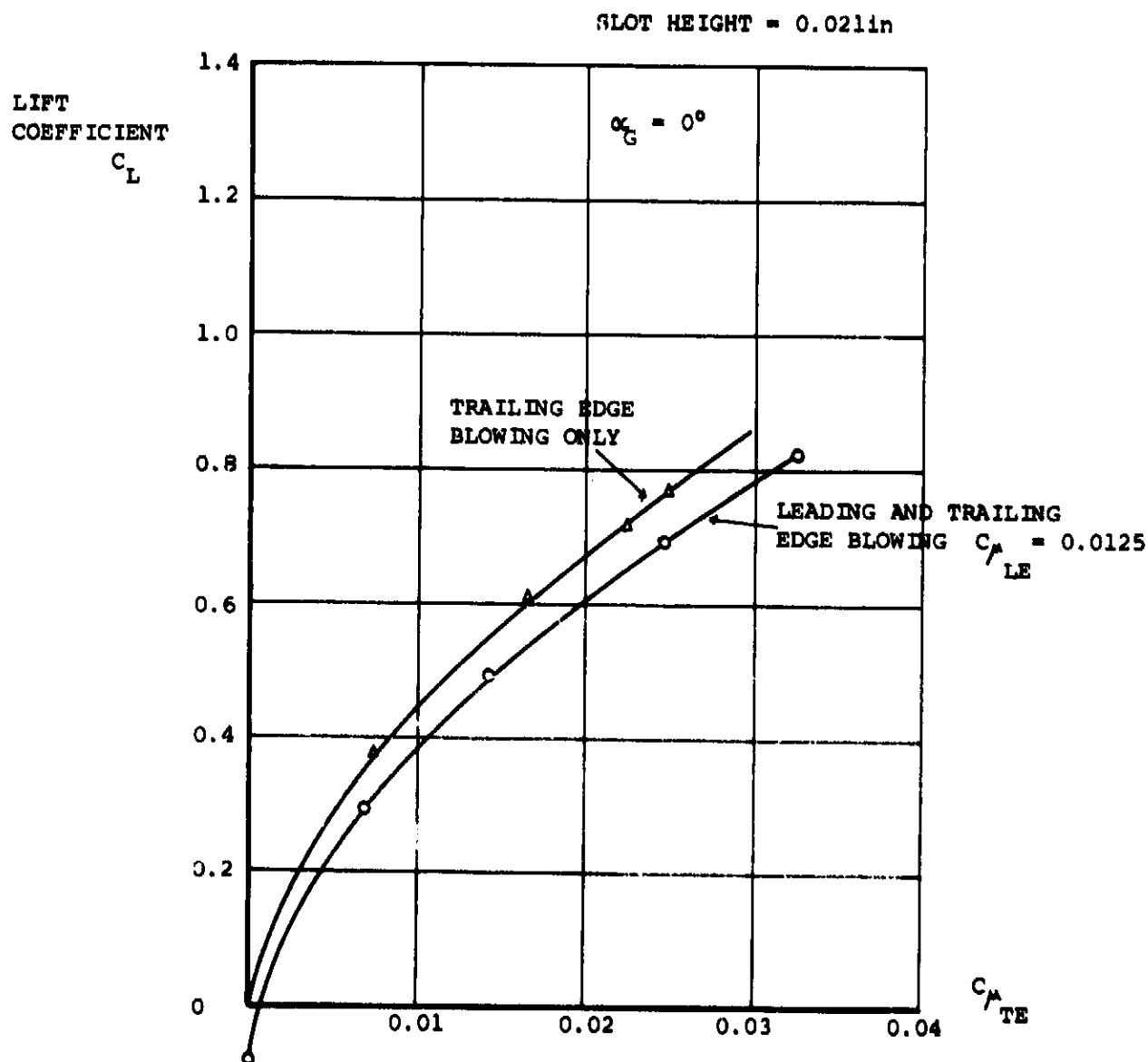


FIGURE 78: EFFECT OF SIMULTANEOUS LEADING AND TRAILING
EDGE BLOWING UPON LIFT COEFFICIENT

FIG 79A

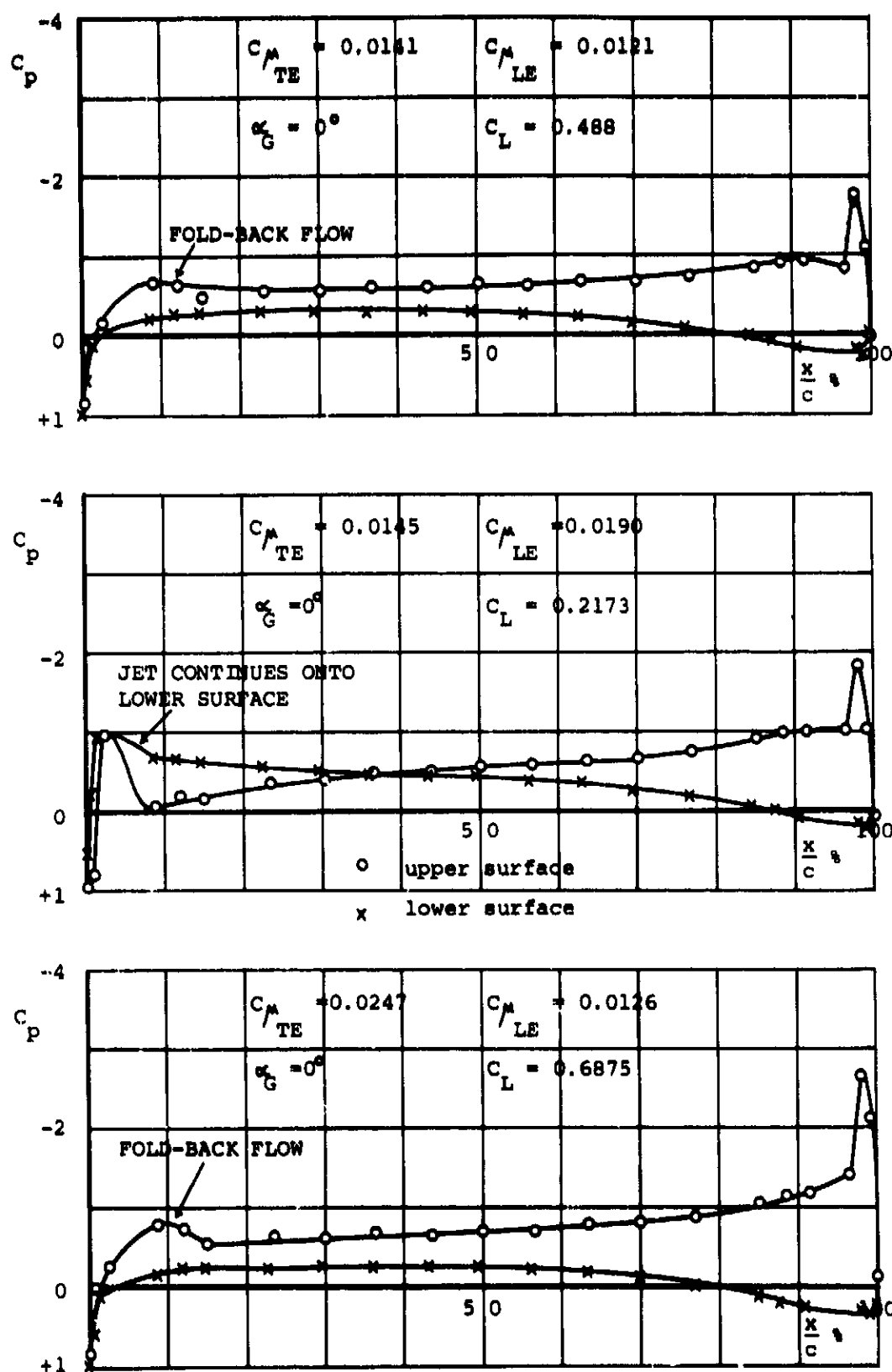
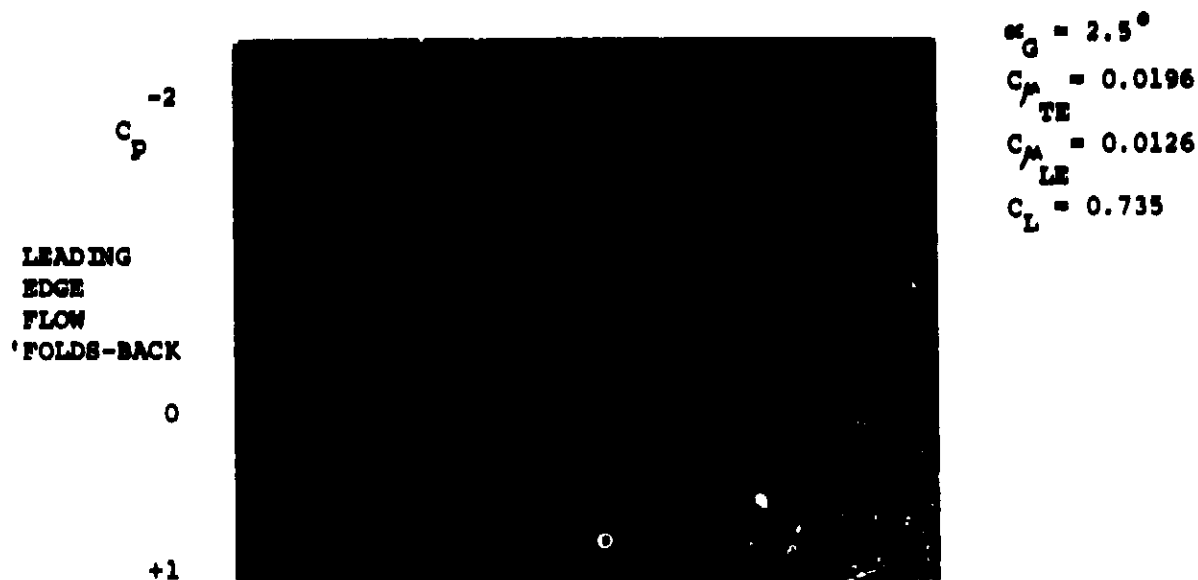


FIGURE 79A: EXPERIMENTAL CENTRELINE PRESSURE DISTRIBUTIONS
FOR SIMULTANEOUS LEADING AND TRAILING EDGE BLOWING

FIG 79B

ORIGINAL PAGE
BLACK AND WHITE PHOTOGRAPH



SOLID LINES INDICATE EXPERIMENTAL RESULTS
CROSSES INDICATE THE EFFECTIVE INCIDENCE CALCULATION



FIGURE 79B: EXPERIMENTAL CENTRELIN PRESSURE DISTRIBUTIONS
FOR LEADING AND TRAILING EDGE BLOWING

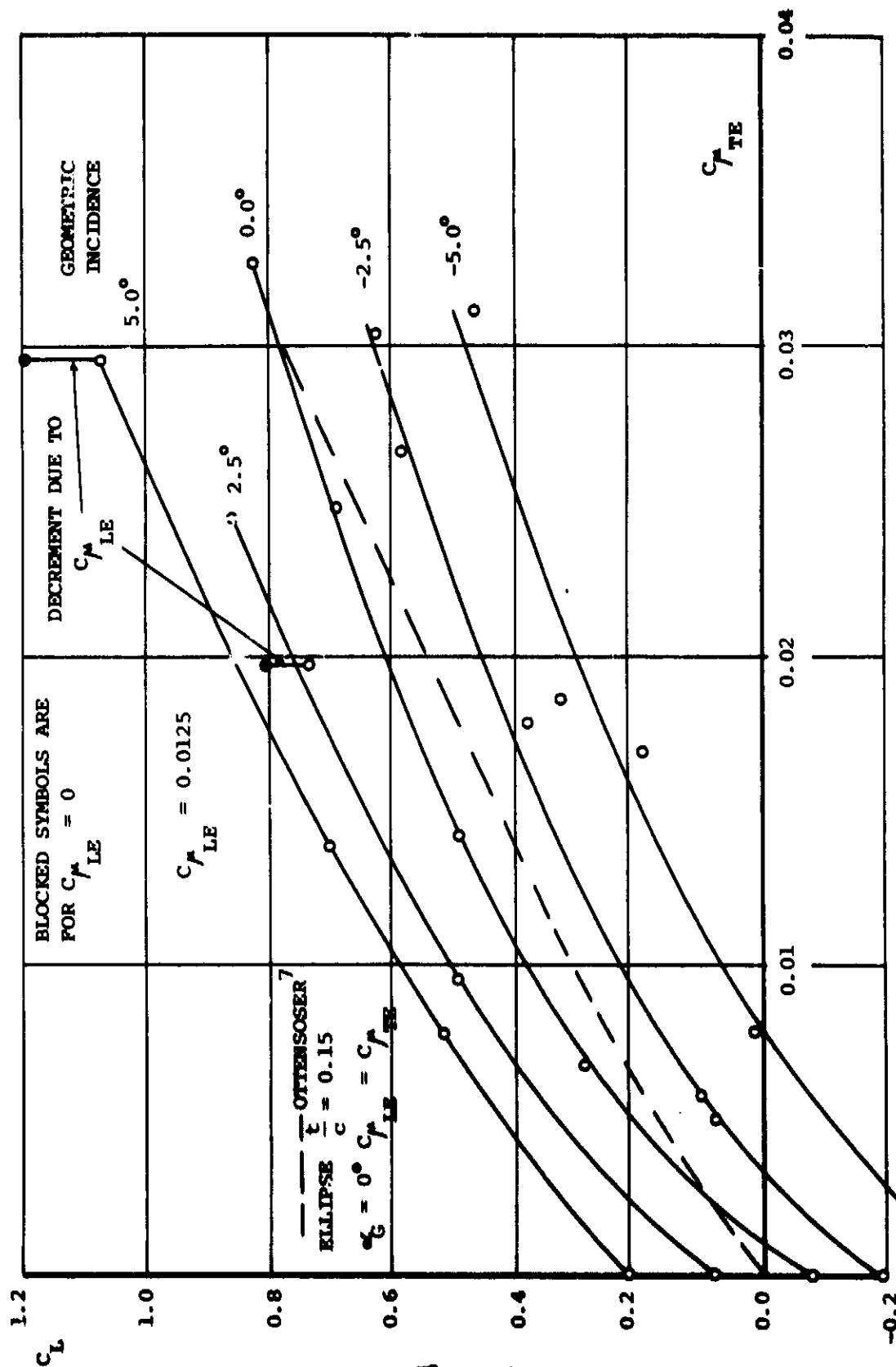
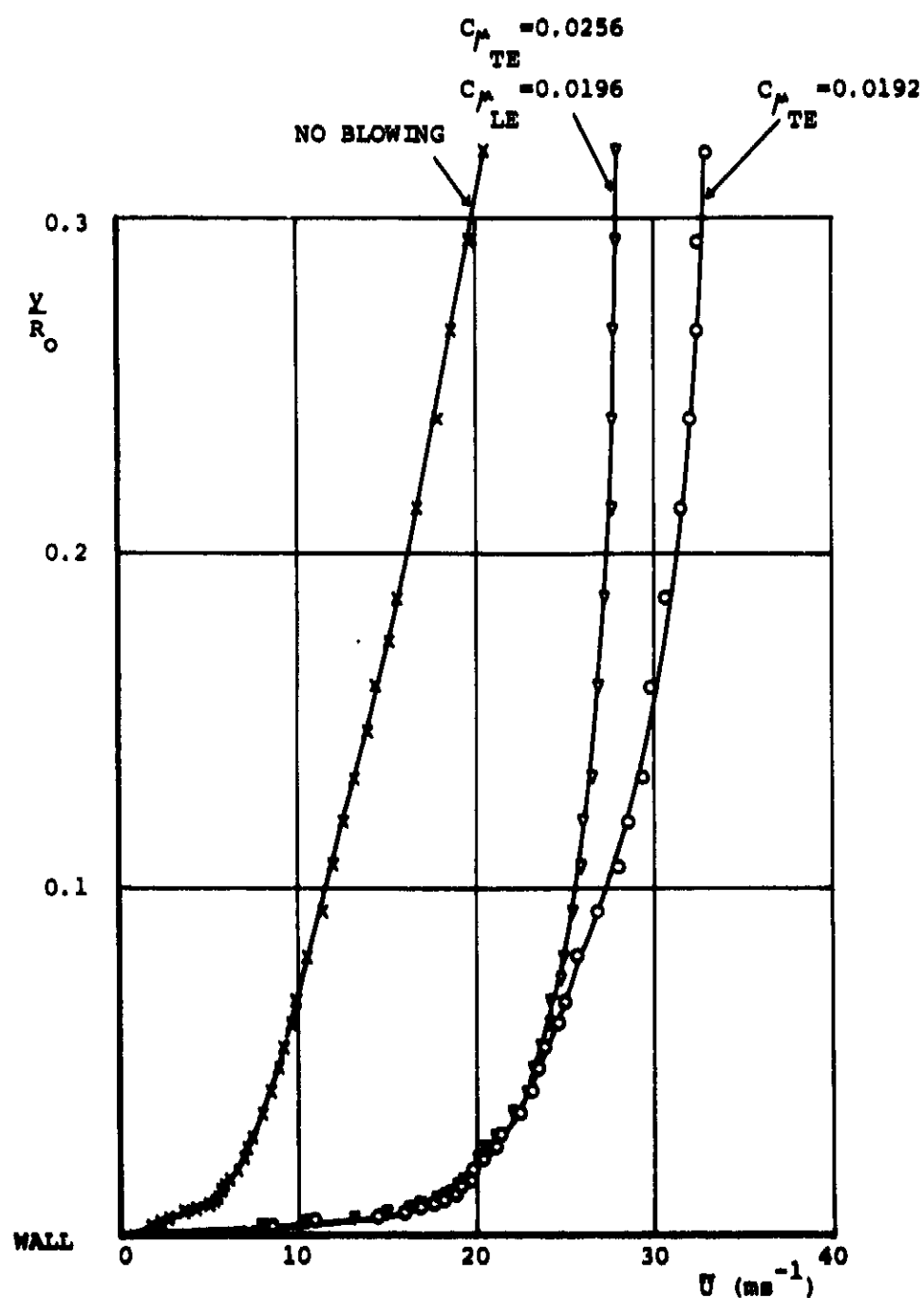


FIGURE 80: VARIATION OF LIFT COEFFICIENT WITH TRAILING EDGE BLOWING FOR A FIXED LEADING EDGE BLOWING RATE $C_{f_{LE}} = 0.0125$

FIG 81

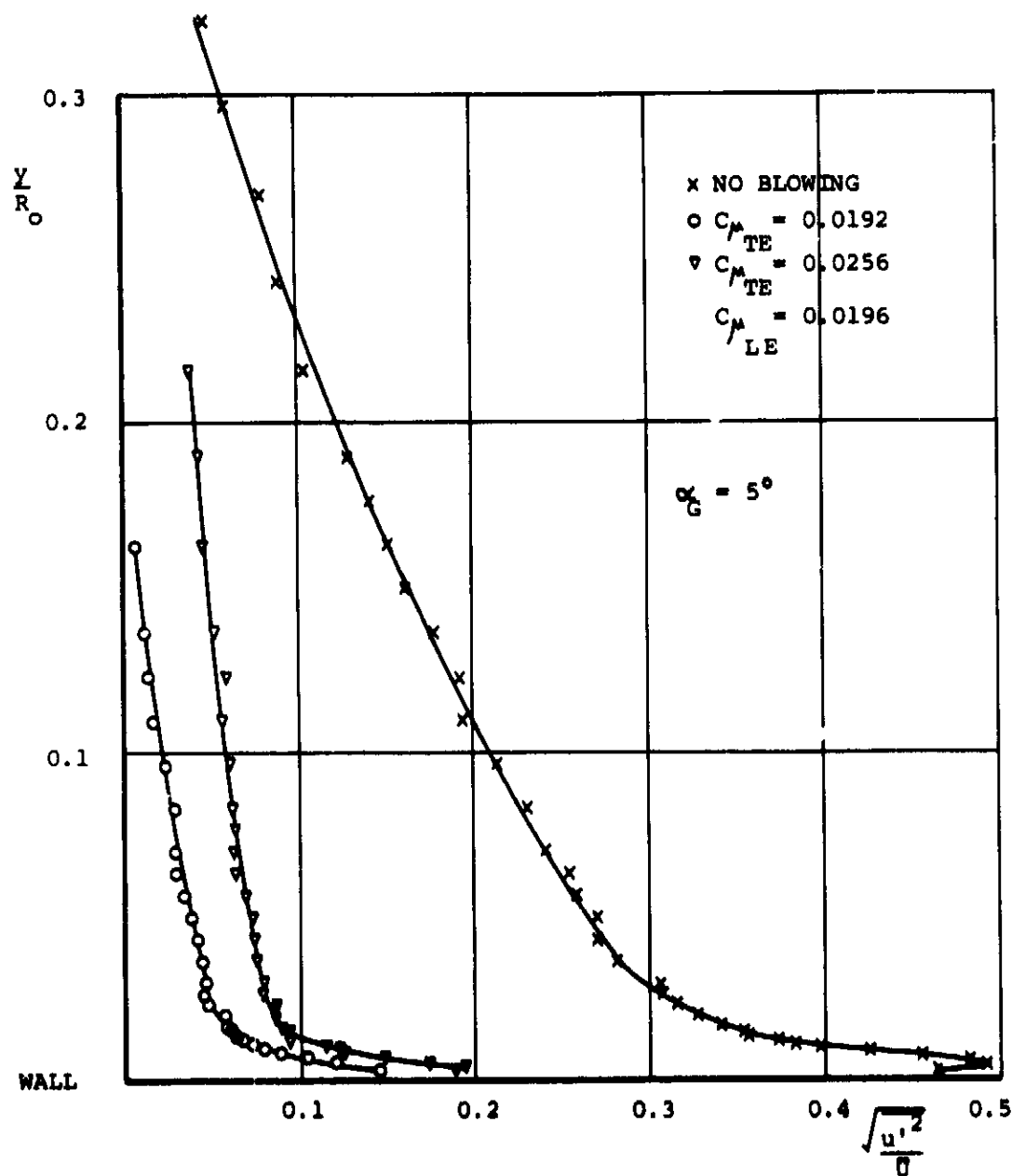


HOT WIRE RESULTS

$\alpha_0 = 5^\circ$

4 SLOTWIDTHS (0.084in, 2.1mm)
UPSTREAM OF SLOT

FIGURE 81: BOUNDARY LAYER VELOCITY PROFILES UPSTREAM OF SLOT



HOT WIRE RESULTS
 4 SLOTWIDTHS (0.084in, 2.1mm)
 UPSTREAM OF SLOT

FIGURE 82: LONGITUDINAL TURBULENCE INTENSITY THROUGH THE BOUNDARY LAYER UPSTREAM OF THE SLOT

FIG 83

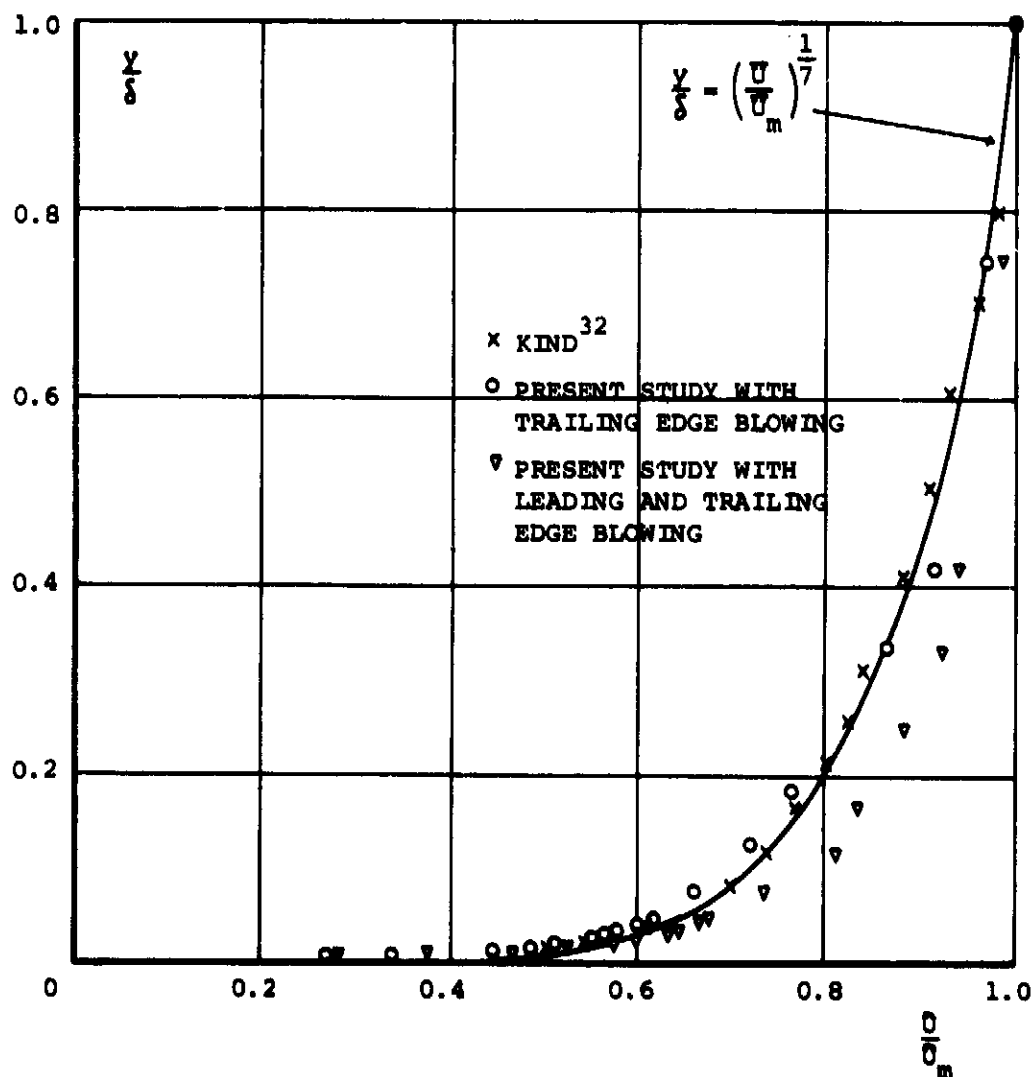
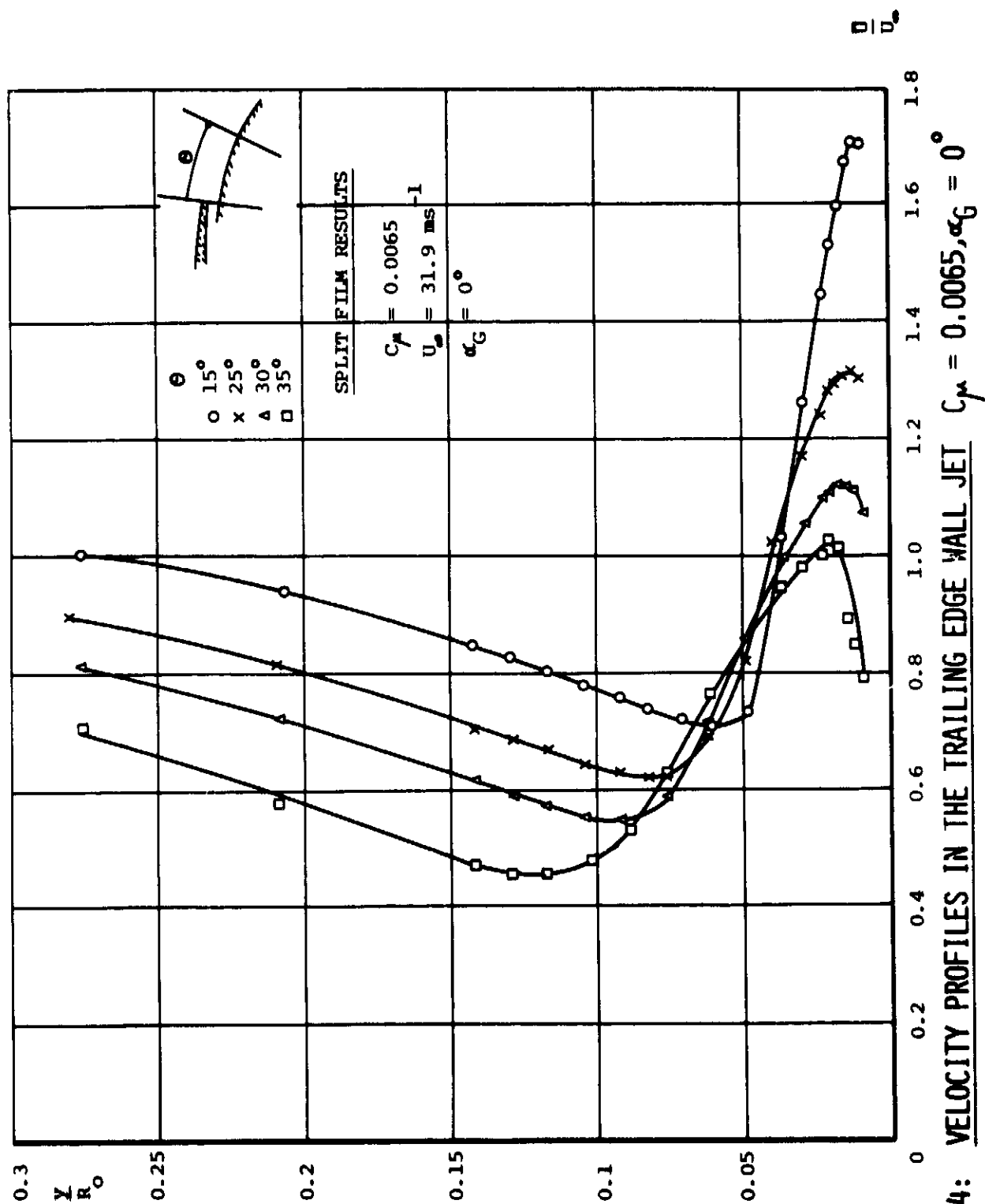


FIGURE 83: VELOCITY PROFILES IN THE BOUNDARY LAYER UPSTREAM OF THE SLOT COMPARED WITH $\frac{y}{\delta} = \left(\frac{u}{U_m}\right)^{\frac{1}{7}}$



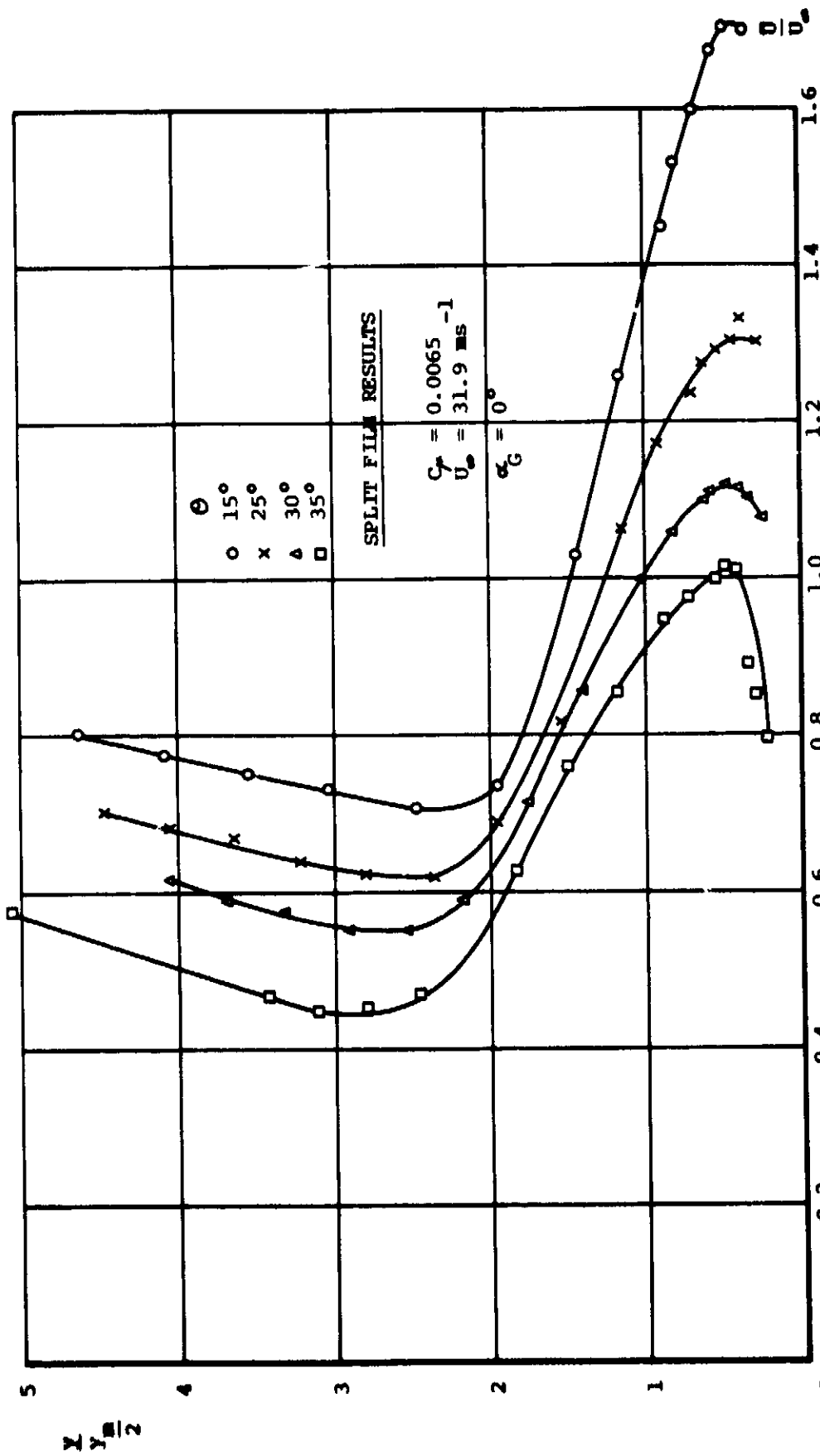


FIGURE 85: VELOCITY PROFILES IN THE TRAILING EDGE WALL JET AS A FUNCTION OF THE HALF VELOCITY POINT y_m , $C_p = 0.0065$, $\alpha_G = 0^\circ$

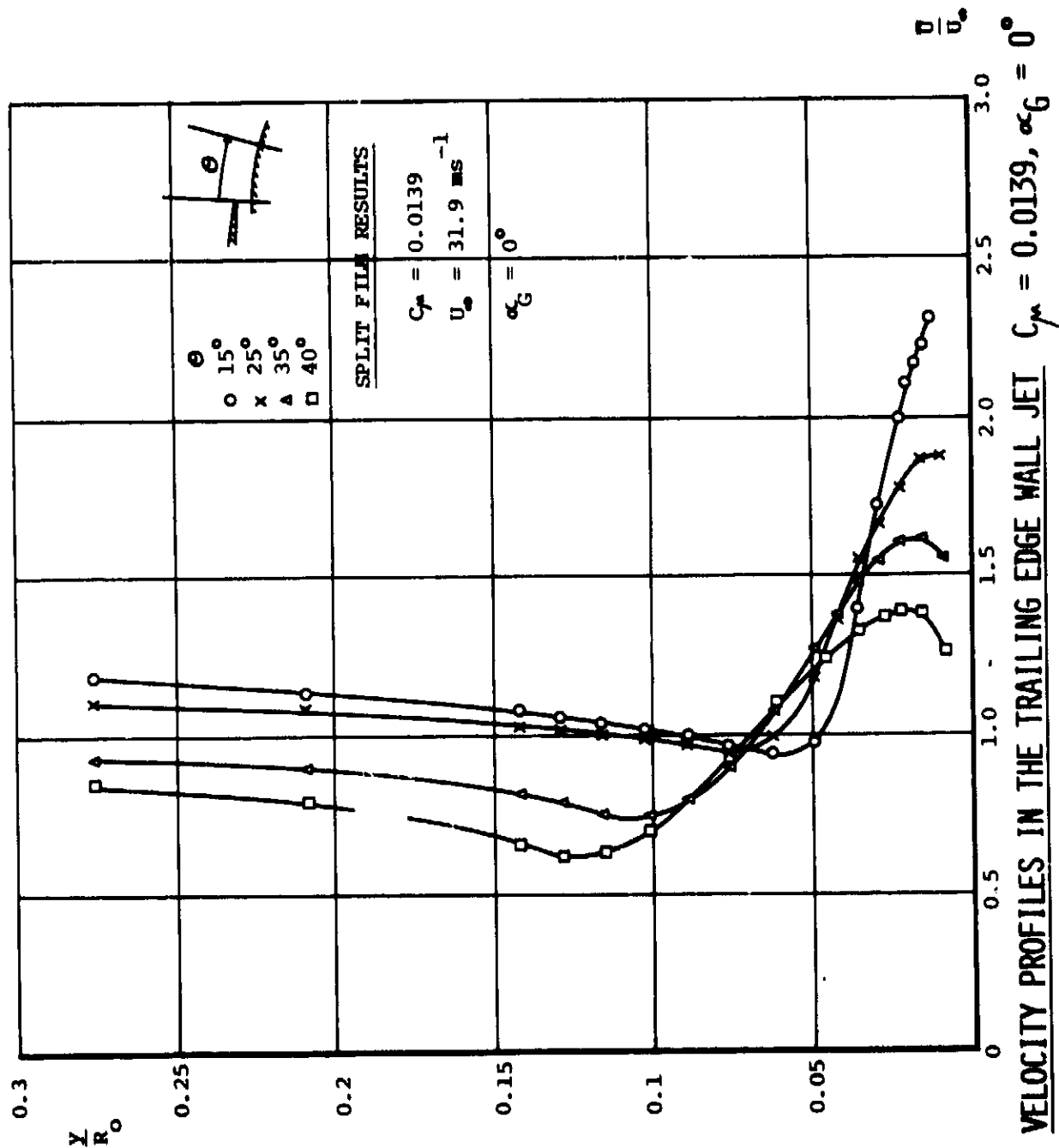
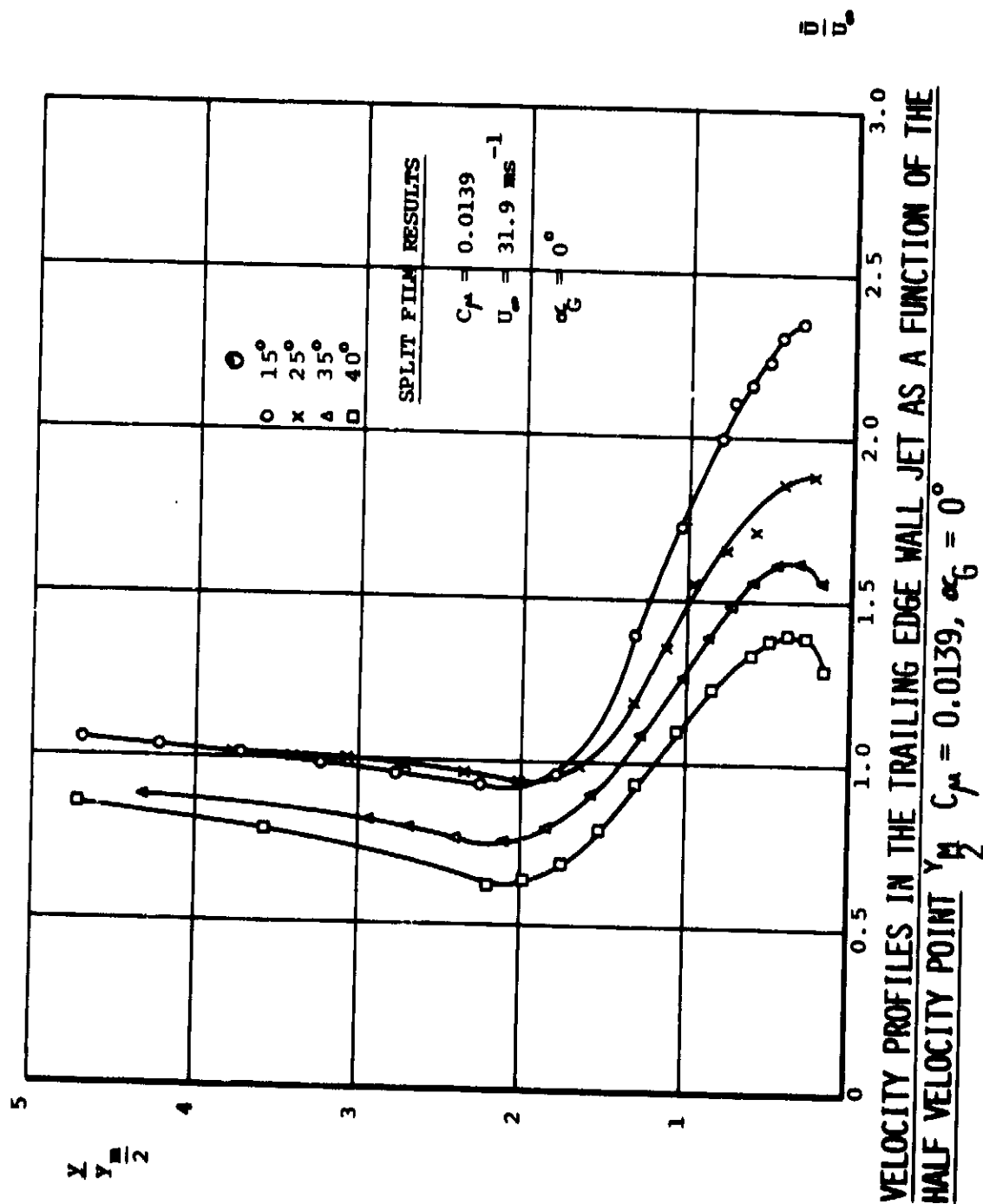
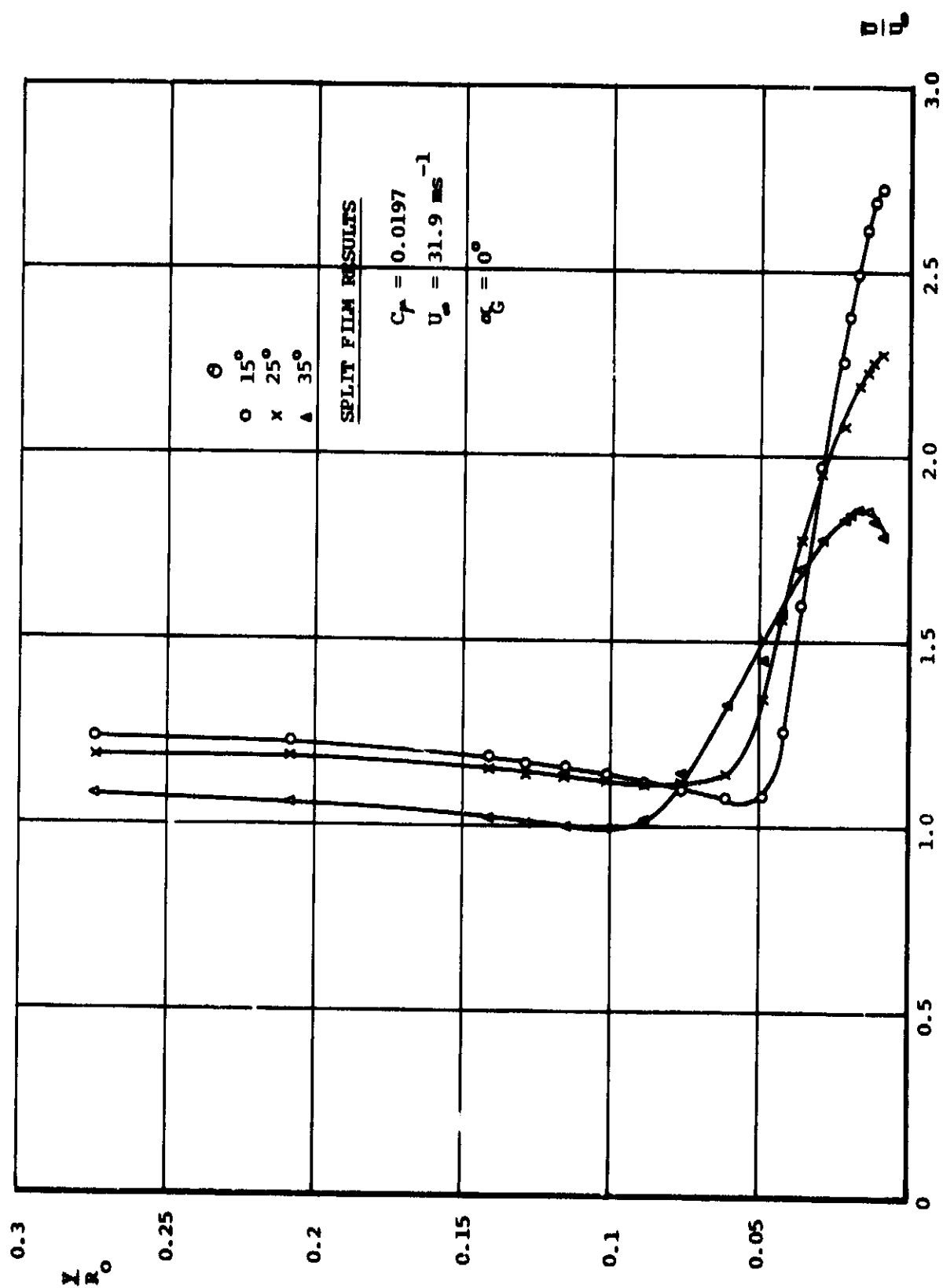


FIGURE 86: VELOCITY PROFILES IN THE TRAILING EDGE WALL JET $C_\mu = 0.0139, \alpha_G = 0^\circ$




 FIGURE 88. VELOCITY PROFILES IN THE TRAILING EDGE WALL JET $C_f = 0.0197$, $\alpha_G = 0^\circ$

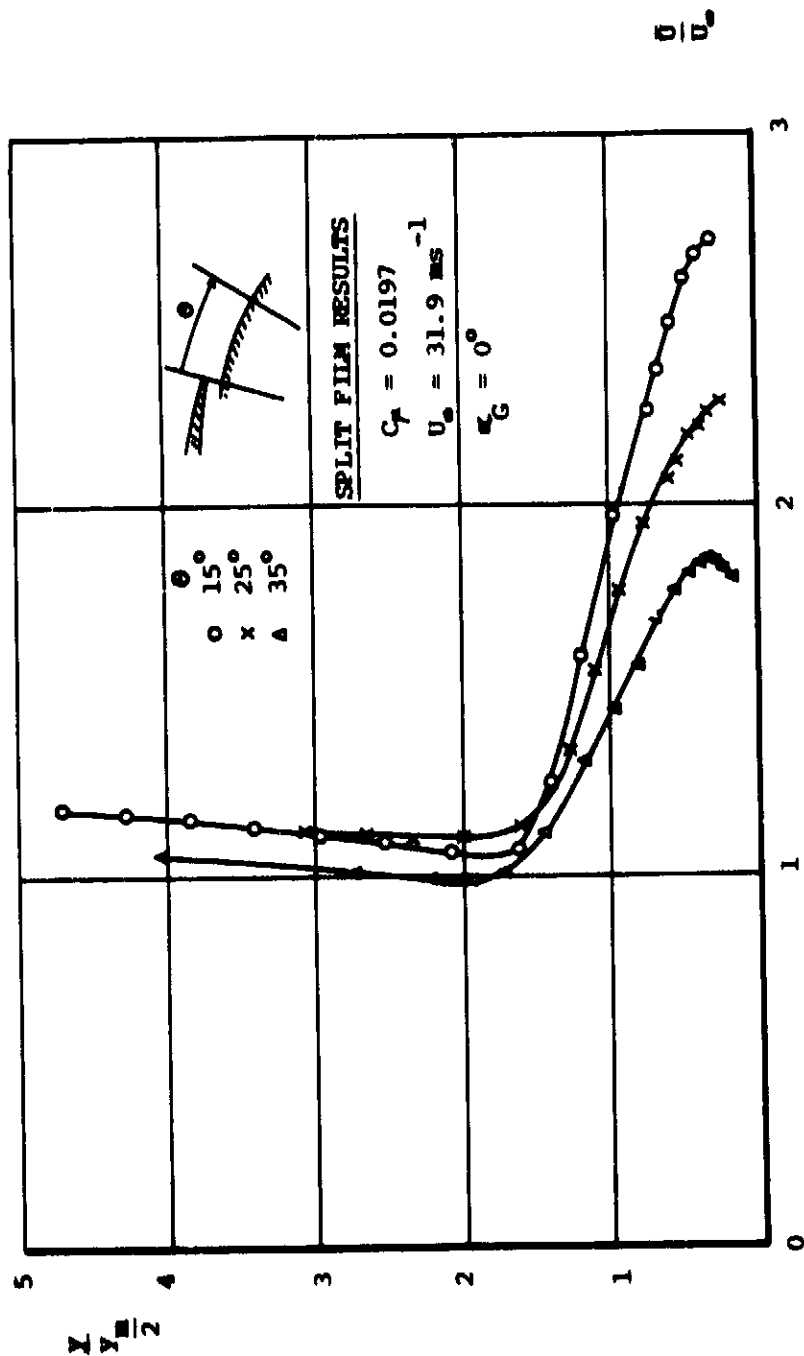


FIGURE 89: VELOCITY PROFILES IN THE TRAILING EDGE WALL JET AS A FUNCTION OF THE HALF VELOCITY POINT Y_m $C_f = 0.0197$, $\alpha_G = 0^\circ$

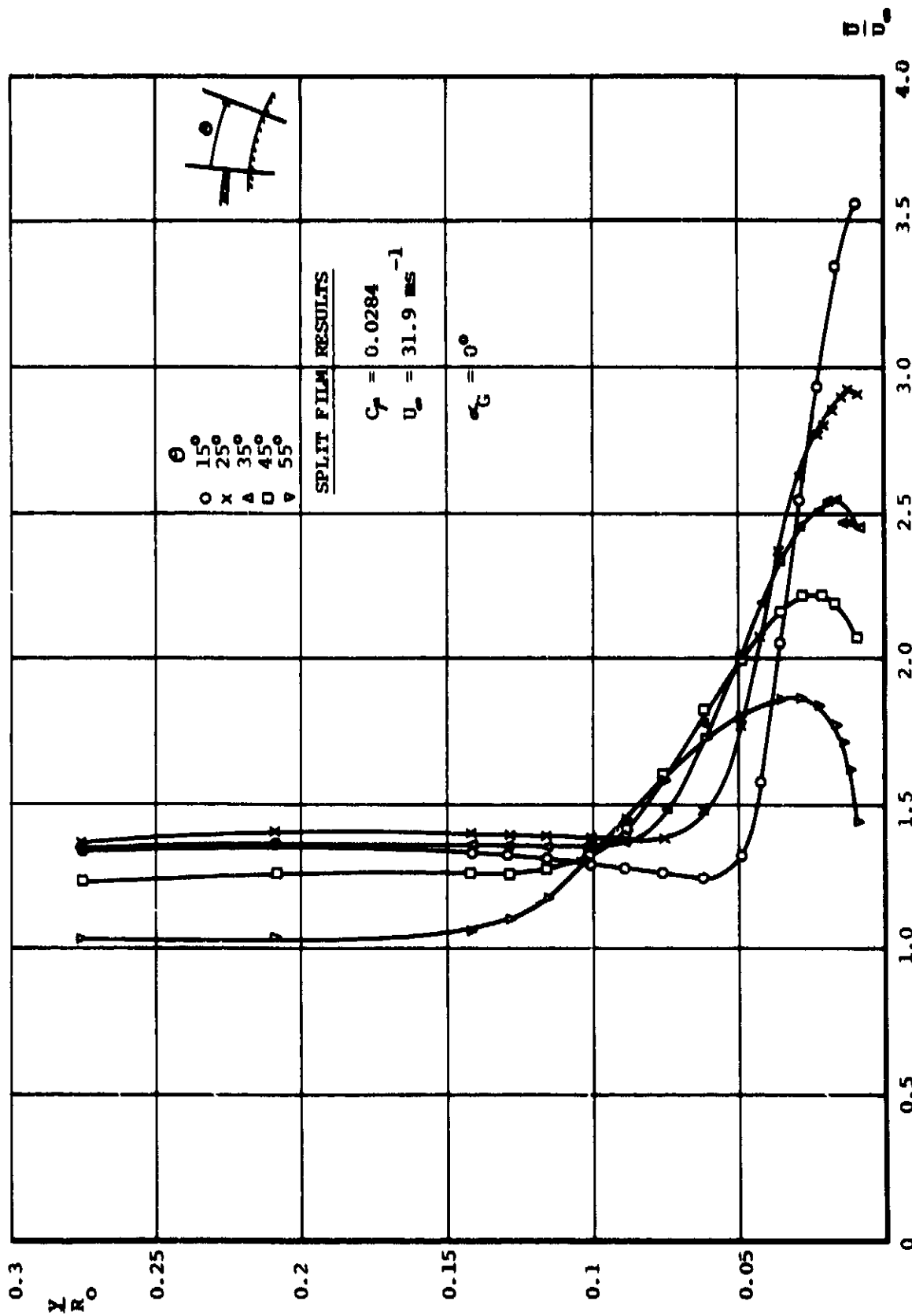


FIGURE 90: VELOCITY PROFILES IN THE TRAILING EDGE WALL JET $C_f = 0.0284$, $\alpha_G = 0^\circ$

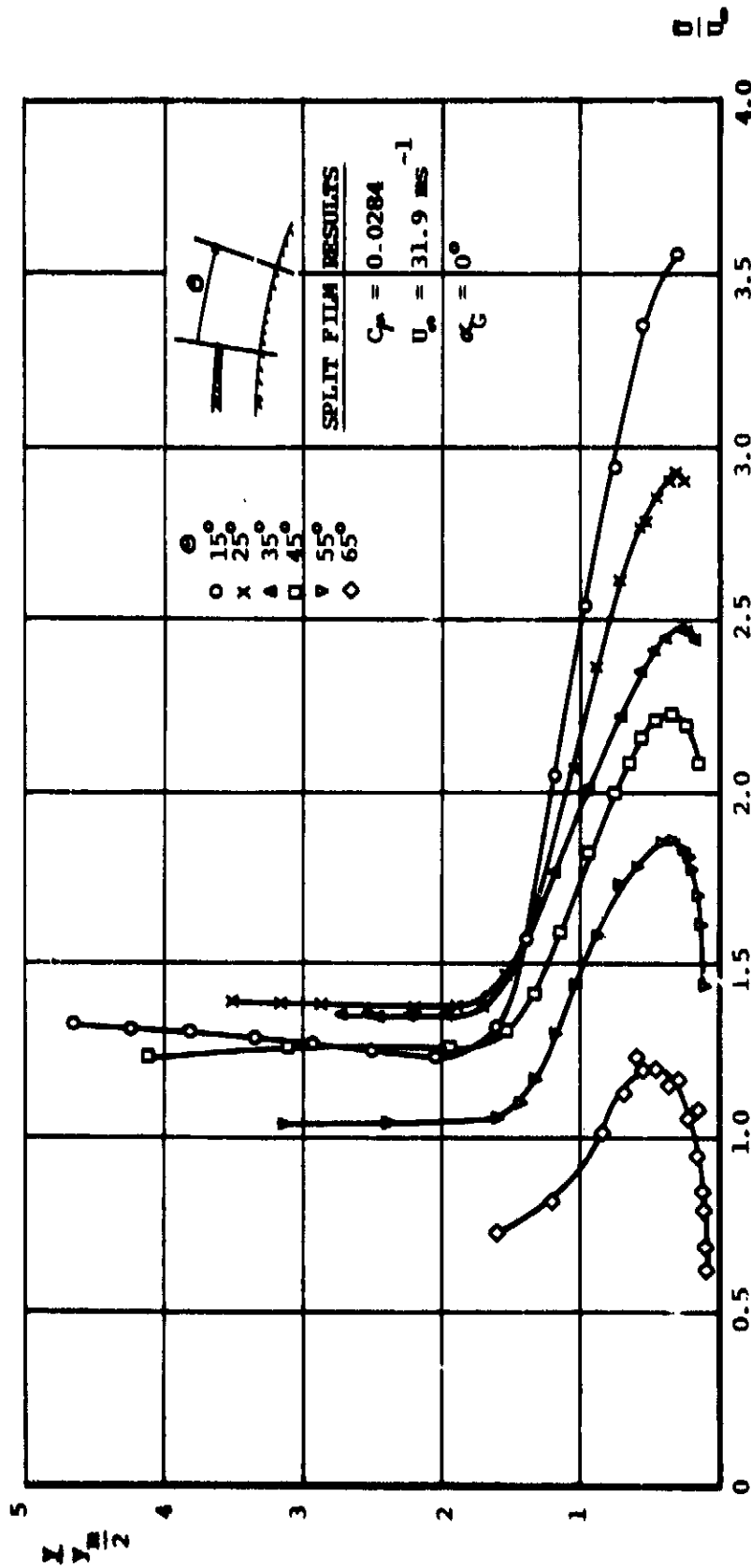


FIGURE 91: VELOCITY PROFILES IN THE TRAILING EDGE WALL JET AS A FUNCTION OF THE HALF VELOCITY POINT Y_m $C_p = 0.0284$, $\alpha_G = 0^\circ$

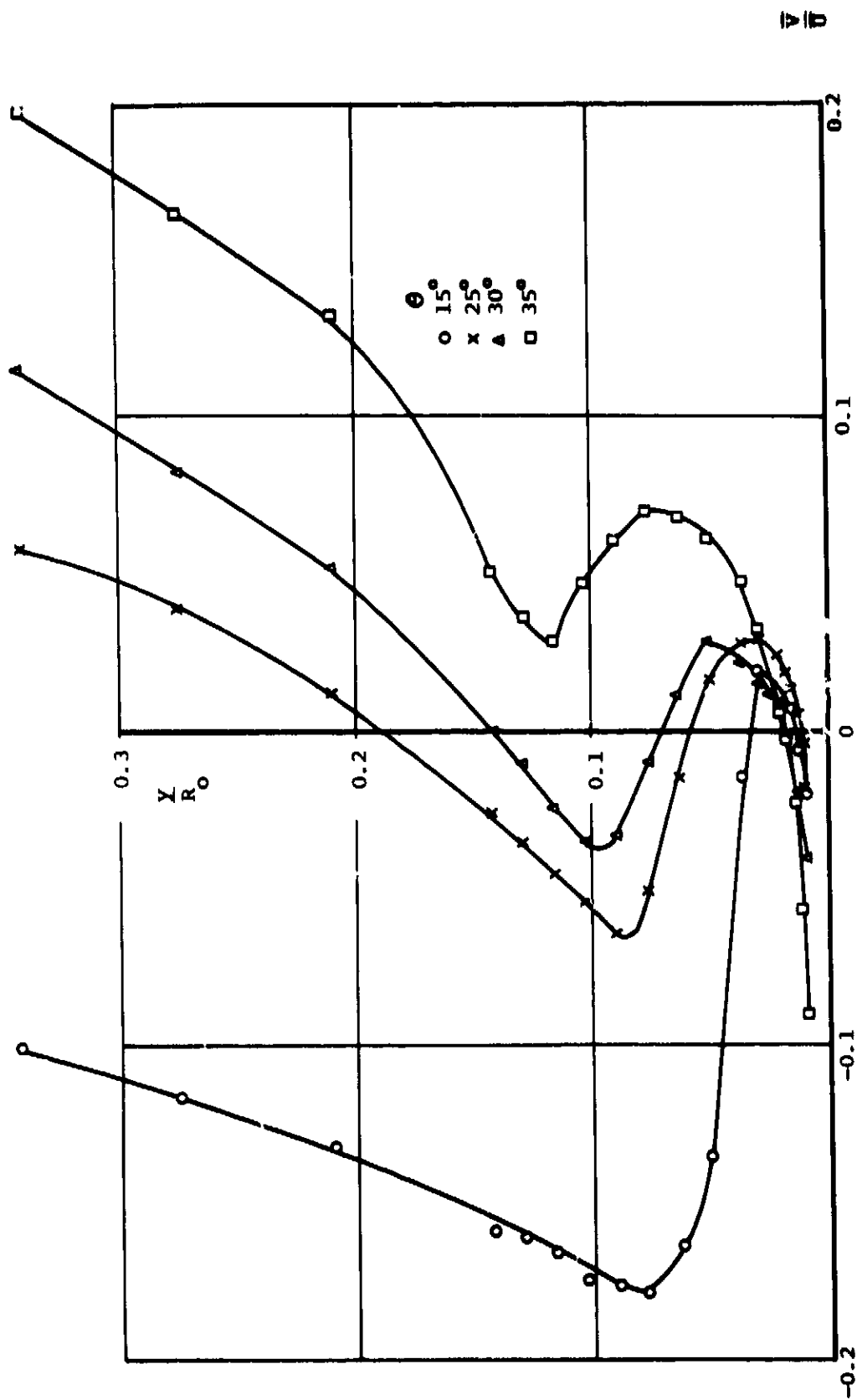


FIGURE 92: LOCAL FLOW ANGLE IN THE TRAILING EDGE WAKE JET $C_\mu = 0.0065$, $\alpha_G = 0^\circ$

FIG 93

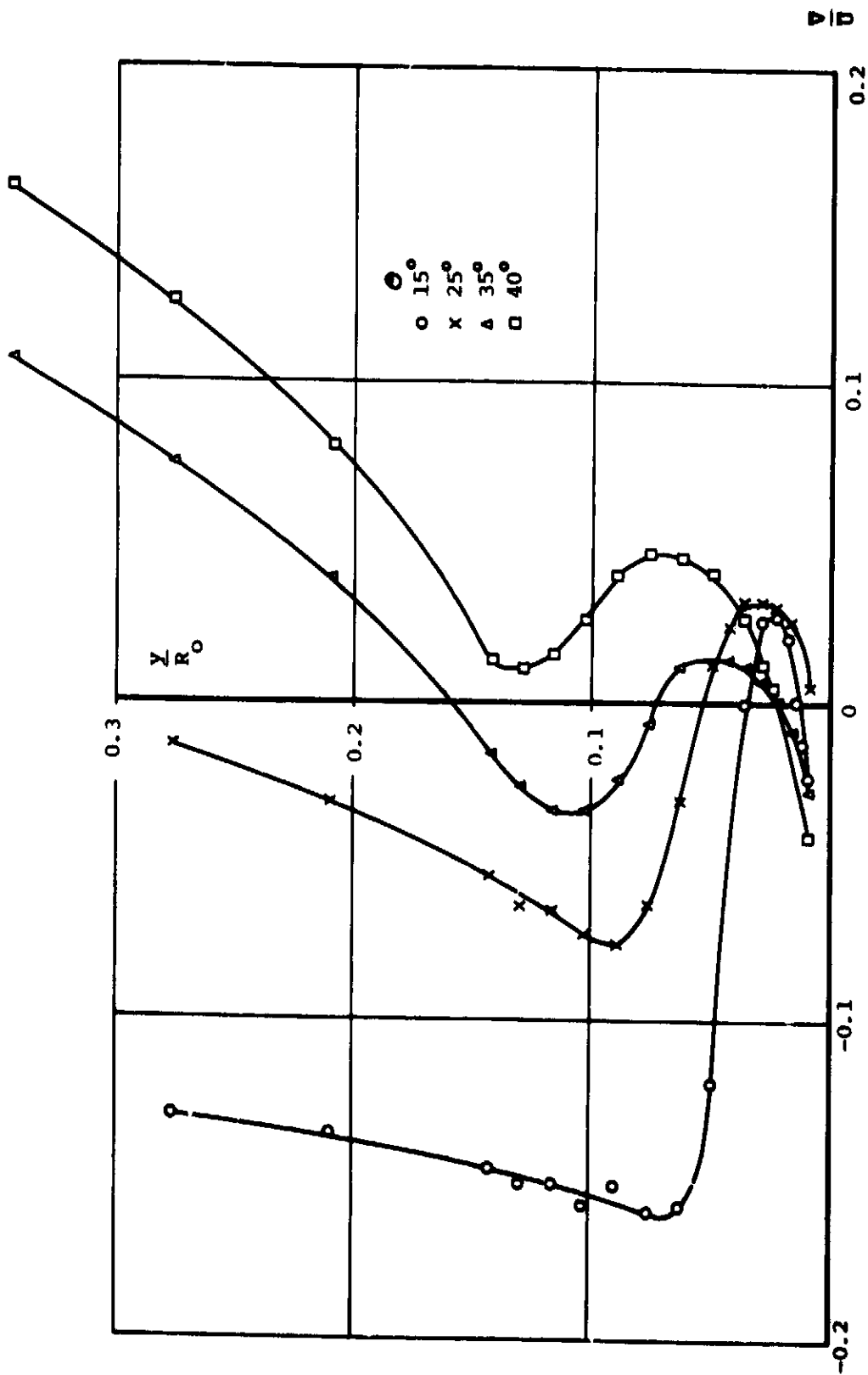


FIGURE 93: LOCAL FLOW ANGLE IN THE TRAILING EDGE WALL JET $C_f = 0.0139$, $\alpha_G = 0^\circ$

FIG 94

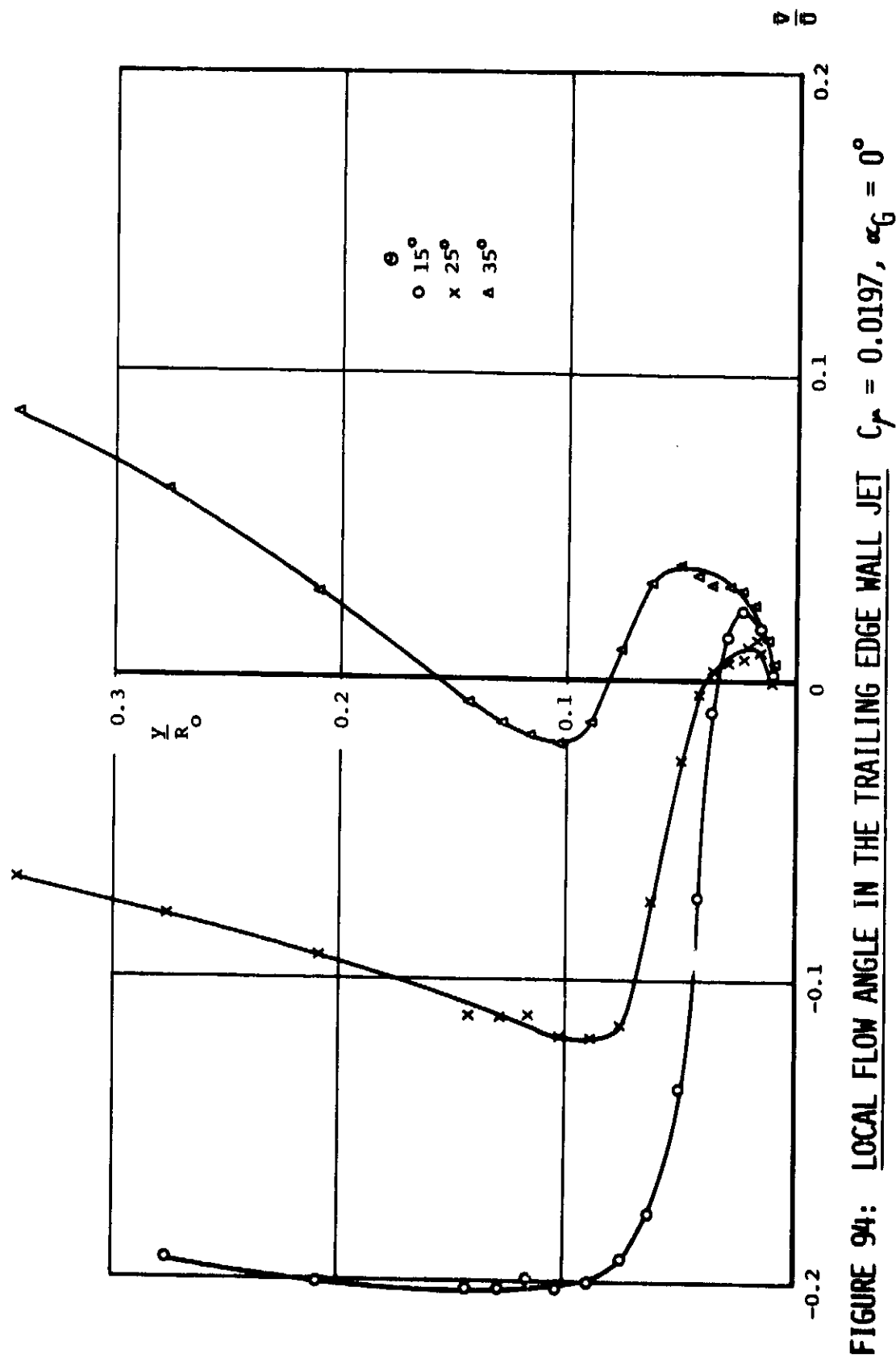


FIGURE 94: LOCAL FLOW ANGLE IN THE TRAILING EDGE WALL JET $C_p = 0.0197$, $\alpha_G = 0^\circ$

FIG 95

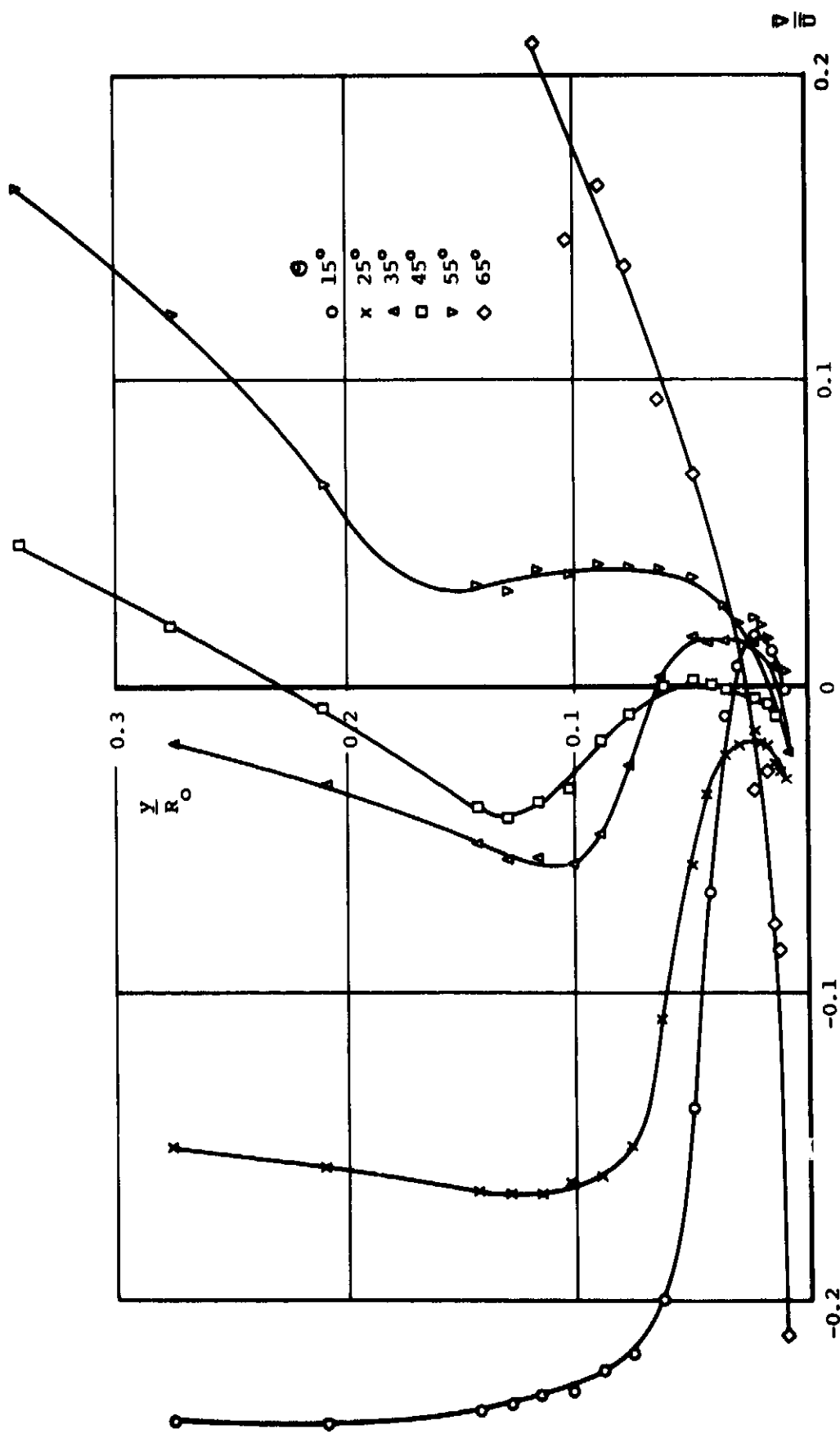


FIGURE 95: LOCAL FLOW ANGLE IN THE TRAILING EDGE WALL JET $C_{\mu} = 0.0284$, $\alpha_G = 0^\circ$

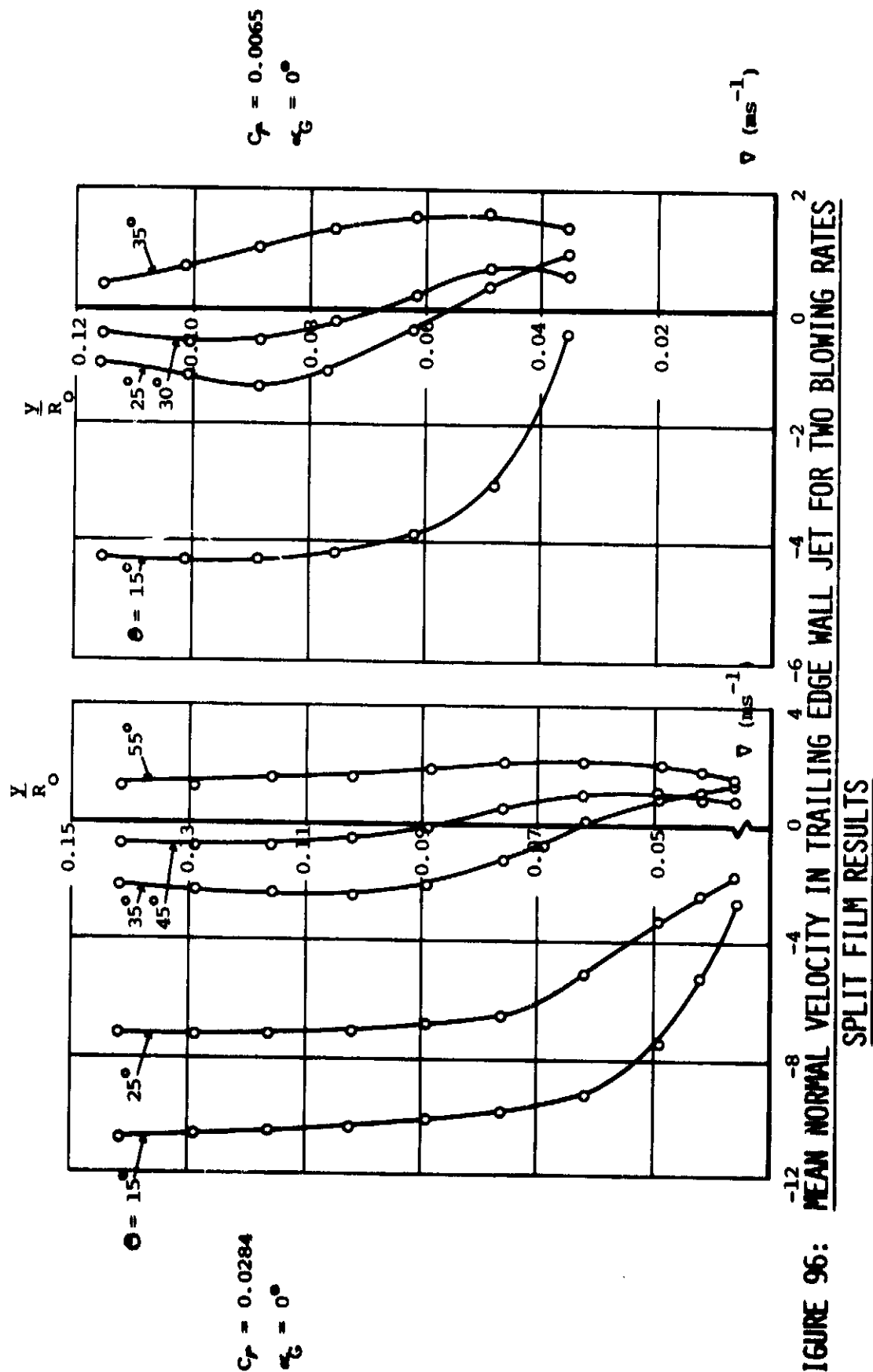


FIGURE 96: MEAN NORMAL VELOCITY IN TRAILING EDGE WALL JET FOR TWO BLOWING RATES
 SPLIT FILM RESULTS

FIG 97A

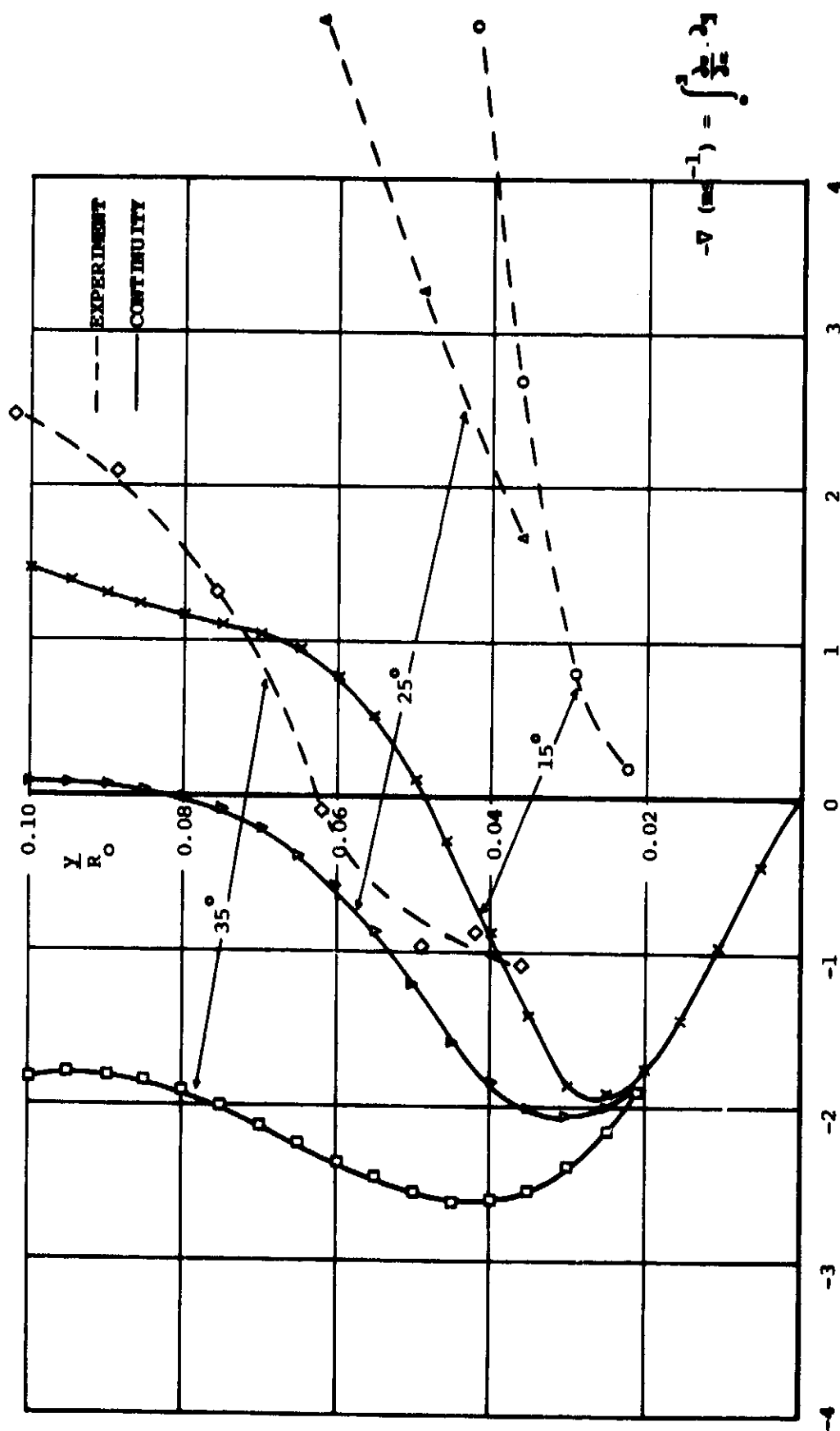


FIGURE 97A: COMPARISON OF EXPERIMENT WITH CONTINUITY IN PREDICTION OF MEAN NORMAL
VELOCITY \bar{V} $C_F = 0.0284$, $\sigma_G = 0$

FIG 97B

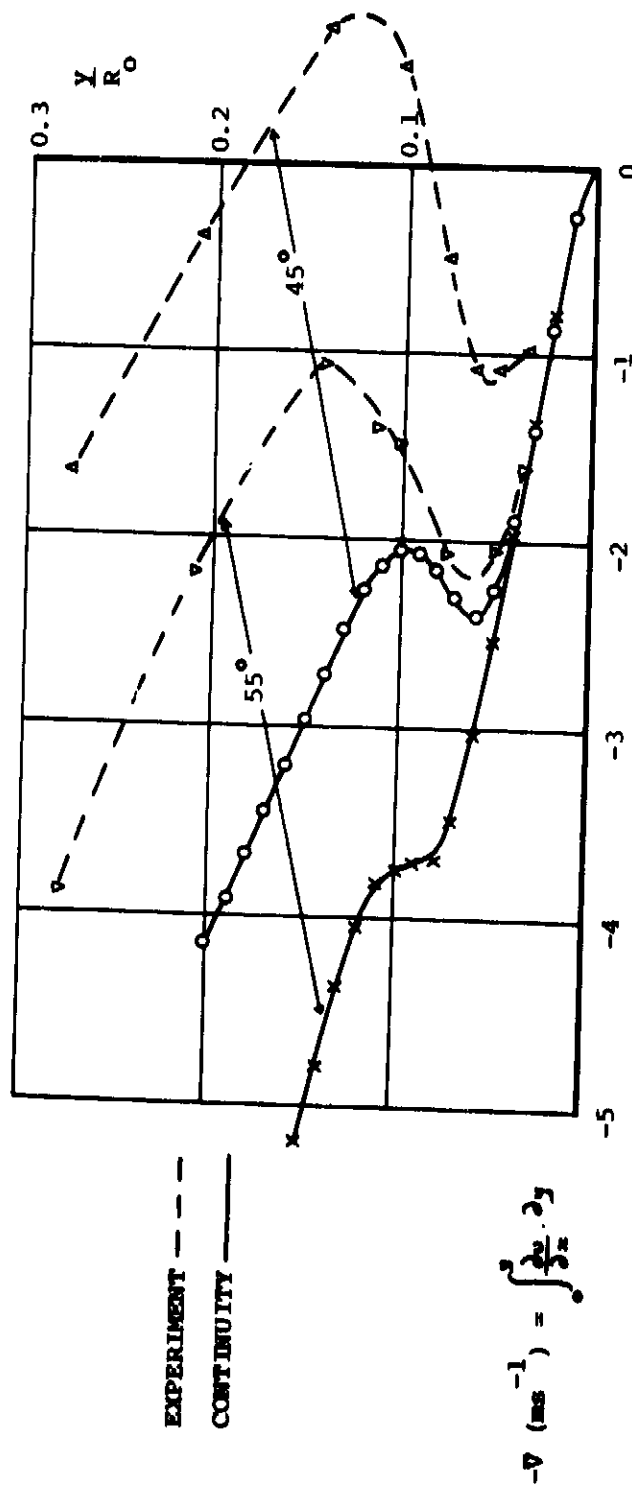


FIGURE 97B: COMPARISON OF EXPERIMENT WITH CONTINUITY IN PREDICTION OF MEAN NORMAL
VELOCITY V $C_{\mu} = 0.0284$, $\alpha_G = 0^\circ$

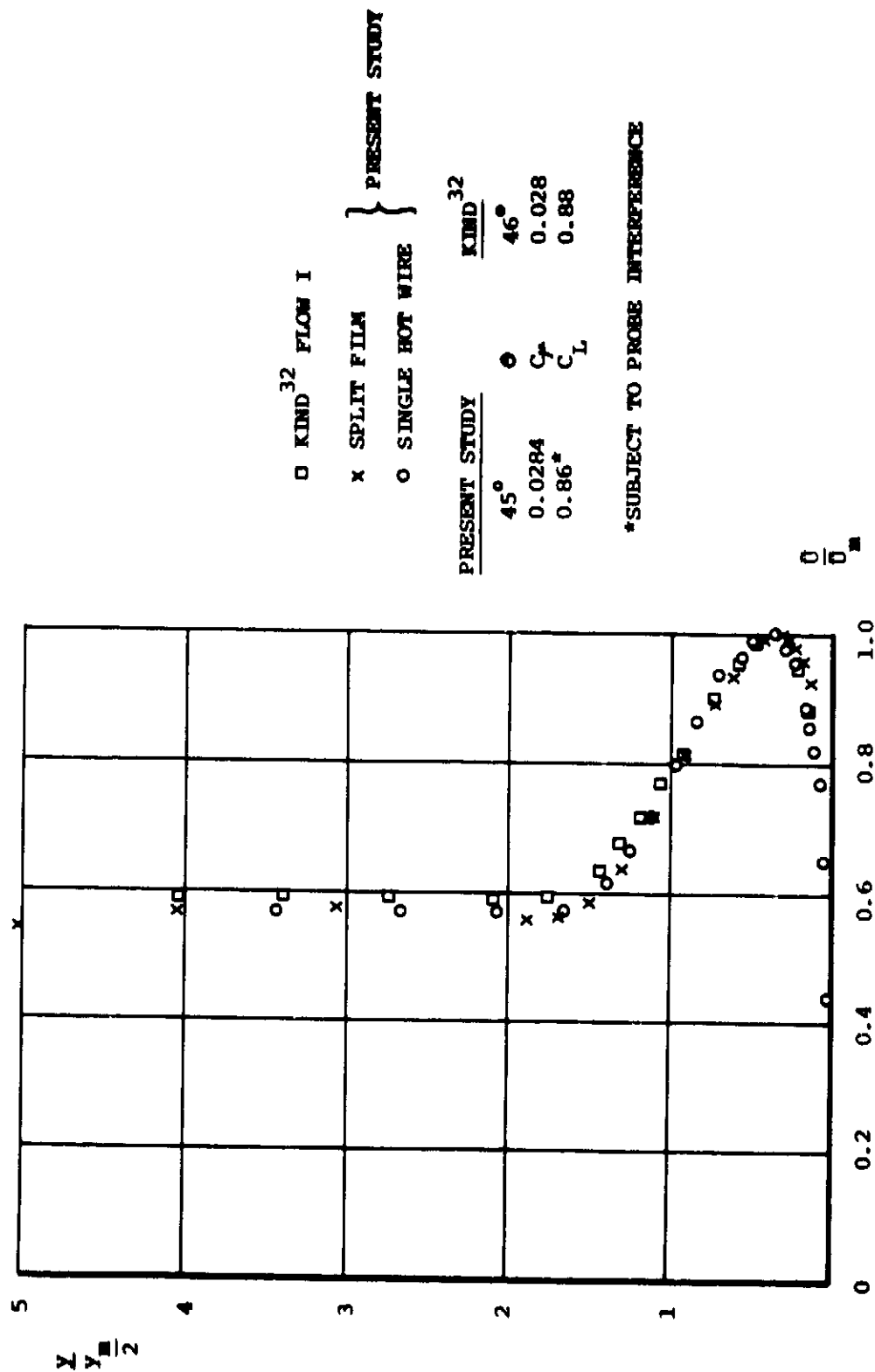


FIGURE 38: NON-DIMENSIONAL VELOCITY PROFILE COMPARISON WITH KIND ³²

FIG 99A

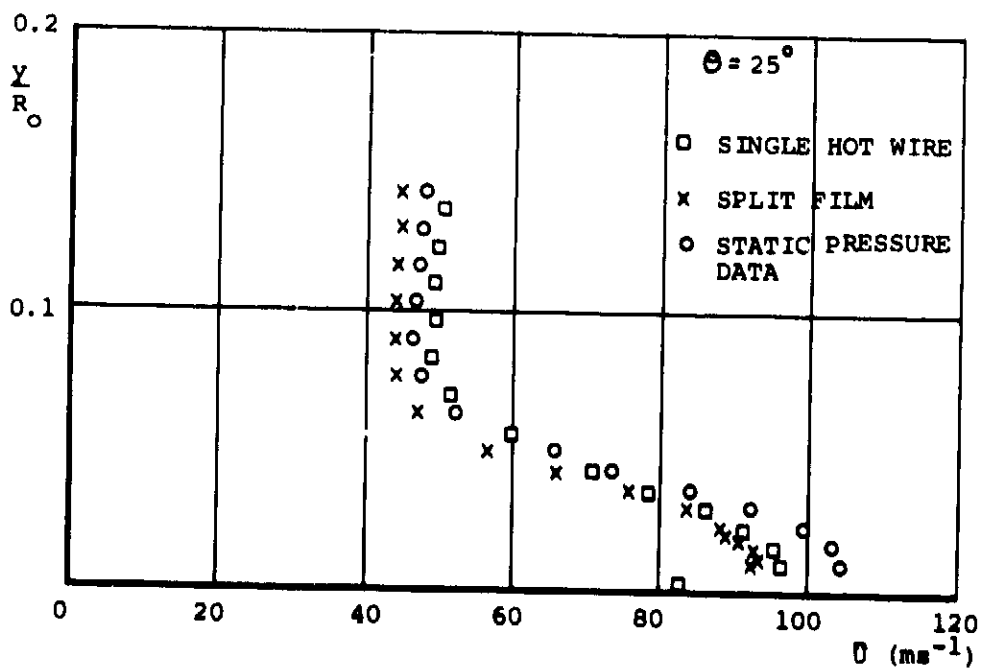
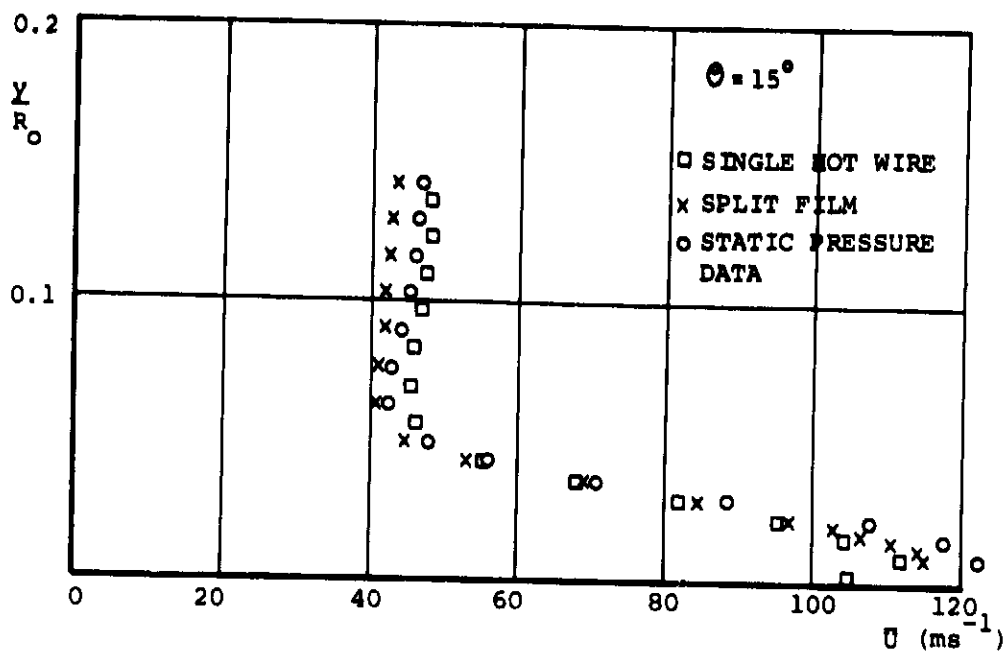


FIGURE 99A: COMPARISON OF VELOCITY PROFILES IN THE TRAILING EDGE WALL JET FROM THREE DIFFERENT MEASUREMENT TECHNIQUES $C_\mu = 0.0284$, $\alpha_c = 0^\circ$

FIG 99B

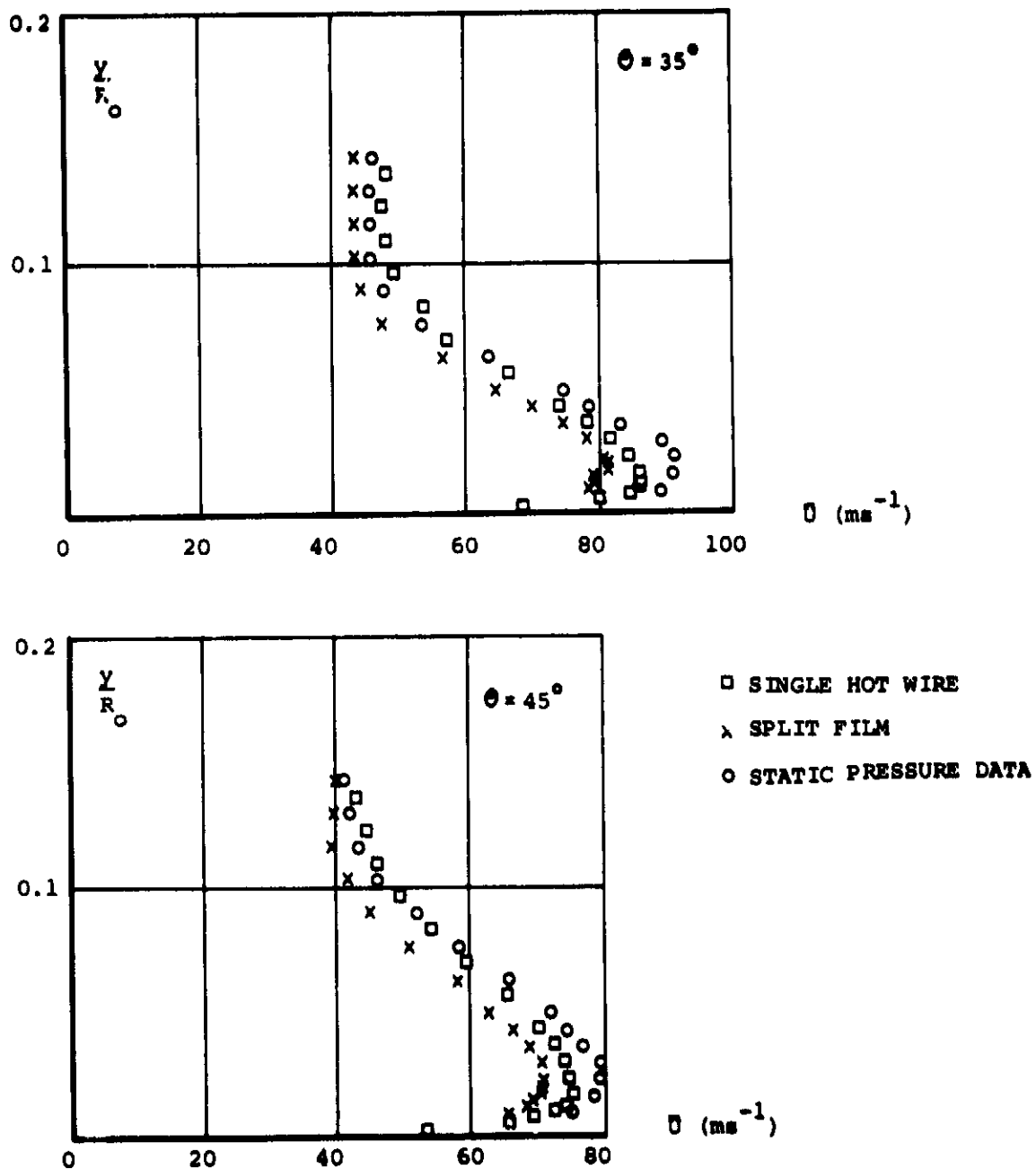


FIGURE 99B: COMPARISON OF VELOCITY PROFILES IN THE TRAILING
EDGE WALL JET FROM THREE DIFFERENT MEASUREMENT
TECHNIQUES $C_\mu = 0.0284$, $\alpha_G = 0^\circ$

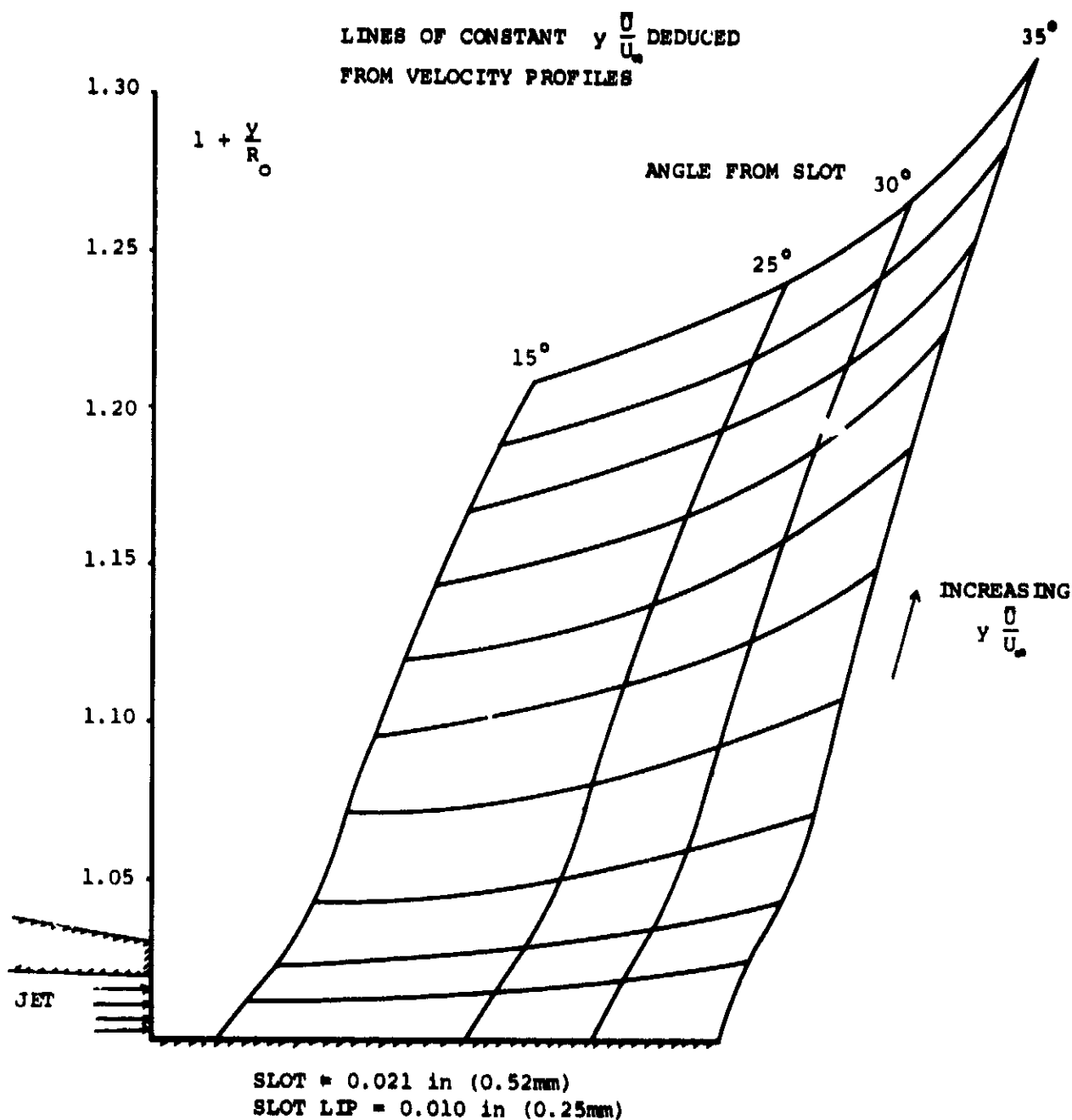


FIGURE 100: MEAN STREAMLINE PATTERN IN THE TRAILING EDGE
WALL JET $C_{\mu} = 0.0065$, $\alpha_G = 0^\circ$

FIG 101

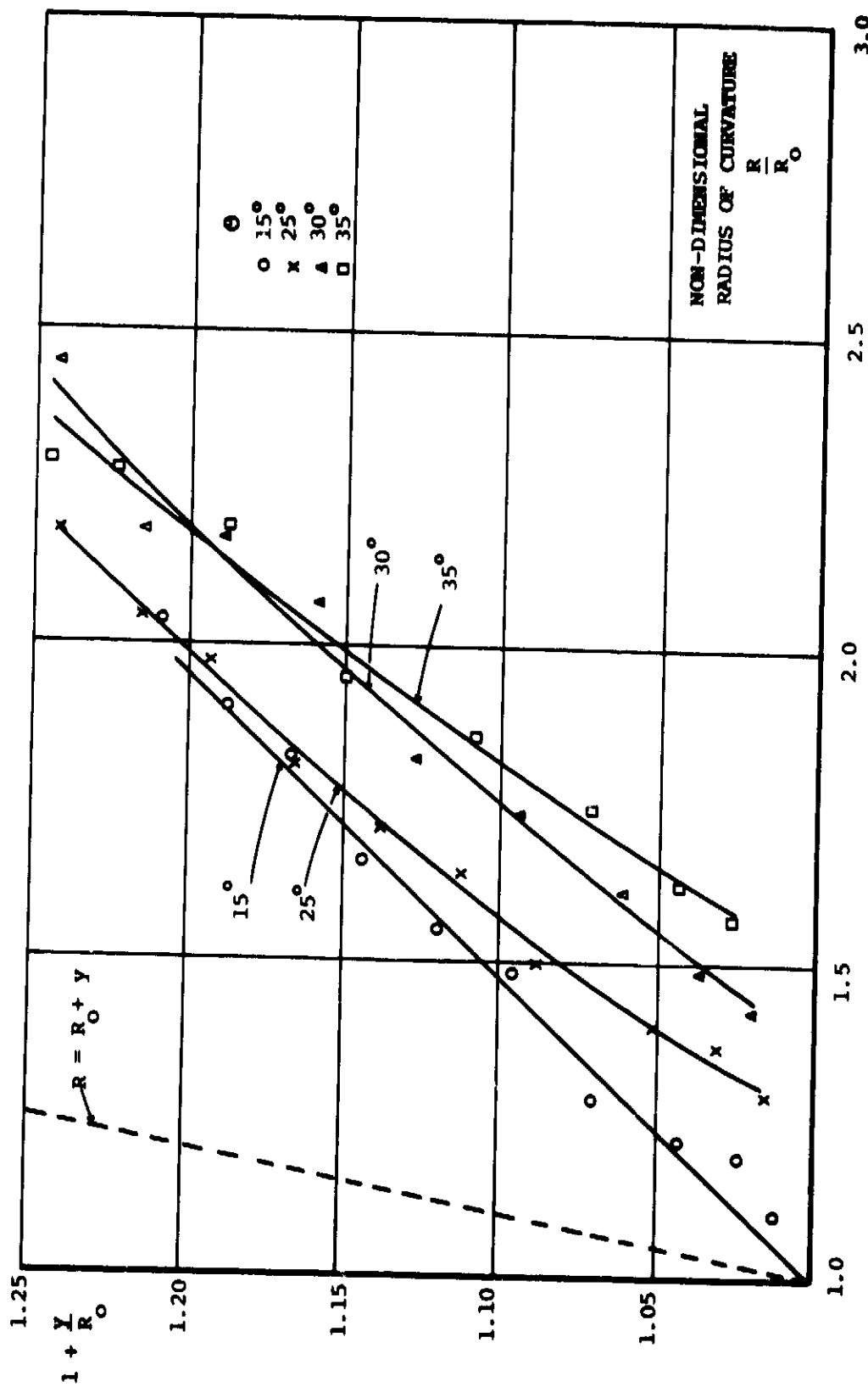


FIGURE 101: DEDUCED MEAN STREAMLINE RADIUS OF CURVATURE $C_p = 0.0065$, $\alpha_G = 0^\circ$

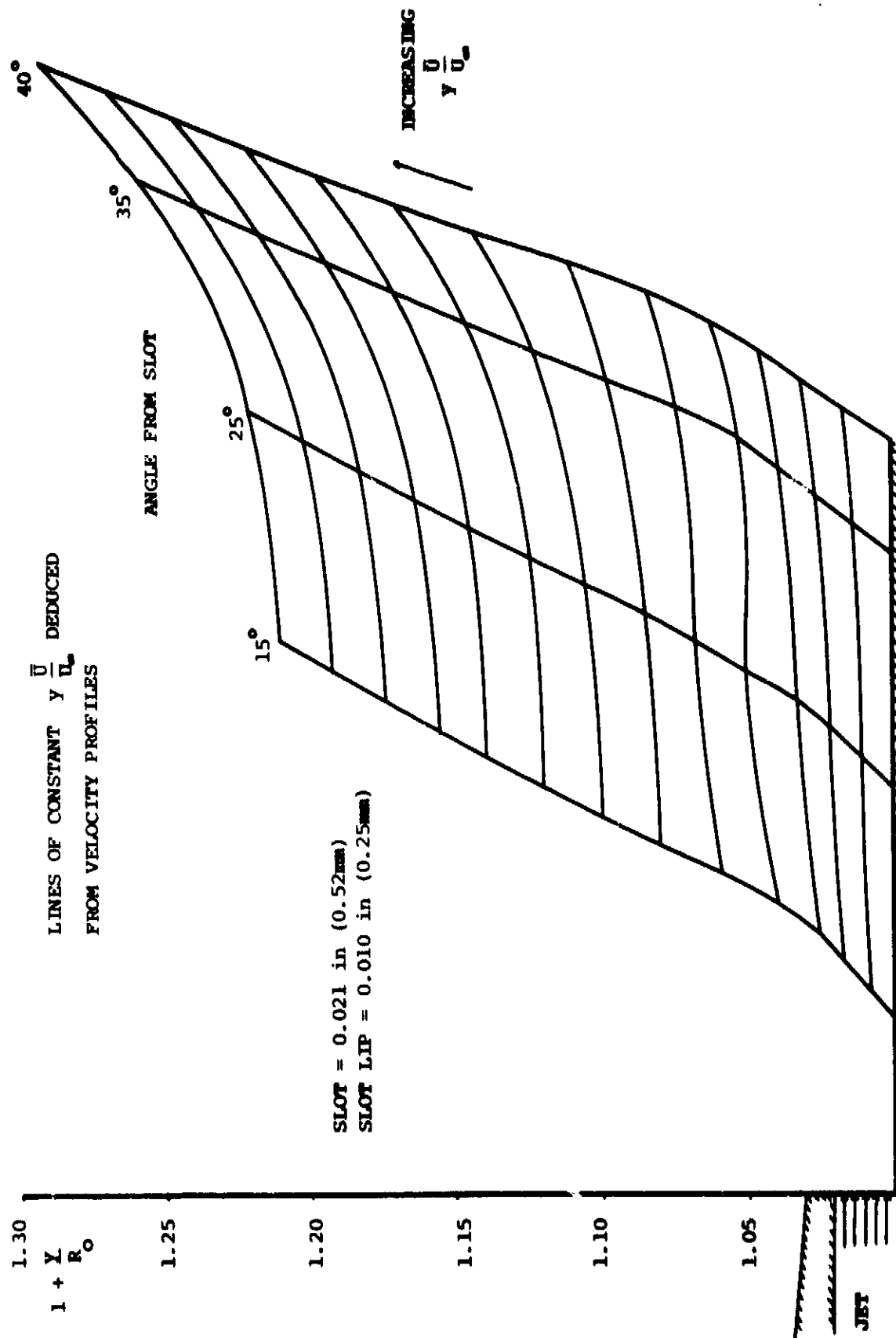


FIG 102

FIGURE 102: MEAN STREAMLINE PATTERN IN THE TRAILING EDGE WALL JET $C_{\mu} = 0.0139$, $\alpha_G = 0^\circ$

FIG 103

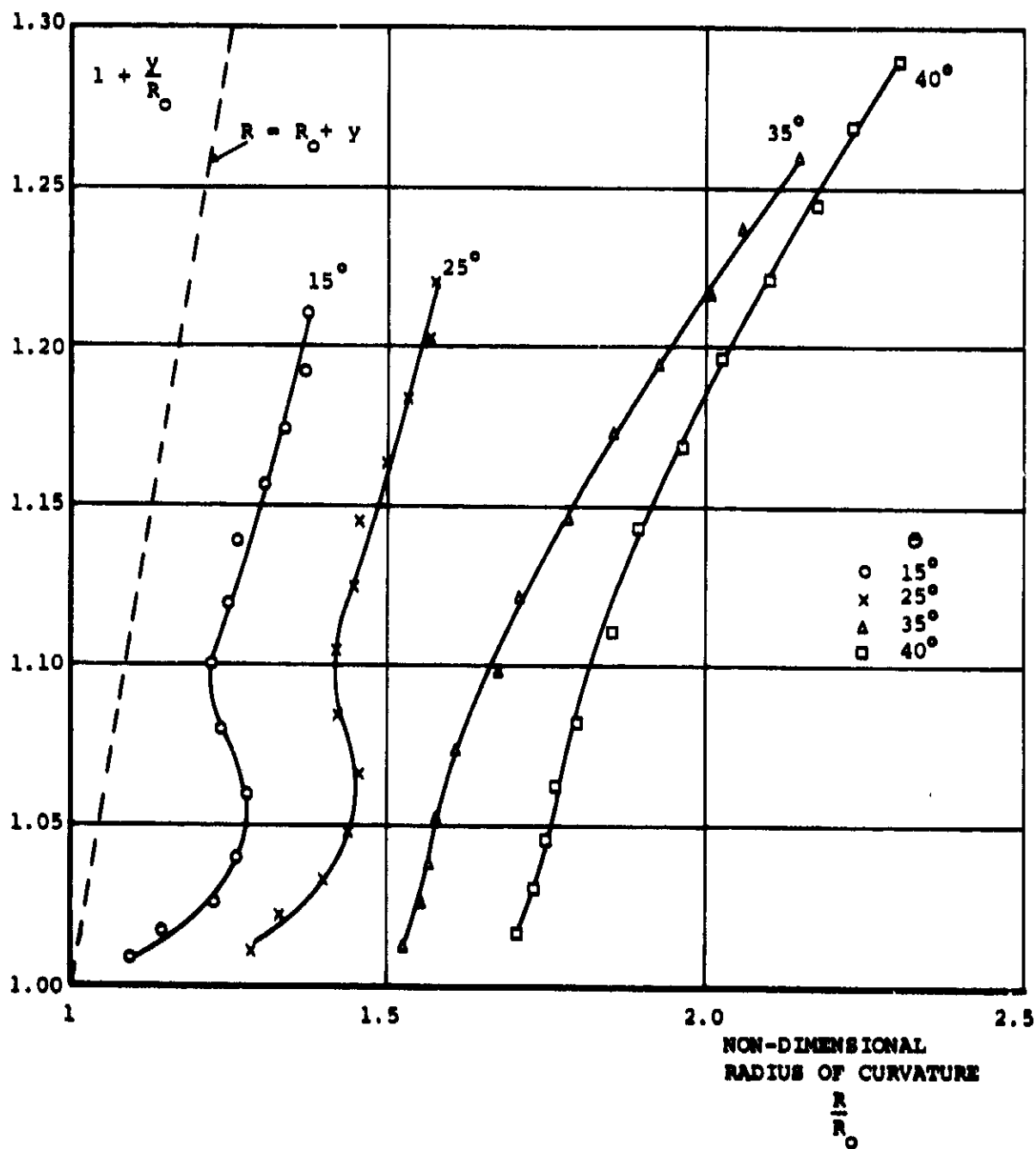


FIGURE 103: DEDUCED MEAN STREAMLINE RADIUS OF CURVATURE
 $C_\mu = 0.0139, \alpha_G = 0^\circ$

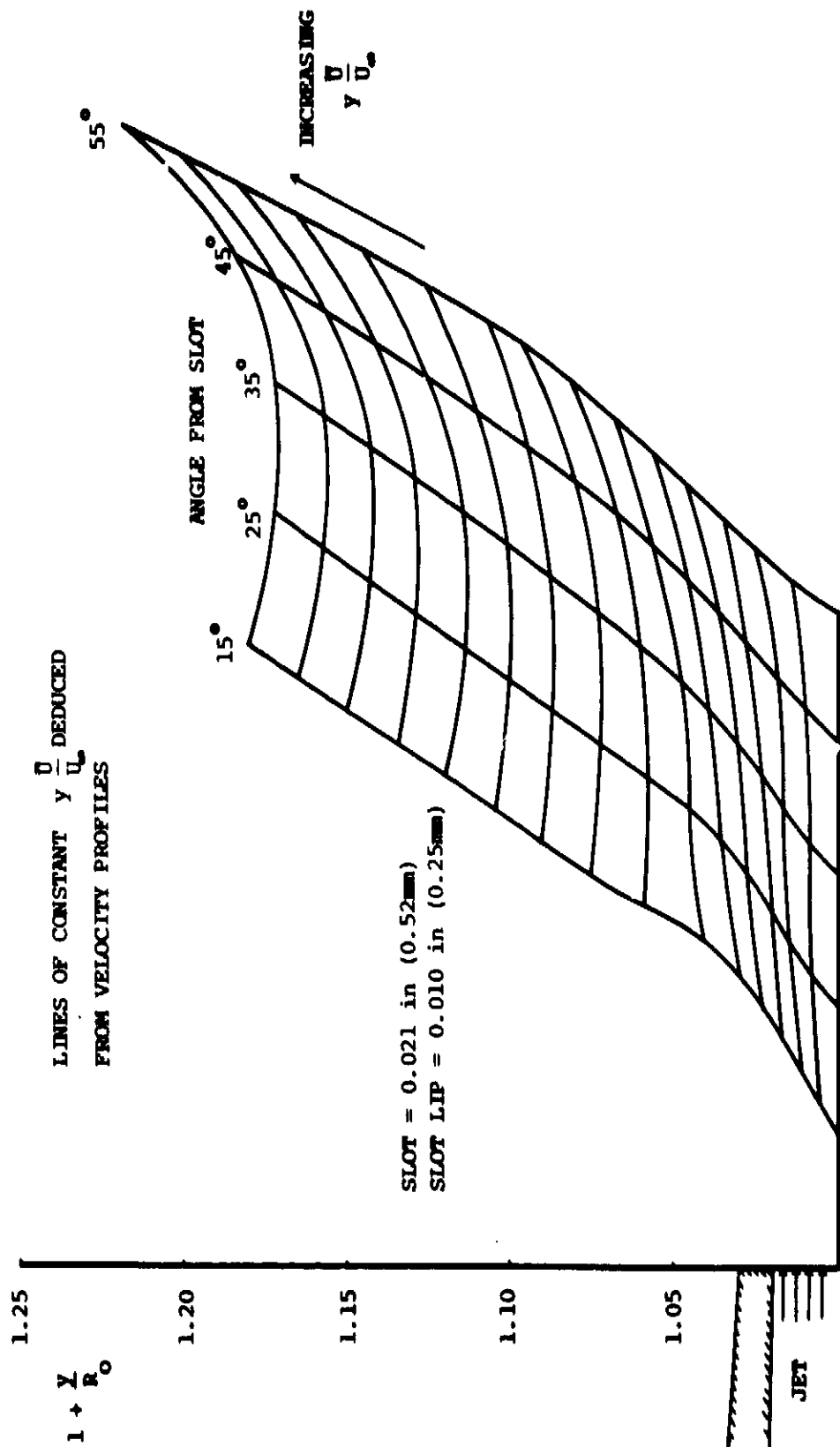


FIGURE 104: MEAN STREAMLINE PATTERN IN THE TRAILING EDGE WALL JET $C_p = 0.0284$, $\alpha_G = 0^\circ$

FIG 105

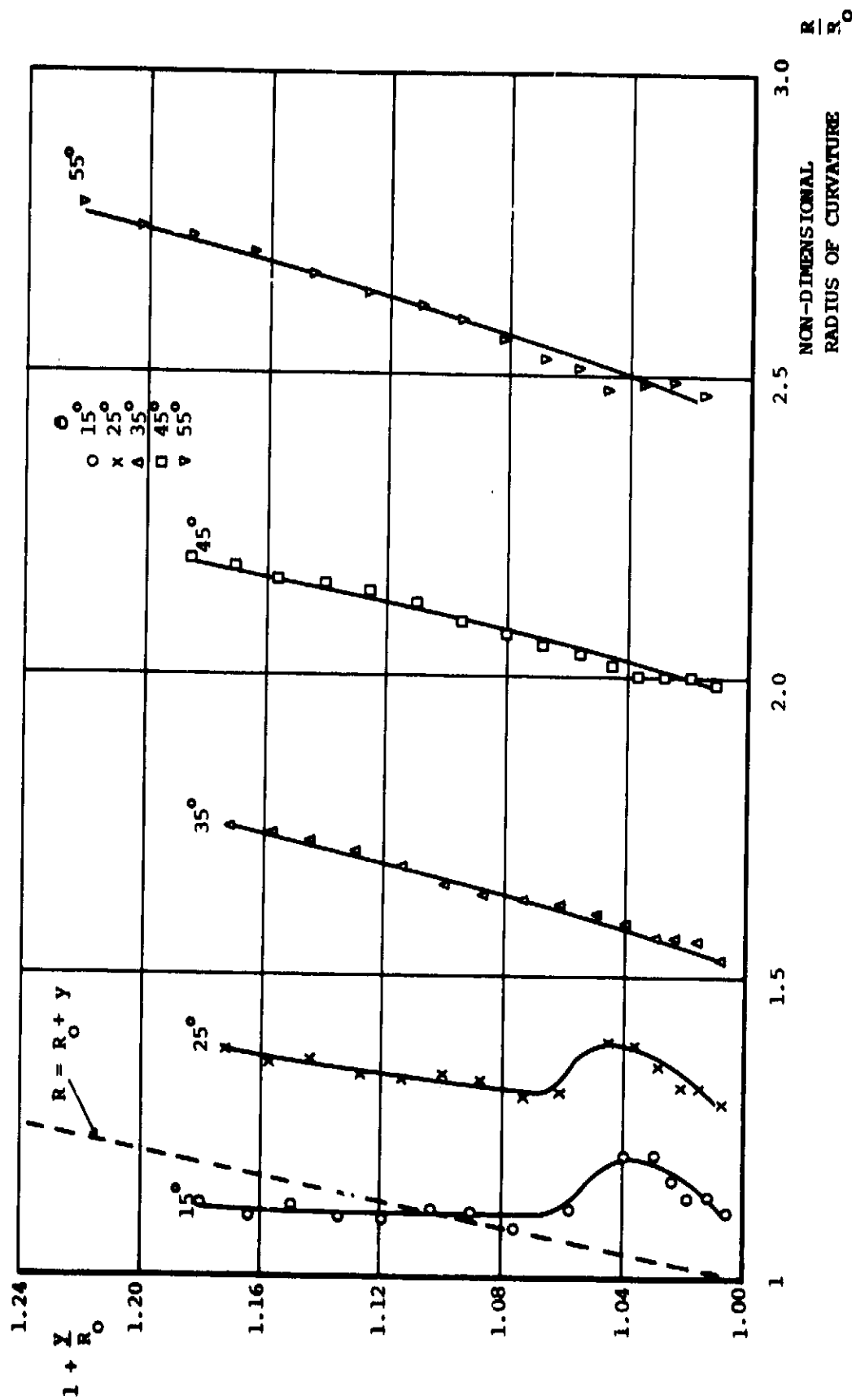


FIGURE 105: DEDUCED MEAN STREAMLINE RADIUS OF CURVATURE $C_p = 0.0284, \alpha_G = 0^\circ$

C_p	LIP THICKNESS	
0.0219	○ 0.024"	} SLOT HT 0.040"
	× 0.017"	
	△ 0.010"	
0.0197	□ 0.010"	SLOT HT 0.021"

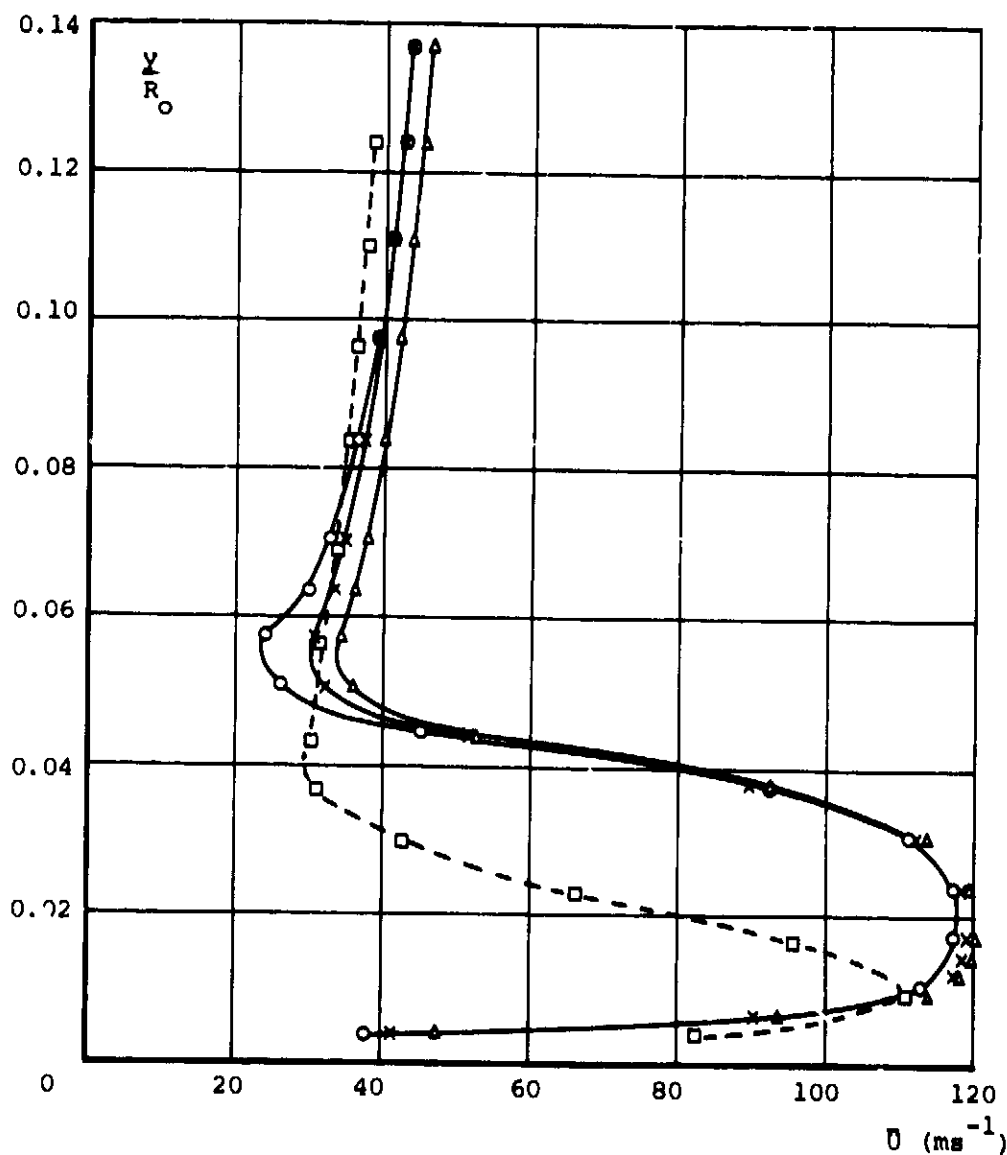


FIGURE 106: EFFECT OF SLOT HEIGHT AND LIP THICKNESS ON THE VELOCITY PROFILE 5° FROM SLOT

FIG 107

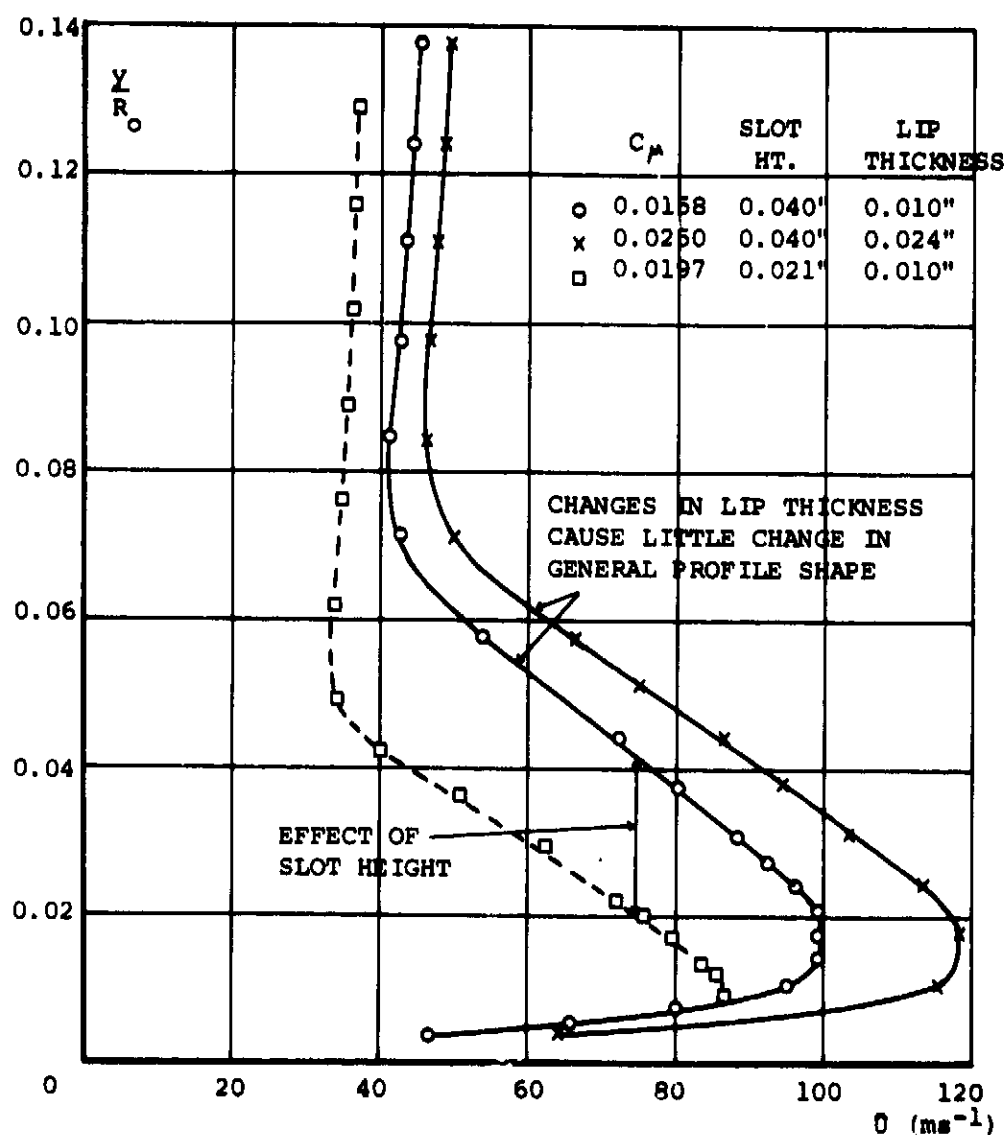


FIGURE 107: EFFECT OF SLOT HEIGHT AND LIP THICKNESS ON THE VELOCITY PROFILE 15° FROM SLOT

FIG 108

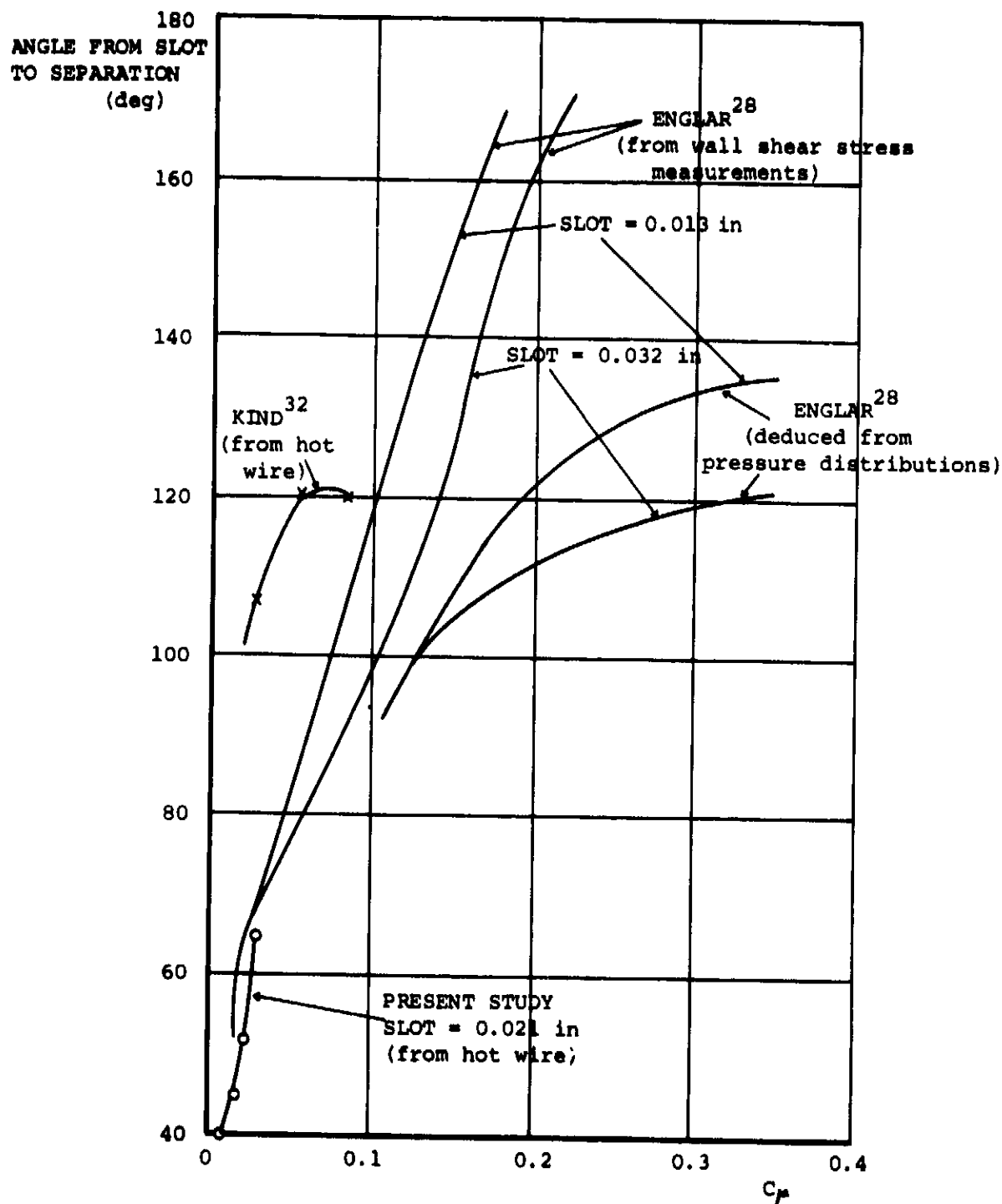
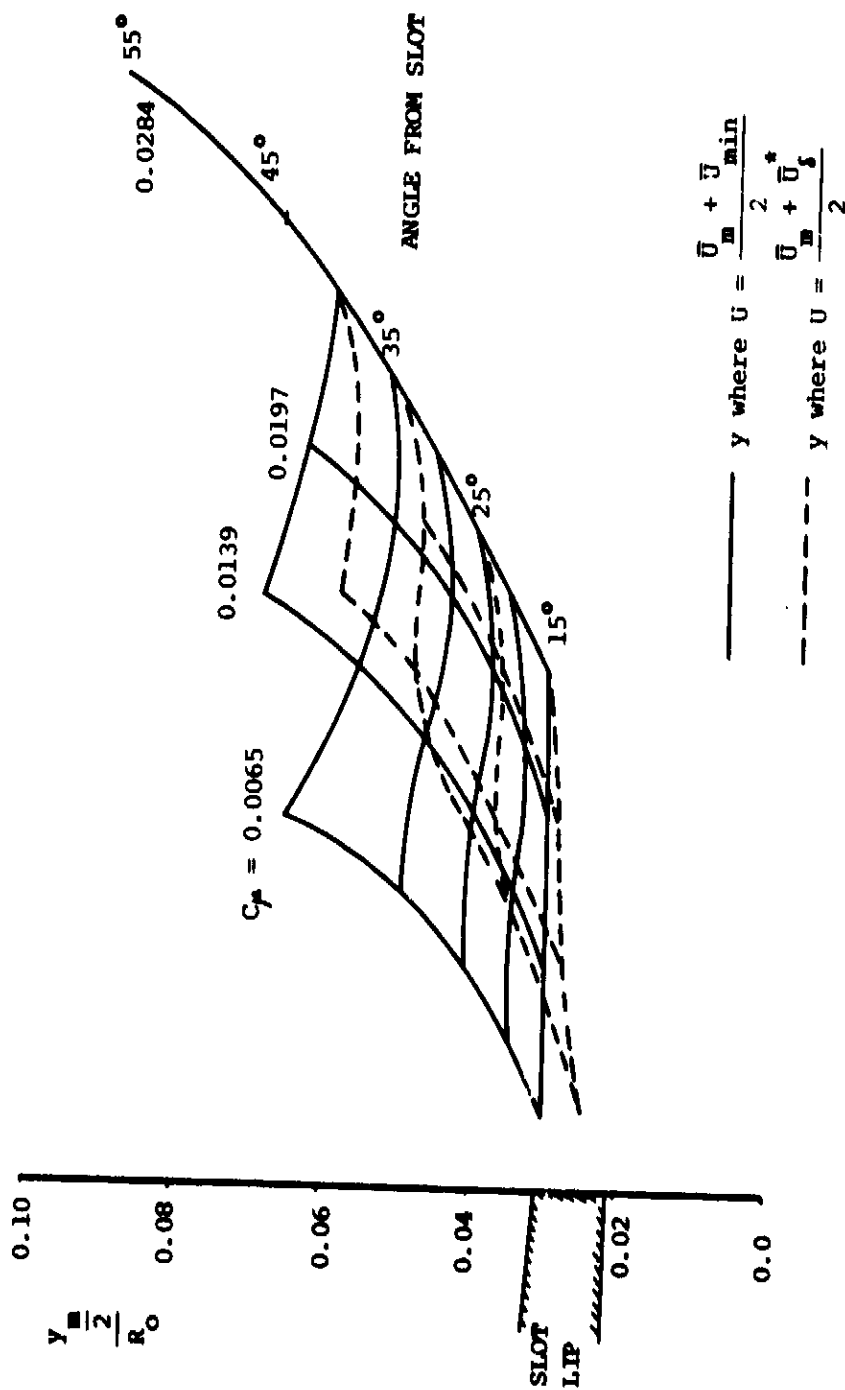


FIGURE 108: CHANGES IN ANGLE FROM SLOT TO SEPARATION WITH TRAILING EDGE BLOWING FOR A VARIETY OF AEROFOILS AND EVALUATION TECHNIQUES



* NOTE THAT AT THE LOWER BLOWING RATES
AN ESTIMATED VALUE OF u_s^* IS USED

FIGURE 109: LOCUS OF HALF VELOCITY POINT FOR VARYING C_p

FIG 110

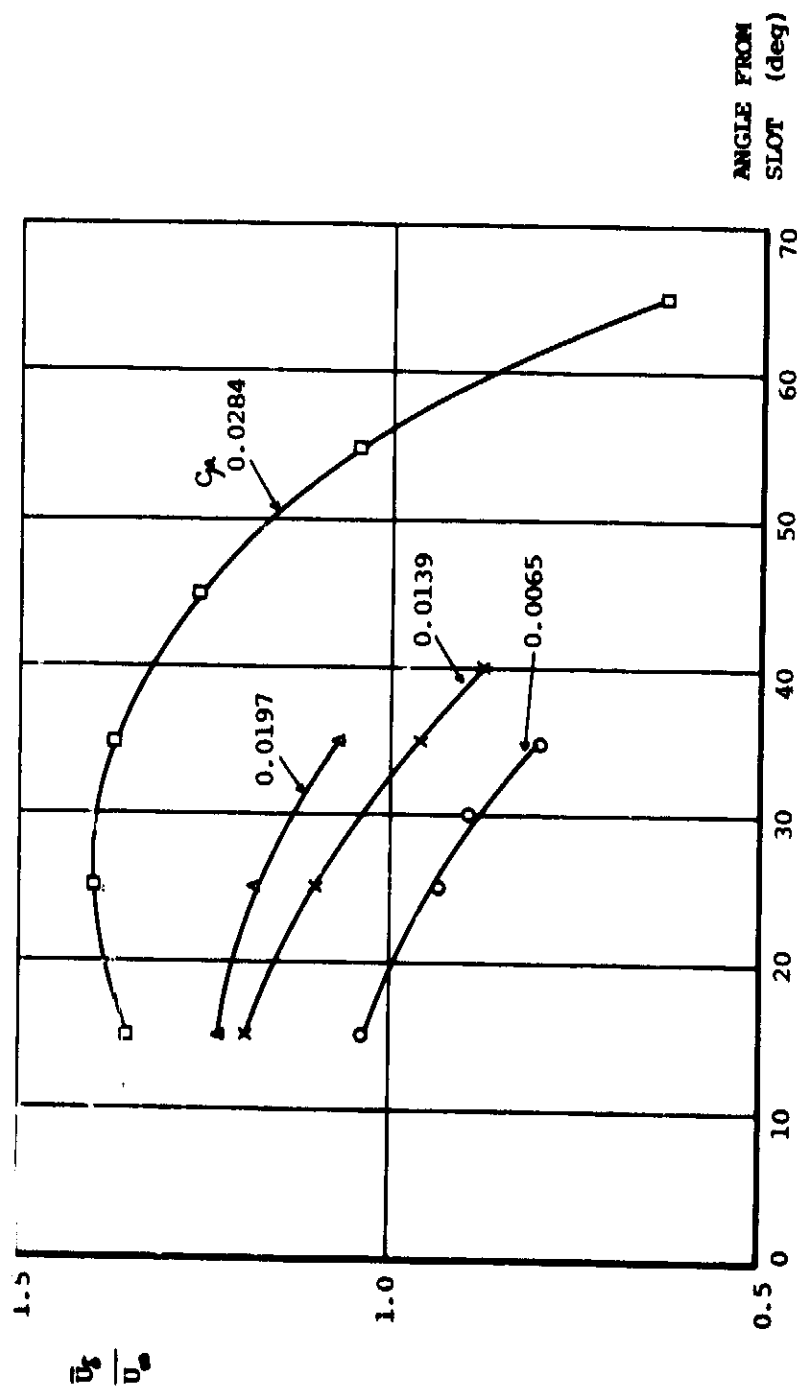


FIGURE 110: DECAY OF WALL JET EDGE VELOCITY WITH DISTANCE FROM SLOT

FIG 111

5° DATA TAKEN FROM ADDITIONAL HOT WIRE RESULTS

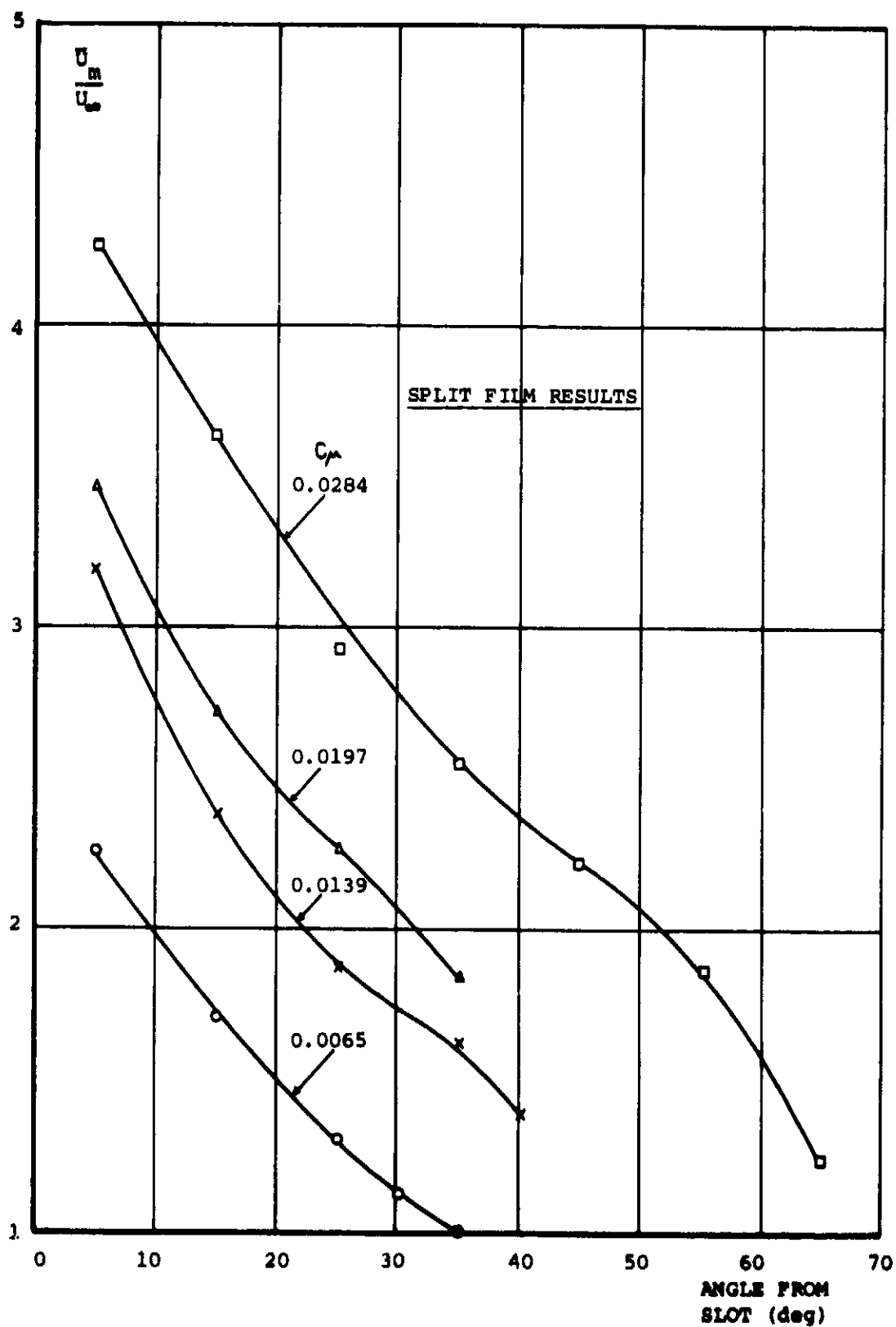


FIGURE 111: DECAY OF WALL JET MAXIMUM VELOCITY WITH DISTANCE FROM SLOT

FIG 112

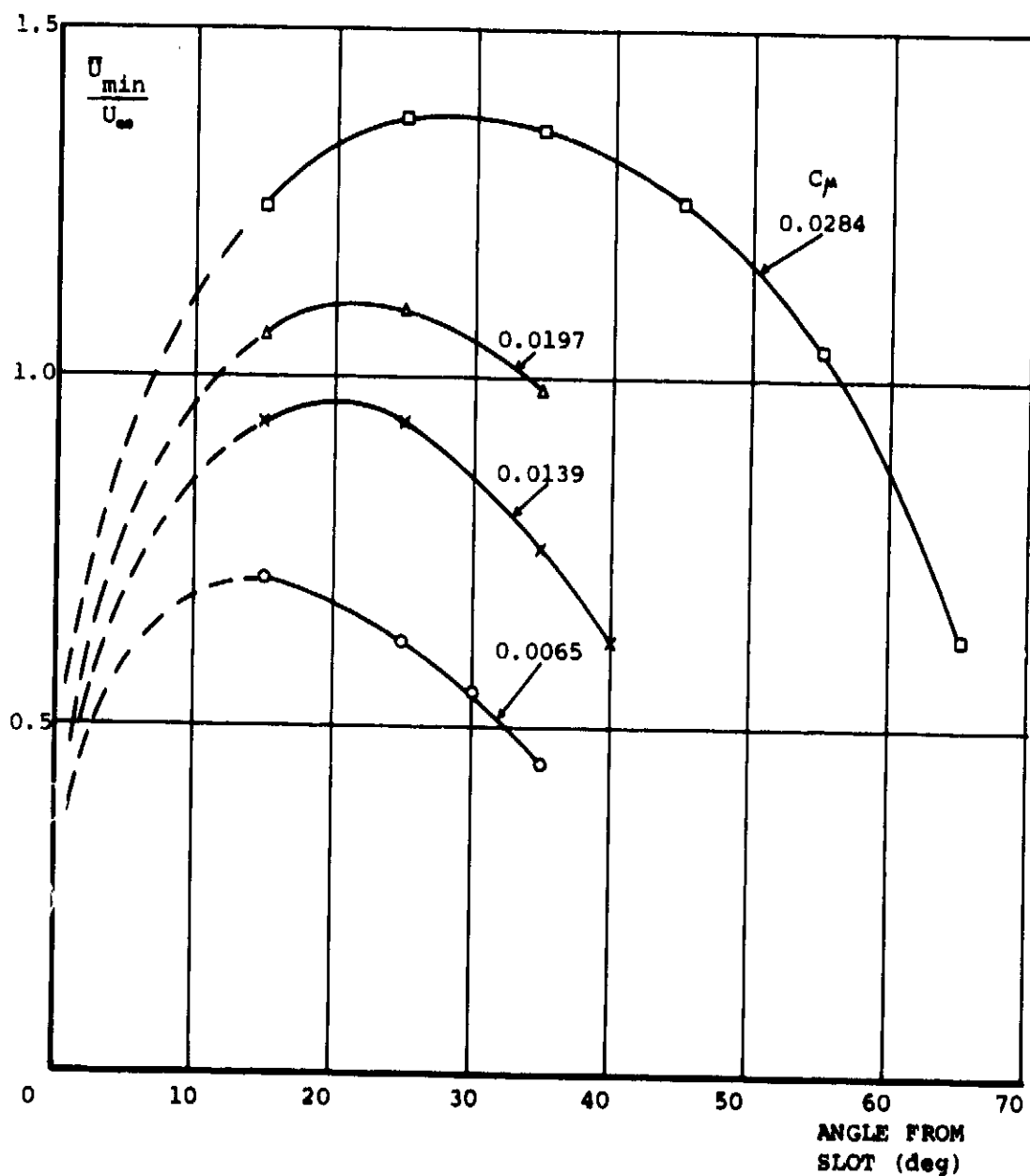
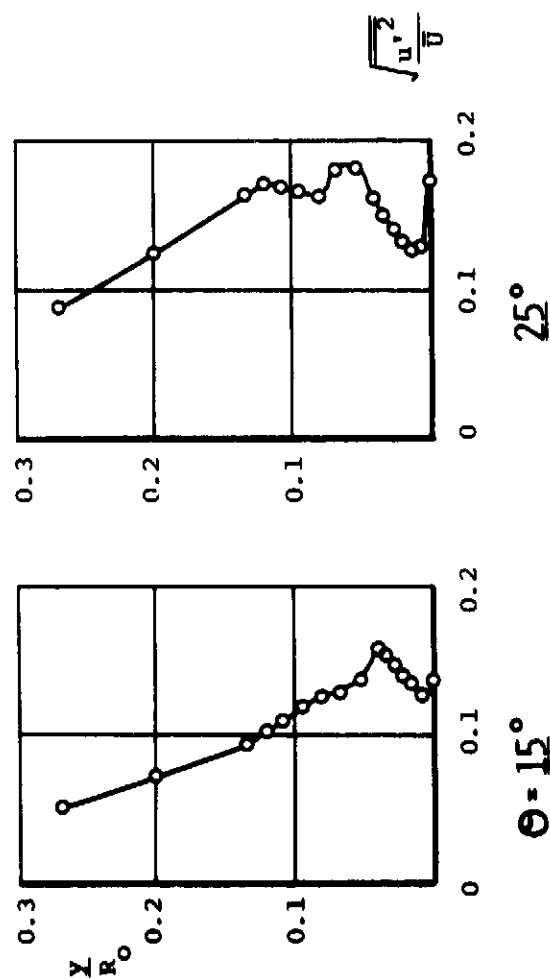
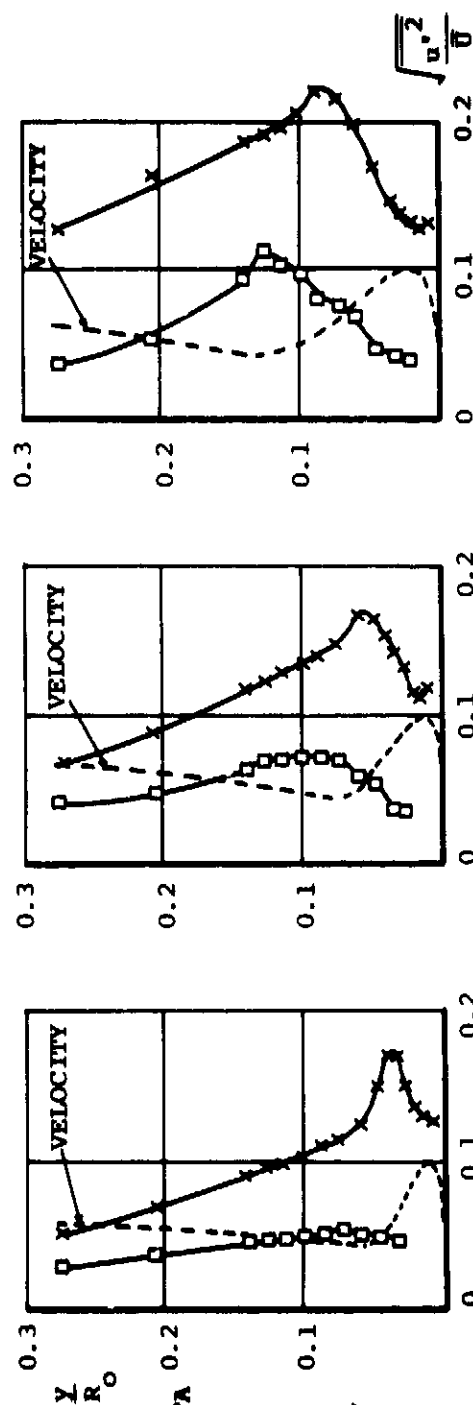


FIGURE 112: VARIATION OF WALL JET MINIMUM VELOCITY WITH DISTANCE FROM SLOT



○ SINGLE WIRE DATA



x STATIC PRESSURE DATA

□ SPLIT FILM DATA

○ NON-DIMENSIONAL

VELOCITY PROFILES

ARE SHOWN FOR CLARITY

FIGURE 113: LONGITUDINAL TURBULENCE INTENSITY IN THE TRAILING EDGE WALL JET $C_{\mu} = 0.0065$, $\alpha_G = 0^\circ$ FIG 113

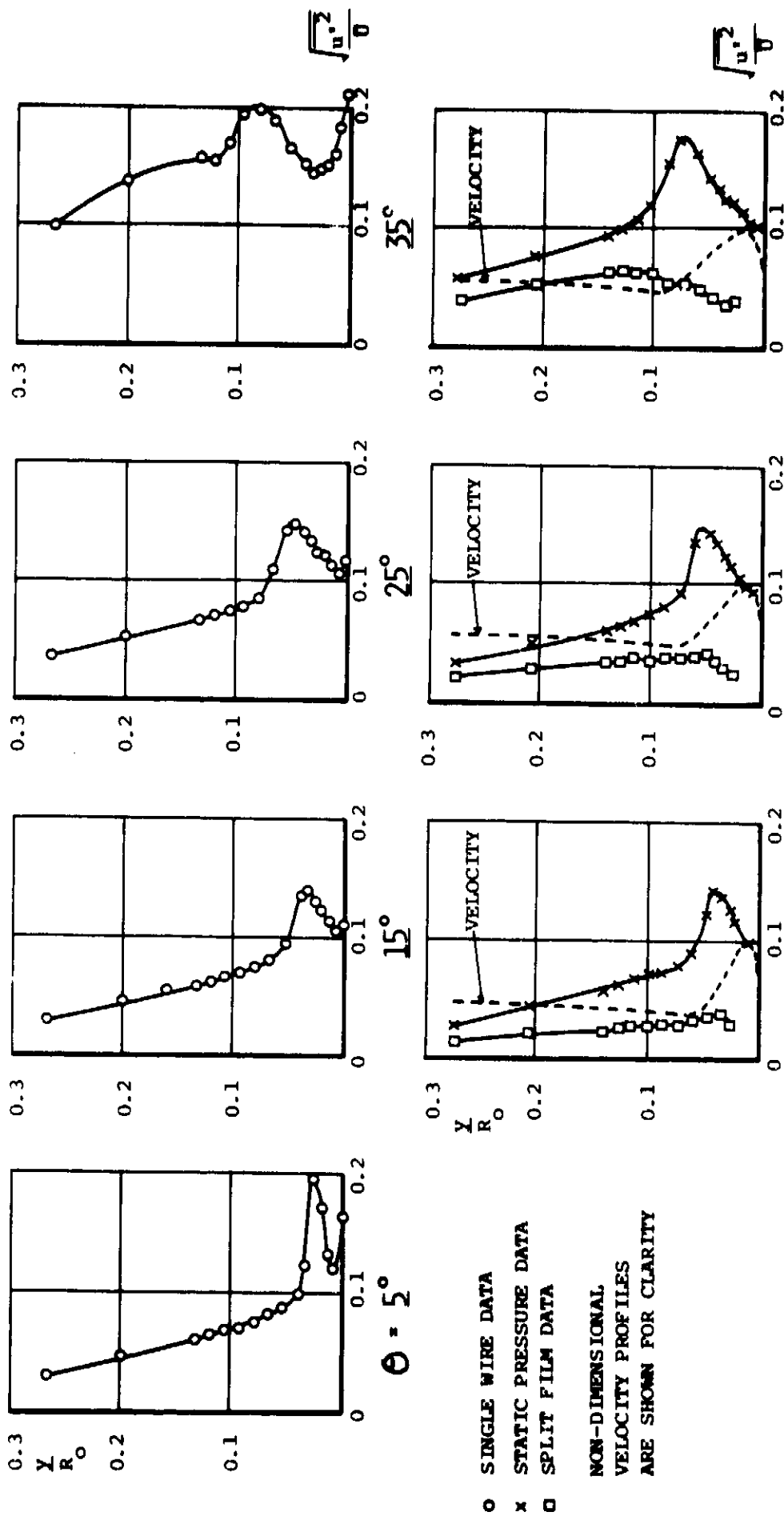


FIGURE 114: LONGITUDINAL TURBULENCE INTENSITY IN THE TRAILING EDGE WALL JET $C_p = 0.0139$, $\alpha_G = 0^\circ$

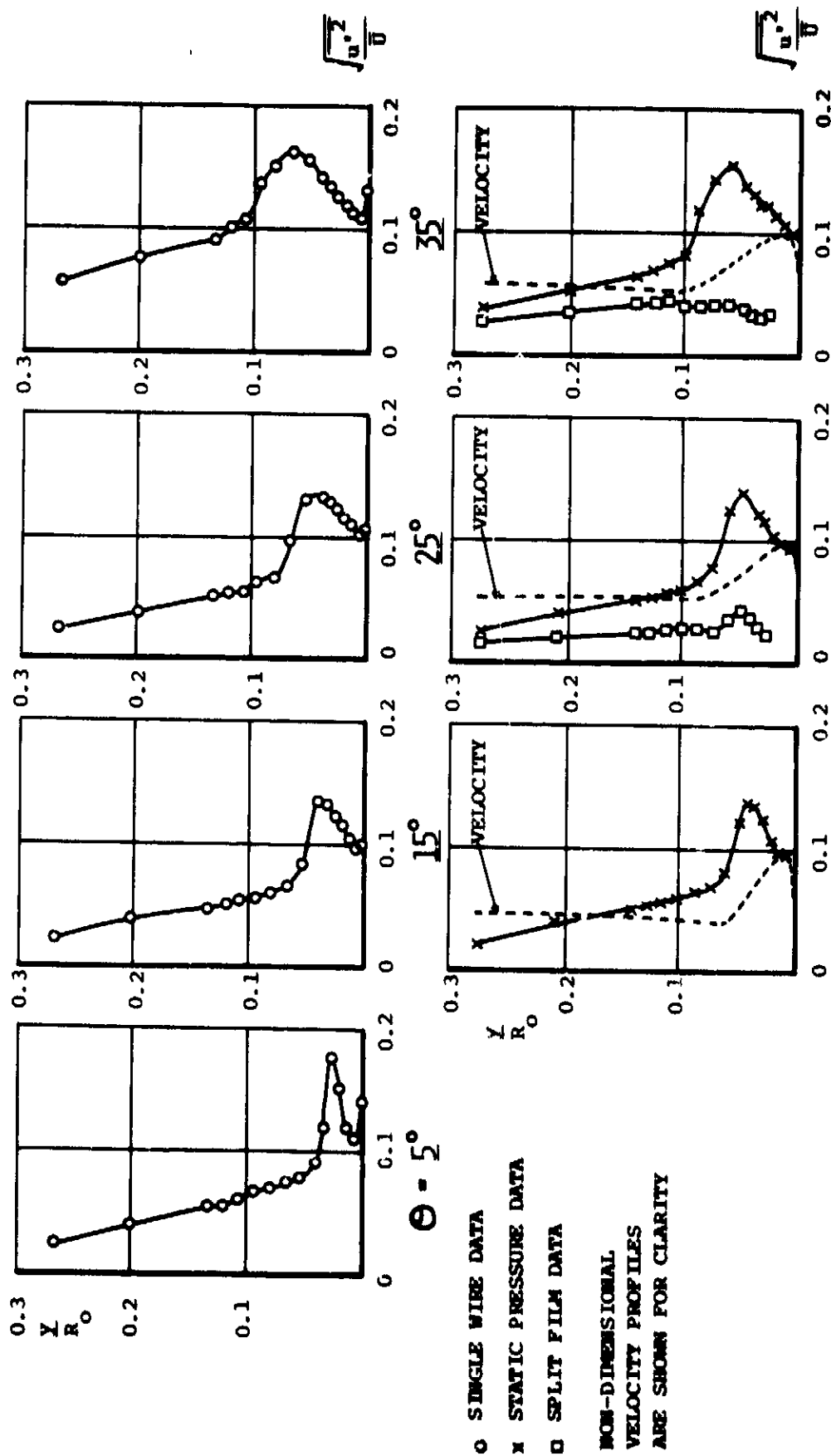


FIGURE 115: LONGITUDINAL TURBULENCE INTENSITY IN THE TRAILING EDGE WALL JET $C_{\mu} = 0.0197$, $\alpha_G = 0^\circ$ FIG 115

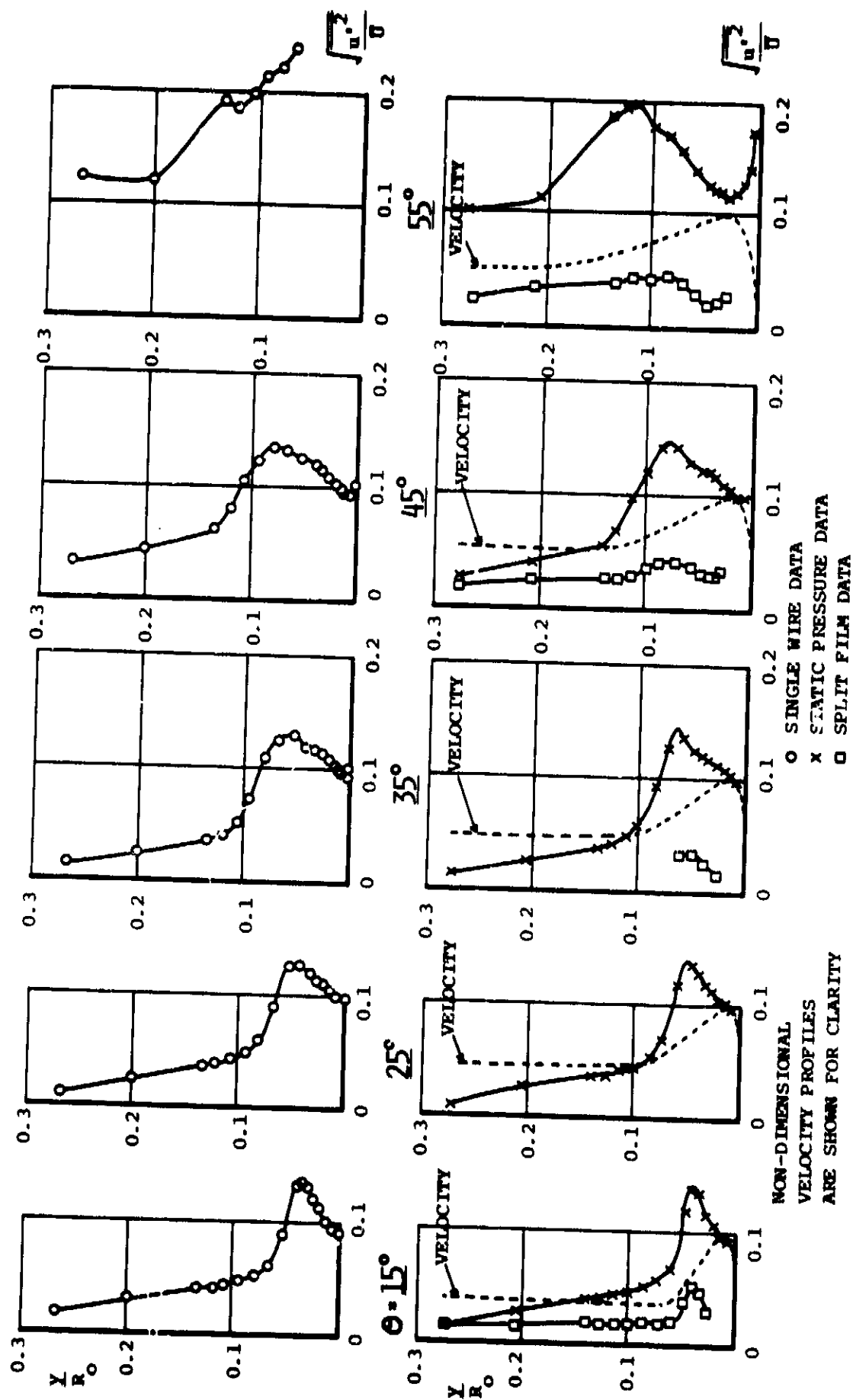
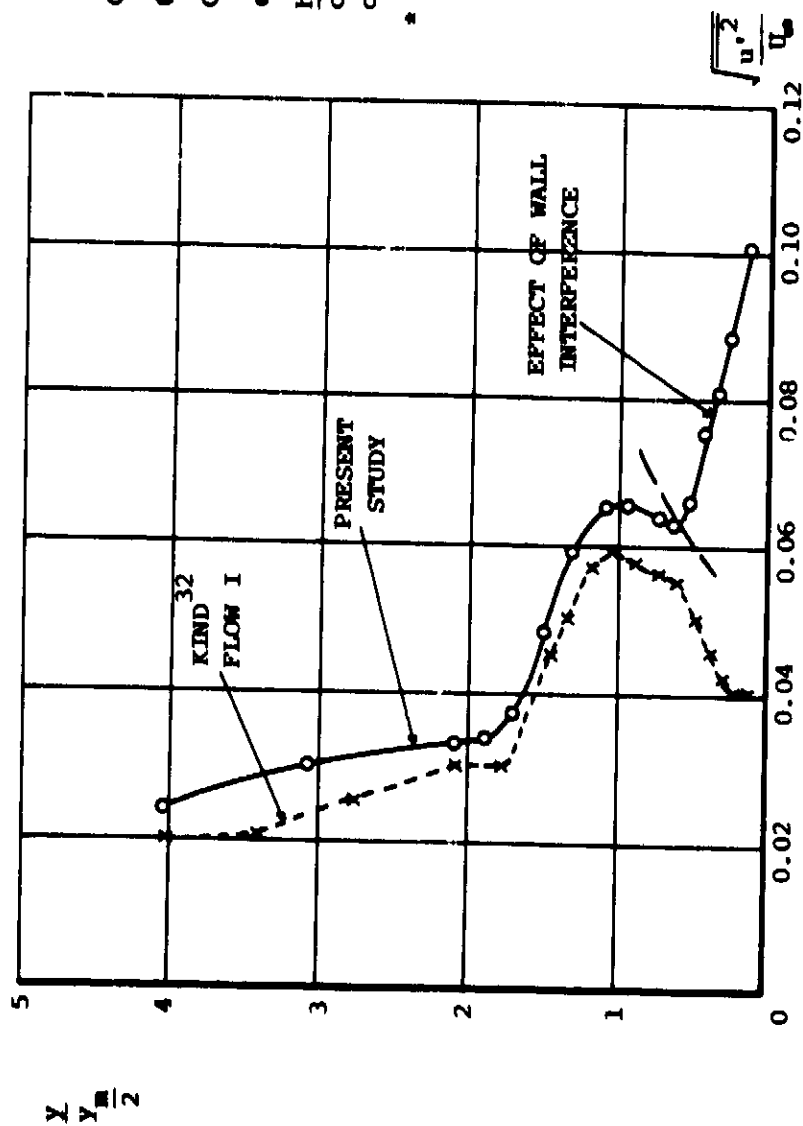


FIGURE 116: LONGITUDINAL TURBULENCE INTENSITY IN THE TRAILING EDGE WALL JET $C_p = 0.0284$, $\alpha_G = 0^\circ$



	KIND ³²	PRESENT STUDY
C_p	0.028	0.0284
θ	46	45
C_L	0.88	0.86*
α_{eff}	-3.5	-4.0
$\frac{h}{c}$	0.0012	0.0009
chord	14.435"	23.425"

* C_L subject to probe interference

FIGURE 117: COMPARISON OF LONGITUDINAL TURBULENCE IN THE TRAILING EDGE WALL JET WITH THE RESULTS OF KIND³²

FIG 117

FIG 118

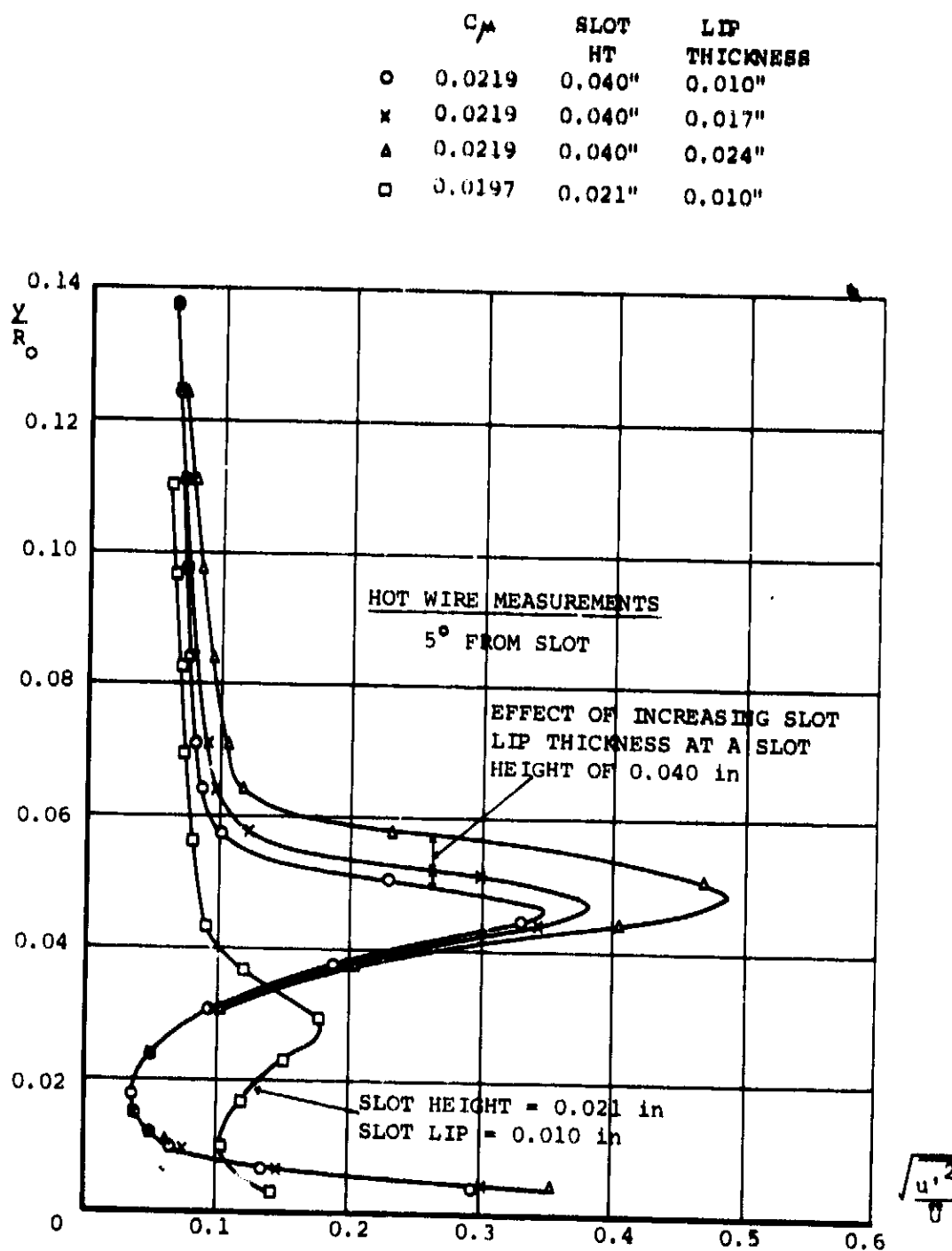


FIGURE 118: EFFECT OF SLOT HEIGHT AND LIP THICKNESS UPON THE LONGITUDINAL TURBULENCE INTENSITY IN THE TRAILING EDGE WALL JET

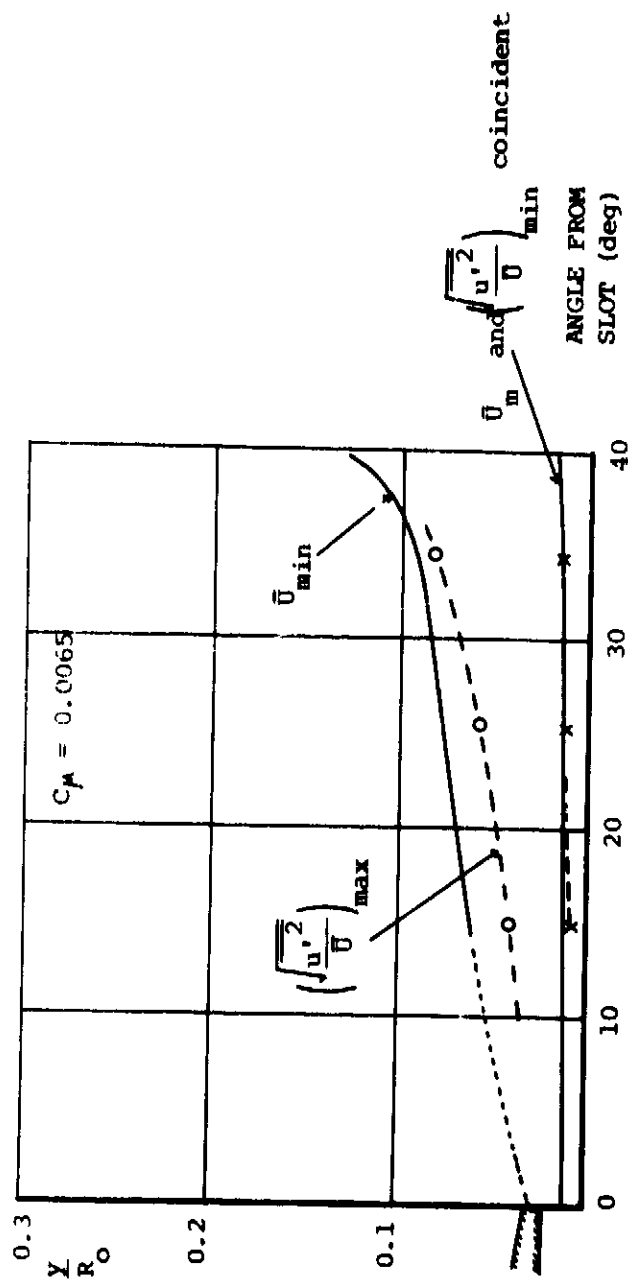


FIGURE 119: LOCI OF THE MAXIMA AND MINIMA OF THE MEAN VELOCITY AND THE LONGITUDINAL TURBULENCE INTENSITY IN THE TRAILING EDGE WALL JET $C_\mu = 0.0065$, $\alpha_G = 0^\circ$

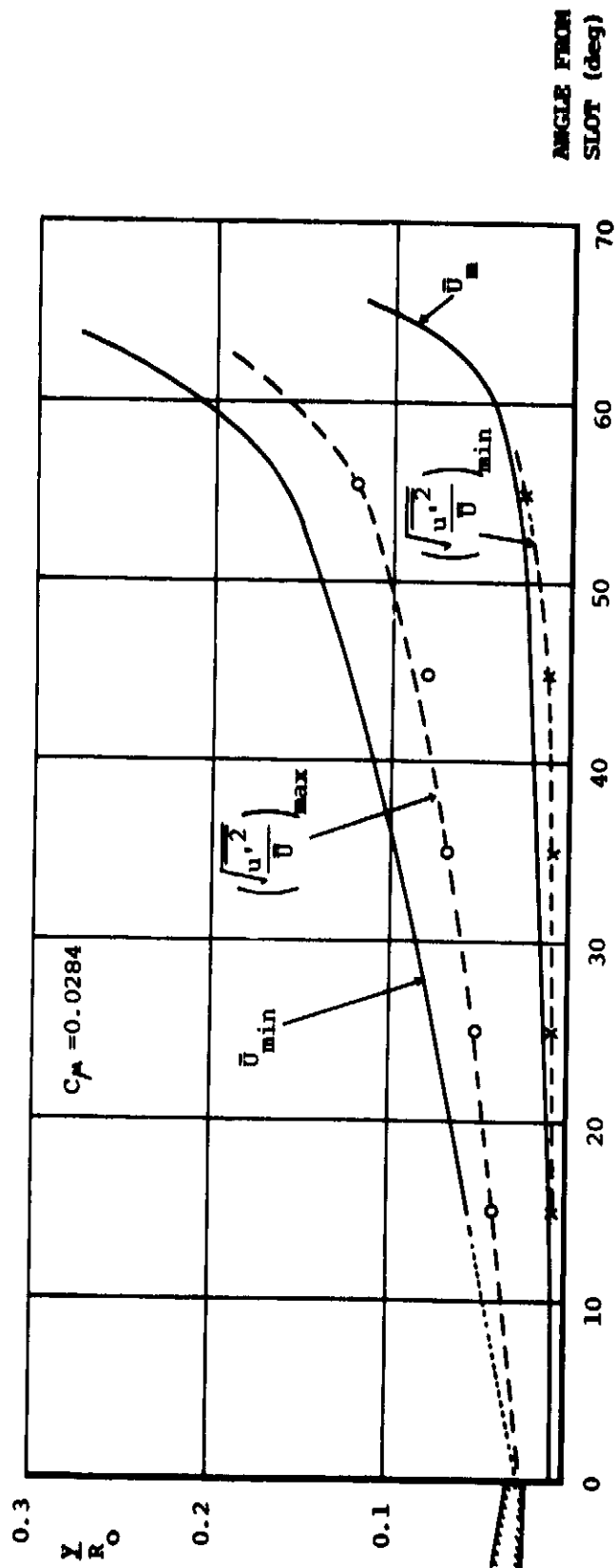
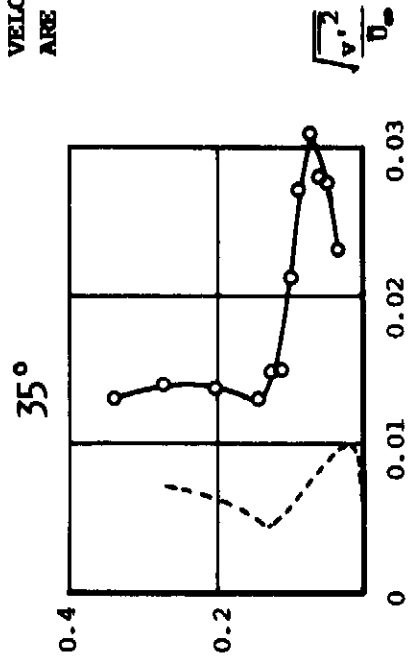
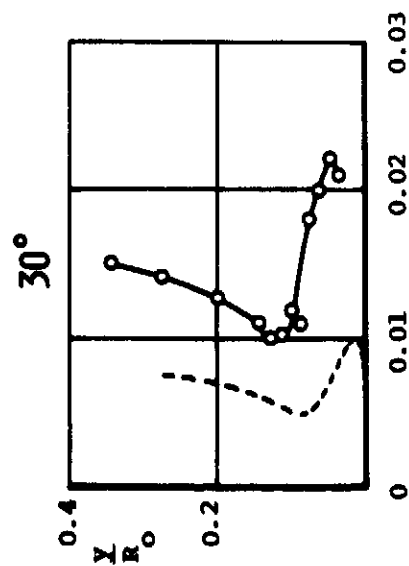
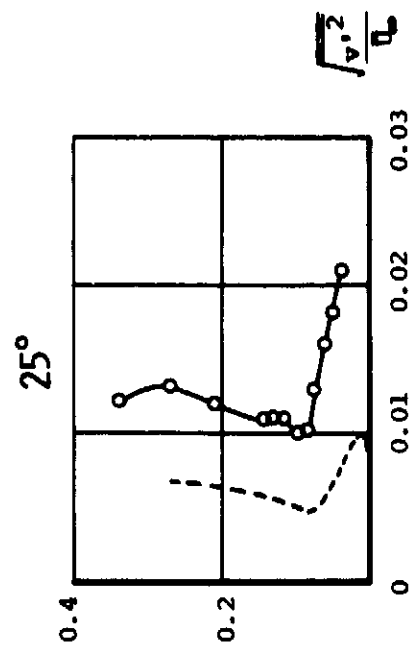
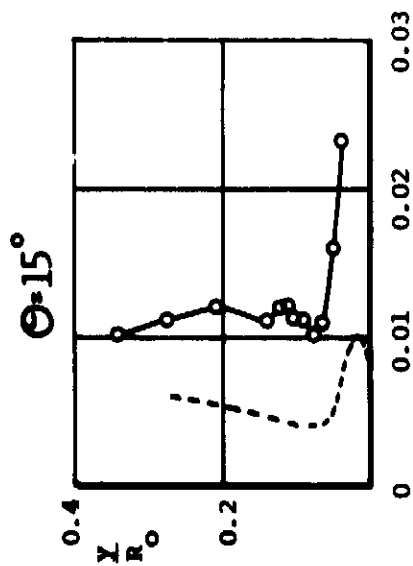
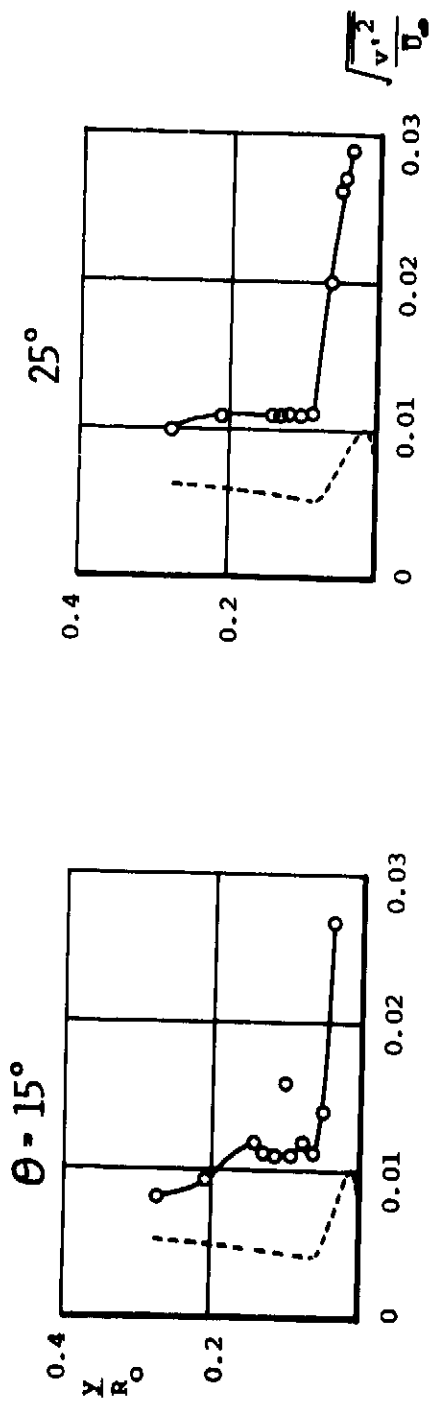


FIGURE 120: LOCI OF THE MAXIMA AND MINIMA OF THE MEAN VELOCITY AND THE LONGITUDINAL TURBULENCE INTENSITY IN THE TRAILING EDGE WALL JET $C_p = 0.0284$, $\alpha_G = 0^\circ$



NON-DIMENSIONAL
VELOCITY PROFILES
ARE SHOWN FOR CLARITY

FIGURE 121: NORMAL TURBULENCE DISTRIBUTION IN THE TRAILING EDGE WALL JET $C_\mu = 0.0065, \alpha_G = 0^\circ$



NON-DIMENSIONAL
VELOCITY PROFILES
ARE SHOWN FOR CLARITY

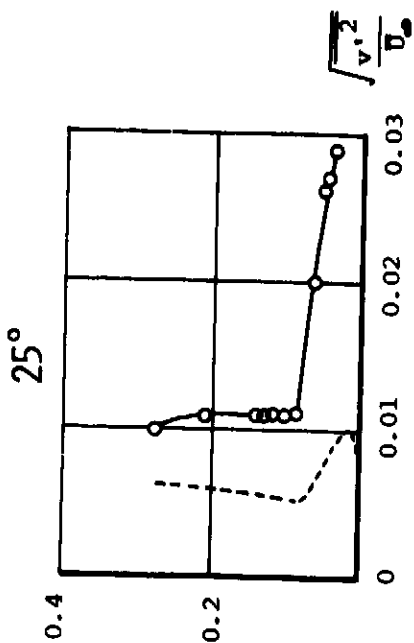
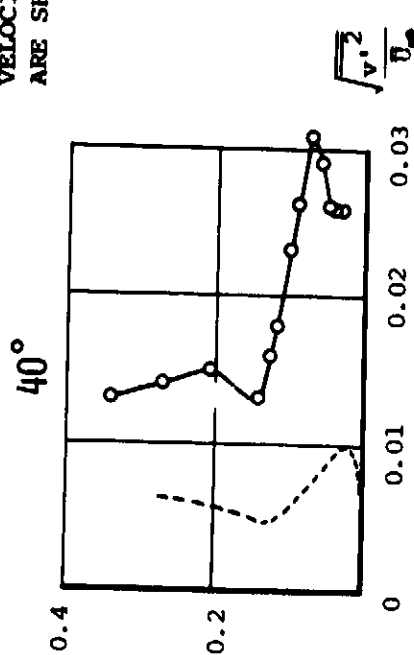
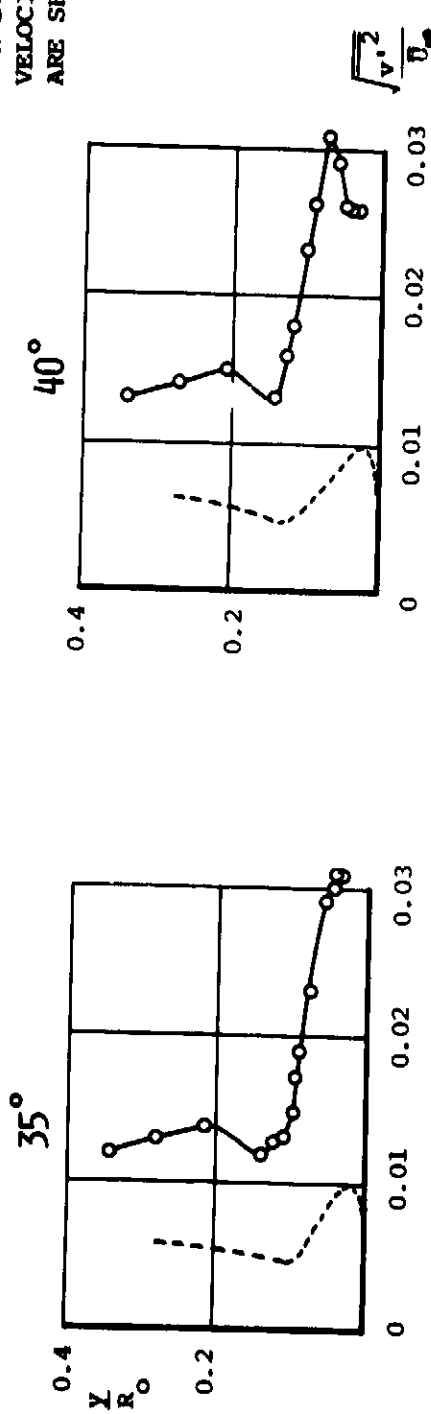


FIGURE 122: NORMAL TURBULENCE DISTRIBUTION IN THE TRAILING EDGE WALL JET $C_\mu = 0.0139$, $\alpha_G = 0^\circ$

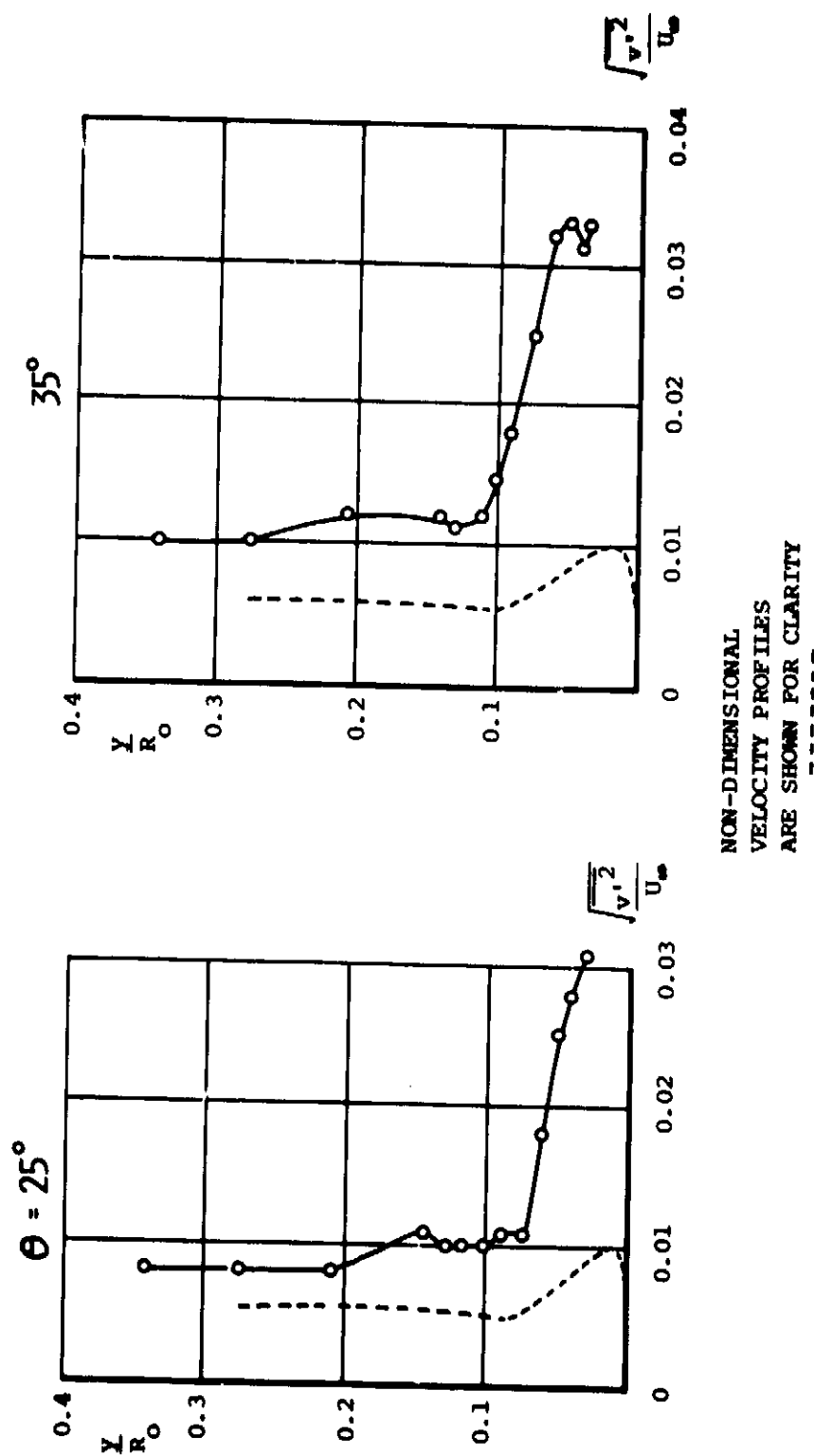


FIGURE 123: NORMAL TURBULENCE DISTRIBUTION IN THE TRAILING EDGE WALL JET $C_\mu = 0.0197$, $\alpha_G = 0^\circ$

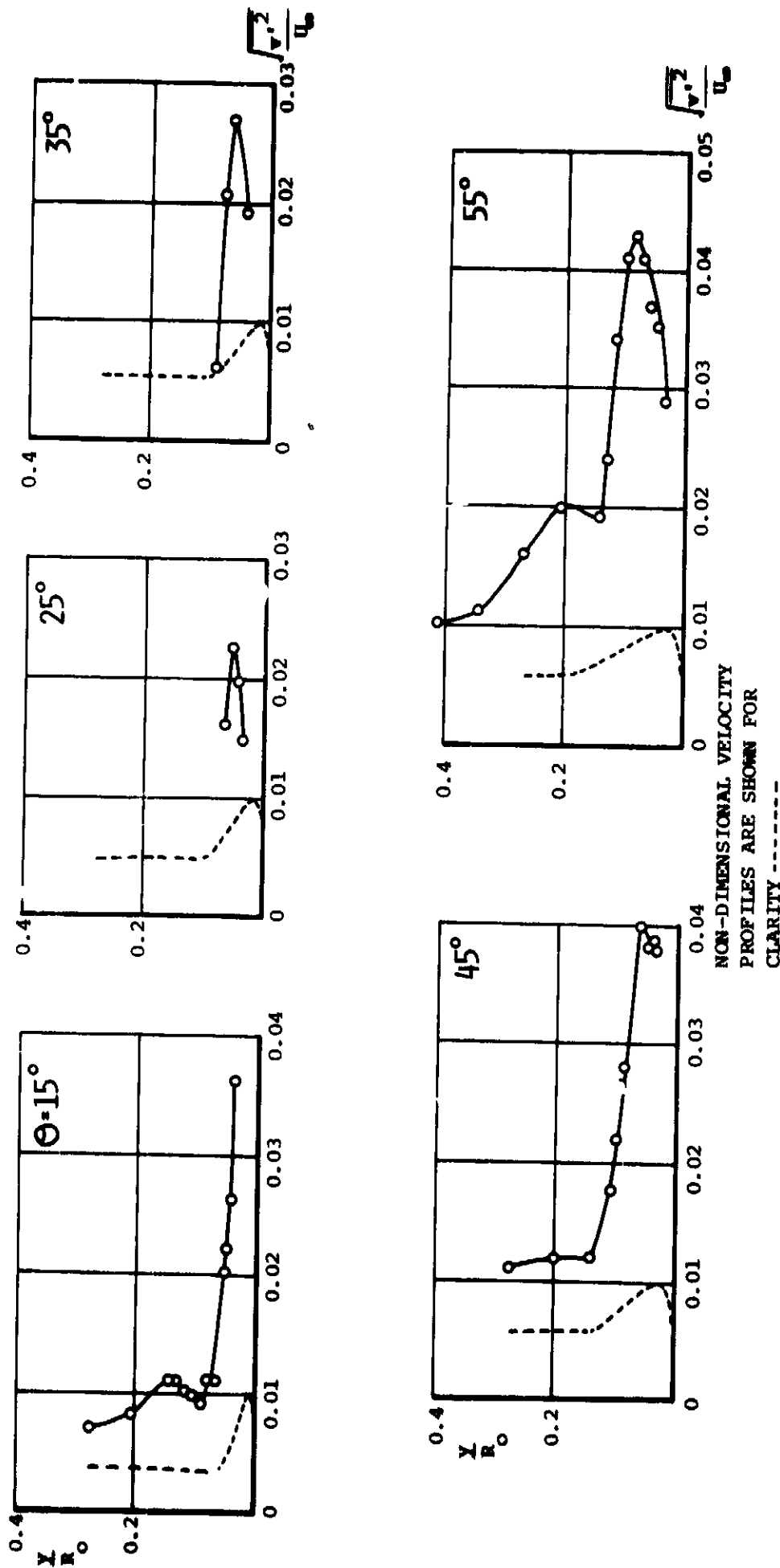


FIGURE 124: NORMAL TURBULENCE DISTRIBUTION IN THE TRAILING EDGE WALL JET $C_{\mu} = 0.0284$, $\alpha'_G = 0^\circ$

FIG 125

ORIGINAL PAGE IS
OF POOR QUALITY.

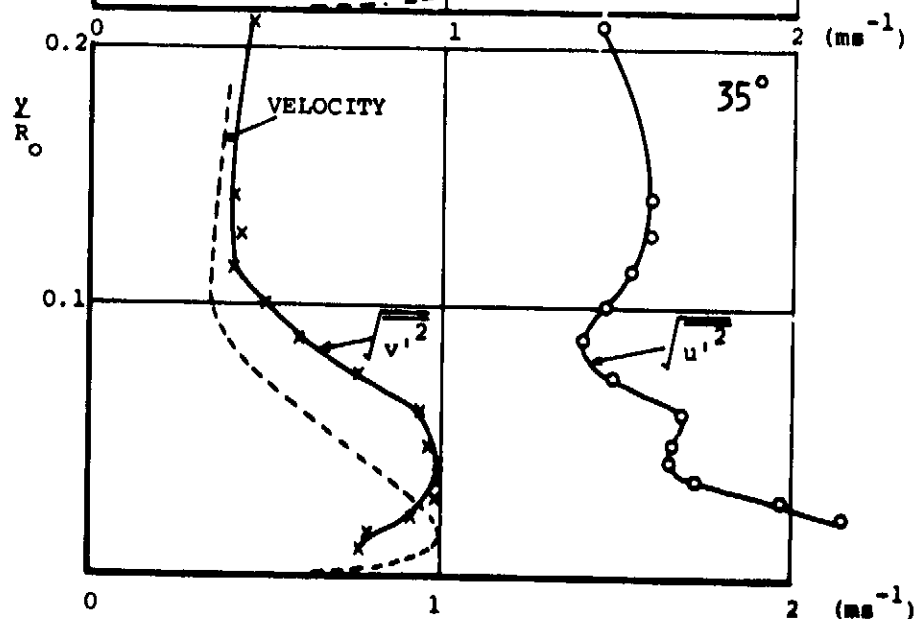
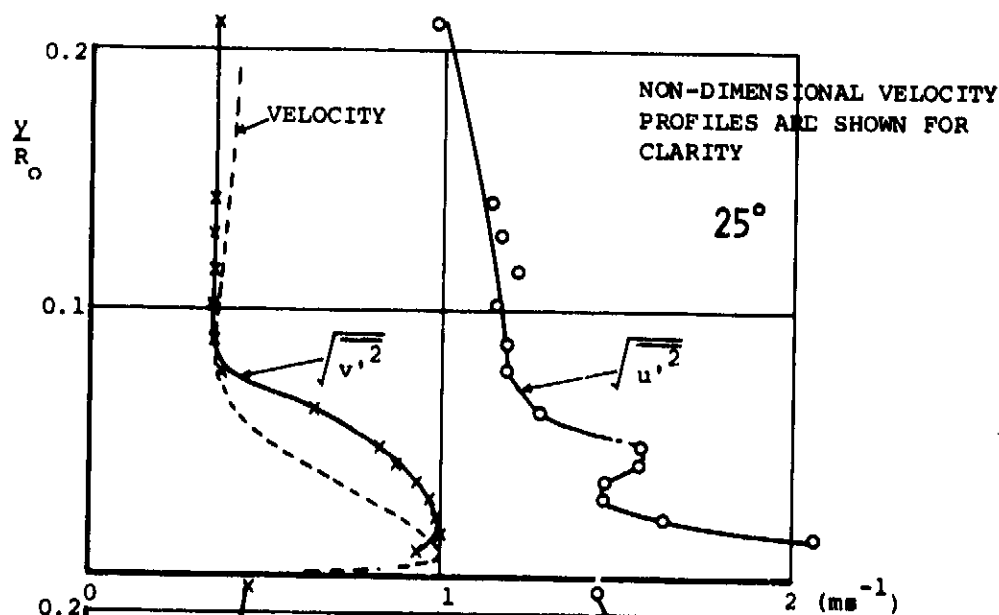
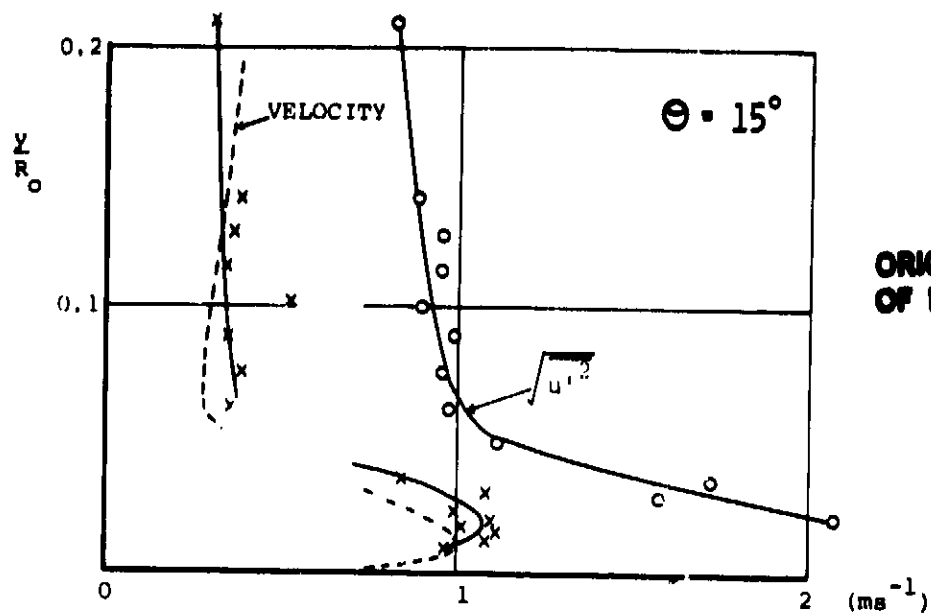


FIGURE 125: COMPARISON OF LONGITUDINAL AND NORMAL TURBULENCE QUANTITIES IN THE TRAILING EDGE WALL JET
 $C_p = 0.0139, \alpha_G = 0^\circ$

FIG 126

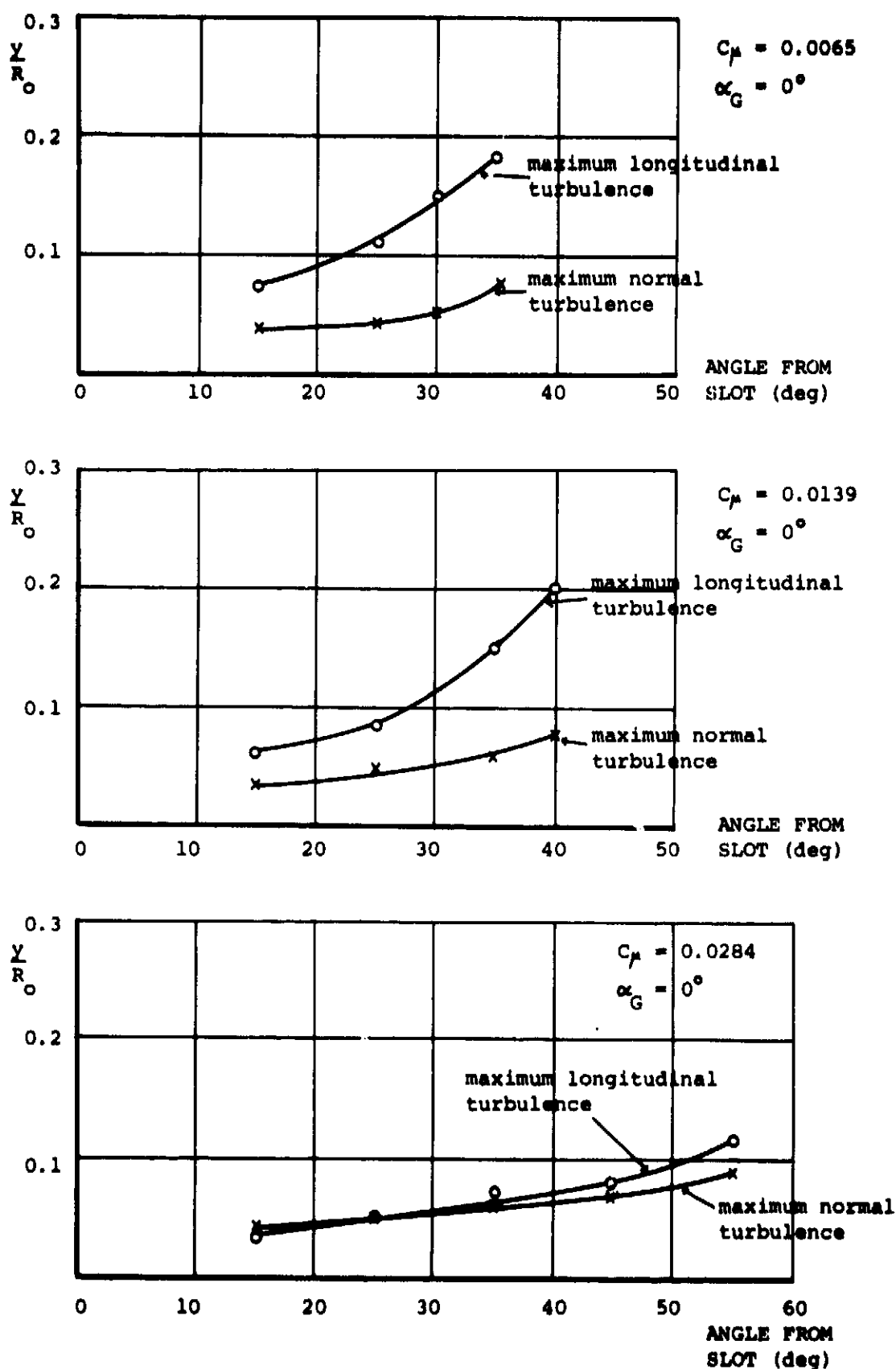


FIGURE 126: COMPARISON OF DEVELOPMENT OF THE LONGITUDINAL AND NORMAL TURBULENCE MAXIMA IN THE TRAILING EDGE WALL JET

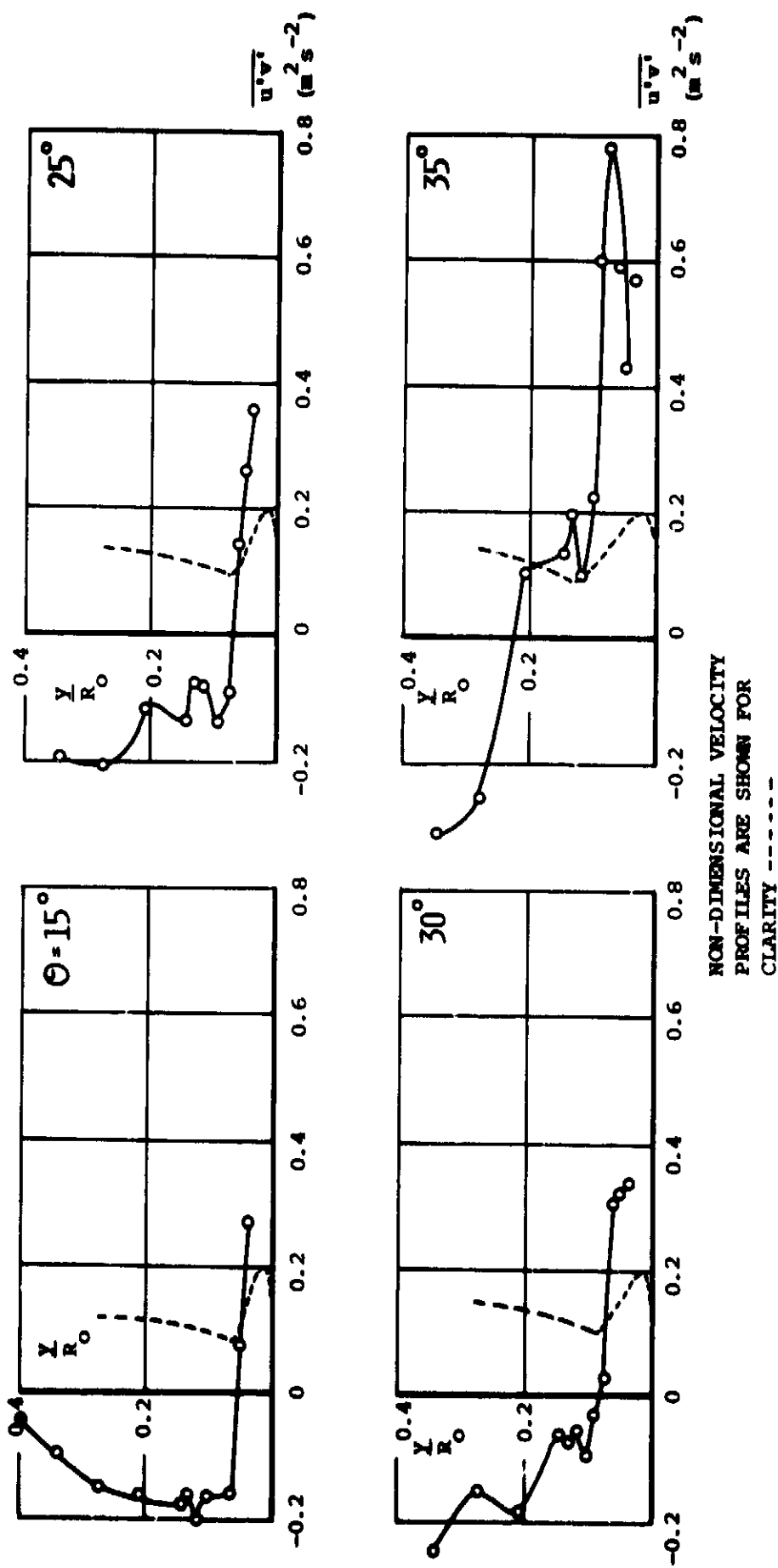


FIGURE 127: REYNOLDS SHEAR STRESS DISTRIBUTION IN THE TRAILING EDGE WALL JET $C_\mu = 0.0065$, $\alpha_G = 0^\circ$

FIG 127

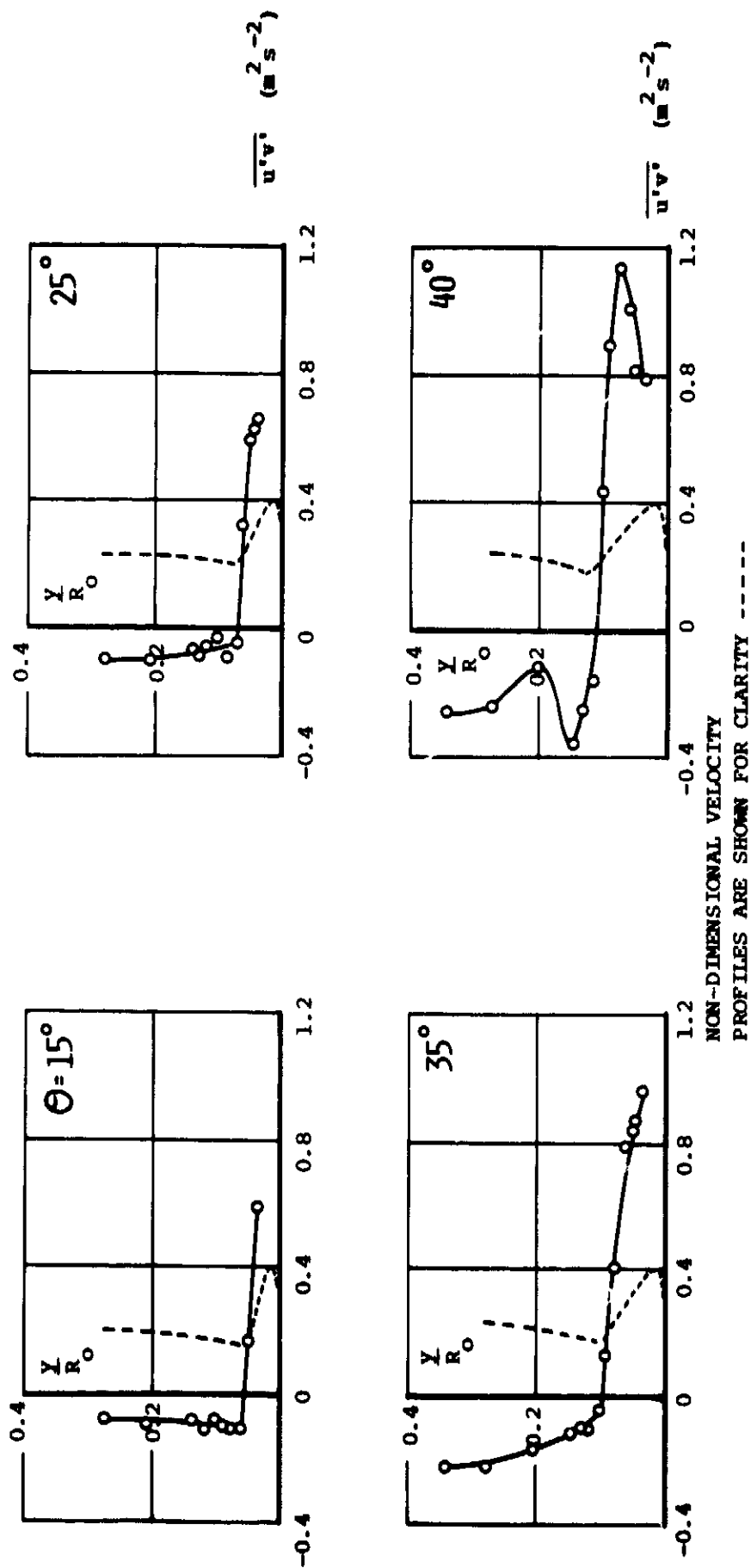


FIGURE 128: REYNOLDS SHEAR STRESS DISTRIBUTION IN THE TRAILING EDGE WALL JET $\alpha_0 = 0.0139$, $\alpha_6 = 0^\circ$

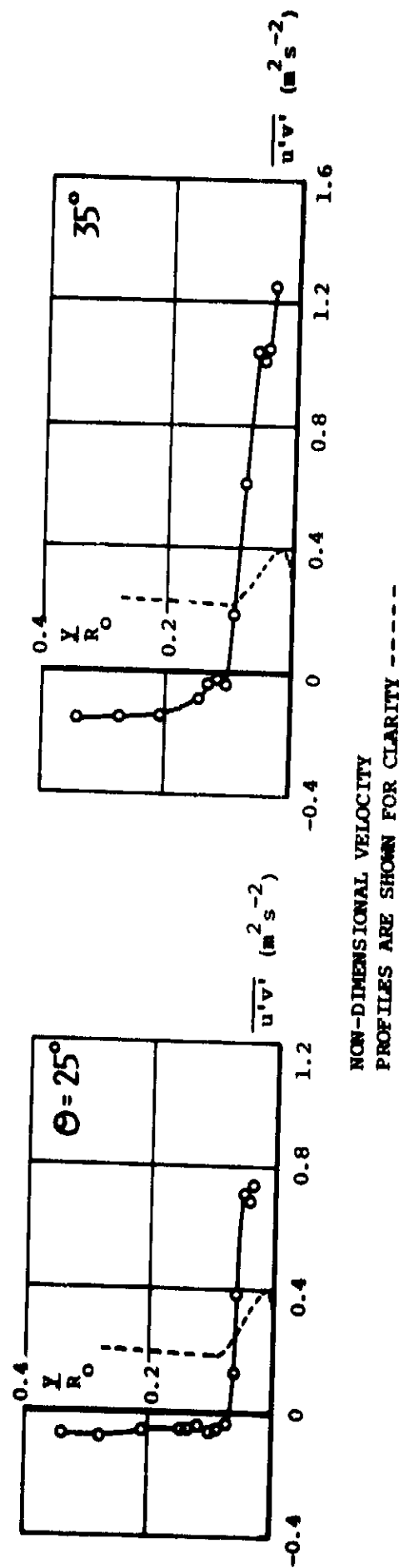
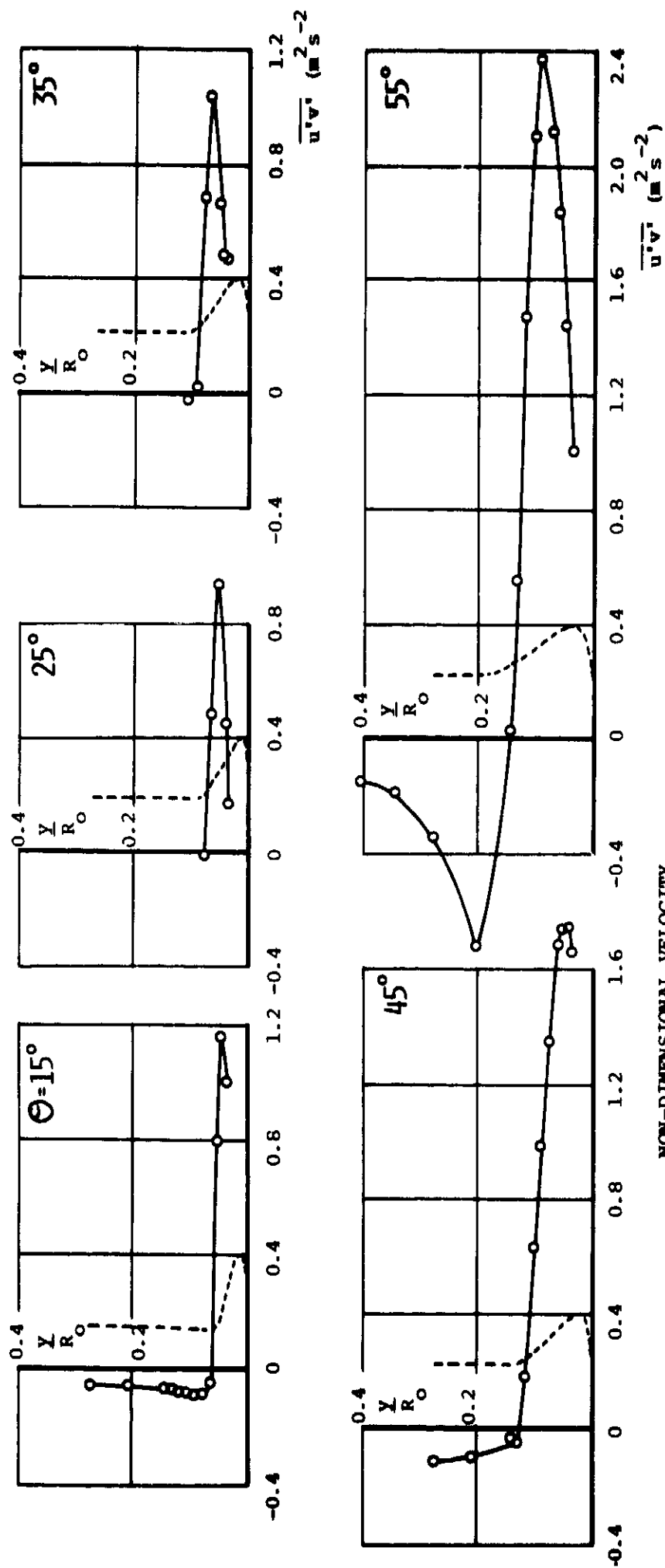


FIGURE 129: REYNOLDS SHEAR STRESS DISTRIBUTION IN THE TRAILING EDGE WALL JET $C_\mu = 0.0197, \alpha_G = 0^\circ$

FIG 129



NON-DIMENSIONAL VELOCITY
PROFILES ARE SHOWN FOR CLARITY -----

FIGURE 130: REYNOLDS SHEAR STRESS DISTRIBUTION IN THE TRAILING EDGE WALL JET $C_p = 0.0284$, $\alpha_G = 0^\circ$

FIG 130

FIG 131

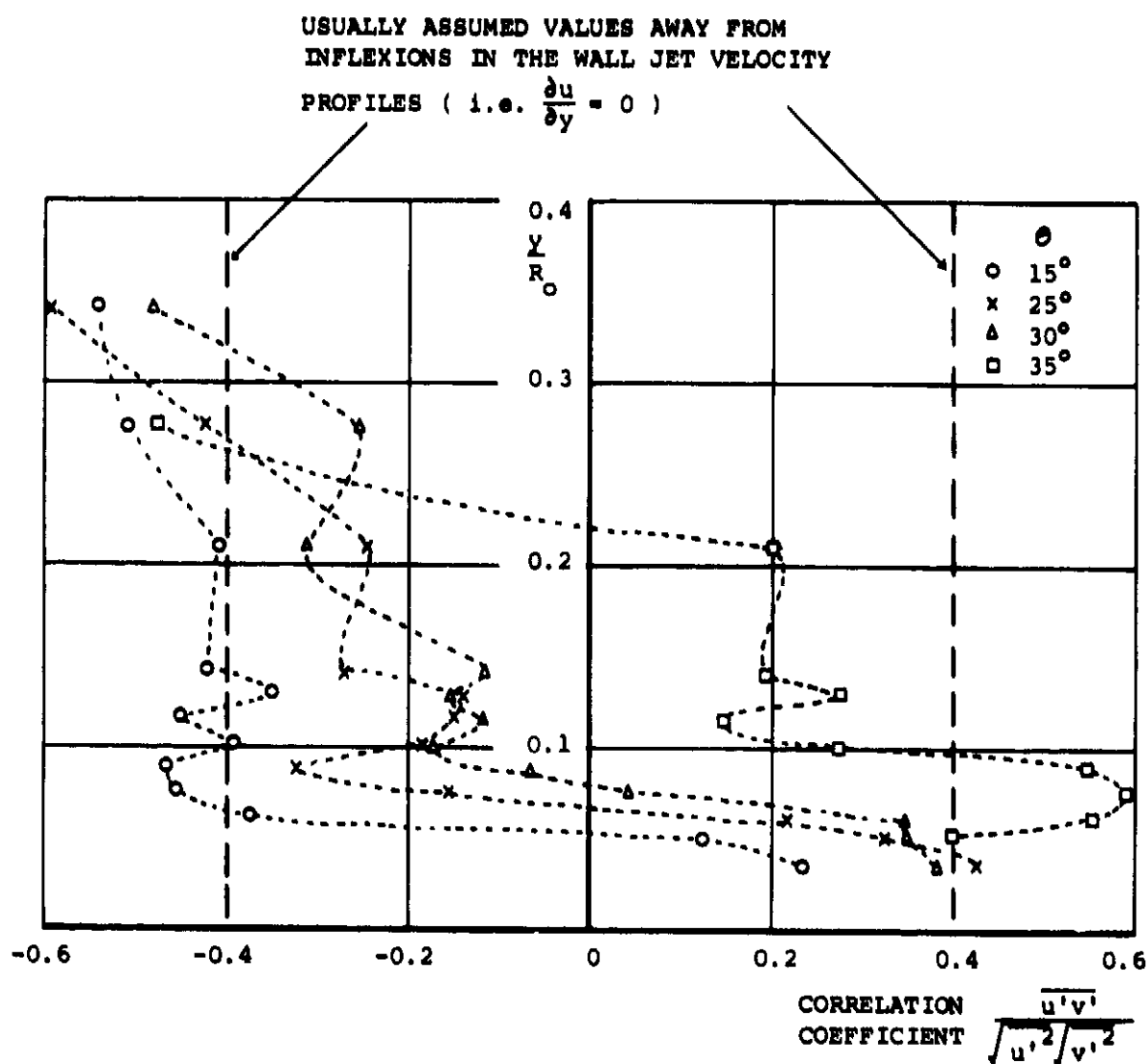


FIGURE 131: CORRELATION COEFFICIENT OF SPLIT FILM RESULTS IN
THE TRAILING EDGE WALL JET $C_{\mu} = 0.0065$, $\alpha_G = 0^\circ$

$$\left(\frac{\sqrt{v'^2}}{U}\right)_{\text{wire}} = \left(\frac{\sqrt{v'^2}}{\sqrt{u'^2}}\right)_{\text{film}} \times \left(\frac{\sqrt{u'^2}}{U}\right)_{\text{wire}}$$

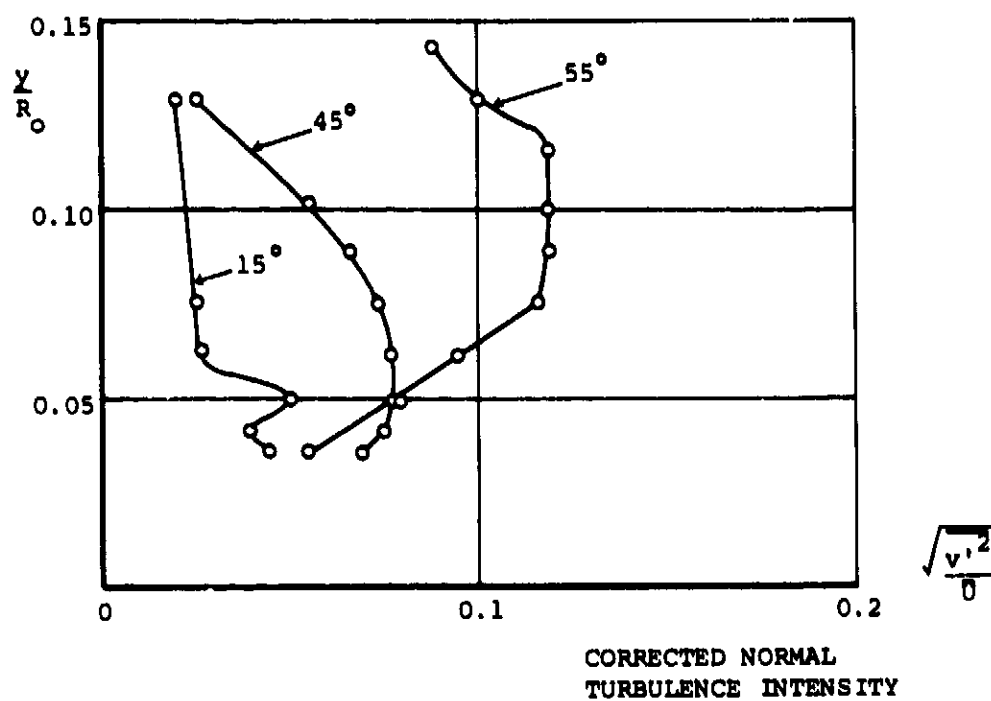


FIGURE 132: AN EXAMPLE OF THE PROPOSED CORRECTION FOR LOW ANEMOMETER BANDWIDTH ON THE NORMAL TURBULENCE INTENSITY $C_p = 0.0284$, $\alpha_G = 0^\circ$

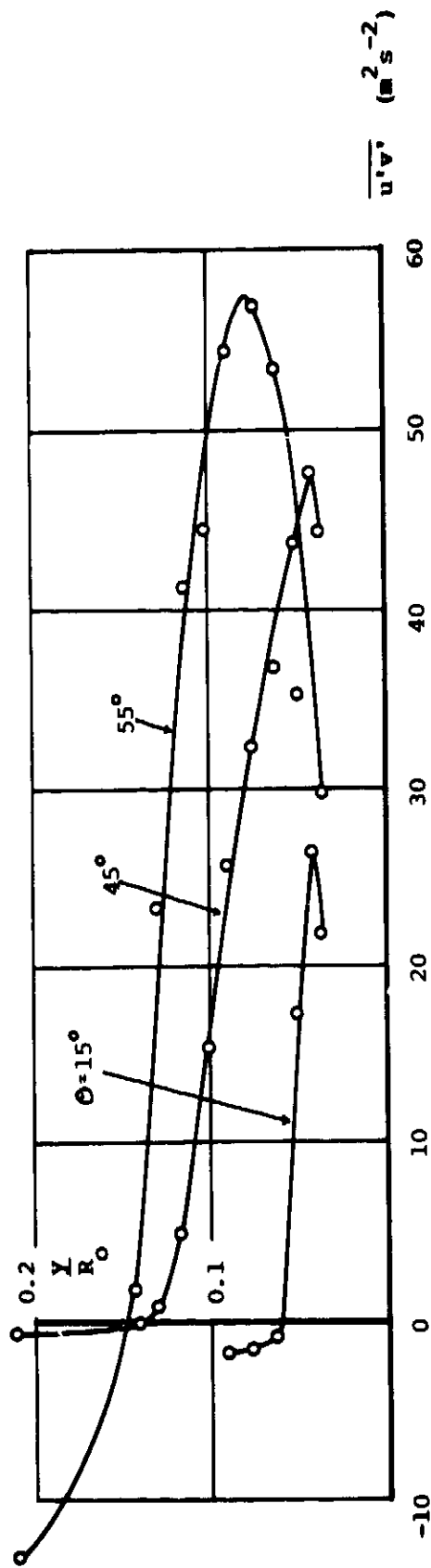


FIGURE 133: AN EXAMPLE OF THE PROPOSED CORRECTION FOR LOW ANEMOMETER BANDWIDTH ON THE REYNOLDS SHEAR STRESS $C_\mu = 0.0284$, $\alpha_G = 0^\circ$

FIG 134

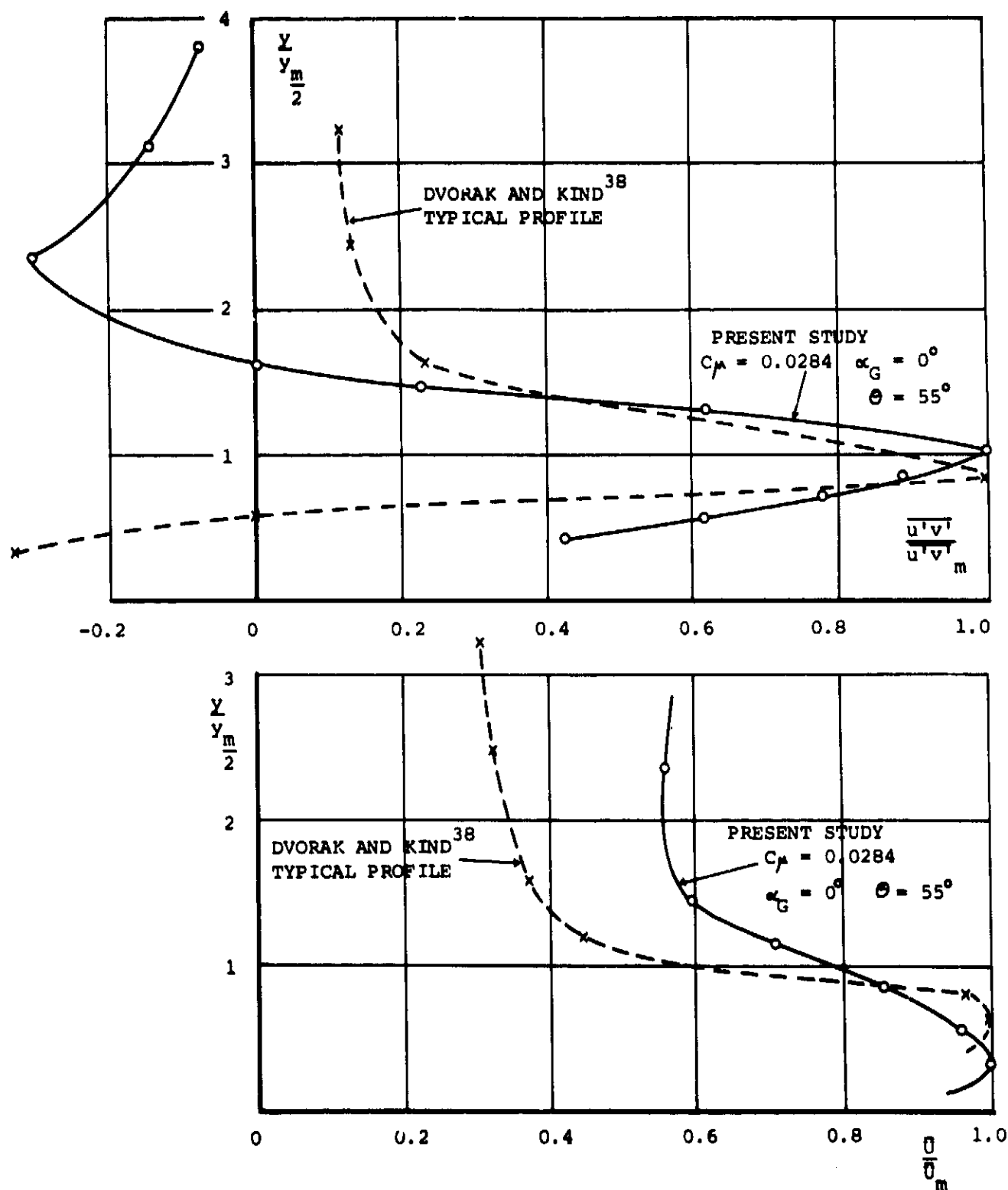


FIGURE 134: COMPARISON BETWEEN THE SHEAR STRESS RESULTS OF THE PRESENT STUDY AND TYPICAL VALUES FROM THE CALCULATION METHOD OF DVORAK AND KIND³⁸

FIG 135

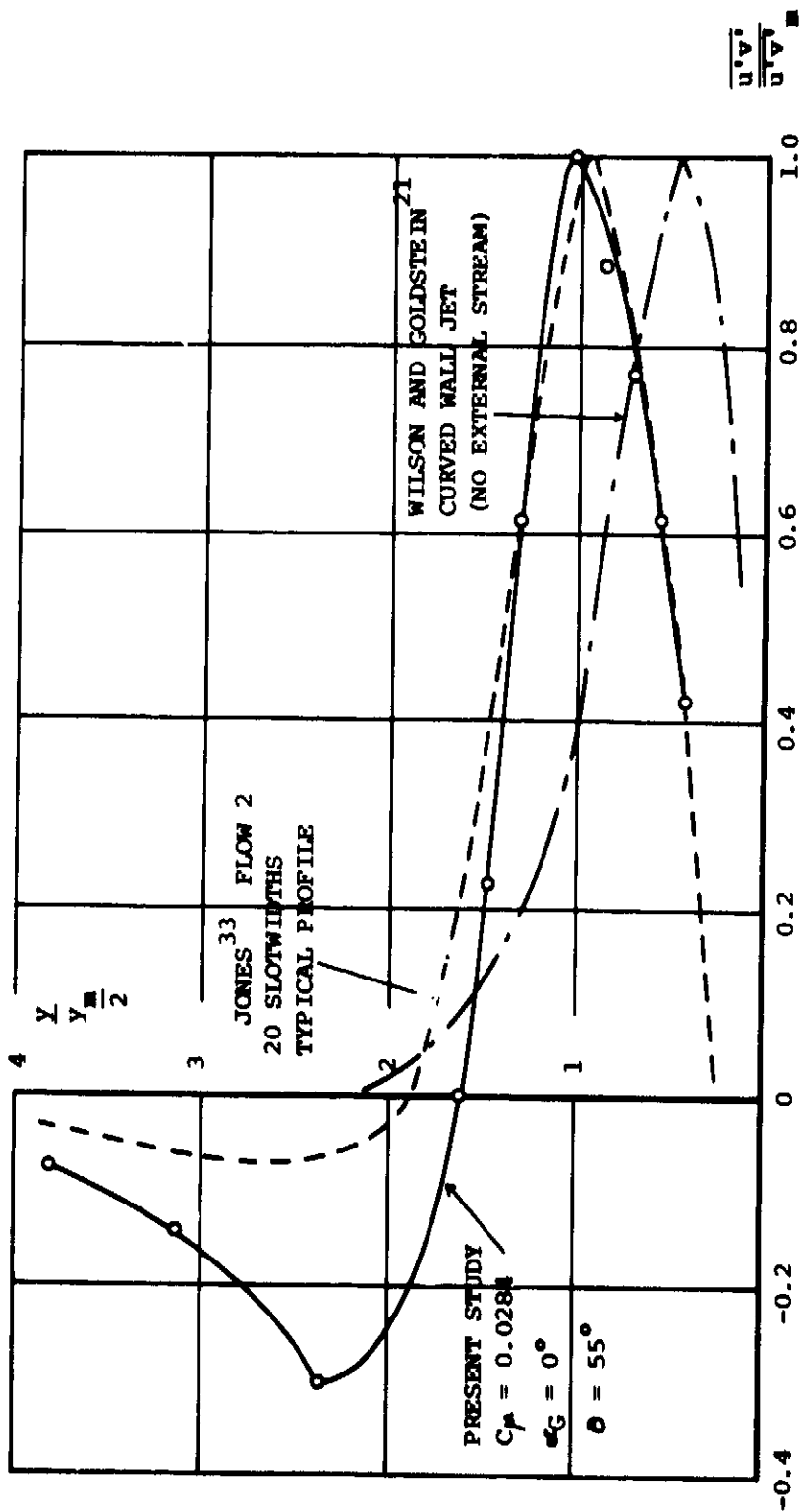


FIGURE 135: COMPARISON BETWEEN THE SHEAR STRESS RESULTS OF THE PRESENT STUDY AND THOSE FROM JONES³³ AND WILSON AND GOLDSTEIN²¹

FIG 136

SEE FIGURE 62 FOR THE GEOMETRY
OF THE MEASURING PROBES

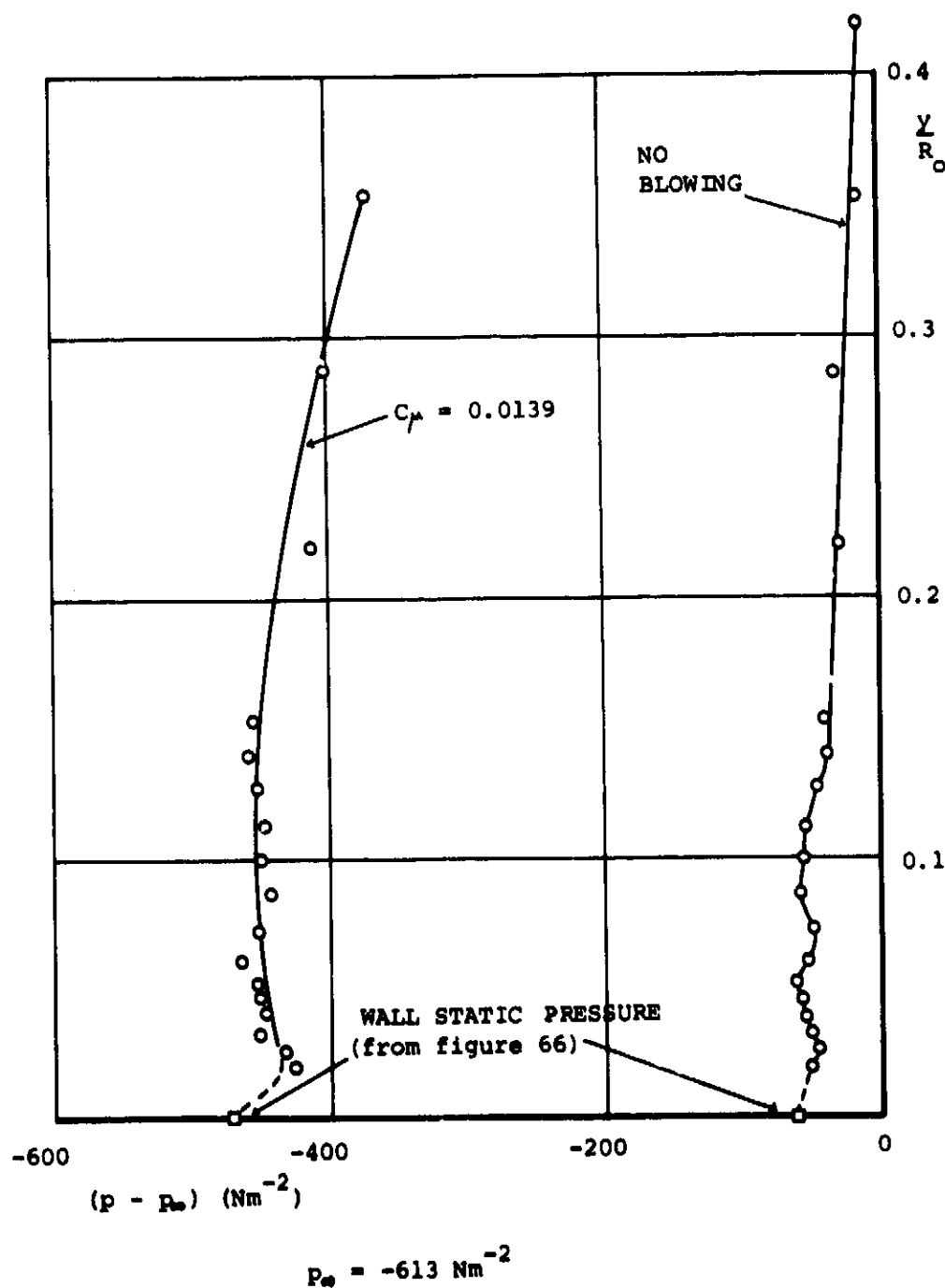


FIGURE 136: UPSTREAM BOUNDARY LAYER RADIAL STATIC PRESSURE DISTRIBUTION $\alpha_G = 0^\circ$

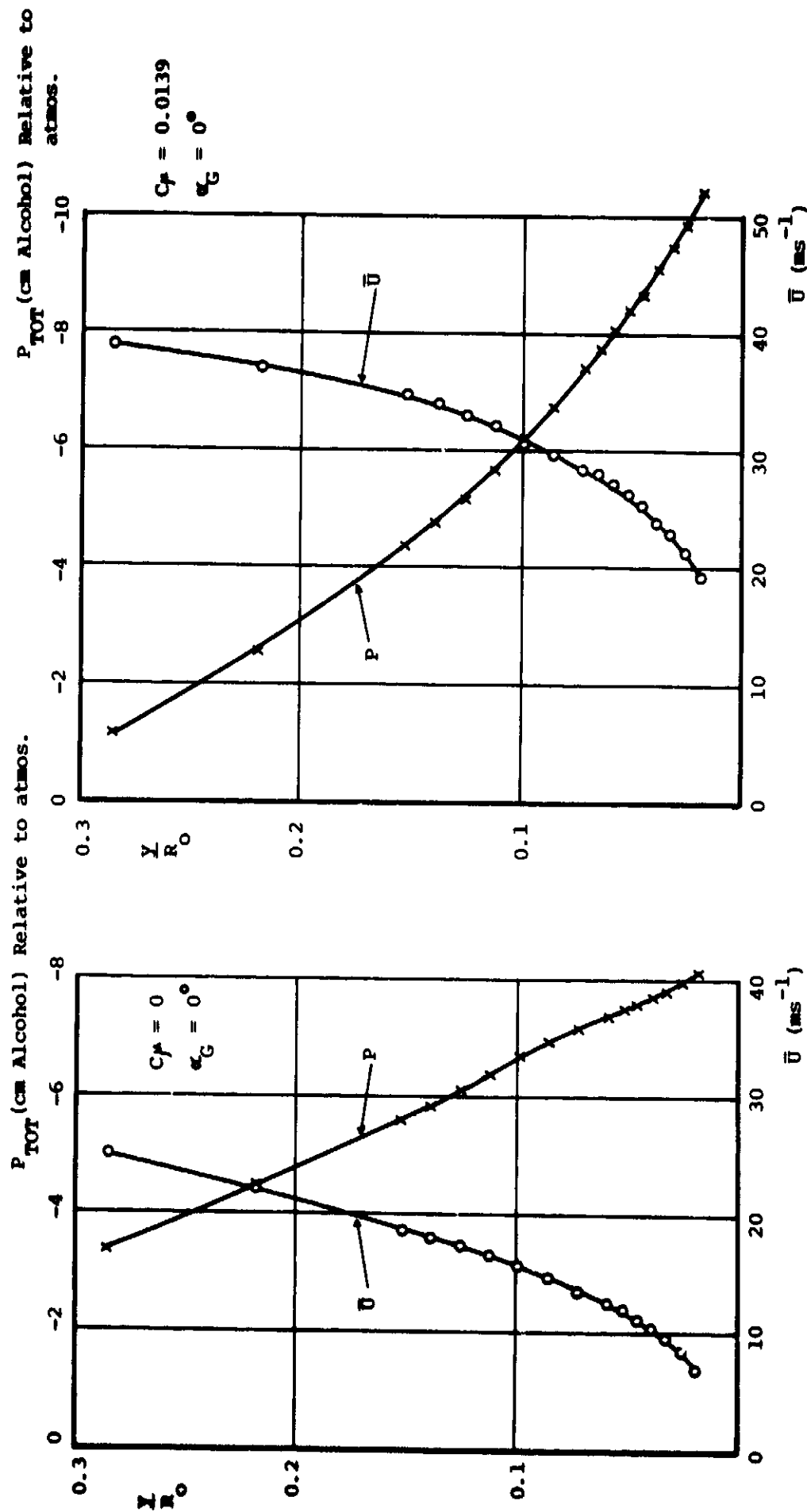


FIGURE 137: ACTUAL MEASUREMENTS USED TO DERIVE FIGURE 136

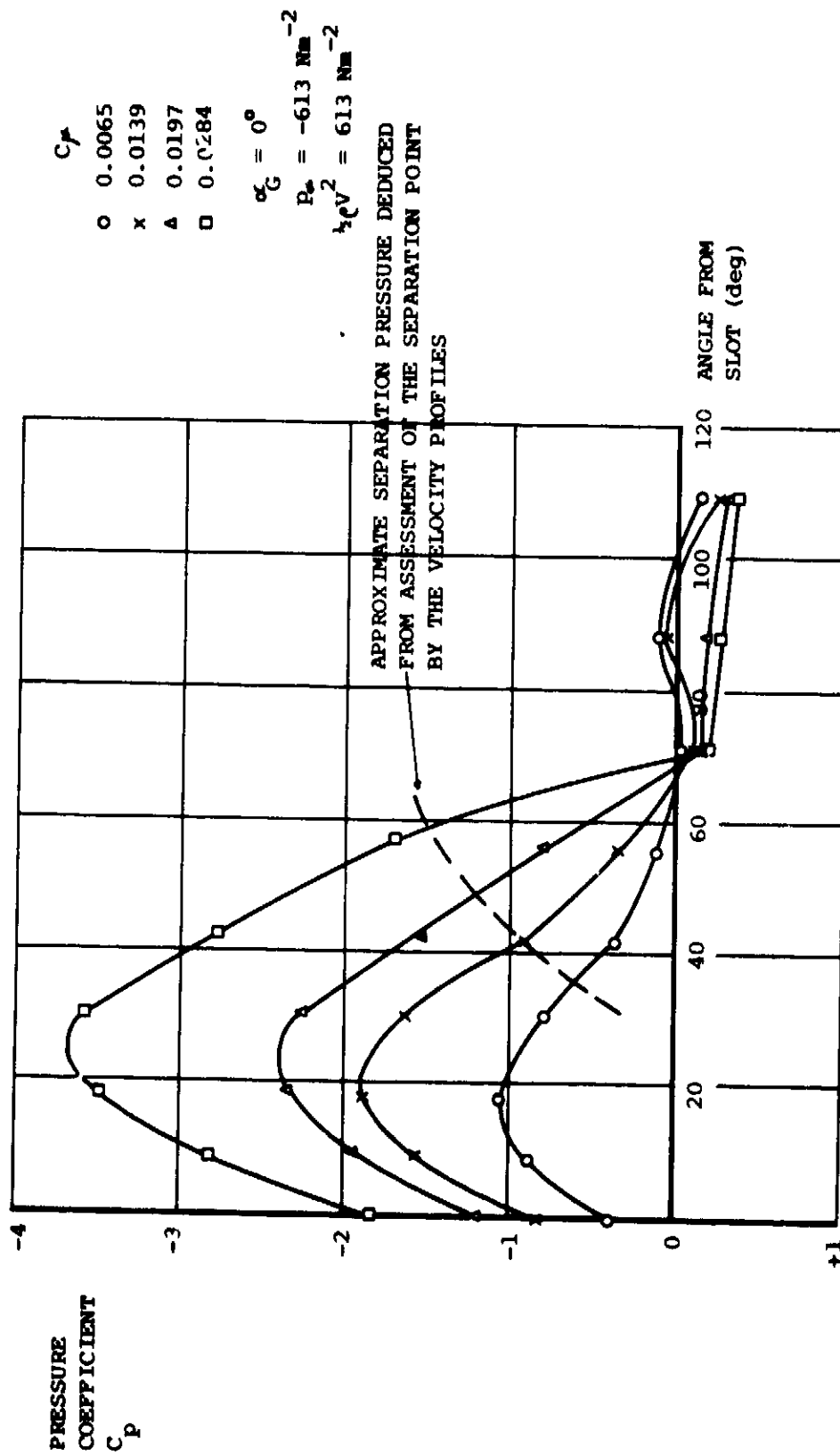


FIGURE 138: TRAILING EDGE STATIC PRESSURE DISTRIBUTIONS INDICATING SEPARATION POINT

FIG 139

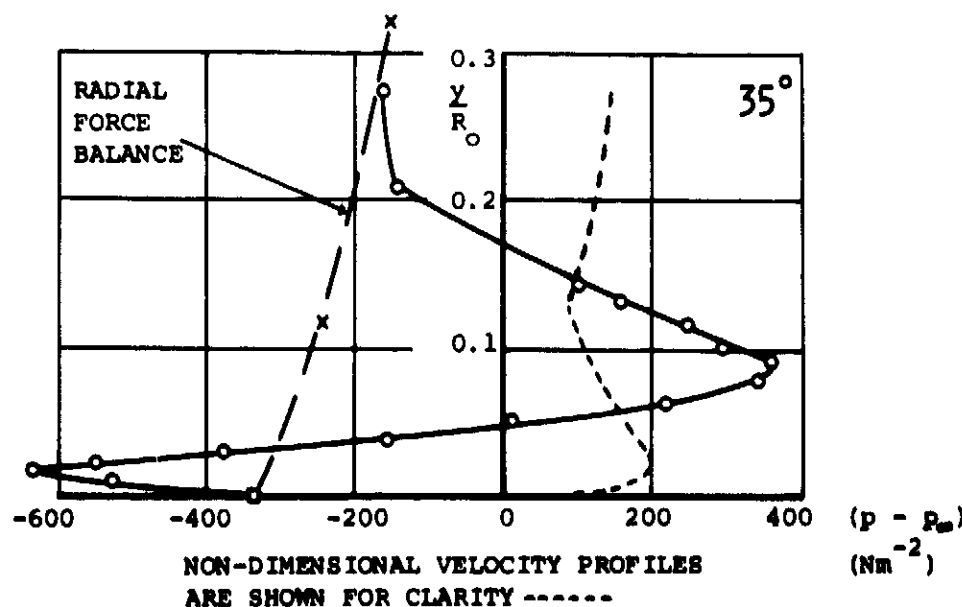
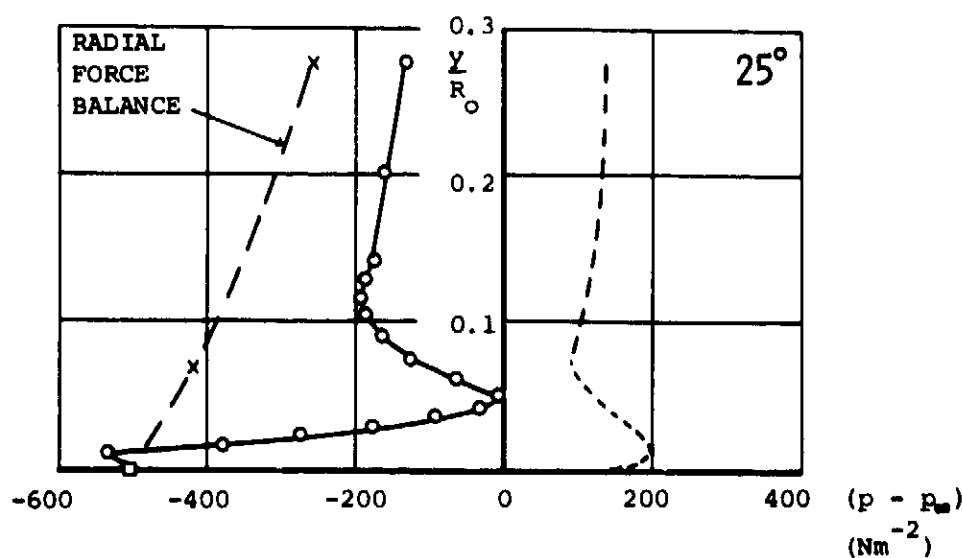
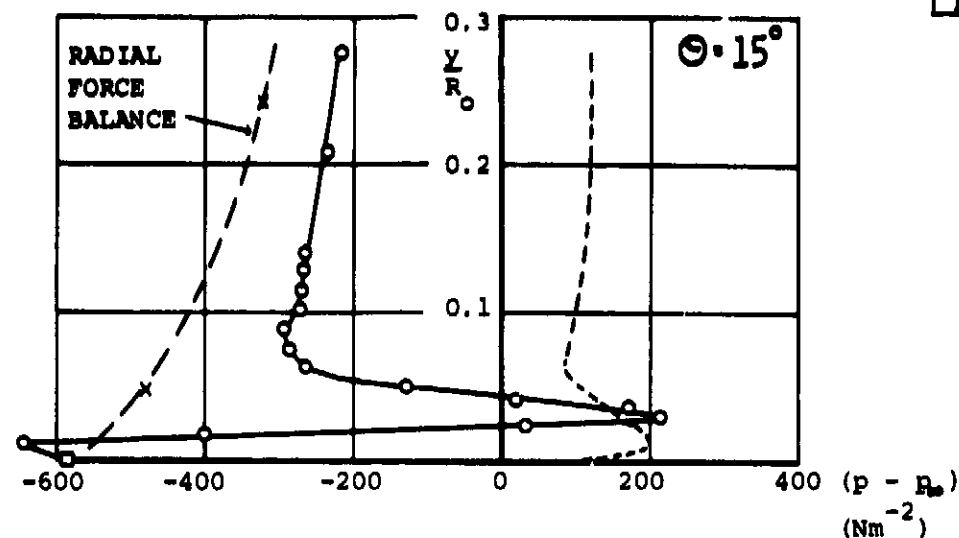


FIGURE 139: RADIAL STATIC PRESSURE DISTRIBUTION IN THE TRAILING EDGE WALL JET $C_\mu = 0.0065$, $\alpha_G = 0^\circ$

FIG 140

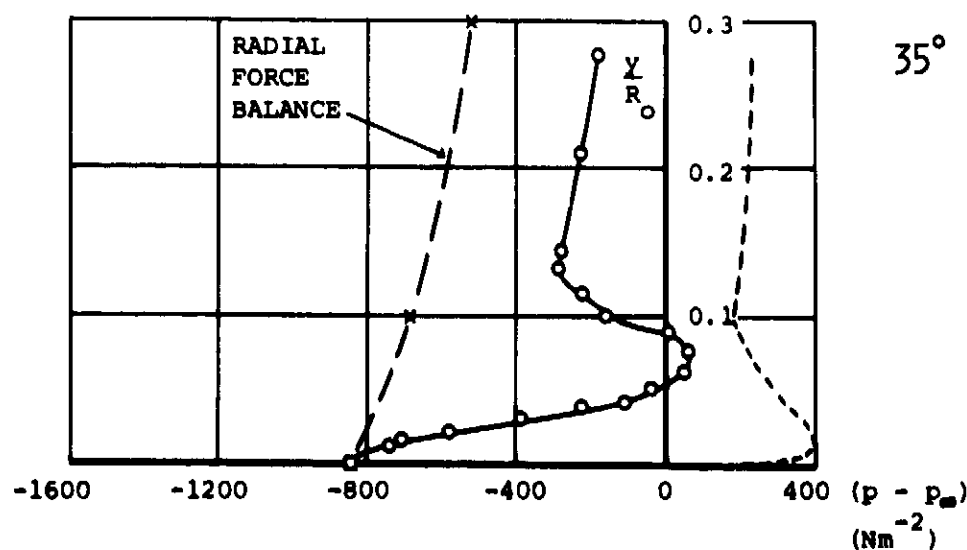
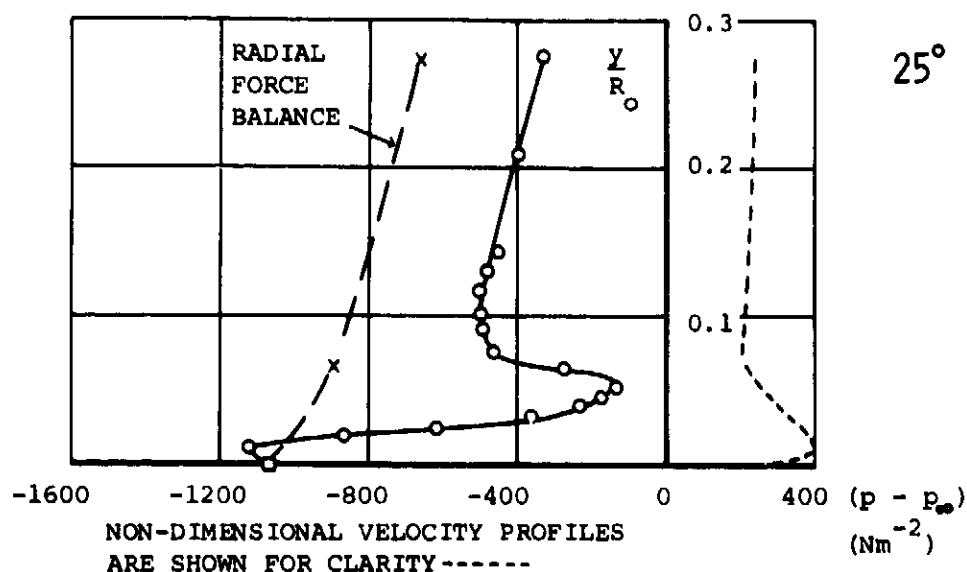
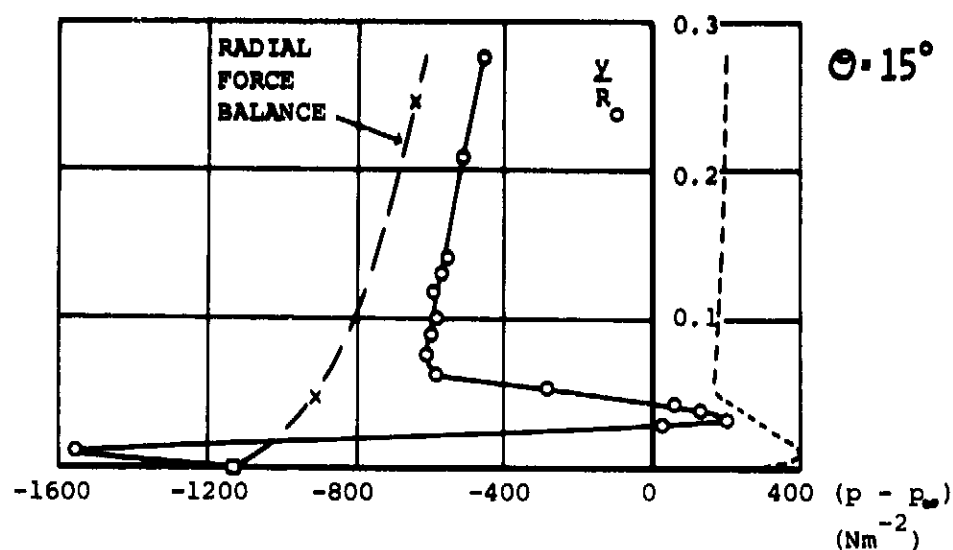


FIGURE 140: RADIAL STATIC PRESSURE DISTRIBUTION IN THE TRAILING EDGE WALL JET $C_\mu = 0.0139$, $\alpha_G = 0^\circ$

FIG 141

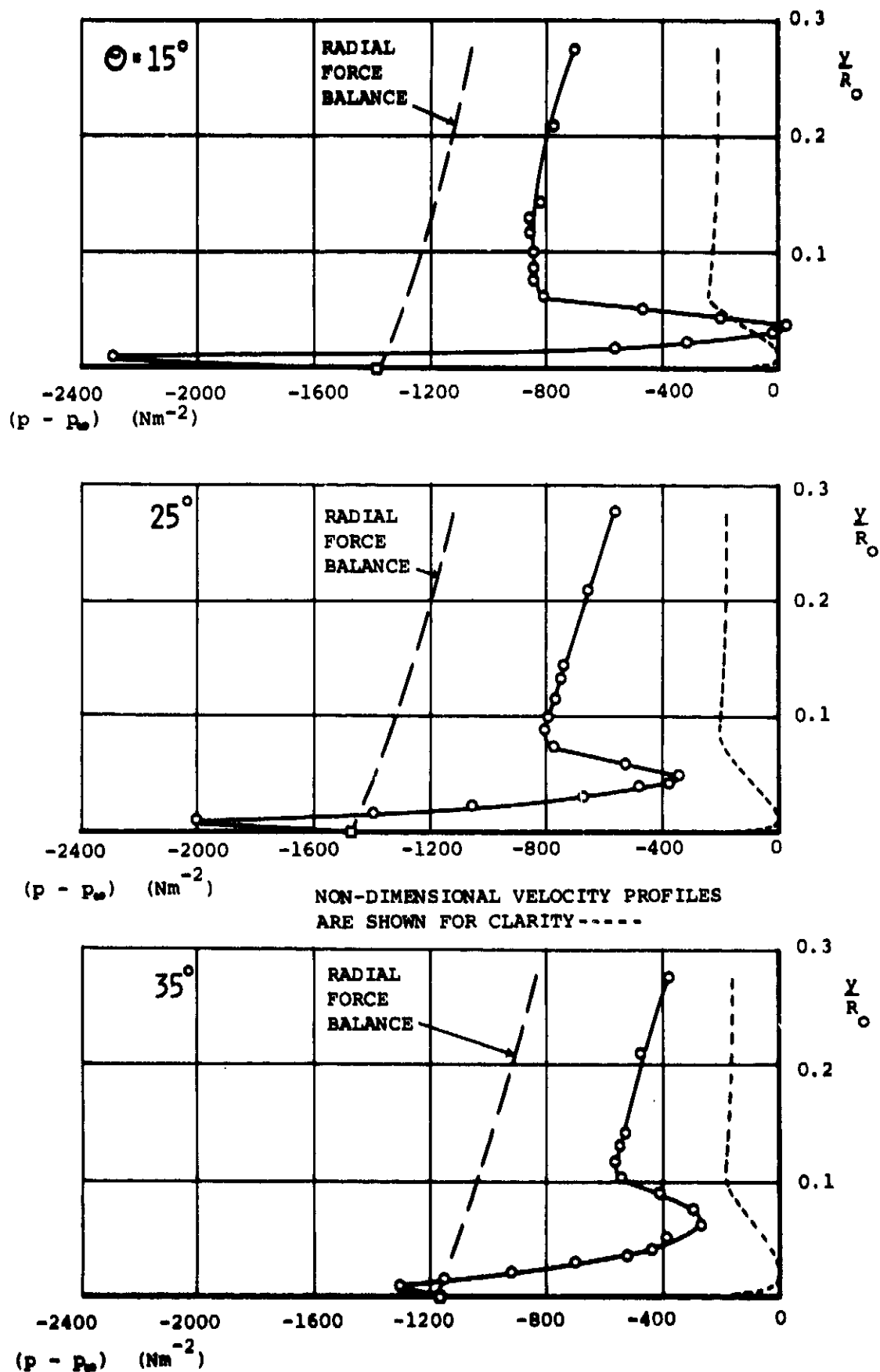


FIGURE 141: RADIAL STATIC PRESSURE DISTRIBUTION IN THE TRAILING
EDGE WALL JET $C_{\mu} = 0.0197$, $\alpha_G = 0^\circ$

FIG 142A

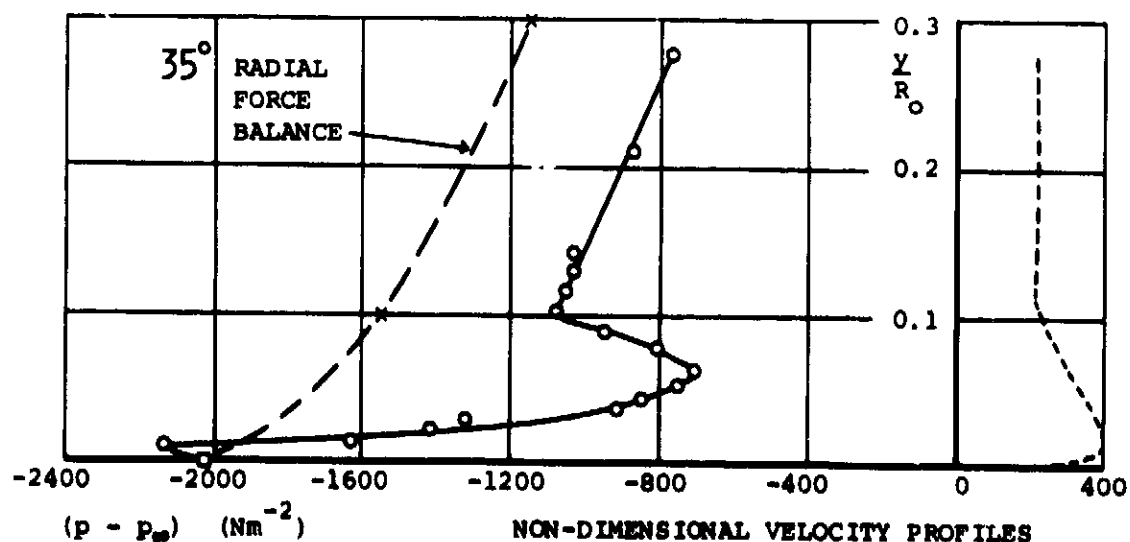
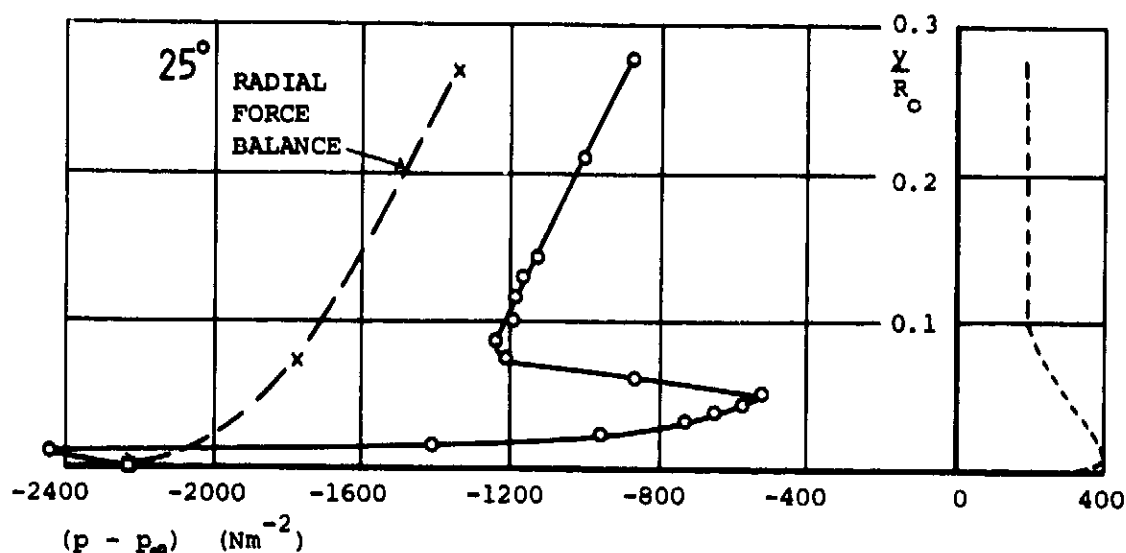
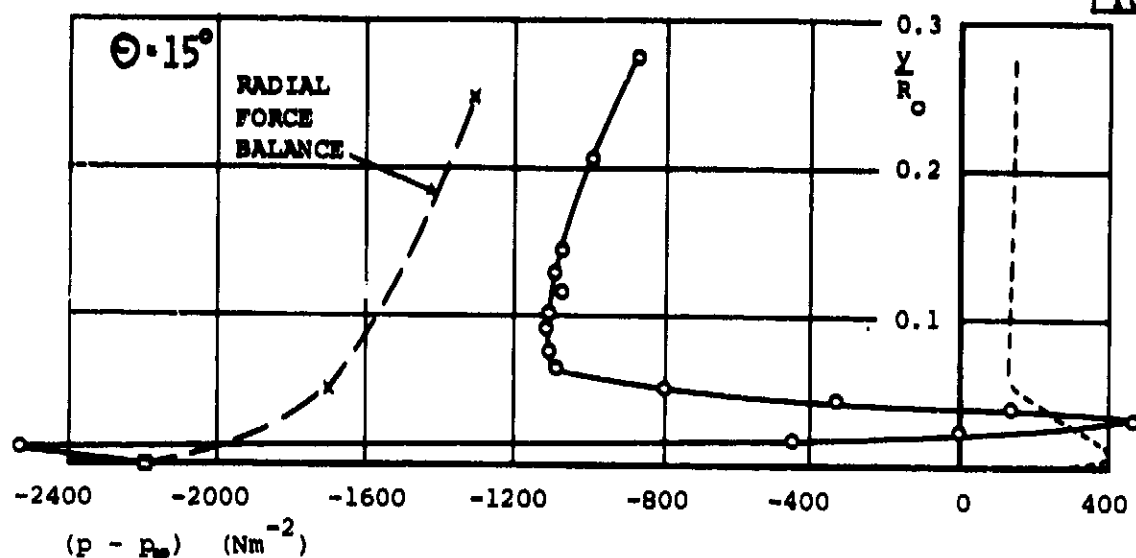
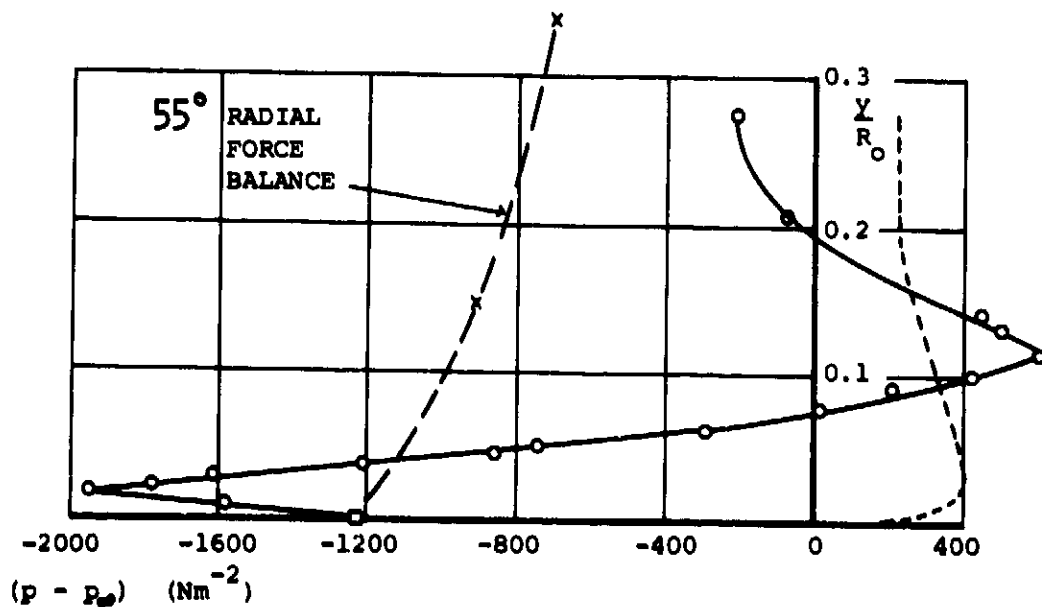
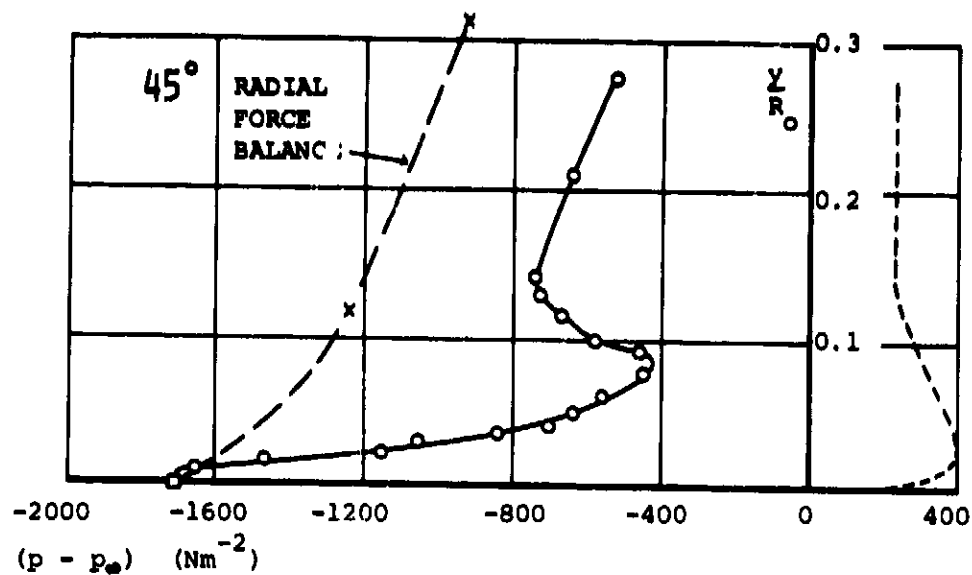


FIGURE 142A: RADIAL STATIC PRESSURE DISTRIBUTION IN THE TRAILING EDGE WALL JET $C_\mu = 0.0284$, $\alpha_G = 0^\circ$

FIG 142B



NON-DIMENSIONAL VELOCITY PROFILES
ARE SHOWN FOR CLARITY -----

FIGURE 142B: RADIAL STATIC PRESSURE DISTRIBUTION IN THE TRAILING
EDGE WALL JET $C_\mu = 0.0284$, $\alpha_G = 0^\circ$

FIG 143



DETAILS OF THE MAGNITUDES OF THE AXES ARE NOT
GIVEN IN REFERENCE 49

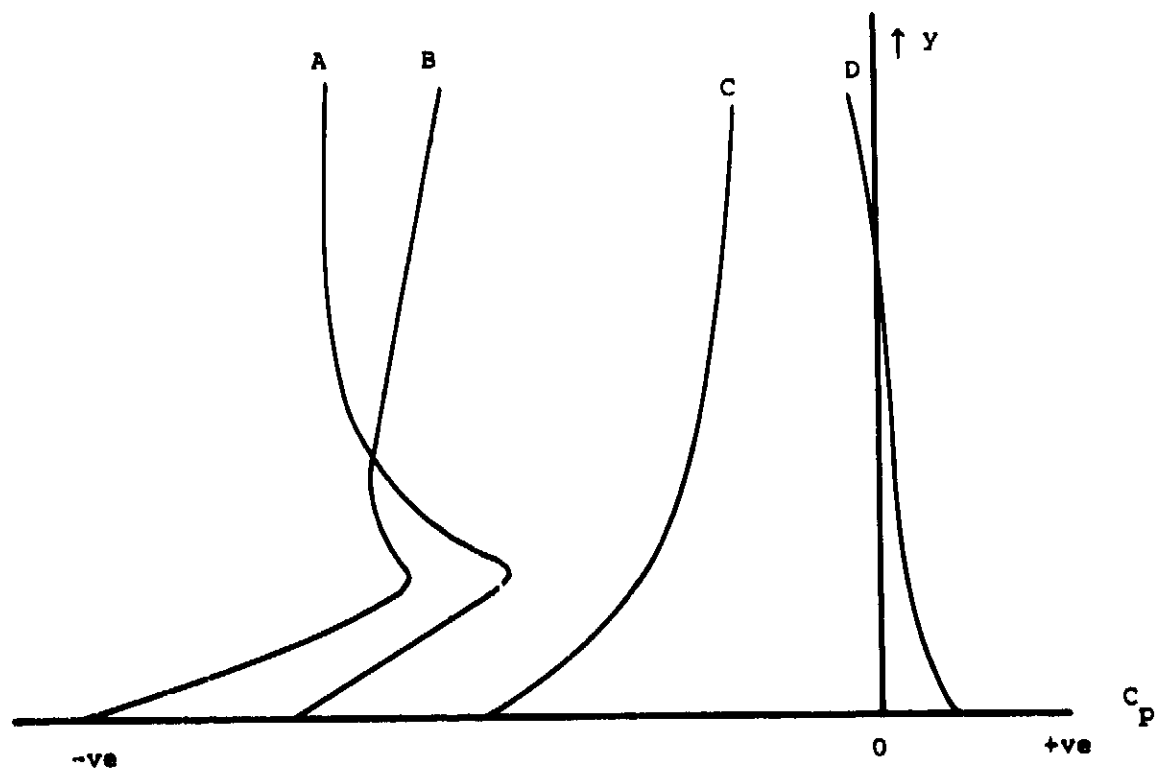


FIGURE 143: STATIC PRESSURE VARIATION NORMAL TO A SLOTTED FLAP SURFACE FROM REFERENCE 49

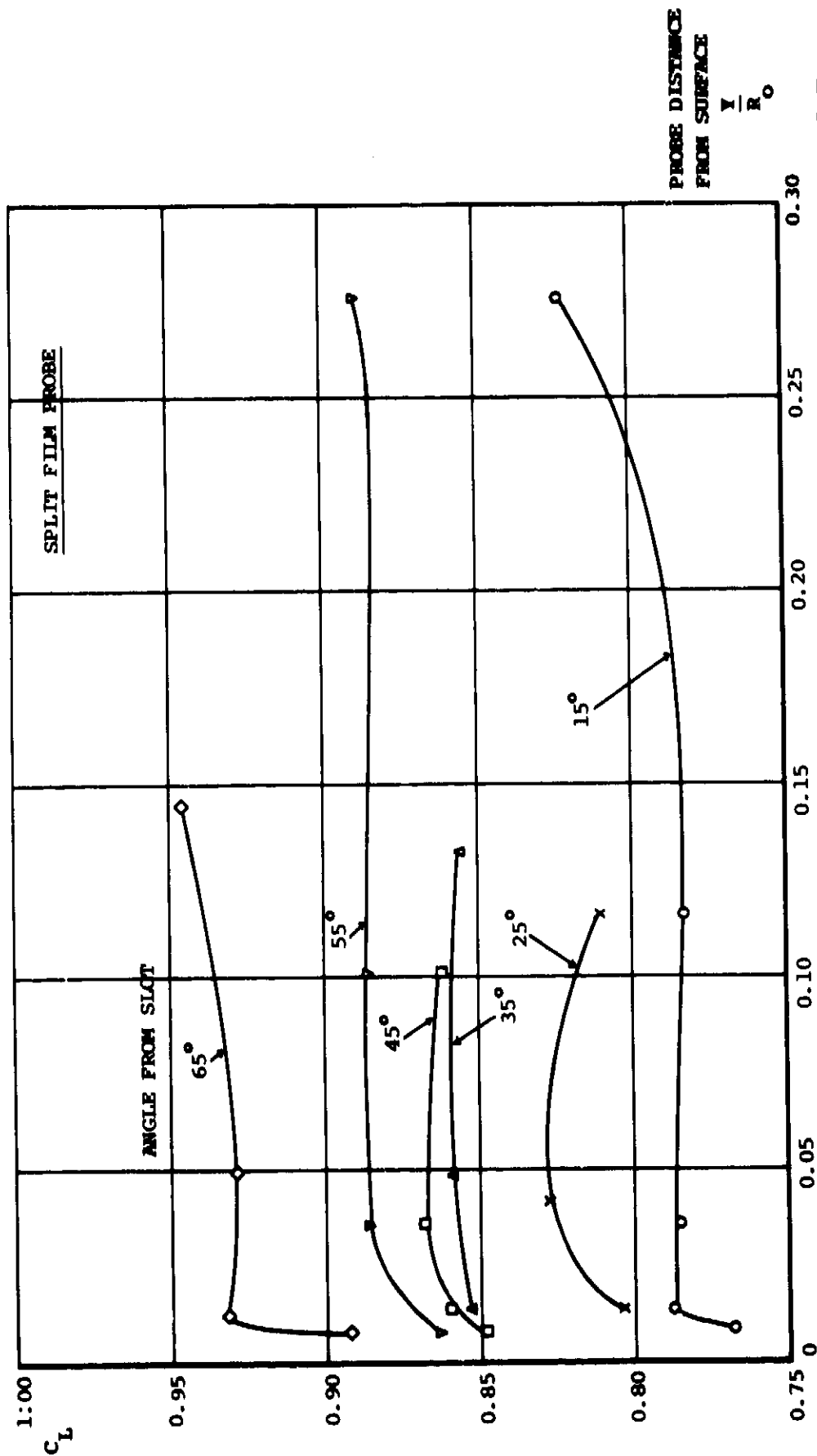


FIGURE 144: EFFECT OF SPLIT FILM PROBE POSITION ON THE MEASURED CENTRELINE LIFT COEFFICIENT

$$C_{ps} = 0.0284, \alpha_G = 0^\circ$$

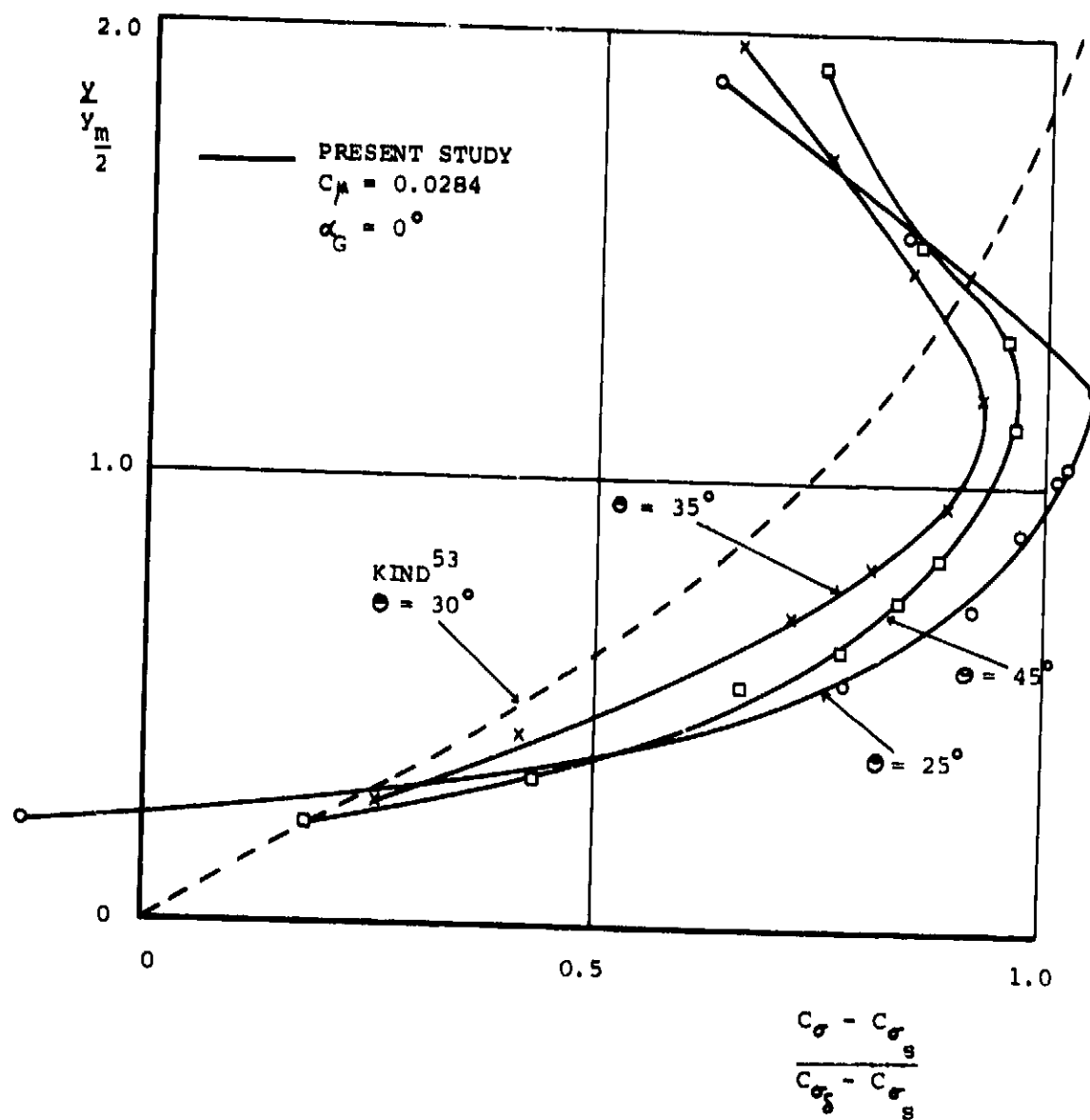


FIGURE 145: A COMPARISON BETWEEN THE PRESENT RESULTS AND THE THEORETICAL NORMAL STRESS CALCULATION OF KIND⁵³

FIG 146

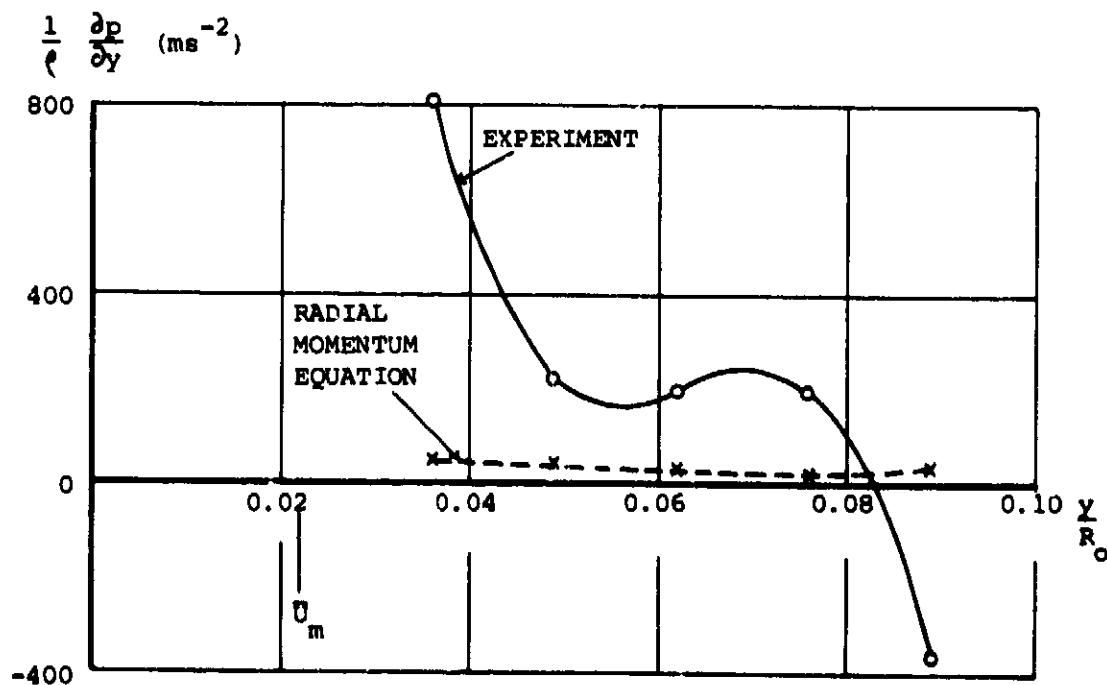
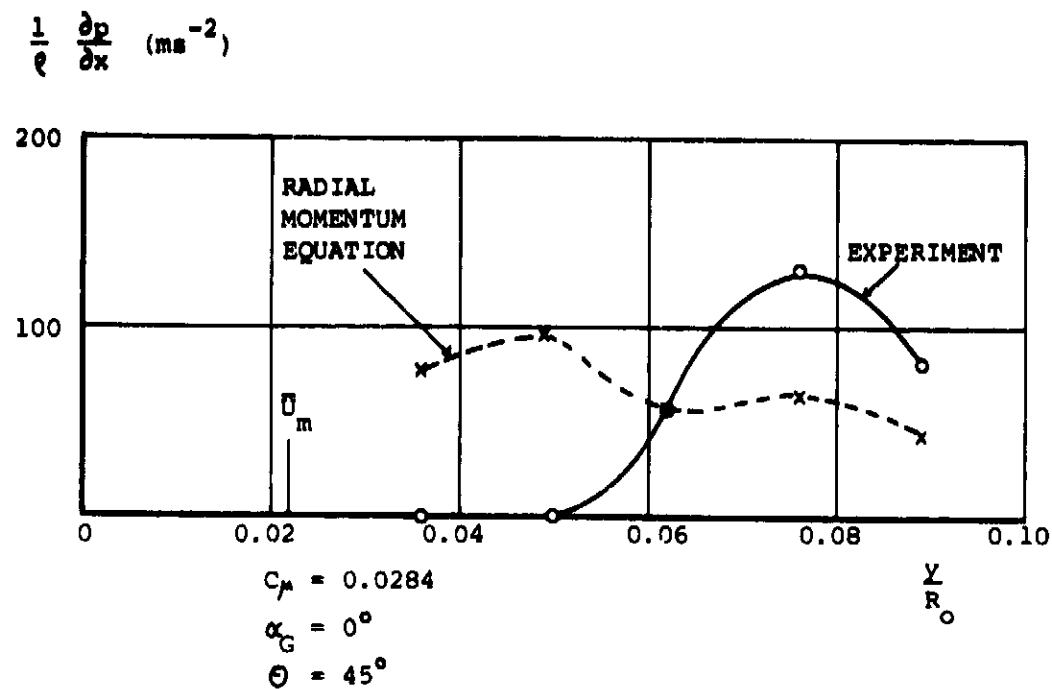
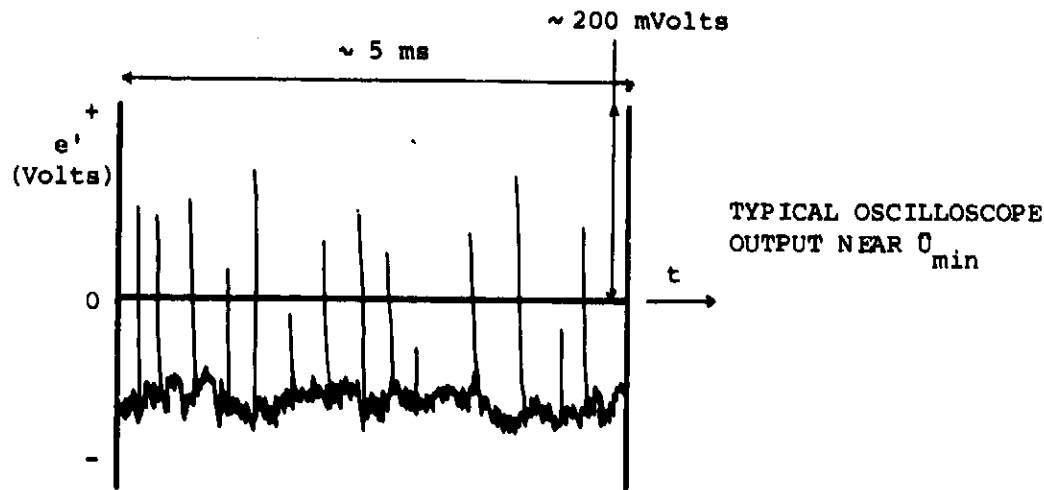
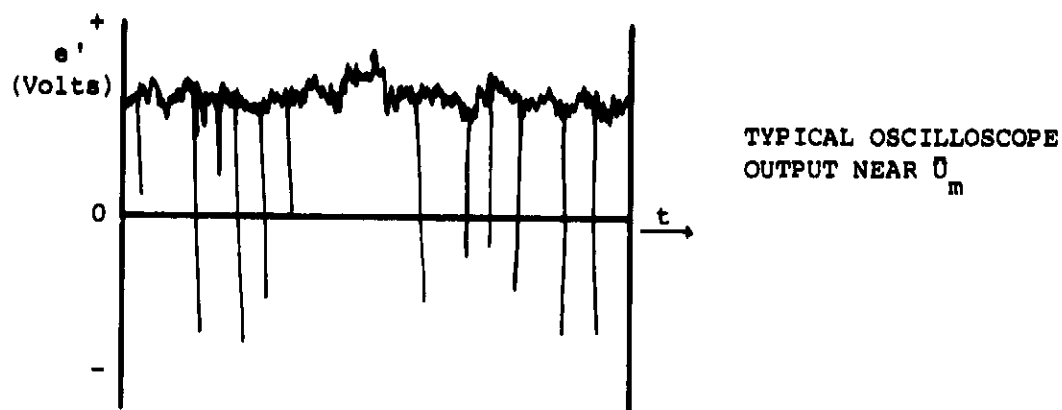


FIGURE 146: COMPARISON BETWEEN MEASURED STATIC PRESSURE GRADIENTS AND THOSE OBTAINED FROM THE RADIAL MOMENTUM EQUATION

FIG 147



TYPICAL OFFSETS WERE 100 mV
HIGH PASS FREQUENCY = 2 Hz

FIGURE 147: SKETCH OF OBSERVED HOT WIRE OUTPUT SIGNALS

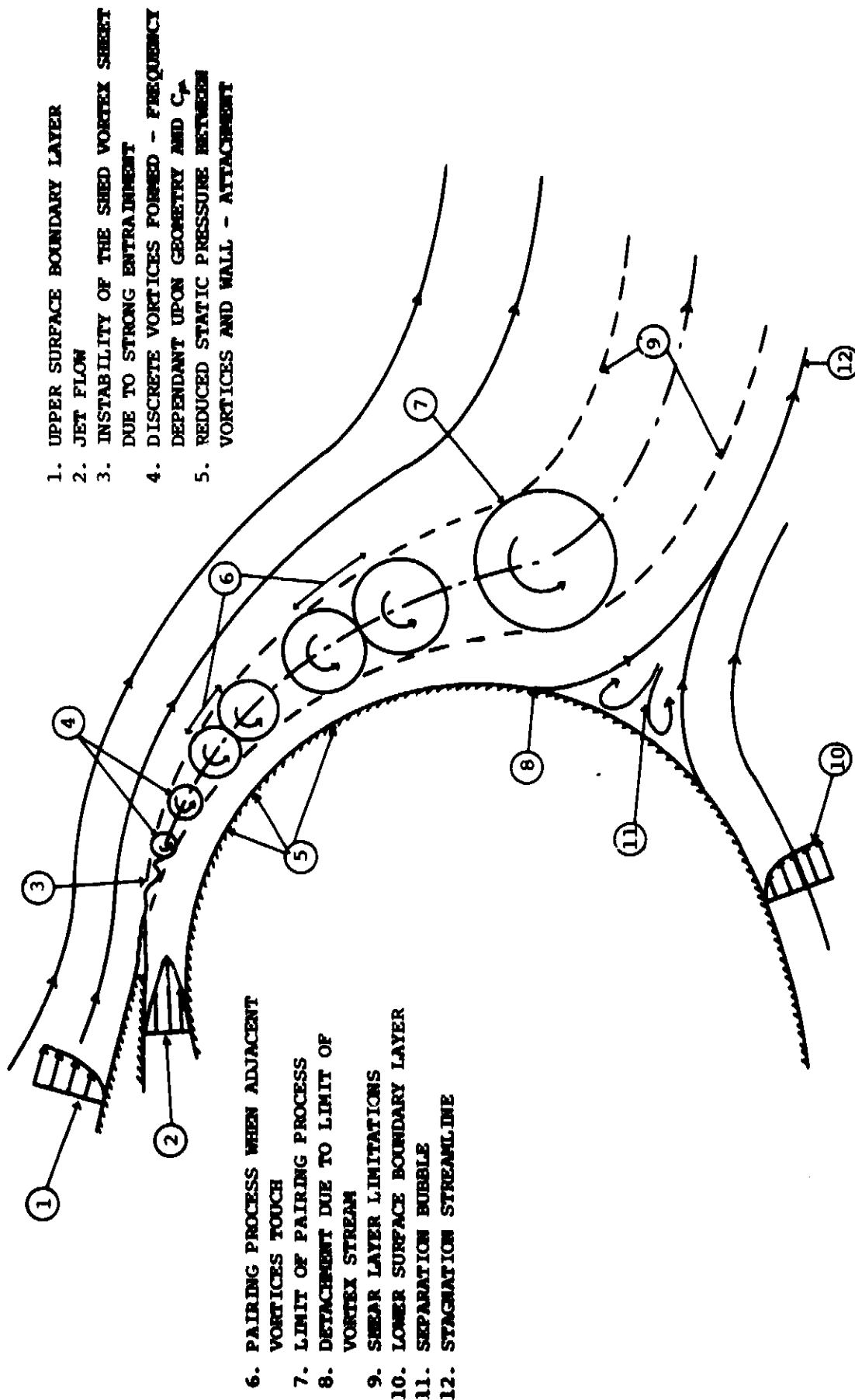


FIGURE 148: PROPOSED COANDA FLOWFIELD

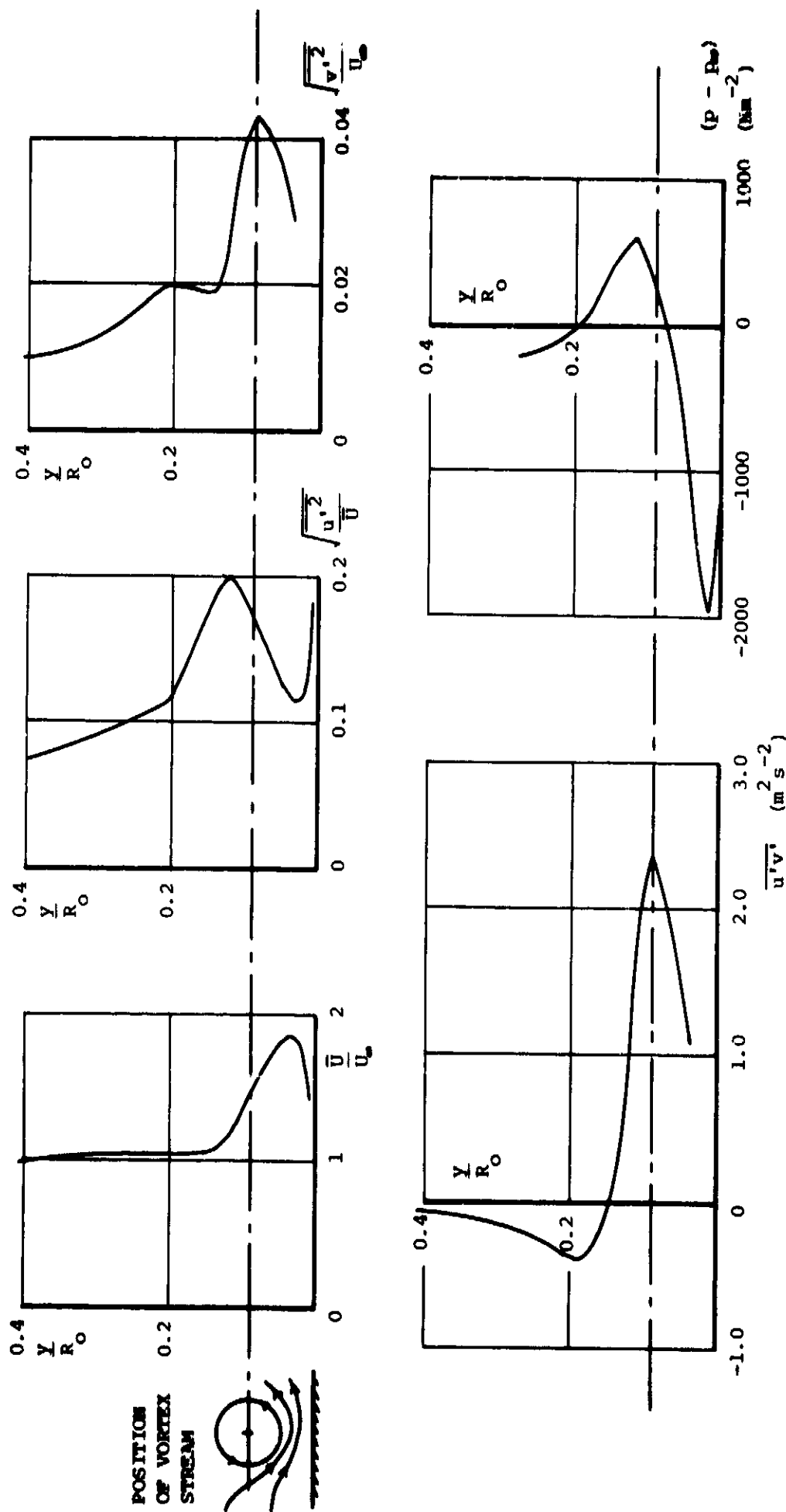


FIGURE 149: SPATIAL CORRELATION OF THE EXPERIMENTAL RESULTS WITH THE PROPOSED VORTEX STREAM
 $C_p = 0.0284$, $\alpha_G = 0^\circ, 55^\circ$ FROM SLOT

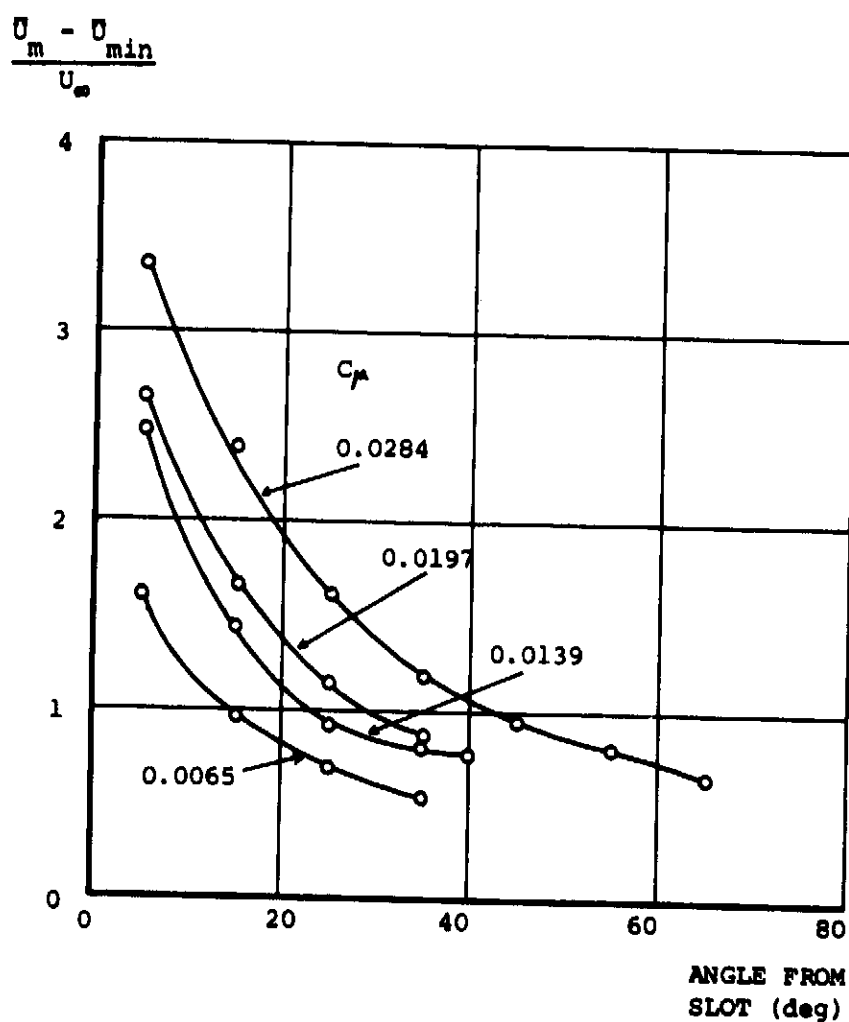


FIGURE 150: DECAY OF THE VELOCITY DIFFERENCE ACROSS THE FREE SHEAR LAYER WITH ANGLE FROM THE SLOT

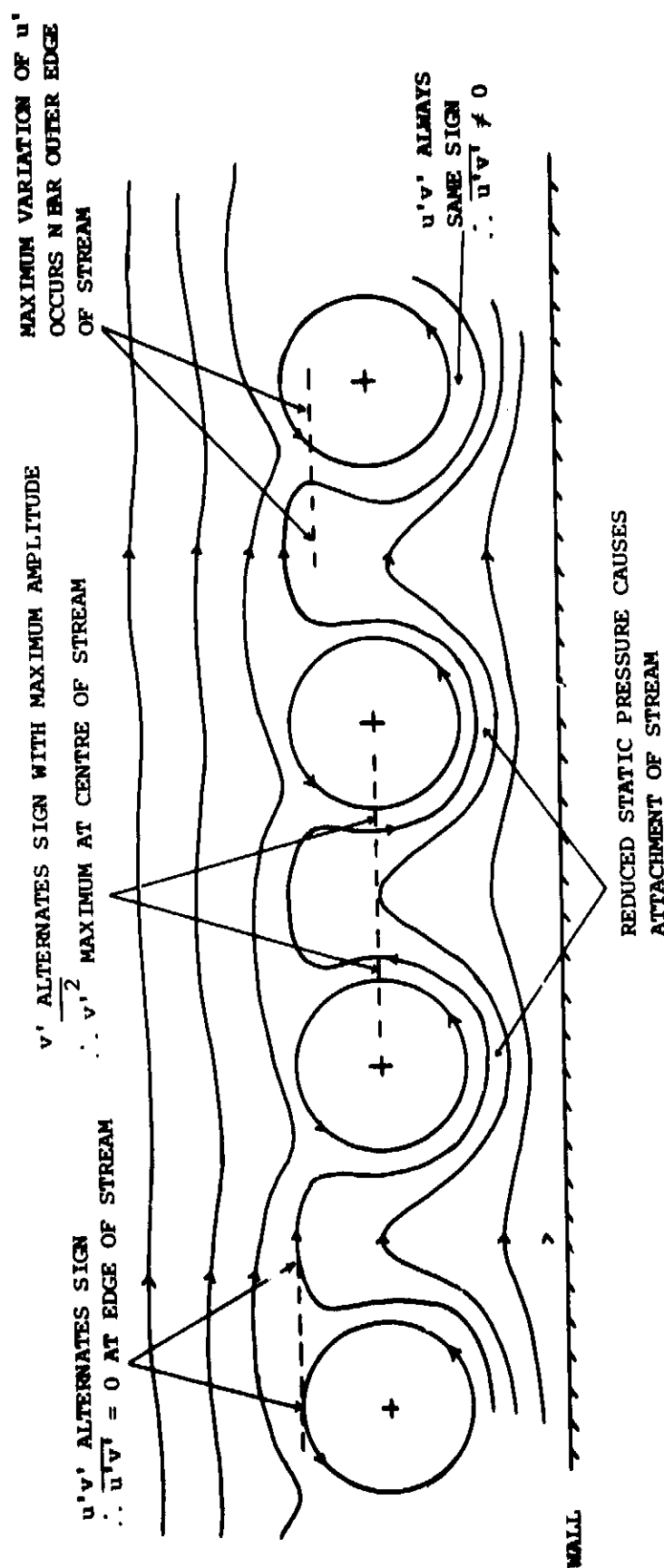


FIGURE 151: INTERPRETATION OF THE MEASURED TURBULENCE QUANTITIES WITH RESPECT TO THE PROPOSED VORTEX STREAM

WALL SHEAR STRESS

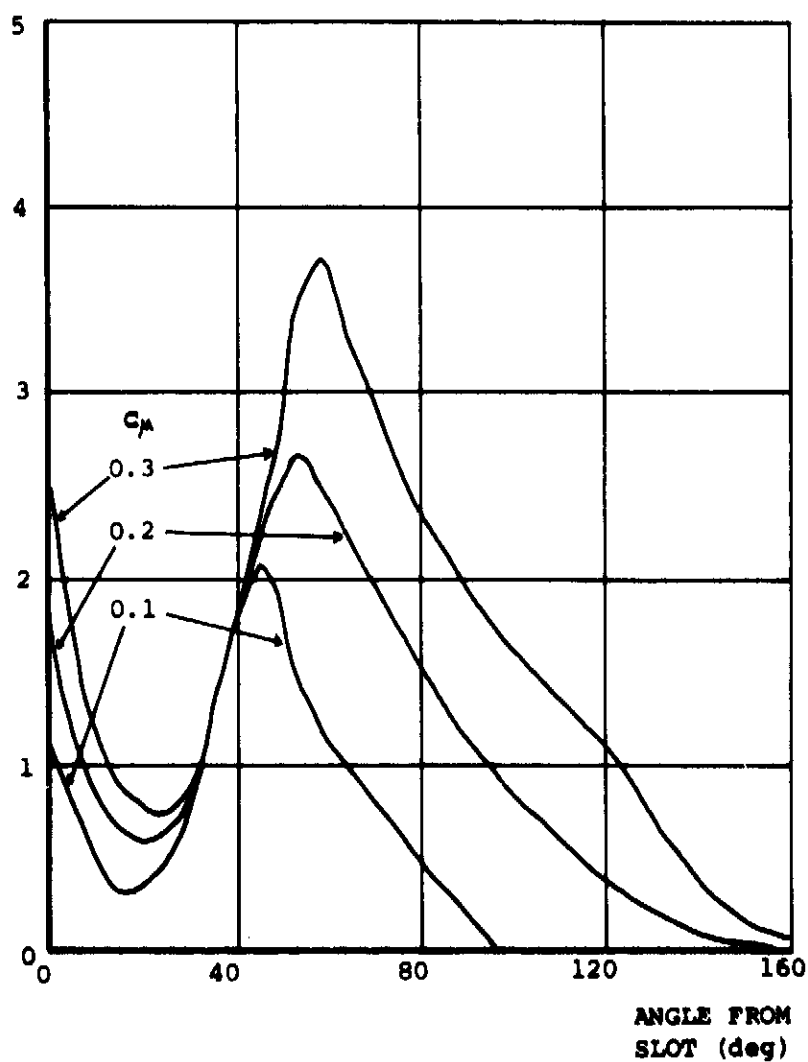
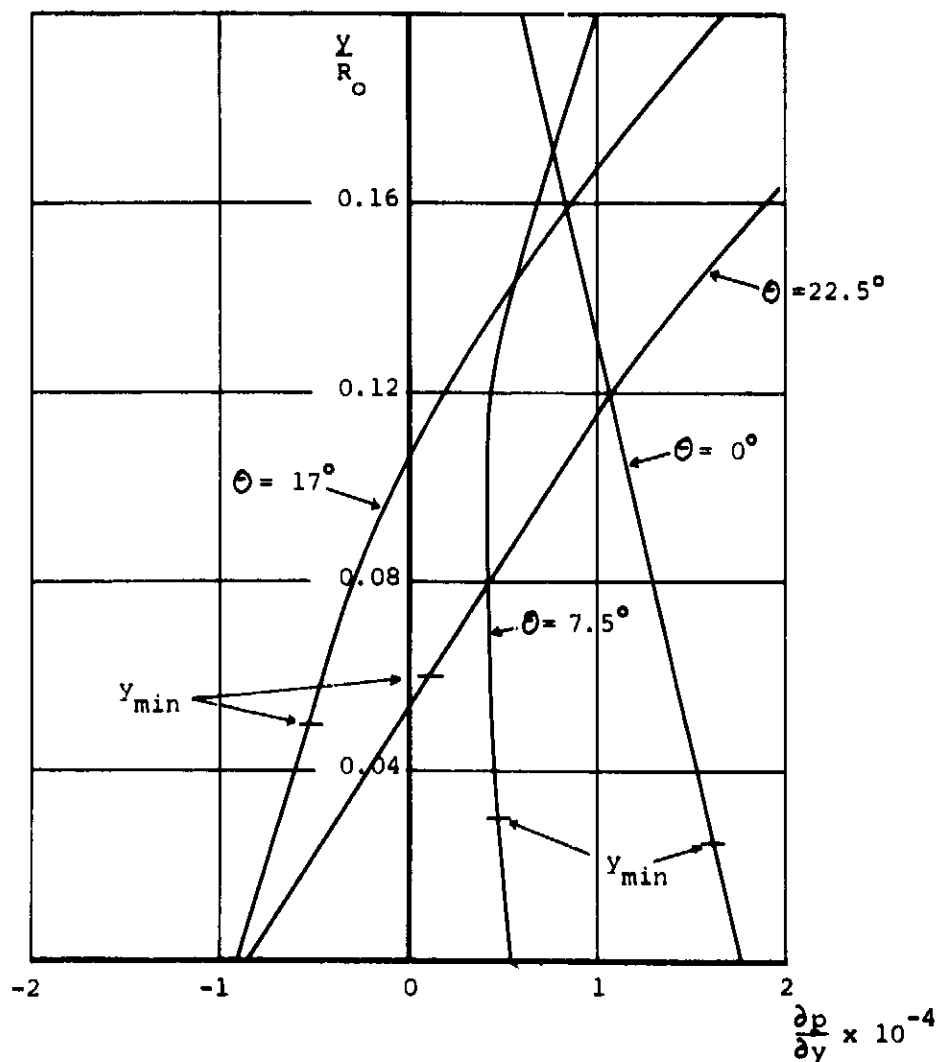
 $q_w = 27.5 \text{ psf}$ $\tau_w \text{ (psf)}$ $V_\infty = 46 \text{ ms}^{-1}$ 

FIGURE 152: WALL SHEAR STRESS UNDER A HIGHLY CURVED WALL JET
MEASURED BY A SURFACE MOUNTED HOT FILM SENSOR
FROM ENGLAR²⁸



THESE RESULTS ARE TAKEN DIRECTLY FROM A COMPUTER OUTPUT FROM CIRCON⁵⁸. THE RUN WAS BASED UPON THE PRESENT AEROFOIL WITH $C_{\mu} = 0.0284$.

THE UNITS FOR $\frac{\partial p}{\partial y}$ ARE UNCLEAR AND ARE ASSUMED TO BE lb ft^{-3} .

FIGURE 153: A SAMPLE OF THE VARIATION OF RADIAL PRESSURE GRADIENT IN THE TRAILING EDGE WALL JET FROM THE CALCULATION PROGRAM CIRCON⁵⁸

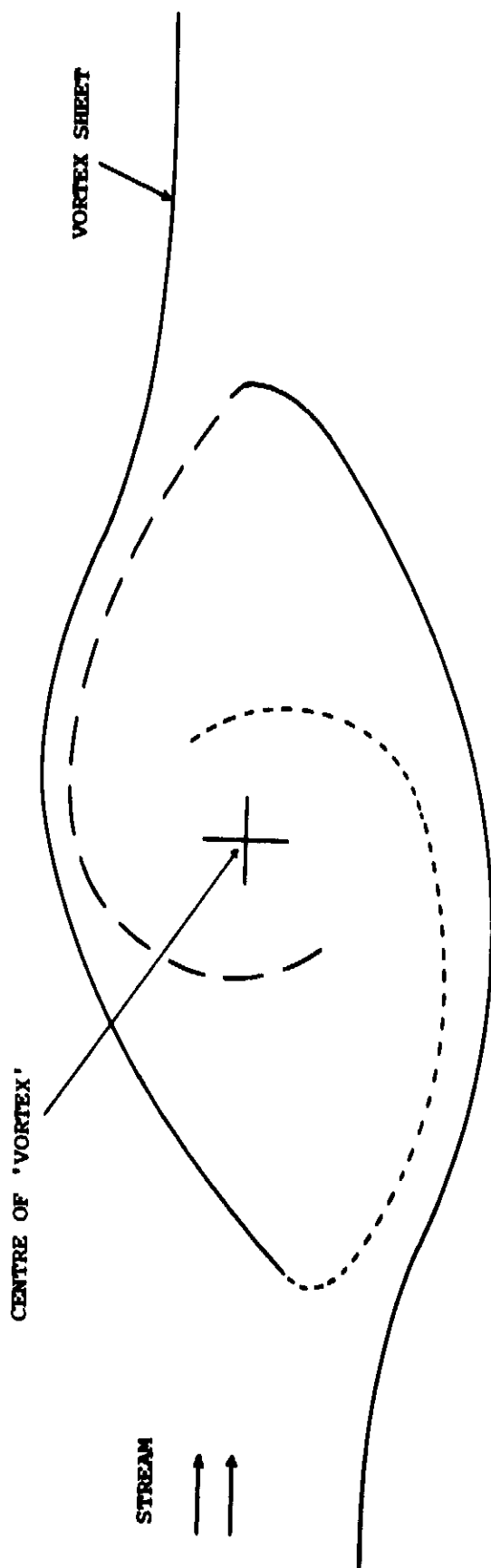


FIGURE 154: THE ROLL-UP OF A UNIFORM VORTEX SHEET TO PRODUCE THE 'CATS-EYE' SHAPE

VORTICES ARE ASSUMED TO BE INFINITELY LONG IN THE Z DIRECTION

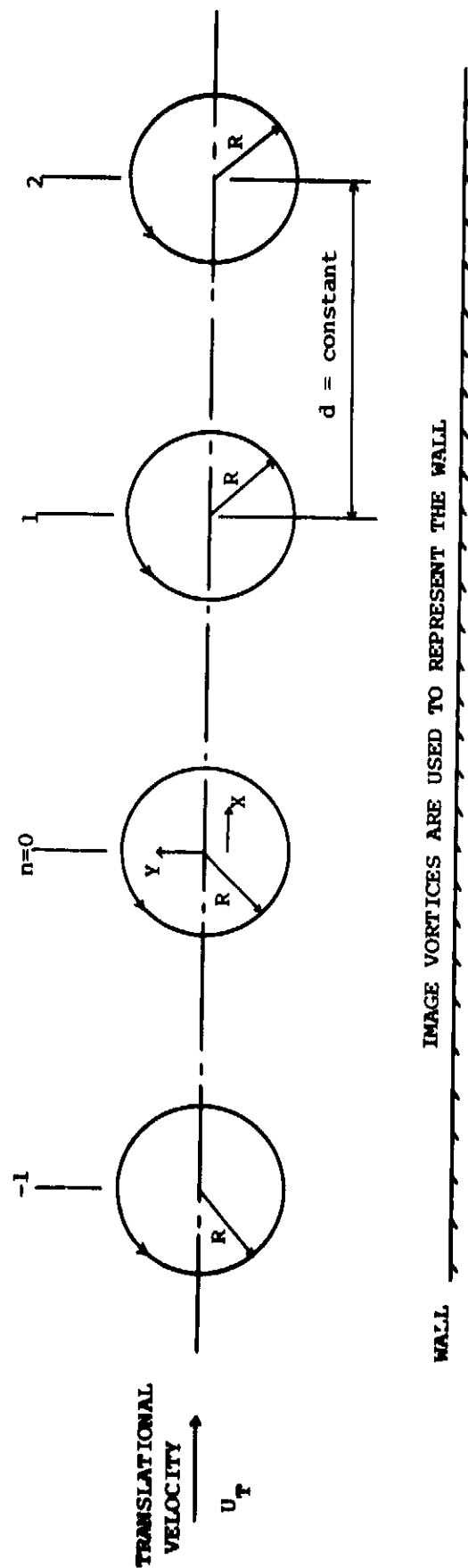


IMAGE VORTICES ARE USED TO REPRESENT THE WALL

MODEL ASSUMES CONSTANT VORTEX STRENGTH, κ

FIGURE 155: SIMPLIFIED VORTEX ARRAY TO DETERMINE THE TRUE VORTEX STRENGTH FROM A TIME AVERAGED VELOCITY PROFILE

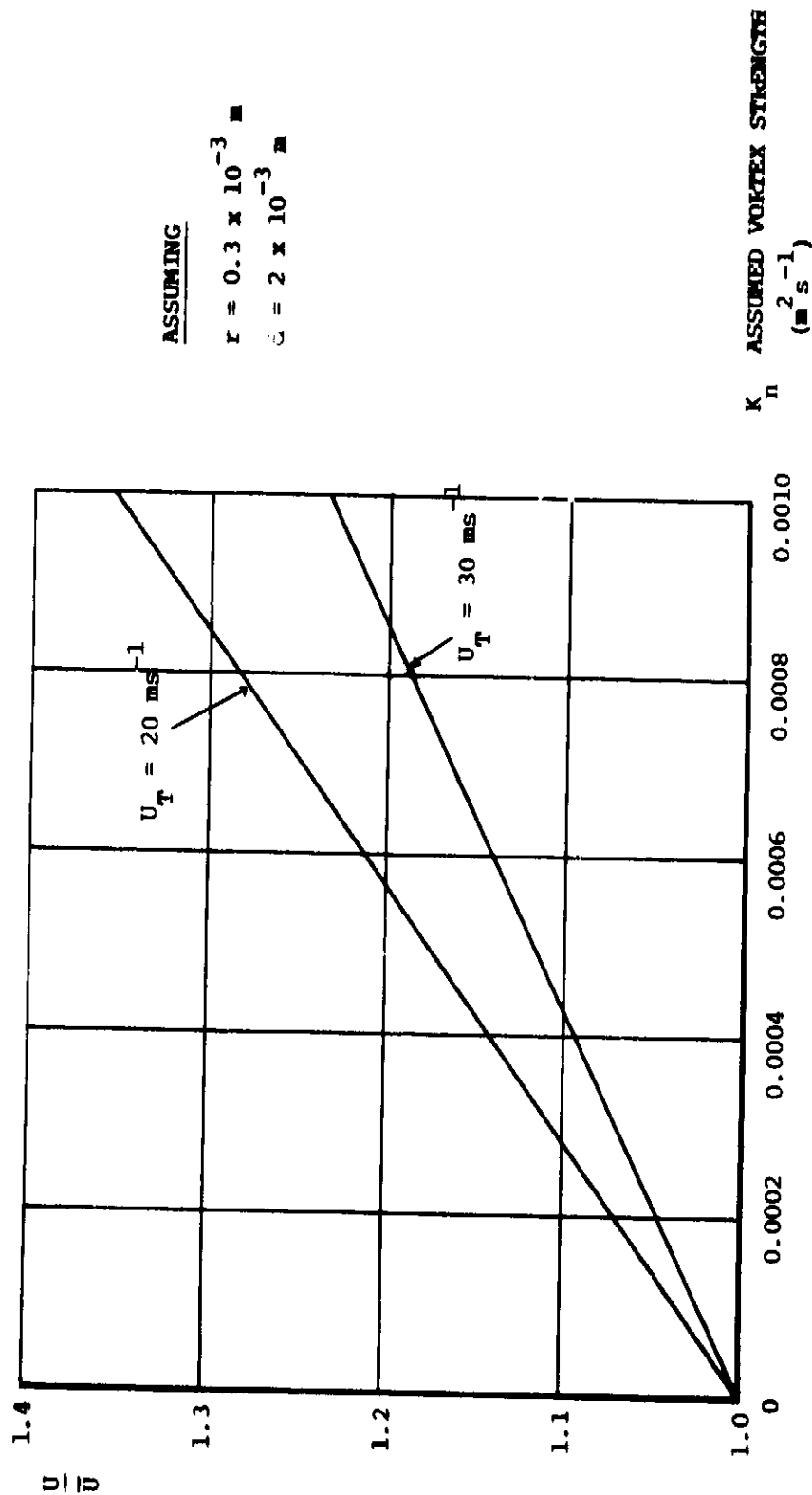


FIGURE 156: AN EXAMPLE OF THE VARIATION OF INSTANTANEOUS TO TIME AVERAGED VELOCITY AT THE EDGE OF THE PROPOSED VORTEX STREAM AS A FUNCTION OF VORTEX STRENGTH, STREAMING SPEED AND GEOMETRY

FIG 157

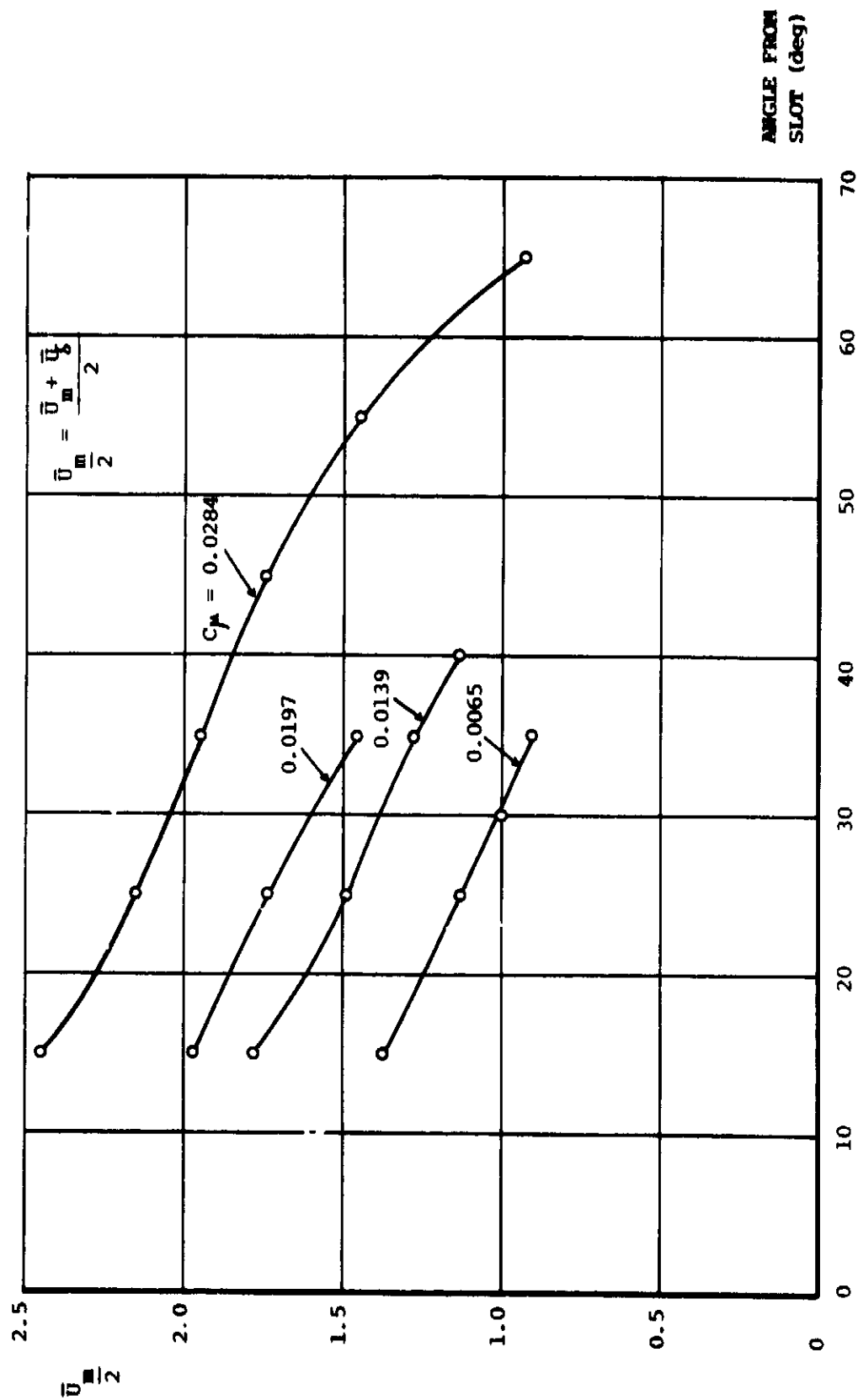


FIGURE 157: VARIATION OF THE PROPOSED VORTEX STREAMING SPEED WITH ANGLE FROM THE SLOT

FIG 158

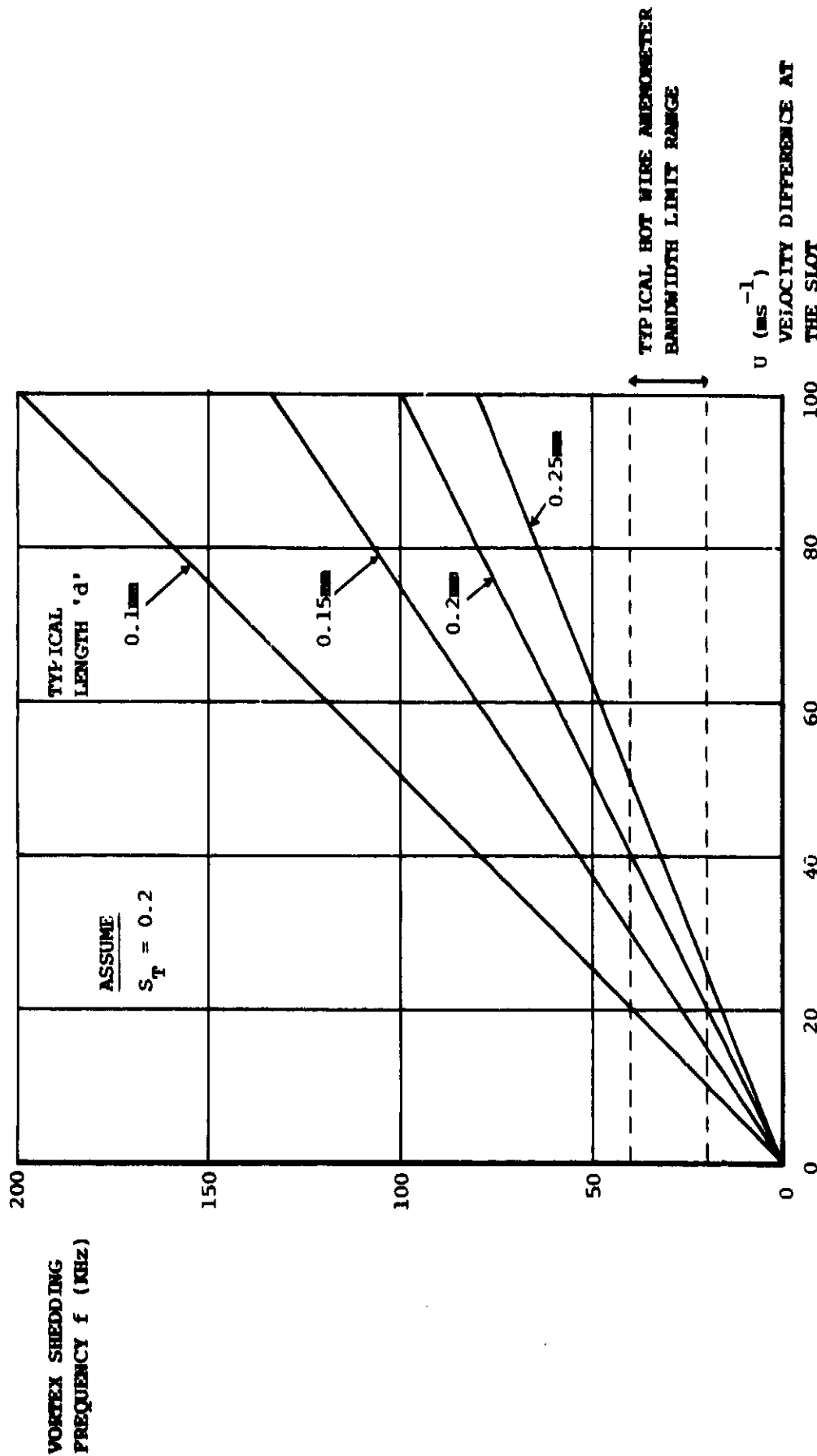


FIGURE 158: THE PROPOSED VORTEX SHEDDING FREQUENCY AS A FUNCTION OF THE VELOCITY DIFFERENCE AT THE SLOT FOR A VARIETY OF TYPICAL LENGTH SCALES

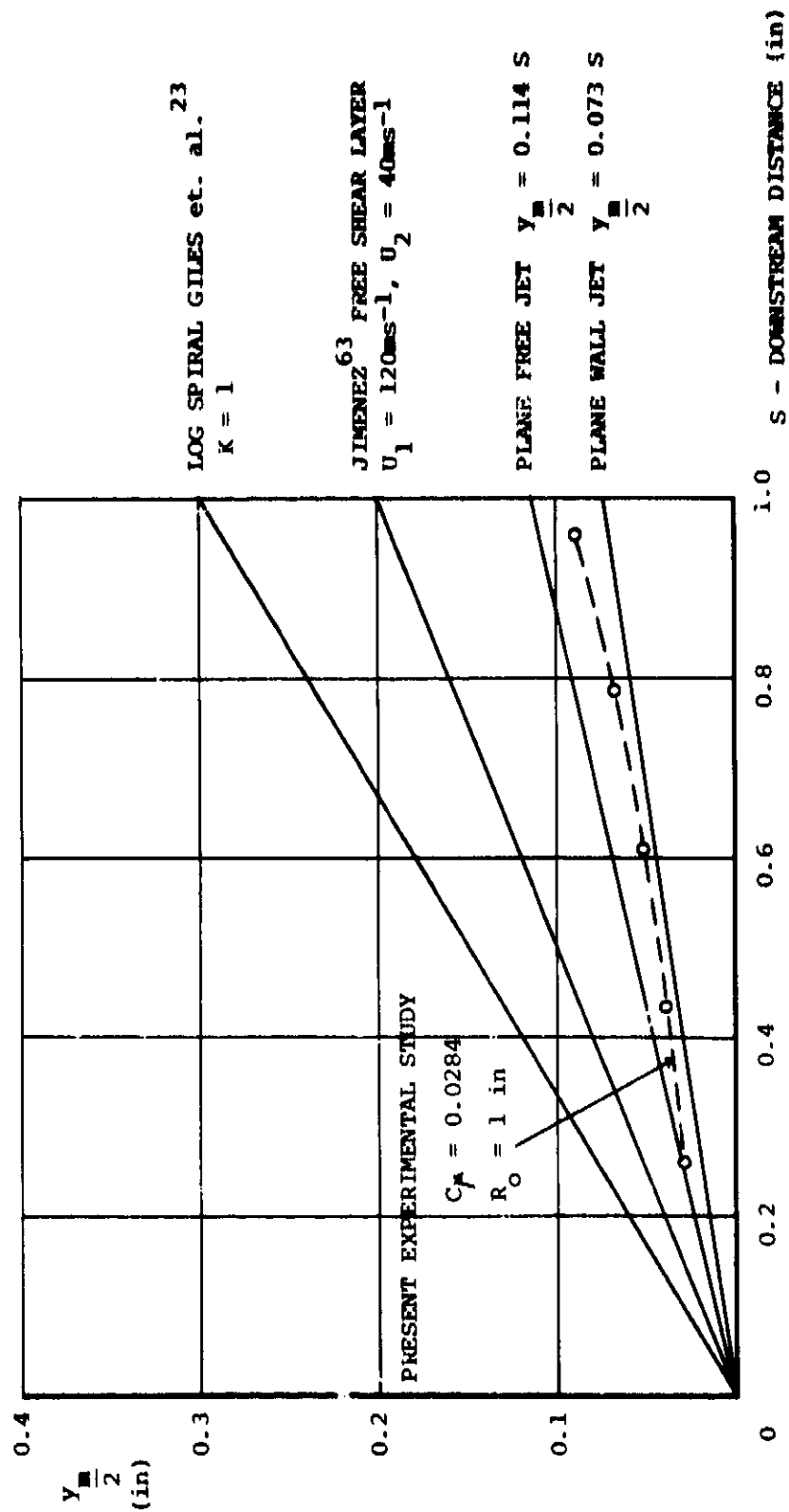


FIGURE 159: A COMPARISON OF HALF VELOCITY POINT GROWTH RATES FOR VARIOUS WALL JET CONFIGURATIONS

FIG 159